CZECH TECHNICAL UNIVERSITY IN PRAGUE

Faculty of Nuclear Sciences and Physical Engineering

DISSERTATION THESIS

Radiation hardness and performance of the hadron calorimeter designed for Projectile Spectator Detection in the framework of international collaboration CBM@FAIR

Prague 2021 Vasily Mikhaylov

Dedicated to my beloved girlfriend Daria

Bibliographic Entry

Author	Ing. Vasily Mikhaylov Czech Technical University in Prague Faculty of Nuclear Sciences and Physical Engineering Department of Physics
Title of dissertation	Radiation hardness and performance of the hadron calorimeter designed for Projectile Spectator Detection in the framework of international collaboration CBM@FAIR
Degree program	Application of Natural Sciences
Field of study	Nuclear Engineering
Supervisor	RNDr. Andrej Kugler, CSc. Czech Academy of Sciences Nuclear Physics Institute Department of Nuclear Spectroscopy
Supervisor specialist	Vasily Kushpil, CSc. Czech Academy of Sciences Nuclear Physics Institute Department of Nuclear Spectroscopy
Academic year	2020/2021
Number of pages	333
Keywords	Hadron calorimeter, PSD, CBM, FAIR, GSI radiation hardness, silicon photomultipliers, polystyrene scintillators, particle flow, reaction plane resolution

Bibliografický záznam

Autor	Ing. Vasily Mikhaylov České vysoké učení technické v Praze Fakulta jaderná a fyzikálně inženýrská Katedra fyziky
Název práce	Radiační odolnost a výkonnost hadronového kalorimetru navrženého pro Detekci Projektilových Spektatorů v rámci mezinárodního programu CBM@FAIR
Studijní program	Aplikace přírodních věd
Studijní obor	Jaderné inženýrství
Školitel	RNDr. Andrej Kugler, CSc. Akademie věd České republiky Ústav jaderné fyziky Oddělení jaderné spektroskopie
Školitel specialista	Vasily Kushpil, CSc. Akademie věd České republiky Ústav jaderné fyziky Oddělení jaderné spektroskopie
Akademický rok	2020/2021
Počet stran	333
Klíčová slova	Hadronový kalorimetr, PSD, CBM, FAIR, GSI radiační odolnost, křemíkové fotonásobiče, polystyrenové scintilátory, tok částic, rozlišení roviny srážky,

Acknowledgments

I express my gratitude to:

- my supervisors Andrej Kugler and Vasily Kushpil for the amazing opportunity to work at Nuclear Physics Institute as well as for the guidance during the conduction of my research and writing this thesis.
- Ondřej Svoboda for the invaluable guidance and shaping of my scientific evolution. He was always ready to selflessly help me and taught me how to deal with complex problems which may have many solutions.
- Vladimir Wagner for great theoretical teachings, huge patience for any kind of questions, and a tremendous help with organizational problems like obtaining a visa and acquiring financing that I faced during my work.
- A. Sadovsky, S. Seddiki, I. Selyuzhenkov, and P. Tlustý for their great teaching and invaluable discussion related to the nuclear collision simulations.
- E. Bratkovskaya, V. Friese, M. Golubeva, Y. Leifels and V. Vovchenko for the help in handling the heavy-ion collision generator codes.
- F. Guber, D. Finogeev, A. Ivashkin, A. Izvestnyy, N. Karpushkin, and S. Morozov from INR Moscow for the useful discussions on the SiPM radiation hardness and opportunity to test it at CERN. I am eternally thankful to S. Morozov who was the first to believe in my plan to investigate SiPMs at CERN and spent many days and nights with me during our shifts, teaching me how to operate the calorimeter and analyze the data.
- M. Majerle and M. Štefánik from the NPI Department of Accelerators for their kind help in the organization of neutron irradiation experiments and excellent beam conditions.
- F. Křížek and A. Isakov for the help in the organization of proton irradiation experiments.
- P. Chudoba and M. Fikrle for a possibility to use the HPGe spectrometer and help with activation foil analysis.
- all colleagues from the NPI Department of Nuclear Spectroscopy, CBM and NA61 collaborations, and my friends Dzmitry Makatun, Oleg Sviridov and Pavel Tichý who helped me in the research and proofread this thesis.

Finally, I would have never succeeded in this research without deep love and understanding from my mother Valentina Mikhaylova, and my girlfriend Daria Abramova. Daria selflessly supported me on my journey and helped me with the thesis preparation, embedding of the vector graphics, and grammar checking of this work. Without her, this work would be truly impossible.

This work was financially supported by Czech grant MEYS - LM2015049 and European grant OP VVV - CZ.02.1.01/0.0/0.0/16_013/0001677. Funding for the irradiation experiments was provided by CANAM infrastructure project. Additional financial help in form of granted silicon photomultipliers was provided by F. Guber, V. Ladygin, and Z. Sadygov.

Author's declaration

I declare that I elaborated the submitted dissertation thesis individually and that I stated all the used information sources in accordance with the Guidelines for the ethical preparation of university theses. The dissertation thesis was elaborated in the internal and combined form of postgraduate study at the Department of Nuclear Spectroscopy at the Faculty of Nuclear Sciences and Physical Engineering of the Czech Technical University in Prague and has not been submitted to acquire another qualification at this or any other university. The dissertation thesis was created thanks to the collaboration between the Nuclear Physics Institute of the Czech Academy of Sciences and the Compressed Baryonic Matter (CBM) experiment at the Facility for Antiproton and Ion Research (FAIR) based in GSI Darmstadt, Germany.

In Prague

Ing. Vasily Mikhaylov
(author of the thesis)

Abstract

The Compressed Baryonic Matter (CBM) experiment at the Facility for Antiproton and Ion Research (FAIR) will investigate the phase diagram of strongly interacting matter at neutron star core densities under laboratory conditions. It is a fixed target heavy-ion collision experiment operating in the medium energy range, i.e. 2 – 11 AGeV for gold ions. Projectile Spectator Detector (PSD) reconstructs the collision centrality and reaction plane orientation from the energy distribution of non-interacting nucleons and fragments emitted at very low polar angles in the forward direction. It is a compensating lead/scintillator hadron calorimeter with a light readout via wavelength shifting (WLS) fibers coupled to Silicon Photomultipliers (SiPM). Since it will operate at an extremely high collision rate up to 1 MHz, the expected high radiation load becomes one of the challenges in the design of the detector.

This thesis focuses on the evaluation of the PSD radiation hardness. Active detector components, including polystyrene scintillators, WLS-fibers, and SiPMs, are the most susceptible to radiation damage. The first part of the presented work is devoted to an extensive review of a wide scope of relevant irradiation studies. It includes the interaction of radiation with detectors, the details of detector operation, and radiation-induced effects. As the outcome of this review, anticipated radiation tolerance limits and recommendations for its improvement are provided.

The following part presents PSD design upgrades that helped to reduce the radiation load by a factor of 10. In the final design, dose up to 1 kGy for scintillators and 1 MeV equivalent neutron fluence up to 2×10^{11} n_{eq}/cm^2 for SiPMs are expected after a year of operation. Based on the reviewed data and results of the proton irradiation for scintillators at cyclotron of Nuclear Physics Institute of the CAS, only minor light yield degradation is expected after ten years of operation.

In the next parts, a detailed investigation of the radiation hardness for multiple SiPMs produced by Hamamatsu, Ketek, Sensl, and Zecotek is presented. This includes neutron irradiations at NPI cyclotron, development of the measurement setup and software, laboratory tests, tests at the calorimeter module at CERN, and data analysis. Significant SiPM degradation after irradiation was observed which is in agreement with data reported by other studies. Discrepancies with other studies are addressed. Presented experiments produced several unique observations. The first is the improvement of radiation hardness with the reduction of SiPM pixel size. The second unique observation is the evaluation of the dependence of the calorimeter energy resolution on fluence achieved by SiPMs. Tests at CERN proved that Hamamatsu SiPMs with small 10×10 μm^2 pixels are sufficiently hard to withstand the radiation level at CBM for at least a year. at least a year in the zone with the highest radiation load. After that, they can be exchanged, if necessary. The experiments concluded in detailed recommendations on how to achieve improvement of the SiPM radiation hardness and mitigate calorimeter performance degradation.

Finally, in the last part of this thesis the results of simulations of Au+Au collisions with UrQMD, HSD, DCM-QGSM, and LA-QGSM at the CBM energy range are reported. It was demonstrated that the selection of a generator does not significantly affect the reaction plane

resolution. Based on the simulation results, DCM-QGSM was selected for further PSD performance studies. This generator showed, although marginally, better resolution, which can be explained by the presence of fragments and the strongest directed particle flow.

Abstrakt

Cílem experimentu Compressed Baryonic Matter (CBM), který je součástí zařízení Facility for Antiproton and Ion Research (FAIR), bude zkoumat fázový diagram silně interagující hmoty při hustotách neutronových hvězd v laboratorních podmínkách. Jedná se o experiment s pevným terčem určený pro přesnou rekonstrukci srážek těžkých iontů ve středním energetickém rozsahu, tj. 2 – 11 AGeV pro ionty zlata. Projectile Spectator Detector (PSD) je určen pro měření rozdělení energie neinteragujících nukleonů a fragmentů emitovaných do velmi malých polárních úhlů v dopředném směru, čímž umožňuje rekonstrukci událostí, včetně centrality srážky a stanovení reakční roviny. Jedná se o kompenzační olověný/scintilační hadronový kalorimetr se světelným odečtem využívajícím vlákna wavelength shifting fibers (WLS) spojená s křemíkovými fotonásobiči (SiPM). Vzhledem k tomu, že bude provozován při velmi vysokých četnostech srážek až do 1 MHz, očekává se velmi vysoká radiační zátěž.

Tato práce se zaměřuje na hodnocení radiační odolnosti PSD. Aktivní součásti detektorů, včetně polystyrenových scintilátorů, vláken WLS a SiPM, jsou nejvíce náchylné k radiačnímu poškození. Chybí dostatečně spolehlivý přehled limitů odolnosti. První část předkládané práce je tak věnována rozsáhlému přehledu všech dosud publikovaných studií v této oblasti. Přehled začíná interakci záření s detektory, pokračuje podrobnostmi o činnosti detektoru a účincích vyvolaných zářením, a následně shrnuje očekávané limity odolnosti vůči záření a doporučení pro jeho zlepšení. V následující části je uveden přehled konstrukčních vylepšení, která pomohla výrazně snížit radiační zátěž PSD. V konečném designu se po roce provozu očekává dávka ionizujícího záření až 1 kGy pro scintilátory, a ekvivalentní fluence 1 MeV neutronů až 2×10^{11} n_{eq}/cm^2 pro SiPM. Na základě přezkoumaných údajů a výsledků testů ozařovaní scintilátoru na Cyklotronu Ústavu jaderné fyziky v Řeži (ÚJF) svazkem protonů, je po deseti letech provozu PSD očekávána pouze mírná degradace světelného výtěžku

V dalších částech se pojednává o podrobném výzkumu radiační odolnosti pro řadu SiPM produkovaných společností Hamamatsu, Ketek, Sensl a Zecotek. Výzkum zahrnuje ozařování neutrony na Cyklotronu ÚJF, vývoj měřicí sestavy a softwaru, laboratorní testy, testy modulu kalorimetru v CERNu a analýzu dat. V souladu s řadou předchozích prací byla pozorována významná degradace SiPM po ozáření. Pozorované rozpory s jinými předchozími studiemi jsou podrobně diskutovány. Je zde uvedena řada unikátních výsledků, především zlepšení radiační odolnosti při zmenšení velikosti pixelů SiPM a závislost energetického rozlišení kalorimetru na fluenci, kterou SiPM obdrželi. Testy v CERNu prokázaly, že SiPM s malými 10×10 μm^2 pixely od společnosti Hamamatsu jsou dostatečně odolné a přežijí minimálně rok provozu v zóně s nejvyšší radiační zátěží. V případě potřeby je bude možné po uplynutí této doby vyměnit. Na základě zmíněných měření byla vypracována doporučení ke zlepšení radiační odolnosti SiPM a ke zmírnění degradace výkonu kalorimetru.

V poslední části jsou popsány simulace srážek zlata se zlatem pomocí modelů UrQMD, HSD, DCM-QGSM a LA-QGSM v energetickém rozsahu CBM. Projevily se pouze malé změny v rozlišení roviny srážky pro PSD při použití různých modelů. Pro další zkoumání výkonnosti PSD byl vybrán model DCM-QGSM, protože vykazoval nepatrně lepší rozlišení, pravděpodobně kvůli přítomnosti fragmentů a nejsilnějšímu směřovanému toku částic.

Glossary

AGS – Alternating Gradient Synchrotron at BNL
APD – Avalanche PhotoDiode
ATLAS – A Toroidal LHC ApparatuS experiment at CERN
BES – Beam Energy Scan program at STAR
BM@N – Baryonic Matter at Nuclotron experiment at NICA
BNL – Brookhaven National Laboratory
BUU – Boltzmann Uhling-Uhlenbeck dynamics collision model
CANAM – Center of Accelerators and Nuclear Analytical Methods
CBM – Compressed Baryonic Matter experiment
CBMRoot – Extension of CERN Root software for CBM experiment
CERN – European Organization for Nuclear Research
CV – Capacitance-Voltage dependence
DAQ – Data AcQuisition system
DCM-QGSM – Dubna intranuclear Cascade collion Model coupled with Quark-Gluon String Model
Dharma -= Software for (not-only) SiPM measurements which I developed
DLTS – Deep Level Transient Spectroscopy
E877, E895 – Heavy ion experiments at AGS
ECAL – Electromagnetic calorimeter
FAIR – International Facility for Antiproton and Ion Research
FLUKA – Particle through matter transport code
FOPI – Detector for the physics of nuclear reactions at GSI
G-APD – APD operating in Geiger region
GEANT4 – (GEometry ANd Tracking) particle transport platform
GPIB – General Purpose Interface Bus for data transfer
GSI – Helmholtz Centre for Heavy Ion Research in Darmstadt, Germany
HADES – High Acceptance DiElectron Spectrometer at GSI
HCAL – Hadron calorimeter
HEP – High energy physics
HPGe – High Purity Germanium spectroscopic detector
HSD – Hadron-String Dynamics collision model
iQMD – Isospin Quantum Molecular Dynamics collision model
INR – Institute for Nuclear Research of Russian Academy of Sciences in Moscow, Russia
IV – Current-Voltage dependence
JLC – Electron-Positron Linear Collider Project
KaoS – Kaon spectrometer at GSI
KERMA – Kinetic energy released per unit mass
LA-QGSM – Los Alamos Quark-Gluon String collision Model
LET – Linear energy transfer

LHC – Large Hadron Collider at CERN
LHCb - Large Hadron Collider beauty experiment at CERN
MCNPX – Monte Carlo N-Particle eXtended transport code
MIP – Minimum Ionizing Particle
MPD – Multi Purpose Detector at NICA
NA61/SHINE – Heavy ion collision experiment at North Area at CERN
NCE – Nuclear Counter Effect
NICA – Nuclotron-based Ion Collider fAcility in Dubna
NIEL – Non-Ionizing Energy Loss radiation damage model
NPI – Nuclear Physics Institute of the Czech Academy of Sciences in Řež, Czech Republic
PET – Proton emission tomography
PHSD – Parton-Hadron-String Dynamics collision model
PKA – Primary Knock-On Atom
PMT – PhotoMultiplier Tube
POPOP – 1,4-di-(5-phenyl-2-oxazolyl)-benzene, $C_{24}H_{16}N_2O_2$
PS – Polystyrene, $(C_8H_8)_n$; or Proton Synchrotron at CERN
PSD – Projectile Spectator Detector
PTP – Paraterphenyl, $C_{18}H_{14}$
PVT – Polyvinyl toluene, $(C_9H_10)_n$
QCD – Quantum ChromoDynamics
QGP – Quark-Gluon Plasma
QMD – Quantum Molecular Dynamics collision model
RD50 collaboration at CERN – studies the radiation hardness of semiconductor devices
RHIC – Relativistic Heavy Ion Collider at BNL
SEE – Single Event Effect
SiPM – Silicon Photomultiplier. Also called MAPD, MPPC, SPD, PPD, etc.
SIS18, SIS100, SIS300 – Heavy ion synchrotrons at GSI
SPAD – Single Photon Avalanche Diode
SPICE – Simulation Program with Integrated Circuit Emphasis
SPS – Super Proton Synchrotron at CERN
SRIM – Stopping and Range of Ions in Matter software packages
STAR – Solenoidal Tracker At RHIC
STS – Silicon Tracking System (i.e. of CBM)
TCAD – Technology Computer-Aided Design
TDR - Technical Design Report
TID – Total ionizing absorbed dose
TOF – Time Of Flight detector (i.e. of CBM)
UrQMD – Ultrarelativistic Quantum Molecular Dynamics
WA97 – Lead-lead collision experiment at CERN
WLS-fiber – Wave-Length Shifting optical fiber
ZEUS – was an uranium/scintillator calorimeter at HERA (Hadron Elektron Ring Anlage) accelerator at DESY, Hamburg

List of parameters

b – Impact parameter of collision
B – Magnitude of magnetic field

μ_B – Net baryon density
E_{beam} – Ion beam energy
p_{beam} – Ion beam momentum
$R_E = \sigma_E/E$ – Relative energy resolution (i.e. of a calorimeter)
Ψ_{EP} – Event plane angle (experimentally determined Ψ_{RP})
Ψ_{RP} – Reaction plane angle
$Q - vector$ – Flow vector determining the reaction plane
R_{n} – Reaction plane resolution correction factor of n-order
R_A – Nuclear radius
v_n – Collective flow coefficient of n-order
p_T – Particle transverse momentum
y – Particle rapidity
y_{norm} – Particle rapidity normalized to center of mass system
ϕ – Azimuthal angle of particle (in XY plane)
θ – Polar angle of particle (in YZ plane)

C_{pix} – Pixel capacitance
CCE – Charge Collection Efficiency of sensor
DCR – Dark Current Rate
E_b – Beam energy
ENC – Equivalent Noise Charge
ENF – Excess noise factor
η – Pixel occupancy
G – Gain (amplification factor)
I_{rev} – Reverse (leakage) current of sensor
I_{dark} – Reverse current of light-sensitive sensor in the darkness
I_{forw} – Forward (dark) current of sensor
N_{eff} – Effective impurity concentration in sensor material
N_{pix} – Number of pixels
P_{av} – Avalanche triggering probability
PDE – Photon Detection Efficiency
R_q – Quenching resistance
$SE\ [\%] = \frac{Signal_{after\ irradiation}}{Signal_{before\ irradiation}}$ – Signal efficiency of sensor after irradiation
$SNR = \frac{Signal\ integral}{\sigma_{Noise\ integral}}$ – signal-to-noise ratio of sensor
τ_r – Recovery time of a SiPM pixel
V_{bd} – Breakdown voltage for sensor operating in Geiger regime
$V_{ov} = V - V_{bd}$ – Overvoltage for sensor operating in Geiger regime
V_{FD} – Full depletion voltage of sensor

Contents

Chapter 1

Introduction

Nowadays, heavy-ion collisions are of huge interest in the physics community. Their study can reveal answers to the very basic theoretical questions about our universe's existence. Conditions similar to the formation of the universe in the very beginning of the "Big Bang" can be accessed in the heavy ion collision with very high energy when a nuclear medium with high temperature T is created. The requirement for this research is the highest now accessible energies $\sqrt{s_{\mathrm{NN}}}$ in nucleon-nucleon center of mass in the range from hundreds of a GeV up to a few TeV [1]. This is presently studied with help of very high-energy colliders such as CERN Large Hadron Collider (LHC) and BNL Relativistic Heavy Ion Collider (RHIC).

Another interesting physics case corresponds to the high net baryon density μ_B i.e., the density of protons and neutrons (baryons) minus the density of antibaryons, and can reveal the theory behind the existence of very dense matter which can be found in the core of a neutron star. This requires $\sqrt{s_{\mathrm{NN}}}$ in the range from a few GeV up to several tens of a GeV [2].

It is presently studied with the RHIC Beam Energy Scan (BES) program in STAR, but unfortunately, at the required low energies, it has very limited luminosity and hence limited statistics [3]. The NA61 experiment at CERN-SPS has access to this region as well, but also has a limited amount of data due to the slow response of the Time-Projection Chamber [4]. A solution to the requested increase of statistics can be found at the future very high luminosity high energy nuclear physics facilities such as International Facility for Antiproton and Ion Research (FAIR) and Nuclotron-based Ion Collider fAcility (NICA).

Figure 1.1 shows the two-dimensional QCD phase diagram for temperature T and net baryon density μ_B (μ_B is divided by $\mu_{B,0}$ – the normal nuclear matter density; referred as $\mu_B = 1$ on the axis). The different physics cases that can be accessed by heavy-ion collisions at different energies, conditions similar to the formation of the early universe, and the compact neutron stars are indicated.

For the experimental study of heavy-ion collisions, one needs a dedicated detector setup providing the measurement of particles produced in the collision. Probably the most difficult part is to build a robust system of particle tracking and identification. However, it is important as well to have the basis for this – detectors describing the general properties of the event itself. The most common properties that can be accessed on the event-by-event basis are the centrality i.e. the value of the impact parameter and the reaction plane. They can be accessed with the internal tracking system or with help of the very forward hadron calorimeter situated downstream of the target in case of the fix-target experiment. It is shown in section 4.5 that these two methods are complementary in FAIR Compressed Baryonic Matter experiment (CBM) and the data obtained by both detectors allows to get very good precision of event characterization for the whole covered energy range of the experiment.

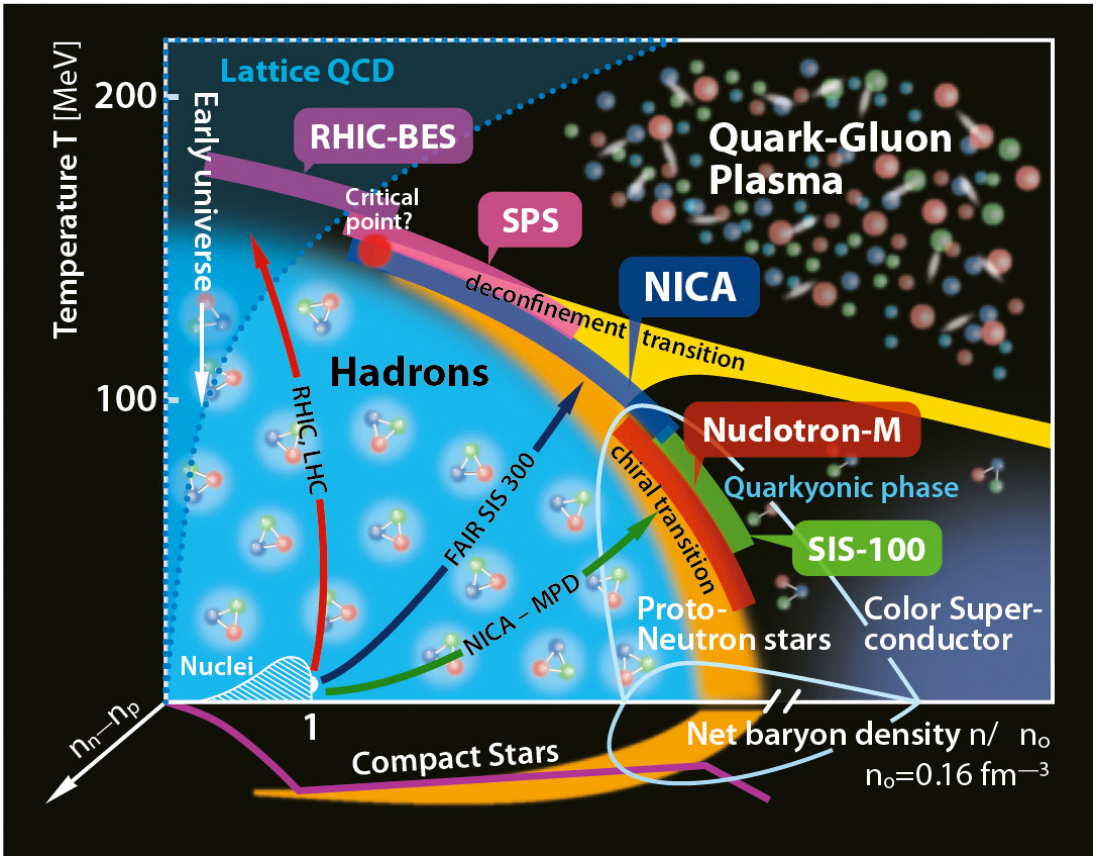

Figure 1.1: A sketch of the QCD Phase Diagram. Drawing from [5].

The idea of the very forward calorimeter which provides high and uniform energy resolution was already successfully applied as the Projectile Spectator Detector at the NA61 experiment at CERN [4]. The very similar calorimeters are being designed and built for the future high energy nuclear physics experiments, such as CBM at the future FAIR facility [2] and Baryonic Matter at Nuclotron (BM@N) [6] and Multi-Purpose Detector (MPD) at the future NICA facility [7]. Those calorimeters allow the detection of the non-interacting nucleons and fragments i.e. spectators emitted at very low polar angles in the forward direction in heavy-ion collisions. They will be used to determine the collision centrality and the orientation of an event plane by measurement of the spatial position and energy of these nucleons and fragments.

The expected performance of the calorimeters that are currently being designed and built has to be analyzed to assure that they fit the experiment's requirements. This PhD study is focused on the discussion of the several performance aspects of the Projectile Spectator Detector (PSD) being built for the CBM experiment.

Main goals of the PhD study

- investigate the radiation hardness of CBM PSD detector including passive (scintillators) and active (light readout) components, namely
  - assess the possible deterioration of the light yield for scintillators used in PSD;

  - investigate the suitability of various Silicon Photomultipliers (SiPMs) for the PSD light readout;
  - conduct the irradiation tests of the investigated SiPMs under conditions corresponding to the anticipated CBM radiation environment;
  - test the performance of irradiated SiPMs to determine the most radiation-hard model and assess its limitations for application at the CBM PSD.

- compare generators based on different models of heavy ion collisions in the CBM beam energy range in terms of
  - produced collective particle flow to determine which one agrees best with the available experimental data;
  - simulation of the reaction plane reconstruction by the CBM PSD detector to assess the application of different collision generators;

Workflow of the thesis

Chapters 2 – 4 of the thesis are dedicated to the discussion of the general theory, CBM experiment, PSD detector, and the review of existing data on the calorimeter radiation hardness. Chapters 5 – 9 focus on the simulations, experiments, and analysis that I conducted during the PhD study. There are few exceptions in those chapters where I describe work that was done by my colleagues and I explicitly note that further.

Chapter 2 discusses the relation between the particle-matter interaction and radiation damage in various materials. The discussion continues with the basics of particle showers generation and calorimeters design.

Chapter 3 presents my substantial effort to review and systematize all the studies on the radiation hardness of plastic scintillators and silicon photomultipliers conducted during the last decades (> 150 publications) to produce, I believe, the most comprehensive review on the subject up to date. The chapter also describes the principles of sensor operation, mechanisms of the radiation damage production, and detector characterization techniques after irradiation. At the end of the respective sections, I summarize the takeaway information on the radiation hardness limits and approaches that can be utilized to improve it.

Chapter 4 overviews the general concept and physical goals of the CBM experiment, compares the existing NA61 PSD calorimeter with the proposed CBM PSD calorimeter, and highlights its construction, design, and performance challenges. Similar calorimeters that are being built for NICA are also mentioned.

Chapter 5 discusses the problem of the radiation hardness of the PSD based on the predicted radiation environment for the very high luminosity CBM experiment. It also reviews the PSD design changes that were recently implemented by other PSD team members and were not yet fully described anywhere else. At the end, results of my measurements of irradiated polystyrene scintillators in the laboratory are presented.

Chapter 6 describes the necessary details on the NPI cyclotron facility and neutron experiments that I conducted there. Activation foil analysis that I carried out to determine the neutron fluence is discussed. At the end of the chapter, proton irradiation experiments where I participated and my calculation of the proton ionizing doses are described.

Chapter 7 discusses our laboratory measurement setup and software that I developed for the SiPM tests. SiPM measurements that I conducted in the laboratory before and after irradiation

are presented. I provide a comprehensive discussion on changes in various macroscopic parameters of tested SiPMs and their possible influence on the detector operation. I determine the SiPM that is suitable for the application at CBM PSD as a light readout sensor.

Chapter 8 discusses the performance of Silicon Photomultipliers that were chosen in the previous chapter at CERN. Specifics of tests that I conducted with help of INR PSD team at PS T9/T10 and SPS NA61 beamlines with proton beams are described. I present my analysis of the degradation of PSD module energy resolution after SiPMs' irradiation and conclusion about its applicability at CBM.

Chapter 9 discusses the results of heavy ion collisions simulations that I performed during the PhD research. I briefly describe the heavy ion collisions with an emphasis on the evaluation of collision centrality and reaction plane. Further, I present the performance analysis for various generators of heavy ion collisions currently available in the CBM energy regime. I compare the particle flow produced by these generators and discuss its relation to the PSD reaction plane resolution which I simulated with their input. Moreover, I present the results of the particle flow simulation for the HADES experiment that I voluntarily conducted upon request from the HADES group.

Chapter 10 draws overall conclusions on the results achieved during my PhD study and discusses the further steps and improvements that can be taken to expand research on this topic.

Chapter 2

Interaction of particles with detectors and radiation damage

Understanding the interaction of particles with matter is essential to construct the detector with desired functionality and reliability. Detector's radiation hardness is a widely studied topic for high energy physics experiments. Nowadays, it is gaining even higher impact due to the rapid increase in the beam intensities the accelerators can provide. It results on the one hand in the higher luminosity and therefore better statistics essential for the precise measurements of rare physics observables, and on the other hand in higher radiation emission and stricter requirements for the detector's radiation hardness.

In chapters 2 and 3, I aimed to create a roadmap that can be used to understand the radiation damage induced in complex detectors from the very first principles of particle interactions with matter. This chapter provides an overview of the basic mechanisms of particles-matter interaction with an emphasis on the radiation damage production in different materials irradiated by various particles. General aspects of the particle cascade (shower) evolution and its detection in the electromagnetic and hadronic calorimeters are discussed.

2.1 Interaction of particles with materials

Different devices have different susceptibility to radiation based on their structure and potential ways of particle interactions. Figure 2.1 shows the typical damage ranges for different materials in terms of both ionizing and non-ionizing energy losses. One can see that semiconductors that have the most complicated structure suffer the most while metals are obviously the most radiation hard. Polymers also show significant radiation effects due to complex structures and low bonding energies of several eV. Generally, incident particles can introduce damage to the material by:

- Interaction with atomic electrons. The atom can become excited and consequently emit photons during the deexcitation, or the ionization can occur in form of the release of free electron and hole pairs. In crystalline conductive materials such as metals and semiconductors, this typically produces only temporary effects because generated free carriers quickly drift towards terminals. In amorphous non-conductive materials produced charge may not dissolve and cause permanent changes in mechanical, optical, and electrical properties. Ionizing radiation can further induce chemical reactions altering the material structure by rearranging its chemical bonds and producing free radicals.

- Interaction with atom via non-ionizing energy loss. In crystalline materials atom can be displaced from its original position which produces permanent defects in the lattice and changes the material properties. On contrary, the concept of atom displacements does not necessarily apply to amorphous materials which do not have a regular structure [8].
- Nuclear reactions. An incident particle can cause the nuclear transmutation of the atom which alters the material structure in the most fundamental way. In conductive materials, this changes the intrinsic doping profile. In other materials production of hydrogen and helium can change the mechanical properties of the materials and cause swelling and embrittlement. Neutron activation or photodisintegration in presence of high-energy gamma radiation can force materials to become radioactive. Nevertheless, there is no straightforward way to include nuclear reactions which do not directly cause ionization or atomic dislocations into the overall damage prediction. Generally, these effects tend to be relatively low and are often neglected during the radiation damage studies, but in some cases, they may become considerable, see discussion in sections 2.3 and 3.4.1. The simplest and probably the best way to account for it is to choose the radiation source which produces the particle spectrum closest to the anticipated detector environment.

High energy particles may first lose their energy by radiative processes such as Bremsstrahlung, electron-positron pair production, Cherenkov, and Transition radiation. This results in the creation of new particles or even particle showers which in turn may interact with the detector material in one of the aforementioned ways, see section 2.4. Low energy particles can also interact with the lattice itself in form of collective excitations or phonons which do not result in radiation damage.

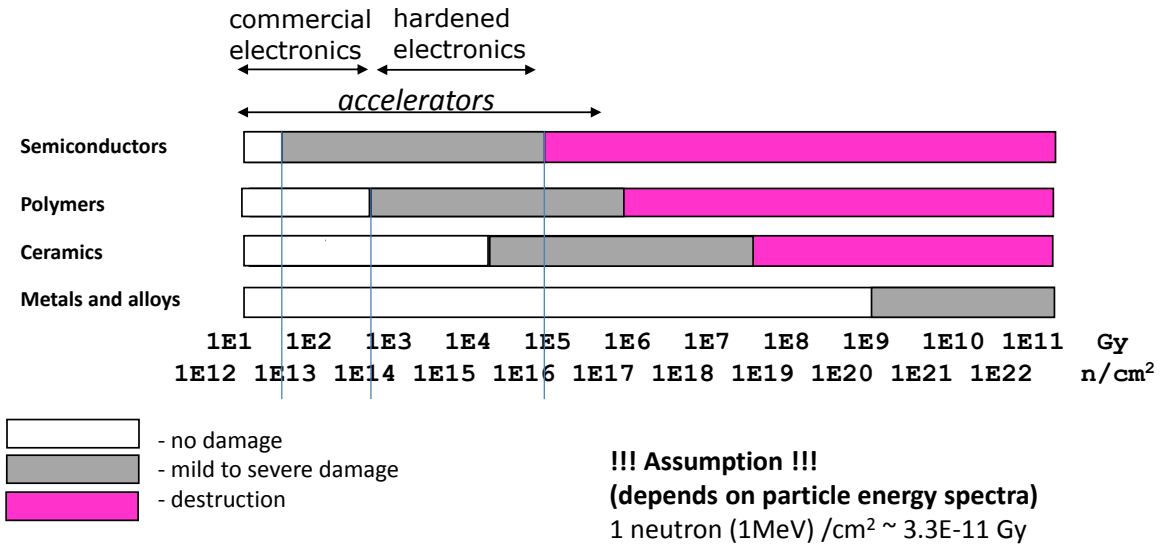

Figure 2.1: Rough estimation of tolerance levels for radiation damage in materials. Data compiled by [9].

The simplest way to quantify the radiation load is to use the total fluence of impinging particles, typically given in particles per cm^2 of the device area. However, the nature of the interaction of different particles with the device material as well as variation of particle's energy leads to a substantial variation in the produced damage. Two concepts presented in the following sections are used to unify the radiation load.

2.2 Ionizing energy loss and absorbed dose

Particles traversing the material undergo inelastic collisions with atomic electrons and nuclei and consequently lose their energy. The stopping power of the material determines the amount of energy transferred by a particle to the material per unit distance. Ionization can be produced in Coulomb collisions with atomic electrons or nuclei, however, for most particles and energies nuclear stopping power is lower by several orders of magnitude.

2.2.1 Ionizing energy loss by heavy charged particles

Electronic stopping power for heavy charged particles is described by the famous Bethe equation ([10])

$$\left\langle \frac{dE}{dx} \right\rangle = \left(\frac{1}{4\pi\varepsilon_0} \right)^2 \cdot \frac{4\pi z^2 e^4}{m_e c^2 \beta^2} \cdot \frac{N_A \cdot Z \cdot \rho}{A} \cdot \left[\ln \left(\frac{2 m_e c^2 \beta^2}{I \cdot (1-\beta^2)} \right) - \beta^2 - \frac{\delta(\beta\gamma)}{2} \right], \tag{2.1}$$

where multiplicands are divided by their physical origin, expect for the first one being a constant for expression in SI units. The second multiplicand represents the main dependence on particle's charge z and speed $\beta = v/c$. Third – main dependence on the material atomic number Z, atomic mass A and density ρ. Fourth – minor dependence on particle's and material's properties which rises at relativistic energies. I is the mean excitation energy of the material which is approximately equal to $(10 \pm 1)Z$ eV as proposed by Bloch, however nowadays more accurate tabulated values of I exist [11]. $\delta/2$ is Fermi's density correction which accounts for media polarization limiting the electric field extension of the incoming particle at higher energies. Other physical constants include vacuum permittivity ε_0, electron mass m_e and charge e, and Avogadro number N_A.

Figure 2.2 presents an example of the complex dependence of mass stopping power on momentum. Note that the Bethe equation is valid with an accuracy of a few % only for intermediate-Z materials in the region of intermediate energies corresponding to $0.1 < \beta\gamma < 1000$ [11]. In this region, the stopping power at first falls as $\sim 1/\beta^{1.5}$ and reaches a broad minimum around $\beta\gamma = 3.0 - 3.5$. In practice, most relativistic particles have mean energy loss rates close to the minimum and they are called minimum-ionizing particles or mip. Accelerator-produced or cosmic ray muons are especially useful because they do not indulge in the strong interaction.

For $\beta\gamma < 0.1$, e.g. for protons with energy lower than 10 MeV, more corrections have to be included in the Bethe equation because the projectile's velocity becomes comparable to that of the atomic electrons. In this case, electrons cannot be considered free anymore and atomic binding must be taken into account. Nuclear stopping power which accounts for collisions between the impinging particles and nuclei may become dominant for heavy ions impinging on heavy materials. The interval $0.01 < \beta\gamma < 0.05$ is described by the phenomenological fitting formulae developed by Andersen and Ziegler [11]. For particles slower than $0.01c$ (more or less the velocity of the outer atomic electrons), Lindhard described electronic stopping power to be proportional to β. At even lower energies, e.g., for protons below 100 eV, non-ionizing nuclear recoil energy loss dominates the total energy loss.

For $\beta\gamma > 1000$ radiative losses start to dominate increasing linearly with the particle energy and the corresponding energy limit is called critical energy E_c. Depending on material E_c scales from 1 – 100 MeV for low mass particles like photons and electrons up to hundreds GeV for heavier muons and even higher for protons. See section 2.4 for more information.

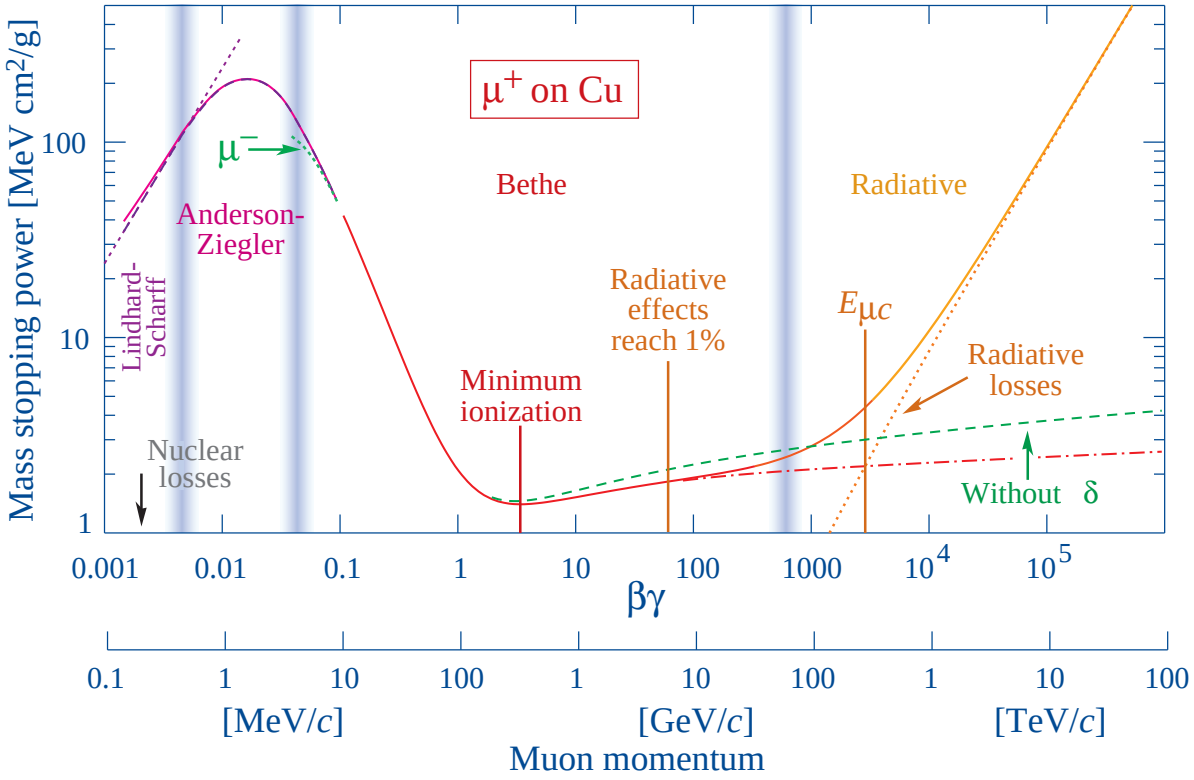

Figure 2.2: Mass stopping power for positive muons in copper as a function of $\beta\gamma = \beta/\sqrt{1-\beta^2} = p/Mc$. Taken from [11].

2.2.2 Ionizing energy loss by electrons and positrons

For both electrons and positrons, the Bethe formula takes a bit different forms due to their small mass making them easier deflected, and incident and target electrons being indistinguishable from each other after the collision, see [11] for details. Still as one can see in figure 2.3, the general tendencies of the energy loss described for heavier particles also hold for electrons: at lower energies, below few tens MeV, the ionization dominates, while at higher energies radiative losses dominate.

The mass stopping power is about the same for most solids and is typically expressed in MeV$cdot$cm^2/g. On contrary, the linear stopping power also called the linear energy transfer (LET) is material dependent. LET is typically expressed in MeV/cm and can be obtained by multiplication of mass stopping power by material density ρ.

2.2.3 Total ionizing absorbed dose (TID) and kerma

TID (or just dose in this thesis) is used to quantify and compare energy deposited in the matter by various ionizing radiation per unit mass. Its SI unit is the gray (Gy), which is defined as one Joule of energy absorbed per kilogram of matter. However, the older CGS unit rad = 0.01 Gy is still often used in the radiation studies, for instance, I provided the equivalent dose in Gy for results in rad that I reviewed in section 3.2. The fluence of charged particles can be easily converted to the absorbed dose by

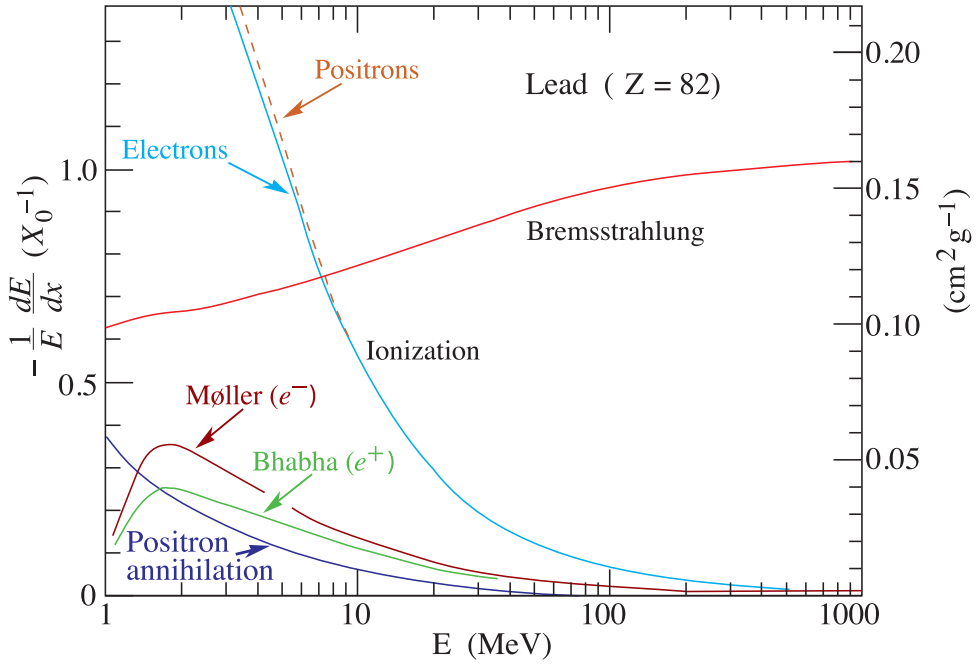

Figure 2.3: Dependence of fractional energy loss per radiation length in lead on the electron (positron) energy. Radiation length of the material X_0 is defined in subsection 2.4.1. Collision is considered as ionization when the energy loss per collision is below 0.255 MeV, and as Møller (Bhabha) scattering when it is above. Taken from [11].

$$D_{charged}[Gy] = 1.602 \cdot 10^{-10} \cdot S_m(E) \left[\frac{MeV \cdot cm^2}{g}\right] \cdot \Phi[cm^{-2}], \tag{2.2}$$

where $S_m(E)$ is the mass stopping power for the material, Φ is the fluence of impinging particles per cm^2 and E is the particle energy. In the case of thin structures when total energy loss in the sample is relatively small, one can go by the assumption that $S_m(E)$ is constant. Tables of mass stopping power of various materials can be found at Standard Reference Database on Stopping-Power & Range Tables for Electrons, Protons, and Helium Ions at National Institute of Standards and Technology (NIST) [12].

Particles with zero charge can produce ionization only indirectly as they do not indulge in Coulomb interaction. For them, one may calculate **kerma** K **– kinetic energy released per unit mass** as

$$K = dE_{tr}/dm = k_\Phi \cdot \Phi \tag{2.3}$$

where dE_{tr} is the sum of initial kinetic energies of all secondary charged particles that are produced in the sample by initial particle, dm is the sample mass, k_Φ is the kerma coefficient depending on the material, particle, and its energy, and Φ is the fluence of initial particles per cm^2.

Kerma factors are expressed in either keV·cm^2/g or MeV·mb, in the latter units they can be extracted from ENDF/B database [13]. I find Java-based Nuclear Data Information System JANIS at Nuclear Energy Agency (NEA) to be extremely helpful for the data extraction from ENDF/B and other databases [14].

2.2.4 Ionizing energy loss by photons

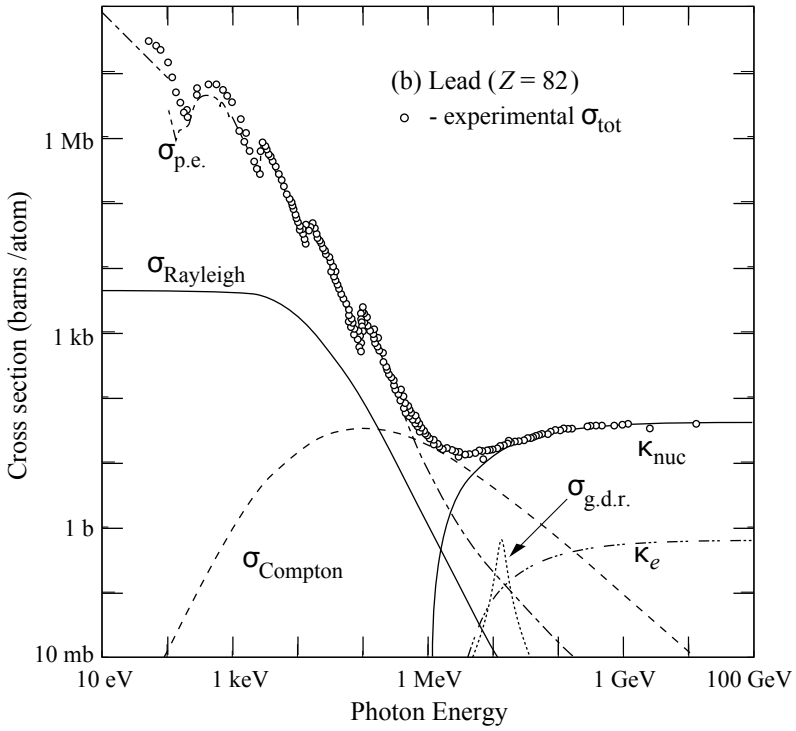

Figure 2.4: Dependence of photon total cross section and its individual components on energy for lead. Taken from [11].

Photons interact with matter and produce secondary ionization by the three dominating processes shown in figure 2.4 for lead. At energies below 50 keV, photon transfer all the energy to free the atomic electron in a process called the photoelectric effect. Its cross section decreases with photon energy as Z^5/E and eventually, Compton scattering of photons start to dominate [10]. But $\sigma_{Compton}$ also decreases as Z/E for energies above 511 keV (electron mass) and after 1.02 MeV threshold (double the electron mass) the incident photon may undergo conversion into an electron-positron pair. It can happen via interaction with the electric field of a nucleus with $\sigma_{pair} = \kappa_{nuc} \sim Z^2 \ln 2E$ or atomic electron also called triplet production with $\sigma_{trip} = \kappa_e \sim Z \ln 2E$ [10]. The smaller contributions to the total cross section σ_{tot} come from scattering which does not produce ionization, i.e Rayleigh scattering on a single electron or Thomson scattering on an entire atom. Another contribution comes from photonuclear reactions creating nuclear resonances – quasi-stationary excited states of nuclei, e.g. giant dipole resonance (g.d.r.). These states quickly decay with the evaporation of protons, neutrons, pions, or other particles.

Since photons are readily absorbed in the matter, Beer-Lambert law is used to define the attenuation of the number of photons traversing through the sample as

$$I(t) = I_0 \cdot e^{-\mu \cdot t} \rightarrow I(x) = I_0 \cdot e^{-(\mu/\rho) \cdot x} \tag{2.4}$$

where I_0 is the initial intensity of monoenergetic photon beam, $I(x)$ is the intensity after traversing the sample with density ρ, thickness t and corresponding mass thickness $x = \rho \cdot t$. $\mu = \sigma_{tot} \cdot n$ is the exponential attenuation coefficient with n being the number of atoms per volume

unit. The exponential mass attenuation coefficient is therefore defined as $\mu/\rho = \sigma_{tot} \cdot A \cdot m_u$, where $m_u = m(^{12}C)/12 = 1.66 \times 10^{-27}$ kg is the atomic mass constant. For compounds $\mu/\rho = \sum_i w_i \cdot (\mu/\rho)_i$, where w_i is the fraction by weight of the i-th atomic constituent.

Photon kerma is calculated as

$$K_\gamma = \mu_{tr}/\rho \cdot \Phi \cdot E \tag{2.5}$$

where Φ and E are the photon energy and fluence per cm^2. $\mu_{tr}/\rho = (f_{pe}\sigma_{pe} + f_{Compton}\sigma_{Compton} + f_{pair}\sigma_{pair} + f_{trip}\sigma_{trip}) \cdot A \cdot m_u$ is the mass energy-transfer coefficient, and f_i is the average fraction of photon energy that is transferred to kinetic energy of charged particles. The coherent scattering is omitted here due to negligible energy transfer. Photonuclear absorption is omitted due to the lack of theoretical models and gaps in experimental data on $\sigma_{ph.n.}$, see information provided in [15] for details.

Note, that secondary charged particles produced by the initial photon can further emit radiation which can, in turn, escape the material. Thus, for high-energy gammas kerma is significantly higher than the absorbed dose. To account for this, the factor g is introduced, which is the average fraction of the kinetic energy of secondary charged particles that is lost in radiative processes. Finally, the **absorbed dose for photons** can be calculated as

$$D_\gamma = (1 - g) \cdot \mu_{tr}/\rho \cdot \Phi \cdot E = \mu_{en}/\rho \cdot \Phi \cdot E \tag{2.6}$$

where μ_{en}/ρ is the mass energy-absorption coefficient. Tables of both μ/ρ and μ_{en}/ρ for various materials and mixtures can be found at NIST Standard Reference Database on X-Ray Mass Attenuation Coefficients [15].

2.2.5 Ionizing energy loss by neutrons

Interactions of neutrons with matter are depicted in figure 2.5. Neutrons are divided by their energy into cold < 3 meV, thermal < 0.5 eV (the most probable energy at room temperature is 0.025 eV), epithermal < 1 keV, middle energy < 0.5 MeV, fast < 20 MeV, high energy < 100 MeV, relativistic < 10 GeV and ultrarelativistic > 10 GeV [10]. All neutrons with E < 1 keV are called slow. Elastic scattering dominates most of the energies. Since the maximal energy transfer to the nucleus occurs when it has a mass comparable to neutron, materials with a low atomic mass number (H, D, Be) are used as moderators to slow down the neutrons. Inelastic scattering may also occur when part of energy goes into nucleus excitation with the following release of gamma rays.

Further inelastic interactions (nuclear reactions) happen when the neutron is absorbed to form a compound excited nucleus. At lower energies neutron capture is prominent: after neutron, absorption nuclei emit high energy gamma photons. At energies > 1 MeV nuclei either emits new particles and light fragments (γ, n, p, d, α, etc.) in processes called evaporation and γ-deexcitation, or if it is heavy enough undergoes fission producing new light nuclei. Nuclear reactions may be endothermic requiring certain threshold energy, and exothermic releasing some amount of energy. This is exploited in nuclear reactors, for example typical reaction (i.e. $n + ^{235} U \rightarrow ^{141} Ba + ^{92} Kr + 3n$) requires just 6.5 MeV, but releases 202.5 MeV. If the initial neutron energy exceeds hundreds of MeV, spallation and cascades of particles are produced which are discussed in subsection 2.4.2. Cold and thermal neutrons may also undergo diffraction on the crystal lattice with no change in either energy or momentum magnitude.

Kerma factor for neutrons can be calculated as [17]

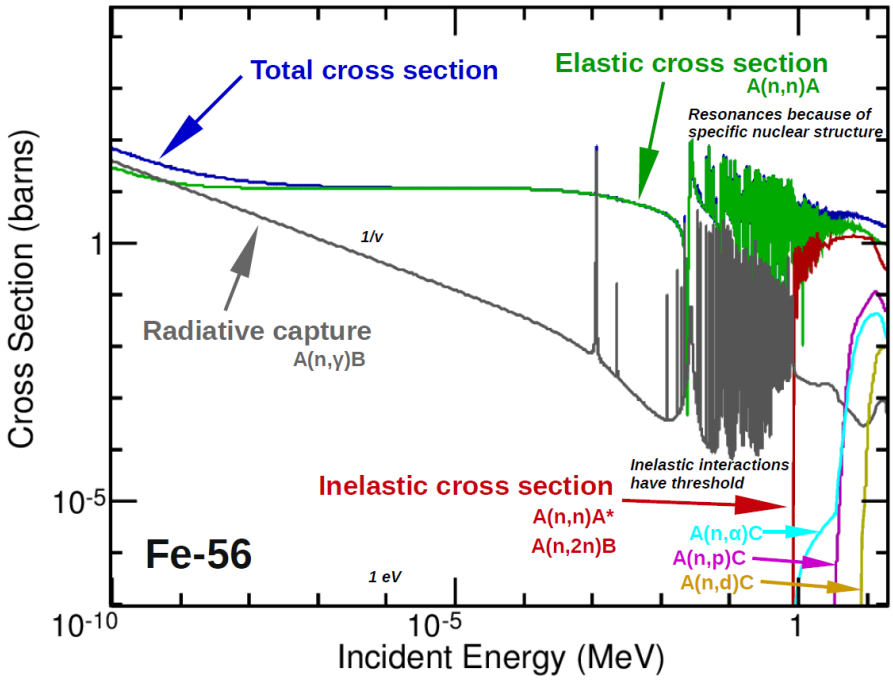

Figure 2.5: Dependence of neutron total cross section and its individual components on energy for iron. Picture produced by [16][lechner] based on data from ENDF/B-VII.1 database [13].

$$k_{\Phi n} = N \cdot \sum_i \int E \frac{d\sigma_i(E_n)}{dE} dE \tag{2.7}$$

where $N = N_A/A$ is the number of nuclei per unit mass of material, E is the energy of the secondary charged particle and $d\sigma_i(E_n)/dE$ is the energy-differential cross section for emission of charged particle i at the neutron energy E_n.

As it was previously discussed for photons, some secondary particles could escape the material volume which would result in the absorbed dose being lower than kerma. Radiological conversion coefficients for ambient air and tissues are collected in a report by International Commission on Radiation Units and Measurements (ICRU) [18]. For the specific detector, conversion of kerma to dose requires running a neutron transport code for the used geometry and material composition. However, it is not clear to which extent this neutron dose can be compared with the dose deposited by charged particles or photons due to the very different nature of the particle-matter iteration and damage production. Discussion for organic materials can be exemplified for polystyrene scintillators in subsection 3.2.5. In inorganic materials with the crystal lattice, radiation load is generally quantified by the 1 MeV equivalent neutron fluence. This arises from the fact that radiation damage is mainly produced by the atom dislocations which are described in the following section.

2.3 Non-ionizing energy loss (NIEL) and 1 MeV equivalent neutron fluence

The non-ionizing energy loss (NIEL) is responsible for the lattice damage production in crystalline materials. Neutrons participate in head-on collisions with nuclei described by elastic

scattering, while charged particles also interact with atoms by Coulomb interaction. Both interactions can displace the lattice atom, which in turn occupies some Interstitial (I) position leaving Vacancy (V) in the lattice. Altogether I and V are called Frenkel pair. The minimal energy required to displace an atom E_d varies from study to study, often being set around 25 eV for silicon. The maximum recoil energy achieved by the Primary Knock-On Atom (PKA) in a head-on collision through non-relativistic elastic scattering is defined as [19]

$$E_{R,max} = 4E_p \frac{m_p m_{Si}}{(m_p + m_{Si})} \tag{2.8}$$

where E_p and m_p are energy and mass of an incident particle.

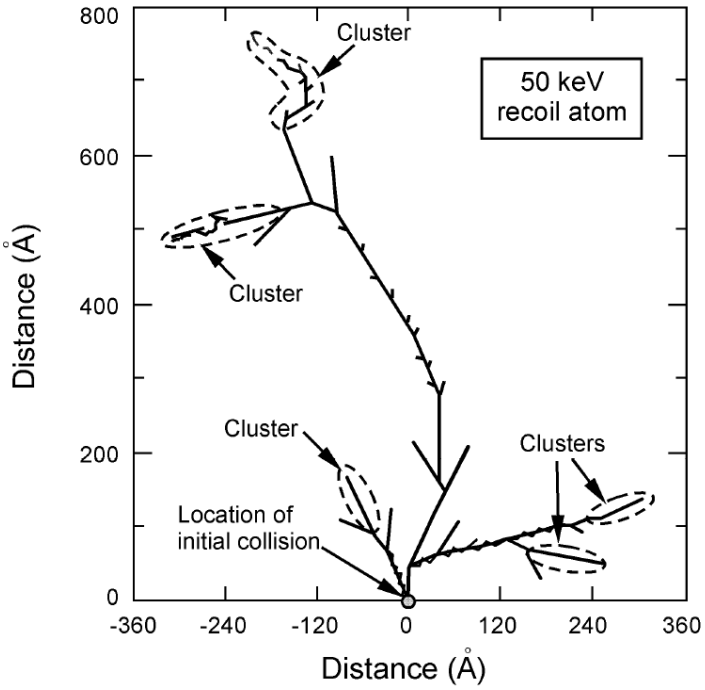

Figure 2.6: Monte Carlo simulation of track in silicon for a recoil atom with energy 50 keV. 50 keV is an average kinetic energy transferred by a 1 MeV neutron to PKA. Taken from [19].

By this formula, one can calculate that incident neutron should have more than 185 eV to displace the silicon atom, while electron needs at least 255 keV. Neutrons and protons have similar mass and thus recoil energy, but protons tend to lose energy in small fractions and create more point defects because of Coulomb interaction. Every PKA which achieved energy greater than 25 eV can produce further Frenkel pairs by itself and even result in a cluster of defects, if it's E_R exceeds 5 keV which can be recalculated to incident energy of 35 keV for neutron or 8 MeV for electron [19]. Figure 2.6 illustrates the typical track of a recoil atom which produces both ionization and further defects on its way. Cluster defects are present at the end of produced branches because non-ionizing interactions prevail at low energies just before the recoil atom is stopped [20].

2.3.1 NIEL function for displacement damage

The NIEL-scaling hypothesis has been introduced for the comparison of damage produced by different radiation [21]. It assumes that the NIEL value or damage function D is proportional to

the resulting damage effects. The NIEL value can be viewed as kinetic energy released to matter (kerma) that resulted in atom displacements [22]. For silicon with A=28.086 g/mol, $D = 100$ MeV·mb is equal to NIEL = 2.144 keV·cm^2/g. Damage function values can be extracted from ENDF/B database [13], again I recommend using Java-based JANIS system [14]. Alternatively, simple tabulated data collections are available on the webpage of RD50 collaboration [23].

NIEL radiation damage is solely dependent on the non-ionizing energy loss of an impinging particle which resulted in lattice dislocations. It does not account for ionization and (de)excitation of atoms, the initial spatial distribution of the displacement defects in one PKA cascade, annealing sequences after the initial damage event, etc. [24].

NIEL damage function or displacement damage cross section for a given particle type and energy E is calculated as

$$D(E) = \sum_i \sigma_i(E) \cdot \int_0^{E_{R,max}} f_i(E, E_R) P(E_R) dE_R \tag{2.9}$$

where damage function is calculated over all possible interactions with the incident particle with a cross section of i-th interaction $\sigma_i(E)$, a probability $f_i(E, E_R)$ of generation of a PKA with a recoil energy E_R and a fraction of energy $P(E_R)$ that goes into the displacement of a silicon atom (also called Lindhard partition function) [20].

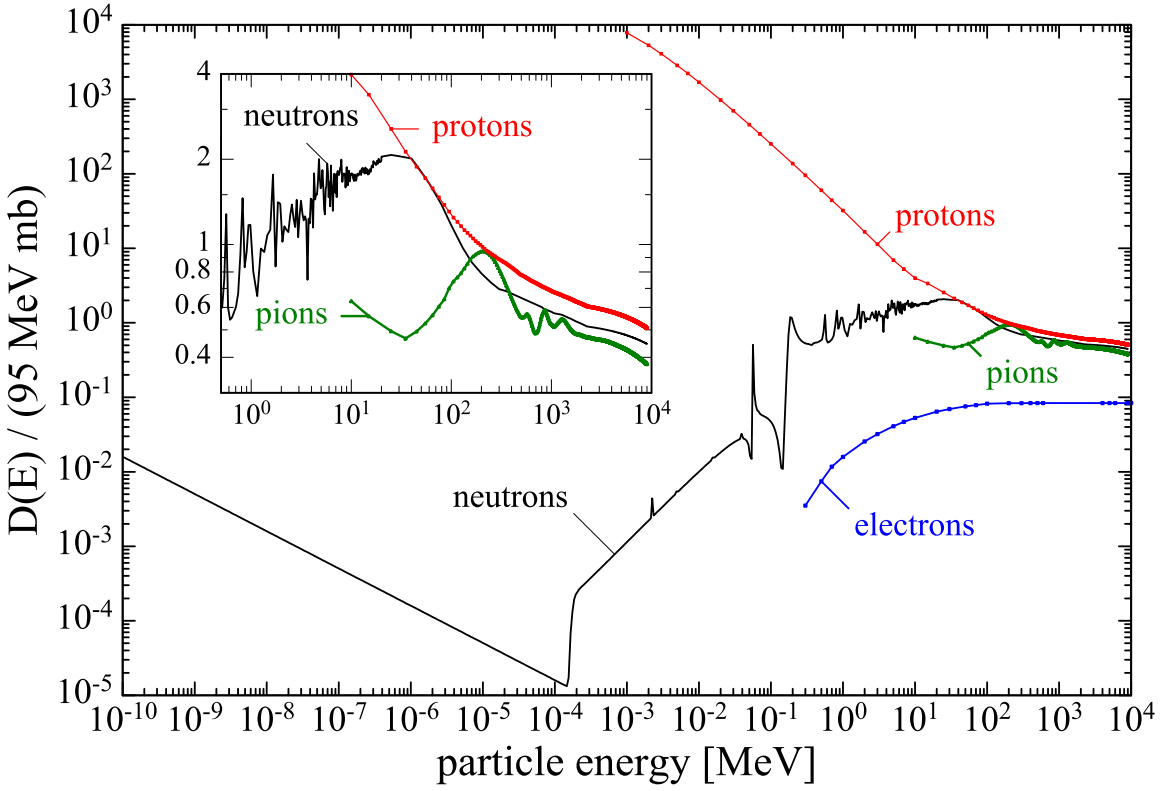

Figure 2.7: Displacement damage functions normalized to 95 MeV mb for neutrons, protons, pions and electrons in silicon [25]. The 1 MeV neutron equivalent fluence is indicated as a cross of the vertical and horizontal lines.

Figure 2.7 represents the displacement damage functions calculated for various types of particles in a wide range of energies. The direct knock-on of silicon atoms by impinging of

incident particles starts at an energy of about 185 eV for neutrons. The damage function is non-zero for the lower energies due to the possibility of thermal neutrons to be captured by silicon atom which can subsequently gain enough energy to escape the lattice [26]. Cross-section of this process is inversely proportional to the velocity of the incident neutron. From 185 eV up to 10 MeV, the elastic scattering of neutrons on atoms dominates with $\sigma \sim E$ governed by equation (2.8). Around 50 keV nuclear resonances start to play an important role in introducing edgy fluctuations on the graph. Deflection from the linearity around 1 MeV can be explained by the fact that part of the transferred energy is spent on the change of nucleons allocation within the nuclei. From 10 MeV direct head-on collisions on individual nucleons start to dominate with following knock-out of these nucleons. This is the reason why damage functions of protons and neutrons converge to similar values, while for lower energies protons have much higher damage function due to the high probability of the Coulomb interaction [26].

Gamma-rays can also produce damage due to electrons from the photoelectric effect, Compton scattering, or pair production [20]. For instance, γ-rays with energies of 1.17 and 1.33 MeV emitted by ^{60}Co-source mostly produce secondary electrons by the Compton effect. These electrons with an average energy of about 1 MeV generate much less damage on the order of 5×10^{-3} MeV·mbarn because they can only point defects [20].

NIEL for compounds can be determined by means of Bragg's rule, i.e., the overall NIEL in units of keV·cm^2/g is obtained as a weighted sum in which each material contributes proportionally to the fraction of its atomic weight. Alternatively, it can be estimated based on the number of vacancies produced in each material, which can be calculated with SRIM/TRIM software [27] as done in [28].

2.3.2 1 MeV neutron equivalent fluence

The damage produced by various particles can be compared in terms of the damage caused by 1 MeV neutrons $D(E_{n(1\,MeV)})$, which is considered as a reference [20]. Due to the fact that resonances give significant contribution around 1 MeV, ASTM [1] standardized $D(E_{n(1\,MeV)})$ as 95 MeV mb to avoid discrepancies in calculations with different routines, energy steps, etc. **The hardness factor** κ is used to compare the damage produced by various radiation sources in terms of the damage caused by 1 MeV neutrons

$$\kappa = \frac{\int D(E)\Phi(E)dE}{D(E_{n(1\,MeV)}) \cdot \int \Phi(E)dE} \tag{2.10}$$

where $\Phi(E)$ stands for the energy spectrum of a given particle source.

The equivalent fluence of 1 MeV neutrons can be calculated by [20]

$$\Phi_{eq}(1\ MeV\ neutrons) = \kappa \cdot \Phi \tag{2.11}$$

where Φ is the actually measured fluence.

This equivalent fluence is widely utilized for the unified cross-comparison of fluences achieved in various irradiation experiments but shall be used carefully as it does not account for many side effects. For instance, point-like and clustered defects affect the device parameters such as the effective space charge very differently, see section 3.4. Another example is the 1 – 2 orders of magnitude lower damage by electrons than by hadrons, see figure 2.7. This is likely because many displacement clusters are produced by hadrons via nuclear interactions generating high current. Also, electrons transfer energy only by Coulomb interaction, so PKA achieves way less energy and produces many close Frenkel pairs which later have a high chance to recombine [23]. At

[1] ASTM International standards organization, formerly American Society for Testing and Materials.

last, γ-rays can produce damage via electrons from the photoelectric effect, Compton scattering, or pair production.

2.4 Particle cascades and calorimeters

When a $\sim$ GeV energy particle hits a thick material it produces further particles initiating the cascade also called a shower. Showers are generally divided into electromagnetic and hadron based on the dominant interaction of the initiating particle.

2.4.1 Electromagnetic (EM) showers

EM showers, which are initiated by electrons or photons, are composed of particles that were multiplied via two main processes repeating many times after each other. One is called Bremsstrahlung which happens when an electron with $E > 10$ MeV (see figure 2.3) is slowed down and deflected by a Coulomb field of atomic nucleus emitting electromagnetic radiation. In another a photon with $E > 1.02$ MeV (see figure 2.4) converts into an electron-positron pair. Eventually, when the majority of the initial energy is dissipated shower ceases via low energy processes.

The critical energy E_c required for the showering process to continue can be simply defined as the energy at which the ionization and radiative loss rates are equal. However, E_c definition by Rossi [] as energy at which the ionization loss per radiation length X_0 is equal to the electron energy was found to describe the EM-shower development more accurately. E_c is approximated by $610/(Z + 1.24)$ MeV in solids [29].

The main EM-shower characteristic is the radiation length X_0 – the mean distance over which a high-energy electron loses all but 1/e of its energy by bremsstrahlung [11]. At the same time, $9/7X_0$ is the mean free path for pair production by a high-energy photon. X_0 is approximated as

$$X_0 \approx \frac{716.4A}{Z(Z+1)\ln\frac{287}{\sqrt{Z}}} \left[\frac{g}{cm^{-2}}\right] \tag{2.12}$$

The shower develops longitudinally by the high-energy particles, so its length scales as the material radiation length. At some point, the particle multiplication process reaches a maximum t_{max} and then slowly degrades as shown in figure 2.9. The shower also grows laterally by the multiple scattering of electrons and positrons as well as by isotropic production of photons and electrons (via Compton scattering and photoelectric effect). Averaged practical approximations of the shower dimensions given in units of X_0 are [29]

$$\begin{aligned} t_{max} &\approx \ln(E/E_c) + t_0 \\ t_{95\%} &\approx t_{max} + 0.08Z + 9.6 \\ R_M &\approx 21/E_c \end{aligned} \tag{2.13}$$

where t_{max} is the shower maximum, $t_{95\%}$ is the longitudinal material thickness containing 95% of the shower energy, R_M is the Molière radius – transverse radius of a cylinder containing 90% of the shower energy ($2R_M$ contain 95%), parameter t_0 is -0.5 for electrons and 0.5 for photons.

One can see that X_0 scales as A/Z^2 while R_M scales as A/Z which makes the latter much less material dependent. For instance, copper and lead have approximately the same value for R_M, while their radiation lengths differ by a factor of 3.

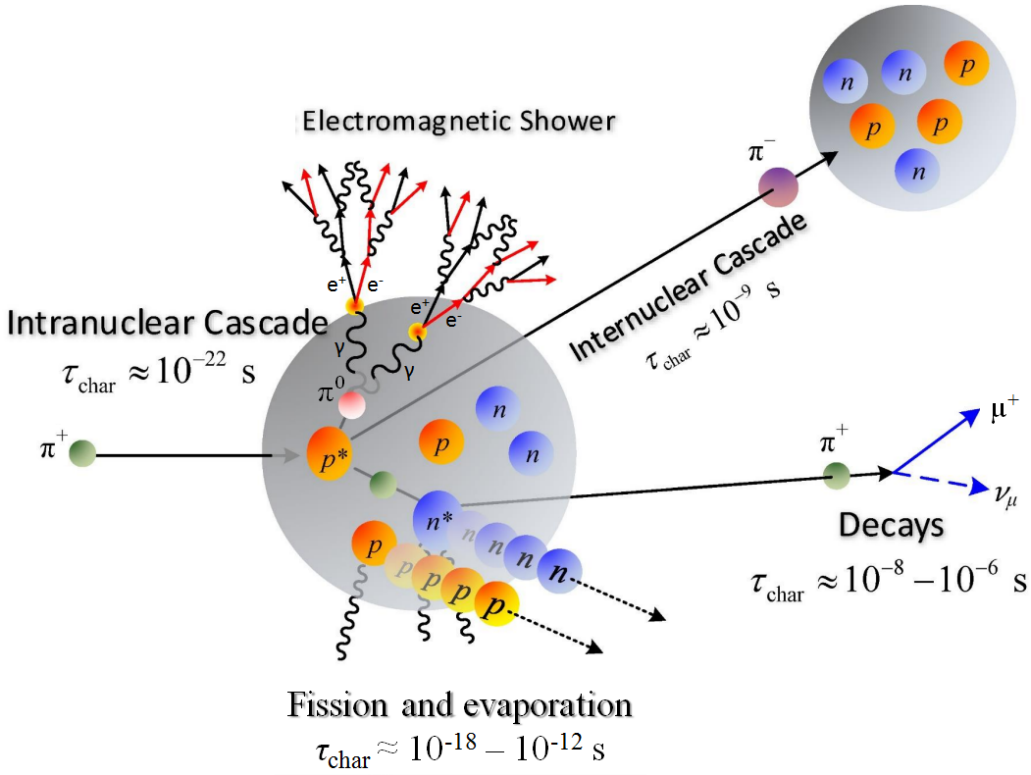

Figure 2.8: Evolution of the hadron shower, including spallation (intra-nuclear cascade, fission and evaporation), particle decays and further electromagnetic and hadron cascades. Characteristic times for all the processes are designated. Modified picture from [30].

2.4.2 Hadron showers

Hadron showers exhibit much more complex behavior because they are initiated by hadrons which indulge in a variety of hadronic interactions. Many secondary particles are produced in multiple inelastic hadronic interactions which are repeating one after another. The development of a hadron cascade can be described in terms of a spallation reaction [31] presented in figure 2.8. Spallation starts with the intra-nuclear cascade where hadrons, including nucleons and newly produced particles like pions, are released and eventually kicked out from the nucleus to start new cascades. This high energetic component of a shower spreads mainly along the direction of an incident particle. About 1/3 of produced pions are π^0 which promptly decay into a $\gamma\gamma$ pairs which in turn initiate EM showers.

When the incident energy becomes equally distributed in a highly excited nucleus the equilibrium stage of the spallation begins [31]. Here, the nucleus can deexcite by evaporation of soft neutrons, protons or light charged fragments like d, t, and α with energies around 10 MeV. Alternatively, it can deexcite by fission into two fragments similar in proton number which may in turn also undergo evaporation. Finally, when the nucleus excitation energy becomes smaller than the binding energy ~ 8 MeV, so neutrons are not emitted anymore, the nucleus deexcites by γ-emission. The resulting nucleus is usually β-radioactive and decays until the stable state. The remaining soft energetic component of a shower, which is mainly composed of recoil protons, spallation neutrons, and photons, loses its energy via elastic collisions, ionization, excitation and capture processes. It generally does not stick to the initial particle direction.

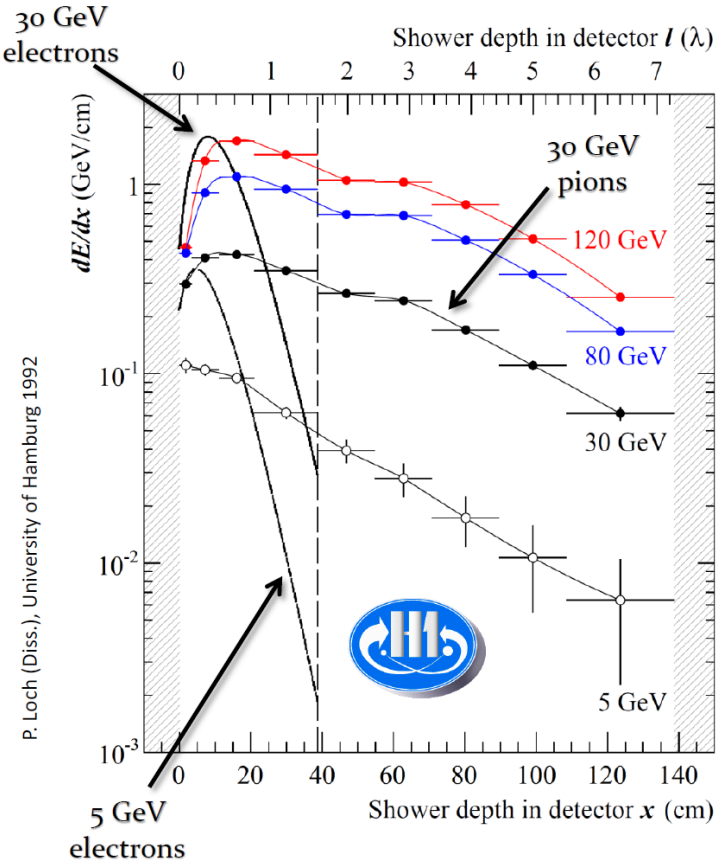

Figure 2.9: Comparison of electromagnetic and hadron longitudinal shower profiles which were measured with the liquid argon calorimeter of H1 detector at HERA (DESY). Picture from [30].

The main hadron shower characteristic is the interaction length $\lambda_{int} \approx 35A^{1/3}$ g/cm^{-2} which is a mean free path between interactions. On average hadron shower develops in a similar fashion to electromagnetic exhibiting a certain shower maximum, see figure 2.9. However, individual showers differ a lot from each other due to many processes involved resulting in much larger fluctuations than observed for EM showers. Typical radius $R_{95\%}$ containing 95% of the shower is relatively energy independent similarly to the case of EM shower. Averaged shower dimensions can be approximated in units of λ_{int} as [29]

$$\begin{aligned} t_{max} &\approx 0.2\ln(E) + 0.7 \\ t_{95\%} &\approx t_{max} + 2.5E^{0.3} \\ R_{95\%} &\approx 1 \end{aligned} \tag{2.14}$$

For heavy absorbers which are required to minimise the volume of a practical shower detector (calorimeter), λ_{int} is much larger than X_0. For example, in lead $\lambda_{int} = 17.6$ cm [11], which results in $t_{95\%} \approx 6.2\lambda_{int} \approx 108.2$ cm and $R_{95\%} \approx \lambda_{int} \approx 17.6$ cm for a shower initiated by a 10 GeV proton. At the same time X_0 in lead is only 0.56 cm [11], which results in $t_{95\%} \approx 22.9X_0 \approx 12.8$ cm and $R_{95\%} \approx 5.7X_0 \approx 3.2$ cm for a shower initiated by a 10 GeV electron. Here one can see that the typical dimensions differ by an order of magnitude for EM and hadron showers. Based on this fact, it is a common practice to design two separate calorimeters for the experimental detection of heavy ion collision products.

2.4.3 Calorimeter types and parameters

Detectors determine the particle energy and/or position by (ideally) complete absorption of an incoming particle. They can detect both charged and neutral particles, except for neutrinos and muons which are not readily absorbed. But in combination with other detectors, including muon chambers, indirect neutrino measurements via event's missing energy are possible [29].

The electromagnetic calorimeter is placed closer to the collision point, i.e. before the hadron calorimeter, because photons and electrons are much quicker absorbed than hadrons. Still, it is essential to minimize the material budget of tracking and other detectors which are placed before the calorimeters, because particles will inevitably lose some fraction of energy there making it unavailable for calorimetric measurements. Furthermore, as a result of this energy loss energetic secondary δ-electrons are being produced creating undesirable tracks which do not carry information on the main collision event.

High transverse segmentation of a calorimeter on the order of $R_{95\%}$ or even less is desired to distinguish between showers produced by different particles. The choice about the longitudinal segmentation evolves into consideration of a calorimeter type to be homogenous versus sampling, see figure 2.10. Homogeneous calorimeters are based on scintillating crystals (e.g. BGO or $PBWO_4$) or noble liquids (e.g. argon or xenon), as well as Cherenkov radiators (e.g. PbO or PbF_2) [11]. Here whole calorimeter material acts as the energy absorber and signal producer at the same time. This way, total shower energy is being absorbed providing the best energy resolution, particularly at lower energies.

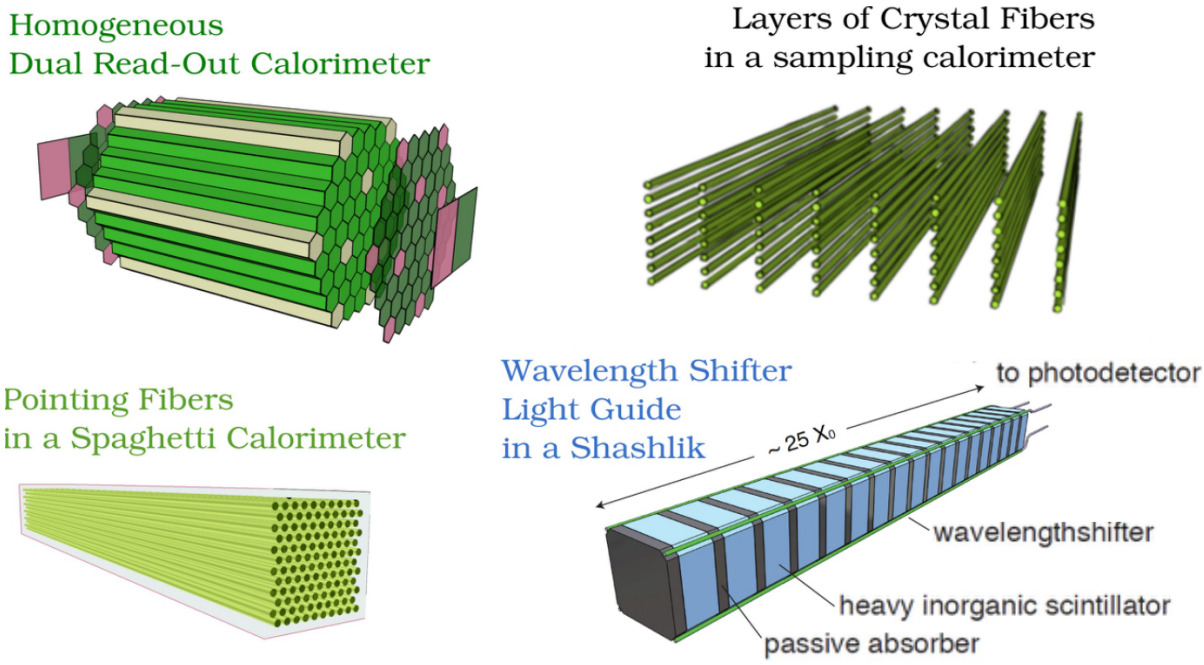

Figure 2.10: Simplified drawings of various calorimeter types and sub parts based on crystal fibres with different readout options. Picture from [32].

Longitudinal shower segmentation is achieved with sampling calorimeters by alternating layers of the passive absorber material (high-Z, e.g. Pb or U) and active material (scintillator, semiconductor, or ionizing detector based on noble liquid or gas) that generates a signal [11].

Most of the operating calorimeters have an analog signal readout, but digital readout, typically in form of resistive-plate chambers, is also used. Micro-pattern gas detectors (e,g, resistive

plate chambers) are another alternative to active material. They provide superior spacial resolution (down to 100 × 100 μm), albeit at the cost of worse energy resolution as the digital pads measure the only number of particles disregarding their energy [33].

Design based on scintillators + photodetectors for the light readout is the most common approach. Various approaches of the scintillating light readout are employed including: "spaghetti" with scintillating fibers running through the absorber, "shashlik" with wavelength shifting (WLS) fibers running through the alternating scintillator and absorber plates, "sandwich" with WLS-fibers embedded in scintillator plates and bent to the side (alternated by absorber plates), and even "accordion" with zig-zag absorber plates. Several mentioned designs are shown in figure 2.10. Another examples of "shashlik" and "sandwich" designs are CBM ECAL and PSD described in sections 4.2 and 4.3.

The advantage of sampling calorimeters is a much lower cost compared to homogenous ones which are very important considering the high material budget of the device. A disadvantage of the sampling is that only a fraction of the energy is detected in the active medium reducing the output signal and introducing the signal fluctuations which limits the detector resolution.

2.4.4 Hadron calorimeters

When hadron showers are detected, there are several features unknown for electromagnetic ones which make them more difficult to handle. About 20 – 40 % of the hadron shower energy is "invisible" for detection because it is spent to overcome nuclear binding energies, or carried away by photons and neutrons which are produced in nuclear reactions with up to 1 μs delay [29]. This reduces the output signal and introduces fluctuations. It also leads to a higher response to EM fraction of the shower than to the hadron fraction (e/h ratio) resulting in a condition called non-compensation. Furthermore, EM fraction increases with energy because π^0 production becomes available at more steps of the shower evolution. For instance EM fraction increases from $\sim$ 30% at 10 GeV to $\sim$ 50% at 100 GeV [34], which makes the calorimeter response non-linear to the initial particle energy. These facts combined make sampling calorimeters the only suitable option for hadron detection.

Compensation condition $e/h = 1$ can be achieved by design with careful tuning of the sampling ratio. It is based on a fact that active and passive materials have a different responses to shower fractions. EM fraction can be decreased with help of low-Z active material because the cross-section of soft γ-s increase with Z^{1-5}, see section 2.2. At the same time, hadron response can be increased by the boost of neutron collection. The use of hydrogenous scintillators is beneficial because hydrogen exhibit 100 times higher energy deposition by elastically scattered soft neutrons than heavy materials [11]. Requirement on compensation makes some materials more attractive than others, for instance, the sampling ratio for Fe/scintillator is about 20, while for Pb/scintillator it is about 4 which is much more practical, for instance, CBM PSD is based on the latter. Earlier compensating calorimeters like ZEUS were made from uranium, however, it is now abandoned due to its radioactivity, inflammability, and worse mechanical properties [35].

Alternatively, compensation can be reached by a complex software that can differentiate between compact EM and broader hadron shower fractions event by event, given the calorimeter has a very fine segmentation. See for example the energy flow method based on the combination of tracking and calorimeter information described in [33] [wigmans]. Another promising way is the dual-readout calorimetry where the EM fraction is measured event by event with a separate readout of scintillation light and Čerenkov light which is generated mainly by relativistic electrons, being promoted by DREAM collaboration [36], see figure 2.10 (top left).

2.4.5 Energy resolution and linearity of a calorimeter

The calorimeter energy resolution improves with energy as $1/\sqrt{\mathrm{E}}$ making them perfect for high-energy physics experiments compared to magnetic spectrometers where momentum resolution decreases linearly with momentum [29]. Exploiting the time structure of the signals Electromagnetic calorimeters are intrinsically linear, while the linearity of hadron calorimeters depends on the fulfillment of the compensation condition. However, non-linearity may arise from the saturation of active detecting parts (gas or photodetectors) or extensive shower leakage.

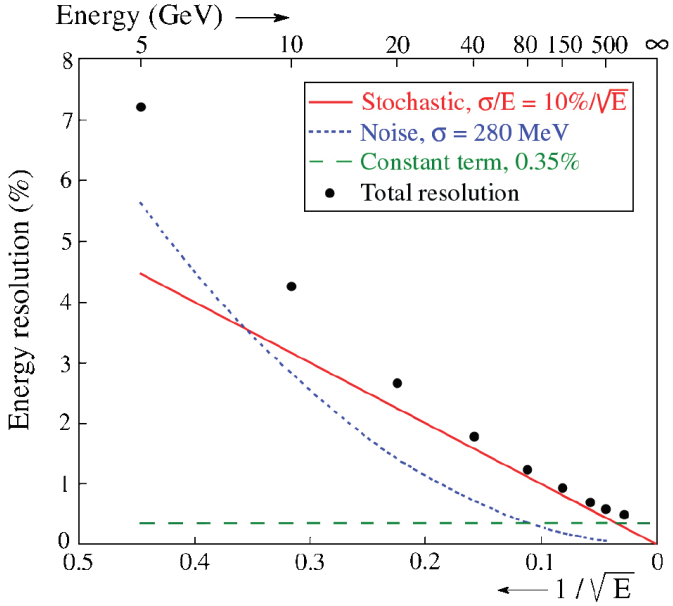

Figure 2.11: Energy resolution of the ATLAS EM calorimeter and its three constituent terms. Picture taken from [37].

Figure 2.11 depicts the relative energy resolution which is expressed as [29]

$$\frac{\sigma_E}{E} = \sqrt{\frac{a^2}{E} + b + \frac{c^2}{E^2}} \tag{2.15}$$

where a, b, and c are stochastic, constant, and noise terms, respectively.

Stochastic term a which is introduced by statistical event-to-event fluctuations usually dominates the resolution. Fluctuation of produced signal quantum, i.e. number of photons or charge carriers n, is the main contribution for homogenous EM calorimeters, i.e. $\sigma_E/E \sim 1/\sqrt{n} \sim 1/\sqrt{\mathrm{E}}$, which have the lowest achievable relative resolution on the order of a few percent per $\sqrt{\mathrm{E}}$ [11]. In case of sampling EM calorimeters, dominant are the fluctuations of number of different shower particles and their energy that is measured in the active layer. It can be expressed as $\sigma_E/E \sim \sqrt{(t/f_{samp}/E}$, where t is absorber layer thickness and f_{samp} is fraction of energy deposited in active layer [11]. Consequently, for sampling EM calorimeters $\sigma_E/E \sim 5 - 20$ % $/\sqrt{\mathrm{E}}$ [29]. Fluctuations in visible energy and EM shower fraction add up to the typical hadron calorimeter resolution of $\sigma_E/E \sim 30 - 90$ % $/\sqrt{\mathrm{E}}$ [37].

Constant term b represents the imperfection in the calorimeter design, i.e. fulfillment of the compensation condition, stability of the calibration (temperature, radiation, etc.), loss of the energy in dead material, and shower leakage fluctuations (if the shower starts in the last

sections). b is typically on the order of a few percent for hadron, or even below a percent for EM calorimeters, making it significant in the very high energy regime.

Noise term c is governed by instrumental effects, i.e. noise of light or charge sensor and readout electronics. Noise ultimately depends on the signal amplification technique. For example, photomultiplier tubes used for light collection provide gain on the order of 10^6 with almost no noise, while when the charge signal is collected it usually requires a preamplifier which introduces extra noise. It is especially important for low energy experiments and may even become dominant below a few GeV [29].

2.4.6 Radiation damage

Due ever-increasing luminosity and consequently the radiation load of modern collision experiments, it is very important to ensure that the calorimeter will remain well function during its lifetime. First, the response of active layers (e.g. scintillators) and sensors may degrade reducing the designed detector uniformity, which though can be partially mitigated by calibration. Second, it may significantly increase the noise of readout electronics and sensors worsening the resolution at low energies, which can be partially mitigated via signal shaping and optimal filtering. These concerns have to be addressed by the thorough study of radiation hardness of the calorimeter components under the envisaged radiation conditions. In the next sections of this chapter, I discuss the theoretical aspects and existing data on the radiation hardness studies of the most sensitive calorimeter components of CBM PSD.

Chapter 3

Extensive review of radiation hardness of calorimeter components

This chapter continues the journey on understanding the detector radiation damage. Section 3.3 overviews the radiation hardness of standard planar silicon detectors which is a well-established field with many books and publications that can provide an exhaustive description of the observed effects. It can be seen as a basis for the discussion on radiation damage in silicon photomultipliers (SiPMs).

On the contrary, general knowledge on the radiation hardness of organic scintillators and SiPMs is lacking. Even though substantial research data are available, there is yet no source that can provide a comprehensive review and understanding of all the data variety. In this chapter, I aimed to analyze and systematize all the existing irradiation studies in order to compose the unified data interpretation and provide a general assessment of the radiation hardness limits. To achieve this, I paid the utmost attention to various internal and ambient effects which are responsible for the vast discrepancies in observed results. Detailed attention is brought to the physics of operation and radiation effects for Polystyrene Scintillators, Wavelength Shifting Fibers, and Silicon Photomultipliers which are used in the CBM PSD calorimeter.

3.1 Scintillators

Scintillators are extensively utilized for particle detection via conversion of the ionization into light since the 1960s. Organic scintillators and fibers can be found in various applications, including high-energy physics, astrophysics, neutrino physics experiments as well as nuclear densitometry, and contamination monitoring. Plastic scintillators are the most popular option for the design of hadron calorimeters. In this section, I provide a short comparison of inorganic and organic scintillators, followed by an overview of the operation principles and properties of plastic scintillators and fibers.

3.1.1 Scintillator types

The most common scintillators are inorganic crystals and organic plastics, however organic liquids and crystals, ceramics, glasses, and noble gases also find their application. Inorganic scintillators produce luminescence due to the band structure of the crystal lattice: carriers released by ionization are captured by the luminescent centers (intrinsic or doped) which then radiate photons. They have high densities about $4-8$ g/cm^3 [11] which provide light output up to 40000 photons/MeV [38] thanks to the photo effect cross section proportional to Z^5. It makes

them ideal for electromagnetic homogenous calorimeters and gamma detectors where excellent energy resolution on the order of a few percent is required. However, high-purity germanium (HPGe) detectors can provide σ_E as low as 0.1 % which makes them even more favorable in gamma-ray spectrometry.

Specific inorganic scintillator crystals like $PbWO_4$, CsI and BaF_2 exhibit very good radiation hardness up to 100 kGy. Recently they were outpaced by Cerium doped crystals like YAG:Ce and LYSO:Ce which can survive well beyond 1 MGy and 10^{15} n/cm^2 [28]. However, the use of inorganic scintillators is not always favored due to the slow decay time of tens – hundreds of nanoseconds, the strong temperature dependence of 0.1 – 2 %/řC, and complicated growing process which results in high cost, non-uniformities, and size limitations [11]. Liquid, gas, and ceramics scintillators also possess great radiation hardness [39], but they tend to have lower conversion efficiency and/or are quite difficult to handle. They are utilized mainly in high-volume detectors like those of neutrino experiments.

Organic plastic scintillators truly shine if the application requires only medium radiation hardness up to 10 – 50 kGy. They are cheaper than inorganic scintillators, have small temperature dependence, and are easily produced in any desired shape. Time-sensitive detectors often utilize plastic scintillators for the superior decay time of a few nanoseconds or even lower. Their low density of about 1 g/cm^3 and high hydrogen content of about 50 % accompanied with a good light yield of about 10000 photons/MeV [38] make them ideal for compensating sampling calorimeters.

3.1.2 Basics of plastic scintillators and fibers

Luminescence of organic scintillators comes from transitions within the single-molecule and therefore does not require the lattice structure. For instance, the crystalline anthracene $C_{14}H_{10}$ which is used as an etalon scintillator can also scintillate as vapor or part of a mixed solution.Luminescence is exhibited by organic hydrocarbon molecules with symmetrical aromatic structure, typically a benzene ring C_6H_6 [40].

Figure 3.1 (left) shows the energy level scheme for transitions in molecule. When ionizing radiation strikes, an electron of the molecule can be excited to higher energy singlet states S_{1N}, S_{2N}, etc. where N is the vibrational level within the state. They radiationlessly relax to S_{10} and then may quickly radiatively decay to ground state S_{0N} in a process called fluorescence. Alternatively, deexcitation can go through triplet states T_{1N}, T_{2N}, etc. which may again decay to S_{0N} in processes called phosphorescence and delayed fluorescence. These take microseconds, and corresponding delayed photons are usually missed by readout electronics.

Organic scintillators are more or less transparent to their own fluorescence emission. This is due to the fact that all emissions except $S_{10} \rightarrow S_{00}$ have lower energy than required for absorption. Based on the Franck-Condon principle $S_{10} \rightarrow S_{00}$ transition is not very probable because the overlap of the two vibrational wave functions is smaller than, for example, for $S_{10} \rightarrow S_{02}$. This results in the Stokes shift – emitted photon has lower energy (longer wavelength) than the absorbed one as shown in figure 3.2.

The base of a plastic scintillator is a polymer chain with aromatic rings, most prominent examples being polyvinyl toluene (PVT, $(C_9H_10)_n$) and polystyrene (PS, $(C_8H_8)_n$), which structures are depicted in figure 3.1 (right). Even though the base scintillates by itself, it usually has low yield and transparency to its own emission and long decay time [40]. To compensate for that, fluors are added in a concentration of 1 – 2 % which is strongly coupled to the base. The light energy absorbed by the base is transferred to the first fluor via radiationless dipole-dipole interaction (Förster resonance energy transfer). Most first fluors emit the energy as ultraviolet radiation. That's why the secondary "wavelength shifter" fluor is added in a concentration of

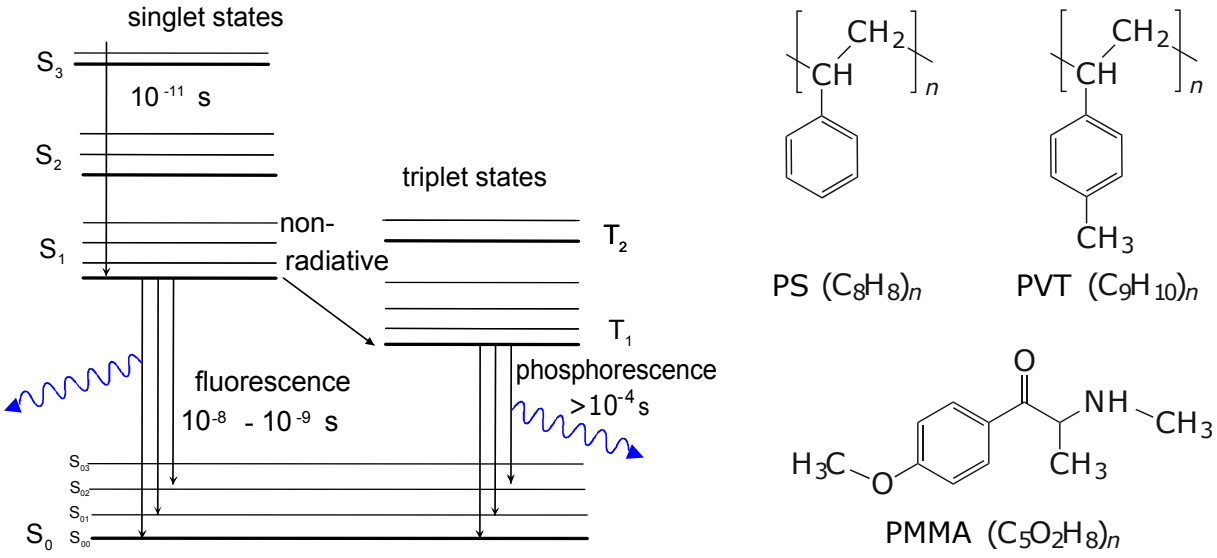

Figure 3.1: (left) Jablonski diagram of energy states in a scintillator molecule showing diffrenece between fluorescence and phosphorescence [41]. Higher vibrational states S_{0N}, S_{1N}, T_{0N}, etc. are depicted as thinner lines. (right) Chemical formulas for polystyrene, polyvinyltoluene and polymethylmethacrylate [42].

about 0.1 % to absorb UV light and reemit visible light [11]. It improves the light transmission and makes the wavelength corresponding to the typical sensitivity region of photomultipliers or photodiodes, compare spectra in figures 3.1 and 3.22 (right). The fluor concentrations are chosen in order to maximize the light yield, but keep fluor-induced self-absorption at a minimum. Schemes based on only a single-fluor like 3-Hydroxyflavone (3HF) with large Stokes shift can be used, but are not very effective [41].

Many base-fluor combinations are made to match their emission-absorption spectra in the scintillator. For example, scintillators of CBM PSD are made of PS with paraterphenyl (PTP, $C_{18}H_{14}$) as first fluor and 1,4-di-(5-phenyl-2-oxazolyl)-benzene (POPOP, $C_{24}H_{16}N_2O_2$) as second "wavelength shifter" fluor, their spectra are shown in figure 3.2 (left). Base and fluors are mixed together and then polymerized with help of molding or cast sheets of various sizes to form the scintillator. Recently 3D-printed scintillator prototypes have been developed which takes the manufacturing to a new level [43]. Examples of popular PVT-based scintillators are BC-408 produced by Bicron division of Saint-Gobain and EJ-260 produced by Eljen. PS-based scintillators are produced by many manufacturers, e.g. Kuraray SCSN-81 scintillators which were very popular in the past but are now discontinued. Industrially produced scintillators have proprietary composition, but for some, it was uncovered, e.g. SCSN-81 was found to be PS + $\sim$ 1 % PTP + (0.05–0.1) % 3HF [44].

Another common material used in scintillators is non-aromatic polymethylmethacrylate (PMMA, $(C_5O_2H_8)_n$) which structure is depicted in figure 3.1 (right). It has high light transparency, durability and robust mechanical properties, especially brittleness. It does not exhibit fluorescence, but can be used as the scintillator base by adding another aromatic component like naphthalene [46].

PMMA is often used for the cladding of scintillating and wavelength-shifting (WLS) fibers, which are used to detect ionizing radiation itself or shift the wavelength of photons already produced by primary scintillators. They provide the possibility to transport the light to the

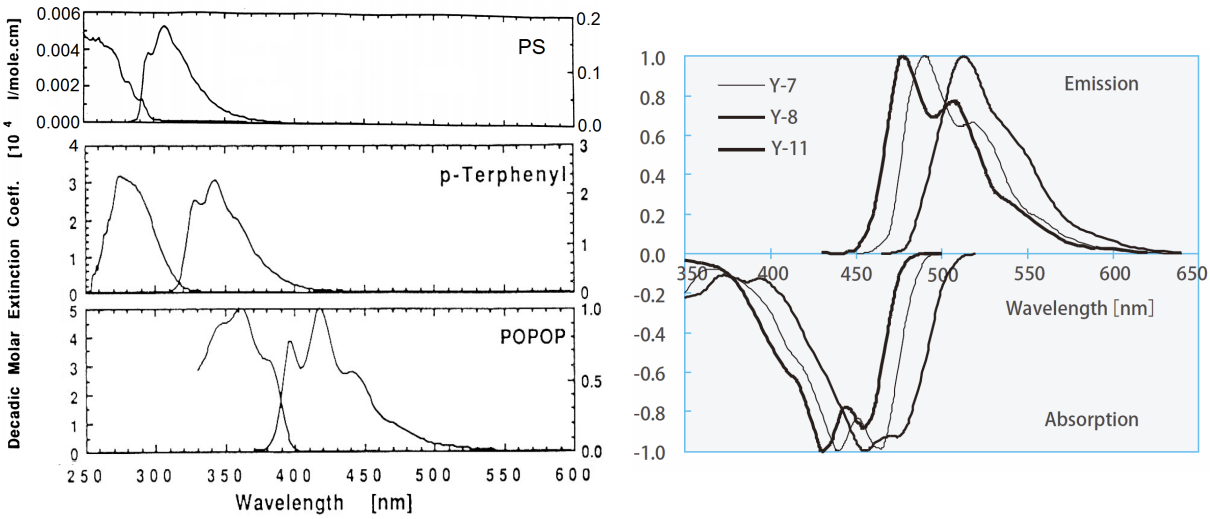

Figure 3.2: (left) Absorption and emission spectra of PS, PTP and POPOP given as molar extinction coefficient which is the measure of the light attenuation in material [41]. For each material absorption spectrum is on the left, emission is on the right. (right) Absorption and emission spectra in arbitrary units for Kuraray WLS-fibers [45].

photodetector which is situated several meters aside. The scintillating core of the fiber is usually PS accompanied by a wide range of fluors which is made into a fiber by extrusion. PMMA has a refractive index of 1.49, which is lower than 1.59 of PS which improves the attenuation length by confining the light within the fiber by reflection [45]. The fiber diameter is in the range of 0.1 – 1 mm, length up to several meters. Currently, there are two major fiber manufacturers: Kuraray and Bicron division in Saint-Gobain [45, 47]. CBM PSD utilizes multilayered cladding fibers Y-11 produced by Kuraray, their absorption/emission spectra are well-matched with the scintillators which are shown in figure figure 3.2 (right). Unfortunately, a fraction of generated light that is captured and transported for several meters by the fiber is only about 10 %, which implies the usage of highly sensitive photodetectors [11].

3.1.3 Advantages and disadvantages of plastic scintillators

Important properties of plastic scintillators and fibers include

- Relatively high light yield up to 25000 photons/MeV [38].
- Good transmission of generated light and consequently relatively long attenuation lengths in the range of 2 – 5 meters [45, 47].
- Fast decay time (time over which the light intensity decreases to 1/e) of 0.7 – 4 ns for scintillators [38, 47] and 10 – 25 ns for fibers [48].
- Optical characteristics aligned with characteristics of photodetectors, namely refractive index about 1.6 and wide range of choice for emission peaks between 370 and 610 nm [38, 45, 47].
- Sensitivity to proton recoils from neutrons due to high hydrogen content of roughly 50 %.
- Ease of fabrication into desired shapes (rectangles, fibers, etc.) and low cost, which is demanded in tracking and calorimetry. Good fiber flexibility is a very important requirement ranging from 5 to 20 cm [45].

- Low degree of the response fluctuation between the samples, usually about a few percent.
- Mild dependence on ambient conditions. Light yield variation as low as 0.01 %/řC were measured up to +50 řC range [49]. Light yield variations of several percent were reported for extreme conditions like high values of oxygen partial pressure or magnetic field [11].
- Saturation of the light yield when the ionization density is very high. It can be related to the finite amount of molecules that can get excited by the incoming radiation [11]. Light yield per unit length of the scintillator is semi-empirically described by the Birks' law

$$\frac{dL}{dx} = \frac{A \cdot dE/dx}{1 + k_B \cdot dE/dx} \tag{3.1}$$

  where A is the absolute scintillation efficiency, dE/dx is the stopping power, and k_B is Birks' constant, which depends on the material – for polystyrene-based scintillators, it is 0.126 mm/MeV.
- Degradation of the properties with time (aging) due to high temperatures, mechanical flexing, rough handling, irradiation, and contact with solvent vapors or even fingerprints [11]. The surface is particularly easily damaged with microcracks reducing the light transmission. Therefore, it is essential to keep the scintillator in closed encasement without the excessive impact of ambient conditions and mechanical forces. Radiation damage is discussed in the further subsection.

3.2 Review of irradiation studies for polystyrene scintillators and WLS-fibers

In scintillators, along with the desired scintillation effects, intensive radiation exposure inevitably causes material changes leading to radiation damage. The degree of damage varies greatly with the device type and technology as well as the radiation dose and source. Radiation conditions expected at HEP experiments are typically in the range of 0.1 – 100 kGy.

Many studies on scintillator performance after irradiation with various sources, doses, and conditions are available now. I would like to thank Yu. Kharzheev [42] for currently the only review article on the radiation hardness of plastic scintillators and fibers which cover a great variety of publications. Authors divide the studies into "old" and "new" (recent years) and conclude that new scintillators can withstand irradiation up to tens of MGy, also promoting the higher radiation hardness of PVT-based scintillators. However, after a closer look into the data, I realized that there are huge discrepancies in the covered results, i.e. scintillator's radiation tolerance in the range between 1 kGy and 100 MGy is claimed by different researchers. It inspired me to extend this work and make a comprehensive review covering all the articles on scintillator irradiation studies available for the last decades. I discuss the observed variation of the radiation effects trying to explain possible origins of discrepancies in the data by internal and external factors, including the scintillator material and design, irradiation, and measurement conditions.

Organic scintillators have highly irregular structure and therefore a study of lattice dislocations is not justified, in the absence of the lattice. Therefore, the non-ionizing energy loss of impinging radiation is expected to be negligible compared to the ionizing energy loss. The latter can cause a variety of chemical reactions altering the highly reactive polymer chains. This explains why most studies are performed with gamma sources which can be seen in the following subsections. To further explore the basics of the radiation damage production in scintillators, I would suggest an old but great guide by C. Zorn [50].

In this section, I start with an explanation of the microscopic effects of radiation in polymers and then discuss the macroscopic effects observed in scintillators paying attention to the variety of factors involved. I also shortly review the performance studies for calorimeters conducted with irradiated scintillators. In the end, I discuss the most discrepant results and their probable origins and provide the final summary on the radiation tolerance limits and general recommendations for the detector choice and operation.

3.2.1 Effects of irradiation in polymers

Passage of the ionizing radiation through the polymer results in ionization and excitation of its molecules producing ions, electrons, and free radicals. Free radicals are atoms or molecules with unpaired valence electrons which can be imagined as "dangling" covalent bonds. They are created via chain scission and dissociation of the units situated at the chain side. Two examples are hydroxyl radical $HO\cdot$ and methylene radical $:CH_2$. The "Dangling" nature of the bonds makes radicals highly chemically reactive and unstable.

Various chemical reactions are initiated and promoted by ionization and free radicals resulting in the following effects, some of which are depicted in figure 3.3 [51]

- Polymerization of single molecules (monomers) present in the material – production of new polymer chains.
- Grafting – conjunction of a newly polymerized monomer onto the base polymer chain.
- Chain branching – conjunction of polymer chains.
- Crosslinking – conjunction of multiple polymer chains to form a complex 3D-network.
- Chain scission – cleavage of polymer chains which reduces the molecular weight of the polymer.
- Oxidation – reaction of polymer molecules with oxygen from radicals and peroxides, e.g. hydrogen peroxide H_2O_2. It greatly enhances the other effects.

The latter effects lead to the elimination of atoms or molecular fragments from the polymer chain [52]. It results in the creation of unsaturated bonds between carbon atoms, i.e. double or triple bonds from single bonds. They are more chemically active than saturated (single) or delocalized bonds of the benzene ring, so they promote further reactions. Atoms that were eliminated from the chain may evolve into gases like H_2 and CH_4 which may lead to material swelling. Impinging ions can be incorporated into the material as in the case of ion implantation (doping) which significantly alters the material properties [53]. Produced defects and molecular species can migrate along the polymer chain, be trapped at specific sites, or recover themselves by recombination.

All the aforementioned processes change the polymer properties, including molecular weight, mechanical stability, shape, color, optical and electrical properties [56]. The introduced changes can be both detrimental or beneficial. Undesirable degradation is common in harsh radiation environments like space or high energy physics facilities, which is the topic of my research. Benefits lie in the currently growing field of radiation polymer modification. Radiation curing is a combination of polymerization and crosslinking, which is used to harden the materials like coatings and composites. Degradation by chain scission and oxidation can be useful for recycling polymer waste to prevent or reduce environmental pollution.

Radiation resistance can be judged on the basis of the G value. G value is defined as the chemical yield of radiation in a number of molecules reacted per 100 eV of absorbed energy. Important are G values for crosslinking (X), chain scission (S), the formation of radicals (R)

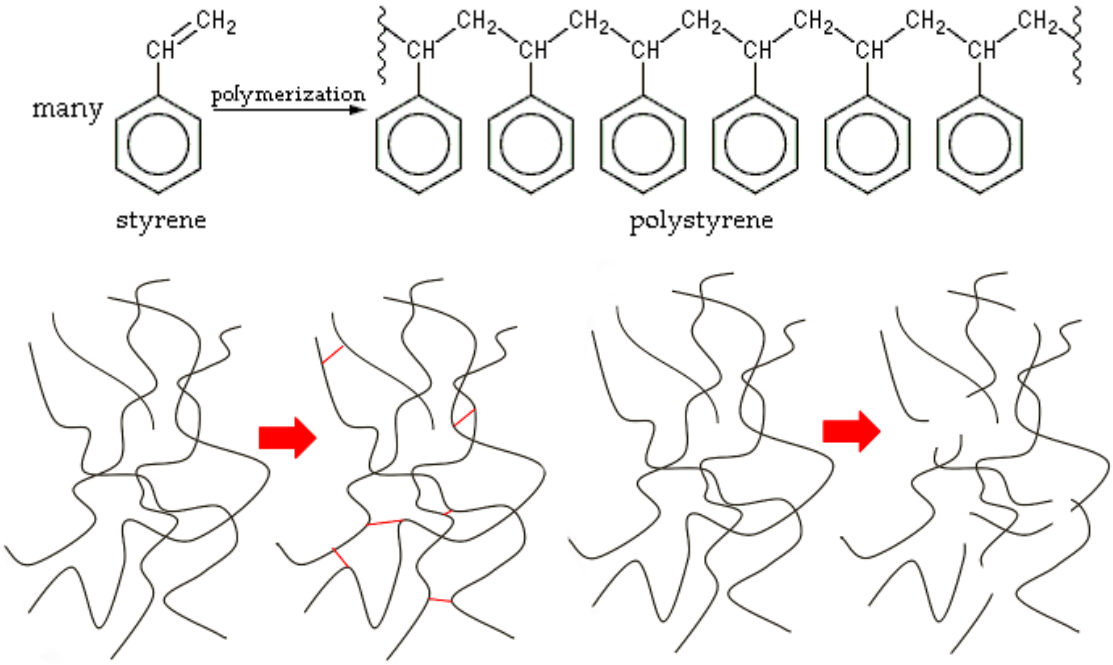

Figure 3.3: (right) Polystyrene chain formation by polymerization of styrene monomer [54]. (bottom) Crosslinking (left) and chain scission (right) of polymer chains [55].

and gases (G). G values increase with the absorbed dose. However, G(X) increases slower than G(S), so the latter inevitably starts to dominate after some threshold resulting in overall degradation [51].

Material	G(S) [reactions per 100 eV]	G(X) [reactions per 100 eV]	G(R) [reactions per 100 eV]	G(G) [reactions per 100 eV]	G(S):G(X)	Physical hardness [kGy]	Optical hardness [kGy]
PS C_8H_{8n}	0.0094 – 0.019	0.019 – 0.051	0.2	0.022	~ 0.4	10000	1 – 100
PMMA $C_5O_2H_{8n}$	1.1 – 1.7	< 0.5	2.4 – 2.5	1.18	> 2	100	1 – 100

Table 3.1: Properties related to radiation hardness for polystyrene (PS) and polymethylmethacrylate (PMMA), namely G values for chain scission (S), crosslinking (X), formation of radicals (R) and gases (G), ratio G(S):G(X), and typical radiation hardness thresholds for degradation of physical and optical properties. Data are from [42, 51, 56]

Different polymers respond differently to radiation. Every polymer is unique and there is no one rule that fits all, but here are some general tendencies. Polymers with more hydrogen atoms on the side (e.g. polyethylene) usually have G(S):G(X) ratio < 1 and therefore tend to crosslink with radiation [51]. Polymers with a methyl group CH_3 (e.g., polypropylene) tend to

have G(S):G(X) ratio > 1 and would more likely undergo degradation. Low radiation resistant materials like polyethylene have G values $\sim 0.5 - 1.5$. Aromatic polymers like PS and PVT have superior radiation resistance. This can be explained by the enhanced stability brought by benzene rings. They have very low G values < 0.1 and G(S):G(X) ~ 0.4 making them rather crosslink the degrade [51]. PMMA is found to be generally less resistant due to the absence of aromatic units and tends to undergo scission due to G(S):G(X) > 2. The G values and typical radiation thresholds for PS and PMMA are presented in table 3.1.

3.2.2 Radiation tolerance limits for PS and PMMA based scintillators

Scintillator physical properties remain stable beyond 0.1 – 10 MGy. However, their optical properties are found to be much more vulnerable. Yellowing starts for both PS and PMMA at doses above 10 kGy and becomes browning at higher doses, though the color tends to at least partially recover after some time [51]. Numerous experiments confirmed that the irradiation creates color centers in scintillators that absorb and scatter the light. This reduces both the attenuation length L_λ (proportional to light transmittance T, see equation (3.2)) and the light yield. However, mechanisms responsible for the scintillator radiation damage are complex and their relation to basic processes which were described earlier are not yet completely understood [11].

$$L_\lambda = \frac{1}{k} = \frac{d}{\ln(1/T)} \tag{3.2}$$

where k is the absorption coefficient defined for the exponential light absorption, d is the scintillator thickness and $T = I/I_0$ is defined as the ratio of photons produced in the scintillator to photons exiting the scintillator.

Significant variations in the degradation were observed in the studies for the same absorbed doses. Laboratory investigations performed by many authors [50, 60–67] indicate that the initial loss of the light yield (5 – 30 %) happens around 1 – 10 kGy, and becomes very drastic (50 – 90 % loss) around 100 – 1000 kGy. For example see black/grey points in figure 3.4. Studies performed at collision experiments environments by ATLAS [67, 68] and CMS [57, 59, 69] collaborations reported much higher losses, see colored points for CMS in figure 3.4. Even more, discrepant results are reported by some authors. For example, Zh. Li et al. [70] measured a huge 90 % transparency loss after just a 10 kGy, while H. Jivan et al. [71, 72] measured only a mild 20 – 40 % light loss after 1 MGy.

Observed data variations are due to the inevitable dependence of scintillator performance on many internal and external parameters, including polymer properties, mechanical stress, heat, light, presence of oxygen and other chemicals, dose rate, and particle species. In the following subsections, I discuss in detail the impact of those parameters which was observed by the researchers.

3.2.3 Scintillator geometry and light readout with WLS fibers

The bigger the scintillator size – the worse is the light transmittance and therefore the light yield, see grey points in figure 3.4. Typical scintillator tile diameters in calorimeters range from 5 to 40 cm which results in lowered light yield if readout directly from the tile side like in ZEUS [73], LHCb [74] and ATLAS [67] calorimeters. For instance, ZEUS collaboration found [73] that light transfer via WLS-bars significantly degraded already after a low dose of 1 kGy, see figure 3.10. The light collection is substantially improved by embedding the fiber inside a grove in the tile in a circular manner which is done in CMS [59] and CBM calorimeters. This way light travels a shorter distance through the scintillator to the fiber which reduces the

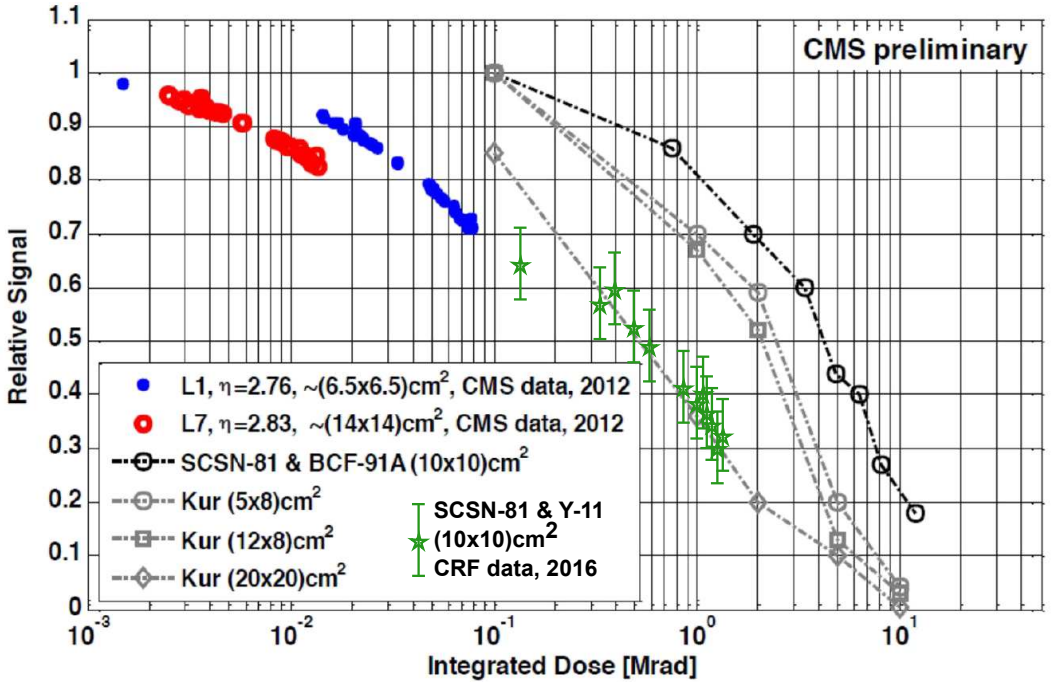

Figure 3.4: Compilation of the degradation of scintillation light yield after irradiation with 0.001 – 10 Mrad (0.01 – 100 kGy) investigated by CMS HCAL [57]. Black/grey data are for laboratory measurements of different scintillator tiles produced by Kuraray after irradiation by ^{60}C gamma source with dose rate of 1 kGy/h [58]. Black data are for PS-based SCSN-81 Kuraray scintillators with embedded BCF-91A WLS-fibers. Colored data are for SCSN-81 scintillators with embedded Y-11 Kuraray WLS-fibers measured at CMS environment [59]. Red/blue data are for scintillator+fiber modules of CMS HCAL irradiated during physics beamtime with dose rate below 1 Gy/h. Green data is for scintillator+fiber samples irradiated at CASTOR radiation facility (CRF) in front of CMS with a dose rate of 42 Gy/h (added to the figure by me). The width of all the scintillators is about 4 mm. Laboratory measurements were done after several months of annealing, measurements at CMS environment were done online without annealing.

absorption and scattering losses. Consequently, light losses due to the radiation damage are also reduced. Embedding multiple WLS-fibers to the scintillator or dividing the scintillator into smaller finger strips with individual fibers in each strip can further significantly improve the light collection [66, 75]. However, such a solution imposes additional design complications, so the provided benefit shall be carefully evaluated.

WLS fibers also suffer from the radiation damage [48, 76–81]. Figure 3.5 presents the deterioration of the light yield at the fiber end after irradiation up to 15 kGy. Fiber attenuation length was found to decrease from 2 – 3 down to 1 – 2 meters after 1 – 10 kGy [61, 74, 82–84] and further down to 10 – 20 cm after 100 kGy [58].

Small-sized scintillators exhibit better light yield due to small light path that reduces self-absorption, but the light path in larger scintillators can be significantly reduced by the embedded WLS-fibers. Studies for irradiated assemblies of 7 – 15 cm wide scintillator tiles with 1 – 2 m long WLS-fibers [57–59, 64, 67, 74, 80, 82, 83] reported total light losses comparable to 1 – 4 cm wide scintillator samples alone [61–63, 65, 81, 85–87]. Namely, a light yield drop of up to 30 % is observed around 10 kGy, and decrease above 50 % around 100 kGy. Figure 3.4 shows the light yield improvement by incorporation of the fiber which is shown by black points compared to

grey points measured without the fibers. The light yield uniformity of the scintillator + fiber system is usually on the level of a few percent before irradiation but can degrade to 5 – 20 % depending on the dose and the assembly properties [64].

A detailed discussion of clear and scintillating fibers is beyond my research topic, but I may note that general trends on their degradation are quite similar to that of scintillators and WLS-fibers, check [42] for further information.

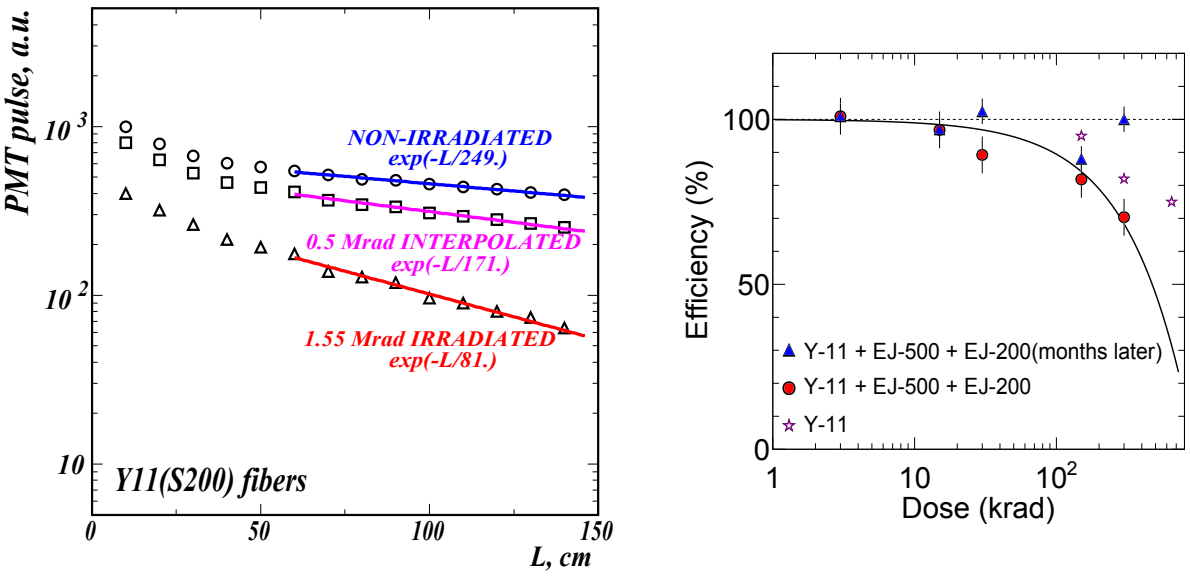

Figure 3.5: (left) Light yield produced by Kuraray Y-11 WLS-fibers depending on the distance to scintillator measured by [74]. Triangles data are for fiber irradiated by 70 GeV protons with dose rate of 3 krad/h (30 Gy/h) to dose 1.55 Mrad (15.5 kGy). Square data points for 0.5 Mrad (5 kGy) are interpolated. Measurements were done after 3 months of annealing. (right) Compilation of radiation-induced deterioration of the scintillation detection efficiency – the ratio of an average signal after irradiation to average signal before irradiation, prepared by [88]. Dose range is 3 – 650 krad (0.03 – 6.5 kGy). Blue triangles and red circles data was measured with the assembly of $12 \times 5.5 \times 0.5$ cm^3 EJ-200 PVT-based scintillators with embedded Kuraray Y-11 WLS-fibers which were glued by EJ-500 optical cement. The assembly was irradiated with a 50 MeV proton beam with a 2.6 kGy/h rate. Measurements were done 4 days after irradiation and after a few months of annealing.

Application of the optical adhesive between the scintillator and fiber improves the light transmission and light yield by up to 50 % [89]. Adhesives are usually epoxy-based in form of glue, cement, or resin, with a wide range of viscosities from 0.01 to 10 Pa·s. More viscous resins were found to have better radiation hardness than less viscous glues % [89]. Several studies of adhesive degradation due to irradiation and environmental conditions were carried out by [88–93]. They revealed that many adhesives are radiation-resistant up to at least 10 kGy, and some even up to 100 kGy. Note, that a popular BC-600 glue was found to have much worse resistance [89, 90], so now it is often replaced by harder ones. Irradiations of plastic scintillator + fiber assemblies coupled by radiation-hard adhesives EJ-500 [88] and SKTN-MED [89] revealed that the light yield losses are mainly caused by the degradation of scintillators and fibers themselves.

3.2.4 Scintillator composition and manufacturing

Irradiation modifies connections both between the base polymer molecules themselves and between the base molecules and the fluors. Damage in the polymer matrix is considered to be the main reason for the radiation-induced degradation because fluor molecules were found to be very radiation resistant [50]. In a few studies [42], scintillators were produced with fluors that were preliminarily heavily irradiated (up to 1 MGy), however, their parameters were comparable to scintillators produced with non-irradiated fluors. Only a few data is available on the comparison of radiation hardness of different base materials, moreover, they behave differently in different environments [57], which leaves ambiguity in the interpretation. Earlier studies reported that PVT-based scintillators can be slightly more ($\sim 10 - 30$ %) resistant than PS-based ones [57,65], but recently the opposite was claimed [59].

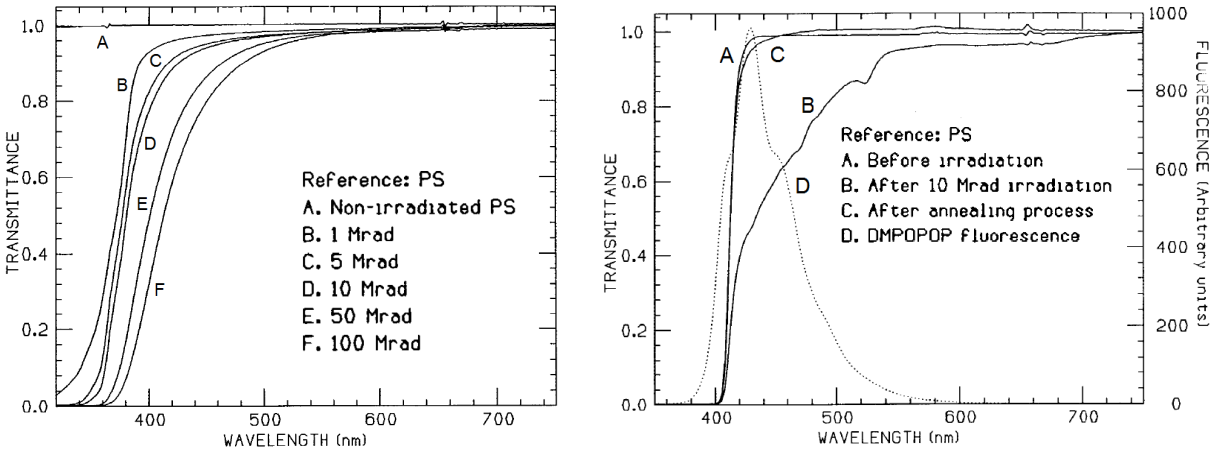

Figure 3.6: (left) Transmittance for pure polystyrene samples (without fluors) after irradiation with doses 1 – 100 Mrad (10 – 1000 kGy). (right) Transmittance for PS + 1.25 % PTP + 0.1 % DMPOPOP sample after irradiation with 10 Mrad (100 kGy) measured before and after annealing, and fluorescence of the non-irradiated sample. Both figures are from [85]. Scintillators are in form of 1 cm thick discs with a 2.2 cm diameter. Samples were irradiated in nitrogen by ^{60}C gamma source with 10 kGy/h rate and measured after two weeks of annealing in oxygen.

Experiments observed that the degradation manifests more strongly in the UV and blue than at longer wavelengths [50,85]. It is explained by the base developing an "absorptive front" shown in figure 3.6 (left) which competes with the absorption between the primary and secondary fluor. Note, that this front is partially masked in the scintillator transmission spectrum due to the intrinsic absorption of the secondary fluor which creates a similar front shown in figure 3.6 (right). This is the reason why the change in the measured light yield is usually more pronounced than the change in the transmittance spectrum, especially for shorter wavelengths. According to this knowledge, the damage is usually partially mitigated by shifting luminescent emissions to the longest practical wavelengths with fluors like POPOP and 3HF [62, 63, 83, 86, 94].

Light transmission of PMMA-based cladding of WLS-fibers also suffers from radiation damage. PMMA does not have the aromatic units which would increase its radiation stability similarly to PS [46]. But the fact that the cladding thickness is only 3 % of the fiber makes its transmission degradation somewhat less significant. The fluorinated polymers and copolymers have lower refractive indices and were found to be more resistant to gamma radiation than PMMA [95]. Nowadays, they are routinely used for second cladding layers which improve the

light transmission and radiation hardness of the fiber.

Multiple further methods were proposed to increase the scintillator radiation resistance. Changes in the manufacturing process, namely molding of granulated polymer instead of bulk monomer polymerization or making it porous was observed to increase hardness by $\sim$ 10 – 30 % [61, 86, 96]. Scintillating and WLS fibers based on fused-silica doped with cerium were claimed to exhibit the radiation hardness up to 100 kGy [97]. Great radiation hardness up to several hundred kGy was reported for polyethylene naphthalate (PEN), polyethylene terephthalate (PET), and polysiloxane (silicone) based scintillators [98, 99]. Higher fluor concentrations up to 10 % for primary and 1 % for secondary were found to increase the energy transfer between the base and fluors which improves the radiation hardness [63, 86, 94], especially for doses above 20 kGy [100, 101], see figure 3.7 (left). These approaches must be applied carefully because they lead to lowered transparency (unusual bases, granules) and an increase in self-absorption (high fluor concentrations), see figure (right). This results in reduced initial light transmittance and light yield, which is especially pronounced for scintillators with dimensions larger than 10 cm, left alone a few meter long fibers [86, 94, 102].

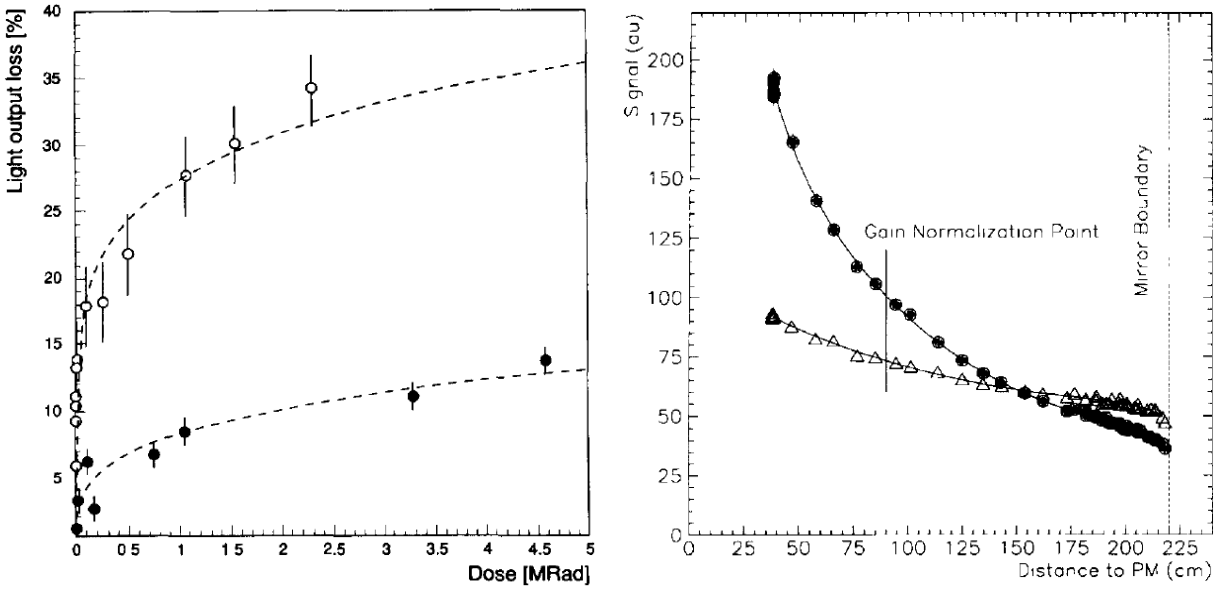

Figure 3.7: Comparison of light output for lead + scintillating fiber calorimeter with different scintillating fibers [101]. Calorimeter modules are of spaghetti type, each module has four 3.6 × 3.7 cm^2 cells with one fiber per cell, module length is 2 m, lead to fiber filling ratio is 4:1. Modules were irradiated by a 5 GeV electron beam, and measured after 10 – 120 hours of annealing. (left) Dependence of the light yield loss on the absorbed dose for standard SCSF81Y9 fibers (clear circles) and fibers with 500 ppm 3HF and fluorinated radiation hard cladding (darkened circles). (right) Dependence of the normalized light yield on distance to the photomultiplier for standard SCSF 38 fibers (darkened circles, 49 kGy dose) and fibers with 500 ppm 3HF and fluorinated radiation hard cladding (triangles, 97 kGy dose).

3.2.5 Radiation sources comparison

Different particle species produce damage in the scintillator structure in a different manner. As I discussed previously in this section, amorphous organic scintillators tend to suffer more from ionizing energy loss which produces ions and radicals and promotes chemical changes. On

contrary, non-ionizing energy loss does not affect them as much because it cannot cause lattice dislocations in already irregular non-crystal structures. That along with the wider availability are the reasons why most of the irradiation studies are performed with gamma sources like ^{60}C or ^{137}Cs.

There are certain microscopic differences in the damage produced by high energy heavy ions (p, α, etc.) and low mass electrons and photons. Low mass particles have low linear energy transfer (LET), therefore they interact sparsely and produce isolated distorted regions with ions and radicals [52]. Massive particles have high LET, and therefore produce clusters of distorted regions that can overlap with each other resulting in non-linear chemical yield along the particle track. This can be also the case for neutrons, even though they do not indulge in Coulomb interaction but can produce high LET recoil protons [103].

Number of authors employed beams of protons [71,72,74,99,104], electrons [58] and secondary hadrons emerging from heavy-ion collisions [59, 67, 78]. Available comparative data [58, 59, 67] suggest that those particles produce slightly (by 10 – 20%) higher damage than γ radiation. This might be explained by the extra damage fraction induced by non-ionizing energy losses and denser energy distribution within the material.

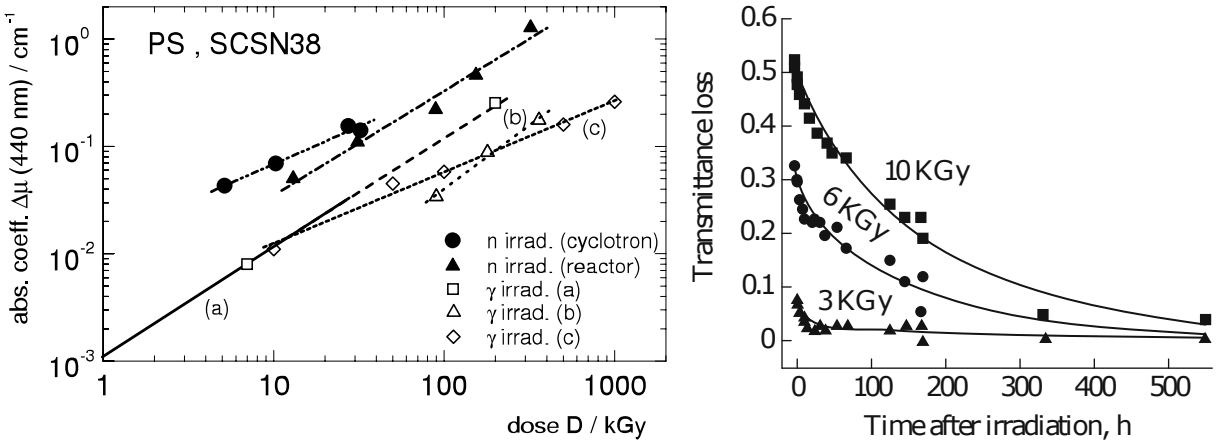

Figure 3.8: (left) Compilation of the absorption coefficient measurements at 440 nm for scintillators irradiated with multiple neutron and γ-ray doses prepared by [105] on a basis of several studies. Neutron data and γ data (a) are for $10 \times 10 \times 2.6$ mm^3 PS-based SCSN-38 scintillators produced by Kuraray. γ data (b) and (c) are for $10 \times 10 \times 3$ mm^3 pure PS samples. Neutron irradiations were performed at reactor and cyclotron with flux about 2×10^{10} n/s·cm^2, γ irradiations were performed with ^{60}C source with rate up to 100 Gy/h. (right) Recovery of the scintillator transmittance measured at 440 nm as a function of time after irradiation with ^{60}C gamma source with dose rate of 8.5 kGy/h [87]. Scintillator samples are PS + 0.4 %PPO + 0.04 % POPOP, produced as cylinders of 2.5 cm diameter and 3.0 cm thickness.

Neutron sources including reactors and cyclotrons gained an attention for scintillator irradiation studies [66, 89, 105–108]. For the comparison with γ-irradiation, neutron radiation can be characterized by its KERMA which is released by secondary recoil protons, gammas, etc. To exclude the high energy secondaries which escape the material, authors typically measure the dose absorbed by film dosimeters, which however also count the contribution from γ-background. Due to the differences in the neutron spectra and γ-background, the ratio between the neutron fluence and dose varies around 0.73 – 5.4 kGy per 10^{14} n/cm^2. Reported total neutron fluences range from 10^{12} up to 10^{17} n/cm^2 which approximately represents the range of 0.05 – 5000

kGy in absorbed dose. Minor degradation (< 30 %) of the scintillator parameters starts around $10^{13} - 10^{14}$ n/cm^2 ($\gtrsim 1$ kGy). It becomes crucial (> 50 %) after $\sim 10^{15} - 10^{16}$ n/cm^2 ($\gtrsim 10$ kGy). Authors [66, 105] indicate that for the same accumulated dose neutrons produce significantly larger damage than gammas, see figure 3.8 (left) for example. It can be explained by the additional damage coming from the non-ionizing energy loss produced by these extremely high neutron fluences. Just compare that particle fluence required to deposit the dose of 10 kGy amounts for approximately 10^{15} neutrons/cm^2 while it is only 3×10^{11} protons/cm^2 (for 30 MeV protons, see section 6.6).

3.2.6 Ambient conditions during the scintillator irradiation, recovery and operation

Recovery of the scintillator and fiber properties manifests with time and is called annealing. Below 10 kGy total recovery can be observed as shown in figure 3.5 (right), for higher doses it is usually incomplete and stops at a certain residual level. This means that the damage after annealing is usually several times lower than right after the irradiation as shown in figure 3.8 (right). Most of the scintillator properties are restored in about a week time for doses below 10 kGy [61, 80, 87, 107, 109]. For higher doses, it can take a much longer time from several weeks up to a few months [63, 81, 88, 107, 110–112]. However, fully complete annealing of highly irradiated scintillators may even take a year, especially if done in an artificial atmosphere [110].

Annealing is accelerated by the oxygen diffusion and elevated temperatures [50, 60, 109, 111, 113]. The temperature increase promotes the crosslinking, chain-scission, radical production, and other reactions due to increased species mobility in the polymer [51]. Even though scintillator heating speeds up its annealing, temperatures above 50 řC increase the permanent damage [91, 113, 114]. Lowered temperatures considerably slow down the annealing, which is important for detector systems that are kept cool with, e.g. liquid nitrogen [57].

Ambient oxygen readily diffuses into the scintillator and reacts with free radicals assisting the material changes via oxidation [52]. The oxygen influence can be beneficial if it helps to quench the radicals but more often the scintillator degradation due to color center creation is observed. Keeping the scintillator in an oxygen-free atmosphere was found to reduce both the permanent damage and recovery [60, 109, 110], see figure 3.6(right). The ideal atmospheric conditions for different materials and radiation are not yet determined.

K. Wick et al. [115] reported that photobleaching can also reduce the damage. The authors illuminated the scintillators with the light of different wavelengths during the irradiation experiment. The shorter (blue) wavelengths provided the best result than green or red. However, scintillator illumination during the experimental data taking is pointless, but post-irradiation photobleaching was not reported.

Natural aging of scintillators, namely mild light yield deterioration and development of microcracks after > 10 years of exploitation was reported by [116, 117]. For a shorter time span of 4 years only negligible < 5 % changes were recorded [118]. Aging is enhanced by operational conditions including radiation degradation, mechanical stress, temperature, humidity, and oxygen presence. Therefore, natural degradation is important for detectors with a long projected lifetime, low expected dose below few kGy, or unusual operating conditions. An example is ZEUS calorimeter which was operated for 17 years and received a dose of just ~ 100 Gy but the scintillator transmittance deteriorated by 7.4 % [117]. For higher radiation loads the radiation effects will likely dominate during the experiment lifetime.

3.2.7 Dose accumulation rate

The rate at which scintillators are irradiated was found to have a striking effect on the induced damage [59, 62, 65–67, 69, 87, 107, 109]. This is greatly enhanced by the oxygen diffusion, but other factors including scintillator structure, geometry, environment, and temperature also play a role in the process [59]. At a high dose rate, radicals form very fast and oxygen does not have enough time to diffuse into the entire material volume to assist the degradation. This results in an inverse relationship between the dose rate and radiation damage which is shown in figure 3.9.

Figure 3.9 (bottom) presents the damage in terms of the dose constant D which depends on the dose rate R. The light yield typically decreases exponentially with the dose increase, i.e. $I = I_0 \cdot \exp(-d/D)$, where I_0 and I are the light yields before and after irradiation and d is the dose. The seeming change of $D(R)$ slope around 10 Gy/h might be interpreted as a point where the oxygen is no longer able to penetrate the entire PS sample thickness of 4 mm [59]. A detailed discussion of the dose rate and oxygen role in irradiation-induced scintillator degradation can be found in a recent work by CMS collaboration [59].

3.2.8 Characterisation of the scintillator performance after irradiation

Light yield and transmittance are commonly used for scintillator characterization [57]. Light yield is measured with help of a conventional or silicon photomultiplier. β-emitter like ^{90}Sr can be used to induce the scintillation. Dependence of transmittance or absorption on wavelength is measured with help of a spectrophotometer. Time resolution investigation can be performed with help of a photomultiplier and oscilloscope with fast readout [98]. Spectrofluorometry was also utilized by several authors [44, 72, 87, 99, 104, 107, 112, 119] to measure the dependence of fluorescence on wavelength, which allows understanding the response of different dopants by varying the excitation wavelength.

A few authors performed even more sophisticated measurements trying to uncover the structural changes of irradiated scintillators with Electron Spin Resonance [103], Electron Paramagnetic Resonance [120] and Raman spectroscopy [71,106,121]. Up to now, results of such sophisticated scintillator studies are scarce and therefore the comprehensive interpretation remains ambiguous. Nevertheless, these studies are of utmost importance for understanding the basics of the radiation-scintillator interaction. Examples of other useful techniques include Positron Annihilation Lifetime Spectroscopy, Differential Scanning Calorimetry, Residual Gas Analysis, Elastic Recoil Detection Analysis, and Quadrupole Mass Analysis [52]. They find an extensive application in industrial polymer processing which strives to produce the desired material properties with radiation curing [51].

3.2.9 Performance of calorimeter modules with irradiated scintillators

Several studies investigated the performance of calorimeters equipped with irradiated scintillators in terms of response to the test beam, including teams from ZEUS [73], SSC [75,83,100] and LHC [81,101] collaborations. All the tested modules were built for electromagnetic calorimeters and only electron test beams were employed. Test modules were composed of lead and scintillators or scintillating fibers, light transfer was done via WLS-bars or WLS-fibers, the light was read out by PMTs. Module transverse dimensions were 4 – 20 cm, lengths were 5 – 25 cm. Scintillators and fibers were based on polystyrene and PMMA with standard or radiation hard (3HF) dopants. Irradiations were performed by ^{60}Co $\gamma-$source or 0.5 – 1 GeV electron beam. Up to the dose of 10 kGy scintillation, yield decreased relatively mildly up to 20 – 30 % which is comparable to results of laboratory measurements described above. Figure 3.10 shows that such scintillator degradation affected the calorimeter performance and energy resolution only

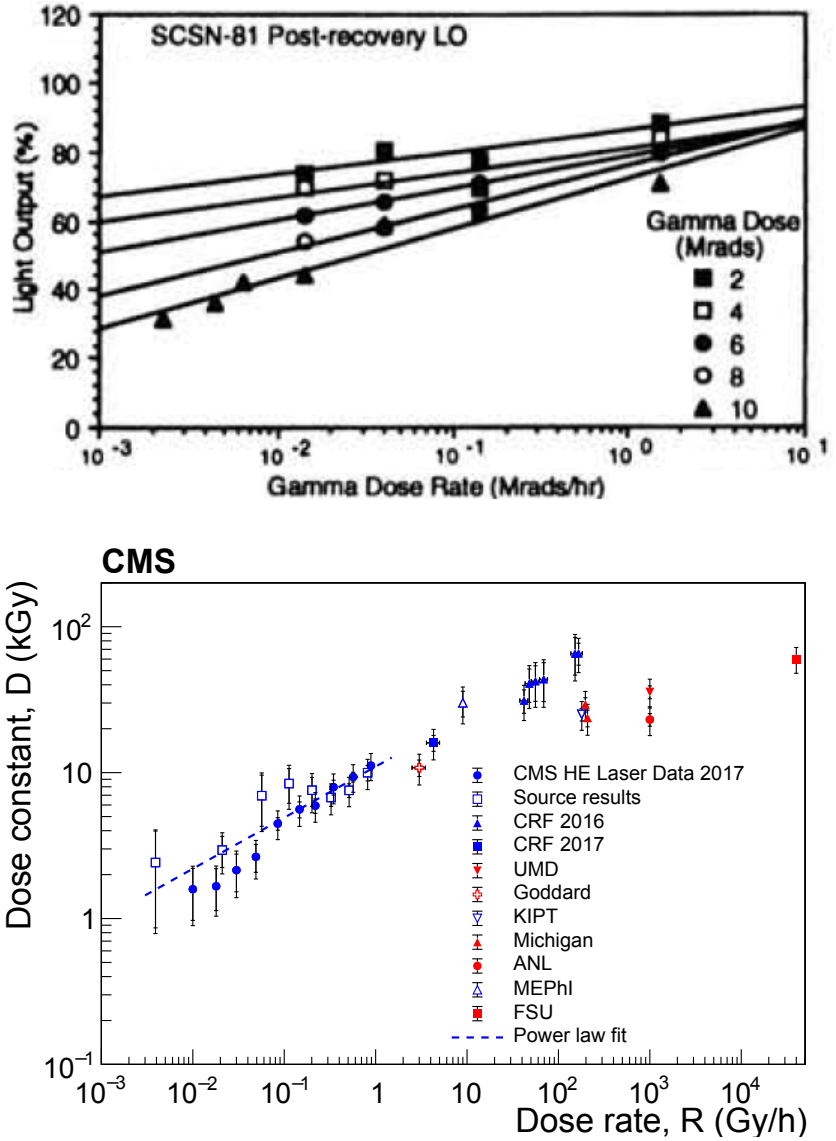

Figure 3.9: (right) Dependence of light yield on dose rate for Kuraray SCSN-81 scintillators irradiated to 2 – 10 Mrad (20 – 100 kGy) [44]. Irradiation was done with ^{60}Co source with rates in the range of 0.02 – 15 kGy/h. Scintillator samples were in form of 4 mm thick disks with 2.54 cm diameter. Measurements were done after 7 days of recovery. (bottom) Compilation of the dependence of dose constant on dose rate prepared by [59]. Low rate data are measured after physics beamtime at CMS HCAL with help of a laser and ^{60}Co source, and at the collider environment of CASTOR radiation facility (CRF) in front of CMS. High rate data are taken with gamma sources at KIPT, MEPhI, Goddard, Michigan, ANL, and UMD, an electron beam at FSU. Information on the scintillator size is included in the next figure.

negligibly. At doses around 100 kGy or above the light yield, degradation was so big, that it was advised to replace or refurbish the scintillators [75, 100, 101].

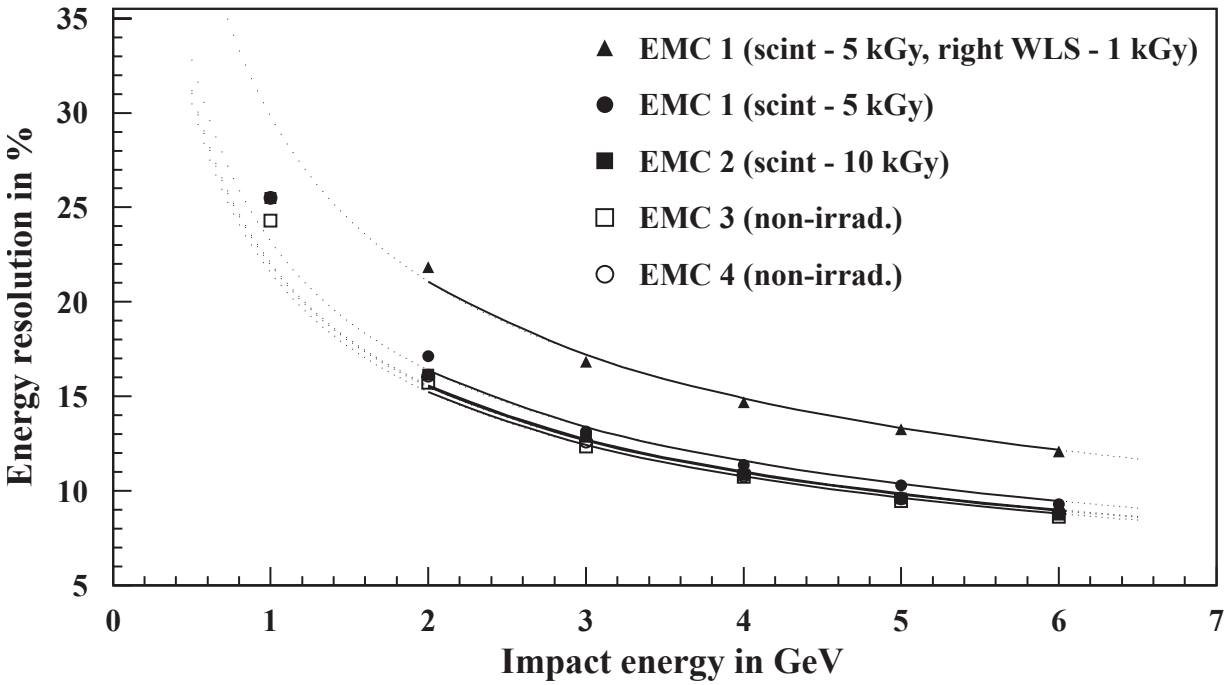

Figure 3.10: A relative energy resolution of four vertical sections of test electromagnetic calorimeter (EMC) as a function of the electron energy [73]. 21 layers of SCSN-38 scintillators formed a section and were read out altogether with two PMMA-based WLS-bars. Scintillators of EMC1 were irradiated with ^{60}Co source by 5 kGy, scintillators of EMC2 – by 10 kGy. A single right WLS-bar of EMC1 was irradiated by 1 kGy, the upper curve was measured with the light readout from only this bar (omitting the left bar).

3.2.10 Discussion of the data discrepancies

The unique mixture of the aforementioned internal and external parameters in each experiment produces the wide variation of radiation degradation which is observed by different authors. Here are several very prominent examples:

- Data from the CMS collaboration [57, 59, 69] which shows the influence of scintillator composition and manufacturing along with the dose rate effect presented in figure 3.4. One can clearly see the detrimental effect of the HCAL low dose rates below 2 Gy/h compared to laboratory studies with high rates up to 1 kGy/h. Note that in CRF, the initial ~ 20 % degradation was caused by instrumental effects and additional 10 % recovery after the annealing, which are not corrected in the presented data. A similar observation of the dose rate effect was made by ATLAS collaboration [67, 68].
- Relatively small transmission loss even after 1 MGy shown by A. Bross et al. [85] in figure 3.6 (right) is presumably due to irradiation with an extremely high dose rate of 10 kGy/h in an oxygen-free atmosphere.
- Extraordinary radiation hardness measured by H. Jivan et al. [71, 72] might be explained by the fact they used very thin scintillators with dimensions of just $5 \times 5 \times 0.35$ mm^3 and irradiated only a 1.8×1.8 mm^2 spot of it. This probably resulted in a greatly improved light transmission which allowed the scintillator to operate even after doses of 1 – 100 MGy.

- Zh. Li et al. [70] reported that a scintillator barely survived just a 10 kGy. It is easily explained by the fact that the measurement was performed right after the irradiation without waiting for the annealing to manifest. The authors reported the annealing time study but only for scintillators irradiated by 0.57 Gy with expectedly no visible effects.
- I. Bohnet et al. [73] observed significant degradation of energy resolution from 22 to 30 % for ZEUS test ECAL module, in the case when WLS-bar was irradiated with a relatively low dose of 1 kGy, see figure 3.10 (triangles). It can be explained by the fact that the entire bar is made from very radiation susceptible PMMA. The effect was further amplified by relatively low light collection due to readout from only a single 2 m long WLS-bar at one side for all the scintillators, instead of two bars from both sides. In modern calorimeters with WLS-fiber embedded in each scintillator, this should not be a problem.

3.2.11 Summary and recommendations

Based on the afore described data, it is advised to use PS or PVT-based scintillators manufactured with a high-quality process with blue or better green-emitting fluors (e.g. POPOP and 3HF). Embedding a high-quality WLS-fiber with help of high-grade glue significantly improves light collection, especially for > 5 cm wide scintillator. Both scintillators and fibers exhibit relatively good radiation hardness up to 10 kGy if irradiated in the air at room temperature by a high rate (> 100 Gy/h) laboratory source. They may be operated even up to 100 kGy if the excessive light yield degradation can be tolerated or mitigated by calibration.

Variation of any internal or external parameters affects the performance, so the best practice is to study the exact scintillator type under the anticipated experimental conditions. If this is not possible, like in the case of a low rate environment of a collision experiment (< 1 Gy/h), its additional effect shall be evaluated based on the available data. This is essential because depending on the dose rate, scintillator hardness can be reduced by as much as an order of magnitude. Although, ionizing energy loss produces much more damage than non-ionizing, above very high neutron fluence of $\sim 10^{15} - 10^{16}$ scintillator performance also deteriorates significantly.

Scintillator radiation tolerance can be further improved by the utilization of different bases and/or very high fluor concentrations. However, these approaches are only justified for very harsh radiation environments > 10 kGy, because they significantly decrease the intrinsic transmission and light yield.

3.3 Silicon sensors

Silicon detectors belong to the most important detectors in particle physics. They are used for the detection of ionizing particles, photon detection, and gamma-spectrometry. Similar to scintillators they suffer from radiation exposure, but in quite a different manner. Radiation hardness limits vary by many orders of magnitude depending on the detector technology on the particle species. Unanticipated radiation load varies from experiment to experiment usually in range of $10^{10} - 10^{16}$ n_{eq}/cm^2.

3.3.1 Semiconductor detector materials

Semiconductor detectors are made from inorganic materials and usually require just a few eV for electron-hole (e-h) pair creation which is much less than ~ 100 eV for scintillators or ~ 30 eV for gases (electron-ion pair) [118]. This results in a much higher signal providing superior energy resolution and detection efficiency. However, the complex production technology and cost

make scintillators and gaseous detectors much more appealing for high-volume applications. The small sensitive area used to detect radiation (μm – mm scale) is unmatched for precise position measurements, i.e. particle tracking. The small detector volume and high carrier mobility provide an excellent charge collection time $\sim 10^{-8}$ s [11] which is crucial for timing applications, e.g. fast decay measurements.

Silicon sensors dominate the detector market because of the great material availability (Si composes 27.7 % of the Earth's crust), the moderate band gap of 1.12 eV allowing the room temperature operation, and maturity of the microelectronics processing technology. The latter offers large surface (15 — 20 cm diameter) sensors with high quality and fair price, which can also be integrated with readout electronics during the manufacturing. Silicon's low atomic mass of 14 makes it ideal for tracking detectors where energy loss in the detector should be minimal (see $dE/dx \sim Z$ in 2.1) [11].

Germanium is the next material by usage. Due to higher Z = 32 it is widely applied in gamma spectroscopy (see $\sigma_\gamma \sim Z$ in 2.2). High-purity germanium detectors (HPGe) provide astounding energy resolution down to 0.1 %. But due to a very small band gap of 0.66 eV HPGe have to be cooled down to reduce the thermally generated noise, which is typically done with liquid nitrogen at 77 °K [122].

Diamond is the third popular material in particle physics, although it is actually an insulator with a 5.5 eV band gap. Therefore, there is no need for doping and bias voltage supply, but at the same time produced signal is much smaller than for Si. It is the most radiation-hard material among semiconductors due to its low noise generation and long mean free path for carriers, it can be utilized up to 10^{16} n_{eq}/cm^2 [28]. However, signal response and consequently signal-to-noise ratio for detected particles is also much lower than for Si. Moreover, diamond crystals are very expensive and difficult to grow. So, diamond is usually applied in tiny beam monitoring or vertex detectors which are placed inside the beam or closest to the collision point.

At last, there are compound semiconductors, including GaAs, CdTe, CdZnTe, and others. They have moderate band gaps ∼1.4 eV to allow room temperature operation combined with high-Z providing better energy resolution than Si. Unfortunately, they typically suffer from charge collection problems, characterized by the product of carrier mobility μ and carrier lifetime L. Namely, for silicon μL is bugger than 1 cm^2 V^{-1}, whereas in compound semiconductors it is in the range 10^{-3}˘10−8 cm^2 V^{-1} [11]. Nowadays, a major effort is made to overcome the downsides of compound semiconductors or find better ones.

3.3.2 Silicon detector structure and operation

When an ionizing particle strikes the semiconductor it releases electrons from atoms which are left with unfilled "holes" in the electronic structure as shown in figure 3.11 (left). Electrons and holes are the signal carriers – they migrate within the material and can be collected by metallic contacts at the surface if the bias voltage is applied. The value of the gap between conduction and valence bands is very important for semiconductor properties. The lower the band gap the less the energy for e-h pair production. This results in a larger signal but at the same time in higher thermally excited intrinsic carriers (noise). The energy required to form an electron-hole pair is higher than the band gap, as part of the energy goes into excitation of lattice vibrations (phonons), i.e. for silicon $E_{gap} = 1.12$ eV while $E_{e-h\ pair} = 3.6$ eV. The most probable charge deposition in a 300 μm thick silicon detector by MIP is about 3.5 fC or 22000 electrons [11]. However, due to thermal vibrations, there are about 4 orders more intrinsic charge carriers in the material. Therefore, detector volume has to depleted of the intrinsic carriers for operation. This can be achieved by very high purity and cryogenic cooling as in the case of HPGe.

Alternatively, pn-junction operated under reverse bias voltage can be implemented as in the

case of silicon sensors. It is a junction of the n-type silicon layer (excess of electrons) with a p-type layer (excess of holes). When these layers are connected, electrons diffuse from n-region to p-region and holes diffuse from p-region to n-region, and they recombine around the junction. Ions that are left behind by recombined carriers, attract further electrons and holes until the equilibrium between electric fields created by ions and excessive carriers is settled. The region around the junction becomes depleted. The depletion region can be extended through the detector volume by application of reverse bias voltage (V^+ to n-type layer, V^- to p-type) which will force the remaining charge carriers to diffuse and recombine as shown in figure 3.11 (top right). This can be explained as the increase of the potential barrier between the valence and conduction layers by eV as depicted in figure 3.11 (bottom right) [123]. It suppresses the further diffusion across pn-junction.

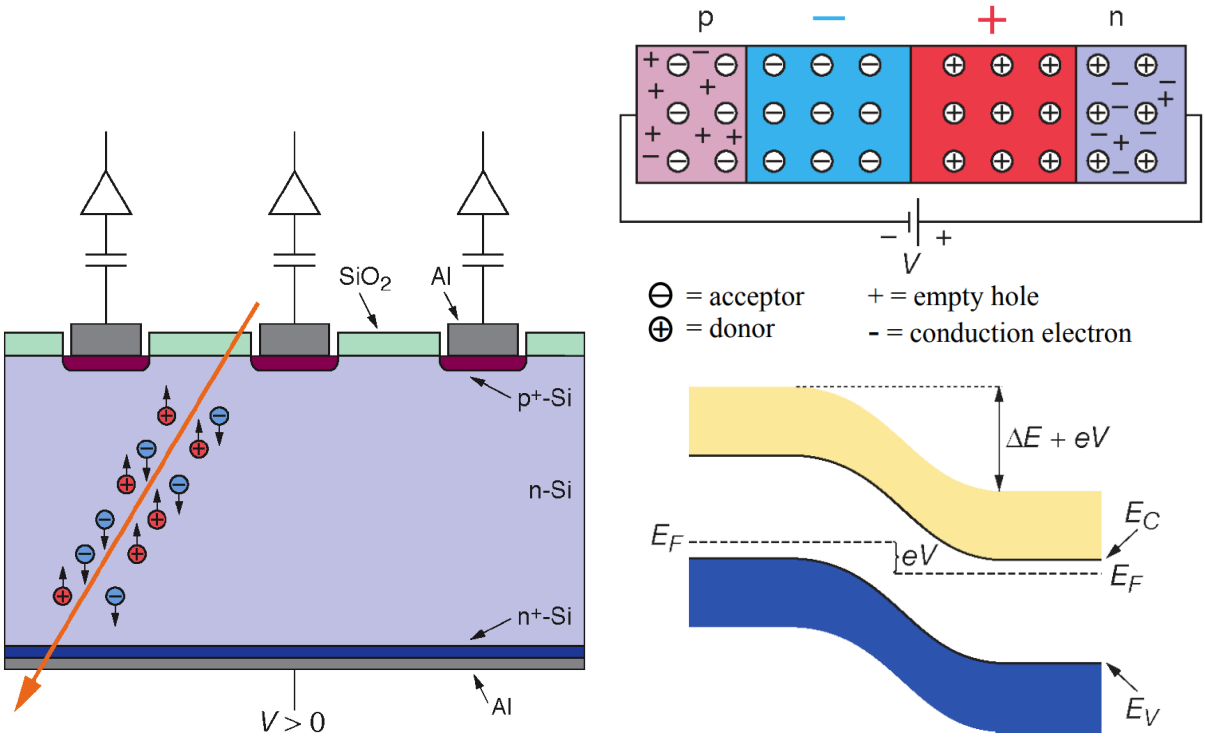

Figure 3.11: (left) Typical internal structure of n-type silicon detector operated in reverse bias regime which is struck by an ionizing particle producing electron-hole pairs along the track. Electrodes are connected to basic readout consisting of coupling capacitors and charge amplifiers. (Top right) Pn-junction with applied reverse bias voltage. (bottom right) Diagram of energy levels for this pn-junction. E_F is the Fermi level, E_C is the conduction band, ΔE is the difference between Fermi levels of n and p-type layers which causes the diffusion of excessive carriers. All pictures are from [123].

Monocrystalline silicon used in semiconductor devices and detectors is obtained from ultra-purified polycrystalline silicon which is in turn produced from SiO_2 [20]. The most widespread single-crystal growth techniques are Czochralski (Cz) and Float Zone (FZ) [122]. In Czochralski method, polycrystalline silicon is melted with dopants, then rod-mounted seed crystal is dipped into and slowly pulled up and rotated extracting a large single-crystal cylindrical ingot from the melt. In the Float-zone method, a seed crystal is attached to the end of a polycrystalline rod which is passed through an RF heating coil, which creates a localized molten zone from

which the crystal ingot grows. Czochralski method provides more than two times bigger crystal diameters (up to 46 cm) and is much cheaper than Float-zone, while the latter offers much lower impurity concentrations ($<$ 1 ppm impurities and $<$ 0.1 ppb electrically active impurities) and more homogeneous dopant concentration. Shortcomings of Cz silicon could be overcome with the MCz method which is a variation of the CZ method with a magnetic field, perpendicularly applied to the melted silicon surface allowing to better control the crystal properties. The active thickness of FZ sensor can be altered via high-temperature deep-diffusion of dopants from the rear sensor side (dd-FZ).

Yet another option is the epitaxial (EPI) silicon which is usually grown by vapor-phase epitaxy (VPE) deposition of $SiCl_4$ or a similar compound on the low resistivity Cz wafer. Usually, it requires a substrate thickness of at least 300 – 600 µm which introduces the undesired non-active layer in the sensor. Therefore, it is rarely used for tracking detectors which require the whole sensor volume for detection of high energy particles [20]. On contrary, epitaxy is commonly used for bipolar transistors, complementary metal-oxide–semiconductors (CMOS) devices, silicon photomultipliers, and compound semiconductors. However, along with the significant cost advantage, it brings many challenges including control of the growth process and surface purity, prevention of diffusion of dopants from the substrate to the EPI layer, and surface protection during manufacture resulting in higher variations of doping density, resistivity and thickness.

The produced silicon ingot is sliced into 3 – 500 µm thin wafers which are further lapped, etched, polished, and cleaned. Then wafer passivation is performed via surface oxidation producing $\sim$ 300 nm SiO_2 layer to eliminate surface leakage current. Extra layers of Si_3N_4 can be added for improved protection. After this specific regions are doped to create optimized electric properties, including highly doped p+ and n+ areas forming the desired electric field; p-stops, p-sprays, guard rings for isolation of neighboring junctions and leakage current protection; and readout connection via capacitors, resistors, and transistors. Implantation or diffusion of phosphorus or arsenic produces the n-type region, boron is used for p-type. Doping is performed with help of photolithography and etching which create windows within the SiO_2. Unwanted radiation damage is annealed in the oven, e.g. at 600 °C for 30 minutes [20]. Electric contacts are created with aluminum metallization, again with help of photolithography and etching. Finally, a wafer can be cut into individual devices and sensors.

3.3.3 Applications of silicon detectors in HEP

Today, a wide variety of detector types are designed for different applications. N-type bulk is the most widespread basic sensor structure where a few µm thin highly doped p+ region is used for charge readout and several hundred µm wide lightly doped n region is used as the sensitive volume as shown in figure 3.11 (left). The reverse structure of the p-type bulk sensor with n+ electrodes requires more complicated manufacturing, but offers improved properties including radiation hardness, see section 3.4.

Individual electrodes are organized as cm-scale pads and strips, or µm-scale pixels. Pixels offer the most straightforward way to achieve 2D particle tracking, they provide a large signal-to-noise ratio and low leakage current due to small pixel volume, but require a large number of readout channels which together with complex structure results in large power consumption of electronics and high cost. 2D tracking can also be achieved when multiple strips are aligned at a specific angle either as separately or within double-sided sensors like the CBM STS tracking system, see section 4.2. Many layers of sensors form the 3D tracking detector.

Readout electronics can be connected by thin bonding wires ($\sim$ 25 µm), by two-dimensional arrays of solder bumps, i.e. hybrid pixel sensors, or integrated together with the sensor, i.e. Monolithic Active Pixels (MAPS) [11]. Other important silicon particle detectors include Silicon

Drift Detectors, 3D silicon detectors, Depleted Field Effect detectors (DEPFET), Silicon On Insulator (SOI) [122].

Semiconductor photodetectors are commonly applied for particle identification and energy measurements, e.g. in Cherenkov detectors and calorimeters. Silicon-based photosensors are realized either as single padded PIN diodes and Avalanche Photo Diodes (APD), or as pixelated Charge-Coupled Devices (CCD), CMOS sensors and Silicon Photo Multipliers (SiPM). Furthermore, germanium detectors are widely utilized in gamma spectrometers.

Detector performance is limited by its structure, material properties, ambient effects, and readout electronics. Ultra-pure silicon with high resistivity ρ ($\rho > 1$ kΩcm or doping of $10^{12} - 10^{15}$ cm^{-3}) is required to minimize the amount of thermally excited intrinsic charge carriers. Collection time also depends on the material quality, namely carrier mobility, and on the sensor volume.

Position and energy resolution depend on statistical fluctuations of the energy loss, diffusion of charge carriers which is often influenced by the ambient magnetic field, the distance between centers of strips or pixels (detector pitch), signal readout characteristics and signal-to-noise ratio. Statistical fluctuations occur because of electronic and lattice excitations that can be described by the Fano factor (about 0.1 in Si and Ge) multiplied to the energy resolution $\sigma E/E = \sqrt{FE_{eh}/E}$, where E is the deposited energy and E_{e-h} – energy required for the creation of electron-hole pair [11]. Another source of fluctuations is the deviation of actual energy loss from its mean or most probable value. However, usually, fluctuations are dominated by the deviation of actual energy loss from its mean or most probable value and noise produced by the readout electronics.

3.4 Radiation hardness characterisation for silicon sensors

Silicon sensors utilized for direct detection of charged particles are of big concern to the radiation studies, particularly due to the fact that they are usually situated closest to the collision point and irradiated more than other components [124]. Optoelectronic components are also affected by radiation effects resulting in increased leakage current and degradation of main performance parameters including: illumination output of light-emitting diodes and lasers, current transfer ratio of optocouplers, a power output of solar cells, efficiency of charge-coupled devices, photocurrent of photodiodes and signal-to-noise ratio of silicon photomultipliers. The frequency of crystal oscillators can also be affected. Bipolar transistors and diodes suffer from increased leakage current and gain degradation due to the radiation damage.

The radiation hardness of standard planar silicon detectors is already thoughtfully studied for more than 50 years. It is essential to understand the silicon sensor fundamentals to properly evaluate the new sophisticated devices like Silicon Photomultipliers (SiPM) which are not yet well studied. In this section, I present the most important information on the silicon detector performance in harsh radiation conditions and ways to improve it. For more exhaustive information, I advise looking into the PhD thesis [20] and great recent overview by M. Moll [25], who is the co-spokesperson of RD50 collaboration. RD50 concentrates on radiation hardness investigation for semiconductor devices used in very high luminosity colliders [125]. I also briefly discuss the possibilities for optimization of detector signal processing and electronics for radiation-damaged sensors, for an extensive overview of the subject I recommend checking the Lecture Notes by H. Spieler [126]. For a comprehensive review on the damage mitigation techniques for CMOS microelectronics, their firmware and software, refer to PhD thesis of J. Gebelein [127].

3.4.1 Defects produced in a silicon sensor

Radiation can produce permanent damage to the sensor structure or just transient effects which disrupt the sensor operates in the present moment. Transient change of device's state may occur if an ionizing particle with sufficient energy stroke a sensitive node of the semiconductor logic. These phenomena are called single event effect (SEE) and it is being intensively studied for microelectronic devices like microprocessor, memory, FPGA, or power transistors [128]. Most frequent are the Single Event Upsets (SEU) – soft non-destructive errors. They normally appear as transient pulses in logic or support circuitry, or as bitflips in memory cells or registers. Some devices like MOSFETs may experience hard errors: Single Event Latchup (SEL), Power Burnout and Gate/Dielectric Rupture resulting in a very high current flow through the device. They may be cleared by a timely power reset or may cause a permanent device failure. Nevertheless, SEE is usually not related to cumulative damage in silicon sensors which is described further.

Cumulative damage can be divided into bulk and surface damage in terms of origination inside a sensor structure or ionizing and non-ionizing energy loss induced damage in terms of the interaction mechanism. Considering the ionizing damage, produced electron-hole pairs do not lead to damage in sensor active volume, as it is meant to conduct current and therefore only temporal current transients can occur. However, it is particularly important for the sensor surface to be commonly made of silicon dioxide (see figure 3.11 (left)) which has a highly irregular structure. Produced highly mobile electrons escape SiO_2 quickly, while many holes can be trapped there creating "build-up charge" [129]. Consequently, a conductive layer of electrons attracted to this charge is created in silicon bulk near SiO_2–Si interface increasing the surface leakage current. Note, that some trapped holes can recombine with bulk electrons by tunneling effect, so manufacturers can make the dioxide layer thinner to decrease this effect.

Depending on the technology and crystal orientation, the amount of build-up charge saturates at around $1.5 - 3.5 \times 10^{12}$ e/cm^2 resulting in the surface leakage current of $2 - 6\mu$A/cm^2 after irradiation with a total dose of about 100 –1000 kGy [130]. Typical values before irradiation are on the order of 10^{10} e/cm^2 and an nA/cm^2, respectively. Surface damage is of big importance for MOSFETs which have thick oxide layers, their gate threshold voltage and leakage current can be severely affected. It is also very important for strip detectors where it leads to larger signal sharing and increased interstrip capacitance producing noise [122]. Compound semiconductors suffer the least because of the higher surface state density.

The main reasons for the permanent sensor damage originate in the structural changes of the silicon lattice. They include atom displacements and transformations inside the sensor bulk via non-ionizing energy losses of the incident particle. Lattice changes are not so important for the surface dioxide, as it has a highly irregular structure.

Moreover, particles, e.g. neutrons, striking the atomic lattice can invoke nuclear reactions such as $^{30}Si + n \rightarrow {}^{31}Si + \gamma$; $^{31}Si \rightarrow {}^{31}P + e^- + \overline{\nu}$ and other secondary processes leading to the change of the initial doping concentration [131]. Such effects can be very significant especially for the boron-doped silicon under high fluence of thermal neutrons. The ^{10}B dopant has extremely high cross section of 3840 barns for thermal neutron capture ($n+ {}^{10}B \rightarrow {}^{7}Li+ {}^{4}He$) that can lead to extra damage not predicted by NIEL model for the pure silicon if boron concentration exceeds 10^{17} cm^{-3} [132].

Displaced atoms often end up in interstitial (I) positions in the lattice leaving vacancies (V) at original positions. Both I and V do not remain stable, but often recombine with each other, i.e. undergo the annealing which is elevated with temperature. The recombination rate depends on the ratio of the distance between I and V and the lattice constant. On average about 60 % of all produced Frenkel pairs recombine, while this rate can reach up to 95 % in regions with very high defects concentration [133]. Defects that did not recombine with each

other can combine with defects of the same type (V+V) or with dopant atoms and impurities creating different long-living defect centers, e.g. E-center (V+P), A-center (V+O_2), etc. [26]. These centers can form complex cluster defects, dissociate and recombine depending on the temperature and presence of other defects around. Interestingly, there is yet no clear evidence for dependence on the bias voltage applied, so irradiation tests are generally performed without bias [134].

Generated lattice defects may be electrically active and together with the change in initial dopant concentration, they can affect the sensor operation. Carrier recombination in silicon sensors is governed by Shockley-Read-Hall statistics where electron transits between bands through energy states attributed to dopants or defects which are called traps. Various types of introduced states in the electronic band model of the device are shown in figure 3.12. Introduced states can be divided into deep and shallow level defects with respect to their location within band diagram or effective interaction distance and probability (shallow defects are located closer to conduction or valence band). The defects can affect the sensor properties in the following ways [135]:

- Increase the leakage current by the generation of extra charge carriers (electrons and holes), trapping and following the emission of carriers and helping carriers to tunnel through the band gap.
- Change the space charge density in the active volume and the electric field distribution around the pn-junction, therefore changing the resistivity, full depletion voltage, and the amplification (gain).
- Decrease the charge collection efficiency by recombination and trapping of the signal carriers and compensation of the initial dopant centers.

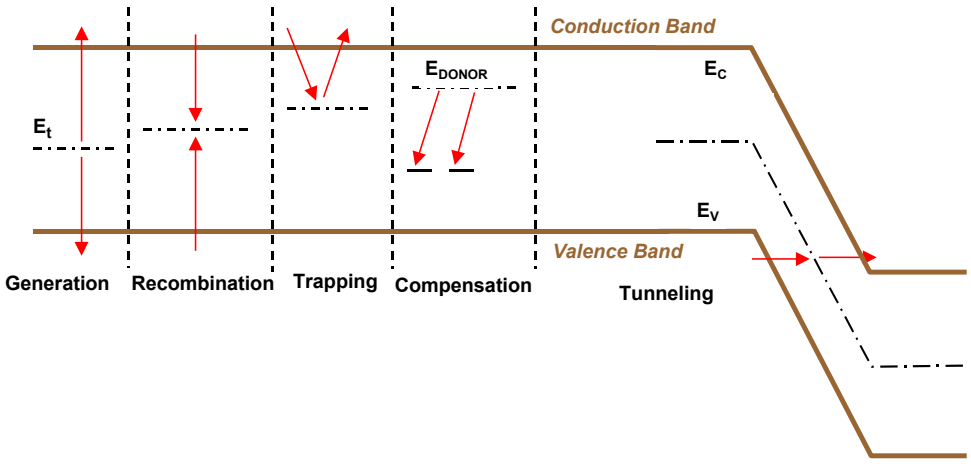

Figure 3.12: Energy levels and disruptive functions of various defects in the band zone diagram of silicon [134].

Multiple experimental techniques are utilized to study the parameters of microscopic defects as capture cross sections, level position in the band gap, concentration, and annealing behavior. They include Capacitance Deep Level Transient Spectroscopy (C-DLTS), Thermally Stimulated Current spectroscopy (TSC), Transient Current Technique (TCT), Photoluminiscense methods, etc. [20]. In conjunction with them, techniques studying the changes in a lattice structure and

chemical configuration of the material can be used, such as Annealing studies, Transmission Electron Microscopy (TEM), Electron Energy Loss Spectroscopy (EELS), Energy-Dispersive X-ray spectroscopy (EDX), Electron Paramagnetic Resonance spectroscopy (EPR), Fourier Transform Infrared Spectroscopy (FTIR), etc. [136]. Extensive correlation studies employing various techniques on the same device are required for the proper identification of the various defects. Moreover, the applicability of these methods is limited due to the empirical and non-comprehensive understanding of the microscopic defect kinetics, so relating it to the degradation of the device's macroscopic properties is not always possible [25, 136]. Data from irradiations by hadrons, especially neutrons, is even more difficult to analyze and interpret as the complex defect clusters are abundantly produced there in addition to single defects. Therefore, extensive tests of the device's performance are always required to gain basic knowledge of its radiation hardness. The principles of these experimental tests are described in the following subsections.

3.4.2 Basic characteristics of pn-diodes

In a nutshell, silicon sensors are based on reverse biased pn-junction, so I provide a short description of their basic electric characteristics to aid further discussion.

Current-voltage (IV) characteristic expresses general electric behavior of pn-diode under applied bias voltage as shown in figure 3.13 (left). Shockley diode equation describes the IV curve of an ideal diode as

$$I = I_S \left(e^{\frac{eV_{bias}}{\eta k_B T}} - 1 \right) \tag{3.3}$$

where I is the diode current, I_S is the saturation leakage current in the absence of particles, V_{bias} is the bias voltage, k_B is the Boltzmann constant, and η is the ideality factor. η has a value between 1 and 2 depending on the dominant charge movement process being diffusion or recombination [20].

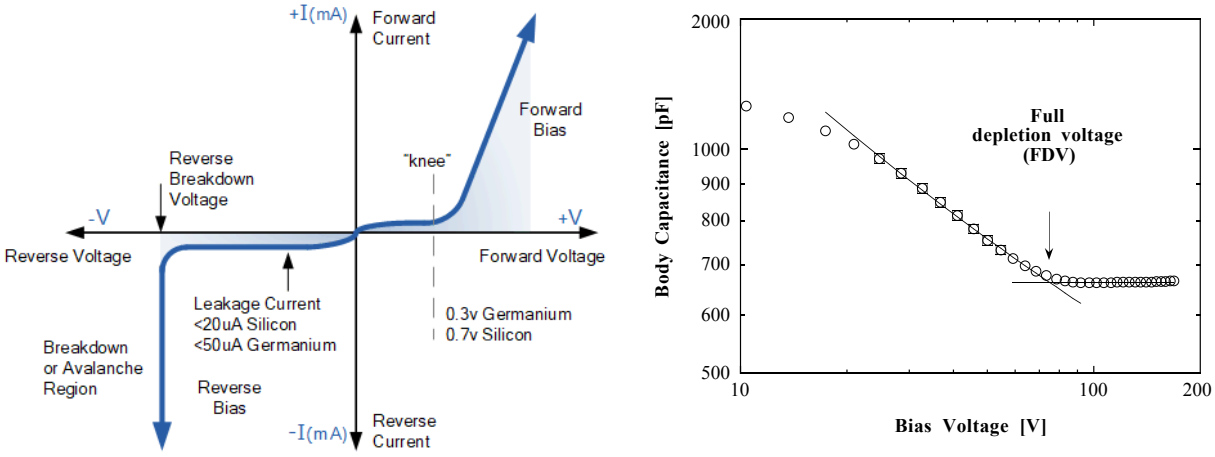

Figure 3.13: (left) Dependence of typical pn-diode current on bias voltage [137]. (right) Dependence of standard strip sensor capacitance on bias voltage [138]. Sensor was made from high-resistivity n-type bulk silicon with a 300 µm thickness and 50 µm pitch.

In the forwarding bias regime just a small current flows over the junction until the built-in voltage is exceeded allowing the current to flow freely ("knee" in figure 3.13 (left)). The built-in voltage corresponds to the width of the intrinsic depletion region created by ionized donors and

acceptors around the junction. When the forward current is sufficiently large, IV curve becomes a straight line whose slope represents the bulk resistance.

Detectors are operated in a reverse bias regime with their sensitive volume depleted of free carriers, so only a very small leakage current caused by the sensor impurities and other imperfections remains. However, if the breakdown voltage V_{bd} is reached, an extremely high current starts to flow through a diode due to avalanche carrier multiplication which usually results in permanent damage and failure. But avalanche diodes are designed to work in this region, see subsection 3.5.2. Measurement of the reverse IV curve allows to estimate the typical leakage current and locate the breakdown voltage for avalanche diodes.

Capacitance–voltage (CV) characteristic describes the amount of charge stored in the sensor volume as shown in figure 3.13 (right). The capacitance decreases with the increase in reverse bias voltage until the whole sensor volume is depleted from the charge carriers where it reaches the value defined by the sensor geometry

$$C = \frac{\epsilon\epsilon_0 A}{D} \tag{3.4}$$

where ϵ is the relative permittivity of silicon, ϵ_0 is the vacuum permittivity, A is the sensor area and D is the sensor thickness.

One can determine the voltage required for the full depletion from the kick in CV curve shown in figure 3.13 (right). Note, that in real sensors capacitance continues to slightly decrease even after the sensor was fully depleted due to the lateral extension of the depletion zone around the individual strips or pixels.

For simple one-sided abrupt junction, CV measurement can be used to obtain the built-in voltage and the doping density profile. However, for more complex junctions one would need at least some degree of knowledge on the device's internal structure to make assumptions required for precise calculations.

3.4.3 Leakage current

Arguably the easiest characteristic to be measured, leakage current can be also called reverse current as it is measured for a reversely biased sensor or, in the case of optical sensors for which it is measured in the darkness, dark current. Usually, leakage current increases after irradiation mainly due to three mechanisms related to the increase of defect amount in the lattice [20]. Firstly, extra charge carriers are generated by defect levels close to the middle of the band gap, which is unrelated to the useful collected signal. Secondly, carriers from the useful signal can be trapped and then released after the collection time window. Thirdly, some carriers can tunnel through the band gap via new intermediate states in the band gap. Leakage current increases linearly with the sensor volume, applied bias voltage and equivalent irradiation fluence according to [124]

$$\Delta I_{leak} = \alpha \cdot V \cdot \Phi_{eq} \tag{3.5}$$

where α is the current related damage factor, ΔI_{leak} is the change in the leakage current after irradiation and V is the detector volume. α in silicon is usually measured to be in range from 10^{-17} A/cm to 10^{-18} A/cm depending on the incident particle type, temperature and time after irradiation (annealing) [135]. For example, $\alpha = (3.99 \pm 0.03) \times 10^{-17}$ A/cm was observed for data presented in figure 3.14 (left).

As one can see in figure 3.14 (left), the value of leakage current divided by the sensor volume scales with the equivalent fluence and is usually independent of the detector material including resistivity, impurity concentration, crystal orientation, silicon type, and manufacturing process.

Therefore α remains constant over several orders of fluence and can be utilized for the fluence measurement [139]. Note that this holds for bulk-generated currents, like in the case of hadron (p, π, n, etc.) irradiation which mostly affects the sensor bulk and tends to generate defect clusters. But in the case of gamma irradiation surface oxide is heavily affected and mostly point-like defects are produced along with which results in I_{leak} dependence on the oxygen concentration in the material and quadratic dose-dependence [25].

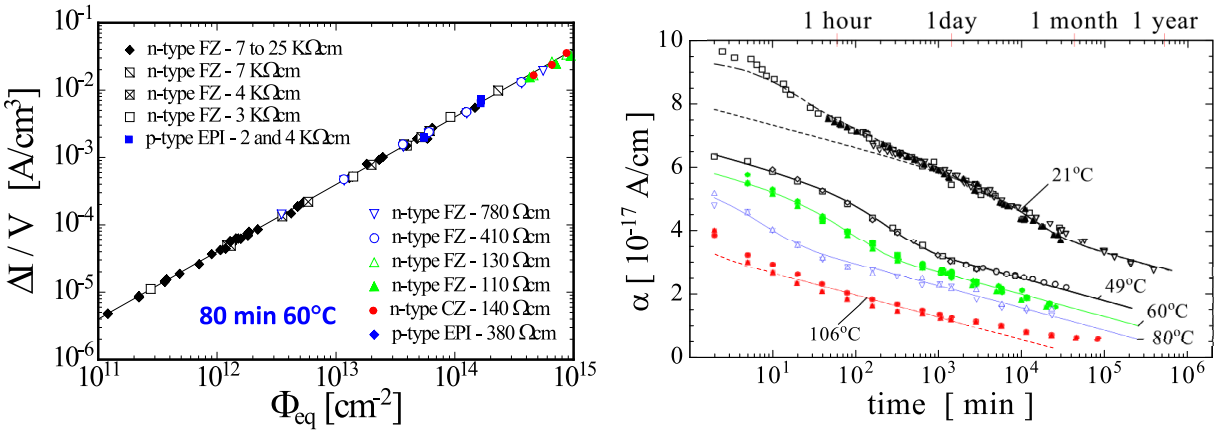

Figure 3.14: (left) Dependence of the leakage current density on the 1 MeV equivalent fluence for single padded sensors produced with different silicon materials and technologies after fast neutron (5.2 MeV mean energy) irradiation. Current measurements were performed after annealing of 80 min at 60 °C and are normalized to the current measured at 20 °C. (right) Annealing of the current related damage factor α with time elapsed after irradiation measured at different temperatures. Both plots are from [25].

Leakage current strongly depends on the sensor temperature because the defect energy levels in the band gap and the band gap itself depend on it. If a temperature-controlled environment is not available for the measurements, a measured value of I_{leak} can be scaled to reference temperature (often "room temperature" like 20, 22, or 25 °C) by the following equation which is derived from equation (3.3) [25]

$$I_{leak}(T_{ref}) = I_{leak}(T) \cdot \left(\frac{T_{ref}}{T}\right)^2 \cdot \exp\left(-\frac{E_{eff}}{2k_B} \cdot \left(\frac{1}{T_{ref}} - \frac{1}{T}\right)\right) \tag{3.6}$$

where E_{eff} is the effective activation energy recently determined for Si as 1.214 ± 0.014 eV [140] which is close to band gap (1.12 eV [141]), and k_B is the Boltzmann constant. In practice, one can apply a rule of thumb stating that the leakage current changes in ~ 2 times with the change of temperature by 9 řC [124].

Almost any radiation-dependent parameter changes after some time because of migration and recombination of defects produced in the sensor. This process is called annealing or self-annealing and is getting faster if carried out under the increased temperature. Commonly, a standard annealing time of 80 minutes at 60 °C is applied that scales to approximately 100 days at room temperature. Leakage current decreases after annealing, for example after standard annealing for sensors irradiated with fluence around 10^{13} n_{eq}/cm^2 it decreases by a factor of 2 – 3 as shown in figure 3.14 (right) [25].

Leakage current shall be always kept as low as possible, often with help of the sensor cooling and annealing. The lower I_{leak} is, the lower is the noise and the higher is the maximal bias

voltage that can be applied to the detector not leading to the thermal runaway. Contemporary detectors consist of hundreds to millions of sensors and, consequently, power supply channels, so increased leakage current leads to significantly increased power consumption. Typical current before irradiation is measured in units of μA or even nA, and its increase up to mA is often considered as a limitation. Therefore, it is important to measure I_{leak} for irradiated sensors to see whether they still meet the technical requirements.

3.4.4 Full depletion voltage and effective space charge

The depletion voltage is the bias voltage that is reversely applied to the sensor nodes, which produces electrical field throughout the sensor and removes the initial free carriers, so even a small amount of charge deposited by the ionizing particle can be measured. The full depletion voltage V_{FD} is the bias voltage required to deplete the whole sensor volume of free carriers and it is especially important for detectors with large sensitive volume which are operated at several hundred Volts. It is known to be directly related to the effective space charge N_{eff}, which can be seen as effective doping (impurity) concentration of electrically active shallow levels [135]. N_{eff} is the difference between the amount of donor-like and acceptor-like impurities inside the bulk, therefore representing the number of free carriers that shall be removed from the bulk for the sensor to become fully depleted. Dependence of V_{FD} on N_{eff} and sensor thickness D is expressed by [124]

$$V_{FD} = \frac{e}{2\epsilon\epsilon_0} \cdot \mid N_{eff} \mid D^2 \tag{3.7}$$

where e is the electron charge, ϵ is the relative permittivity of silicon and ϵ_0 is the vacuum permittivity.

Figure 3.15 (left) shows the evolution of V_{FD} and N_{eff} depending on the accumulated fluence for the n-type bulk sensor, which can be described by [124]

$$N_{eff}(\Phi_{eq}) = N_D \cdot exp(-c\Phi_{eq}) - N_A \cdot exp(-d\Phi_{eq}) + (\beta_D - \beta_A)\Phi_{eq} \tag{3.8}$$

where N_D is the initial donor concentration, N_A is the initial acceptor concentration, c and d are corresponding doping removal constants, and β_D and β_A are introduction parameters for donor-like and acceptor-like defects.

For small fluences effective doping exponentially decreases until it reaches a minimum and then further increases with fluence. The minimum around fluence of 2×10^{12} n_{eq}/cm^2 corresponds to the point of type inversion, where the concentration of acceptors becomes equal to the concentration of donors corresponding to almost intrinsic silicon [25]. Afterward, initially n-doped silicon bulk becomes effectively p-doped. It happens due to the experimentally found fact that the introduction of acceptor-like defects is dominant over the donor-like ones, at least for high-resistivity detector grade float-zone (FZ) silicon [124]. As one would expect, no type of inversion is generally found for the p-type bulk devices. However, in some irradiation experiments, silicon sensors produced by non-standard floating zone (FZ) technology were observed to deviate from this rule, i.e. p to n-type bulk inversion or no inversion for n-type sensors up to high fluences [25].

Unlike the monotonic decrease of I_{leak} with the annealing time, N_{eff}/V_{FD} exhibits a more complex trend presented in figure 3.15 (right). At first, it undergoes beneficial annealing (decreases), but after approximately 100 minutes under 60 °C, the reverse annealing (increase) starts to manifest. This puts a limitation on the application of the sensor annealing which is absolutely beneficial for the leakage current but can be become detrimental for V_{FD}. Sensor

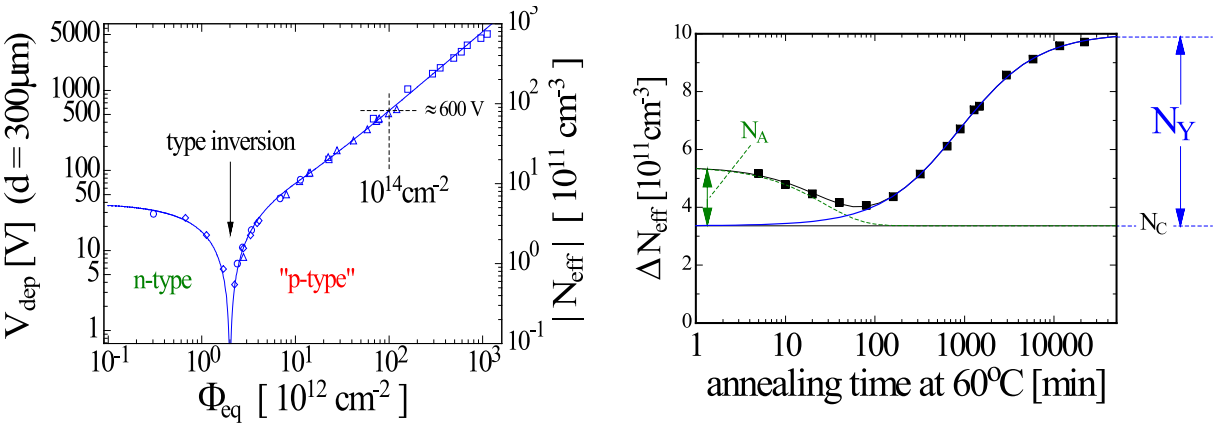

Figure 3.15: (left) Dependence of full depletion voltage and effective impurity concentration on the 1 MeV equivalent fluence for a single padded n-type detector produced from standard FZ silicon after fast neutron (5.2 MeV mean energy) irradiation. Data was measured right after irradiation, i.e. without annealing. (right) Change of the effective impurity concentration with time after irradiation measured during the annealing at 60 °C. Here N_C is the stable damage component, N_A is the beneficial annealing component, and N_Y is the reverse annealing component. Both plots are from [25].

cooling during the operation can help to decelerate or even freeze down this process but will require extra effort and costs to maintain during the experiment shutdown or maintenance.

Generally, an increase of the depletion voltage is directly related to an increase of N_{eff} following equation (3.7). However, in very irradiated detectors the space charge may not be identical to the free carrier concentration which may be trapped by other defects [25]. Furthermore, space charge may become inhomogeneously distributed over the sensor volume which may result in the creation of junctions on both p and n sides of the sensor (double junction), in a shift of the highest electric field to unexpected regions. In general, it can be seen as the formation of a complex 3D electric field distribution in the sensor bulk, i.e. it is no longer a linear function of the sensor depth. Non-linear distribution can be found in non-irradiated devices with very complex junctions consisting of multiple regions with very different doping concentrations like Avalanche Photodiodes (APD) and Silicon Photomultipliers (SiPM) where it is not always possible to clearly define the depletion voltage, see section 7.7.2 for discussion. Therefore, the change of V_{FD} shall be investigated for real sensors experimentally to understand their radiation hardness.

Depletion voltage is usually determined from the kink in capacitance versus voltage (C–V) measurements in a parallel connection which is shown in figure 3.13 (right). Slight dependence of V_{FD} on measurement parameters for damaged detectors was reported, which can become significant for high variations, for example a 21 % decrease in C between f = 10 kHz and 100 Hz, and a 5 % increase in C between +20 and -10 °C [142]. Therefore, it is advised to conduct the measurements at "standard" frequency–temperature point of $\sim$ 10 kHz and room temperature $\sim$ 20 °C.

V_{FD} is limited at around 1000 V/channel by the sensor technology because its increase will eventually lead to the breakdown, and by the cost of power supply. Figure 3.15 (left) shows that these requirements may be exceeded after irradiation with fluences higher than 10^{14} n_{eq}/cm^2. It may so happen that p-type bulk devices will be operated in an under-depleted regime after high irradiation resulting in decreased sensitive volume and collected signal. For n-type bulk

devices, type inversion results in relocation of pn-junction to the opposite side of the sensor (from p-side to n-side), from where the space charge region will develop under the reverse bias voltage applied, which brings the limitation to use such devices in under-depleted regime [25].

3.4.5 Charge collection efficiency and relative signal response

Charge collection efficiency CCE is a measure of how many signal carriers were collected at the sensor nodes during the acquisition time of the readout electronics. It is directly proportional to the number of charge carriers initially produced by the ionizing particle hitting the sensor, which in turn is proportional to the particle's energy [122]. One of the ways to unify this measurement for different detectors is to collect the charge produced by the minimum ionizing particles (MIP). This can be done with help of a common laboratory particle source like Sr-90 emitting electrons. It can be further coupled with the absorbers and triggers to select electrons with certain energies.

Defects accumulated inside the silicon during irradiation decrease the charge collection efficiency by several mechanisms. They can trap electrons or holes created by ionization and then emit them with a delay which is usually longer than the integration time of the readout electronics [135]. Therefore, re-emitted carriers contribute not to the read-out signal but to the detector noise via the increase in leakage current. Another mechanism is a compensation of the initial dopant centers leading to the change of space charge density. In this case, the designed configuration of the electric field inside the device is disrupted. It can lead to operation in an under-depleted regime, so the carriers produced outside the depleted region are not collected [139]. Or the amplification (gain) of the sensor can decrease, which is particularly the case for sensors working in the avalanche regime.

The amount of the produced defects increases linearly with fluence leading to a decrease of the effective carrier lifetime τ_{eff} or increase of effective trapping probability $1/\tau_{eff}$ as [143]

$$\frac{1}{\tau_{eff}} = \frac{1}{\tau_{eff,0}} + \Phi_{eq} \sum_k g_k (1 - P_k^{e,h}) \sigma_{k_{e,h}} \nu_{th_{e,h}} = \frac{1}{\tau_{eff,0}} + \beta_{e,h}(t,T) \cdot \Phi_{eq} \tag{3.9}$$

where in the sum over all defects $\nu_{th_{e,h}}$ is the thermal velocity of carriers, g_k is the introduction rate of the defect k with occupation probability $P_k^{e,h}$, $\sigma_{k_{e,h}}$is the cross section for capturing electrons and holes, and $\tau_{eff,0}$ is the effective carrier lifetime before irradiation.

If the evolution of defects is usually governed by the first-order dynamics, so the effective trapping probability can be simply described by a proportionality damage coefficient $\beta_{e,h}(t,T)$ depending on the time passed after irradiation t and sensor temperature T. This is the case for fluences below 10^5 n_{eq}/cm^2 with reported $\beta_{e,h}(t,T)$ values in the range of $4 - 8 \times 10^{16}$ cm^2/ns, while at higher fluences deviation from this behavior was found with the extracted trapping rates being a factor of 2 – 3 lower than expected from the linear extrapolation from low-fluence data [25].

The amount of charge collected at the sensors nodes can be expressed in electron units as

$$N_{e,h}(t)[e-] = N_{e,h}(0) \cdot \exp\left(- \frac{t_c}{\tau_{eff}} \right) \tag{3.10}$$

where $N_{e,h}(0)$ is the amount of charge initially deposited in the sensor by ionization and t_c is the signal collection time, which is directly dependent on the drifting charge acceleration by the "sharp" pn-junction. Hence, in the radiation environment it is important to utilize fast detectors to collect the maximally possible amount of charge.

Examples of the reduction in CCE with fluence are depicted in figure 3.16 (left). Trapping probability decreases linearly with temperature by about 20 – 30 % for the temperature increase

from -50 to +20 °C [144]. It also undergoes annealing, albeit differently for different carriers: electrons experience less and holes more trapping as time goes by. This results in again a rather complex annealing behavior of the collected charge with time: initial increase of CCE is followed by the degradation as shown in figure 3.16 (right). Moreover, annealing is influenced by the detector technology being more pronounced for thicker sensors.

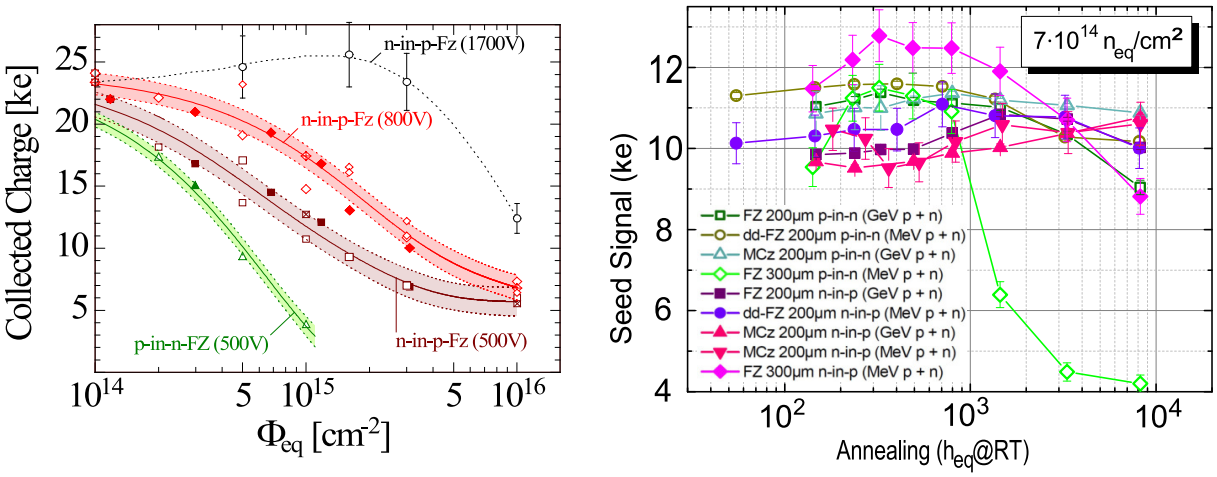

Figure 3.16: (left) Dependence of charge collection efficiency on the 1 MeV equivalent fluence for 300 µm FZ silicon strip sensors produced with different technologies after irradiation with 23 GeV protons, 26 MeV protons, and reactor neutrons [25]. During the measurements sensors were cooled down to -20 °C to -40 °C and different bias voltages were applied. (right) Annealing of charge collection efficiency for silicon strip sensors produced with different materials and technologies as a function of room temperature equivalent annealing time [145]. Strip pitch is 100 µm, irradiation particle mixes are indicated in the legend.

Relative signal response or signal efficiency is utilized to describe the reduction of collected charge after irradiation relative to collected charge before irradiation. In the case of the measurement performed with the full setup consisting of sensor + amplifier + digitizer, the measured value represents the complex process of signal production, conversion, and collection, and is expressed in ADC units. Relative charge or signal response is calculated simply as

$$Q/Q_0\ [\%] = \frac{Charge(e-)_{irradiated}}{Charge(e-)_{non-irradiated}} \tag{3.11}$$

Usually, the signal produced by a unified source like MIP-particles is utilized to be measured either directly as the number of free carriers or as the resulting integration of the output signal. Usually abrupt degradation of signal efficiency after some threshold fluence is observed similarly to CCE. An example of such a trend measured for different silicon and diamond sensors manufactured by various conventional and new technologies is presented in figure 3.17 (left).

3.4.6 Equivalent noise charge and signal-to-noise ratio

The noise of the detector system shall be minimized to achieve the best performance. Noise sources include the detector itself, readout electronics, cabling, and external electronics. Figure 3.18 (left) presents the typical connection scheme of the detector [11]. Most detectors can be represented by single the capacitance C_d, reverse biased parallel resistance R_b which includes intrinsic resistance of the sensor. In the case of DC coupling, the signal goes to the amplifier

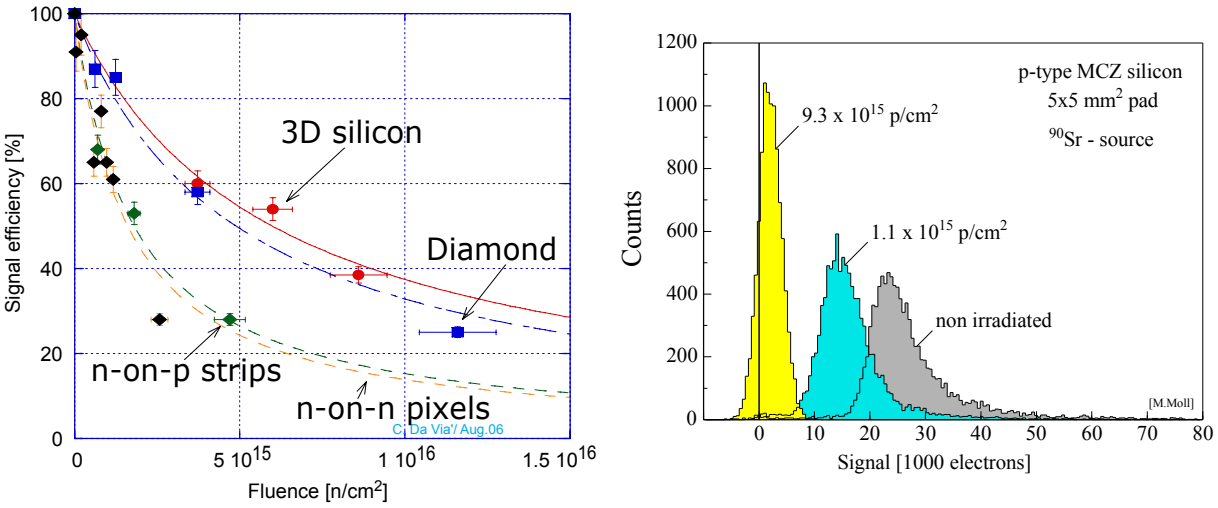

Figure 3.17: (left) Dependence of the signal efficiency on the 1 MeV equivalent fluence for various sensors compiled by [146]. Pixel sensors were produced from diffusion oxygenated float zone (DOFZ) silicon with thickness of 300 µm, 125 µm pixel pitch, irradiated with 24 GeV protons [147]. Strip sensors were produced from standard silicon with 2kΩcm resistivity, 300 µm thickness, and 1 cm long strips with 80 µm pitch, irradiated with with 24 GeV protons [148]. 3D sensors were produced from n-type bulk high-resistivity silicon with p-type active edges, 230 µm thickness and 50 µm pixel pitch [146], irradiated with "white" spectrum fast neutron source of NPI cyclotron which is described in section 6.1. Diamond sensors were produced from polycrystalline chemical vapor deposited material with 300 µm thickness and 50 × 400 µm^2 "pixels", irradiated with with 24 GeV protons [149]. Data extrapolations are linear, i.e. $SE \sim 1/\Phi_{eq}$. (right) Degradation of the signal magnitude manifesting as a decrease in signal-to-noise ratio measured for simple PAD MCz silicon sensors [150].

through a capacitance C_c as in the figure, while in the case of AC coupling it can go through a polysilicon resistor, punch through bias or FOXFET bias which can be external or integrated within the sensor [122]. Series resistance R_s is comprised of sensor intrinsic resistance, electrode resistance, and parasitic resistances in the amplifier input. The amplifier provides additional gain for very small signals ($\sim$ fC) and modifies input pulse duration and shape in a way suitable for digitization and processing. Amplification can be performed by single or multiple devices, e.g. preamplifier + pulse shaper. Signal digitization can be realized as a measurement of amplitude and/or time (ADCs, discriminators, TDCs), several examples studied for CBM PSD are presented in section 4.4.

Similarly to the collected signal, the detector's noise can be expressed in the number of elementary electron charges by the Equivalent Noise Charge (ENC). ENC is the number of electrons one would have to collect from a silicon sensor in order to create a signal equivalent to the noise of this sensor. For a typical amplifier with CR–RC shaper, it can be estimated as [126]

$$ENC^2 = 12 I_{leak} \tau_{sh} + 6 \cdot 10^5 \frac{\tau_{sh}}{R_b} + 3.6 \cdot 10^4 \nu_n^2 \frac{C^2}{\tau_{sh}} \tag{3.12}$$

where I_{leak} is the detector leakage current in nA, τ_{sh} is the shaping time constant in ns, R_b is the parallel resistance in kΩ, ν_n is the equivalent input noise voltage spectral density of the amplifier in nV/$\sqrt{Hz}$, and C is the total input capacitance in pF.

Typical noise levels can be as low as $\sim$ 1 electron for CCD, but usually is about $10^2 - 10^3$

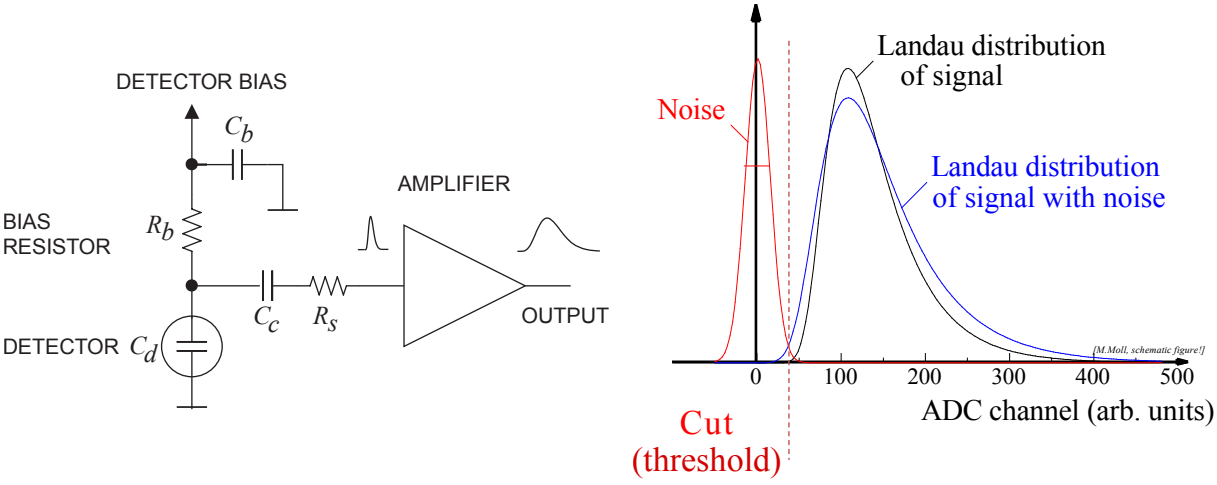

Figure 3.18: (left) Simplified equivalent scheme of a detector connection to readout circuit [126]. (right) Sketch of a measurement histogram consisting of noise and signal distributions, and signal acquisition threshold [139].

electrons for unirradiated silicon detectors [11]. After irradiation, the noise can increase by several orders of magnitude.

signal-to-noise ratio (SNR) is perhaps the most comprehensive parameter for the sensor performance characterization. It can be estimated based on values of signal and noise expressed in electrons or integral signal measurements

$$SNR = \frac{Charge(e-)}{ENC(e-)} \tag{3.13}$$

Note, that ENC can be also estimated with help of SNR. For this, one needs to inject known signal charge into the sensor, e.g. irradiate it with MIP, and measure the input charge for which SNR is equal to 1 [126].

signal-to-noise ratio is a very simple and versatile tool for the sensor assessment which allows to quickly estimate its radiation-induced degradation and get an insight into the change of its dynamic range. Unfortunately, data on the signal-to-noise ratio degradation with fluence are rarely presented, probably because of the complex noise dependencies on the power supply, readout electronics, amplification, digitization, and data processing which makes these measurements hardly reproducible in different laboratories. Still, SNR is a great tool for the comparison of different sensors when done with the same laboratory detector setup under well-controlled conditions.

Sketch of signal and noise histograms collected from the detector is presented in figure 3.18 (right). For relatively thin detectors the energy loss probability is described by the Landau distribution where the mean value is significantly larger than the most probable. The long tail at high energies occurs due to very rare high-energy-transfer collisions. The signal distribution is further blurred by the noise which is described by a Gaussian distribution as individual noise contributions are usually random and uncorrelated [11]. During the operation, one needs to set a threshold for the detector output signal to cut out the noise. Often there is an overlap between noise and signal distributions resulting in some amount of noise acquired over the threshold (noise occupancy) and some amount of actual signal lost under it (efficiency loss) [122]. Usually, after the irradiation noise pedestal gets wider, so the threshold must be elevated. At the same

time amplitude of signal or collected charge decreases as shown in figure 3.17 (right). Combined, these effects lead to the gradual decrease of the detector SNR which is directly related to the decrease in dynamic range. Change of the signal-to-noise ratio shall be always investigated for the detector after irradiation to understand the degradation of its performance. Commonly, SNR around 10 is considered as a safe limit for the detector operation [139].

3.4.7 Approaches for sensor radiation hardening

Optimization of material engineering, sensor design, treatment during the operation, and readout optimization can be used to significantly improve device tolerance. Generally, the choice of high-quality silicon with low impurity concentrations is crucial for the best sensor performance, i.e. advanced FZ or MCz over a standard Cz silicon, see figure 3.16 (right). But it is not always that simple: RD48 collaboration found that after p and π irradiations V_{FD} increased roughly by 3 times slower for sensors produced with oxygen-enriched silicon [25]. Even though no difference was found for neutron irradiated sensors and leakage current trends, ATLAS and CMS pixel detectors at the LHC have been made from oxygen-enriched silicon. Other impurities were studied as well, e.g. carbon produced the opposite effect (fast V_{FD} increase).

Detector design plays a foremost role in the hardening. The collected charge can be increased by the utilization of sensors with n+ collecting electrodes (on ether p- or n-substrate) because under the reverse bias they collect electrons that have higher mobility than holes and therefore better chance of not being trapped by defects on the way to the node, see figure 3.16 [11]. Furthermore, the electric field around n+ electrodes is reduced by the increased oxide charge, which provides extra protection against breakdown and noise (the opposite is true for p+ electrodes). This design guideline was approved for future ATLAS and CMS detectors to be based on n-in-p concept (current sensors are p-in-n) [25].

Reduction of the sensor thickness offers the improvement of charge collection efficiency along with the reduction of required bias voltage because of the reduced charge drift length (faster collection time -> lower trapping probability). Of course, it will reduce the overall deposited charge, but still can be beneficial after irradiation due to the lowered charge trapping and improved electric field distribution. Optimum device thickness can be found to maximize the measured signal depending on the particle fluence and the applied voltage, e.g. 150 μm for 2×10^{15} n_{eq}/cm^2 and 300 V [25] (instead of a 300 μm standard), see figure 3.16 (right). Recently developed 3D sensors with columnar electrodes etched perpendicularly to the wafer surface at a small distance of 50 – 100 μm represent a competing option. Even though compared to planar sensors, 3D devices have higher pixel capacitance (higher noise), dead regions around the columns and larger production costs, they were recently successfully installed and tested at the ATLAS experiment, see figure 3.17 (left).

Protective microlayers and elements can be utilized during the sensor design. Single or multiple guard rings (p+ implants) are placed around the sensor sensitive nodes to protect them from currents originating at the edges and to precisely define the active volume Further implants like p-stop and p-spray are utilized to isolate neighboring nodes from each other reducing the parasitics internode capacitances and leakage current. The surface passivation layer can be manufactured with the use of only depleted boron ^{11}B which does not have a huge neutron capture cross-section like ^{10}B. Sensor shielding by can be made from composite materials like isophthalate resin polymer with lead oxides [127].

Technology computer-aided design packages like Synopsys Sentaurus TCAD are a vital part of the sensor development allowing to understand, test, and optimize the device design. They include modeling of the manufacturing process, i.e. doping by implantation or diffusion, which allows simulating the electric field and behavior of the device. Furthermore, parameters of

radiation-induced defect levels can be embedded in the simulation to optimize the silicon material, device thickness, geometry, and field distribution for the prediction of the radiation damage and creation of radiation hard sensors. The achieved device model can be then translated into a compact SPICE model and combined with the model of the readout chain to investigate the overall detector performance. There is big progress in the field of the radiation effects TCAD simulations in recent years. However, the significant number and complexity of experimentally observed defects complicate the simulation, so fewer effective defect levels are usually parametrized and benchmarked against the measured detector parameters. The available TCAD simulations achieved by different researchers may show very different results when applied to highly irradiated silicon diodes, so the accuracy and conformity of the simulation are still to be improved [25]. Sensor design studies and optimization is based on the detailed knowledge of its doping profile and geometry. This demands a very close contact and information exchange with the manufacturer which is often achievable for standard large-scale expensive detectors but can be very challenging for commercially produced devices which design is kept as a commercial secret like the SiPMs.

Temperature treatment is useful to improve the detector performance because the defect states occupancy is strongly temperature-dependent. First of all, temperature stabilization or cooling can be applied during the operation to stabilize the sensor characteristics, e.g. gain of SiPM; reduce the leakage current and noise; avoid detrimental annealing. Depending on the radiation load, detector design and available budget, the sensor can be kept at a stable room temperature like SiPMs in NA61 PSD (see section 4.7), cooled down to -5 or -20 ° like tracking (STS) and vertex (MVS) detectors in CBM (see section 4.2), or even kept at cryogenic temperatures like HPGe spectrometers. Periodical annealing can partially recover the performance of the irradiated detector reducing the leakage current and noise (see figure 3.14 (right)), reducing effective space charge and depletion voltage, improving the carrier trapping and charge collection efficiency, which altogether will improve the signal-to-noise ratio. However, the annealing time and conditions shall be well chosen based on the extensive detector studies to avoid detrimental annealing or malfunction which can happen for instance for 300 μm thick sensors as shown in figures 3.15 (right) and 3.16 (right).

Noise minimization starts with the sensor optimization and extends to the evaluation of full readout chain design which is schematically depicted in figure 3.18 (left). Before irradiation, the most important noise contribution usually comes from the value of input capacitance. It can be minimized by lowering the detector capacitance (detector area) and increasing the signal shaping time. After the detector irradiation, fluctuations of the leakage current start to dominate. It can be minimized by the high-quality detector material and radiation hard design as well as by decreasing the signal shaping time and proper resistor choices [122]. Parallel bias resistance, which is often integrated into the sensor, is to be maximized, but its value is limited by the production process and the voltage drop across the resistor. Serial resistance between the sensor and readout shall be minimized by the implementation of low resistance interconnection lines (e.g. thick aluminum layer) and making external connections as short as possible. The amplifier further contributes to the total noise in the extent depending on its design and features.

Correct digitization is also important for noise minimization following the development trends of high speed and low power. If the sampling rate of the ADC is much lower than the signal frequency, a fast component of the pulse could be missed and high-frequency components could be transferred to lower frequencies increasing the noise level [11]. To avoid this a low-pass filter can be added before the ADC limiting the noise bandwidth. Furthermore, the higher amplifier gain can help to override the equivalent input noise of ADCs which can be quite high. Noise mitigation can be also performed on the firmware and software levels by the choice of appropriate

acquisition time window and application of the noise threshold for individual sensors/channels.

Additional noise often comes from external sources such as RF interference from electronics within the detector system or outside. It can also come from the "common ground" of the sensor, electronics, or power supply. Minimization of cross-coupling, power decoupling, and sensor shielding can be beneficial to reduce the noise.

Radiation tolerance of the readout electronics shall be evaluated as well to ensure the proper detector operation. The most obvious way to protect the readout electronics from radiation is positioning it as far as possible from the harsh radiation area, e.g. at the detector side or even farther. The readout chain can be divided into a radiation hard preamplifier which is connected as close as possible to the sensor to reduce noise interference on the cables when a signal is yet very small (pC). Second stage amplification and signal digitization can be situated several meters aside if possible. From there the digital signal can be transferred as far away as desired, even to another building.

The circuit sensitivity to radiation generally increases with increasing levels of integration and decreasing size of individual structures. Various techniques are applied to protect the innermost electronics from single event effects (SEE) changing the cell state and the circuit operation. Surface damage represented by the "build-up" charge in SiO_2 can be mitigated by utilization of the substrate with a wide band gap like silicon on insulator (sapphire, silicon carbide, or gallium nitride) instead of the usual silicon wafers. Edgeless layout transistor (ELT) NMOS transistors have source and drain enclosed by polysilicon gate reducing the leakage current [127]. Larger transistor size and increased distance between the nodes is beneficial as it increases the node capacitance, so higher energy deposition (critical charge) is required for SEE to happen effectively reducing SEE probability. Extra wiring and special selector units can also help to tolerate the hardware damage. Capacitor-based DRAM is more vulnerable and is often replaced by tolerant MOSFET-based SRAM or even more tolerant Magnetoresistive RAM [151]. Their tolerance can be further improved if they are based on more than usual 4 – 6 MOSFET proving the system redundancy. Unfortunately, these approaches limit the application of the newest and fastest device families based on smaller process nodes resulting in overall higher cost and power consumption per cell.

As it is not possible to mitigate all the SEE, circuitry logic is further protected by various levels of redundancy. Spacial triple modular redundancy utilizes the straightforward way of replacing the most important and sensitive device units, be it electric node, single bit, register, microprocessor, or the whole chip, by three identical units [127]. The unit states or signals are compared via the special "voting logic" elements or circuits forming a majority decision of two against one. Temporal redundancy is based on widening the between sampling cycles, so that transient pulse will be lost during the transfer from one element to another. Error correcting (ECC) memory utilizes the additional parity bits to check the data and mark it for correction if it is corrupted. The watchdog timer is implemented on the system level with the task to periodically check the "aliveness" trigger and perform a hard reset if it is not valid. A scrubber circuit can be added to continuously sweep and rewrite the RAM, or reconfigure the chip logic [127]. Similar redundancy approaches can be implemented at the software level, e.g. multiple (three or more) program instances running in parallel with their calculation results cross compared to each other, program instructions can be duplicated and software signatures can be transferred to ensure the proper operation.

Some of the aforementioned conditions can be contradictory or not so easy to implement, therefore it is important to design the detector, readout electronics, and power supply as one system to optimize its performance.

3.4.8 Summary

Generally, degradation can start already after exposure to several hundreds of Gy or $10^{10} - -10^{12}$ n_{eq}/cm^2 for highly susceptible devices [134]. Radiation hardness is ultimately dependent on the device's material, technology, and design and can be optimized via various methods. Well-designed novel strip and pixel detectors remain functional at fluences beyond 10^{15} n_{eq}/cm^2 as shown in figures 3.14, 3.15, 3.16 and 3.17. Electronics produced by standard "deep submicron" complementary metal-oxide–semiconductors (CMOS) processes have rather a small gate oxide volume and high doping, so it can withstand fluences above 10^{15} n_{eq}/cm^2 [11].

New technologies are also being investigated for future applications. Low Gain Avalanche Detectors provide higher collected charges with help of the avalanche carrier multiplication with a gain of about 10, for more details on the avalanche process, see next section. HV-CMOS sensors allow benefiting from the standard CMOS manufacturing process with high-bias voltages applied to the substrate of CMOS sensors and charges collected from deep n-wells in a p-type substrate. Both technologies are yet very young and shall be properly investigated, e.g. significant radiation damage was observed above 10^{14} n_{eq}/cm^2 [25]. Even very radiation sensitive devices like APDs and SiPMs are very popular for HEP applications, even though they may degrade dramatically already above 10^{12} n_{eq}/cm^2 which is discussed in the next section.

For fluences higher than 10^{15} n_{eq}/cm^2, 3D silicon sensors which have 3 – 6 shorter collection distances than planar sensors and diamond sensors which have carrier mobilities 3 – 8 times higher than silicon can be utilized as shown in figure 3.17 (left) [11]. For fluences above $10^{16} - 10^{17}$ n_{eq}/cm^2 radiation-hard scintillators like YAG:Ce can be used, e.g. for primary beam monitoring [28]. However, both diamond and scintillators are not semiconductors and have very different properties and challenges, namely much lower charge deposition and utilize different charge readout approaches.

3.5 Silicon Photomultipliers (SiPMs)

Silicon Photomultiplier (SiPM) is a very promising detector that is widely utilized in applications requiring light readout in the wide dynamic range, single-photon counting, and excellent timing. It is a relatively new device commercially available only for last 10 – 20 years, and due to its novelty every manufacturer has its own name for it, eg. SiPM [152, 153], Pixelized Photon Detector (PPD [11]), Solid State PhotoMultiplier (SSPM), Micro-pixel Avalanche PhotoDiode (MAPD [154]), Multi-Pixel Photon Counter (MPPC [155]), etc [156]. Regardless of the name, it can be generally described as a multi-pixel avalanche photodiode operating in Geiger regime.

Nowadays, SiPMs are widely applied in the positron emission tomography nuclear medicine, gamma spectroscopy, and experiments of the high energy and neutrino physics, and recently it started to arrive at biomolecular science, astroparticle physics, light detection and ranging (LIDAR), and even to quantum physics and informatics [157]. The most common applications in HEP are found for sampling calorimeters, other examples include tracking detectors, particle identification systems, large-volume detectors, and time of flight detectors [158]. Usually, the spectral range covers only visible light, but new developments extend it to ultraviolet or near-infrared. SiPM is considered a competitor to the renowned PhotoMultiplier (PMT) due to SiPM's very compact size, low price, low bias voltage, comparable gain and dynamic range, and insensitivity to the magnetic field.

In this section, I provide a relatively short SiPM overview. For more details on the SiPM properties and design, I advise referring to the great guide by D. Renker [159] and a more recent one by S. Gundacker [160]. A detailed discussion of the SiPM parameters characterization can be found in comprehensive reviews by R. Klanner [161], and F. Acerbi [157], the latter one also

offers an insight into the SiPM simulations. Finally, extensive summaries of SiPM applications in particle and nuclear physics as well as in other fields can be found in a special volume of NIMA journal on SiPMs [162].

3.5.1 Operation principle of photodiodes and SiPMs

Just like other silicon radiation sensors, silicon photodiodes are based on a reverse-biased p-n junction. They detect light by the intrinsic photoelectric effect when the energy of an incident photon is absorbed by the electron of silicon atom producing the ionization. For this to happen, photon shall have energy higher than the silicon band gap of 1.12 eV or wavelengths shorter than ~ 1 μm. Figure 3.19 (left) shows that the sensor thickness shall exceed 100 μm to provide the light absorption in the full visible spectrum.

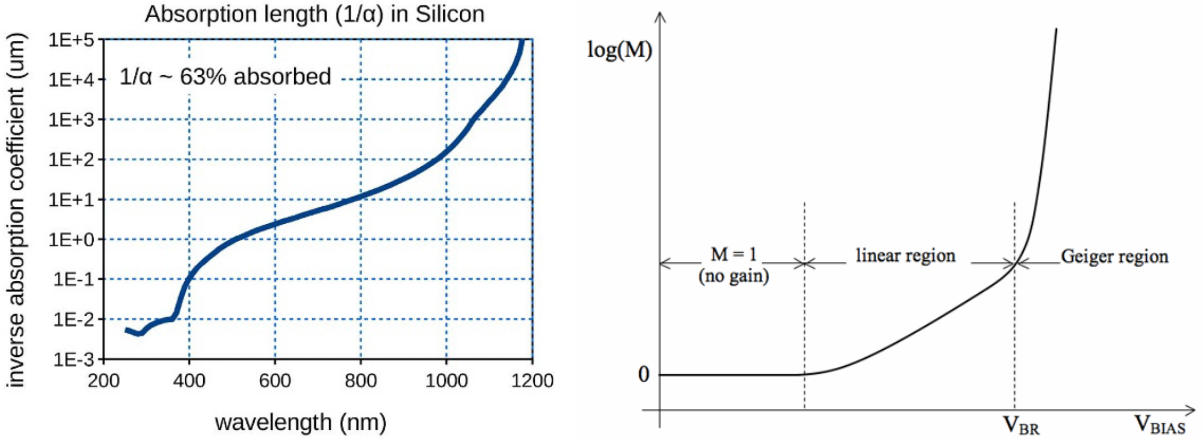

Figure 3.19: (left) Dependence of penetration depth ($1/\alpha$) in silicon on wavelength [160]. (right) Dependence of gain on applied bias voltage discriminating between regular photodiode without gain, APD operating in linear avalanche region and G-APD operating in Geiger-mode avalanche region [163].

The simplest PIN photodiode is composed of a 300 – 500 μm thick intrinsic silicon layer with two heavily doped n+ and p+ regions on the sides. Low doping of the intrinsic layer allows to operate it with a small voltage with minimal thermal generation current, large thickness results in small capacitance and hence low noise as well as sensitivity to red and infrared light and light detection efficiency up to 90 % [159]. However, it has no internal signal amplification which demands the use of rather slow low-noise amplifiers and limits the minimum detectable signal to 200 – 300 photons at room-temperature [164]. Many large scintillation gamma calorimeters, including CLEO, L3, Belle, BaBar, and GLAST, use PIN photodiodes for the light readout. Pixelized photodiodes including charge-coupled devices (CCD), CMOS sensors, and hybrid detectors are utilized in both consumer and scientific photography.

Low light levels can be detected with the introduction of the internal amplification in form of an avalanche multiplication process creating the cascade of secondary carriers. Avalanche PhotoDiodes (APD) is operated at a high voltage of several hundred Volts which coupled with the cleverly designed highly doped regions produces a very high electric field $> 2 \times 10^5$ V/cm [159]. Figure 3.19 (right) shows the dependence of photodiode gain on the voltage where the gain is defined as the number of secondary carriers produced per each primary one. Simple pn and pin photodiodes operate in a flat area without gain. APDs operate in the linear region just below the complete avalanche breakdown, where the amount of produced secondary carriers is

linearly proportional to the number of incident photons. In this region, only electrons create the avalanche (they have intrinsically higher probability), which goes towards the n-node and stops by itself when electrons reach the low field area. On contrary, after the breakdown holes also start to participate which results in an uncontrollable self-sustaining process that can lead to the device failure. Therefore, voltage stability and temperature monitoring are important for linear-mode operation, and substantial cooling is often necessary like in the case of CMS crystal-based electromagnetic calorimeter [145]. APDs usually offer a moderate gain of 10 – 300, detection efficiency up to 70 %, and detection minimum of 10 – 20 photons [164].

If one increases the electric field further and goes beyond the diode's breakdown voltage V_{bd}, the avalanche starts to grow uncontrollably, so any amount of incident photons would ideally produce an infinite number of carriers. In this case, APD operates in Geiger region and is called G-APD or Single Photon Avalanche Diode (SPAD) due to very high gain allowing the light detection on the single-photon level. The quenching mechanism is applied to stop an avalanche at some point protecting the device from burning out due to the extreme current flow and providing a fast signal output. Often, passive quenching is implemented in form of the large resistance ($R_Q = 100\ k\Omega - 1\ M\Omega$) connected in series with the photodiode [165]. Because R_Q is much larger than the coupled resistance of the diode (typically about 1 kΩ [160]), a voltage drop is developed on the quenching resistor which reduces the voltage on the photodiode to V_{bd} and SPAD returns to the idle state for the next photon detection. Alternatively, an active quenching technique can be utilized, particularly suitable for CMOS-compatible G-APDs. It can be implemented as an integrated circuit detecting the SPAD pulse signal and generating a delayed signal to turn on a quench driver recharging SPAD actively.

Regular SPAD is built as a single pixel and therefore produces the same signal for any amount of detected photons which does not allow for the photon counting. SiPM is an array of $10^2 - 10^5$ SPAD-like pixels connected in parallel which inherit the very high gain of regular SPAD of about $10^4 - 10^7$. Due to the pixel structure, SiPM signal is linearly proportional to the number of detected photons in a wide dynamic range. Figure 3.21 (right) represents the typical electrical connection scheme for SiPM application as well as SiPM internal structure consisting of many SPADs coupled with quenching resistors. Depending on the SiPM gain and necessity to detect single photons, its signal is usually amplified by a conventional fast amplifier with a gain of around 10 – 1000 [157]. It can be seen as quite a convenient solution, opposed to lower-gain photodiodes which require complex low noise amplifiers that are limited in bandwidth for noise suppression [159].

3.5.2 SiPM structure

The design of the SiPM silicon structure depends on the requested light wavelength region. Electrons have a higher avalanche initiation probability than holes, so a high field region shall be designed in a way that electrons undergo the maximal acceleration [159]. Figure 3.20 shows the shallow p-on-n structure which has a peak sensitivity for the blue light and its field distribution. Short wavelength photons are readily absorbed in the first few μms of the device allowing created electrons to move through all the high field regions towards the back n-node. The opposite is true for the reach-through n-on-p structure which is better suitable for the green or red light which penetrates tens or hundreds of μm deep from where created electrons travel to the n-node situated in the surface.

Usually, SiPM structure is created on the low doped 500 μm thick silicon substrate with 1 – 10 μm thick epitaxially grown layer. The epitaxial layer is consequentially doped to create a complex structure consisting of the first very thin (0.1 – 0.5 μm) highly doped layer, and several further layers with opposite doping to create a p-n junction with a high-field distribution as

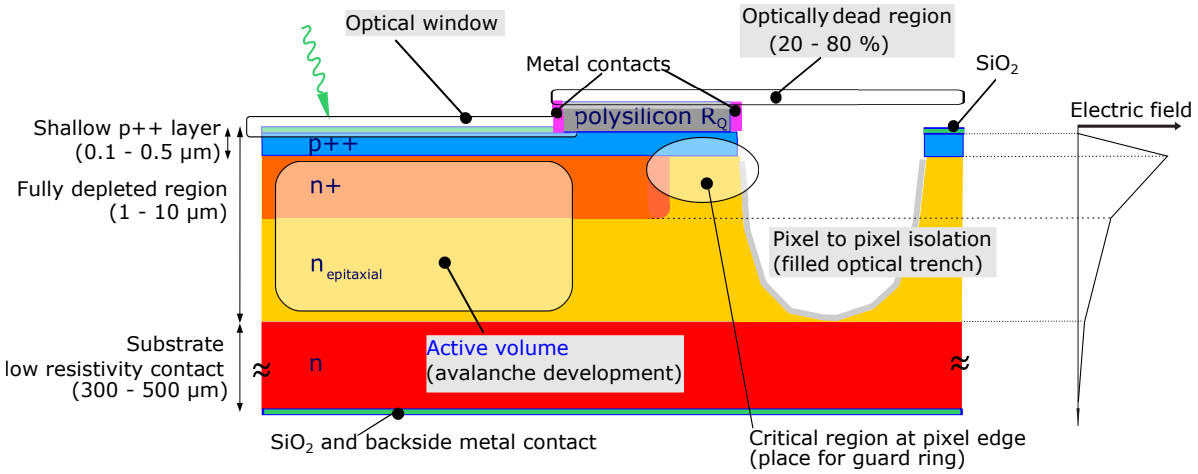

Figure 3.20: Typical internal technological structure of SiPM pixel optimized for blue light (side view) with the electric field distribution along with its depth. R_q represents the quenching resistor. The figure is taken and modified from [156] [Collazuol2019].

shown in figure 3.20. Passivation with SiO_2 serves both for the sensor protection and as the front optical window, which is added with an anti-reflective coating to minimize the losses of photons during the passage through the optical window down below 10 percent over the entire visible spectrum. At the side polysilicon quenching resistors, trenches for the optical isolation between pixels, and guard rings are implemented. The structure is divided into pixels with sizes in the range of $5 \times 5 - 100 \times 100$ μm^2.

Photon which successfully passed the window and is absorbed inside the active volume has a probability to generate an electron-hole pair. Electrons will drift to the n+ side (the hole will drift to the p+ side) under the applied reverse electric field. The field abruptly maximizes around the p-n boundary with the highest doping difference which increases the probability of avalanche creation. Finally, multiplied carriers are collected at the sensor nodes and the avalanche is stopped by the quenching resistor.

Guard rings are placed at the pixel edges to tune the high gradients of the E-field, reduce leakage currents and surface charges, and prevent Premature Edge Breakdown (PEB). PEB happens when an avalanche is firstly initiated at the junction edge before the intended photo sensing area reaches its breakdown, thus confining the multiplication region at the corner and preventing the spreading of the avalanche [165]. Both optical trenches and guard rings are significantly improving the sensor operation, but at the same time take the space at pixel sides creating regions that are "dead" for photon detection.

Another interesting design was invented by Zecotek manufacturer which is based on 8 μm deep micro-wells buried within the epitaxial layer representing pixels. There the avalanches take place in independent channels that do not have charge coupling between themselves resulting in better operation stability, increased sensitivity, and radiation hardness. However, the pixel recovery time of these devices is rather slow which makes them unsuitable for high rate experiments, see discussion in section 7.1.

Digital SiPM utilizing the active quenching circuits is a promising area of research for timing and CMOS integrated imaging applications. It can provide unprecedented rate capability above 1 MHz and time resolution on the order of ten ps [160]. However, quenching circuits require much more design which makes digital SiPMs more expensive. They also require more space on

the SiPM side reducing the geometrical detection efficiency due to the more dead space, which is especially crucial for SiPMs with small pixels. The latter problem can be potentially solved by 3D sensor design consisting of separate layers of SiPM pixels and processing electronics.

3.5.3 Equivalent circuit and SiPM parameters

Figure 3.21 (left) presents a common variant of the SiPM equivalent circuit. Every pixel is represented by a diode with internal resistance R_d (also called R_{pix}) and capacitance C_d (also called C_{pix}) connected in parallel. C_d is a sum of the depletion layer capacitance and perimeter capacitances around the pixel. The quenching circuit consists of quenching resistor R_q and parasitic capacitance C_q in parallel. Value of R_q shall be high enough to quench the avalanche, i.e. several hundred kΩ for the critical current of 10 — 20 μA required to sustain the avalanche process [166]. But values too high would result in long recovery (dead) time τ_r when a pixel is not available to detect photons. C_q is the coupling capacitance of the quenching resistor to the pixel bulk and is an important design parameter that can be made bigger to make the initial pulse narrower for fast signal extraction [161].

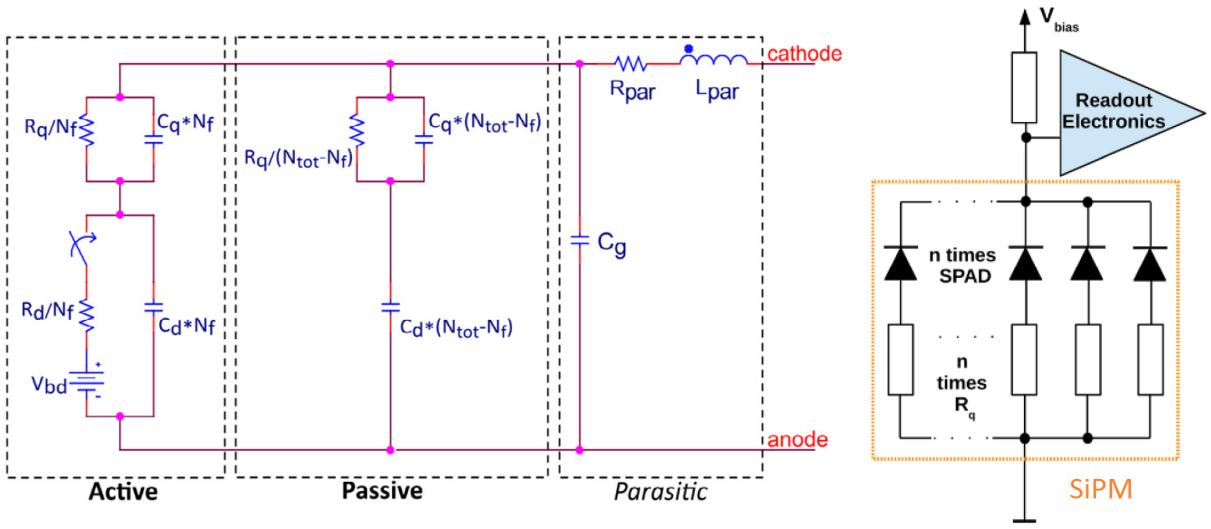

Figure 3.21: (left) Equivalent electrical circuit of the SiPM. Fired SiPM pixel is discharged when the switch is closed represents. R_d is the pixel series resistance, C_d is the pixel capacitance. R_q is the quenching resistance, C_q is the quenching (parasitic) capacitance. Active part represents N_f fired pixels, passive part – remaining $N_{tot} - N_f$ pixels. Parasitic components include resistance R_p, inductance L_p and capacitance C_p of the pixel grid and connection to readout [157]. (right) Example of SiPM connection schematics. SiPM is shown as a number of individual SPADs complemented with quenching resistors and connected in parallel [160].

In an idle state, the switch is closed and C_d is charged to the SiPM bias voltage V_{bias} applied on the anode and cathode. When an avalanche is triggered the switch is closed leading to a Geiger discharge of the capacitance C_d via the resistor R_d, and the switch opens when the voltage on the diode drops below the breakdown voltage V_{bd}. The voltage drop at the internal node is called overvoltage V_{ov} (or excess voltage) and is the difference between V_{bias} and V_{bd}. In-circuit presented in figure 3.21 (left) V_{bd} is modeled as the DC power supply source which allows describing the avalanche quenching or non-quenching. Alternatively, V_{bd}, R_d and the switch can be replaced by a pulsed current source to model take the time structure of the

avalanche development [160]. High initial current through the diode ($\sim$ several mA) is equal to the overvoltage divided by $R_q + R_d$.

All the fired pixels n_f contribute to the SiPM signal, while not fired ones $N_{tot} - n_f$ represent extra parasitic capacitance. Further parasitic components are the connections and grid resistances R_p, inductances L_p, and capacitances C_p which can be expanded to take into account parameters of the amplifier and readout electronics. All of them shall be minimized to achieve the best SiPM timing capabilities.

Absolute admittance of a single-pixel and the whole SiPM is frequency dependent and can be estimated as [157]

$$\begin{aligned} Z(\omega) &= \left| j\omega L_{par} + R_{par} + (j\omega C_g + N_{tot} Y_{pix})^{-1} \right| \\ Y_{pix}(\omega) &= \left[\frac{1}{j\omega C_d} + \frac{1}{R_q^{-1} + j\omega C_q} \right]^{-1} \end{aligned} \tag{3.14}$$

where Y_{pix} (also called Y_{cell}) is the single-pixel admittance and N_{tot} is the total number of pixels (assumed to be idle).

Simple connection of SiPM to the readout electronics is shown in figure 3.21 (right). Frequency characteristics of the SiPM output depend on parasitic components and the amplifier design. Pulse shape has a steeper rise time when the SiPM parasitic impedance and capacitance are low which is usually the case for small area devices with small pixels. For instance, Sensl SiPMs feature the third "fast" readout node with much lower capacitance $\sim$ 1 pF than compared to the standard output with $\sim$ 100 pF, though when the signal is read out from the low capacitance output the gain is decreased by a factor of 50 [152].

Low amplifier input impedance below 10 Ω is desirable if the fast signal component is meant to be extracted from the SiPM. This is important to achieve the best timing resolution, e.g. for trigger or PET applications, where fast voltage or transimpedance amplifiers with the bandwidth in the GHz range are preferred. On contrary, a high impedance value on the order of 100 Ω slows down the rising edge of the pulse but also provides higher gain and a smooth signal shape without initial fast component overshoot. This approach is exemplified by charge sensitive amplifiers which have very low noise levels, albeit at the cost of the narrower bandwidth in 100 – 300 MHz range, and therefore provide superior performance in applications where the dynamic range is more important than the timing accuracy, eg. in spectrometers and calorimeters like CBM PSD.

3.5.4 Advantages and disadvantages of SiPMs

Silicon Photomultipliers possess many advantageous properties which make them a great photodetector of choice, namely

- Capability to detect single photons.
- Low bias voltage: from 20 up to 100 V. Most of the SiPM parameters depend on the overvoltage (see figure 3.22, left), so it is tuned in the range of 0 – 10 V for the needs of a specific application.
- Very high gain: from 10^4 up to 10^7 [164]. It allows detecting very low amounts of light down to single photons well above the electronics noise threshold without the application of complex amplification circuits.
- Wide dynamic range: directly proportional to the number of pixels or inversely proportional to the pixel pitch, and measures from single photons up to N_{pixels} photons.

- Relatively high photon detection efficiency (PDE): up to 60 % for SiPMs with large pixels.
- Wide spectral response range: from 300 up to 900 nm. New vacuum-UV devices allow to start from $\sim$ 100 nm, standard near-IR devices can go up to 1050 nm, while SiPMs based on InGaAs can extend the range up to 1700 nm [156]. Many SiPM parameters depend on the wavelength of incoming light, for example see PDE dependence in figure 3.22 (right). Thus, SiPMs are chosen for the specific application by their intrinsic peak sensitivity, which depends on the SiPM structure as was described in subsection 3.5.2.
- Low noise devices available. Uncorrelated noise in terms of dark current I_{dark} is in the range from 0.1 up to 100 nA/mm^2, in terms of the dark current rate: in the range from a 1 up to 100 kHz/mm^2 (for new devices [164]). Correlated noise contributions of afterpulsing and optical crosstalk are also relatively low in the range from 1 to 10 %. For high-quality SiPMs and light intensities, signal-to-noise ratio SNR can reach a value of few thousand.
- Low power consumption: below < 50 μW/mm^2 [159].
- Excellent time resolution: from few ns for regular SiPMs down to 80 ps for the fastest ones [160]. By connection of several SiPMs in series, it can be further improved down to 20 ps albeit at cost of higher operating voltage [158]. In general, a signal pulse can be shaped by an amplifier providing a trade-off between the fast pulse component, signal amplitude, and recovery time.
- Insensitivity to the magnetic field is an intrinsic property of a silicon sensor. PMTs are on contrary very sensitive to it due to the electron travel and amplification in a vacuum. It can be very important for detectors of High Energy Physics situated inside or near the magnet.
- Absence of the nuclear counter effect (NCE). NCE happens when charged particles or gammas which were not supposed to be collected invoke avalanches inside the sensor. This can be an issue for convenient APDs resulting in signal resolution deterioration or fake signals production [159]. In SiPMs only a single will be fired due to the particle passage and therefore the change in total signal will be negligible. For instance, this can be important for the calorimetric detectors where sensors can react to the leftover shower particles created in the modules [167].
- Compactness, lightweight, mechanical endurance, and ability to tolerate accidental illumination.
- Low cost: about 20 – 100 EUR/device for the commercially available SiPMs.

The aforementioned attributes make SiPMs superior to PMTs in many applications. However, PMTs are still better than SiPMs in applications requiring low light readout from large areas and/or high radiation tolerance due to the following SiPM drawbacks [159]

- Smaller device area: up to 6×6 mm^2 for individual devices available now. Though they can be connected in arrays of $> 50 \times 50$ mm^2 but at quite a high price [164].
- Higher noise rate per unit area.
- Increase of the signal rise time due to the large parasitic capacitance of large-area devices, e.g. 80 nF for 51×51 mm^2 SiPM array [164].
- Necessity to make a trade-off between PDE, gain and dynamic range. Quenching resistors, trenches, and guard rings do not scale with the pixel size and greatly reduce the fraction of the pixel area available for photodetection and consequently PDE for small pixels, see figure 3.22 (right).

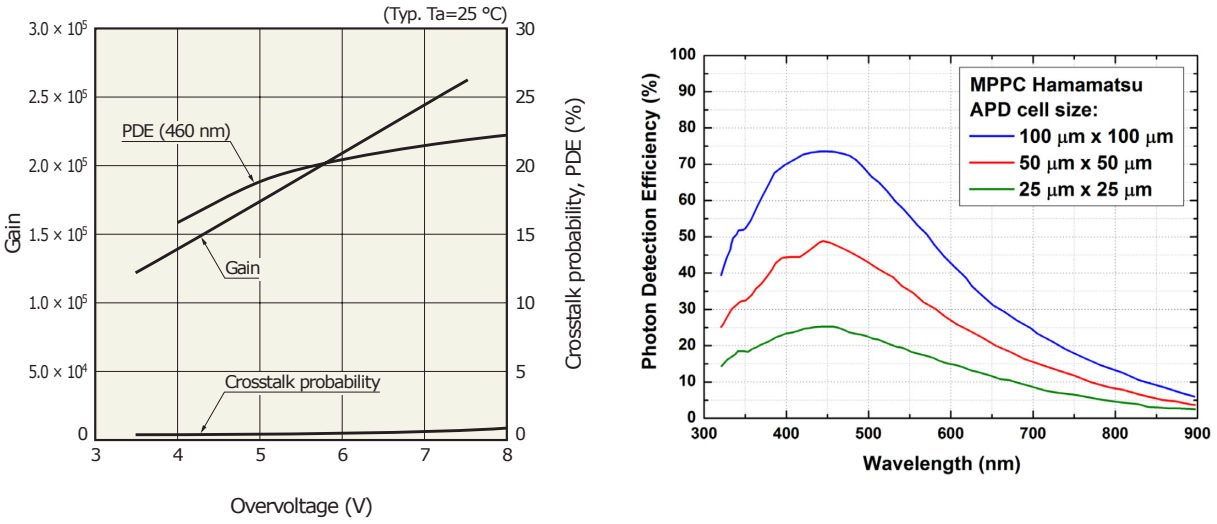

Figure 3.22: (left) Dependence of gain, crosstalk and photon detection efficiency on overvoltage for Hamamatsu S14160-1310PS SiPM [] [hamanewdata]. (right) Dependence of photon detection efficiency on wavelength for Hamamatsu SiPMs with different pixel pitch [164]. Presented SiPMs are optimised for blue light detection, i.e. presumably have p-on-n structure.

- Strong correlation of V_{bd}, PDE and gain to overvoltage and temperature, raising requirement for their precise control. An increase of gain with overvoltage $1/G \times dG/dV$ is usually about 2 %/dV. The temperature coefficient for V_{bd} is about 0.1 %/°C, and temperature coefficients for gain are in the range of 0.5 – 7 %/°C.
- Several orders lower radiation hardness: silicon internal structure is complex and easily disrupted by radiation, while metal and simple electronics components of the voltage divider (commercial resistors and capacitors) in PMT can withstand very high fluences.

If one considers using SiPMs for the applications of small area light readout, e.g. a readout from light-guiding fibers with a diameter of few mm^2 complemented with the continuous online calibration system, the radiation hardness is the main issue that has to be studied.

3.6 Review of SiPM irradiation studies

The study of the SiPM radiation hardness is gaining more popularity during the last decade due to the rapid increase of interest for its application in harsh radiation environments such as high luminosity physics experiments, PET scanners, and satellites. In HEP experiments fluences in the range of $10^9 - 10^{16}$ n_{eq}/cm^2 are anticipated.

Today, there are plenty of studies on SiPM performance after irradiation with various sources, spectra, and fluences (doses). I would like to thank E. Garutti and Yu. Musienko [130] for currently the only review article on the SiPM radiation hardness which excellently summarizes the main issues on SiPM radiation hardness. Authors draw a conclusion that even though dark current and noise increase greatly, the relative response of SiPMs does not degrade up to a fluence of 10^{12} n_{eq}/cm^2. However, other research results presented in this section (mainly in subsections 3.6.6 and 3.6.15) and my own results presented in subsection 7.8.2 show that this is not true for every device and experimental conditions. My understanding is that the authors' conclusion is only valid for novel SiPMs with small pixels operated at -30 °C. It inspired me

to extend their work and make a comprehensive review covering all the available articles on SiPM irradiation studies. I discuss a variation of the effects induced by different particles with a different energy, paying maximal attention to various discrepancies in the data and trying to explain their possible origins comparing the parameters of SiPM design, irradiation, and measurement conditions.

As previously discussed, in silicon sensors including SiPMs which have a regular crystal structure, the most radiation damage usually arises from lattice dislocations. The fast hadron irradiation has the largest probability to produce those lattice defects in the silicon bulk and therefore it is considered the most dangerous. Thus, I start my review explaining the change of various SiPM properties after irradiation by fast neurons and protons with energies in the range of 10 – 800 MeV produced by accelerators, fast neutron generators and reactors (though reactors produce neutrons from meV up MeV energies, the most effective is expected to arise from MeV neutrons). Then I move to other particle sources in subsections 3.6.10 – 3.6.14. In the end, I provide a short overview of performance studies for complex detectors conducted with irradiated SiPMs, possible ways to improve the SiPM radiation hardness, and the final summary. Note, that most covered results correspond to blue light sensitive SiPMs, but a few results for red light sensitive SiPMs are explicitly indicated. The majority of data was measured at room temperature after several days of recovery, unless specifically indicated otherwise.

3.6.1 Dark current and dark count rate

Dark current I_{dark} originates from carriers that were thermally generated, captured, and released by trap states or tunneled through the band gap as was explained in subsection 3.4.3. In SiPM I_{dark} consists of surface (carriers not participating in avalanches) and bulk (carriers multiplied in avalanches) components. Bulk current is mainly defined by the concentration of doping and defects in the epi-layer where avalanches are created. Value of I_{dark} is proportional to SiPM volume, pixel pitch, overvoltage, temperature, and defect concentration, including initial sensor doping and radiation-induced defects. IV curve is usually measured with a high precision micro- or even pico-ammeter.

Figure 3.23 shows the current increase after irradiation. Dark current may be stable below V_{bd} if the surface carrier generation dominates. On contrary, if bulk current dominates, it increases with the bias which is often the case for irradiated SiPMs. One can see that current density J_{dark} increases linearly with fluence with a rate of about 1 $\mu A/mm^2$ per 10^9 n_{eq}/cm^2. Similar data are reported in [157, 168–179]. Therefore, it can be used as a very rough estimate of the fluence. For instance for SiPMs with small 10 – 20 μ pixels operated at typical overvoltage of 3 – 4 V and room temperature, J_{dark} before irradiation is usually about 1 – 10 nA/mm^2, and after irradiation it becomes 0.5 – 5 $\mu A/mm^2$ for 10^9 n_{eq}/cm^2, 5 – 50 $\mu A/mm^2$ for 10^{10} n_{eq}/cm^2, 50 – 500 $\mu A/mm^2$ for 10^{11} n_{eq}/cm^2, and $>$ 1 mA/mm^2 for $> 10^{12}$ n_{eq}/cm^2 [157, 173–175, 177–198].

Furthermore, figure 3.23 reveals that J_{dark} decreases with pixel area. This can be explained by the decrease of an effectively depleted region with a decrease of effective fill factor. Consequently, for SiPMs with large 30 – 60 μ pixels J_{dark} is approximately 5 – 30 times higher than for 10 – 20 μ SiPMs [168, 169, 171, 172, 174–177, 179–181, 186–188, 190, 199–209].

SiPM dark current I_{dark} can be expressed via dark count rate DCR – a number of avalanches measured in darkness per second, usually measured for avalanches above 0.5 p.e. threshold [161]. Equation (3.15) and figure 3.24 (left) describe the linear dependence of DCR on I_d which is valid if gain and excess charge factor do not change as in the case of low fluences.

$$I_{dark} = e \cdot G(V_{ov}) \cdot DCR(T, V_{ov}) \cdot ECF(V_{ov}) \tag{3.15}$$

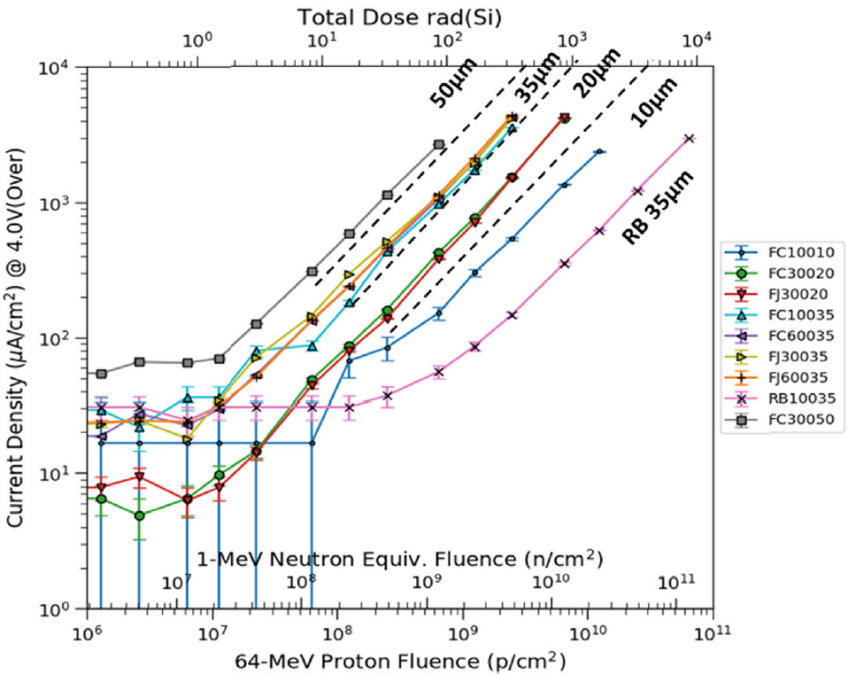

Figure 3.23: Dependence of dark current density on accumulated proton fluence for SiPMs with different pixel pitches operated at overvoltage of 4 V [180]. Note that J_{dark} here is presented in units of μA/cm^2, while in the text I use units of μA/mm^2. Proton fluence data is also recalculated to 1 MeV equivalent for neutrons as well as ionizing dose. All SiPMs were produced by Sensl (now ON Semiconductor) and have a size in the range of 1 – 36 mm^2. All except one SiPMs belong to C- and J-series which are optimized for blue light detection, i.e. presumably have p-on-n structure. RB10035 SiPM belongs to R-series and is optimized for red light detection, i.e. presumably have an n-on-p structure. I discuss the probable reason for differences in radiation hardness between p-on-n and n-on-p structures in subsection 3.6.16.

where G is the SiPM gain, and ECF is the excess charge factor which is described in the next subsection.

Figure 3.24 (right) shows the linear dependence of dark count rate on fluence with rate about 1 MHz/mm^2 per 10^9 n_{eq}/cm^2. Similar data are reported in [186,188,210]. At room temperature, before irradiation DCR is usually below 100 kHz/mm^2, while already after 10^9 n_{eq}/cm^2 it rises to MHz levels, and reaches GHz levels after 10^{11} n_{eq}/cm^2 [172, 177, 178, 181, 186, 188, 189, 191–194, 198, 204–207, 210–213].

The dark count rate is usually assessed as the number of Geiger-discharges exceeding the threshold level of 0.5 photoelectrons in SiPM charge spectra measured in dark conditions, see [161] for discussion. However, the latter can be performed only for moderate DCR where the peaks for noise from Geiger discharges are well separated from the electronics noise, which is not valid for highly irradiated SiPMs, see subsection 3.6.5. In this case, DCR can be determined only from I_{dark} measurement (by equation (3.15)), or from the measurement of the standard deviation of SiPM noise in darkness (see [161] for details), though both methods rely on the knowledge of gain and ECF.

As was explained in subsections 3.4.2 and 3.4.3, dark current generation in silicon is described by Shockley–Read–Hall (SRH) statistics and it is strongly dependent on temperature, see equations 3.3,3.6. Dependence of I_{dark} and DCR on temperature is depicted in figure 3.25.

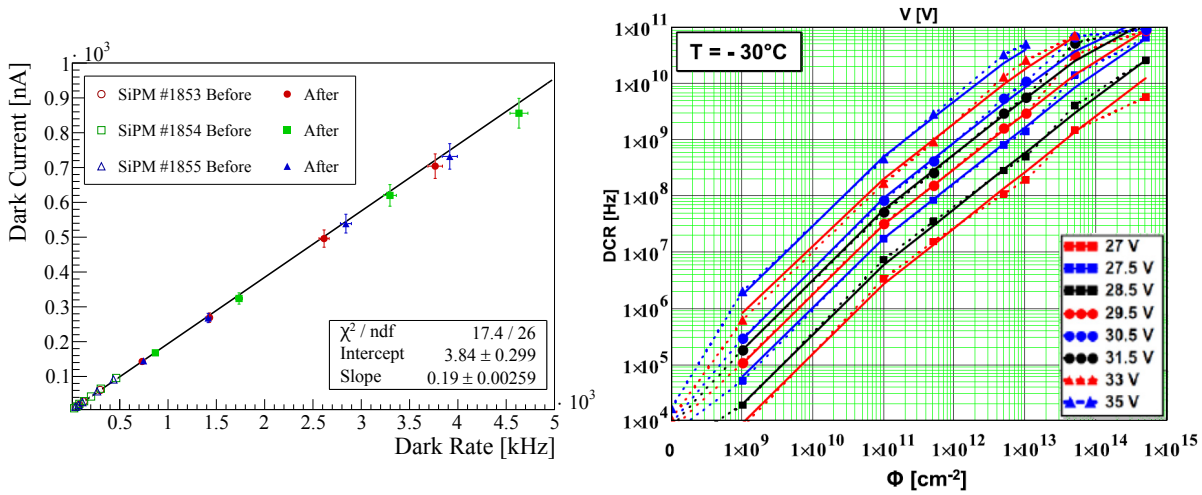

Figure 3.24: (left) Dependence of the dark count rate on dark current for SiPMs before and after neutron irradiation with fluence of 3.7×10^9 n_{eq}/cm^2 [178]. Different values for the same SiPMs were measured at various temperatures between -5 °C and 25 °C. SiPMs were irradiated by fast neutrons. SiPMs were manufactured by Hamamatsu and have 1 mm^2 area with 50 µm pixels. (right) Dependence of the dark count rate on 1 MeV equivalent fluence for SiPMs operated at different bias voltages, determined from the dark current measurements at -30 °C [193]. SiPMs were irradiated by reactor neutrons. SiPMs were manufactured by Ketek and have 1 mm^2 area with 15 µm pixels.

Before irradiation, the temperature coefficient is usually around 9 – 11 %/K similar to what is observed for regular silicon sensors. Several researchers found that after irradiation with $10^9 - 10^{10}$ n_{eq}/cm^2 it can decrease down to 4 – 6 %/K [171, 178, 179] which can be seen in figure 3.25 (left). SiPMs with higher operating voltages typically demonstrates higher temperature coefficients [214]. M. Vignali et al. [194] proposed a parametrization of the dark current in terms of fixed band gap energy $E_g = 1.12$ V and current activation energy. The latter term decreased from 0.63 down to 0.59 for 15 µm Ketek SiPMs after irradiated with 10^{12} n_{eq}/cm^2.

More exotic approaches include SiPM imaging by a high-resolution CCD camera to see the light produced by thermally generated discharges [189,216,217] or DCR measurement for digital SiPM with individual pixels disabled one by one [210, 211], which are presented in figure 3.26. Both methods allow estimating DCR individually for each pixel. They revealed that some pixels produce 20 times more noise than average probably due to high defect concentration [161]. Observed light hot-spots have a diameter of about 10 µm probably corresponding to the diameter of the avalanche (pixel size was 50 µm). The size of these micro-discharge channels does not depend on V_{ov}.

3.6.2 Noise parameters

Figure 3.27 depicts the increase of SiPM noise with radiation damage which introduces new defects in the silicon lattice.

The contribution of SiPM noise to total equivalent noise charge of the detector system described by equation (3.12) can be expressed as [218]

$$ENC^2_{SiPM} = 2 \cdot e \cdot B \cdot \left[(I_{light} + I_{d-bulk}) \cdot G^2 \cdot ENF + I_{d-surf} \right] \tag{3.16}$$

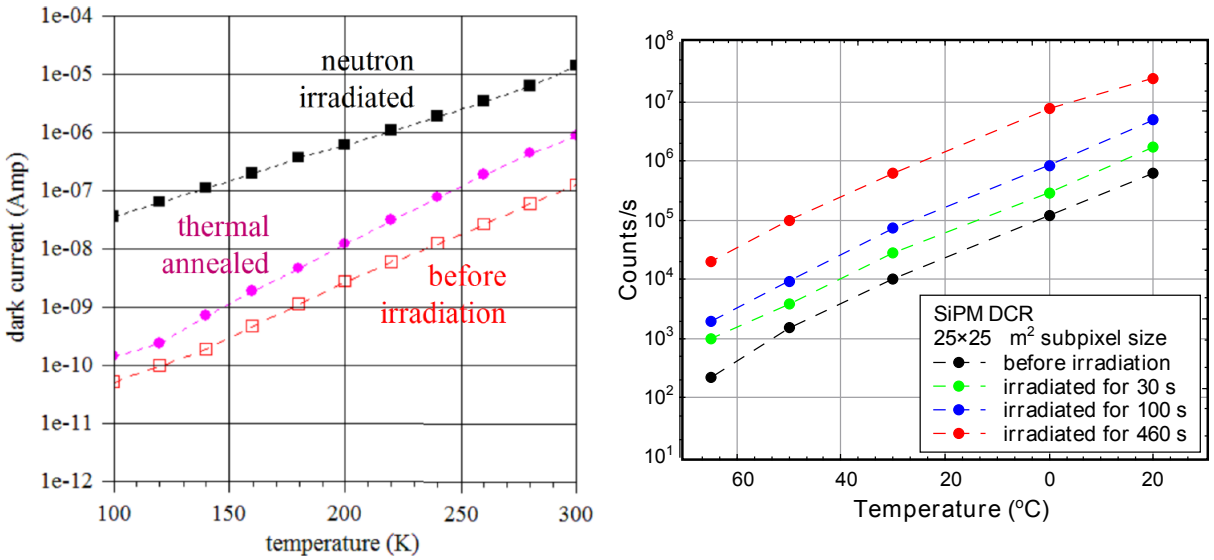

Figure 3.25: (left) Dependence of the dark current on SiPM temperature before and after neutron irradiation with fluence of 1.8×10^9 n_{eq}/cm^2 [179]. SiPMs were irradiated by fast neutrons. SiPMs are Hamamatsu S13360 and have 9 mm^2 area with 50 µm pixels. Measurements were performed before and after high temperature annealing at 250 °C accelerated by applied forward bias. (right) Dependence of the dark count rate on SiPM temperature before and after 170 MeV proton irradiation [215]. Irradiation times of 30, 100, 460 s correspond to fluences of 3×10^8, 1×10^9, and 4.6×10^9 n_{eq}/cm^2, respectively. SiPMs were manufactured by Hamamatsu and have 9 mm^2 area with 25 µm pixels. Data on SiPMs with 50 and 75 µm pixel size is available in [215].

where B is the readout bandwidth, ENF is the excess noise factor, I_{light} is the current due to light pulses, I_{d-bulk} is the bulk dark current, and I_{d-surf} is the surface dark current. Only I_{light} and I_{d-bulk} are multiplied by gain.

The equivalent noise charge of SiPM can be estimated in units of photoelectrons with equation (3.16) from dark current measurements. Alternatively, noise variance presented in figure 3.27 (right) can be measured with an oscilloscope and normalized by a single photoelectron value estimated with spectral measurement. However, both methods rely on the knowledge of SiPM gain and ENF or the assumption that they did not change after irradiation. Example of such a measurement is presented in figure 3.28. Similar data are reported in [203].

SiPM noise can be divided into uncorrelated and correlated with respect to the signal. Uncorrelated noise originates from the dark current, while correlated noise follows the photon-induced avalanches in the forms of afterpulsing (inside the pixel) and crosstalk (in neighboring pixels). Before irradiation, surface dark current and/or correlated noise may dominate the performance of high-quality SiPMs, but after irradiation drastic increase of bulk dark current becomes superior. Therefore, noise exhibits the temperature dependence similar to I_{dark} as shown in figure 3.29.

Afterpulsing (AP) is caused by the carriers that are trapped by lattice defects and released afterward causing an additional avalanche breakdown of the pixel. Optically-induced afterpulsing can happen if during the avalanche secondary photons were produced and later reabsorbed generating a secondary avalanche. Optical crosstalk (XT) happens when during the avalanche in one pixel secondary photons are emitted producing avalanches in neighboring pixels. Optically-

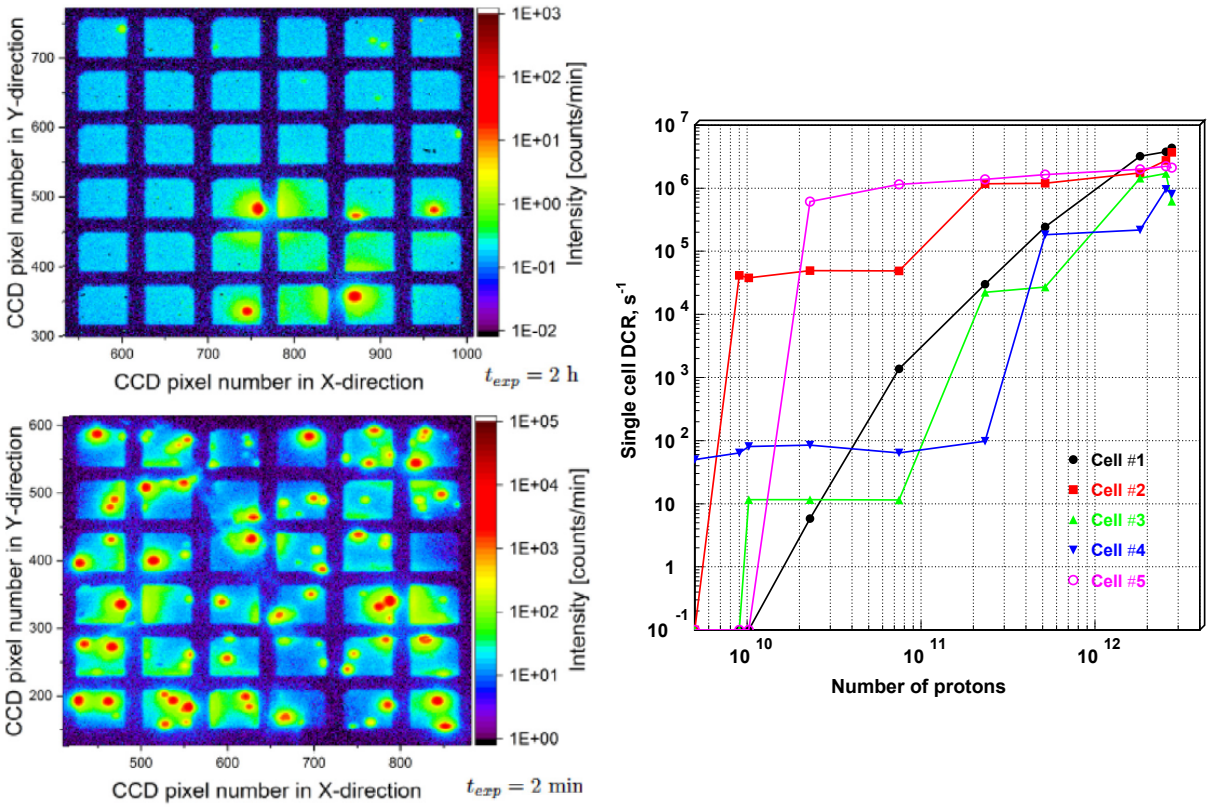

Figure 3.26: (left) Light hot-spots on images taken for SiPM before irradiation (top) and after (bottom) irradiation operated at overvoltage of 4 V. SiPM were irradiated up to 10^{10} n_{eq}/cm^2 []. SiPMs were manufactured by Ketek and have 9 mm^2 area with 50 µm pixels. (right) Dependence of the dark count rate on fluence per SiPM for several individual pixels of digital SiPM measured during the irradiation [210]. Irradiation was performed with 800 MeV protons up to maximal fluence of 4×10^{11} p/cm^2 or 5.7×10^{11} n_{eq}/cm^2. SiPMs were cooled down to -20 °C. SiPMs were manufactured by Philips and have 9 mm^2 area with 50 µm pixels. The maximal DCR of 2 MHz for a single pixel corresponds to DCR of 400 MHz per mm^2.

induced afterpulsing and crosstalk can occur right after the initial pulse (prompt XT/AP) or be delayed by several ns or µs. Delayed XT/AP happens if a secondary photon generated an electron–hole pair in a neutral non-depleted region and carriers have to diffuse to the active region. In case if pixel recovery time is much longer than the effective carrier lifetime, the afterpulsing and crosstalk probability can be considered negligible [157].

Figure 3.30 presents the dependence of afterpulsing and crosstalk on fluence for low fluence range. They can be evaluated from the charge spectra measurement either in darkness, same as for DCR, or with low light pulses with low amplitude producing a few photoelectrons, see [161]. Unfortunately, like in the case of DCR, the distinction between the peaks or areas corresponding to different noise sources is usually not possible for high noise levels, e.g. for highly irradiated SiPMs.

Alternatively, current transients can be recorded. Extraction of correlated noise parameters is more difficult than plain DCR measurement, because though prompt crosstalk events produce high pulses and are easily distinguishable, but afterpulsing and delayed crosstalk events are mixed with primary light events [157]. Furthermore, correlated noise contribution to the

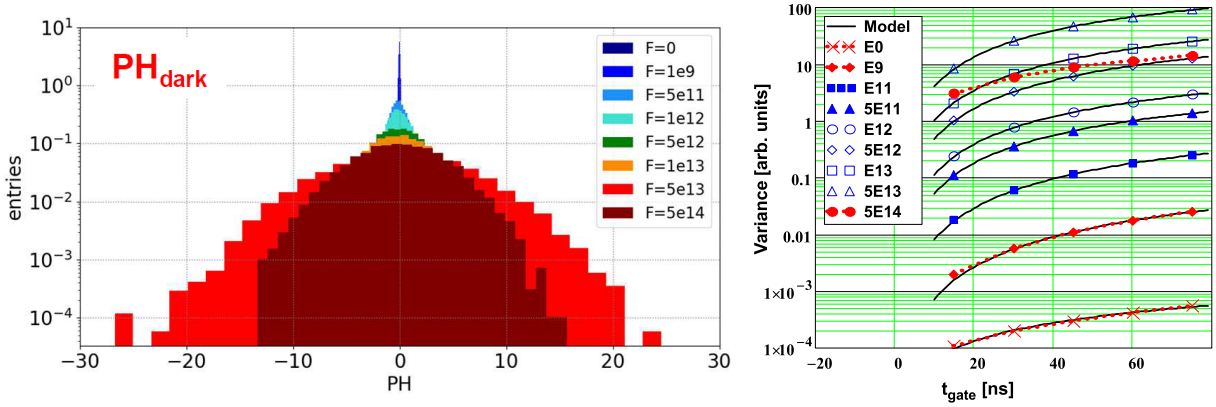

Figure 3.27: (left) Dark noise spectra measured at -30 °C after irradiation to different 1 MeV equivalent neutron fluences [161]. SiPMs were irradiated by reactor neutrons. SiPMs were manufactured by Ketek and have 1 mm^2 area with 15 µm pixels. (right) Dependence of variances of the noise spectra as a function on the gate width for the same data.

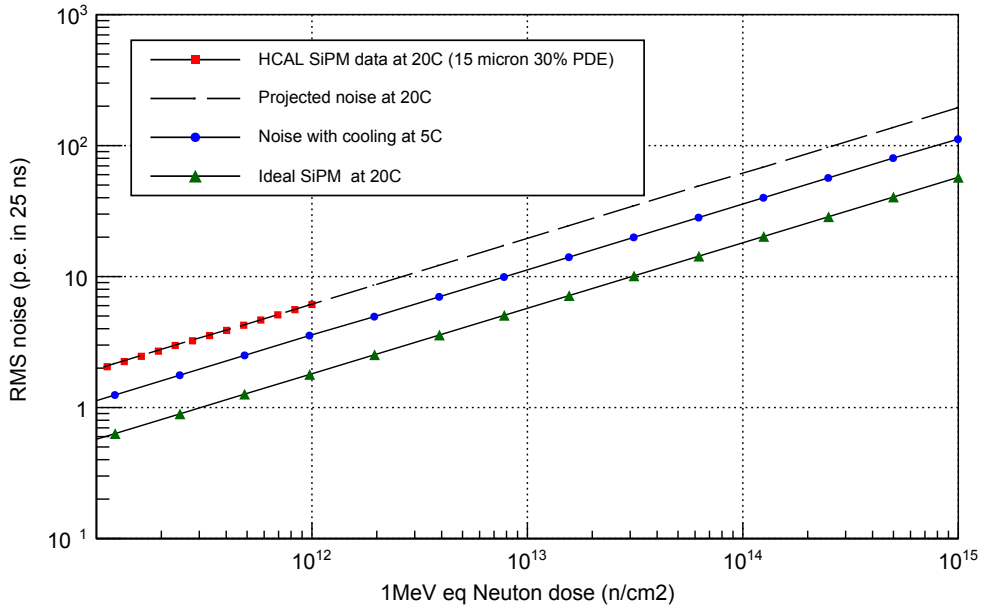

Figure 3.28: Dependence of dark noise RMS on 1 MeV equivalent neutron fluence for proton irradiated SiPMs [182]. SiPMs were measured at 5 and 20 °C. SiPMs were manufactured by Hamamatsu and have 1 mm^2 area with 15 µm pixels. "Ideal SiPM" refers to model calculation, see [182] for discussion.

measured signal depends on integration time, readout, and analysis method. The common way to disentangle different events is to plot the amplitude versus inter-time between the events and fit individual contribution areas is utilized for this analysis, alternatively, pulse counting with a variable threshold can be employed [161].

Correlated noise parameters increase the charge and its standard deviation measured with real SiPM compared to the ideal photodetector. Distribution for the latter is described by the Poisson statistics: for a number of primary photoelectrons triggered by the incoming photons

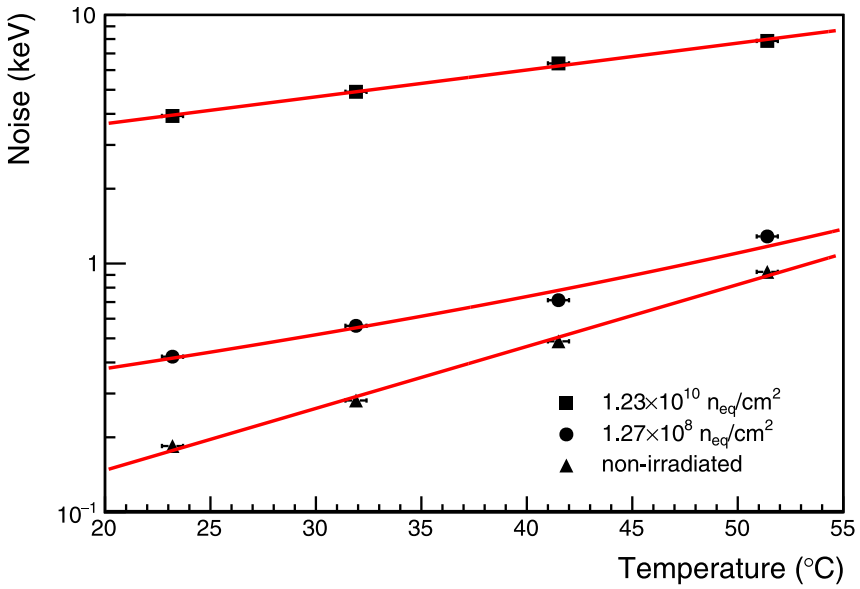

Figure 3.29: Dependence of dark noise on temperature for SiPM arrays before and after proton irradiation operated at overvoltage of 3.65 V [171]. Measurements were performed after half a year of annealing at room temperature followed by 168 hours of annealing at 79 °C. Sensors are Sensl J-series (now ON Semiconductor) 2×2 arrays which have 1.27 cm^2 area with 35 µm pixels.

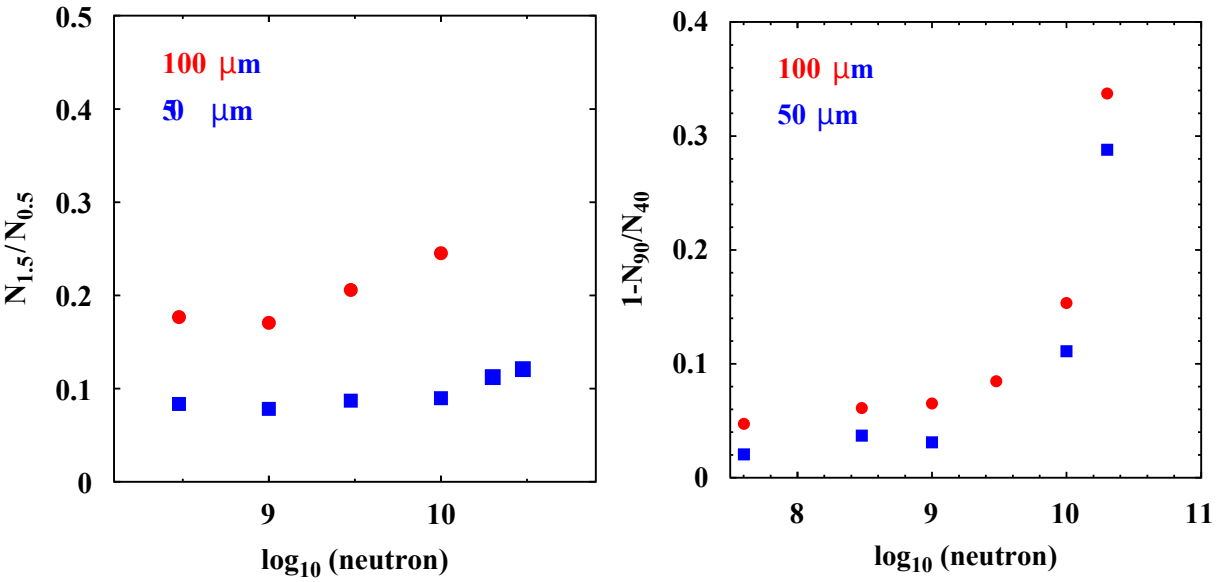

Figure 3.30: Dependence of crosstalk (left) and afterpulsing (right) probabilities on reactor neutron fluence [177]. Fluence can be converted to 1 MeV equivalent fluence by multiplying a factor 0.4. Here crosstalk is defined as DCR with 1.5 p.e. threshold divided by that of a 0.5 p.e. threshold. Afterpulsing is defined as a difference in DCR measured with 1 p.e. threshold with 40 and 90 ns veto durations after the pulse. SiPMs were manufactured by Hamamatsu and have 1 mm^2 area with 100 µm pixels.

N_{pe}, the event to event fluctuations are given by the standard deviation equal to $\sqrt{N_{pe}}$. Excess charge factor ECF accounts for the increased charge as

$$ECF = (1 + P_{AP})(1 + P_{XT}) = \frac{\overline{Q}}{\overline{Q_N}} \tag{3.17}$$

where P_{AP} is the afterpulsing probability, P_{XT} is the crosstalk probability, $\overline{Q}$ is the average measured charge and $\overline{Q_N}$ is the average charge of primary photoelectrons.

Therefore, ECF adds an artificial gain to the SiPM signal and noise, which also deteriorates its resolution that can be expressed via excess noise factor as

$$ENF = \frac{(\sigma_Q/\overline{Q})^2}{(\sigma_{Q_N}/\overline{Q_N})^2} \tag{3.18}$$

where σ_Q is the standard deviation from the average measured charge $\overline{Q}$, and σ_{Q_N} is the standard deviation from the average charge of primary photoelectrons $\overline{Q_N}$ [160].

For novel non-irradiated SiPMs value of excess charge, a factor is usually below 1.2 [161]. It and approaches unity around V_{bd} and rises with the overvoltage, best low crosstalk SiPMs exhibit $ECF \approx 1$ up to $V_{ov} = 5$ V. Crosstalk also depends on the surface reflections which can originate at covering epoxy layer or scintillating crystal wrapped in reflective material placed on top of the SiPM. In most cases for non-irradiated SiPMs at room temperature $ECF \approx ENF$ [161]. ENF also depends on the gain variations, but for SiPMs these are usually negligible (< 0.1 %) which is in contrast to APDs [164, 219]. Unfortunately, for irradiated SiPMs which can not resolve single photons, there is no straightforward technique to estimate ECF and ENF [161].

3.6.3 Breakdown voltage

Knowledge of breakdown voltage V_{bd} is essential for SiPM characterisation and operation since most of its parameters depend on the overvoltage $V_{ov} = V_{bias} - V_{bd}$. The value of breakdown voltage is defined by the critical electric field E_{crit} required to start and sustain the avalanche which depends on the SiPM design, i.e. doping profile, and ionization probabilities of electrons α_n and holes α_p for silicon. α_n is several times higher than α_p depending on the electric field strength, so electrons initiate most of the avalanches [218]. Breakdown voltage is the integral of the electric field over the depletion width, so the higher voltage is required to deplete a wider region. On the one hand, a wide highfield region provides a higher number of possible collisions, thus a higher probability of avalanche generation. This results in a lower E_{crit}, which tends to reduce the field-enhanced noise generation [157].

Changes in the doping profile after irradiation result in a shift of breakdown voltage, usually, it increases. No shift was observed for fluences below $10^9 - 10^{10}$ n_{eq}/cm^2 [169, 176, 195, 204]. Figure 3.31 presents the change of breakdown voltage with fluence observed for different SiPMs. For fluences up to 10^{13} n_{eq}/cm^2 modest V_{bd} shifts up to 0.5 V were reported by [177, 179, 181, 188, 215]. For very high fluences change of V_{bd} seems to depend a lot on the SiPM structure, or respectively, manufacturer technology. Shifts only below 0.5 V were observed for FBK and Ketek SiPMs [182,193,195,213] irradiated by $1 \times 10^{14} - 5 \times 10^{14}$ n_{eq}/cm^2. Drastic V_{bd} increase of 1 – 4 V was reported in [182, 188, 213] for Hamamatsu SiPMs irradiated by $1 \times 10^{14} - 5 \times 10^{14}$ n_{eq}/cm^2.

Critical value of electric field increases with temperature, so if increment in E_{crit} is multiplied by a value of higher breakdown voltage, larger variation of V_{bd} with temperature is observed. Indeed, SiPMs with $V_{bd} \sim 25$ V usually have $dV_{bd}/dT \sim 20$ mV/°C [152,153], while SiPMs with $V_{bd} \sim 75$ V have $dV_{bd}/dT \sim 60$ mV/°C [154, 155]. Only one paper by S. Cerioli et al. [193]

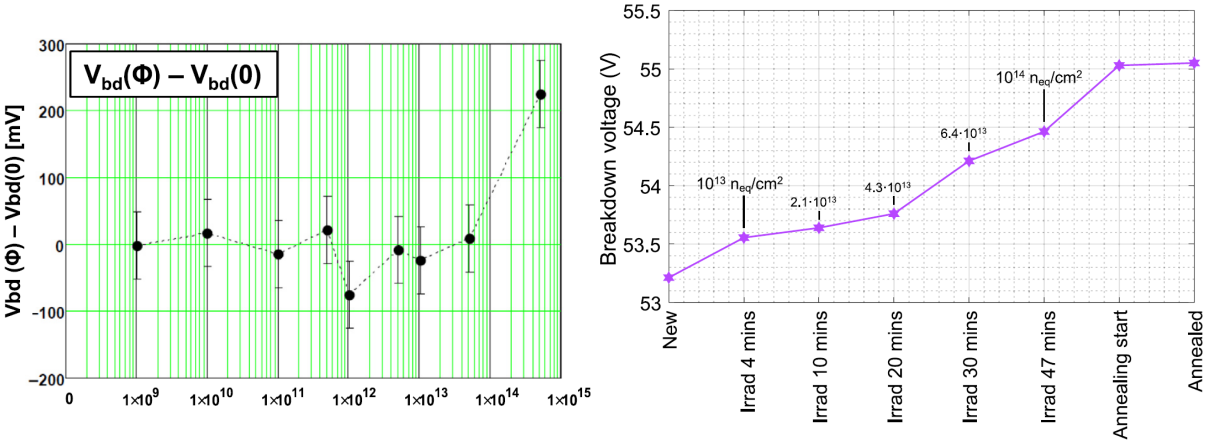

Figure 3.31: Dependence of the breakdown voltage on 1 MeV equivalent fluence for 15 µm Ketek (left, $V_{bd} \sim 27$ V) [193] and 50 µm Hamamatsu (right) [188] SiPMs. Both SiPMs were measured at room temperature after irradiation by reactor neutrons. Both SiPMs have 1 mm^2 area.

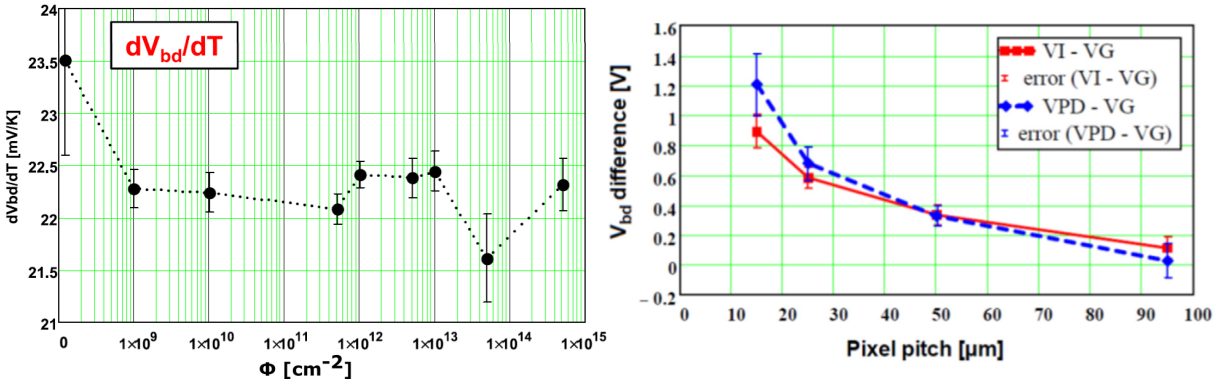

Figure 3.32: (left) Relative change of the breakdown with temperature in range from -30 °C to +30 °C on 1 MeV equivalent fluence [193]. SiPMs were irradiated by reactor neutrons. SiPMs were manufactured by Ketek and have 1 mm^2 area with 15 µm pixels. (right) Differences in the breakdown voltage values estimated with dark current (VI), gain (VG) and *PDE* (VPD) depending on the pixel pitch (SiPMs were not irradiated) [220]. SiPMs were manufactured by Ketek and have 1 mm^2 area with 15, 25, 50 and 100 µm pixels.

reported investigation of V_{bd} temperature coefficient after irradiation, and observed almost no change up to fluence of 5×10^{14} n_{eq}/cm^2, see figure 3.32 (left).

Breakdown voltage can be determined from the extrapolation of G(V_{bias}) to zero (measured with charge spectra) or from the bending point of the IV curve, both methods are described in details in chapter 7. These methods give comparable results for SiPMs with big pixels, but the value measured with gain extrapolation can be lower by up to 1.2 V for devices with small pixels as shown in figure 3.32 (right). V. Chmill et al. [220] explains it by the fact that higher voltage is required to initiate an avalanche while it can be further sustained even at a slightly lower voltage, but why it scales with the pixel size is not yet understood. Another rarely used option of V_{bd} determination is based on *PDE* measurements, it is in good agreement with IV method, see figure 3.32 (right).

Unfortunately, there is no general agreement on which method is preferential, and also which fitting method to apply for V_{bd} extraction from IV curve. Different manufacturers and researchers use various approaches and, unfortunately, do not always explicitly specify how the breakdown voltage was obtained. I will follow the convention described in [220] that the IV curve measurement provides the voltage when an avalanche is turned on V_{on} which I will reference as V_{bd}, while the gain to zero extrapolation provides the voltage when an avalanche is turned off V_{off}. Note, that in reality the SiPM gain at V_{bd} can not be zero since the SiPM already has a small avalanche gain below V_{bd} similarly to APD [160].

3.6.4 Electrical parameters

The main capacitive parameters of the SiPM equivalent circuit C_d and C_q can be extracted by measurements with LCR-meter which is discussed in detail in sections 7.7.1 and 7.7.2. Before irradiation, pixel capacitance varies in range from 1 fF up to 1 pF (see [161] and table 7.1), increasing with the pixel area. Quenching capacitance is typically ten times lower [161]. Up to now, only one research group studied the change of pixel capacitance after irradiation with fluence up 5×10^{14} n_{eq}/cm^2 [191,193,194]. Figure 3.33 (left) shows that no change was observed. Furthermore, measurement results do not depend on the temperature.

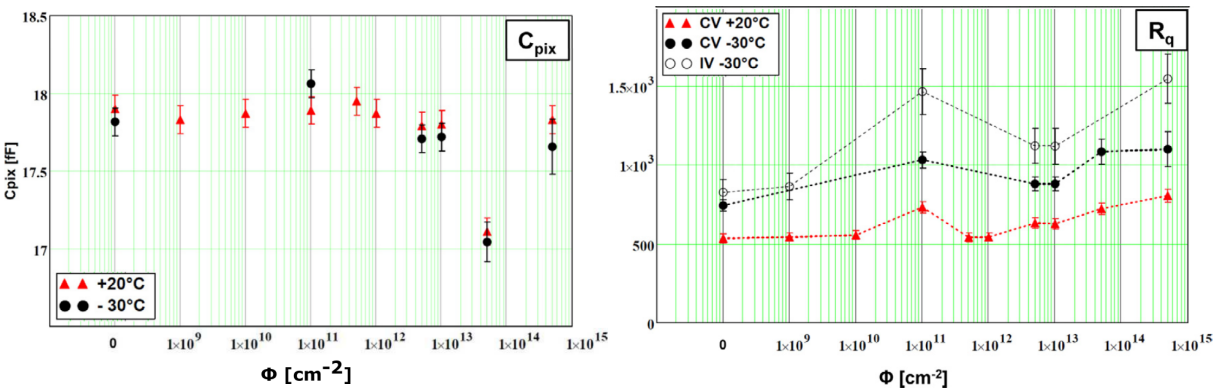

Figure 3.33: Dependence of pixel capacitance (left) and quenching resistance (right) on 1 MeV equivalent fluence [193]. SiPMs were irradiated by reactor neutrons. SiPMs were manufactured by Ketek and have 1 mm^2 area with 15 µm pixels. Measurements of capacitance (CV) were performed at -30 °C and +20 °C. R_q was also measured with help of dark current at a forward bias (IV) at -30 °C.

Quenching resistance can also be determined with LCR meter (see [161] for details), or by a much easier approach of forwarding current measurement which is described in subsection 7.6. However, these methods give somewhat different results which are presented in figure 3.33 (right). Before irradiation, the value of quenching resistance is usually in the range of 0.1 – 5 MΩ. No change of R_q was observed for fluence below 10^{11} n_{eq}/cm^2 [169, 176, 204]. For higher fluences increase of R_q up to 20 – 50 % can be seen, however, the authors indicate that it can be explained by initially different R_q values in different SiPM samples [193, 194].

Most commonly, a quenching resistor is made out of polysilicon, so its resistance decreases with temperature as shown in figure 3.33 (right), which can alter the recovery time and signal shape. Nevertheless, the temperature coefficient is typically below 2 %/°C [161,193], so for room temperature operation, it can be considered negligible.

Parasitic parameters can also be evaluated by solving equations 3.14 or fitting the complex

impedance-frequency dependencies with known main parameters, see [161]. The value of R_d can be theoretically estimated by the single-pixel signal rise time, but the readout bandwidth limitations make it hard to accomplish. The value of R_d is typically on the order of 500 – 1000 Ω and its precise knowledge are usually not that important [157].

Knowledge of the parameters of the SiPM equivalent circuit allows us to simulate the SiPM response and calculate several important operational parameters. The intrinsic limit of the signal rise time (with ideal amplifier and readout) is given by $\tau_{rise} = (C_d + C_q)/(R_d^{-1} + R_q^{-1}) \approx C_d R_d$ because $R_q \gg R_d$ and usually $C_d \gg C_q$ (especially for small pixels), τ_{rise} can be as low as tens of ps. The pixel recovery time is given by $\tau_{recovery} = (C_d + C_q) \cdot R_q^{-1} \approx C_d R_q$, depending on the SiPM design it can be anywhere between few ns and several ms. Since both pixel capacitance and quenching resistance do not seem to change after irradiation, value of $\tau_{recovery}$ can be considered unchanged as well [191].

Full depletion voltage which is very important for common silicon sensors as discussed in subsection 3.4.4, is not straightforward to define for SiPMs. Indeed, SiPM usually has total width (∼ substrate width) of about 300 – 500 μm and operates at voltages below 100 V, so its volume is never fully depleted of carriers. Though the most important is the depletion of the epitaxial region which is only 1 – 10 μm wide, and it usually becomes depleted much below the breakdown voltage. For example, SiPMs with the $V_{bd} \sim 70$ V were found to have the $V_{FD-epi} \sim 20$ V, and SiPMs with the $V_{bd} \sim 25$ V had the $V_{FD-epi} \sim 1$ V [165]. V_{FD-epi} can be estimated from the kick dependence of the capacitance on bias voltage $C(V)$. However, due to the complex doping profile, it does not always have a precisely defined value, see discussion in section 7.7.2.

In summary, in calorimetric application values of C_d and R_q are the most important because they allow estimating the SiPM gain (see next subsection) and recovery time.

3.6.5 Single photon detection and gain

SiPMs are popular due to their ability to detect light on a single-photon level due to their high gain and low noise. As was explained earlier, after irradiation noise level increases dramatically which reduces the resolution for single photoelectron peaks. Usually, SiPMs completely lose the ability to detect single photons after fluence in the range of $10^9 - 10^{10}$ n_{eq}/cm^2 depending on the SiPM structure, see figure 3.34 [157, 169, 175, 177, 179, 186, 191, 201, 205, 207, 215, 221]. Note, that this is only true for room temperature operation at low overvoltages after annealing of at least 10 days. Right after irradiation noise is much higher, more so at high overvoltages, which can make SiPMs unable to resolve single photons already after 10^8 n_{eq}/cm^2 [175, 181]. At the same time, if special annealing is applied or SiPMs are operated at very low temperatures, they will resolve photons up to much higher fluences, see figure 3.43.

Gain or multiplication factor is defined as the number of secondary carriers produced per each primary one. Process of Geiger discharge can be described by the avalanche triggering probability of electrons P_e and holes P_h, with P_e is usually 2 – 3 times higher than P_h [160].

The most precise way to extract gain is to use SiPM charge spectra measurement at the low light level where single-photon peaks are distinguishable as done in subsection 7.8.1. Alternatively, the gain can be calculated as the total charge of the SiPM pulse divided by elementary charge e via equation (3.19), based on electrical measurement of breakdown voltage from IV curve and capacitance with LCR meter, see subsection 7.5 for example capacitance calculations.

$$G = \frac{(C_d + C_q) \cdot (V_{bias} - V_{bd})}{e} \approx \frac{C_d \cdot (V_{bias} - V_{bd})}{e} \tag{3.19}$$

No significant gain degradation after irradiation was observed for fluences below 10^{10} n_{eq}/cm^2 where single-photon peaks can be distinguished [169, 179, 201, 207]. But deviations from linearity

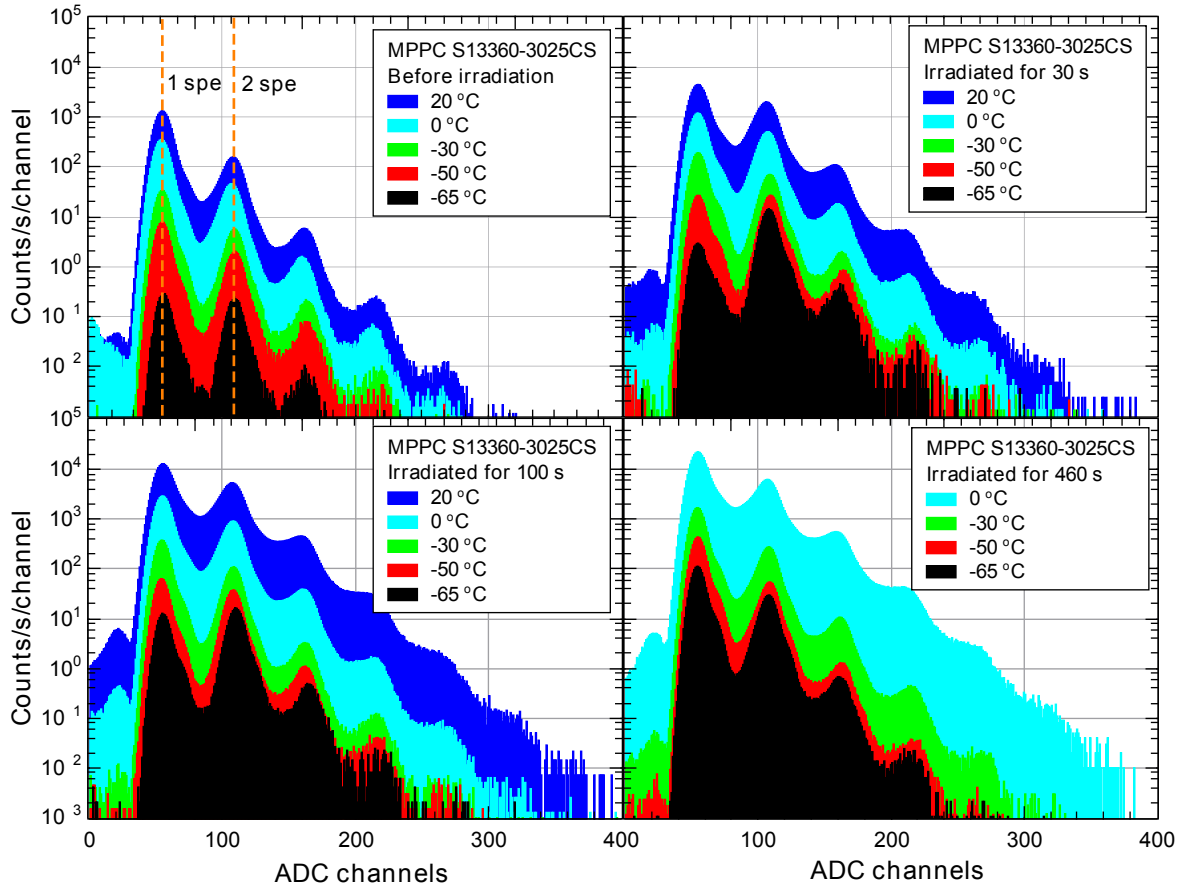

Figure 3.34: Single photon spectra measured for SiPMs before and after 170 MeV proton irradiations of different duration [215]. Irradiation times of 30, 100, 460 s correspond to fluences of 3×10^8, 1×10^9, and 4.6×10^9 n_{eq}/cm^2, respectively. Measuremnts were performed at -65 °C, -50 °C, -30 °C, 0 °C and +20 °C. SiPMs were manufactured by Hamamatsu and have 9 mm^2 area with 25 μm pixels. Data on SiPMs with 50 and 75 μm pixel size is available in [215].

up to 10 % for gain dependence on overvoltage were reported for irradiated samples operated above $V_{ov} = 1.5$ V (i.e. at maximal overvoltage where single-photon peaks were still distinguishable) [169, 201]. For higher fluences, the gain can be estimated only based on pixel capacitance C_{pix} (C_d). Because no change in C_{pix} was found up to a fluence of 5×10^{14} n_{eq}/cm^2 (see the previous subsection), one may assume that gain did not change either. However, the situation might be more complicated, see chapter 7 for discussion.

As was indicated earlier, gain depends on overvoltage and temperature, with coefficients about $G^{-1} \cdot dG/dV \sim 2$ %/V and $G^{-1} \cdot dG/dT \sim 0.5 - 7$ %/°C, respectively [152, 153, 155, 222]. SiPMs with large areas and small pixels have lower gain due to their lower capacitance and higher parasitic components. The latter include bigger grid capacitance and longer connections between pixels and output nodes which act as a low pass filter on the output current.

3.6.6 SiPM response and photon detection efficiency

SiPM response for relatively small light pulses (see next subsection for discussion of the dynamic range) can be expressed in terms of the number of produced photoelectrons as [222]

$$R(\lambda, V_{ov}) = N_\gamma \cdot PDE(\lambda) \cdot G(V_{ov}) \cdot ECF(T, V_{ov}) \tag{3.20}$$

Figure 3.35 shows the decrease of SiPM pulse amplitude with fluence. Depending on pixel technology (notably pixel pitch), annealing and operation conditions, degradation can start already at very low fluence, or no degradation might be observed even after very high fluence. For instance, for SiPMs with pixel pitch > 50 µm signal decrease was reported to start already after $10^9 - 10^{10}$ n_{eq}/cm^2 [175, 177, 178, 203–205], but for SiPMs with pixel pitch < 15 µm degradation was observed only after $10^{11} - 10^{12}$ n_{eq}/cm^2 by [182, 196, 197, 223, 224], or even $10^{13} - 10^{14}$ n_{eq}/cm^2 by [182, 193, 213].

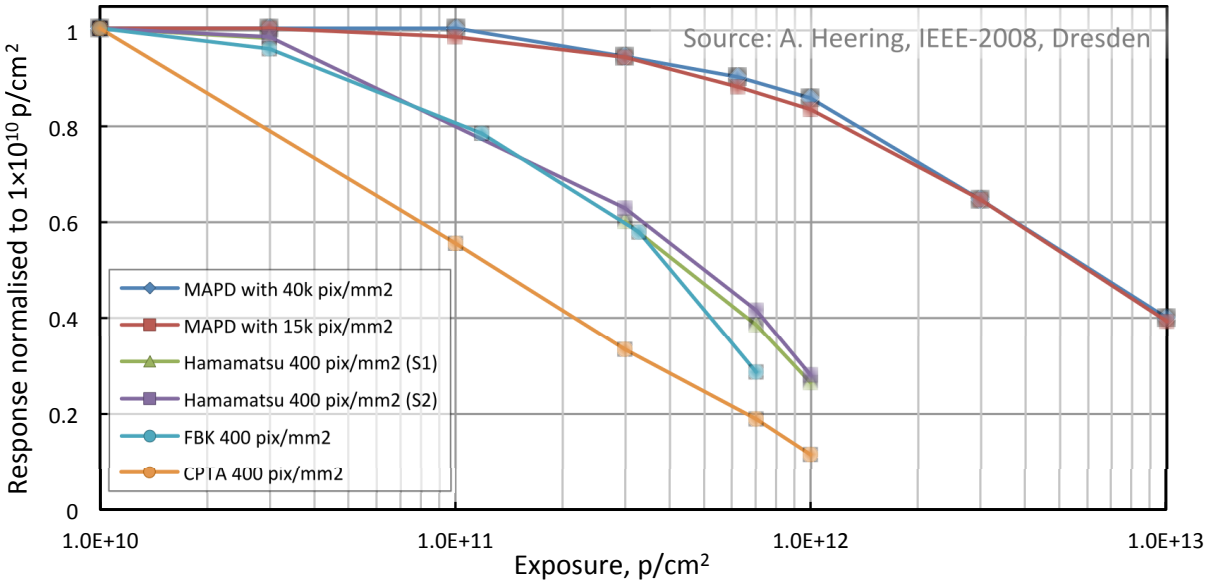

Figure 3.35: Dependence of SiPM response on proton fluence for SiPMs with different pixel (cell) densities [154, 183]. Fluence is indicated here for 212 MeV protons, but it is roughly equal to 1 MeV neutron equivalent fluence. SiPMs manufactured by FBK, CPTA/Photonique, Hamamatsu has 1 – 16 mm^2 areas and 50 µm pixels. SiPMs manufactured by Zecotek has 9 mm^2 area and 5 and 8 µm pixels.

According to equation (3.20), degradation of response can be explained by the decrease of either gain or PDE (or both). Obviously, ECF is expected to only increase after irradiation along with noise. A. Heering et al. [182] provide an interesting explanation stating that when the DCR per pixel becomes comparable to the pixel recovery time, the pixel is effectively busy all the time due to dark counts and can not respond to incoming photons anymore. This way, SiPMs with smaller pixel pitch exhibit higher level of radiation tolerance because they have more pixels per area and shorter recovery time.

Figure 3.36 presents the simple calculation of SiPM pixel occupancy before and after irradiation. These data was calculated as the ratio between SiPM current and maximally possible current which will flow through SiPM if all the pixels will be active simultaneously, i.e. $\eta = I/I_{max} = I \cdot R_q/(V_{ov} \cdot N_{pix})$. Current data was acquired based on SiPM current measurement in darkness and under continuous illumination [192, 194, 195]. Note, that pixel occupancy increases by up to an order of magnitude with a temperature increase of 50 K, which can be compared to DCR increase with temperature is shown in figure 3.25 (right).

Photon detection efficiency PDE is the ratio of detected photons (primary photoelectrons)

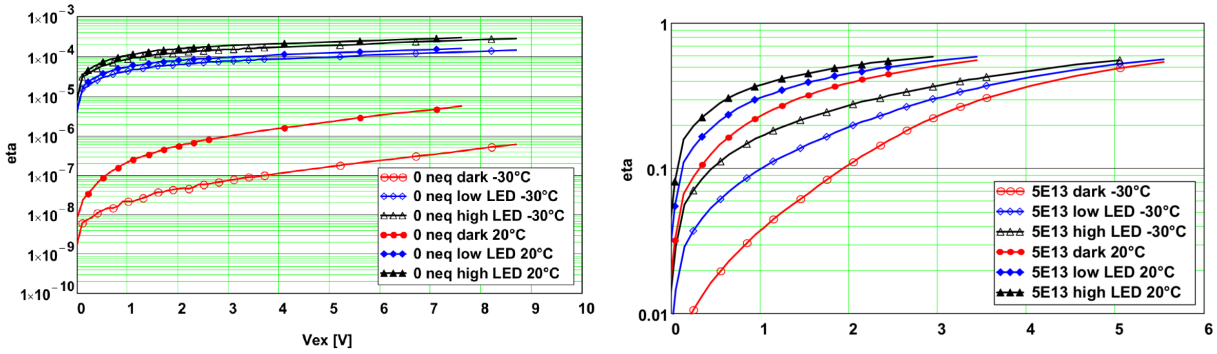

Figure 3.36: Dependence of SiPM pixel occupancy on overvoltage for SiPMs before (left) and after irradiation (right) with 5×10^{13} n_{eq}/cm^2 [192]. SiPMs were irradiated by reactor neutrons. SiPMs were manufactured by Ketek and have 1 mm^2 area with 15 μm pixels. Dark current measurements were performed at -30 °C and +20 °C, in darkness and under LED illumination with high and low intensities.

n_{pe} to the number of photons hitting the SiPM N_γ, and is described by the combination of three intrinsic SiPM properties

$$PDE(\lambda, V_{ov}) = \frac{n_{pe}}{N_\gamma} = FF_{eff}(\lambda, V_{ov}) \cdot QE(\lambda) \cdot P_{av}(\lambda, V_{ov}) \tag{3.21}$$

where FF_{eff} is the effective fill factor – the percentage of the pixel area sensitive to photons, QE is the quantum efficiency – a probability of photon to produce an electron-hole pair by photoeffect, and P_{av} is the probability of produced carriers to trigger an avalanche.

The value of QE lies between 20 and 90 % depending on the transmittance of the entrance window and the photon absorption coefficient, both of which have wavelength dependence. P_{av} varies greatly in the range of 0.1 – 100 % depending on the silicon properties (SiPM design), electric field (overvoltage), carrier type (electron or hole) and position, where the photon was absorbed (wavelength) [159] [renker]. FF_{eff} is the ratio of sizes of pixel active and passive parts which is higher for large pixels, and can be in the range of 20 – 75 % [225]. It also depends on the electric field distribution at pixel borders which is defined by the guard rings and optical trenches. Electric field strength depends on overvoltage and depth, therefore photon wavelength.

PDE is measured from the SiPM response with help of a setup including a fast pulsed light source (laser or LED) and integrating sphere by comparison of the light signal from SiPM and calibrated photodiode as described in [157]. Measurement is performed individually for several different wavelengths between 300 and 1000 nm with the data extrapolation between measured points.

Figure 3.37 presents the decrease of the signal response with fluence. It was attributed to a decrease of photon detection efficiency calculated as $PDE = \mu = \overline{Q}/(G \cdot ECF)$, based on measurement of SiPM transient pulses by S. Cerioli et al. [193]. Signal deterioration starts only after 10^{13} n_{eq}/cm^2, probably because the SiPMs were produced by the newest technology with small 15 μm pixels, and were measured at -30 °C which significantly reduced dark counts and corresponding pixel occupancy. Similar considerations can probably explain data in [182, 213]. E. Garutti et al. [192] proposed another approach to investigate the SiPM signal degradation based on a comparison of the SiPM current ratio before/after irradiation measured under illumination.

Unfortunately, there is no straightforward way to disentangle all the unknown parameters

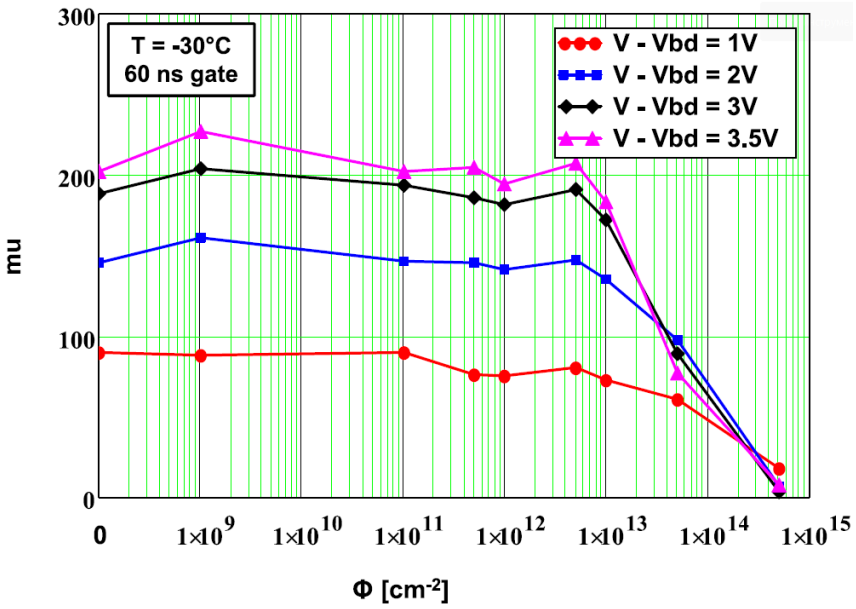

Figure 3.37: Dependence of SiPM response to sub-nanosecond laser pulses on 1 MeV equivalent fluence [193]. SiPMs were irradiated by reactor neutrons. SiPMs were manufactured by Ketek and have 1 mm^2 area with 15 µm pixels. Dark current measurements were performed at -30 °C and +20 °C, in darkness and under LED illumination with high and low intensities.

including gain, PDE and ECF from the measured change of signal or current. For instance, S. Cerioli et al. [193] measured gain and ECF only before irradiation and considered them to be unchanged after irradiation. This lead to a conclusion that the signal amplitude degradation was caused by a decrease in PDE. Though, ECF is often considered to be close to 1 before irradiation, it is expected to increase after irradiation along with the increase of noise, afterpulsing, and crosstalk which is presented in figure 3.30. Therefore, the value of ECF may become non-negligible for the calculation, especially after high irradiation. Furthermore, the assumption that gain did not change after irradiation does not have to be correct either, even though pixel capacitance measurements suggest it, see discussion in chapter 7. Similarly, E. Garutti et al. [192] described the decrease in light-induced current by the degradation of avalanche triggering probability $P_{av} \cdot ECF$. Although authors explicitly included the correlated noise value into the final variable, they assumed that gain and QE did not change after irradiation.

3.6.7 signal-to-noise ratio and dynamic range

Dynamic range is very important for applications where the amount of measured light varies by many orders of magnitude like in spectrometers and calorimeters. In its simplest form, it can be expressed as

$$N_{fired} = N_{pixels}\left[1 - \exp\left(\frac{N_{photons} \cdot PDE}{N_{pixels}}\right)\right] \tag{3.22}$$

where N_{fired} is the number of fired pixels, N_{pixels} is the total number of pixels and $N_{photons}$ is the number of incident photons. An example of dynamic range calculation with this equation for non-irradiated SiPMs is presented in section 7.1.

In a real experiment, the dynamic range also depends on light frequency, pixel recovery time $\tau_{recovery}$ and pixel occupancy due to dark counts and correlated noise ECF, all of which could be theoretically incorporated in equation (3.22). Fast SiPMs with $\tau_{recovery}$ on the order of a few ns effectively increases the dynamic range because pixels will be able to be triggered multiple times within the same light pulse if its duration is long enough [226]. The opposite happens for slow SiPMs detecting high-frequency pulses [226]. An example of such behavior is depicted in figure 3.38. High noise, e.g. due to SiPM design or radiation damage, cause a decrease of PDE and consequently dynamic range due to more pixels being in the recharging state after Geiger discharges caused by spurious events.

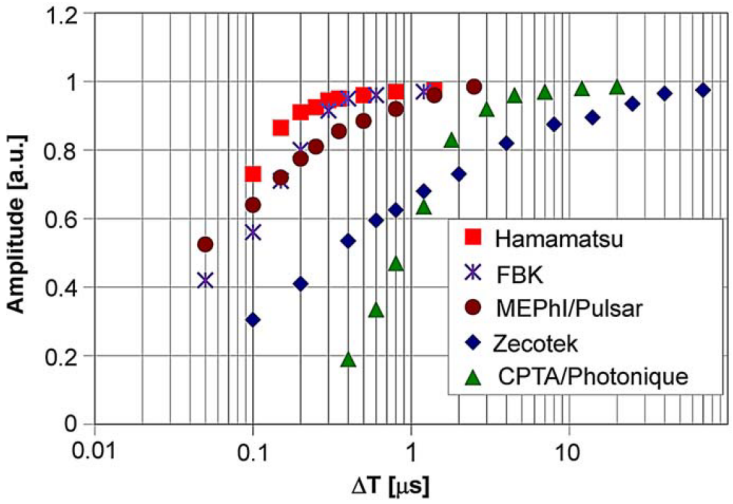

Figure 3.38: Dependence of SiPM response to the second LED to pulse on the delay between the first and second LED pulses (SiPMs were not irradiated) [204]. Pixel pitches of SiPMs are: 50 μm for Hamamatsu and FBK, 30 μm for MEPHi/Pulsar, 40 μm for CPTA/Photonique and Zecotek. All SiPMs have 1 mm^2 area. It is clear that all the SiPMs have a quite slow recovery time on the order of 0.1 – 10 μs, probably due to old technologies dated by 2009 and big pixel sizes.

SiPM response is usually linear as long as the number of simultaneously fired pixels is below 20 % of total pixels. Otherwise, the probability of multiple Geiger discharges in a pixel within its $\tau_{recovery}$ becomes significant resulting in non-linearity. Unfortunately, a comprehensive model of the SiPM response incorporating all the aforementioned effects is quite complicated and not yet available [161]. Therefore, it is essential to check the linearity both in the laboratory and during the real detector operation as the response nonlinearity depends on the arrival-time distribution of the photons and readout electronics.

Noise level increases and PDE decreases dramatically after the SiPM irradiation. This results in effectively shortening and shifting dynamic range towards the higher numbers of detectable photons while low numbers of photons become indistinguishable from noise. Therefore, signal-to-noise ratio SNR can be seen as a determining factor for the SiPM dynamic range.

In continuous operation mode, the signal-to-noise ratio can be measured in terms of current consumed by SiPM as [227]

$$SNR = \frac{I_{light}}{ENC} = \frac{P_\lambda \cdot PDE \cdot G \cdot e}{hc/\lambda \cdot 2eB \cdot \left[(I_{light} + I_{d-bulk}) \cdot G^2 \cdot ENF + I_{d-surf} \right]} \tag{3.23}$$

where P_λ is the optical power of the light source and hc/λ is the photon energy.

For pulsed operation, SNR is measured with charge sensitive amplifier or oscilloscope as

$$SNR = \frac{Signal(e-)}{Noise(e-)} \quad or \quad SNR = \frac{Signal\ integral(nV \cdot s)}{\sigma_{Noise\ integral}(nV \cdot s)} \tag{3.24}$$

where signal $Signal\ integral(nV \cdot s)$ and standard deviation of $\sigma_{Noise\ integral}$ are measured in the same acquisition window with and without light pulses, respectively.

Unfortunately, data on SNR change after irradiation is rarely published, probably because signal and noise levels differ significantly from experiment to experiment which makes it difficult to compare data acquired by different research groups. Up to now only Yu. Musienko et al [184, 196, 197, 213]. published SNR measurements after irradiation. Unfortunately, data before irradiation are not presented, so I can not make a before/after comparison.

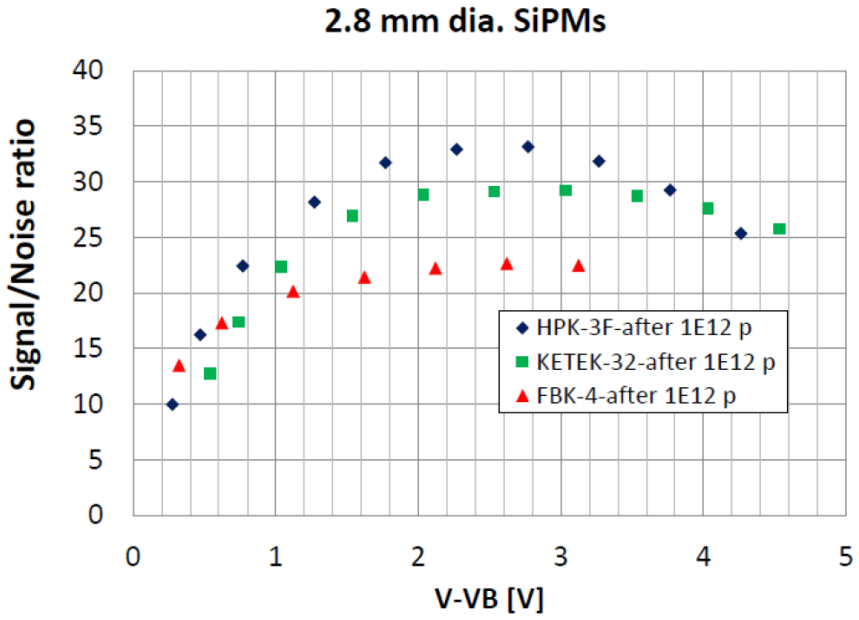

Figure 3.39: Dependence of SiPM signal-to-noise ratio on overvoltage after proton irradiation with 1 MeV equivalent fluence of 1.6×10^{10} n_{eq}/cm^2 [184]. data was acquired by an oscilloscope measurement with a 50 ns gate at room temperature. SiPMs response was measured with 515 nm LED emitting about 4200 photons per pulse. SiPMs were produced by Hamamatsu, Ketek, and FBK. They have 5 – 6 mm^2 area and 15 μm pixel pitch.

Figure 3.39 presents the example of signal-to-noise ratio measured after irradiation for different SiPMs. One can see that there is a maximum SNR at some overvoltage. Therefore, this measurement can be used to determine the optimal overvoltage for a specific light level in the considered application, taking into account the properties of SiPM and the amplification/readout chain. This is explained by the fact that photon detection efficiency and gain increase with overvoltage, but dark counts, afterpulsing and crosstalk (noise) increase as well, see figure 3.22, (left).

3.6.8 Annealing

Characteristics of SiPM improve with time passing after irradiation in a similar way to other irradiated detectors. Again, the most abundant data is available for the dark current anneal-

ing [168,169,171–175,178–180,187–190,199,203,208,209]. Figure 3.40 (left) presents an example of long time annealing for I_{dark}. Only a few studies on the dark count rate recovery are currently available [188,211]. Figure 3.40 (right) shows an example of short term annealing of DCR which exhibits a trend similar to I_{dark} as was expected from equation (3.15).

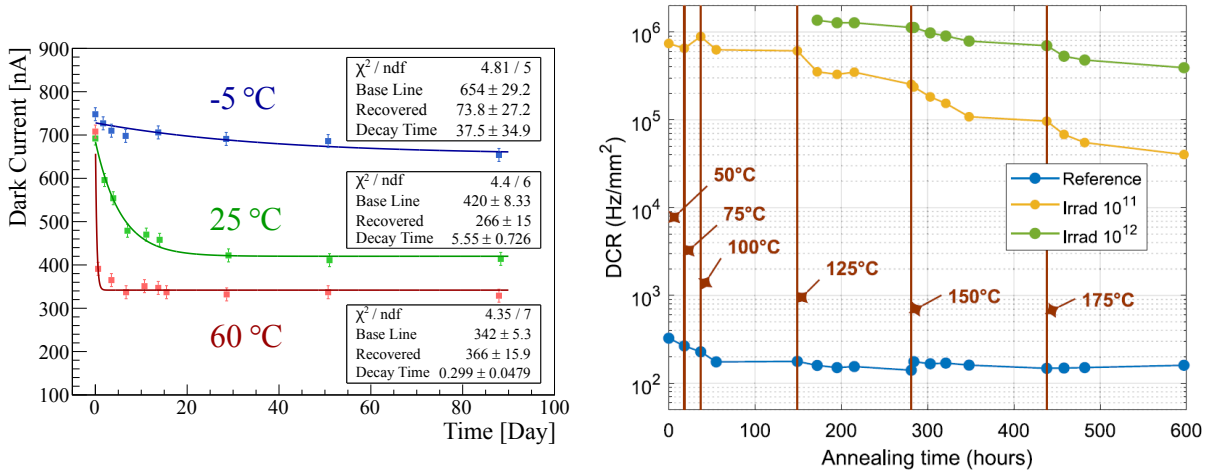

Figure 3.40: Annealing of dark current (left) [178] and dark count rate (right) [188] after irradiation. SiPMs in (left) were irradiated by fast neutrons with fluence of 3.7×10^9 n_{eq}/cm^2. SiPMs in (right) were irradiated by reactor neutrons with fluence of 10^{11} and 10^{12} n_{eq}/cm^2. Annealing was performed at various temperatures from -5 °C up to 175 °C, see comments in the plots. Both SiPMs were manufactured by Hamamatsu and have 1 mm^2 area with 50 μm pixels. The decrease of DCR for non-irradiated SiPM might be explained by the annealing of defects that were introduced during fabrication.

At room temperature dark current exhibits exponential decrease that can be described as $I_{dark} = b + a \cdot exp(-t/\tau)$ by with a time constant τ about 3 – 15 days [172, 178, 180, 199]. However, in reality, different defects have different decay times, so fitting with a single exponent may produce results with limited precision as can be seen in figure 3.40 (left). The majority of annealing usually manifests after a month [178, 180, 189, 190, 199], while several months or even years are required for the absolutely complete annealing [169, 171, 174, 175, 178, 180, 203]. Also, several researchers observed a very fast recovery of current (about 10 – 20 %) during the first minutes right after irradiation for high fluence rates above 2×10^8 $n_{eq}/(cm^2 \cdot s)$ [171,172,180,203].

Effective annealing time depends on many parameters, i.e. increased temperature extremely accelerates the annealing because defect mobility increases with temperature as was explained in subsection 3.4.1. Only a little change in dark current was observed at temperatures below 0 °C [173, 178, 199], while at high temperatures annealing time can be as low as few hours, see figures 3.40 (left) and 3.41 (left). At elevated temperatures, not only recovery goes faster, but also the current decrease is more pronounced. For instance, up to 50 (70) % current decrease is usually observed after a month (several months) of storage at room temperature [169, 171–175, 178, 180, 199, 209]. Figure 3.40 (left) shows that up to 10 % more recovery can be achieved at 60 °C [173, 178, 185, 223]. A huge decrease of I_{dark} and DCR by up to 10 – 15 times was observed at very high temperatures of 150 – 250 °C [179, 188, 190], see figure 3.40 (right). However, note that keeping SiPMs above 100 °C for a long time could change other important SiPM properties, like the color of resin that covers the device, which may lead to a loss of short-wavelength sensitivity [188].

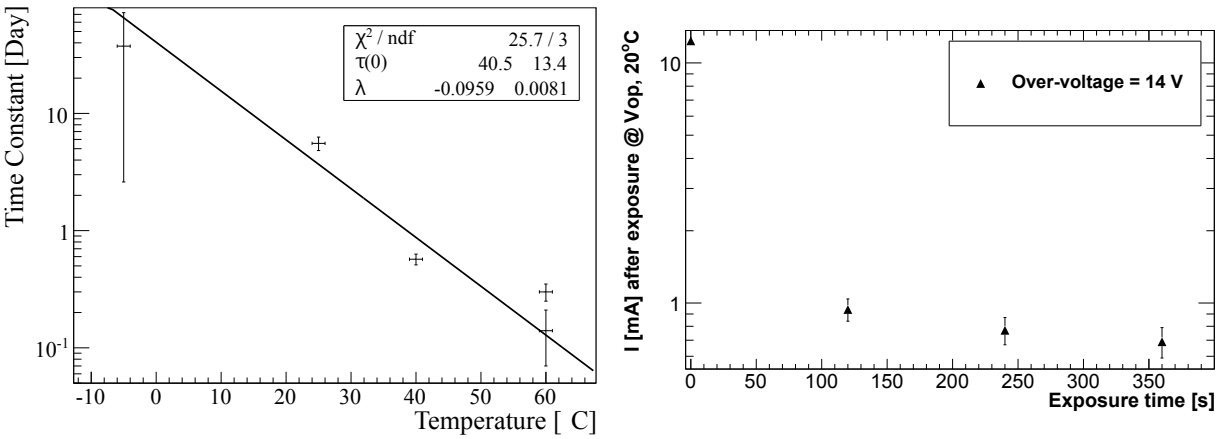

Figure 3.41: (left) Dependence of exponential time constant on annealing temperature calculated based on data from figure 3.40 (left) [178]. This time constant can be described as $\tau(T) = 41 \cdot exp(-0.1T)$ days. (right) Annealing of dark current for SiPM kept at overvoltage of 14 V [208]. SiPM was irradiated by fast neutrons with fluence of 8×10^{11} n_{eq}/cm^2. SiPMs were manufactured by Sensl (now ON Semiconductor) and have 6 mm^2 area with 50 μm pixels.

Recovery can also be improved by 20 – 50 % if SiPMs are kept biased at high (forward or reverse) voltages during annealing [171, 179]. This results in a device self-heating due to high current consumption and also creates a strong electric field helping to re-order the displaced atoms and defects. For instance, M. Cordelli et al. [208] kept SiPMs at overvoltage of 8 – 14 V to reduce I_{dark} by up to 15 times, see figure 3.41 (right). However, very high overvoltages are way beyond the operation range recommended by manufacturers, so it may result in SiPM failure which was observed when authors try to increase V_{ov} to 17 V [208]. Furthermore, the current of highly irradiated SiPMs at these overvoltages can reach hundreds of mA effectively heating up the sensors, so external thermal dissipation is required to keep them below the breaking temperature of 200 – 250 °C.

Figure 3.42 (left) presents the annealing of SiPM signal amplitude after irradiation with 3×10^9 n_{eq}/cm^2. Complete recovery (90 % -> 100 % signal) was observed for this low fluence. Unfortunately, up to now, there is no data on annealing of signal amplitude at higher fluences. Figure 3.42 (right) shows that single photodetection can be also recovered with time for low fluence irradiation.

3.6.9 Low temperature operation

As was discussed in subsection 3.6.1, dark current and dark count rate decrease dramatically at low temperatures, see figure 3.25. For instance, I_{dark} below nA were observed for SiPMs that were thermally annealed (250 °C) and operated at cryogenic temperatures after irradiation with 10^9 n_{eq}/cm^2. DCR decrease by several orders magnitude was achieved with cooling down to -65 °C. Moreover, DCR as low as 100 Hz/mm^2 is reported in figure 3.43 (left) for SiPMs that were thermally annealed (175 °C) and operated at cryogenic temperatures after irradiation with 10^{14} n_{eq}/cm^2.

SiPM cooling during operation significantly reduces the noise and may also restore sensor response if it decreased due to high pixel occupancy by dark counts, see subsection 3.6.6. Combined, these effects can substantially increase the fluence range suitable for operation. Figure 3.34 shows that the signal photon detection capability can be restored with moderate cooling

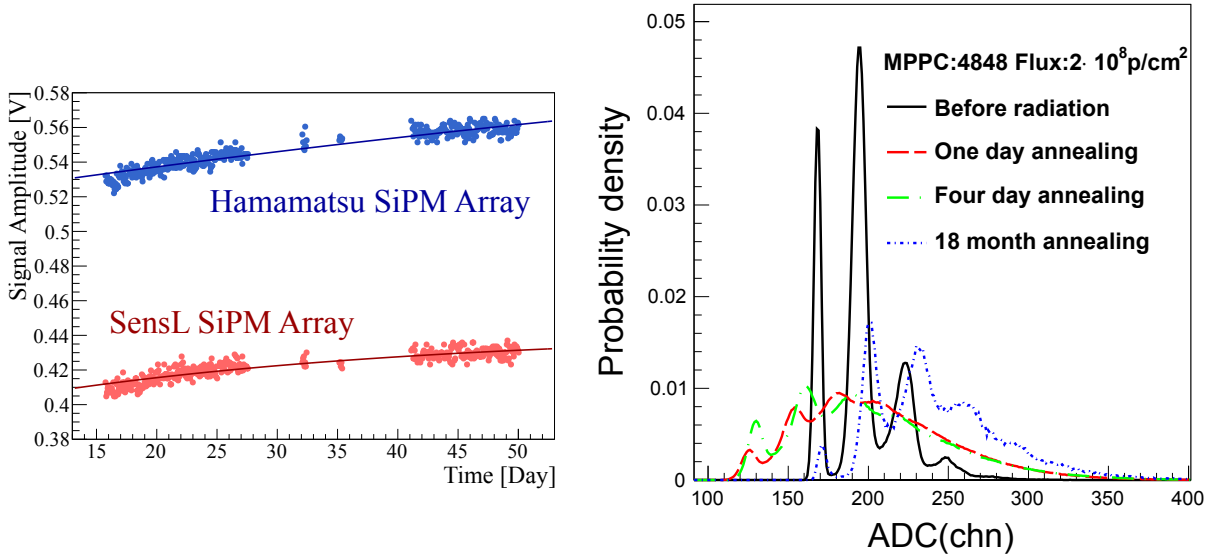

Figure 3.42: (left) Annealing of signal amplitude for SiPM arrays irradiated by fast neutrons with fluence of 3.7×10^9 n_{eq}/cm^2 [178]. Each array consists of 4×4 SiPMs, 9 mm^2 area each. Pixel pitches are 35 μm for Sensl (now ON Semiconductor) SiPMs, and 50 μm for Hamamatsu SiPMs. (right) Recovery of single photon detection capability for SiPMs irradiated with protons up to 5.4×10^8 n_{eq}/cm^2 after a very long storage at room temperature [169]. SiPMs were produced by Hamamatsu and have 9 mm^2 area and 50 μm pixels.

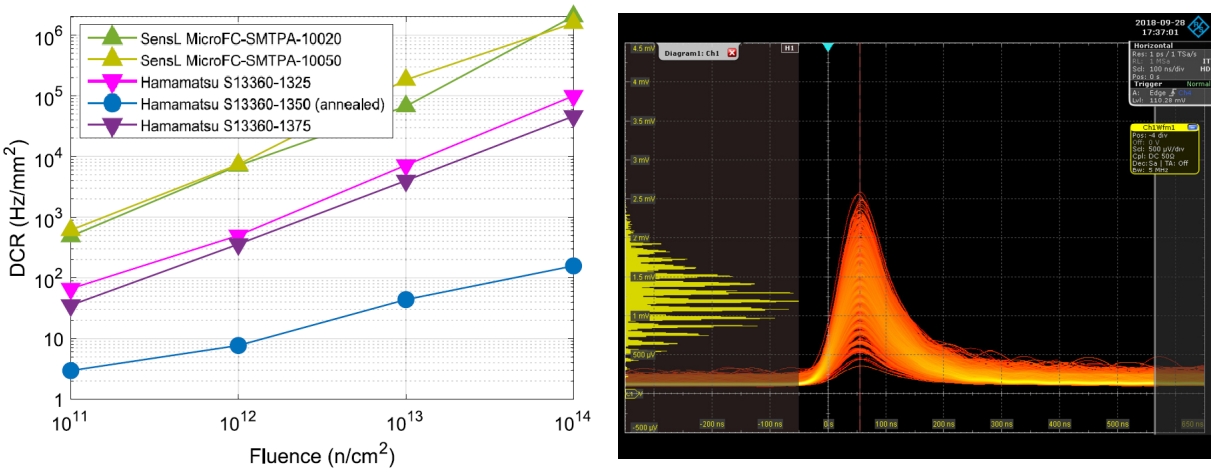

Figure 3.43: Performance of SiPMs irradiated up to 10^{14} n_{eq}/cm^2 measured at 77 K [188]. (left) Dependence of dark count rate on 1 MeV equivalent fluence. SiPMs were manufactured by Hamamatsu and Sensl (now ON Semiconductor) have 1 – 1.7 mm^2 area with pixel pitches in the range of 20 – 75 μm (see last two digits in device code in the legend). (right) single-photon peaks detected by 50 μm Hamamatsu SiPM after irradiation with 10^{14} n_{eq}/cm^2. Horizontal scale is 100 ns/div, vertical is 0.5 mV/div.

down to -30 – -60 °C for medium fluence about $10^9 - 10^{10}$ n_{eq}/cm^2. Moreover, figure 3.43 (right) shows that even after very high fluence of 10^{14} n_{eq}/cm^2, SiPMs can detect single photons if operated at cryogenic temperatures. Similar data are also presented in [179] for SiPMs irradiated

with 10^{12} n_{eq}/cm^2. However, trap-assisted tunneling starts to dominate the current generation process at temperatures 100 K which limits the achievable I_dark reduction due to the much high electric field in SiPMs compared to standard silicon sensors [160] .

3.6.10 Irradiation with low energy neutrons

Although, SiPMs irradiation studies are mostly conducted with high energy neutrons, one research group explored the effects of cold neutrons [228–230]. Figure 3.44 shows the increase of dark current and dark count rate with the achieved neutron fluence for several different SiPMs. After irradiation with 10^{12} n_{cold}/cm^2, I_{dark} increases to a few $\mu A/mm^2$, and DCR to several MHz/mm2 [228]. Furthermore, response degradation for SiPMs irradiated with 6×10^{12} n_{cold}/cm^2 is reported, namely up to 11 % decrease in signal amplitude [229] and up to 9 % worsening of time resolution [230].

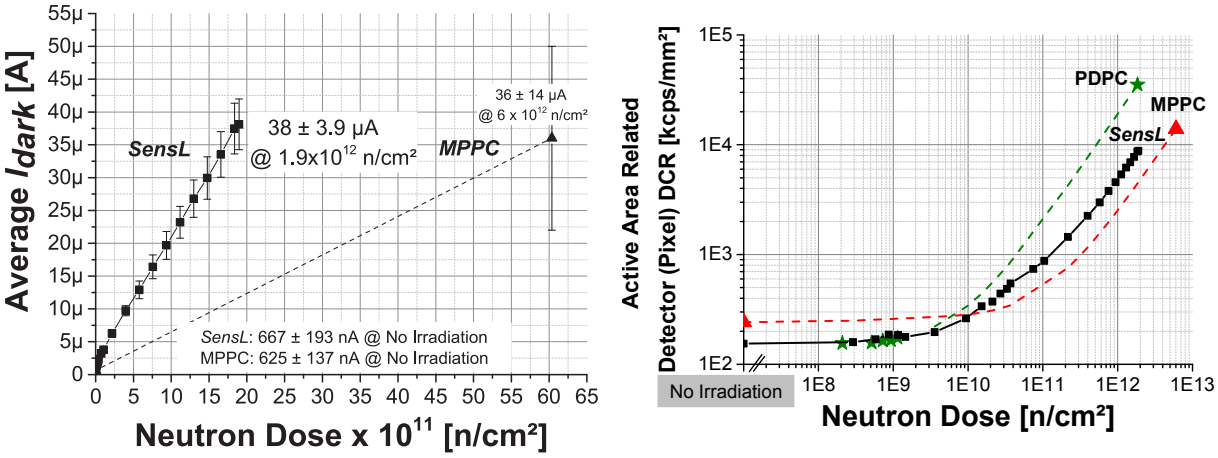

Figure 3.44: Dependence of dark current (left) and dark count rate (right) on the cold (3.3 meV) neutron fluence [228]. SiPM areas are 9 mm^2 for Hamamatsu and Sensl (now ON Semiconductor), 9 mm^2 for Philips. Pixel pitches of SiPMs are: 50 µm for Hamamatsu, 35 µm for Sensl, and 43 µm for Philips.

Comparing to data presented in subsection 3.6.1, one can conclude that similar damage is expected after irradiation with just $10^9 - 10^{10}$ n_{eq}/cm^2 for MeV hadrons. This is in agreement with the fact that NIEL value of 3.3 meV neutrons is 350 lower than NIEL value for 1 MeV hadrons as shown in figure 2.7. As I noted in section 2.3 cold neutrons can also invoke nuclear reactions which are not described by the NIEL hypothesis and can lead to increased damage than predicted solely by NIEL. However, presented data are not enough to discuss such effects.

3.6.11 Irradiation with electrons and positrons

Several scientific teams studied the SiPM radiation hardness after exposure to electrons and positrons produced by ^{90}Sr source (2.28 MeV) and accelerators with energies ranging from 8 up to 28 MeV. Figure 3.45 presents measurements of I_{dark} at room temperature and overvoltage of 3 – 4 V. One can see that dark current values of 1 – 10 $\mu A/mm^2$ were observed for SiPMs with 10 – 25 µm pixels after irradiation with $10^9 - 10^{10}$ n_{eq}/cm^2 equivalent 1 MeV neutron fluence [180, 223]. Higher values of 10 – 100 $\mu A/mm^2$ were reported for SiPMs with 50 µm pixels [180, 223, 231, 232].

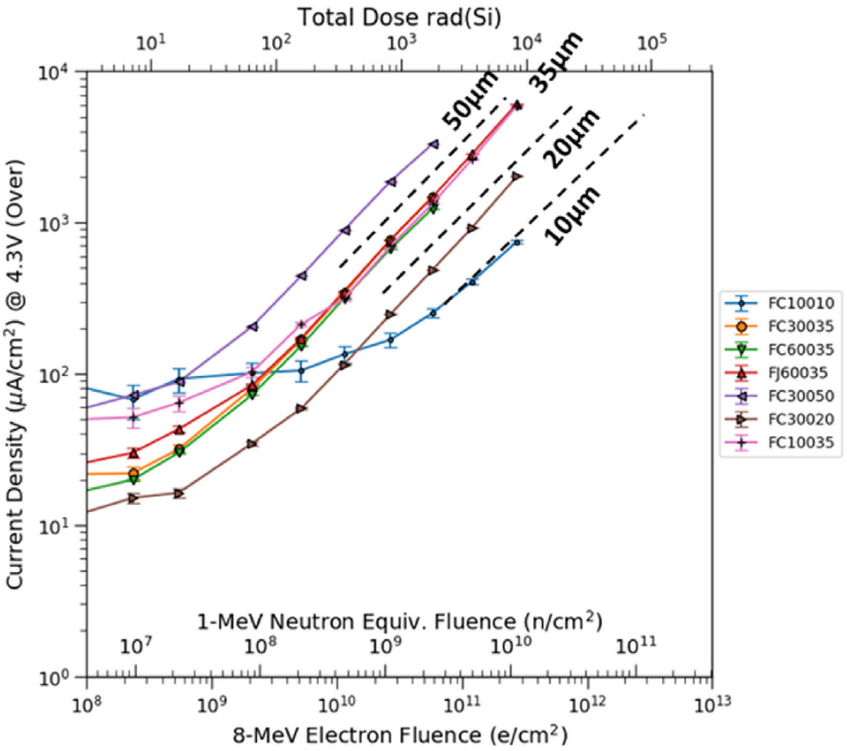

Figure 3.45: Dependence of dark current density on accumulated electron fluence for SiPMs with different pixel pitches operated at overvoltage of 4 V [180]. Note that J_{dark} here is presented in units of $\mu A/cm^2$, while in the text I use units of $\mu A/mm^2$. Electron fluence data is also recalculated to 1 MeV equivalent for neutrons as well as ionizing dose. All SiPMs were produced by Sensl (now ON Semiconductor) and have a size in the range of 1 – 36 mm^2.

Figure 3.46 (left) shows that dark count rate is on the order of tens MHz after irradiation with 10^9 n_{eq}/cm^2. No change in breakdown voltage was reported for fluences up to 10^{10} n_{eq}/cm^2 [180, 231, 232]. Loss of single-photon detection capability and deterioration of signal amplitude was observed after 10^{10} n_{eq}/cm^2 [233, 234], see figure 3.46 (right). Recovery of $\sim$ 30% of signal amplitude is reported after two weeks of annealing at 80 °C [233].

Reported values of I_{dark} and DCR are comparable to values presented in subsection 3.6.1 for high energy neutron and proton irradiation with similar equivalent fluences. Another important fact is that the total ionizing dose in case of electron irradiation is larger by an order of magnitude compared to proton irradiation for the same equivalent fluence, compare figures 3.23 and 3.45. This confirms that the main reason for SiPM degradation due to irradiation by charged particles is their non-ionizing energy loss.

3.6.12 Irradiation with gamma-rays

Photons can be seen as an ideal source to study the effects of ionizing energy loss because their probability to produce lattice dislocations is by 4 orders of magnitude lower than for 1 MeV neutrons, see subsection 2.3.1. ^{60}Co gamma source emitting 1.17 and 1.33 MeV photons is the most popular choice for irradiation. Available data show that for SiPMs with 50 μm pixel pitch dark current is below 1 $\mu A/mm^2$ for doses below 1 kGy, and rises up to 1 – 10 $\mu A/mm^2$ after 1 – 10 kGy [168, 187, 189, 217, 224, 235]. Reported dark count rates are below 10 MHz for doses

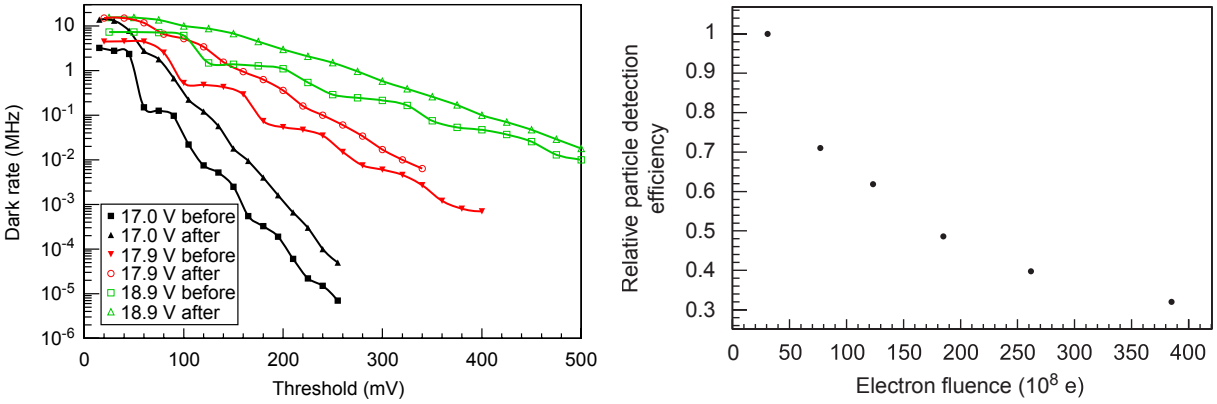

Figure 3.46: SiPM performance after irradiation with 14 MeV electrons [234]. (left) Dependence of dark count rate on the cut-off threshold for SiPMs measured at different bias voltages. Electron fluence of 3.1×10^8 e/mm^2 corresponds to 1.7×10^9 n_{eq}/cm^2. The step structure is related to the multi-pixel events caused by optical cross-talk. (right) Dependence of detection efficiency on electron fluence in units of e/mm^2. Covered range of $3.1 \times 10^9 - 3.8 \times 10^{10}$ e/mm^2 corresponds to $1.7 \times 10^{10} - 2.1 \times 10^{11}$ n_{eq}/cm^2. SiPMs were produced by CPTA/Photonique and have 1 mm^2 area and 45 µm pixels.

below 1 kGy, and reach up to 100 MHz after 1 – 10 kGy [189, 217, 235].

Figure 3.47 presents the change of I_{dark} after irradiation of identical SiPMs with gammas and fast neutrons. As expected for γ-irradiation, there is a huge increase in I_{dark} below the breakdown voltage, which means that most part of the observed damage is related to surface effects in Si-SiO_2 border. Based on the data one may conclude that increase in the dark current after a 1 kGy dose is approximately comparable to the dark current generated by 2×10^8 n_{eq}/cm^2.

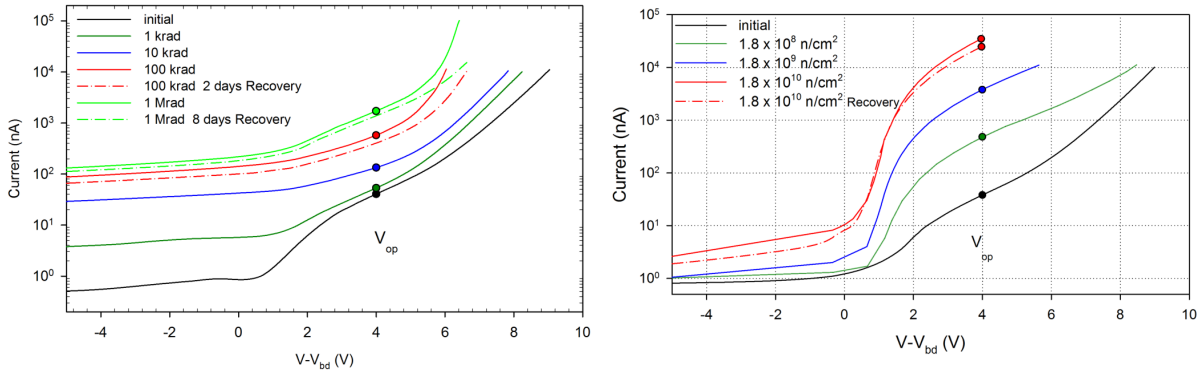

Figure 3.47: Dependence of dark current on overvoltage for SiPMs irradiated with gamma rays (left) and fast neutrons (right) [187]. Gamma irradiations were performed with ^{60}Co source with doses in the range of 1 – 1000 krad which corresponds to 0.01 – 10 kGy. Neutron irradiations were performed with a fast neutron generator, fluences were converted to 1 MeV equivalent. SiPMs were produced by Hamamatsu and have 9 mm^2 area and 15 µm pixels.

Figure 3.48 (left) shows that the radiation hardness of irradiated SiPMs improves with a decrease of pixel size which is consistent with data presented for high energy hadron irradiation in

subsection 3.6.1. Also, a similar exponential annealing trend was reported for I_{dark} in [168,217]. No change in breakdown voltage or signal amplitude was observed [189, 217, 224, 235]. Figure 3.48 (right) presents the relative change of I_{dark}, DCR, crosstalk and gain after irradiation. No change in crosstalk was reported below 300 Gy, but a significant increase was observed for doses above 1 kGy [217,235]. The capability to detect single photons was lost above 1 kGy [235].

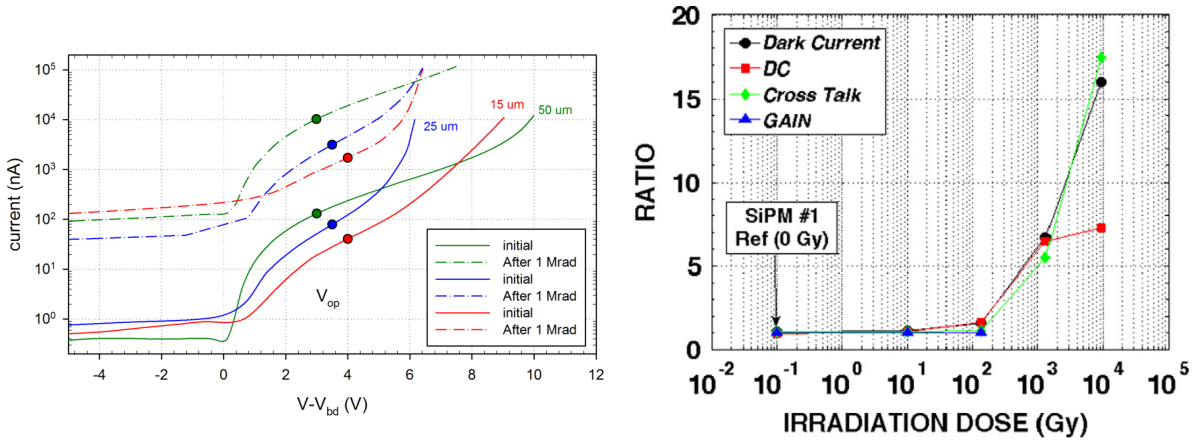

Figure 3.48: (left) Dependence of dark current on overvoltage for Hamamatsu SiPMs with different pixel pitches irradiated with gamma rays [187]. Gamma irradiations were performed with ^{60}Co source with doses in range of 1 – 1000 krad which corresponds to 0.01 – 10 kGy. SiPMs were produced by Hamamatsu and have 9 mm^2 area. (right) Dependence of ratios of different SiPM parameters on total dose of gamma radiation measured at overvoltage of 3 V. SiPMs were manufactured by STMicroelectronics and have 0.64 mm^2 area and 40 µm pixels.

Figure 3.49 shows the study of optical transmission for several SiPM window materials after irradiation with gammas and fast neutrons. While no change is visible in the case of neutron irradiation, a little up to 10 % decrease is observed for gammas. This can be explained by the fact that materials with the highly irregular atomic structure are more prone to damage by ionizing radiation loss, which is in line with data described in section 3.2 for plastic scintillators.

3.6.13 Irradiation with X-rays

Ch. Xu et al. [130, 165, 236] studied the SiPM radiation hardness after irradiation with X-rays in a very wide dose range from 3 kGy up to 20 MGy. This is a very interesting case because X-rays with energies below 300 keV, which were used in this study, should not cause the lattice dislocations. The value of dark current above the breakdown was smaller than 1 µA/mm^2 up to the dose of 20 kGy, but after 2 MGy it increased dramatically up to 1 µA/mm^2, see figure 3.50 (right).

Surprisingly, single photons were detectable even after a huge dose of 20 MGy. DCR increased by an order of magnitude, i.e. on the level of 10 MHz, which is however quite modest comparing to GHz levels of DCR observed for similar I_{dark} values after hadron irradiation. Those peculiar results could be explained by the fact that the majority of dark current was generated at the Si-SiO$_2$ interface at the SiPM surface. This assumption is reasonable for data up to 20 kGy, where current increased by several orders of magnitude below breakdown voltage, but only a slight current increase was observed above V_{bd}, see figure 3.50. However, this does not explain the huge dark current increase above V_{bd} for doses of 2 and 20 MGy which is probably related to bulk-generated current.

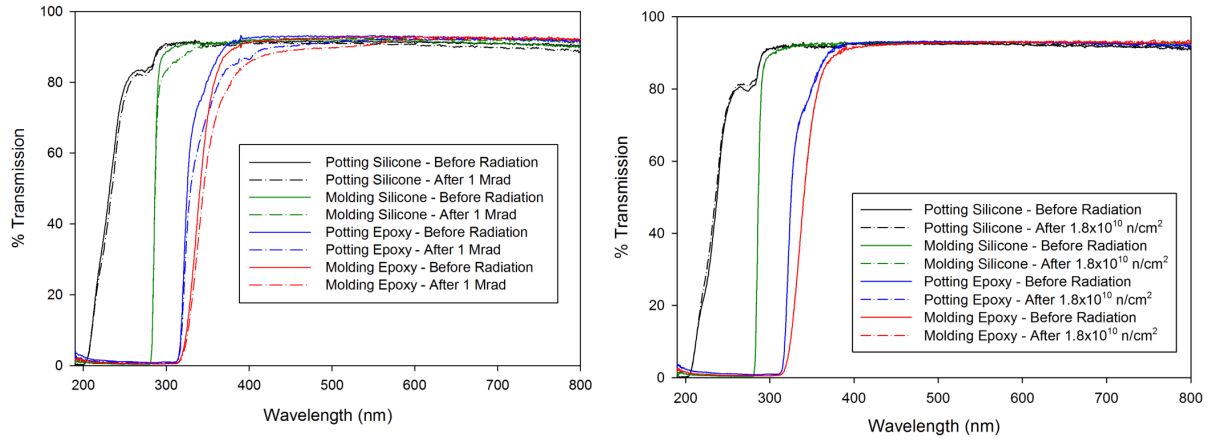

Figure 3.49: Dependence of optical transmission on wavelength for different window materials irradiated with gamma rays (left) and fast neutrons (right) [187]. Gamma irradiations were performed with ^{60}Co source with a dose of 1 Mrad which corresponds to 10 kGy. Neutron irradiations were performed with a fast neutron generator, fluence was converted to 1 MeV equivalent.

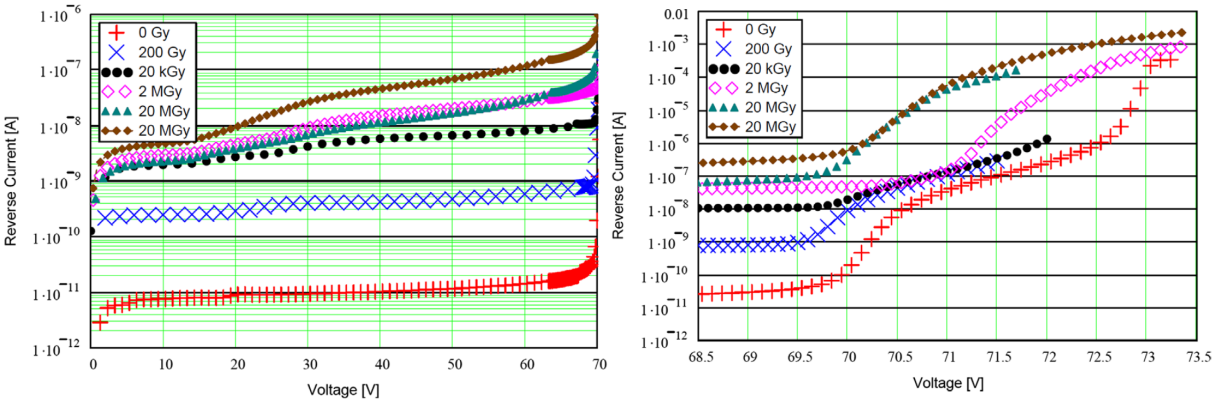

Figure 3.50: Dependence of dark current on overvoltage for SiPMs irradiated by X-rays below (left) and above the breakdown voltage (right) [236]. SiPMs were produced by Hamamatsu and have 1 mm^2 area and 50 µm pixels.

Only a little change up to 10 % was reported for pixel capacitance and quenching resistance, however, no change in signal amplitude or shape was detected. No change in breakdown voltage was observed. Crosstalk probability increased by 50 %.

3.6.14 Irradiation with ions and background radiation

Several studies report the various degrees of radiation damage to SiPMs after irradiation with carbon and lead ions [237–239], and with background radiation [211, 237]. These unusual radiation conditions are usually chosen to simulate the complex radiation field in the environment where SiPMs will be operated. Unfortunately, this usually means that the radiation load either was not quantified at all or was assessed only in non-standard units, like time of exposure or

total ion fluence. Since 1 MeV neutron equivalent fluence per cm^2 is not available here, I can not compare it with results presented in previous subsections. As I discussed before, the total ionizing dose in Gy can not really describe the damage by high-energy heavy charged particles or ions, because the damage is mainly caused by non-ionizing energy loss. However, I present a couple of examples in figure 3.51 to provide some insight into these tests.

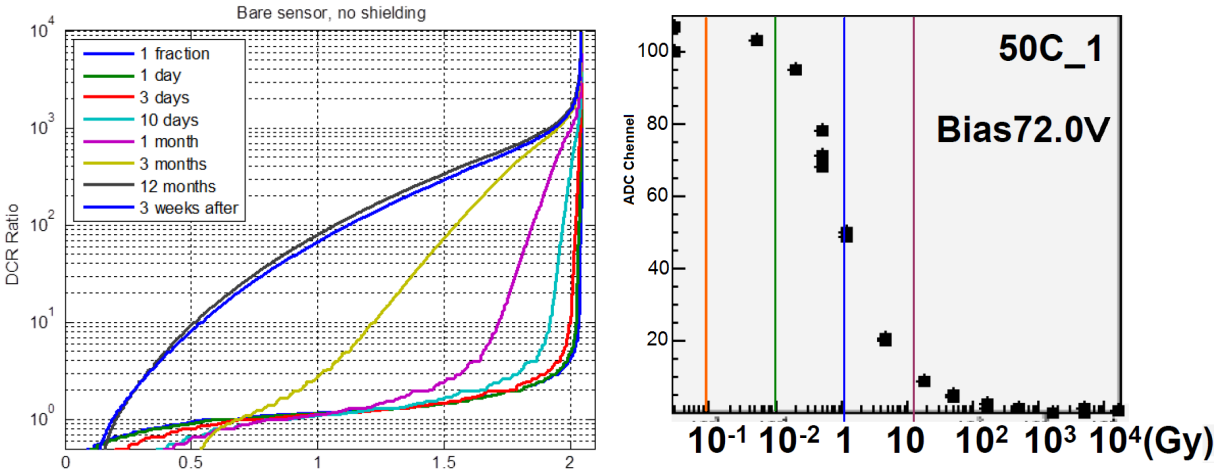

Figure 3.51: (left) Dependence of dark count rate on the amount of active pixels (cell) of digital SiPMs before and after irradiation with background radiation [211]. 150 MeV proton beam was fully stopped in a $35 \times 28 \times 18$ cm^3 water target, SiPMs were located at 25 cm from the target side, perpendicular to the beam. Different curves correspond to expected durations of operation of PET therapy room. Curve "12-months" corresponds to 10^{15} protons, curve "three weeks after" curve is the same but after three week annealing at room temperature. (right) Degradation of the response to illumination with Xe lamp after irradiation with $^{6+}$C ions [238]. The total achieved fluence was 1.2×10^{12} C/cm^2 which corresponds to an ionizing dose of 16 kGy. SiPMs were produced by Hamamatsu and have 1 mm^2 area and 50 µm pixels.

3.6.15 Performance of detectors based on SiPMs

It is essential to check how irradiated SiPMs perform with real detector signals because their time and amplitude distributions may differ significantly from the LED test signals. Several groups measured the SiPM response to light produced by MIPs (cosmic muons, electrons from ^{90}Sr source or particle mix from accelerator) in plastic scintillators [172, 175, 205, 206, 231, 232]. Few other groups studied the response to gamma rays in crystal scintillators [171,215,237]. Most studies report decrease of signal amplitude in several times after irradiation with fluence in range of $5 \times 10^9 - 2 \times 10^{11}$ n_{eq}/cm^2 [157, 175, 205, 206, 237], see figure 3.52 for example. But some studies report no significant degradation of signal amplitude in the same fluence range [171,172].

An increase of the noise several times was observed in all the aforementioned studies which resulted in broadening of the peaks corresponding to noise and detected particles of different species or characteristic energies. Figure 3.52 shows that the peak corresponding to electrons becomes indistinguishable from the noise, and the peak corresponding to muons is heavily overlapped with the noise. Figure 3.53 presents an increase of the energy resolution for the 662 keV gamma line after irradiation with only 4.6×10^9 n_{eq}/cm^2 which can be restored with cooling. One can also see that the optimum overvoltage can be found to achieve the best energy resolution which is similar to data presented in figure 3.39.

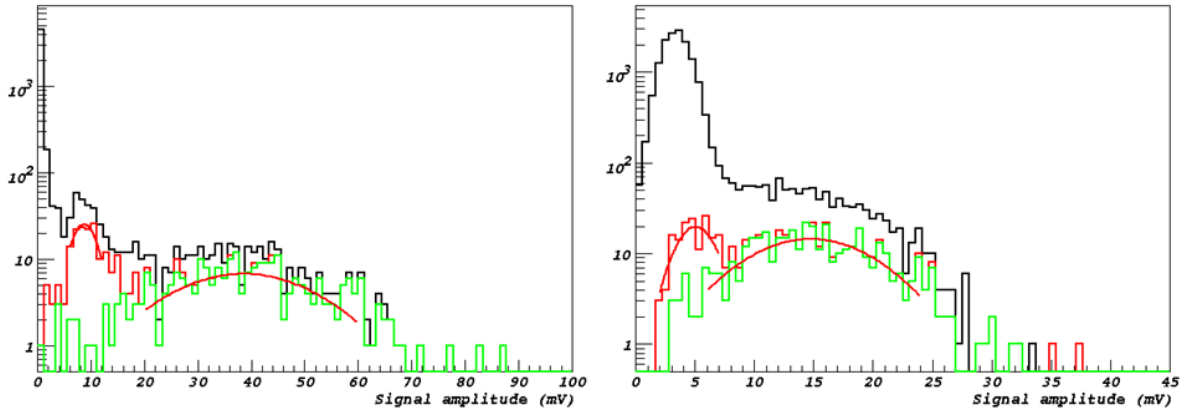

Figure 3.52: Histograms of signal response to 1 GeV/c beam (mix of electrons, muons, and pions) for the shashlik calorimeter test module equipped with non-irradiated (left) and irradiated (right) SiPM boards [240]. Red histograms show electrons and green histograms show mips. The detector consists of 5 layers of iron (1.5 cm thick) + scintillator (0.5 cm thick, covered in Tyvek foils), light is collected by 1 mm diameter Kuraray Y11 fibers, the module has a width of 3×3 cm^2. SiPM board has 9 SiPMs optimized for red light produced by FBK. (right) plot shows data for board irradiated by fast neutrons up to 1.7×10^{10} n_{eq}/cm^2.

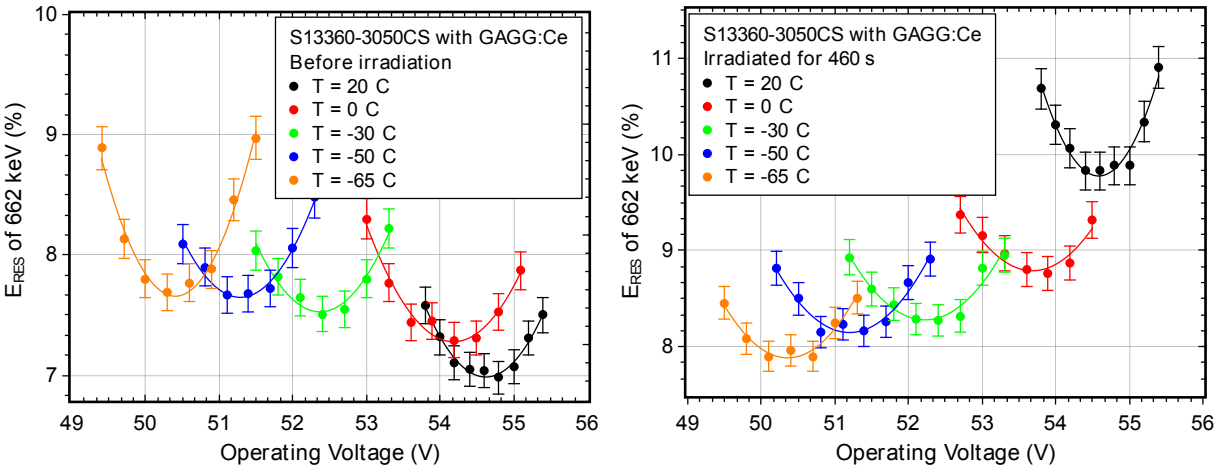

Figure 3.53: Dependence of the energy resolution for the 662 keV gamma line on overvoltage for GAGG:Ce (1 %) scintillator equipped with non-irradiated (left) and irradiated (right) SiPMs [215]. SiPM was irradiated with 170 MeV protons, irradiation time 460 s corresponds to fluence of 4.6×10^9 n_{eq}/cm^2. Measurements were performed at -65 °C, -50 °C, -30 °C, 0 °C and +20 °C. SiPMs were produced by Hamamatsu and have 9 mm^2 area and 50 μm pixels. Data on SiPMs with 25 and 75 μm pixel size is available in [215].

G. Boca et al. [231,232] studied the deterioration of SiPM timing properties after irradiation. Figure 3.54 (left) depicts the degradation of SiPM timing resolution by 20 – 30 % decrease after irradiation with only 3×10^9 n_{eq}/cm^2. Figure 3.54 (right) shows that after irradiation, the time required for the photon detection also becomes slightly longer, probably because an avalanche develops and propagates faster in a stronger electric field of non-irradiated samples. Moreover,

the authors studied the effect of connecting irradiated SiPMs in series and in parallel. They found that timing resolution is the best for series connection if a signal is read out from the side with the most damaged SiPMs, because it compensates the dispersion of signal timings measured by different SiPMs.

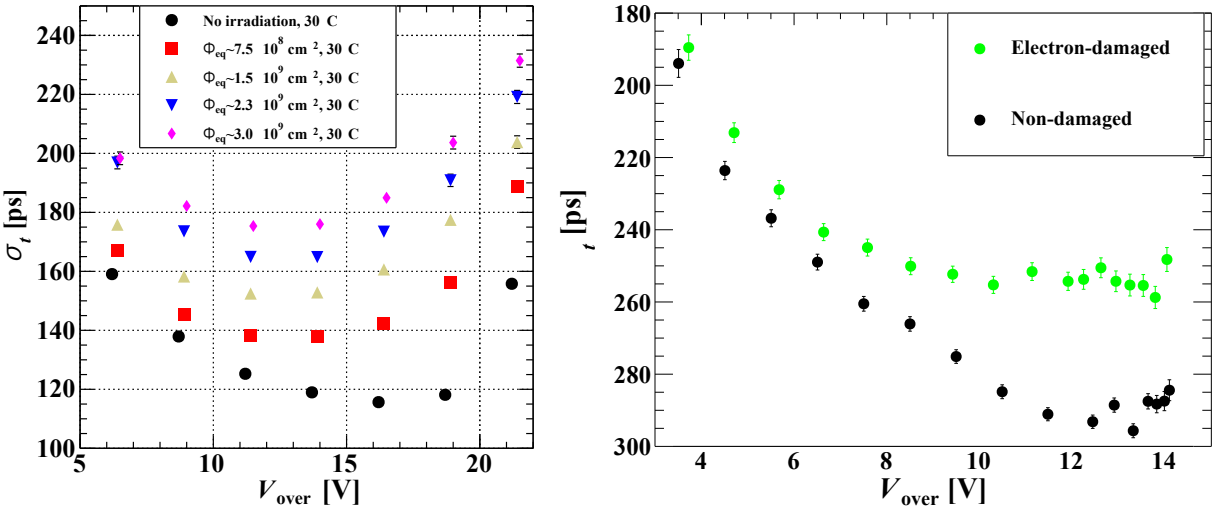

Figure 3.54: Dependence of timing resolution (left) and time center (right) on overvoltage for four series-connected SiPMs before and after irradiation [232]. Some samples were irradiated with electrons and some with protons, but the 1 MeV neutron equivalent fluence of the connected SiPMs was the same. In (left) 1 MeV equivalent fluences are indicated in the legend, in (right) it was 3×10^9 n_{eq}/cm^2. Measurements were performed at 30 °C. SiPMs were produced by AdvanSiD and have 9 mm^2 area and 50 µm pixels.

3.6.16 Approaches to improve SiPM radiation hardness

Several approaches can be beneficial to extend the SiPM radiation hardness based on general techniques listed in subsection 3.4.7 and knowledge of SiPM specifics:

- Optimization of the SiPM structure, namely doping profile distribution, and protection of pixel borders with help of guard rings and optical trenches. However, increasing the size of protection elements will inevitably reduce the optically active volume and, in turn, *PDE*.
- Usage of silicon with low impurity concentrations, both for substrate and epitaxial layer, to reduce the initially present trapping defects. Alternatively, the thickness of the depleted region can be reduced with help of electric field optimization. A decrease of the substrate thickness is also beneficial for the same reason, although it is not easy to achieve with epitaxial silicon, and utilization of FZ or MCz silicon will significantly increase the sensor price.
- Development of SiPMs based on materials with band gap wider than a band gap of silicon (1.12 eV) which will significantly reduce both bulk and surface dark currents. First devices based on GaAs (1.42 eV) and SiC (3.26 eV) are currently being designed [156].
- Replacement of polysilicon quenching resistors with metallic ones, because their resistance does not depend on temperature and they can be made much more compact. Other options include a silicon resistor which is a shallow doping region confined between two trenches, and a bulk resistor under the pixel which allows maximizing the filling factor [156].

- Utilization of n+ collecting electrodes in a p-type structure which is usually done for SiPMs optimized for red light may be beneficial, see figure 3.23. This allows utilizing the higher mobility and avalanche triggering probability of electrons which are collected at positively biased n+ electrodes. Therefore, electrons have a much lower chance to be trapped by irradiation-induced defects because they have to travel only a few micrometers to reach the electrode, opposed to traveling the whole sensor depth (300 – 500 μm) in the case of p+ in the n-type substrate. Although, this is hard to implement for near-UV light which is absorbed within a few hundred nanometers, so electrons won't have enough time to initiate an avalanche before they reach the electrode. But n-in-p structure can be optimized for a green light, it could be used with scintillators and wavelength shifting fibers doped with green-emitting fluors for enhanced radiation hardness. Therefore, dedicated radiation hardness studies comparing n-in-p and p-in-n structured SiPMs are of high interest.

However, usually, SiPM technology is kept secret by the manufacturer, and cooperation with the radiation hardness researchers is not easy to achieve. Moreover, DLTS and TSC techniques, which are used for defect characterization in other silicon sensors, are not applicable to SiPMs due to large capacitance and high dopant concentration [130] making the design optimization with respect to radiation hardness even more difficult.

From the user's point of view, there are several guidelines that I can recommend for the SiPM choice and readout design:

- Pixel miniaturization is now a trend with 10 – 15 μm devices currently available on the market and 5 – 7.5 μm expected to arrive in the near future [182]. Although it reduces initial gain and PDE, it is extremely beneficial for the radiation hardness because
  - Small active volume and surface of a single-pixel results in the decrease of generated dark current (see figures 3.23, 3.45 and 3.48), lowered probability of both afterpulsing and crosstalk, and smaller pixel capacitance.
  - Small capacitance shortens the time required for charge collection and therefore improves collection efficiency, so SiPM response amplitude remains unchanged up to higher fluences, see figure 3.35.
  - Small capacitance also reduces the pixel recovery time which makes it possible to integrate for a smaller time window integrating less dark noise.
  - Small pixel recovery time also increases the effective dynamic range for the high-frequency signals.
- Temperature control is essential to stabilize the SiPM gain and PDE. Breakdown voltage increases and overvoltage consequently decreases with the temperature at fixed V_{bias} which leads to a decrease in SiPM gain and PDE. This effect can be mitigated by either temperature stabilization, e.g. to exactly -30 °C implemented in the CMS calorimeter [145], or by overvoltage stabilization based on the temperature monitoring which is planned for CBM PSD, see section 8.1.4.
- Cooling substantially improves the SiPM performance reducing the noise and restoring the signal lost due to pixels occupied by dark pulses, see figures 3.25 and 3.34. Deep cooling to cryogenic temperatures allows the single-photon detection even for SiPMs irradiated with 10^{14} n_{eq}/cm^2, see figure 3.43.
- Optimization of the readout chain design is essential to achieve the best energy and timing resolution. Distance between SiPM and pre-amplifier shall be minimized to eliminate reflections along the signal trace and RF interference from the outside. In case if timing resolution is of lesser importance, one can utilize the charge sensitive amplifiers with high impedance value and narrow bandwidth.

- Bandwidth can be specifically limited even more to cut out HF part of radiation-induced noise. For instance, an increase of the threshold by 1 p.e. amplitude reduces the dark count rate roughly by an order of magnitude, see figure 3.46 (left). Appropriate acquisition time window and setting of the cut-out threshold for noise can be used individually for each SiPM depending on its noise.
- High-temperature annealing, possibly under high bias, was shown to significantly reduce the dark current of irradiated SiPMs, see subsection 3.6.8.
- In digital SiPMs noise can be reduced by turning off the noisiest pixels, because for medium fluences only a small percentage of pixels is responsible for the most part of the observed dark counts, see figure 3.26.

3.6.17 Summary

It is not simple to derive a general conclusion on the SiPM radiation hardness for application at CBM PSD based on the available data. Initial degradation in form of an increase of dark current and noise starts already after irradiation with 10^8 n_{eq}/cm^2 or 10 Gy. It is followed by the loss of single-photon counting capability around $10^9 - 10^{10}$ n_{eq}/cm^2 or 1 kGy. For SiPMs with large (> 50 μm) pixels, degradation of the response amplitude (combination of gain and PDE) starts to manifest above $10^9 - 10^{10}$ n_{eq}/cm^2, while for SiPMs with small (< 15 μm) pixels it may remain unchanged up to $10^{11} - 10^{14}$ n_{eq}/cm^2. Study of the SiPM signal-to-noise ratio (dynamic range) after irradiation was done only by Yu. Musienko et al. [184, 196, 197, 213] and no comparison with data before irradiation is available. No study of calorimeter performance with irradiated SiPMs in terms of energy resolution is yet available up to my knowledge.

The huge spread in the radiation tolerance by 2 – 3 orders of magnitude in terms of both dark noise and response degradation is reported for different SiPMs in different studies, see figures 3.23 and 3.35. Contradictory information is also reported for electrical characteristics, including breakdown voltage and gain. The foremost reason for this is pixel miniaturization, see the previous subsection. Moreover, SiPM technology is substantially improved almost every year reducing the noise (dark current and dark count rate) and increasing the photon detection efficiency in new device generations. Another complication arises from the very different properties of available devices (total area, pixel size, operating voltage, gain, PDE, dynamic range, spectral range, timing properties, etc.), as well as anticipated operational conditions (temperature, humidity, radiation load, etc.) which demand the careful assessment of particular SiPMs for particular tasks.

The aforementioned considerations provide great motivation for my work to study the radiation hardness of different SiPMs both in the laboratory and in real experimental conditions.

Chapter 4

Projectile Spectator Detector at CBM FAIR

A heavy-ion collision can be characterized with help of different detectors in the experiment such as an internal tracking system or a very forward hadron calorimeter situated downstream of the target in case of the fix-target experiment. In this chapter, the detector system of the CBM experiment being built for FAIR is described with the emphasis on its forward hadron calorimeter. Moreover, existing calorimeters of different high-energy physics experiments with a similar structure including the calorimeter of the NA61 experiment at CERN are reviewed and compared with the one designed for CBM.

4.1 Compressed Baryonic Matter (CBM) experiment

The future Facility for Antiproton and Ion Research (FAIR) in Darmstadt, Germany will provide unique research opportunities in the fields of nuclear, hadron, atomic, and plasma physics [241]. It is designed to provide high-intensity heavy-ion beams with SIS100 and SIS300 accelerator rings. The minimal achievable ion beam energy will be about 2 AGeV. SIS100 synchrotron will be capable of accelerating a primary beam of protons up to $E_b \approx 29$ GeV, gold nuclei up to $E_b \approx 11$ AGeV, and calcium nuclei up to $E_b \approx 14$ AGeV. Later on, SIS300 synchrotron will arrive increasing the magnetic rigidity from 100 to 300 Tm and providing beam energies up to $E_b \approx 90$ GeV for protons, $E_b \approx 35$ AGeV for gold ions, and $E_b \approx 45$ AGeV for calcium nuclei.

The Compressed Baryonic Matter (CBM) experiment will investigate the region of the phase diagram of high net-baryon densities and moderate temperatures and probe the phase transition of hadron matter to the quark-gluon plasma. Transport model calculations for central Au+Au collisions show that very high density about 5 times the density of normal nuclear matter can be already reached at a beam energy of about 5 AGeV (see figure 4.1). A more detailed review of the CBM research program can be found in the CBM Physics Book [2]. CBM is a fixed-target heavy ion collision experiment that will operate with the very high beam intensities expected to reach 10^9 Au ions per second corresponding to a collision rate of 10^7 Hz for the 1% gold target. The comparison of interaction rates for various heavy-ion collision experiments in the few GeV – tens GeV energy range is given in figure 4.2 (left). Here STAR F.t. stands for STAR fixed-target mode.

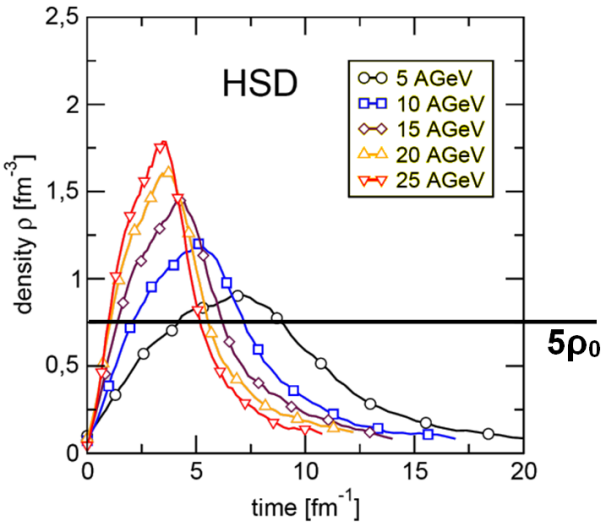

Figure 4.1: The HSD transport model calculations of the baryon density as a function of elapsed time for central Au+Au collisions in the beam energy range $E_b = 5 - 25$ GeV [242].

Due to the high interaction rate, the CBM experiment will be able to measure with unprecedented statistical precision [243]:

- Particles containing charm quarks (D mesons called open charm and J/Ψ mesons called charmonium) to probe very early stage of the highly compressed baryonic matter in the collision and possibly quark-gluon plasma formation.
- Low-mass vector mesons decaying into lepton or muon pairs ($\rho, \omega, \phi \rightarrow e^+e^-$ or $\rho, \omega, \phi \rightarrow \mu^+\mu^-$) carrying information on hadron properties in the hot and dense fireball and expected to be a signature for the chiral symmetry restoration.
- Kaons and hyperons (Ξ, Λ, Ω) produced by the single and double hypernuclei and heavy short-lived multi-strange particle decays carrying strange quarks and expected to be related to the transition from a partonic phase to a hadron final state.
- Photons providing the direct radiation information from the early fireball evolution dynamics.
- The collective flow of above mentioned identified hadrons that carry the information on the equation-of-state of hot and dense matter and can be a signature for a phase transition to the quark-gluon plasma.
- Event-by-event dynamical fluctuations and correlations of observed quantities (e.g. momenta, baryon number, strangeness, particle yields, and production ratios) which can be used to study a first-order phase transition or the critical behavior of the fireball.

Figure 4.2 (right) represents the values of multiplicities times branching ratio for various particles produced in the central Au+Au collisions at $E_b = 25$ AGeV. The black horizontal line indicates those already measured (above) and those not yet measured (below). Here one can see, that huge statistics is required to measure rare probes with adequate precision due to very low particle yields, which is a unique feature that will be available at CBM.

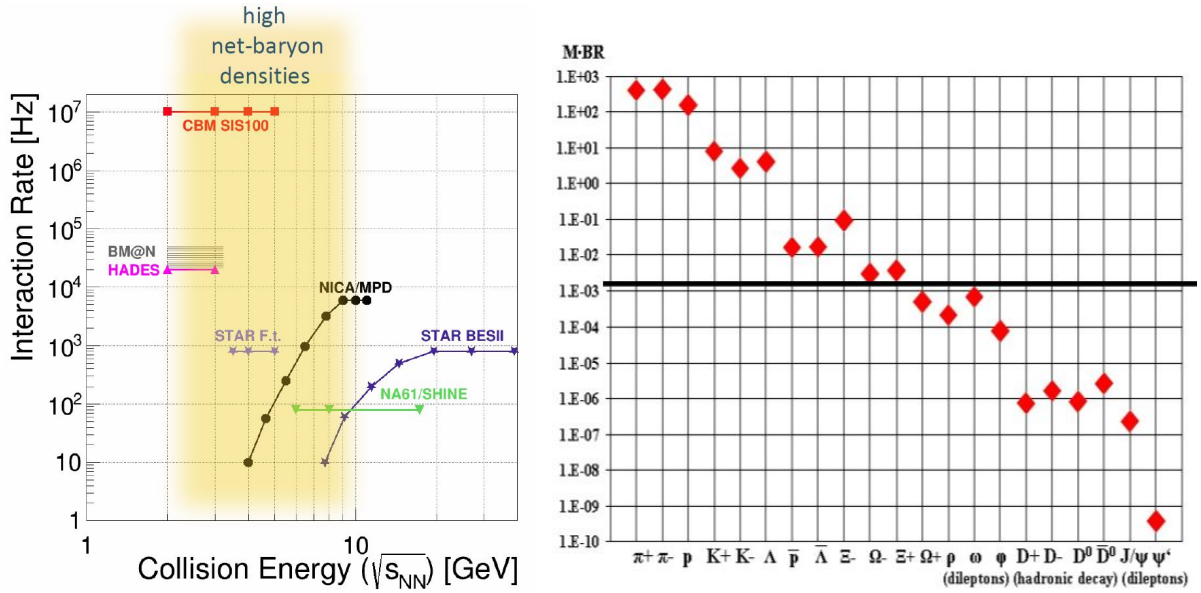

Figure 4.2: (left) Comparison of interaction rate for several heavy-ion experiments [243]. (right) Multiplicity times branching ratio for several rare probes [244].

4.2 CBM detector system

The CBM detector is a multi-purpose device composed of a set of detector systems for effective measurements of various particles produced in beam-target interactions, including very rare particles. Detector systems shall provide efficient charged particle tracking, lepton, and hadron identification and high-resolution determination of decay vertices [244]. Due to extreme rates of the beam collisions with the target (up to 10^7 Hz) with a multiplicity of produced charged particles up to 1000 per collision, the experiment requires its detectors to be fast and radiation hard. To fulfill the first requirement, the high-speed data acquisition system with self-triggered read-out electronics is developed for the experiment without a common multiple-level trigger system which is a paradigm change in data taking by high-energy heavy-ion experiments.

A schematic layout of the full CBM detector setup for the SIS100 with the High Acceptance Dielectron Spectrometer (HADES [245]) detector placed in the same cave as CBM (not discussed here) is shown in figure 4.3. Another unique feature of the CBM detector system is that all the detectors (including the HADES setup) will be movable and will be used in different combinations depending on the physics scenario and beam running conditions. For this purpose, a heavy load crane will be installed in the experimental cave [246]. Two main running scenarios can be considered, while many various configurations can be applied within each of them:

- setup for electron measurements – all detectors can be used except for Muon Chamber;
- setup for muon measurements – Muon Chamber will replace Ring Imaging Cherenkov detector, also Electromagnetic Calorimeter will be moved aside.

The CBM detector system will consist of the following subsystems, technical design reports for most of them are already approved and can be found at [247]:

- Superconducting Dipole Magnet will bend all charged particles created in the collision which is required for the later reconstruction of the exact particle momenta with high

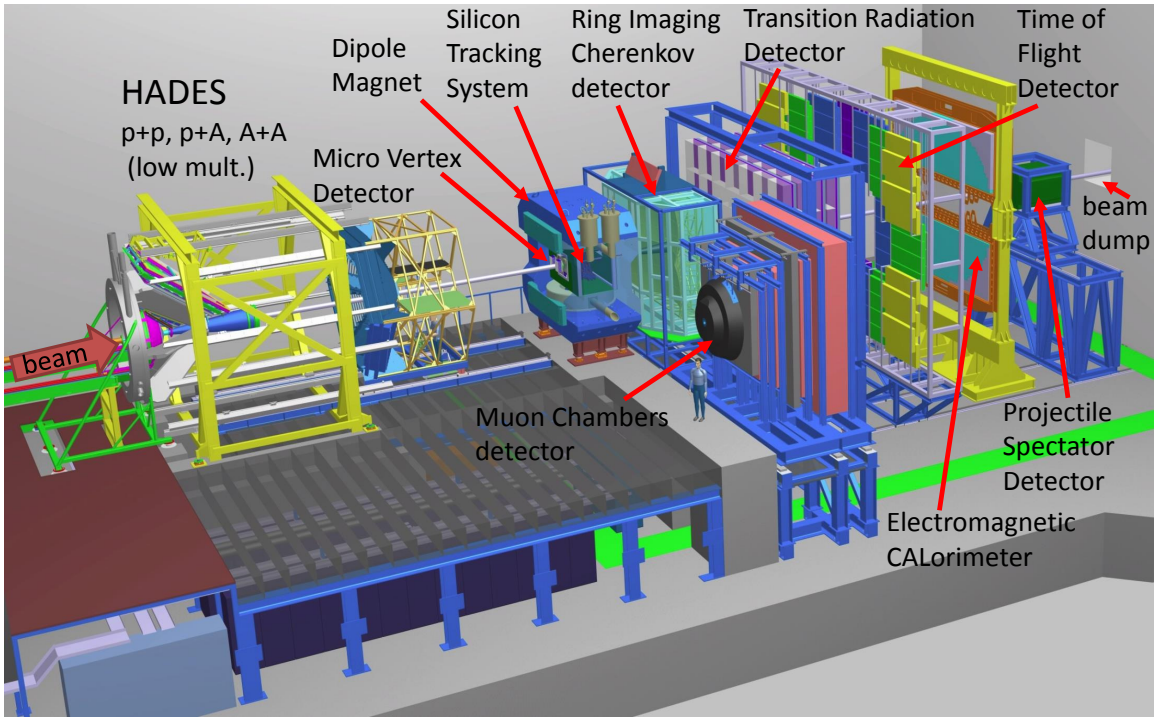

Figure 4.3: Schematic layout of the full CBM and HADES detector setup in the underground experimental cave. Modified artwork from [243].

precision. Magnet has wide polar angle acceptance of ±25 ° and provides an integrated magnetic field up to 1 Teslameter.

- The Micro Vertex Detector (MVD) is the very first particle tracking system situated in a vacuum inside the magnet at 5 cm downstream of the target. It will be used for the reconstruction of secondary vertices allowing identification of very short-lived particles like D^0 ($D^{\pm}$) mesons with decay length of only $c\tau$ = 124 (314) µm. The MVD will have 3 layers of monolithic active pixel sensors (MAPS [248]) with a transverse pixel size of about 18 − 20 µm which allow for a spatial decay vertex resolution of 50 − 100 µm along the beam axis. To avoid multiple scattering a very low material budget is required resulting in a total detector thickness of 300 − 500 µm silicon equivalent.

- Silicon Tracking System (STS) will be the main tracking detector of CBM situated inside the magnet behind MVD. It is designed for charged particle track reconstruction with an efficiency of about 95% and momentum determination within the resolution of $\Delta p/p = 1\%$ over a large momentum range of 0.1 GeV/c – 12 GeV/c. It will be made of 8 tracking layers of double-sided silicon microstrip detectors with a strip pitch of 60 µm, strip lengths between 20 and 60 *mm*, and a silicon thickness of 300 µm. Very low material budget is reached by applying lightweight ladder-like mechanical supports for sensors, placement of front-end electronics outside the STS active area and connection of sensors to the read-out chips via low-mass cables. STS can be used for the event characterization alone or in conjunction with other detector systems which is described in detail in section 9.3.2.

- Ring Imaging CHerenkov detector (RICH) will provide identification of electrons and reduction of the number of background pions in the range of momenta up to 10 GeV/c. RICH

design includes a 1.7 m container filled with CO_2 radiator, glass mirrors of 6 mm thickness with a reflective $Al + MgF_2$ coating and two planes of Multi-Anode Photo-Multiplier Tubes. Detector's idea is based on the detection of radiation emitted by a particle moving in a medium with a speed greater than the speed of light in that medium. During this Cherenkov effect, photons are radiated at a fixed angle forming a cone, which gives a ring on the photodetector plane. As effect depends on particle velocity, electrons with any momenta emit Cherenkov light in CO_2 due to their small mass, while pions start to irradiate at 4.65 GeV/c momentum resulting in an anticipated pion suppression factor of about 500.

- Transition Radiation Detector (TRD) will be placed behind the RICH and will work as the particle tracking the third subsystem also allowing separation of electrons and positrons with $p > 1.5$ GeV/c. Detector idea is based on the effect that a charged particle emits radiation when passing through a boundary between two different media due to the difference in media's electromagnetic properties. The intensity of the radiation depends on the energy of the particle and its type. TRD will consist of 3 layers within a station divided into rectangular modules (pads) with a resolution of 300 – 500 μm across and 3 – 30 mm along with the pad. To ensure an accurate measurement of both coordinates every second layer of the sensors will be rotated by 90 degrees with respect to the previous one. Pion suppression is expected to be up to 100 at 90% electron efficiency.

- Time Of Flight detector (TOF) will provide hadron identification. Its idea is based on the fact that particles with the same momentum but different masses have different speeds and therefore different times of flight between two fixed detectors. The particle's mass can be identified by measurement of its time of flight by TOF together with the measurement of its momentum by STS. TOF will consist of an array of Resistive Plate Chambers covering an active area of about 120 m^2 located about 6 m downstream of the target. The expected time resolution is on the order of 80 ps with a position resolution of σ = 300 – 500 μm across and 3 – 30 mm along with the pad.

- Electromagnetic CALorimeter (ECAL) is designed to measure fast direct photons and decay photons from neutral mesons (π^0 and η). The total energy of incoming photons will be absorbed by interaction with lead producing an electromagnetic shower consisting of electrons, positrons, and secondary photons. Then those particles will produce light in a scintillator which will be read out by photomultipliers. The calorimeter is of a common "shashlik" type composed of modules which consist of 140 layers of 1 mm lead and 1 mm scintillator, with a cell size of 6×6 cm^2 enabling detection of approximately 80 photons in total for a central Au+Au collision at 25 AGeV.

- Muon Chambers (MUCH) detector will be used for measurement of rare particles decaying into muons like low mass vector mesons and J/Ψ. Muons are considered as minimum ionizing particles in a wide momentum range from 100 MeV/c to 100 GeV/c. They can penetrate several meters of iron because they do not interact strongly and are not much scattered by the electromagnetic field of atoms inside the material due to their large mass. The main challenge at CBM is to identify low-momentum muons in an environment of high particle densities. To address this the hadron absorber is divided into 6 layers, each layer followed by 3 gas chambers for tracking of produced charged particles. The first absorber will be made of carbon, all others – of iron. To reduce the muon background from decays of mesons produced in MUCH, the system will have a relatively low total thickness of

only 250 cm. Gas chambers will be based on different technologies such as Gas Electron Multipliers (GEM) and straw tube detectors.

- Projectile Spectator Detector (PSD) is a hadron calorimeter designed for the collision event characterization and described in detail in the next section.

- Data AcQuisition system (DAQ) and First Level Event Selector (FLES) will be responsible for the data collection and analysis in CBM. DAQ will be based on the ultra-fast and radiation tolerant GBTx ASIC data aggregation units. FLES, recently redesigned as Common Readout Interface (CRI), will utilize powerful FPGAs. Considering a recording rate of 1 GByte/s and an event volume of about 40 kByte for minimum bias Au+Au collisions, only an event rate of 25 kHz can be stored. Therefore, the collision rate of 10 MHz CBM requires online event selection algorithms which reject the events containing no interesting signal by a factor of 400 or more. For the most important signals of the CBM physics case, there are no simple criteria for collision triggering and selection on the low hardware level due to the complicated decay topology of particles like λ-hyperons or D-mesons. Data acquired from the detectors by DAQ will be transmitted to the FLES where the full reconstruction of the collision will be done already at the selection stage. It will operate in the free-streaming online mode on a high-performance computer farm "Green IT Cube" equipped with many-core CPUs and graphics cards, where compressed data will be stored afterward.

- 4-dimensional (4D) track finder algorithm will provide time-slice-based online reconstruction in the CBM experiment to analyze time-slices of the hits rather than isolated events. This will be required because at the highest interaction rates the time difference between hits belonging to the same collision will be larger than the average time difference between two consecutive collisions, so events may overlap in time. Detailed information on 4D reconstruction in CBM is presented in PhD thesis of V. Akishina [249]. Track reconstruction, which is the most time-consuming combinatorial stage of the event reconstruction, will be based on parallel track finding and fitting algorithms, implementing the Cellular Automaton and Kalman Filter methods. Detailed information can be found in PhD thesis of M. Zyzak [250] and in [251].

4.3 Design of Projectile Spectator Detector (PSD) at CBM

CBM Projectile Spectator Detector (PSD) is a very forward calorimeter located the most downstream of the beam and designed to detect projectile spectators, i.e. the non-interacting nucleons and fragments emitted at very low polar angles in the forward direction in nucleus-nucleus collisions. It will be used to characterize the collision event including determination of its centrality and reaction plane orientation that is essential for the anisotropic flow measurements.

General design requirements that PSD shall fulfill in CBM are:

- Appropriate energy resolution and modular structure with fine transverse and longitudinal azimuthal segmentation.

- Spectators detection in the beam energy range of $E_b = 2 - 35$ AGeV.

- Operation at beam intensities up to 10^9 Au ions per sec.

- Reaction plane determination with an accuracy better than 40 degrees.

- Determination of collision centrality classes with an accuracy better than 10%.

As it is shown in PSD Technical design report (TDR) [252], PSD can meet those requirements with its current design. It is depicted in figure 4.4 consists of 44 modules with a transverse size of 20×20 cm^2 each, covering a total transverse area of 160×120 cm^2. To avoid radiation damage due to high beam intensities at CBM of up to 10^8 ions/sec, a hole in the center of the PSD is needed for the beam transport to the beam dump through the vacuum-filled beam pipe [253]. Design and delivery of the support platform to GSI were recently accomplished by the joint Czech PSD team from NPI Řež and CTU [254] as an in-kind contribution to FAIR infrastructure. The platform design allows the detector movement along all 3 axes.

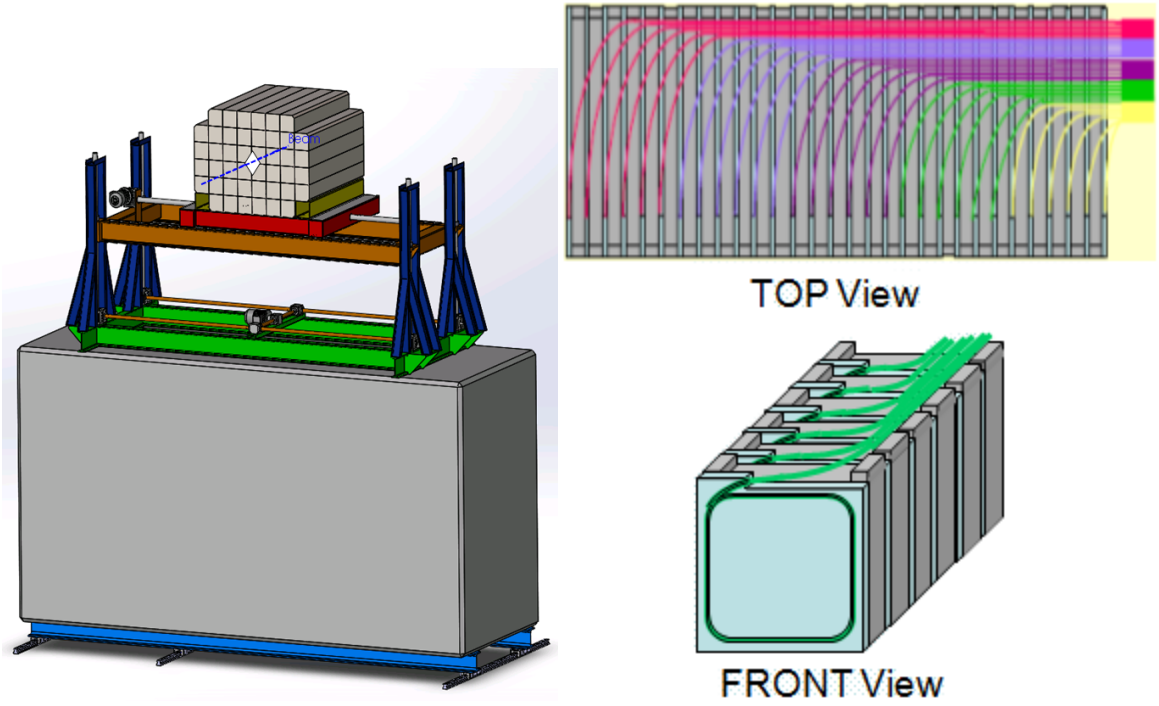

Figure 4.4: (left) Schematic design of PSD with a support platform and a small beam hole [254]. (right bottom) Schematic design of one section of a PSD module. (right top) WLS-fibers connection within a module [252].

Each PSD module consists of 60 pairs of alternating lead plates and scintillator tiles with 16 mm and 4 mm thickness, respectively. The stack of plates is tied together with 0.5 mm thick steel tape and placed in a box made of 0.5 mm thick steel. The steel tape and the box are spot-welded together providing appropriate mechanical rigidity. The total length of the module corresponds to about 5.6 nuclear interaction lengths. Every 6 consecutive layers of scintillators are read out via the WaveLength Shifting (WLS) optical fibers as shown in figure 4.4 (right) by a single Silicon Photomultiplier (SiPM, see section 3.5). Additionally, a simple monitoring and calibration system for the SiPM readout is implemented as an extra WLS-fiber illuminating SiPM by a Light Emitting Diode (LED). The ten sections with the individual light readout provide the longitudinal segmentation within the PSD modules, which ensures the uniformity of the light collection.

4.4 Readout electronics

PSD slow control system will be responsible for the control of the first-level front-end electronics (FEE). FEE will provide the power supply for SiPMs, featuring the automatic voltage adjustment with respect to the ambient temperature to achieve the SiPM gain stabilization, see subsection 8.1.4 for details. SiPM signals will be firstly amplified by the preamplifier board, and then processed with help of the 64-channel digitizer board which was developed for PANDA experiment at FAIR [255]. It is based on fast 125 Msps ADCs with 14-bit digitization resolution. Digitized data will be sent to powerful FPGAs using LVDS links for the data processing based on the Prony-LS fitting procedure, which can distinguish very noise signals and recognize pile-ups [256]. Processed data will be sent to the CBM Common Readout Interface via Gigabit Transceiver (GBT) interface. Clock times of all the detectors in CBM will be synchronized, and measure hit times will be derived into "timeslices" to satisfy the trigger-less readout paradigm [257].

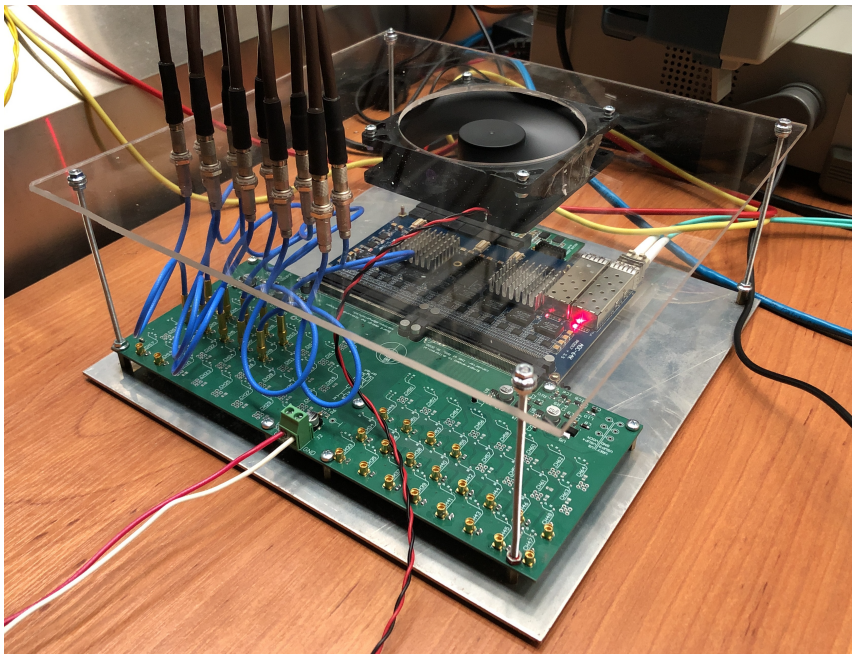

Figure 4.5: ACD64 readout board coupled with amplifier addon [255].

Figure 4.5 shows the described readout setup assembled for tests at GSI. For more details on the PSD readout electronics and its first prototype tests at mini-CBM test-setup at SIS18 in GSI, Darmstadt, Germany, please refer to [258].

4.5 Simulations of CBM PSD performance

4.5.1 Centrality determination with conjunction of PSD and STS

The multiplicity of produced particles in the nuclei overlap zone was used as an experimental proxy of the impact parameter b (or the number of participating nucleons) for a given heavy-ion collision. Figure 4.6 presents the resolution of impact parameter b defined as a ratio of the b-distribution spread σ_b to its average $\langle b \rangle$ for a given centrality. All events are sorted in centrality classes, with the most central ($b \approx 0$ or centrality $\approx 0\%$) being the collisions with the highest multiplicity of the produced particles and peripheral ($b \approx 2$ nuclear radii or centrality $\approx 100\%$)

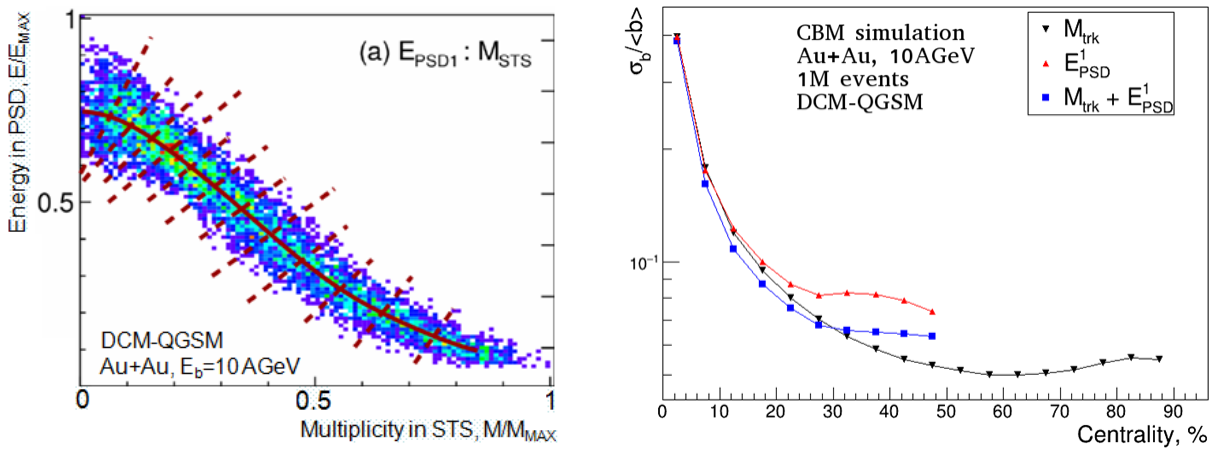

Figure 4.6: Impact parameter resolution for different centrality estimators [259]. 1M events of 10 AGeV Au+Au collisions were generated with DCM-QGSM model. The boundaries between centrality classes are shown by the dashed red lines, the most right line corresponds to the most central event class.

with low multiplicity. Average values of impact parameter for different centrality classes were deduced from a Monte Carlo Glauber (MC-Glauber) model.

Resolutions of b were compared for estimators based on different CBM subsystems. Charged particle tracks multiplicity M_{trk} was reconstructed with STS and MVD detectors. The energy of spectators was reconstructed with the inner four modules of PSD combined into PSD_1 subgroup. The resulting impact parameter resolution is about 5 – 10 % for mid-central and peripheral events. PSD b resolution is comparable to that of STS+MVD for centrality up to 30 %, i.e. for central and semi-peripheral collisions. However, in peripheral events, some fragments go into the beam hole and therefore cannot be detected in the PSD limiting PSD centrality determination to 0 – 50 %. Detailed information on centrality determination in CBM can be found in PhD thesis of V. Klochkov [260].

4.5.2 Reaction plane resolution of PSD vs STS vs TOF

Performance of the reaction plane reconstruction with alternative CBM detector subsystems was studied to show the uniqueness and necessity of the PSD calorimeter in the CBM experiment [252]. It was estimated with STS and PSD CBM detectors and alternative detector setup at forwarding rapidity – a forward time of flight (TOF) detector as shown in figure 4.7.

For the STS, the charged particles in the detector acceptance were required to have at least four hits in the silicon tracking stations. For the TOF, a simplified simulation setup was utilized when only hits from charged particles and fragments coming into the PSD acceptance were considered (see figure 9.9). The event plane resolution of the forward TOF wall was found to be much worse compared to that of the PSD, presumably due to the lack of TOF sensitivity to neutral particles, which are a significant fraction of the spectators. The STS showed the best resolution up to $E_b \sim 4$ AGeV, while its performance degraded at higher energies due to the decreasing STS acceptance for particles produced with large v_1 at forwarding rapidity. PSD showed the best resolutions starting from $E_b \sim 4$ AGeV, because it was optimized mainly for higher energies. For instance, at lower energies, the produced particles have very small rigidity relative to the strength of the magnetic field. Therefore, particles are highly deflected and their multiplicity in PSD acceptance is much lower than in STS acceptance.

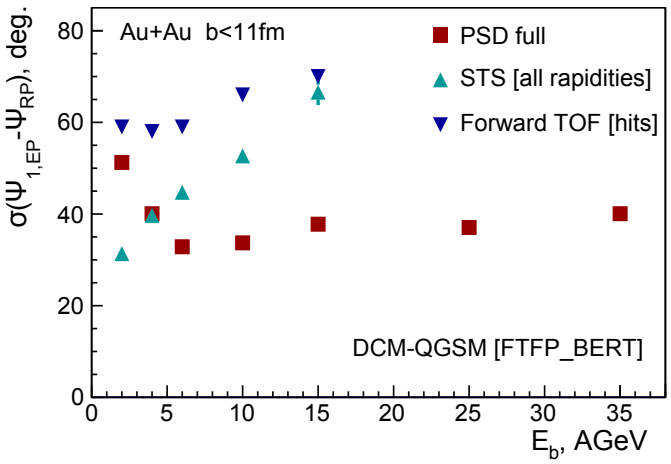

Figure 4.7: Reaction plane resolution measured by PSD, STS, and forward TOF detectors as a function of the beam energy in Au+Au collisions [252]. Impact parameter was chosen to be $b < 11$ fm (about 0 – 57 % central events [259]). The PSD was located at 8 (15) m from the target at SIS100 (SIS300) energies, collision data was generated with the DCM-QGSM event generator.

In summary, PSD and STS detector subsystems were found to be complementary in CBM and together provide the resolution of the reaction plane angle determination better than 40 degrees for the whole expected energy range of the experiment.

4.6 PSD supermodule performance at CERN PS

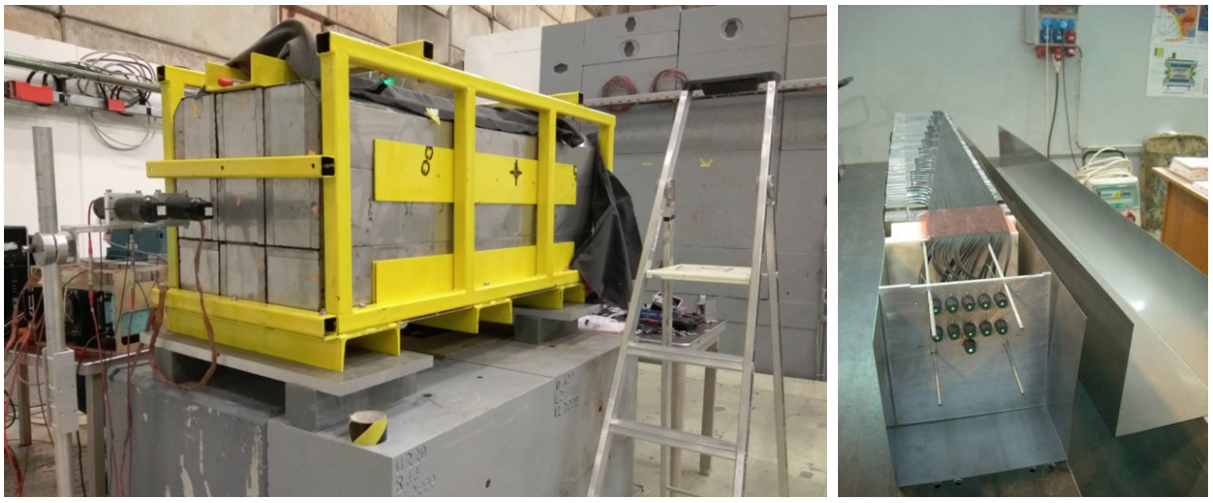

Figure 4.8: (left) PSD supermodule. (right) Single PSD module during assembly.

Figure 4.8 (left) introduces the PSD supermodule consisting of 9 modules assembled in a 3×3 array at CERN for the study of the calorimeter performance. The total weight of the supermodule is about 4.5 tons. Figure 4.8 (right) depicts the module structure.

Supermodule response was studied with proton beams in the momentum range of 2 –

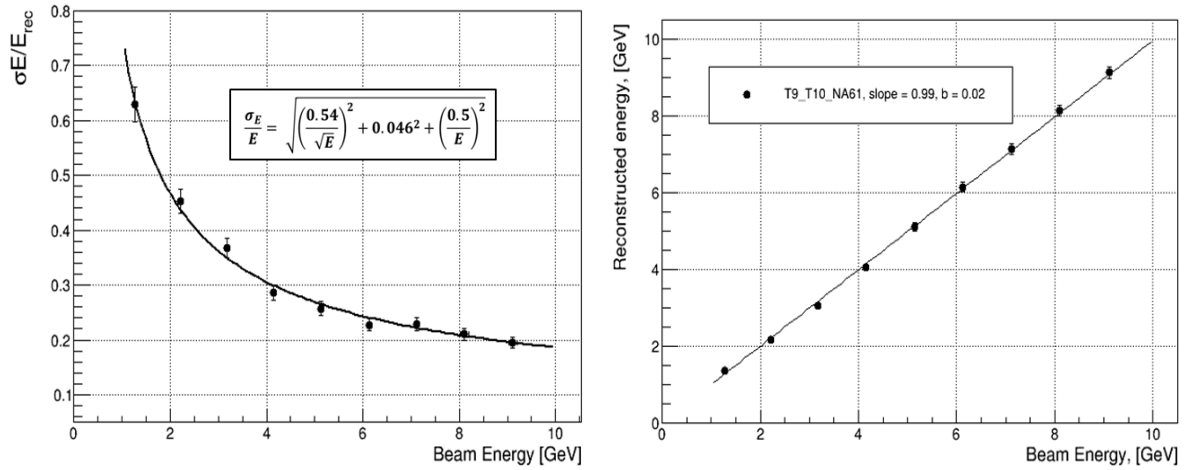

Figure 4.9: Supermodule energy resolution (left) and linearity (right) vs proton beam energy. Data are from [261].

10 GeV/c at the CERN Proton Synchrotron (PS) T9 and T10 beamlines, and in the momentum range of 20 – 80 GeV/c at NA61 H2 beamline. For the first time, the energy resolution and the linearity of the response have been measured at such low energies. Detector calibration was done with help of beam muons acting as MIP particles which produced the light yield of about 8 – 10 photoelectrons/MeV in each section. Protons were identified by the TOF method using two quartz Cherenkov detectors installed in front of the supermodule with a time resolution of about 60 ps.

Figure 4.9 demonstrates the supermodule relative energy resolution (left) and linearity (right) measured at T9 and T10. The energy resolution σ_E/E is estimated to be about $54\%/\sqrt{E(\text{GeV})}$ along with the deflection from linearity less than 1 % which satisfy the requirements of the CBM experiment [252]. A high noise term is explained by the fact that a single module was regarded as an independent calorimeter during the tests. The achieved resolution is in good agreement with the previous measurements at higher beam momenta up to 158 GeV/c and consistent with the CBM PSD requirements.

4.7 Comparison of PSD with similar forward hadron calorimeters

A concept of the calorimeter which registers hadrons via their strong interaction with the detector material was for the first time implemented in the late 1950s in cosmic ray measurements [29]. The hadron calorimeter response can be described in terms of the ratio between the electromagnetic (e) and hadron (h) components of the shower created inside the detector material. PSD is a compensating calorimeter approaching the compensating condition of $e/h \approx 1$ which reduces the energy fluctuations improving the energy resolution of the calorimeter. The other advantages of compensating calorimeters are linearity and Gaussian shape signal of the detector response. This concept started with uranium calorimeters [262] and now is applied to the calorimeters with iron and/or lead absorbers [263]. Compensating condition ($e/h = 1$) depends on the relative absorber/active thickness or sampling ratio and is equal to 20 for Fe/Scintillator, while for Pb/Scintillator it is around 4. Based on the limited space in the CBM cave and smaller sampling fluctuations of the shower, Pb/Scintillator was chosen for the CBM PSD.

Historically, a first lead-scintillator compensating calorimeter with the resolution of about

$58\%/\sqrt{E}$ was built for the WA97 experiment at CERN [264]. This calorimeter had a classical light readout with wave-shifter plates and PhotoMultiplier Tubes (PMTs). Unfortunately, such a readout has a drawback in form of the Cherenkov light in the WLS-plates. Also, it suffers from the nuclear counter effect, i.e. charged particles that were not absorbed in an active volume may hit PMTs placed behind the active part of the calorimeter, and produce an artificial signal. Another similar calorimeter developed for the JLC project [265] has a resolution of about $50\%/\sqrt{E}$. It avoided Cherenkov light by fiber-tile readout providing efficient light collection in the scintillators. It also has finer sampling granting perfect transverse uniformity of the energy resolution. However, a big number of PMTs used for the readout of each scintillator layer resulted in high complexity and cost.

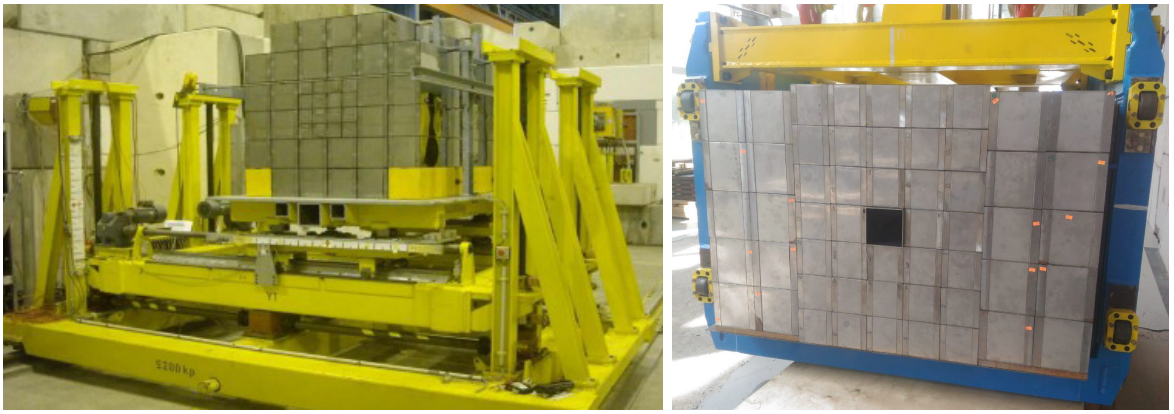

Figure 4.10: Photos of calorimeters NA61 PSD at CERN (left), and FHCAL at BM@N at NICA (right) [266].

Recently, a hadron calorimeter also called Projectile Spectator Detector has been constructed for the NA61 experiment at CERN [267]. It has a very similar 44 module design to that of the CBM PSD except for consisting of 16 small modules with the transverse dimension of 10×10 cm^2 and 28 large 20×20 cm^2 modules as shown in figure 4.10 (left) [268]. Another difference is that due to significantly lower beam intensities reaching only 2×10^5 ions/sec even though energies here reached 150 AGeV for Be beams, no beam hole was required and radiation hardness is not such an issue as it will be in CBM. However, beam intensity was increased during the recent upgrade of the NA61 experiment. To account for this, small inner modules of PSD were replaced by big 20×20 cm^2 standard modules with small edge cut to hold the newly introduced beam hole. Being a currently operating experiment NA61 is a perfect place for the various hardware tests related to CBM PSD within its dedicated test beamtimes supported by a recently signed joint Memorandum of Understanding [269].

The scientific team from Institute for Nuclear Research in Moscow who designed and operated NA61 PSD is now working towards the implementation of other similar calorimeters. One of them is PSD at CBM@FAIR, another will be implemented at BM@N and MPD experiments at NICA. Our team from NPI Řež is also involved in this process. Figure 4.10 (right) shows the Forward Hadron Calorimeter (FHCAL) during the installation at BM@N. For more details, please refer to [266].

Chapter 5

Radiation hardness of CBM PSD

The high-intensity heavy-ion beams provided by FAIR SIS100 accelerator to CBM experiment will reach up to $10^6/10^7$ interactions/second. This will lead to the high radiation emission to the detectors including PSD, especially its parts near the beam hole. PSD modules consist of lead plates, scintillator tiles, and WLS-fibers coupled with Silicon Photomultipliers for the light readout. The performance of all the aforementioned components except lead will probably deteriorate in these harsh conditions. This chapter explores the anticipated radiation environment at the calorimeter and the expected degradation of its components due to radiation damage.

Radiation hardness is discussed separately for passive and active components, namely scintillators + WLS-fibers and Silicon Photomultipliers (SiPMs). Section 5.1 describes calorimeter design changes made by the PSD team which lowered the expected radiation load for the calorimeter components including scintillators and photodetectors. Section 5.2 discusses the proton irradiation tests and measurements of polystyrene scintillators produced for PSD, in which I participated. In the end, I summarize the expectations for radiation hardness in scintillators and SiPMs during their operation in PSD. Due to severe degradation expected for SiPMs, I dedicate chapters 7 and 8 to the investigation of their radiation hardness. In addition, chapter 6 describes in detail the irradiation experiments that I conducted at the NPI cyclotron.

5.1 Radiation load for different PSD geometries

Since PSD TDR approval in 2015, two major changes in the module geometry were made to improve the detector radiation hardness. Because they are not yet fully described in other sources, I decided to summarize them, even though I did not directly participate in it. Though, I would like to note that they are inspired by my research of SiPM radiation hardness, which revealed severe degradation of PSD energy resolution in case of the radiation load expected for the original PSD design.

5.1.1 Shielding of SiPMs with borated polyethylene

The first change is the dedicated neutron shielding for the protection of SiPMs against the neutron-induced radiation damage was proposed by O. Svoboda.

PSD calorimeter being composed of lead and plastic can be regarded as a massive spallation target and neutron moderator, see subsection 2.4.2 for the description of the spallation process. Therefore, very high neutron fluence is emitted behind the PSD, where SiPMs are placed. O. Svoboda performed an MCNPX 2.7 [271] simulation of a single PSD module with added 8 cm shielding made of a 3 % borated polyethylene. The module was irradiated with a "white"

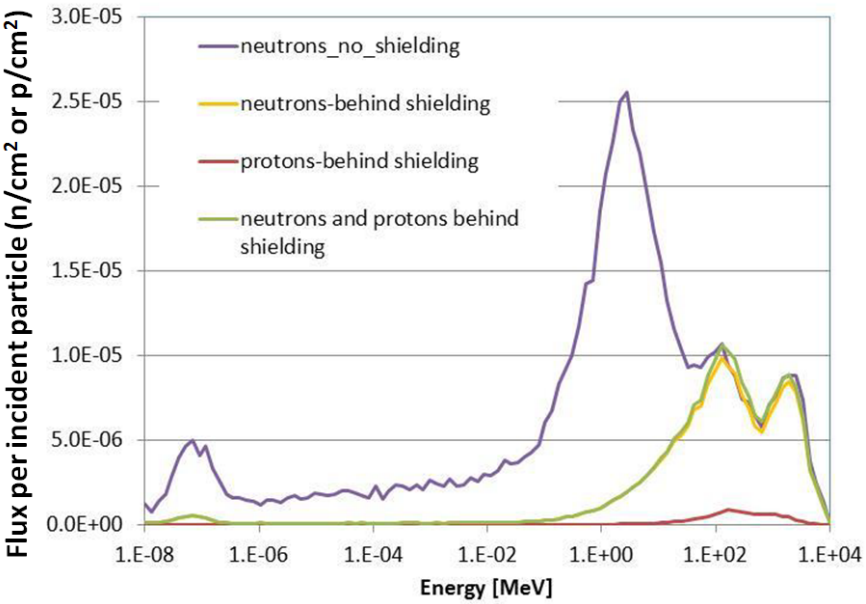

Figure 5.1: Neutron spectrum behind the irradiated PSD module with implemented polyethylene shielding. Spectrum of secondary protons is shown as well. Simulation done by O. Svoboda [270].

beam of 100 MeV – 10 GeV protons [270], a similar result was obtained for the neutron beam of white spectra and the same energy span. Figure 5.1 presents the "spallation" spectra at the end of the PSD module, where the SiPMs are placed. Shielding effectively removed 70 % of the neutrons, mostly below 100 MeV. The number of secondary protons created in the shielding was negligible.

Further simulations were done by A. Senger in FLUKA code [273] with the full CBM setup, turned on the magnetic field and each PSD module supplemented with the neutron shielding. Gold target with 100 μm width was used. The energy of the gold beam was 11 AGeV which is the maximum that SIS100 can deliver. Beam rate of 10^8 ions/second corresponding to reaction rate of 1 MHz is regarded as the maximal rate at which PSD can operate [1]. The 2 months of uninterrupted time is regarded as the typical total time available for the experiments during the calendar year. The neutron fluence is presented in the 1 MeV neutron equivalent according to the Non-Ionizing Energy Loss (NIEL) scaling hypothesis [22], see section 2.3 for details. FLUKA simulations of radiation hardness for all the CBM detectors done by A. Senger can be found at the dedicated webpage [275].

Figure 5.2 (left) demonstrates the reduction in neutron fluence by up to one order of magnitude by the shielding. It is especially efficient for the SiPMs positioned in the most central modules at a radial distance of about 10 – 20 cm from the beam hole. Neutron spectra for different PSD modules with and without shielding can be found in appendix A. The developed neutron shielding – 8 cm thick polyethylene blocks with three percent of boron – was implemented in PSD modules that were produced by the PSD team of Moscow Institute for Nuclear Research as shown in figure 5.2 (right).

[1] Time required for luminescence of WLS-fibers coupled with the SiPM pixel recovery and response is about 40 – 50 ns depending on the amplifier design. It results in a delay between the beam arrival and signal readout which can cause pile-ups at high readout rates [274]. Due to the CBM modular design PSD can be moved away within the cave for the experiments requiring higher rates. However, dedicated pile-up studies were not yet performed, so we might hope to extend the operation regime of PSD up to several MHz.

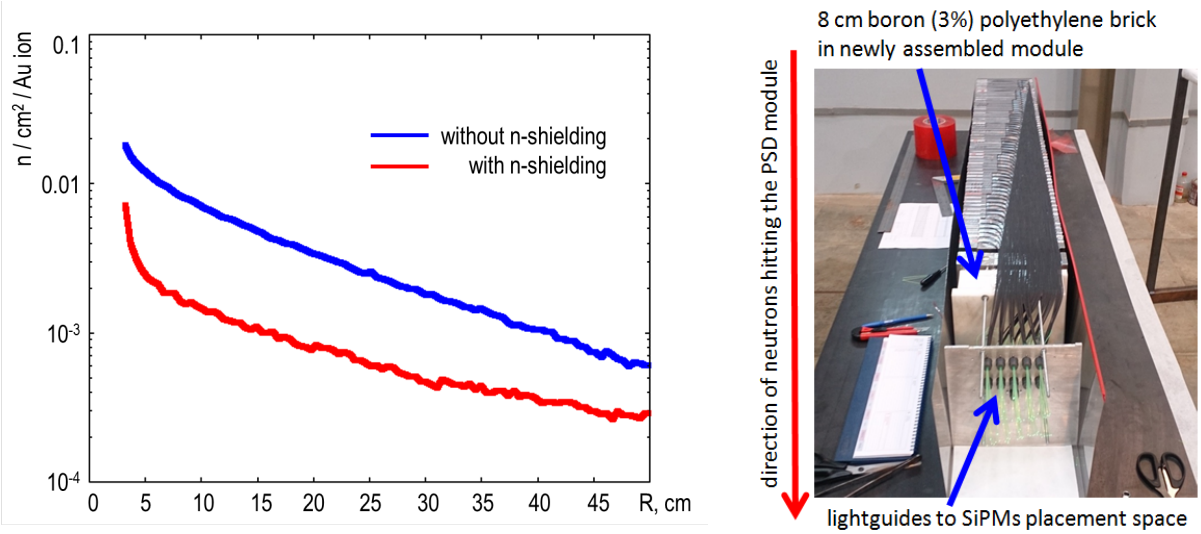

Figure 5.2: (left) Radial distribution of 1 MeV equivalent neutron fluence behind PSD shielding in the plane where SiPMs are placed. Simulations were done by A. Senger for a typical calendar year of operation with the maximal beam settings, i.e. total 2 months of non-stop operation with 11 AGeV Au+Au at beam rate of 10^8 Au/s. (right) PSD module equipped with the neutron shielding during the production in Moscow Institute for Nuclear Research [272].

5.1.2 Enlargement of the beam hole

The second design change is an increase of the beam hole in the center of the calorimeter from a circle with a 3 cm radius to a square of 20 $\times$ 20 cm^2 dimensions, as shown in figure 5.3. This would decrease the radiation load not only within PSD but also for the nearby detectors, most notably TOF which is situated right behind PSD. Two-dimensional X-Y and Z-X distributions of neutron fluence for different beam hole geometries can be found in appendix A. The lowest fluence along the module is accumulated in the case of the diamond-shaped 20 $\times$ 20 cm^2 beam hole, which is now considered to be implemented into the PSD configuration. Four new inner modules with bigger edge cuts were manufactured in Moscow Institute for Nuclear Research.

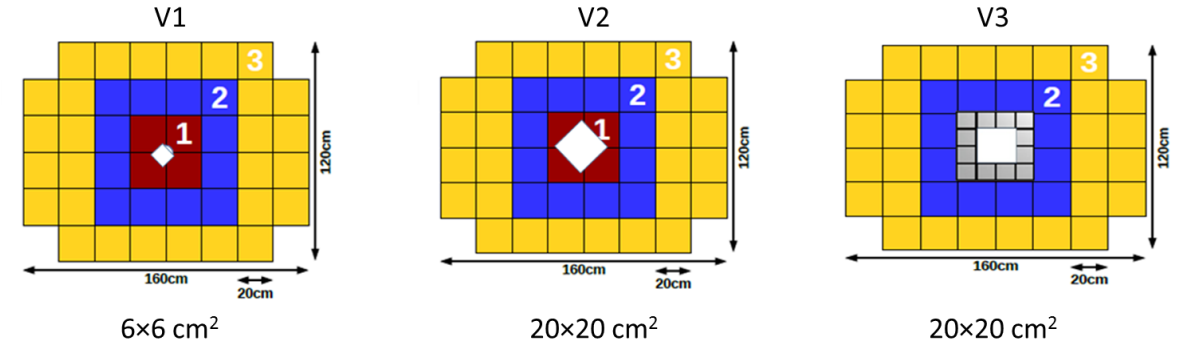

Figure 5.3: Three different geometries of the PSD beam hole, namely geometry with 3 cm radius (left), square-shaped (middle) and diamond-shaped (right) geometries with 20 $\times$ 20 cm^2 dimensions, as used in simulations of A. Senger.

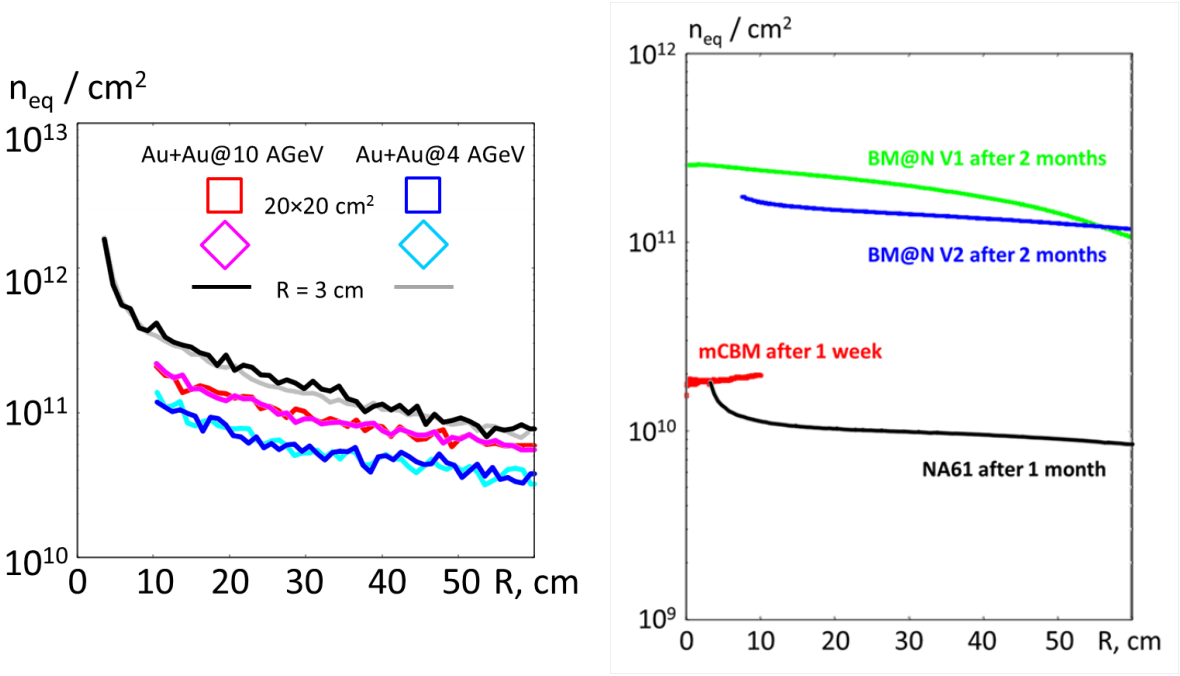

Figure 5.4: (left) Radial distribution of 1 MeV equivalent neutron fluence at the plane of SiPMs for different beam hole configurations of CBM PSD. (right) The same distribution for BM@N at NICA, NA61 at CERN and mCBM at FAIR experiments. BM@N V1 is the configuration without a beam hole, V2 – with the 15 $\times$ 15 cm^2 beam hole in the calorimeter center. Configuration of NA61 calorimeter has a 6 $\times$ 6 cm^2 beam hole in the center. Simulations were done by A. Senger for a typical calendar year of operation with the maximal beam settings, i.e. total 2 months of non-stop operation with 11 AGeV Au+Au at beam rate of 10^8 Au/s for CBM. Beam settings for mCBM, BM@N, and NA61 are described in the text.

Figure 5.4 shows the decrease of the neutron equivalent fluence in about 2 times in the SiPM plane of CBM PSD. It reaches about 2×10^{11} neutrons$_{eq}$/cm^2 closest to the beam hole. A similar situation is expected in the calorimeter of BM@N experiment [2], while roughly one order lower fluence is expected at calorimeter of NA61 experiment [3] as well as at the CBM test-setup at SIS18 called mini-CBM or mCBM [4]. This highlights the importance of the radiation hardness study presented in my PhD thesis for other experiments.

Figure 5.5 illustrates the distribution of the total ionizing dose within the calorimeter. As expected the dose distribution reflects the longitudinal profile of the hadron shower in the calorimeter, see figure 2.9. It reaches the maximum of about 1 kGy near the beam hole in the plane Z = 10 cm along the calorimeter, where it induces the most damage to the scintillators. At the very end of the PSD where SiPMs are located dose is below 100 Gy. Two-dimensional X-Y and Z-X distributions of dose for different beam hole geometries can be found in appendix A.

Both aforedescribed changes in the calorimeter design provide an additional radiation safety reserve and substantially lower the detector degradation during the experiment operation. However, calorimeter physics performance may be an issue in the case of the increased beam hole

[2]BM@N simulation: 4 AGeV Au beam, 100 µm Au target, 2×10^6 ions/second, 2 months of run.
[3]NA61 simulation: 150 AGeV Pb beam, 210 µm Pb target, 2.5×10^4 ions/second, 1 month of run.
[4]mCBM simulation: 1.65 AGeV Ag beam, 4 mm Ag target, 10^8 ions/second, 1 week of the run. The mCBM is used to test and optimize detector modules from all CBM detector subsystems together with the data acquisition system [276].

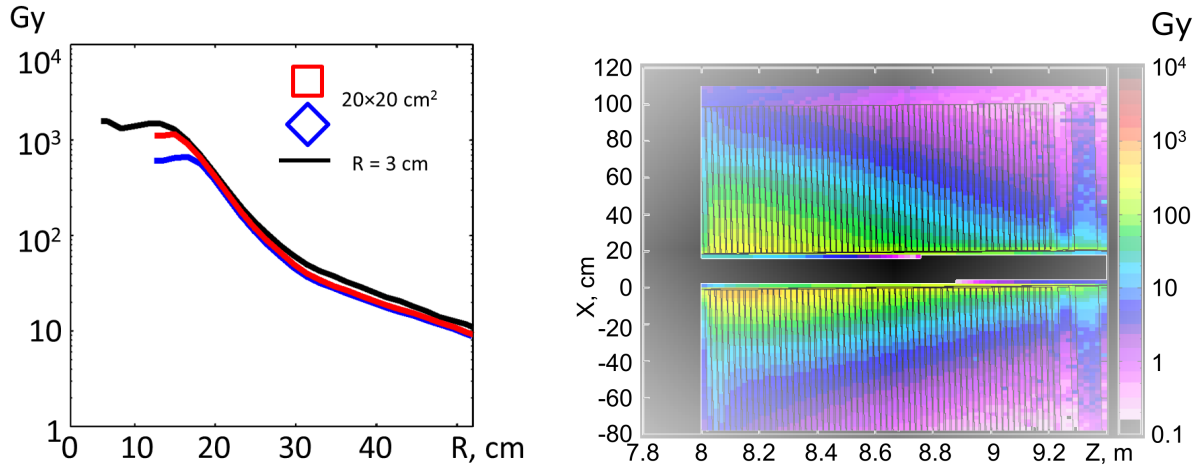

Figure 5.5: (left) Radial distributions of doses from ionizing particles in calorimeter at distance 10 cm from the forward face of the PSD for different beam hole configurations. (right) Longitudinal-radial distribution of the dose along the PSD module for a diamond-shaped geometry of the 20 × 20 cm^2 beam hole. Simulations were done by A. Senger for a typical calendar year of operation with the maximal beam settings, i.e. total 2 months of non-stop operation with 11 AGeV Au+Au at beam rate of 10^8 Au/s.

which is now actively discussed at CBM meetings.

5.2 Radiation hardness of PSD scintillators

Scintillators for PSD are manufactured by Uniplast based in Vladimir, Russia [277] from polystyrene with 1.5 % of para-terphenyl (PTP) and 0.01 % of POPOP, similar samples are utilized in [278]. The scintillator tile has a 4 mm thickness with 1.1 mm depth groove at the surface, where the Kuraray Y-11(200) WLS-fiber [45] with 1 mm diameter and double cladding is glued. Optical cement EJ-500 produced by Eljen is used [279]. Fiber's end situated inside the scintillator is covered with the endcap mirror which reflects the light back significantly improving the light collection on the other end. The shape of the grooves provides a parallel exit of WLS-fiber from the groove relative to the upper side of the scintillator. Each scintillator tile is covered by a white reflector (TYVEK paper) to improve the light collection. The light attenuation length of the fiber is about 4.5 m. Absorption spectra of Y-11 fibers is well-matched with emission spectra of POPOP in scintillators, and emission spectra of Y-11 fibers is well-matched with detection spectra of blue-sensitive SiPMs, see figures 3.2 and 3.22 (right).

In section 3.2 I compiled an extensive review of studies performed by many research groups on the radiation hardness of plastic scintillators and wavelength-shifting (WLS) fibers. Based on the available data, only slight deterioration up to 10 – 20 % is expected for polystyrene scintillators produced with blue/green emitting fluors and PMMA WLS fibers after irradiation up to 10 kGy. These results were obtained for high-quality components produced by well-known manufacturers like Bicron division of Saint-Gobain, Eljen and Kuraray after irradiation in normal conditions with high rate (> 100 Gy/h) sources. The situation can differ significantly if other production processes and operation conditions are involved. Radiation hardness for Kuraray Y-11(200) WLS-fibers and optical cement EJ-500 is already well studied, but it is not

the case for Uniplast scintillators, though they are made with recommended fluors.

In this section, I discuss the radiation hardness tests of small scintillator tiles that we conducted at Nuclear Physics Institute Řež together with my supervisor V. Kushpil and our colleagues from Moscow Institute for Nuclear Research A. Ivashkin and N. Karpushkin. Irradiations were carried out with help of F. Křížek and A. Isakov who built the dedicated proton irradiation setup at the cyclotron, see section 6.6. Final scintillator measurements after irradiation were conducted in our laboratory by internship students from Tomsk Polytechnic University, Tomsk, Russia – M. Balachkov and S. Belyavsky under my guidance. I helped M. Balachkov to analyze the acquired data, which I present hereafter some refinements. Analysis was performed in CERN Root framework [280]. The contribution of S. Belyavsky to the SiPM data analysis is the development of a macro used in subsection 7.6.

5.2.1 Measurement setup

Figure 5.6 presents the scheme of the scintillator measurement setup that we assembled for the tests. Photographs of the described setup placed in the same box with the SiPM measurement setup are presented in figure 5.7, the whole setup including the data acquisition and electronics is shown in figure 7.2. We used twelve small $0.4 \times 2 \times 2$ cm^3 scintillator samples covered in white Tyvek paper. The scintillator sample was inserted into the special 3D-printed holder to minimize the measurement deviations due to the sample positioning.

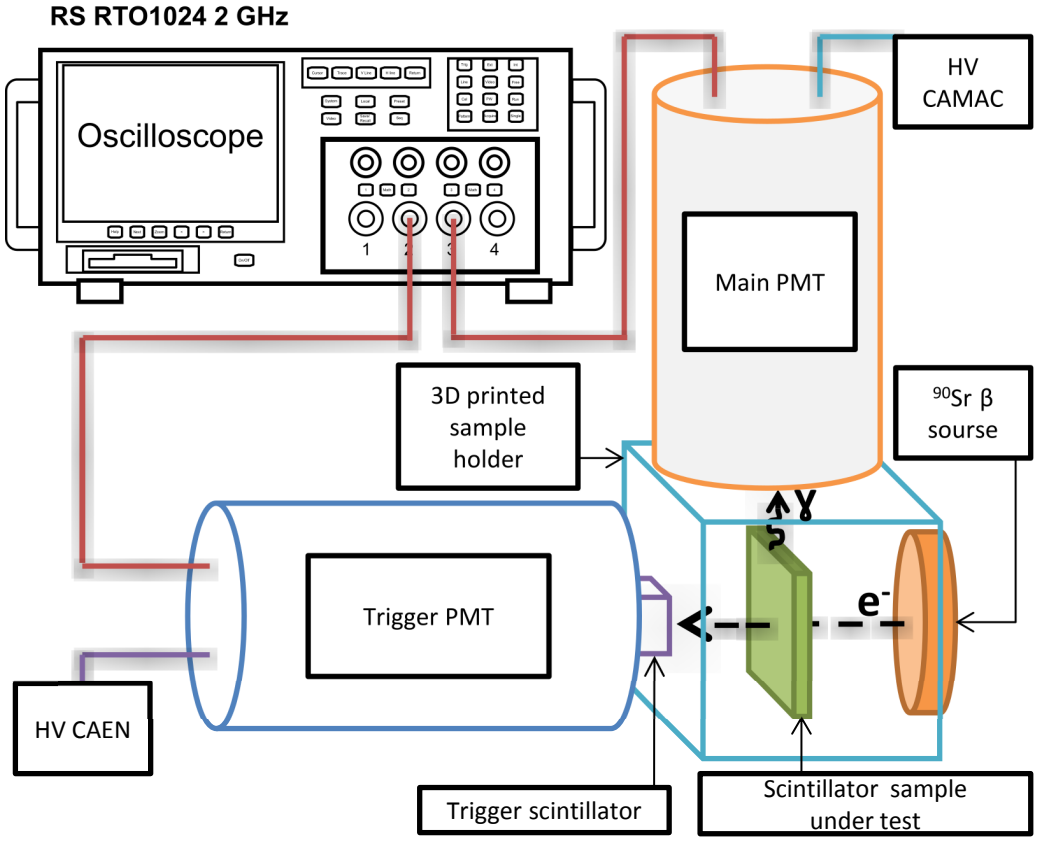

Figure 5.6: Schematic alignment of the setup for measurement of scintillator radiation hardness.

Scintillation was induced by electrons emitted by flat 5.2 MBq ^{90}Sr laboratory source with 0.4 cm^3 active area situated perpendicular to the sample. Figure 5.8 (left) shows that ^{90}Sr

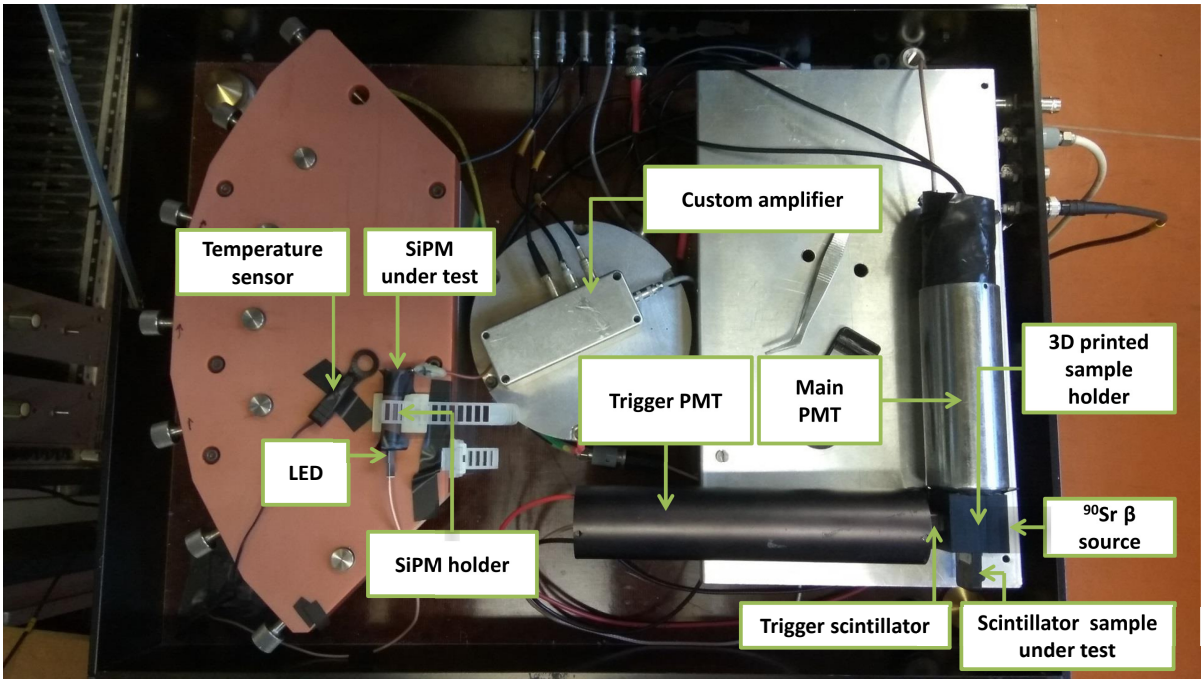

Figure 5.7: Photograph of the SiPM and scintillator measurement setups located in the black box.

and its daughter nucleus ^{90}Y have combined continuous electron spectrum up to 2.2 MeV. In polystyrene range of electrons with energies > 1 MeV is > 0.5 cm, and the most energetic electrons can travel through the scintillator sample under test. Figure 5.8 (right) shows that they can be regarded as MIPs in our experiment. To select only such high energy electrons, Photomultiplier (PMT) coupled with reference $1 \times 1 \times 1$ cm^3 scintillator was placed behind the sample and served as a trigger. Light from the sample was read out with another PMT from the single lateral side that was polished and left uncovered, see figure 6.11 (left).

We used 38 mm (1.5") photomultiplier tubes 9903B with a bialkali photocathode and 10 BeCu dynodes produced by ET Enterprises [283]. They have sensitivity for a blue and green light in the range from 290 nm to 680 nm which covers the range of 370 – 540 nm photons emitted by the POPOP fluor of our scintillators. PMTs were operated at the optimal high voltage (HV) of 1200 V. Voltage to trigger PMT was provided by a standard HV source situated in the CAMAC crate.

For the measurements of scintillator samples before irradiation, we used the old laboratory HV source with precise voltage control which can be seen in figure 5.7 on the left from the black box. Unfortunately, during the measurements, we found out that its voltage was floating with time. This resulted in the deviations of PMT gain and overall 10 % signal decrease after 3 hours of measurements. We tried to correct this effect, but it still resulted in deviations of the peak signal amplitude by 4 – 7 %. Fortunately, our team recently purchased the high-quality HV supply DT1470ET from CAEN which can provide up to 8 kV (3 mA) with the precision of 0.2 V [284]. I used it for the measurements after the irradiation.

Data acquisition was performed with the digital oscilloscope RTO1024 produced by Rohde&Schwarz. It has 4 channels, 2 GHz bandwidth, a maximal sampling rate of 10 Gsample/s and is capable to record 1 million waveforms per second [285]. Both photomultipliers were connected directly to the oscilloscope, which was operated in high 1 MΩ impedance mode. 50 Ω

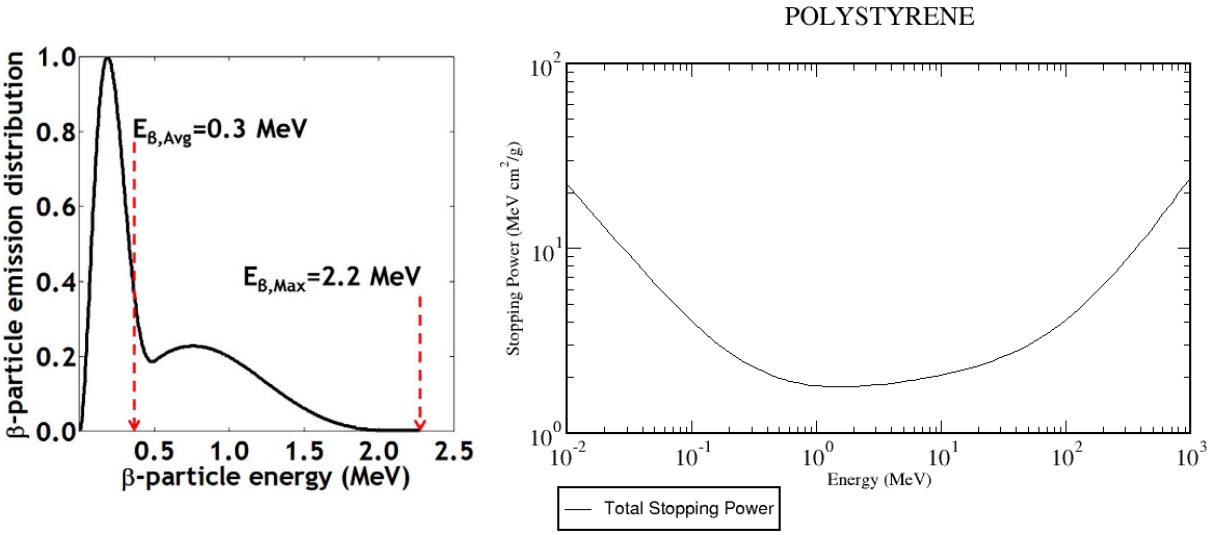

Figure 5.8: (left) Normalized energy spectrum of electrons emitted by ^{90}Sr and ^{90}Y [281]. (right) Energy loss of electrons in polystyrene, figure made via [282].

shunting resistors were connected in parallel to PT outputs for protection from occidental high currents.

Measurements were performed at room temperature. A simple table thermometer with internal and external sensors and sensitivity of 0.3 °C was used to monitor the temperature in the room and inside the black box. The setup was placed inside the light-tight black box. Photomultipliers and scintillators were extra covered by thick black cloth to mitigate the possibility of burn-out of the photomultipliers in case of accidental box opening before the high voltage was turned off.

5.2.2 Measurements of scintillator degradation

We decided to irradiate four scintillator samples №2, №3, №4, №5 with doses 1, 5 and 10 kGy to assess the maximal damage in the scintillator area closest to the beam hole after 1, 5 and 10 years of the CBM PSD operation, respectively, according to simulation presented in figure 5.5. Samples №4 and №5 were irradiated by 10 kGy with an 8 times difference in the dose rate to assess the possible dose rate effects. Sample №1 was used as a non-irradiated reference. These samples were chosen because their light yield was relatively close to each other.

Figure 5.9 shows the very first effect that we observed after the fast 10 kGy irradiation – visible yellowing of the scintillator. However, the scintillator returned to its original white transparent color after a day of annealing at room temperature covered from the light. For samples irradiated with the lower doses and dose rates, this effect was much harder to see.

We also tried to measure the response scintillators on the same day after the irradiation and observed a significant reduction of the signal amplitude by 40 % compared to the non-irradiated sample. But already after a weekend of annealing, it greatly improved. The final measurements that I present here were performed after 4.5 months of storage at room temperature covered from the light. According to the available data presented in subsection 3.2.6, it shall be well enough to call it complete annealing (at room temperature).

PMTs were connected directly to the oscilloscope (without amplifier), signal amplitudes for the tested samples were on the order of 200 mV which provided the signal-to-noise ratio on the

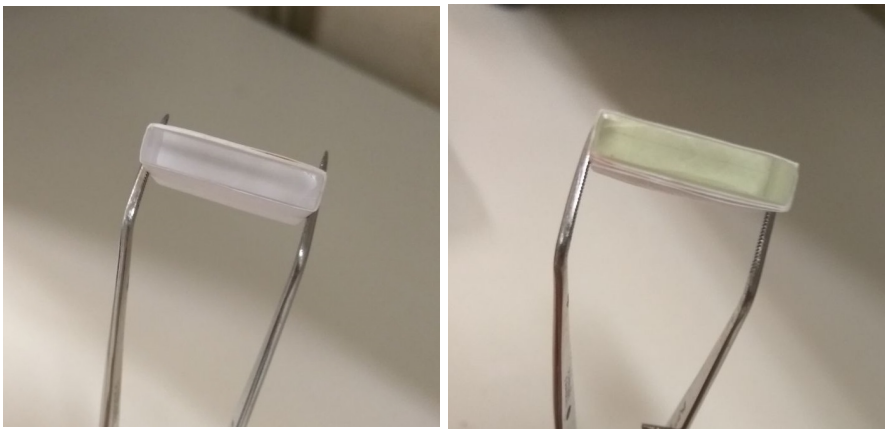

Figure 5.9: Photograph of a scintillator sample before irradiation (left) and right after the irradiation with 10 kGy during 1 hour (right).

order of 10, see figure 5.10. The trigger level was chosen to be 200 mV (signals in trigger PMT were higher due to higher HV setting). Signals were integrated into a short 18.7 ns window, which was chosen to fit the whole light pulse but excludes any extra noise. The resulting values of the collected charge are presented as is, in units of V·s. Statistics of 25000 events were acquired during each measurement.

Figure 5.11 presents the measurement results for all the irradiated scintillators relative to the non-irradiated reference scintillator №1. No light yield degradation exceeding the uncertainty level was observed up to 5 kGy. Light yield decreased by about 15 – 20 % for samples №4 and №5 irradiated with 10 and 11 kGy with the different dose rates. Initially, we wanted to irradiate both samples with 10 kGy, but due to incorrect initial estimation of the time, a higher dose was delivered to sample №5. This and measurement uncertainties made it impossible to derive any conclusions on the dose rate effect from our data.

5.2.3 Uncertainty estimation

The main source of uncertainties is the difference in response of different samples, i.e. sample-to-sample variability due to manual cutting and polishing. It is also complemented by alterations in sample positioning inside the holder. Figure 5.12 (left) shows the spectra collected from 7 non-irradiated samples. The standard deviation of the measured light yield maxima is 10.94 %.

The uncertainty caused by the measurement statistics of each spectrum can be calculated as the standard error of the mean by

$$\sigma_{\overline{x}} = \frac{\sigma}{\sqrt{n}} \tag{5.1}$$

Typical value of the histogram mean is about 1.5×10^{-9} V·s, typical σ is about 2.3×10^{-10} V·s, so $\sigma_{\overline{x}}$ is about 1.5×10^{-12} V·s or ~ 0.1 % of the mean. Therefore, collected statistics of 25000 events was high enough to make uncertainty due to statistics negligible.

All the measurements presented here were performed during a single work-day to minimize the impact of temperature and hardware stability. Figure 5.12 (right) shows the variation of the scintillator response during the day, which was estimated with help of 7 measurements of the reference scintillator №1 made between measurements of other samples. The standard deviation of the measured light yield maxima is 1.33 %. The temperature during the measurements was

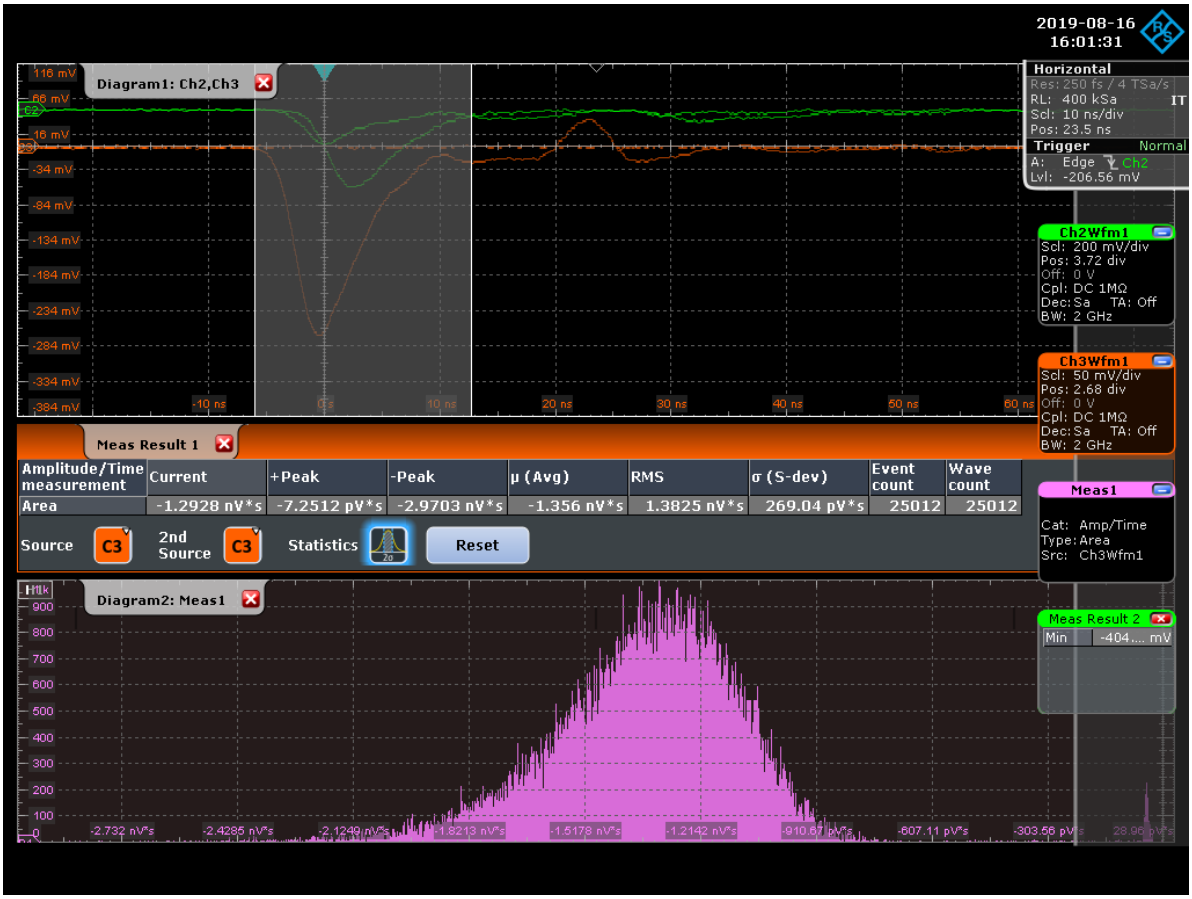

Figure 5.10: Example waveforms of the signal collected from the scintillator sample irradiated with 10 kGy (Channel 3, orange) and trigger (Channel 2, green). Signals were induced by 0.55 MeV electrons from ^{90}Sr laboratory source. Scale of horizontal axis is 10 ns/div, vertical is 50 mV/div for signal and 200 mV/div for trigger. Measurement histogram on the bottom has horizontal axis with 0.3 nV·s/div, vertical axis shows arbitrary values due to oscilloscope software bug.

about 25.5°C with variations on the order of thermometer sensitivity, i.e. ±0.3 °C. One can see that those uncertainties are negligible as well.

Therefore, total light yield uncertainty is dominated by the sample-to-sample variability and is about 11 %. Uncertainty of the dose estimation is dominated by the uncertainty of the proton fluence determination which is estimated to be below 10 %, see section 6.6.

5.2.4 Discussion

Figure 5.13 shows that light yield did not change up to 5 kGy, and after 10 kGy dose, it decreased by about 15 – 20 % for small 2×2 cm^2 scintillator tiles after proton irradiation. Our data is in agreement with the results reported by other researchers, see section 3.2. Performance of Kuraray Y-11 WLS-fibers was already extensively tested after irradiation, and only minor degradation of the light yield of 10 – 30 % for 100 – 200 cm long fibers was observed below 10 kGy [74, 76–79, 84]. No degradation of properties of optical cement EJ-500 was observed up to 3 kGy [88].

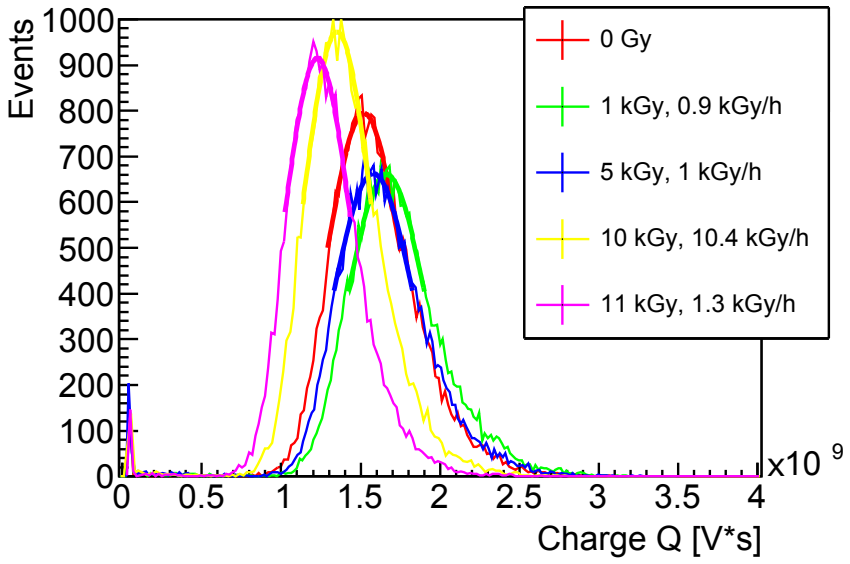

Figure 5.11: Spectra of the response to MIP electrons from ^{90}Sr for non-irradiated and irradiated scintillators.

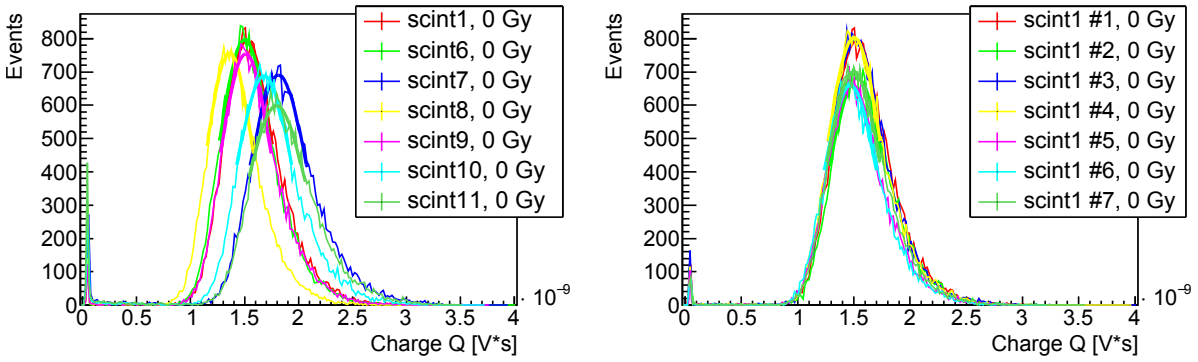

Figure 5.12: Spectra of the response to MIP electrons from ^{90}Sr for 7 non-irradiated scintillators (left) and reference non-irradiated scintillator №1 measused 7 times, every time sample was reinserted in the setup.

In general, light yield degradation is caused by two effects: deterioration of the light emission and reduction of the scintillator and fiber transparency, and consequently light attenuation length. The latter effect increases with the distance that photons travel through the scintillator, i.e. with the scintillator diameter. It is mitigated in big scintillators by embedding WLS-fibers inside the scintillator which significantly improves the light collection. Groups from ATLAS [67, 68] and CMS [57, 58] collaborations irradiated assemblies consisting of scintillator + WLS-fiber and observed overall light yield degradation up to 30 % after 10 kGy, see subsection 3.2.3. Note that ATLAS HCAL WLS-fibers make optical contact only with the lateral side of the tiles, while in the PSD the fibers are embedded into the scintillator providing better light collection. Comparing modules built with embedded fibers, CBM PSD module length is only 1.5 m, while it is 4 – 5.5 m for CMS HCAL, so light attenuation in WLS-fibers is of much higher importance

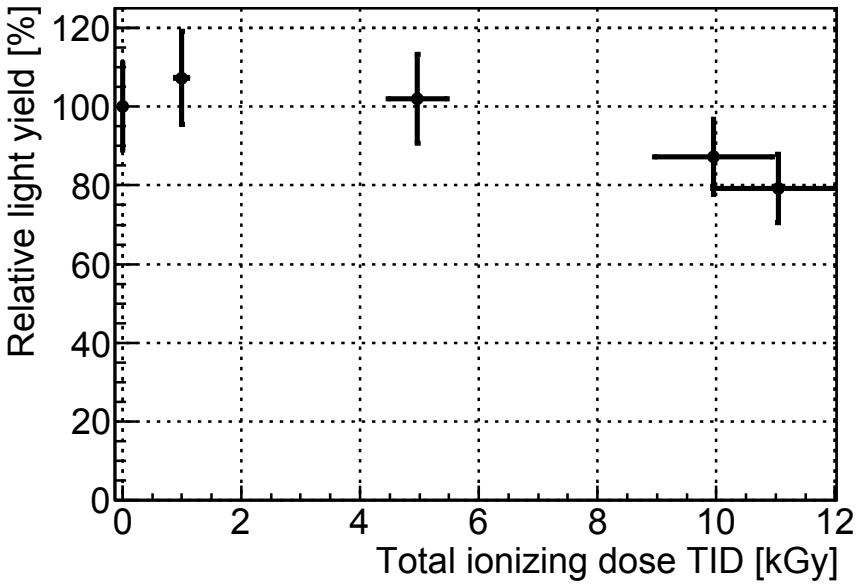

Figure 5.13: Dependence of scintillation light yield (maximums of spectra in figure 5.11) on absorbed dose, relative to reference light yield before irradiation (reference scintillator №1).

for CMS.

All the aforementioned results are obtained for irradiation in normal conditions with high rate ($>$ 100 Gy/h) sources. A significant increase in the radiation damage was reported for scintillators irradiated and operated in conditions with increased oxygen diffusion and elevated temperatures, see subsection 3.2.6. For instance, this is relevant for detectors that are operated in cold or hot environments and surrounded by specific gas mixtures. No such conditions apply for CBM PSD: it will be operated several months per year and always will remain in a normal air environment at room temperature, also no high-temperature annealing is planned. Scintillators will undergo full recovery during months of detector idle state after beamtime because CBM is planned to be operated just a few months in a calendar year.

However, during operation at a 1 MHz collision rate in CBM, PSD will be irradiated with a dose rate of 0.69 Gy/h which is significantly lower than the rate of 1 kGy/h that we used for our tests. A low dose rate will result in the slow creation of defects (radicals) inside scintillators assisted by oxygen diffusion. Because oxygen will have more time to diffuse into the material volume it will result in increased damage production. We tried to assess the dose rate effects in our tests but at 10 kGy we could not achieve a rate below 1 kGy/h because it would require many days of the cyclotron operation. Irradiations with significantly lower dose rates for the 10 kGy dose are not feasible because they would take several days of the cyclotron continuous operation. And only minor effects which will be hard to distinguish within the measurement uncertainties are expected for lower doses.

Fortunately, dose rate effects were already extensively studied by many researchers, see subsection 3.2.7. For instance, results presented in figure 3.9 (top) are very similar to ours, i.e. light yield degradation about 20 % after irradiation with 20 kGy (2 Mrad) with a dose rate of 1.5 kGy/h (0.15 Mrad/h). Note that E. Biagtan et al. [44] irradiated scintillators with gamma rays, while we used protons which were found to produce slightly more damage, see subsection 3.2.5. This combined with the measurement uncertainties might explain the fact that we observed a similar light yield decrease after only 10 kGy. Composition of SCSN-81

scintillator was found to be PS + ∼ 1 % PTP + (0.05–0.1) % 3HF [44], which is very similar to our samples. Presented dependence of the light yield relative to light yield before irradiation I/T_0 on the dose rate R measured after full recovery was approximated as

$$\begin{aligned} I/I_0[\%] &= 86.925 + 6.540 \cdot \log(R[Mrad/h]) \\ I/I_0[\%] &= 60.765 + 6.540 \cdot \log(R[Gy/h]) \end{aligned} \tag{5.2}$$

According to this equation, relative light yield after irradiation shall be 87 % for 10 kGy at 10.4 kGy/h, and 81 % for 10 kGy at 1.3 kGy/h which agrees extremely well with our measurement data. Figure 5.5 shows that anticipated maximal irradiation conditions for PSD scintillators situated closest to the beam hole are 1 kGy at 0.69 Gy/h for two months of operation at a 1 MHz collision rate. This translates to 10 kGy at 0.69 Gy/h for ten years of operation. According to equation (5.2), relative light yield, in this case, will be about 60 %. However, E. Biagtan et al. [44] studied the dose-rate effects only in a range of 0.1 – 10 kGy/h, so mine calculation for lower dose rate shall be considered rather qualitative. Figure 3.9 (bottom) shows the data compilation for low dose rates by A. Sirunyan et al. [59], but data description with exponential fit provided there fails for dose rates above 0.1 kGy/h, so it can not be applied for our data.

5.3 Summary

Only minor degradation of the scintillator and WLS-fiber performance is expected at CBM PSD based on our irradiation tests and the extensive available research from other groups. Total light yield may decrease by up to a factor of 2 for the first sections of the inner-most modules which are located around the beam hole and will achieve dose up to 10 kGy after 10 years of CBM operation at 1 MHz collision rate. For sections and modules located further, the dose will be lower by several times, or even orders of magnitude, so very little to no light yield degradation is expected in the majority of PSD modules.

Observed light yield degradation can be relatively easily mitigated by regular module/section calibration. For instance, ZEUS collaboration [73] observed 10 – 30 % light yield decrease for scintillators irradiated with gamma-rays up to 10 kGy, but this caused little to no effect on the calorimeter energy resolution, see discussion in subsections 3.2.9 and 3.2.10. Note, that they studied the electromagnetic calorimeter which has several times better energy resolution than the hadron calorimeter. Namely, ZEUS ECAL has $22\%/\sqrt{(E(GeV))}$, so it shall be much more sensitive to detrimental effects than CBM PSD which has $60\%/\sqrt{(E(GeV))}$. The modular structure and the longitudinal segmentation of PSD will further ensure the stability of the transverse and longitudinal uniformity of the light collection. Therefore, only very minor, if any, degradation of the energy resolution due to scintillator damage is expected for PSD.

Note, that the most damage to scintillators in PSD will be produced by ionizing energy loss, because neutron fluence in our scintillators is below 10^{13} n_{eq}/cm^2, see appendix A. Existing studies on neutron-irradiated scintillators presented in subsection 3.2.5 did not observe any effect for such a small fluence.

The situation is completely opposite for Silicon Photomultipliers which are situated at the very end of PSD modules. Only very small doses of ionizing radiation below 100 Gy per year of CBM operation are expected there, see figure 5.5. Existing studies on gamma- and X-ray irradiated SiPMs presented in subsections 3.6.12 and 3.6.13 did not observe any significant degradation for such a small dose.

Data presented in section 3.6 show that SiPMs suffer mainly from non-ionizing energy loss. In PSD sensors located closest to the beam hole will receive about 2×10^{11} $neutrons_{eq}/cm^2$ after

a year of operation, or 2×10^{12} neutrons$_{eq}$/cm^2 after 10 years, respectively. However, different SiPMs respond very differently to irradiation, and it is hard to make a conclusion for our fluence range based on the available data. Namely, significant degradation of SiPM performance can start anyway in range of $10^{10} - 10^{14}$ n$_{\mathrm{eq}}$/cm^2. Furthermore, no studies of the calorimeter performance with irradiated SiPMs are available yet. Therefore, I decided to conduct detailed studies of the SiPM radiation hardness, results of which are presented in chapters 7 and 8.

Chapter 6

Irradiation experiments at the NPI cyclotron facility

The most straightforward way to study the radiation hardness of a device is to measure its performance before and after irradiation under the anticipated radiation conditions. Several irradiation experiments were carried out during 2016 – 2019 at the NPI cyclotron. The most radiation susceptible components of PSD, namely scintillators and SiPMs, were irradiated by protons and neutrons, respectively. I secured the funding for irradiations via submission of several experimental proposals to the CANAM [286] project [1]. In this chapter, the irradiation setup, conditions, and corresponding fluence calculations are overviewed.

6.1 Cyclotron U120-M and fast neutron generators

The irradiation experiments were performed at the isochronous cyclotron U120-M at NPI depicted in figure 6.1. U120-M is a multipurpose multiparticle accelerator that can operate in both negative and positive modes and provide beams of various accelerated ions, namely p, H^-, D^+, D^-, $^3He^{2+}$, $^4He^{2+}$ (α) [286].

Figure 6.1: Cyclotron U-120M with neutron generator target attached to the beamline.

[1] Center of Accelerators and Nuclear Analytical Methods (CANAM) is an extraordinary versatile infrastructure that provides open access to scientific laboratories producing beams of accelerated ions for scientists and industry. It is supported by the Ministry of Education, Youth and Sports of the Czech Republic project LM2015056.

Beam energy can vary in a wide range of 1 — 55 MeV, beam currents can be as low as a few nA and reach up to tens of μA. I used a negative mode where H-ions were accelerated and then two electrons from each ion were stripped by a 1 μm carbon foil producing protons. In this case, the proton energy range is 20 – 37.5 MeV. The cyclotron can provide a proton flux up to 10^{14} p/cm^2/s which is very useful for the production of medical radionuclides while several orders magnitude lower fluxes are typically utilized for the radiation hardness tests.

Several unique target stations can be attached to the cyclotron beamline output to create powerful generators of fast neutrons. The quasi-monoenergetic neutron generator is based on the $p+^7 Li$ reaction. Here, protons are directed at a 2 mm thick lithium foil with a 1 cm carbon backing, which fully stopped the protons [287]. The white-spectrum neutron generator is based on the $p+^9 Be$ reaction on an 8 mm thick beryllium target [288]. Targets have 40 mm and 50 mm diameters, respectively. During the operation, they are cooled down to 5 řC by the ethanol. Neutron generators provide a very high neutron flux up to 10^{11} n/cm^2/s at the highest proton currents [289]. Irradiated samples can be placed at a distance from 3 mm up to 2 m from the target.

Neutron spectra of both generators are presented in figure 6.2. Spectral flux at given positions was estimated by neutron generator teams with the activation foil method with an accuracy of 10 – 12 %. Multiple high purity activation foils (Al, Nb, Sc, Y, MnNi, Co, In, Lu, Au, Ti, Fe, Bi) were placed at distances from the target of 15 and 156 mm for white neutron source [288], and 48 and 86 mm for quasi-monoenergetic neutron source [287]. To unfold the neutron spectrum, a modified version of the SAND-II [290] and MCNPX [271] codes were employed. The quasi-monoenergetic neutron spectrum was also measured using the Time-Of-Flight method at a distance of 3.5 – 4.5 m from the target to validate the predictions of the MCNPX simulation. The number of neutrons in the monoenergetic peak was normalized with the measured data on ^{7}Be production in the 2 mm thick Li.

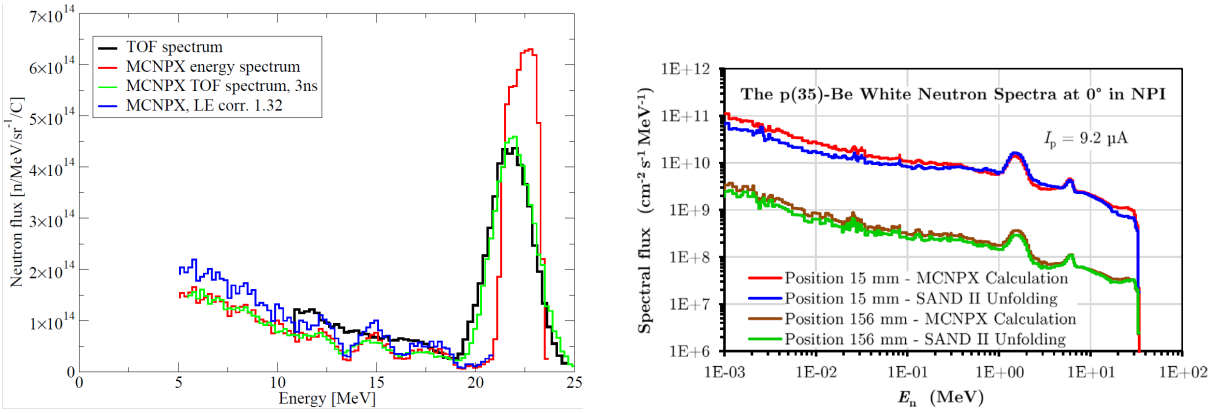

Figure 6.2: Quasi-monoenergetic (left) [287] and white (right) [288] spectra of NPI neutron generators. In the article about quasi-monoenergetic generator there is a cut on energy below 5 MeV, but I used original spectrum without this cut (starting from 250 keV). White spectrum is presented for two irradiation positions in a log-log scale.

The high energy spectrum component corresponds to the production of ground and first excited states in $^7Li(p,n)^7Be$ or $^9Be(p,n)^9B$ reactions forming a mono-energetic peak in the white and quasi-monoenergetic spectrum, respectively. The peak width is defined by the proton beam energy and target thickness. The low-energy continuum is produced by higher excited states and multiple particle emission reactions. In the quasi-monoenergetic spectrum, each

component contains approximately half of the total neutron flux. In the thick beryllium target, the proton beam degrades by ionizing effects and induces the neutron production reactions at low energies forming the broad continuous spectrum without a peak.

Even though the white spectrum is presented starting from 1 keV, fluence calculations are done only for neutron energies above 100 keV according to the guidance of neutron generator teams. Neutron spectrum below this energy was never carefully assessed and depend on many parameters including positions of detectors and various absorbers (sample fridges, etc.) in the cyclotron hall which change from experiment to experiment. Nevertheless, it does not produce any complications in my case because only a few percent of neutrons have lower energy, see section 6.4 for more details.

6.2 Experiments of SiPM irradiation by neutrons

I irradiated about 50 SiPMs produced by six different manufacturers during five experiments in 2016 – 2019:

- At night of 06 – 07.04.2016 eleven different SiPMs were irradiated to compare their radiation hardness at high requested fluences Φ_{req} of 5×10^{11} and 5×10^{12} n/cm^2. Fluence was chosen based on the radiation load estimation for old PSD design with a small beam hole and without shielding, see section 5.1 for details.
- At 10.06.2016 ten Hamamatsu and ten Zecotek SiPMs were irradiated by lower Φ_{req} of 4×10^{10} and 4×10^{11} n/cm^2 (five SiPMs of each type per fluence) to investigate operation of slightly damaged SiPMs at NA61 PSD calorimeter at CERN.
- At 23.11.2016 ten Hamamatsu SiPMs were irradiated by higher Φ_{req} of 1×10^{12} and 3×10^{12} n/cm^2 (five SiPMs per fluence) to investigate their operation at NA61 PSD calorimeter at CERN. Most of SiPMs irradiated at 10.06.2016 were re-irradiated to save the budget.
- At 02.03.2018 ten Hamamatsu SiPMs were irradiated by $\Phi_{req} = 1.3 \times 10^{11}$ n/cm^2 to equip all 10 sections of the calorimeter module. Fluence was chosen according to the newly reduced radiation load at CBM PSD, see section 5.1 in the previous chapter for details.
- At 13.09.2019 three different SiPMs of new versions was irradiated by $\Phi_{req} = 1.3 \times 10^{11}$ n/cm^2 to find out if their radiation hardness will be better than for older ones tested before.

The first irradiation experiment was performed with a quasi-monoenergetic neutron spectrum produced by 25 MeV protons, succeeding irradiations were done with a white neutron spectrum produced by 35 MeV protons. Simulations performed in FLUKA code by A. Senger predict a broad neutron spectrum in the very end of PSD – in a plane where SiPMs are located, see figure 6.3. I chose white spectrum for the further detailed studies because it resembles a broad shape and it was studied in a wider energy range.

Distance from the target, beam current and irradiation time was estimated by the cyclotron team before the experiment to achieve the requested total fluence Φ_{req} for the investigated SiPMs. The experiment with a quasi-monoenergetic spectrum was joint with the neutron generator team of M. Majerle, who was testing new equipment. My samples were placed in the beam for the whole duration of the experiment about 9.5 hours. SiPMs were divided into two groups positioned at 12.6 and 36.6 cm from the target to achieve a ten times difference in fluence. In the further experiments with a white spectrum, irradiation time was 2.5 – 24 minutes. Sample position was 15.6 cm from the target, where the neutron fluence was estimated by the cyclotron team [288]. The beam currents were in a range from 1 μA up to 10 μA. Beam current stability

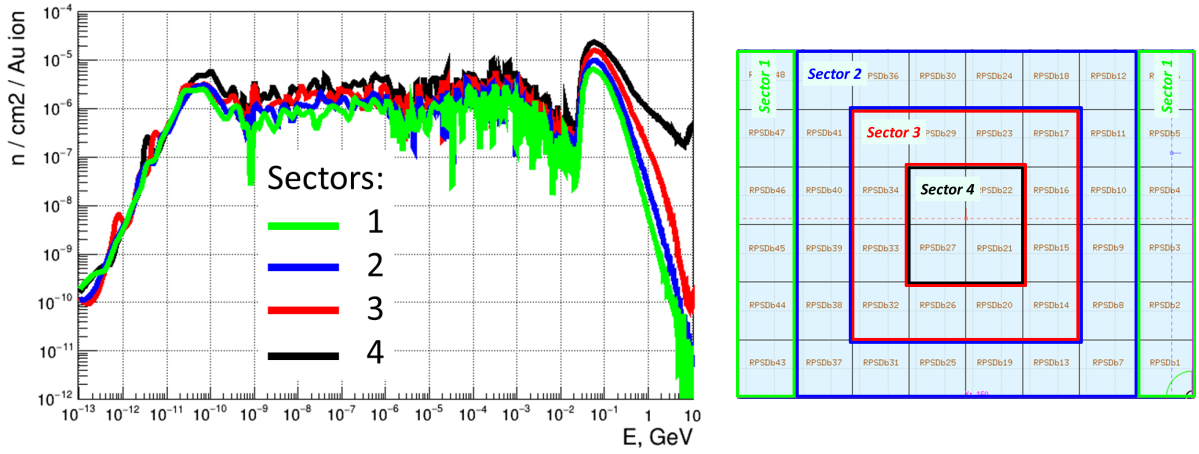

Figure 6.3: Neutron spectrum in a plane where SiPMs are located in PSD for different radial sectors. Simulation was done by A. Senger [275] for a typical calendar year of operation with the maximal beam settings, i.e. total 2 months of non-stop operation with 10 AGeV Au+Au at collision rate of 1 MHz.

at the cyclotron was quite good which is exemplified in figure 6.4. Time series of beam currents for all the other experiments can be found in appendix B.

In the case of quasi-monoenergetic spectrum, I used the following formula to calculate the total neutron fluence achieved by samples per cm^2 during irradiation at a distance D from the target

$$\Phi_{NG} = \Phi_{QMonoEn} \cdot Q \cdot \Omega = N_{^7Be/C} \cdot R_{forw} \cdot R_{abs} \cdot R_n^{peak} \cdot Q/D^2 \tag{6.1}$$

where $\Phi_{QMonoEn} = 2.57 \times 10^{15}$ n/sr/C is the neutron fluence produced by the generator, Q is the total charge of protons produced during the irradiation, Ω is the solid angle at a distance D^2 where my samples where situated. I calculated $\Phi_{QMonoEn}$ with the help of the following parameters provided by M. Majerle: $N_{^7Be/C} = 1.33 \times 10^{15}$ n/C is the amount of produced ^7Be corresponding to neutrons in the monoenergetic peak, $R_{forw} = 0.78$ is the index of forwardness or ratio of forward going neutrons to all produced neutrons, $R_{abs} = 0.88$ is a percentage of neutrons that were not absorbed in 1 cm of carbon and cooling ethanol, $R_n^{peak} = 2.81$ is a ratio of all neutrons in the spectrum to neutrons in the peak.

In the case of the white spectrum, I calculated total neutron fluence per cm^2 by

$$\Phi_{NG} = \Phi_{white}^{156mm} \cdot t_{irr} \cdot \overline{i_p} \cdot i_p^{156mm} \tag{6.2}$$

where $\Phi_{white}^{156mm} = 2 \times 10^9$ n/cm^2/s is the neutron flux at a reference distance 156 mm from target when proton current was $i_p^{156mm} = 9.26$ µA, and $\overline{i_p}$ is the average proton current during duration of my irradiation t_{irr}.

I irradiated samples at normal conditions: room temperature about 25 řC, covered from ambient light by the aluminum or copper foil, SiPM anode and cathode were shortened to lower the charge accumulation, no bias voltage was applied. Thin golden foils were situated behind the irradiated SiPMs for the fluence estimation cross-check by the activation foil method. Samples prepared for irradiation are depicted in figure 6.5. Holder with the samples is situated closely to the neutron target at the beamline end, so no collimators or shielding are applied. In spite of significant variations in the neutron spectra shape, irradiation time, beam current, and distance

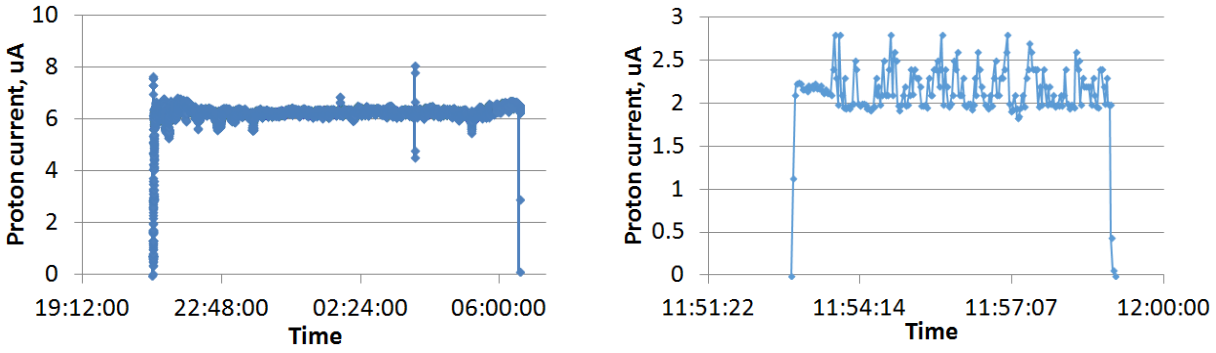

Figure 6.4: Time series of beam currents for irradiation with a quasi-monoenergetic spectrum at 06–07.04.2016 (left) and irradiation with a white spectrum at 13.09.2019 (right).

between the target and samples, no substantial difference was observed for the SiPM performance after irradiations with similar total fluences. This is well visible by the linear dependence of SiPM dark current on neutron fluence presented in figures 7.13 and 7.16, which is discussed in chapter 7.

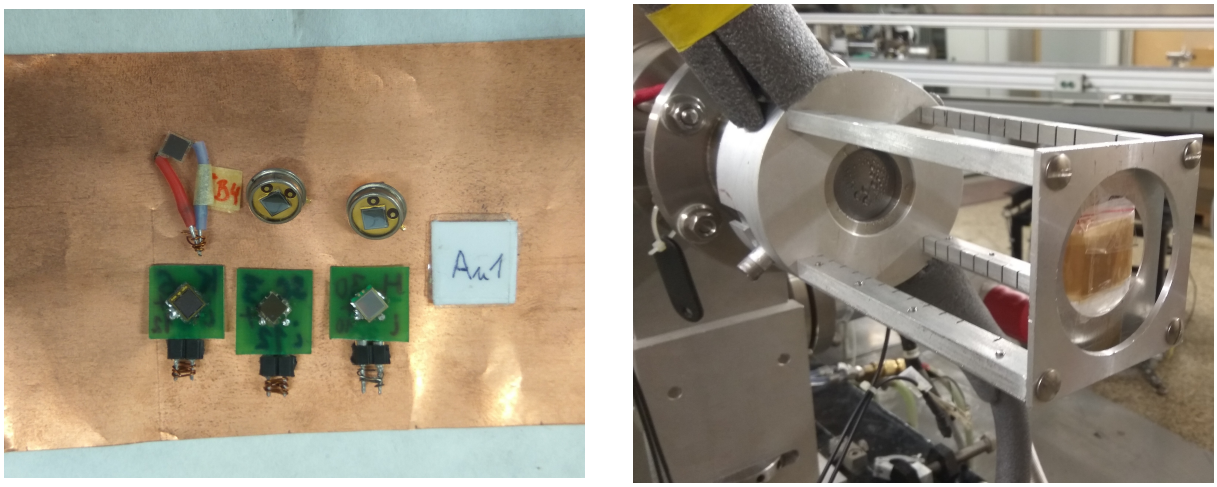

Figure 6.5: SiPM samples and gold foil prepared for irradiation (left) and covered together by copper foil, mounted at the cyclotron holder (right).

6.3 Neutron fluence determination by activation foils

The neutron activation analysis method is widely used for the detection of a small amount of some isotope in a compound. It is based on the measurement of γ-activities of radionuclides produced by the nuclear reactions in irradiated activation foils. It can be used to evaluate cross-sections of nuclear reactions after irradiation with known neutron field and fluence. Alternatively, one can use it to measure the neutron spectrum and/or flux for the reactions with known cross-sections.

6.3.1 Preparation for the activation analysis

I used several thin gold foils in the irradiation experiments to precisely determine the neutron fluence acquired by the samples. The chemical purity of the material was better than 99.99 [291]. Gold is standardly used in nuclear physics because of its well-known microscopic activation cross-section for (n,xn) reactions. I used $^{197}Au(n,2n)Au^{196}$ reaction as a reference because Au^{196} has a half-life of 6.183 days, the cross-section has a maximum below 30 MeV and there is an excellent agreement on its values between existing data and simulations which is shown in figure 6.6 (left).

I weighed and measured the dimensions of foils before irradiation. For the first experiment, I used smaller foils because of the relatively high requested fluence of 5×10^{11} and 5×10^{12} n/cm^2. For further experiments where fluences were lower, I used bigger foils to increase the amount of produced isotopes. Table 6.1 summarizes the measured foil parameters.

Sample	Au1	Au2	Au3	Au4
Weight [g]	0.38	0.74	1.5	1.47
Lateral dimensions [mm]	1.3×1.3	1.3×1.3	2.5×2.5	2.5×2.5
Width [mm]	0.117	0.227	0.124	0.122

Table 6.1: Parameters of irradiated gold foils. Foil Au2 was a composition of two thinner foils similar to Au1. Foil width was calculated based on measured weight, lateral dimensions and gold density.

Total neutron fluence Φ_{foil} can be derived from the equation for nuclear reaction rate

$$r_{n,2n} = \phi \cdot \sigma_{n,2n} = \frac{N_{yield}}{N_0 \cdot t_{irr}} \Rightarrow \tag{6.3}$$

$$\Phi_{foil} = \frac{N_{yield} \cdot M_{^{197}Au}}{\sigma_{n,2n} \cdot N_A \cdot m_{foil}} \tag{6.4}$$

where
$r_{n,2n}$ is the $^{197}Au(n,2n)Au^{196}$ reaction rate per one target nuclei per second,
$\Phi_{foil} = \phi \cdot t_{irr}$ is the total neutron fluence in the sample position per cm^2 of area,
ϕ is the neutron flux in the sample position per cm^2 of area per second,
$\sigma_{n,2n}$ is the microscopic cross-section of the reaction,
N_{yield} is the total yield of ^{196}Au isotope produced in the foil,
m_{foil} is the foil weight,
t_{irr} is the total irradiation time,
$N_0 = N_A \cdot m_{foil}/A_{^{197}Au}$ is the number of target nuclei in the foil,
$M_{^{197}Au}$ is the molar mass of ^{197}Au equal to its atomic mass,
N_A is the Avogadro number.

Due to the fact that my samples were irradiated by neutrons of various energies, I calculated the effective $\sigma^{eff}_{n,2n}$ taking into account shapes of both spectra presented in figure 6.2 according to

$$\sigma^{eff}_{n,2n} = \frac{\int_{0.1\ MeV}^{E_{max}} \Phi(E) \cdot \sigma_{n,2n}(E) dE}{\int_{0.1\ MeV}^{E_{max}} \Phi(E) dE} \tag{6.5}$$

Figure 6.6 (right) shows the convolution of $^{197}Au(n,2n)Au^{196}$ reaction cross-section and spectra provided by neutron generator teams, normalized by the spectrum integral. The influence of the monoenergetic peak is clearly visible here. I used a cross-section that was simulated in TALYS code [292] by O. Svoboda and P. Chudoba in the same energy bins as the neutron spectra. Calculated values of $\sigma^{eff}_{n,2n}$ were 440 and 424 mbarn for white and quasi-monoenergetic, respectively.

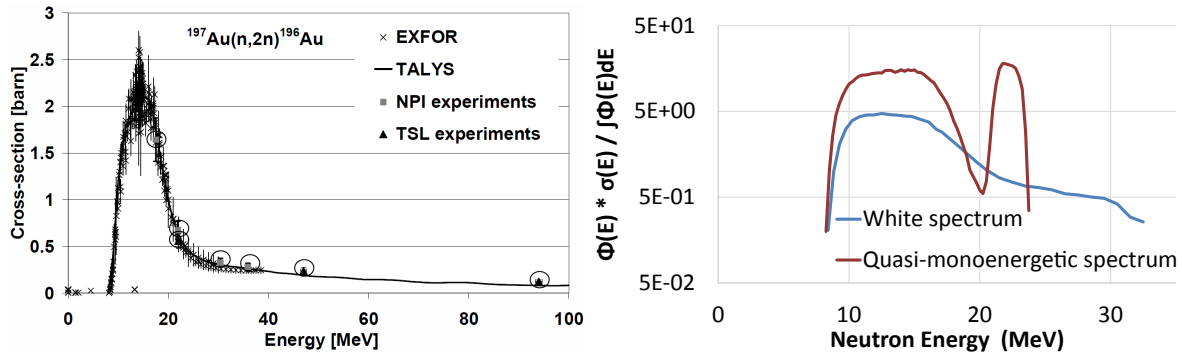

Figure 6.6: (left) Cross-sections of $^{197}Au(n,2n)Au^{196}$ reaction from EXFOR database, TALYS calculation, NPI and TSL experiments conducted by O. Svoboda et al. [293]. (right) Normalized convolutions of this cross-section with two neutron spectra used in my experiments.

6.3.2 Evaluation of the ^{196}Au yield

In this subsection, I briefly discuss details of the spectroscopic measurement, corresponding data evaluation, and corrections. More detailed information on the detector calibration and yield evaluation can be found in the PhD theses of P. Chudoba [294] and O. Svoboda [295] who helped me with the measurements.

Detector setup. I used the spectrometer based on the High Purity Germanium (HPGe) detector for the measurement of activated foils. Spectrometer Canberra GC3018 (CAN35) is situated in our laboratory of the Department of Nuclear Spectroscopy of Nuclear Physics Institute of the CAS in Řež. CAN35 has relative detection efficiency of 35 %, relative energy resolution < 0.7 %, 8192 channels, maximum γ-energy limit of 2 MeV, and it is biased by +4.5 kV. The detector is placed in a closed lead shielding box with the opening doors, which suppresses the background approximately ten times and shields personnel from measured radioactive samples. There is a polycarbonate holder allowing to position samples at 0 – 35 cm from the detector with a 1 cm step. I used a calibrated position = 5 cm for my measurements as an optimum between the maximal measurement efficiency and minimal non-point emitter correction. Detector hosting a gold foil during the measurement is shown in figure 6.7 (left).

Detector efficiency $\varepsilon(E_\gamma)$ is a number of registered gamma photons emitted by a certain transition in a calibration source per second divided by the source activity, recalculated to the day of measurement. Peak efficiency $\varepsilon_p(E_\gamma)$ is mentioned when γ deposits all of its energy in the detector, it is used for the normalization of the detector response. Total efficiency $\varepsilon_t(E_\gamma)$ is mentioned when any part of the energy is deposited in the detector, it is used for the calculation of the correction on true coincidences. Efficiency depends on photon energy, the distance between source and detector, and on the detector characteristics. GC3018 detector calibration was done by P. Chudoba with following sources: ^{152}Eu, ^{133}Ba, ^{60Co}, ^{88}Y, ^{57}Co, ^{241}Am, ^{109}Cd, ^{203}Hg, ^{137}Cs, ^{65}Zn and ^{51}Cr [296]. Calibration uncertainty was up to 2%. Calibrated peak detector efficiency

validated against the Monte Carlo simulation in MCNPX 2.7 [271] is shown in figure 6.7 (right). $\varepsilon_p(E_\gamma)$ has maximum around 100 keV. Because on the one hand, at lower energies, not all the photons can pass through the aluminum end cap and interact in the active volume. On the other hand, some photons with higher energy will just scatter in active volume not depositing their full energy. Coefficients for polynomial fit of peak efficiency curves were reported in [296] by P. Chudoba, for instance for position = 5 cm $\varepsilon_p(E_\gamma) = 0.000368 + 5.99/E_\gamma - 307.3/E_\gamma^2 + 1858.7/E_\gamma^3$.

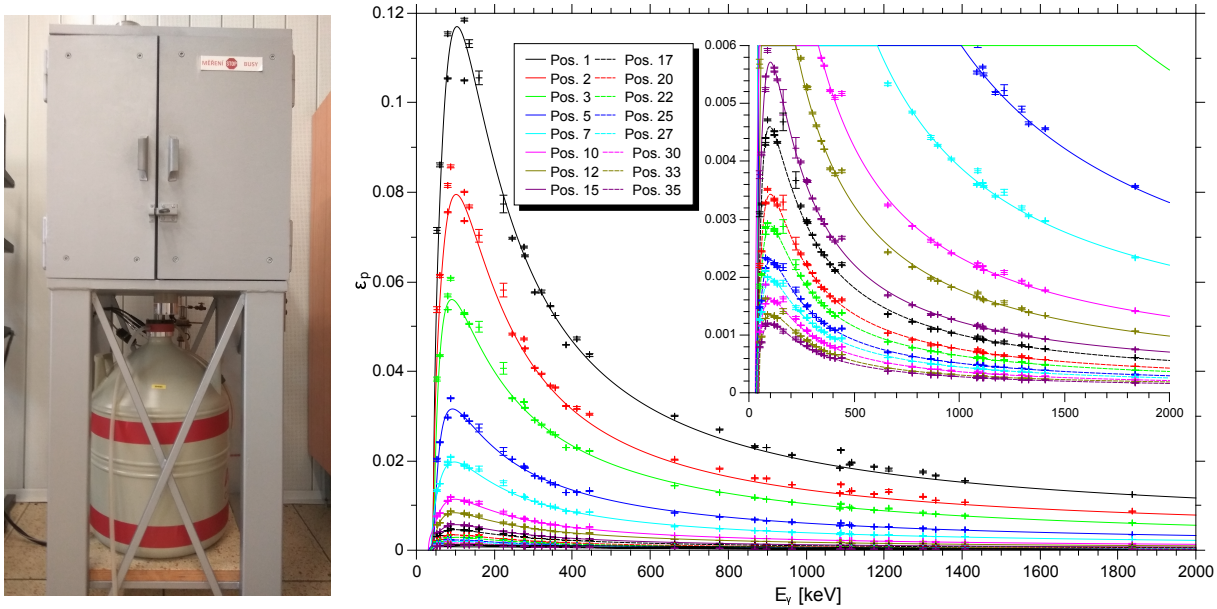

Figure 6.7: (left) HPGe detector of CAN35 spectrometer in our laboratory of Department of Nuclear Spectroscopy. (right) Detector efficiency curves for different sample positions fitted by fifth order polynomial, taken from [294].

True cascade-coincidences happen when several photons are detected simultaneously and interpreted as one event with higher energy. The origin of this effect is the complicated decay schemes of most nuclei where various energy levels are fed which leads to the emission of a complicated set of gamma and x-ray photons. This effect is not to be confused with the random coincidences when two photons from two different nuclei are detected. Random coincidences can be considered negligible because of the low activities of our samples and the small efficiency of the used HPGe detector [294]. Corrections on true cascade-coincidences COI were calculated with the help of TrueCoinc software [297] by P. Chudoba.

Square emitter correction C_{area} becomes important when samples with a few cm^2 are situated at a close distance to the detector. Detector efficiency was determined with a set of point sources, while the geometry of activated samples is not point-like. It is possible to determine this efficiency experimentally by determining the activity of the sample in the furthest geometry where we can assume a point-like behavior. Alternatively, one can perform a throughout Monte Carlo simulation of detector efficiency for both point-like and large geometries to calculate $C_{area} = \varepsilon_p^{area}/\varepsilon_p^{point}$. This was done by P. Chudoba [294] for different sample geometries who provided me the resulting values of C_{area}.

Correction on the detector dead-time accounts for the fact that the detector needs time to collect and process an impulse from incoming photon when new photons can not be registered. Our HPGe detector has a cumulative dead time which increases with a rising number of incoming

gamma photons. The detector records the full measurement time t_{real} along with the time when it was available for the photon registration t_{live}. I calculated the correction on dead time as $C_{dead} = t_{real}/t_{live}$.

Correction on the isotope decay during irradiation, and between the end of irradiation and beginning of the measurement (cooling time t_{cool}) are the most important. They can be derived from the decay law of radioactive materials $dN/dt = P - \lambda N$ which describes how much radioactive nuclei N is produced during the irradiation (see [295] for full derivation). Finally, they are combined into the ratio of number of isotopes produced during the irradiation N_0 to number of decays during the spectroscopic measurement ΔN

$$\frac{N_0}{\Delta N} = \frac{P \cdot t_{irr}}{\Delta N} = \frac{\lambda \cdot t_{irr}}{1 - e^{-\lambda \cdot t_{irr}}} \frac{e^{\lambda \cdot t_{cool}}}{1 - e^{-\lambda \cdot t_{real}}} \tag{6.6}$$

where P is the isotope production rate, t_{irr} is the irradiation time and λ is the decay constant. For ^{196}Au, $\lambda = \ln 2/(6.183\ days) = 1.3 \times 10^{-6}\ \mathrm{s}^{-1}$.

Beam instability correction C_{beam} is implemented to account for deviations in beam rate and consequently isotope production rate P. I calculated it in MS Excel by iterative formula

$$C_{beam} = \frac{1 - e^{-\lambda \cdot t_{irr}}}{t_{irr} \sum_{i}^{N} \left[\frac{1}{t_p(i)} W(i)\, e^{-\lambda \cdot t_e(i)} \left(1 - e^{-\lambda \cdot t_p(i)}\right) \right]} \tag{6.7}$$

where $t_e(i)$ is the time from the end of i-th interval till the end of the irradiation, $t_p(i)$ is the duration of i-th interval, $W(i)$ is the ratio between the number of particles in i-th interval and the total number of particles, and N is the number of intervals.

For the interval, I used the original time binning of proton current data which was one or two seconds. C_{beam} deviated from 1 only by up to 0.01 % which again confirms the great stability of the beam provided by the cyclotron.

Self-absorption or attenuation of photon energy can occur in the activation foil itself during the measurement. This effect is more significant for low γ energies and thick or dense foils. Correction C_{abs} is defined as the ratio between the unattenuated and the attenuated photon fluxes

$$C_{abs} = \frac{\int_0^D \frac{I_0}{D} \mathrm{d}x}{\int_0^D \frac{I_0}{D} e^{-\mu \cdot x} \mathrm{d}x} = \frac{\mu \cdot D}{1 - e^{-\mu \cdot D}} \tag{6.8}$$

where I_0 is the unattenuated intensity of gamma photons, D is the foil thickness, and μ [cm^{-1}] is the total mass attenuation coefficient μ_T [cm^2/g] multiplied by density ρ [g/cm^3]. I have taken the μ_T data from NIST Database [15]. I used a smooth curve between tabular values to extract μ_T values for all three used gamma energies as shown in figure 6.8.

Yield of produced ^{196}Au **isotopes** was calculated with respect to all the aforementioned spectroscopic corrections according to the final equation

$$N_{yield} = \frac{S_{peak}}{I_\gamma \cdot \varepsilon_p(E)} \frac{C_{dead}(E) \cdot C_{beam} \cdot C_{abs}}{COI(E) \cdot C_{area}} \frac{\lambda \cdot t_{irr}}{1 - e^{-\lambda \cdot t_{irr}}} \frac{e^{\lambda \cdot t_{cool}}}{1 - e^{-\lambda \cdot t_{real}}} \tag{6.9}$$

where I_γ is the intensity of the gamma transition defined as the γ-emission probability. S_{peak} is the area of gamma peak representing the number of measured decays of ^{196}Au. Value ranges of applied corrections are presented in table 6.2.

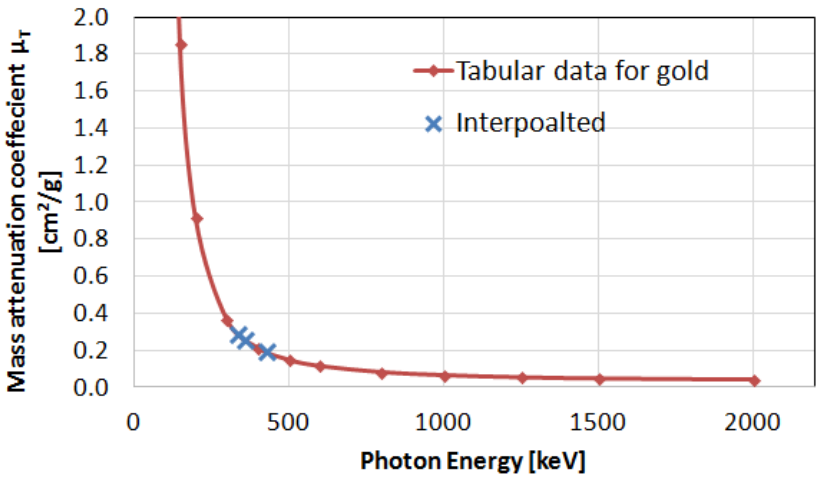

Figure 6.8: Total mass attenuation coefficient for gold extracted from [15].

Correction	$\varepsilon_p(E_\gamma)$	COI	C_{area}	C_{dead}	C_{beam}	C_{abs}
Value range	0.012	0.97	0.975	1.002	0.99991	1.006
	–	–	–	–	–	–
	0.016	0.99	0.981	1.039	1.0	1.035

Table 6.2: Values of detector efficiency and spectroscopic corrections.

6.3.3 Analysis of gamma spectra

I analyzed measured gamma spectra in a semi-automatic manner with the help of Canberra Genie 2000 Spectroscopy software [298] installed on the detector control PC. After completion of data acquisition, I used automatic peak location based on the second derivative method to locate all the peaks that are significantly above the background. Then I used an automatic peak area fitting algorithm based on non-Linear least squares fit by Gaussian function to calculate the peak areas. The background is fitted and subtracted there automatically. Then I generated the report summarising data about the fitted peaks and general measurement data such as t_{real} and t_{live}. I used the keyboard hotkeys to speed up the process consisting of 6 procedures for every analyzed spectrum. The processed spectrum is shown in figure 6.9.

I also analyzed several spectra with the DEIMOS32 code developed at our department by J. Frána [299]. The code provides an option of manual evaluation when peak location and the fitting procedure are done step by step and parameters of the fit can be changed between each step. This is extremely important if one needs to analyze spectra with complicated backgrounds and a lot of closely situated peaks, such a situation is described in the PhD thesis of O. Svoboda [295]. The disadvantage is the extreme time consumption of this procedure. For my spectra where huge intensive peaks are situated on a clear background, the differences between the programs are smaller than the uncertainty of the peak fit in each program, i.e. less than 0.1 %.

For N_{yield} calculation I used three most dominant gamma lines of ^{196}Au decay with intensities: $I_\gamma(332.9\ keV) = 22.9$ %, $I_\gamma(355.7\ keV) = 87.0$ %, $I_\gamma(426.0\ keV) = 7.0$ %. I taken half-life and gamma-line intensities from the Lund/LBNL Nuclear Data Search [300]. I conducted several measurements for each activation foil during the week after irradiation – from one hour up

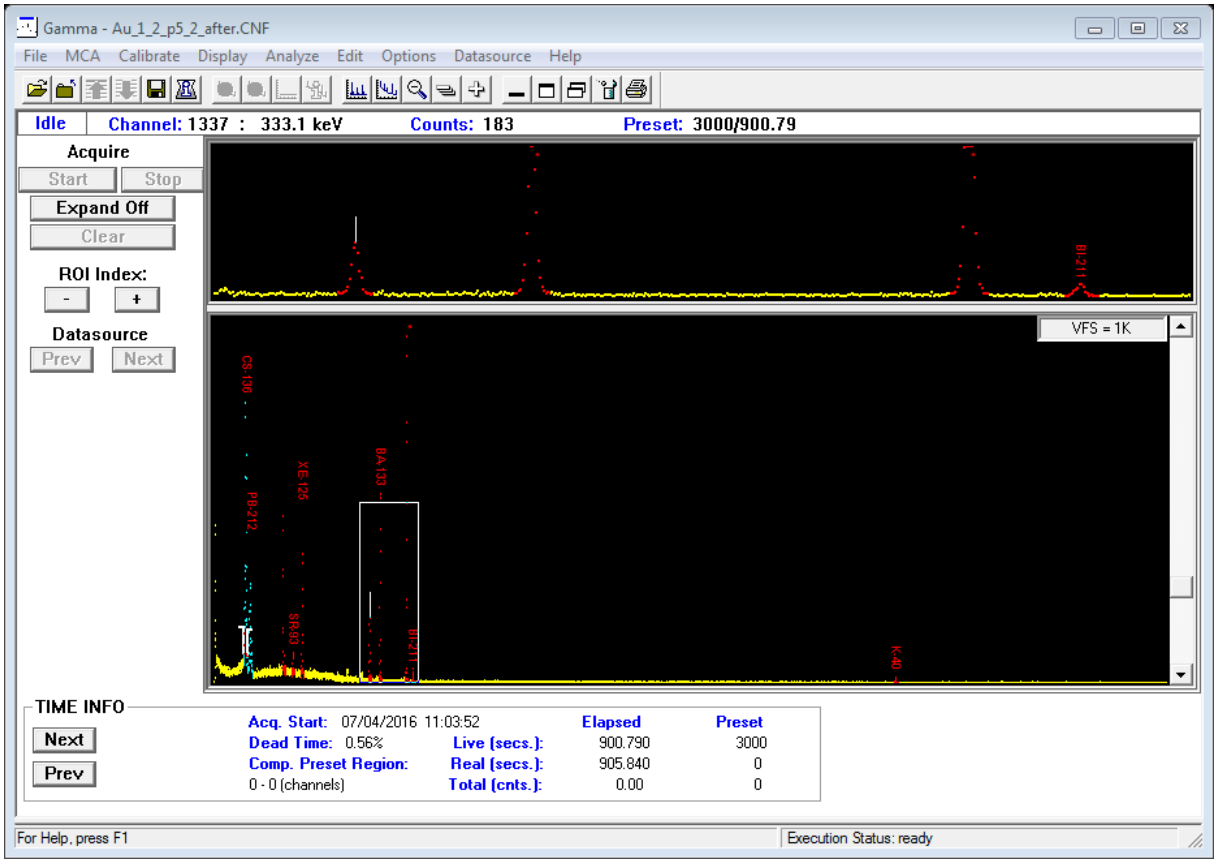

Figure 6.9: Spectrum of photons emitted from gold foil irradiated at 06.04.2016 acquired in Genie 2000.

to three days. Cooling times scaled in a similar manner. This produced the gamma peaks with a count area in the range of $1 \times 10^3 - 1 \times 10^7$. No significant difference in the result due to the isotope decay was observed after the application of corresponding corrections. Uncertainty of the peak area for long measurements was several times lower due to much higher statistics.

I incorporated all the measured data by calculation of weighted average for N_{yield} measured with different durations as

$$\overline{N_{yield}} = \frac{\sum_i^N \frac{N_{yield}^i}{(\Delta N_{yield}^i)^2}}{\sum_i^N \frac{1}{(\Delta N_{yield}^i)^2}} \tag{6.10}$$

where ΔN_{yield}^i is the uncertainty of i-th N_{yield}. Here I used the uncertainty of fitted peak value from Genie 2000 suggested by O. Svoboda [295]. A comprehensive discussion of all the uncertainty sources involved in the fluence estimation can be found in section 6.5.

Then I calculated the weighted average of such weighted averages estimated with different gamma lines. I determined the weighted average uncertainty as

$$\Delta\overline{N_{yield}} = \frac{1}{\sum_i^N \frac{1}{(\Delta N_{yield}^i)^2}} \tag{6.11}$$

6.4 Normalization to 1 MeV neutron equivalent fluence

I converted the total fluence estimated by the activation foil method into the 1 MeV equivalent fluence which is widely used for the comparison of radiation damage produced by various particles and energy spectra. I made a convolution of both neutron generator spectra $\Phi(E)$ depicted in figure 6.2 and NIEL damage $D(E)$ function for silicon caused by neutrons described in section 2.3. I used the data on $D(E)$ from Evaluated Nuclear Data File (ENDF/B-VII.1) [13] extracted from JANIS web [14]. Results of the convolution are shown in figure 6.10.

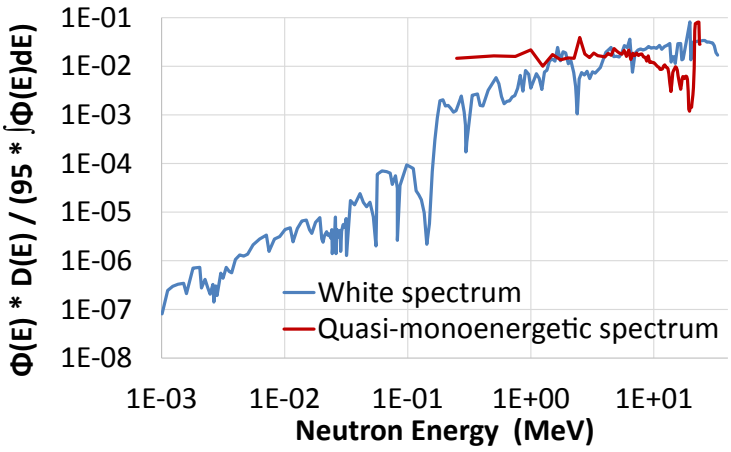

Figure 6.10: Normalized convolutions of NIEL damage caused by neutrons to silicon with two neutron spectra used in my experiments. Spikes are caused by variation in energy bin width and also by nuclear resonances. Data for quasi-monoenergetic spectrum start only from 0.25 MeV because they have fixed bin width of 0.25 MeV, i.e. first bin contains all neutrons from 0 up to 0.25 MeV.

One can see that values of $\Phi(E) \cdot D(E)$ above 100 keV are several orders of magnitude higher than for lower energies, therefore the impact of low energetic neutrons is negligible. Particularly, only 3 % of neutrons have energy below 100 keV which translates into 0.05 % of neutron fluence in the 1 MeV equivalent. This is because thermal neutrons capture and elastic scattering have much lower cross-section than nuclear resonances and direct head-on collisions on nucleons which is visible in figure 2.7. Another reason is that in figure 6.2 flux data are presented in relative units of n/MeV, i.e. divided by the energy bin width. In figure 6.10 I multiplied it by the energy bin width to achieve absolute values that can be convoluted with the NIEL data, and these absolute values became rather small. It justifies the fact that calculations involving neutron spectra are done above 100 keV.

I calculated the hardness factors according to equation (2.10) and achieved $\kappa = 1.54$ and 1.62 for white and a quasi-monoenergetic spectrum, respectively. Therefore, fluence range used in my irradiations converted from $\Phi = 3.3 \times 10^{10} - 4 \times 10^{12}$ n/cm^2 to $\Phi_{eq} = 5 \times 10^{10} - 6 \times 10^{12}$ n_{eq}/cm^2.

6.5 Neutron fluence results and uncertainties

I calculated the neutron fluence for every conducted irradiation by two methods described in this chapter. In the first approach, I used existing data on neutron fluence measured by neutron generator teams in combination with data acquired for my experiments (collected proton charge

or irradiation time + average proton current) according to equations 6.1 and 6.2 to get Φ_{NG}. In the second approach, I calculated the yield of ^{196}Au produced in gold foils which I placed in every experiment according to equation (6.9) and put it into equation (6.4) to achieve Φ_{foil}. Values produced by both approaches as well as essential data on the irradiation experiments are summarised in table 6.3. Relative deviation $\Delta\Phi_{NG}^{foil}$ of Φ_{NG} from Φ_{foil} is also presented.

I consider Φ_{foil} to be a more precise fluence estimate as it was determined by the independent activation foil analysis for every experiment taking into the account all the standard spectroscopic corrections. I converted Φ_{foil} to 1 MeV neutron equivalent fluence multiplying it by $\kappa = 1.54$ and 1.62 for white and quasi-monoenergetic, respectively, calculated in section 6.4. Resulting values of Φ_{eq} are presented in table 6.3 and they are used in all the results provided further along the thesis[2].

Date	Φ_{req} [n/cm^2]	t_{irr} [min]	$\overline{i_p}$ [μA]	Φ_{NG} [n/cm^2]	N_{yield} of Au^{196}	Φ_{foil} [n/cm^2]	$\Delta\Phi_{NG}^{foil}$ [%]	Φ_{eq} [n$_{eq}$/cm^2]
10.06.2016	4×10^{10}	2.48	1.14	3.67×10^{10}	4.4×10^{7}	3.27×10^{10}	10.8	5.04×10^{10}
02.03.2018	1.3×10^{11}	5.98	2.08	1.61×10^{11}	2.25×10^{8}	1.67×10^{11}	3.74	2.58×10^{11}
13.09.2019	1.3×10^{11}	6.07	2.16	1.7×10^{11}	2.1×10^{8}	1.56×10^{11}	7.93	2.41×10^{11}
10.06.2016	4×10^{11}	9.07	3.19	3.75×10^{11}	4.37×10^{8}	3.25×10^{11}	13.34	5.01×10^{11}
06.04.2016	5×10^{11}	570.1	6.31	4.14×10^{11}	5.72×10^{8}	4.42×10^{11}	6.21	7.17×10^{11}
23.11.2016	1×10^{12}	8.35	10.16	1.1×10^{12}	1.36×10^{9}	1.01×10^{12}	7.74	1.56×10^{12}
23.11.2016	3×10^{12}	24.12	10.12	3.16×10^{12}	3.92×10^{9}	2.92×10^{12}	7.84	4.5×10^{12}
06.04.2016	5×10^{12}	570.1	6.31	3.49×10^{12}	5.1×10^{9}	3.94×10^{12}	11.28	6.39×10^{12}

Table 6.3: Requested and calculated neutron fluences, supplemented by auxiliary data on conducted experiments. Data are grouped according to fluence ascending. Differences between requested fluence and achieved fluence are due to difficulty to precisely set the beam current, and finite duration of beam stopping and starting at the cyclotron. $\overline{i_p}$ is the average proton current during duration of irradiation t_{irr}.

Main uncertainties in my measurements come from gamma-detector calibration, spectroscopic corrections, Gaussian function fit of the gamma peaks in Genie 2000, (n,2n) reaction cross-section and neutron spectrum knowledge. HPGe detector was calibrated by P. Chudoba with the set of laboratory etalons so that peak had the area $> 4 \times 10^4$ in order to have the uncertainty of 0.5 % and less. The uncertainty of calibration sources activities was about 0.5 %. I used a set of spectroscopic corrections described in subsection 6.3.2 which are standard in gamma spectrometry. Value ranges of applied corrections are presented in table 6.2. The combined uncertainty brought in by the detector calibration and spectroscopic corrections was below 2 % [294].

I measured gamma peaks with an area in the range of 1×10^3 – 1×10^7 for three dominant gamma lines of ^{196}Au decay (332.9, 355.7 and 426.0 keV). I conducted several measurements during a week after the irradiation. Then I calculated weighted average and its uncertainty by equations 6.10 and 6.11. Due to the rich data combination, the uncertainty of N_{yield} was well

[2]I must note that for requested $\Phi_{req} = 1.3 \times 10^{11}$ n/cm^2 corresponding to 2.16×10^{11} n$_{eq}$/cm^2, slightly different actual fluences were acquired at two different experiments – 2.41×10^{11} and 2.58×10^{11} n$_{eq}$/cm^2. For these data I further use a value of 2.5×10^{11} n$_{eq}$/cm^2 for unambiguity of data comparison. Deviation from original values is about 3 % which is much less than fluence uncertainty discussed in this section.

below 1 %. For N_{yield} estimation I utilized the $^{197}Au(n,2n)Au^{196}$ reaction which cross-section is well known with an uncertainty up to 5 % [14, 301].

The main part of the uncertainty is brought in by the neutron spectrum which was measured by neutron generator teams with an accuracy of 10 – 12 % [287, 288]. I consider that all the uncertainties are independent, so I calculated the total uncertainty of the fluence as a quadratic sum of them and it did not exceed 15 %. This is in good agreement with the deviation of Φ_{NG} from Φ_{foil} which was below 14 %.

6.6 Experiments of scintillator irradiation by protons

Together with V. Kushpil, and colleagues from Moscow Institute for Nuclear Research A. Ivashkin and N. Karpushkin we performed two proton irradiation sessions in March 2019. A. Ivashkin and N. Karpushkin prepared twelve polystyrene-based $0.4 \times 2 \times 2$ cm^3 scintillator samples covered in white Tyvek paper. One lateral side of the samples was polished and left uncovered to emit photons as shown in figure 6.11 (left). We decided to irradiate four samples with doses 1, 5 and 10 kGy to assess the maximal damage after 1, 5 and 10 years of the CBM PSD operation according to simulation discussed in section 5.1.

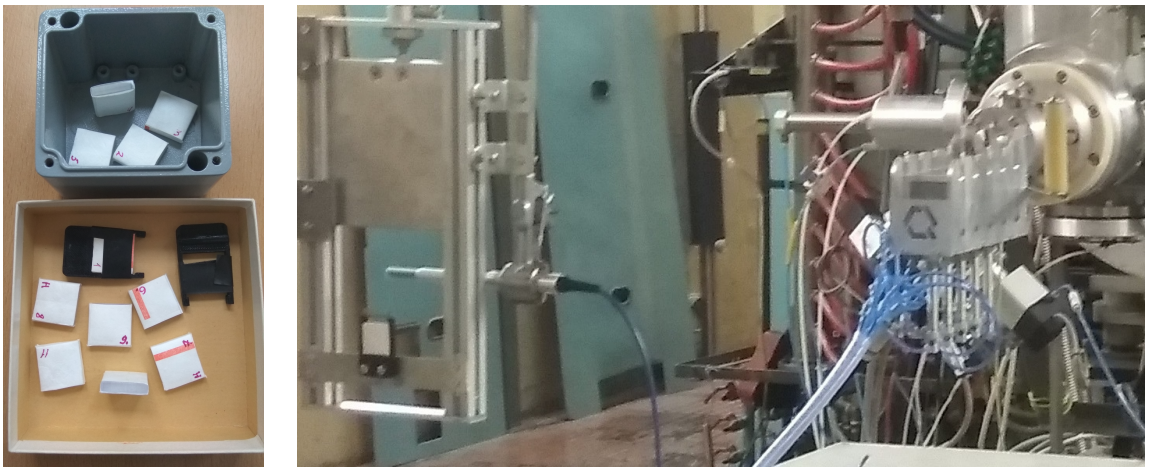

Figure 6.11: Scintillator samples prepared for measurements after the irradiation (left) and fixed at the cyclotron holder together with the ionization chamber (right).

Figure 6.11 (right) presents the scintillator sample placed in front of the cyclotron beamline at the holder of the movable stage. Experiments were carried out with help of F. Křížek and A. Isakov who built the dedicated proton irradiation setup at the cyclotron for the radiation hardness investigations for ALICE CERN [302]. The setup allows monitoring the proton flux in the range of $10^4 - 10^9$ p/cm^2/s with help of ionization chamber Farmer 30010 from PTWFreiburg [303]. The chamber has a sensitive volume of 0.6 cm^3 filled with air. The ionization chamber current is read out with a UNIDOS E Universal Dosemeter [303] which is connected to the chamber using a 50 m long triaxial cable. The chamber and irradiated samples are fixed to a movable stage which allows changing the position of the chamber in the transverse plane relative to the beam axis in a 10 cm range [304]. It is placed at a distance of 130 cm from the exit window of the negative mode beamline. All the equipment is controlled online, for more information on the setup design and logical scheme see [302].

Proton flux during the experiments was quite stable as can be seen in figure 6.12 and in

appendix B.

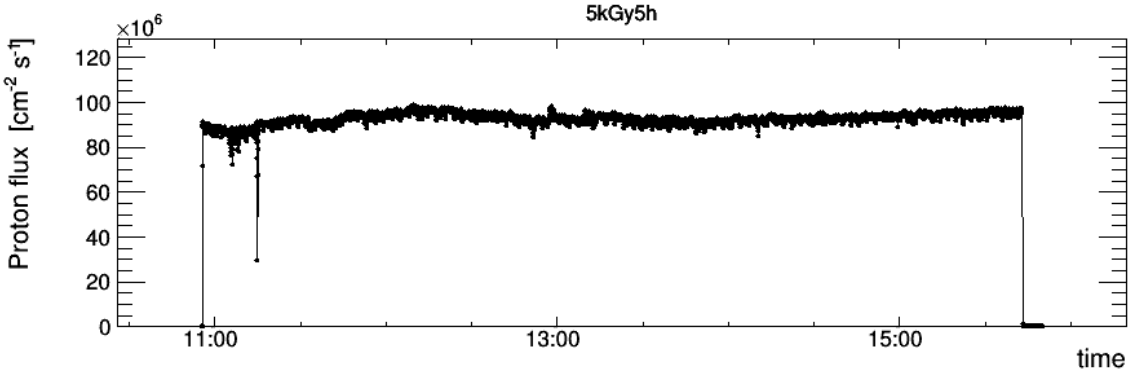

Figure 6.12: Time series of proton flux for sample irradiated by 5 kGy during 5 hours at 27.03.2019.

Figure 6.13 (left) depicts the beam profile along the horizontal axis that was measured using the ionization chamber and movable stage, the beam profile along the vertical axis is similar. Both profiles exhibit Gaussian shape with standard deviation about 12 ± 1 mm, so our small 2×2 cm^2 samples were relatively uniformly irradiated. During the irradiation, samples were placed in the beam center and the ionization chamber was placed 4 cm above the center as shown in figure 6.11 (right). The measured ionization chamber current was corrected for the off-center position using the known Gaussian beam profile by a factor $C_{off} = 350$.

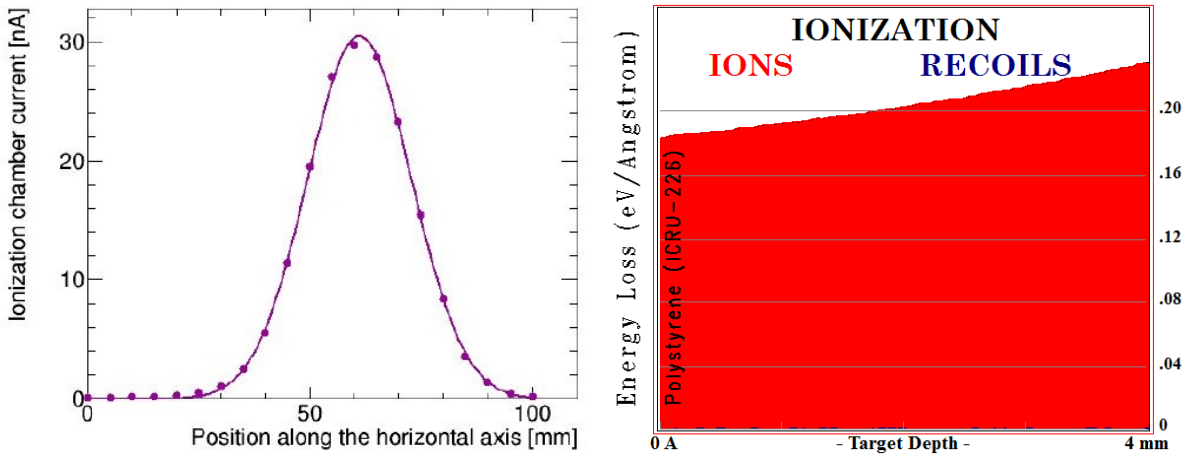

Figure 6.13: (left) Horizontal beam profile measured by F. Křížek with the ionization chamber. Vertical beam profile is similar. (right) Dependence of linear energy transfer (LET) on polystyrene scintillator width for impinging 33 MeV protons, simulated in SRIM 2013 [27].

The response of the ionization chamber to the incoming proton flux ϕ is linear up 10^9 p/cm^2/s. It is parametrized as $\phi = k \times I_{ch}$, where I_{ch} is the ionization chamber current. The calibration factor $k = 15890$ was determined experimentally for low fluxes up to 10^5 p/cm^2/s (to avoid radiation damage) using a 300 µm thick hybrid silicon pixel detector Timepix [302,305]. It was also estimated for high fluxes up to 10^9 p/cm^2/s using the copper activation foils [302]. Here,

Date	D_{req} [kGy]	t_{irr} [h]	$\overline{\phi}$ [p/cm^2/s]	Φ [p/cm^2]	D_{calc} [kGy]
27.03.2019	1	1.06	8.18×10^7	3.13×10^{11}	1.00
27.03.2019	5	4.91	8.83×10^7	1.56×10^{12}	4.97
27.03.2019	10	0.96	9.06×10^8	3.12×10^{12}	9.95
29.03.2019	10	8.38	1.15×10^8	3.47×10^{12}	11.04

Table 6.4: Requested and calculated total ionizing doses with corresponding proton fluences, supplemented by auxiliary data on conducted experiments. Differences between the requested and achieved doses are due to our incorrect initial estimation. $\overline{\phi}$ is the average proton current for the irradiation duration t_{irr}. Uncertainty of the dose (fluence) estimation is below 10 %.

flux determination uncertainty is about 9 % which is the difference between k factor obtained by both methods and fluence ranges. Finally, total proton fluence was calculated by F. Křížek's software as

$$\Phi = k \cdot I_{ch} \cdot C_{off} \cdot t_{irr} \tag{6.12}$$

I estimated the absorbed dose for the sample by equation (2.2) described in section 2.2. If the sample thickness and corresponding energy loss of a proton are relatively small, the stopping power can be regarded as constant and obtained from the NIST Database on Stopping-Power [12]. To ensure the correct calculation, I performed a simulation in SRIM 2013 software [3] which shown that LET changes by 23 % in a 4 mm layer of polystyrene, see figure 6.13 (right). I used statistics of 10000 impinging protons to obtain a smooth distribution. I taken an average LET value of 0.21 eV/Åand multiplied it by polystyrene's density of 1.06 g/cm^3 to achieve $S_m = 19.9$ MeV·cm^2/g. In our experiments, the proton beam energy was 35.3 MeV with RMS about 100 keV measured by the cyclotron team. With help of a similar SRIM simulation, I found that protons lose 2.3 MeV traveling through 130 cm of air to the sample, so I used 33 MeV protons for the polystyrene LET simulation. Final results for the fluence and dose estimation are presented in table 6.4.

[3]The Stopping and Range of Ions in Matter (SRIM) [27] is a powerful collection of software packages that calculate many features of the transport of ions (up to 2 GeV/amu) in matter [12]. Complex targets can be made of compound materials with up to eight layers. SRIM calculates both the final 3D distribution of the ions and also all kinetic phenomena associated with the ion's energy loss: target damage, sputtering, ionization, and phonon production.

Chapter 7

Investigation of SiPM radiation hardness in NPI laboratory

Silicon photomultipliers are very susceptible to the harsh radiation conditions of CBM PSD with neutron fluence reaching 2×10^{11} n_{eq}/cm^2 within the year of experiment operation. This chapter describes the detailed radiation hardness study for eight different SiPMs from various manufacturers which I conducted. SiPMs were irradiated by neutrons with fluence in range from 5×10^{10} to 6×10^{12} n_{eq}/cm^2 which is described in detail the in previous chapter. Based on the achieved results I chose the SiPM for the PSD light readout. Furthermore, I elaborated on several insights considering the reasons of the change of various SiPM parameters which were not yet explored in this fluence range by other investigations.

7.1 Comparison of general sensor characteristics

The photodetectors utilized to read out the light from WLS-fibers at PSD have to fulfill the following requirements [252]:

- Compactness: a set of 10 pieces should fit at the 20×20 cm^2 rear side of the module.
- Sensitive area of several mm^2: sensor should read out a signal from a full section, i.e. it shall fit a bunch of 7 WLS-fibers with 1 mm^2 area each (six for scintillating tiles and one for LED calibration).
- Wide dynamic range on the order of few thousands: to measure signals produced in a hadron calorimeter module ranging from few MeV up to several GeV.
- High gain: to detect light at a level of tens of photons necessary for the initial muon calibration, without a need for the sophisticated amplifier.
- Short pulse width about tens nanoseconds: to operate at the SIS100 reaction rates at least up to 1 MHz.
- Low cost: i.e. photodetector cost, its ability to operate without cooling, low cost of a power supply (low photodetector operating voltage), etc.
- Relatively high radiation hardness: to remain operational up to accumulated fluence of at least 2×10^{11} n_{eq}/cm^2.

Looking at the SiPM properties listed in section 3.5.2 it is clear that this is a great candidate for the mentioned application. Moreover, it has other great features like an absence of nuclear

counting effect, insensitivity to the magnetic field, and mechanical endurance. For the comparison, I selected eight SiPM models with a maximal amount of pixels available at the moment of purchase from several manufacturers.

The list of investigated SiPMs and their parameters, namely breakdown voltage V_{bd}, number of pixels N_{pix}, pixel pitch, gain, photodetection efficiency PDE, pixel recovery time $\tau_{recovery}$, pixel capacitance C_{pix}, quenching resistance R_q, difference between turn-on and turn-off voltage for the Geiger avalanche $V_{bd} - V_{off}$, are presented in table 7.1[1]. The cost of the devices ranged from 30 to 50 EUR/piece. They have gain on the order of 10^5 – 10^6 comparable to the gain of conventional PMTs, which is enough even for the single-photon detection, see subsection 7.8.1.

	Zecotek MAPD [306]		Hamamatsu MPPC [155]		Ketek SiPM PM33 [153]		Sensl SiPM [152]	
	3A	3N	S12572 -010P old	S14160 -1310PS new	15 -WB-A0	50	B-series 30020	C-series 30020
V_{bd}, V	64	88	67	38	27	23	25	25
N_{pix}	135000	135000	90000	90000	38800	3600	11000	11000
Pitch, μm	8.2	8.2	10	10	15	50	28.6	28.6
Gain	6×10^4	10^5	10^5	10^5	3×10^5	6×10^6	10^6	10^6
PDE, %	20	30	10	18	22	40	24	24
$\tau_{recovery}$, ns	2000	10000	10	10	13	2000	100	100
C_{pix}, fF	1.5	1.2	3.2	6.4	19.5	280	63	63
R_q, MΩ	2.7	2.8	2.8	1.6	0.72	0.49	0.42	0.4
$V_{bd} - V_{off}$, V	–	0.43	1.7	0.97	0.72	0.15	0.17	0.18

Table 7.1: Parameters of investigated SiPMs produced by various manufacturers before irradiation. Most of the parameters are typical and may vary from sample to sample by up to 20 %. All SiPMs have 3×3 mm^2 area to fit the WLS-fiber output. Pixel pitch for Sensl (now ON Semiconductor) SiPMs is calculated based on the number of pixels and SiPM area, it is bigger than claimed by the manufacturer because they did not include the dead area around the pixels. Values of C_{pix}, R_q and $V_{bd} - V_{off}$ are based on typical values from my measurements described further in this chapter.

The big difference between the samples arises from the variation in the number of pixels which is directly connected to the dynamic range. Limited number of pixels N_{pixels} results in non-linear dependence of the number of fired pixels N_{fired} on the number of incident photons $N_{photons}$ that can be described by [225]

$$N_{fired} = N_{pixels}(1 - \exp\{-N_{photons} \times PDE/N_{pixels}\}) \tag{7.1}$$

Figure 7.1 (left) represents the dynamic range calculated for the investigated SiPMs using this formula. One can see that SiPMs produced by Zecotek and Hamamatsu with about 10^5 pixels show a dynamic range wider at least by one order of magnitude compared to SiPMs produced by Ketek and Sensl with 3.6×10^3 and 1.1×10^4 pixels, correspondingly.

Furthermore, in practice, the dynamic range can be further shortened due to the long pixel recovery time. It is especially influential at high particle rates when the time before the next

[1]Note, that before my measurements Zecotek MAPD-3A SiPMs were utilized at NA61 PSD for several years and were already slightly irradiated. $V_{bd} - V_{off}$ was not measured for these samples because they were unable to distinguish single-photon peaks, see subsection 7.8.1.

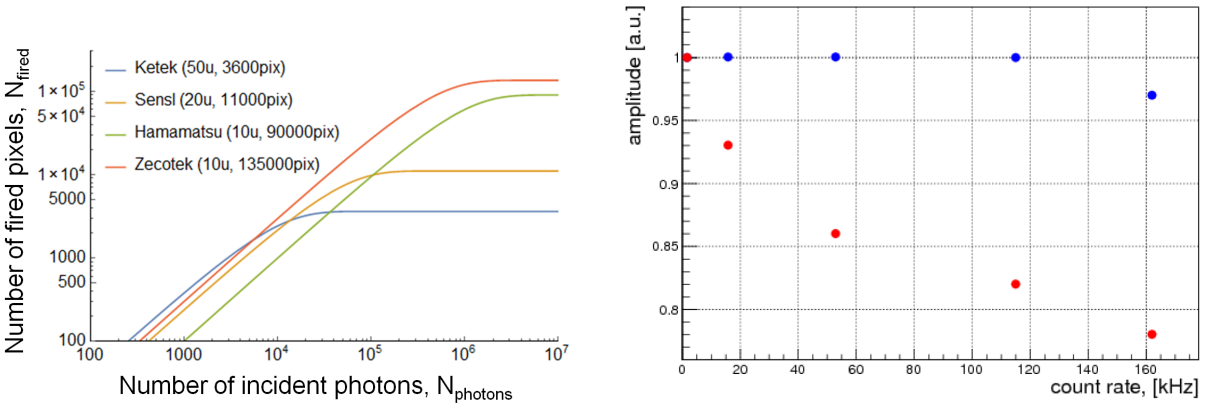

Figure 7.1: (left) Dynamic range calculated for the investigated SiPMs in terms of dependence of fired pixels number on incident photons number. Calculation was done in Mathematica software. (right) Normalized response of Zecotek MAPD-3A (red) and Hamamatsu S12572-010P (blue) SiPMs at various proton beam rates [307].

photon bunch arrival can be too short for fired pixels to recover, reducing the effective number of sensitive pixels and consequently the dynamic range. For most SiPMs it can be defined as $\tau_{recovery} \approx C_d R_q$, see subsection 3.6.4. But it is not always that simple.

For instance, Zecotek SiPM are designed by special dense pixel technology without a physical resistor, where an extra p-n junction is used as a well for charge collection and quenching, which results in extra large recovery time [308]. They have $\tau_{recovery}$ on the order of 10 µs [309] and are expected to perform significantly worse than Hamamatsu SiPMs with recovery time on the order of 10 ns, in terms of both time resolution and dynamic range. It was confirmed by the PSD group of NA61 experiment during the dedicated test, where the dependence of calorimeter response on beam rate was measured as shown in Fig. 7.1 (right). One can see that Zecotek SiPMs exhibited more than 20% signal decrease at rates higher 100 kHz. A small amplitude reduction observed for Hamamatsu SiPMs at high rates was due to the limitation of current read-out electronics. Consequently, it was decided to replace the initially utilized Zecotek MAPD-3A with Hamamatsu S12572-010P SiPMs during the NA61 PSD upgrade for the new physics program [307]. It is even more essential for CBM PSD to utilize SiPMs that can withstand operation at increased light readout rates up to 1 MHz.

Even though Hamamatsu SiPMs have the lowest PDE of about 10 %, it was confirmed to be enough for the detection of muons (MIPs). PSD team from INR Moscow measured about 40 – 50 photoelectrons with these devices for a MIP in a single calorimeter section [272]. Therefore, from the point of view of the performance for PSD readout before irradiation, Hamamatsu SiPMs considerably outpace the other investigated samples due to the wide dynamic range and small pixel recovery time. The latter may even improve the effective dynamic range of the SiPM as was discussed in subsection 3.6.7.

7.2 Measurement setup

I conducted many SiPM tests using the measurement setup which is situated in our laboratory in the Department of Nuclear Spectroscopy of Nuclear Physics Institute of the CAS in Řež. The setup consists of two parts as it is shown in figure 7.2.

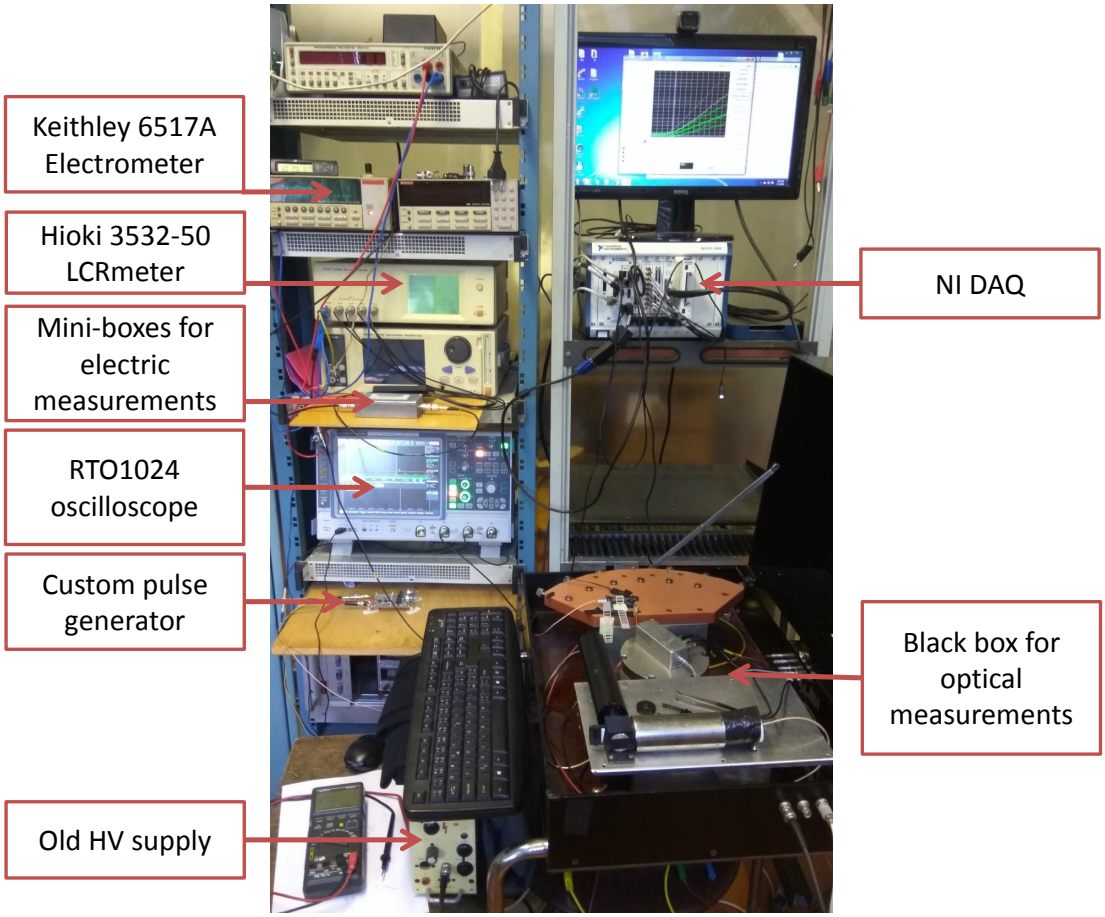

Figure 7.2: Photograph of the full measurement setup used in my work, including setup part for measurements of SiPM electric characteristics, setup part for measurements of SiPM optical response, and setup part for measurements of scintillator response (see section 5.2.1 for the description of the latter). Detailed description of the black box is presented in figure 5.7.

7.2.1 Setup for measurement of SiPM electric characteristics

This setup was made by my supervisor V. Kushpil. I used it to measure current-voltage I(V), capacitance-voltage C-R(V), and capacitance-frequency C-R(F) curves. Measurement modes are described in section 7.3 dedicated to the measurement software that I developed. SiPMs are placed in one of the small light-tight boxes shown in figure 7.3. They are also extra covered by thick black cloth for complete light isolation. Note, that the setup can be used not only for SiPM tests, but also for other electrical components and sensors, e.g. MOS-capacitors, pin-diodes, or avalanche photodiodes.

Keithley 6517A Electrometer is used to measure the current in a wide range from 1 fA up to 20 mA. It has a basic accuracy of 0.1 – 1 % depending on the measurement range. It also supplies the bias voltage for both mini-boxes in the range from 5 mV to 100 V, voltage is defined with an accuracy of ±0.15 %±10 mV.

Hioki 3532-50 LCR HiTester [310] is used to measure the complex impedance in terms of capacitance (C) and resistance (R) in the range from 0.32 pF up to 370 mF. The calculation is performed by the HiTester for both series and parallel equivalent circuits. Tested sample can be presented as a series connection of capacitance and resistance, which is the best approach for

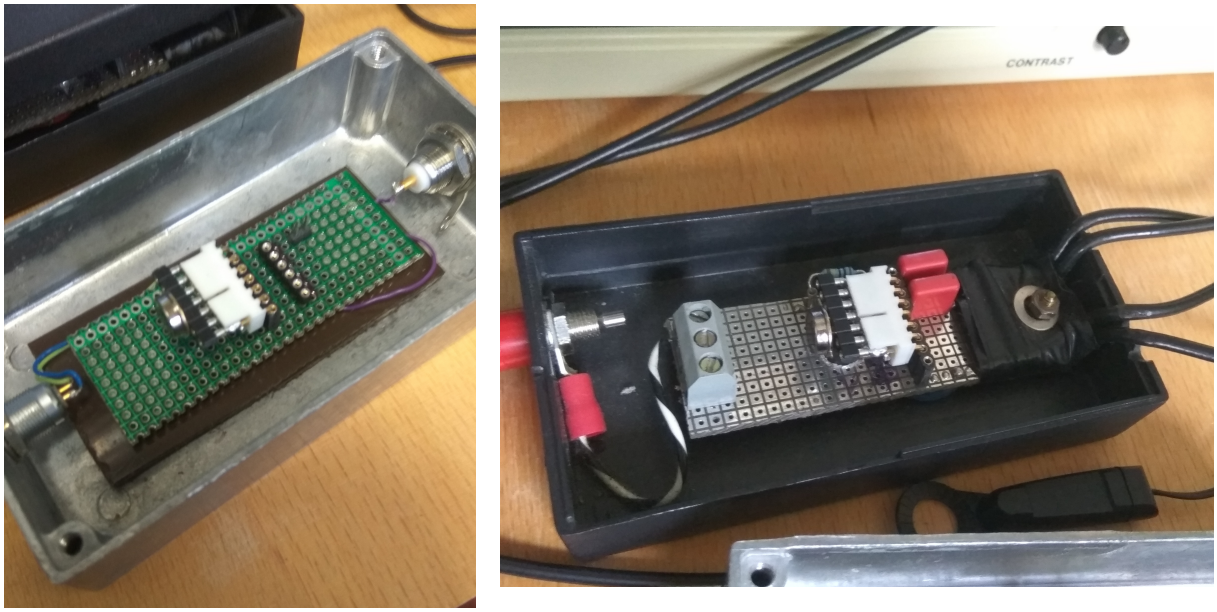

Figure 7.3: Photograph of the SiPM connection mini-boxes used in this setup. (left) is used for dark current measurement, (right) is used for capacitance measurements.

samples with low capacitance (below 10 pF) and high impedance (above 10 kΩ) [311]. Alternatively, it can be presented as a series connection of capacitance and resistance, which is the best for samples with high capacitance (above 1 nF) and low impedance (below 100 Ω). For SiPMs I used parallel equivalent circuit mode because SiPMs have very low capacitance and very high impedance, see table 7.1. Both open and short circuit corrections are used to increase the measurement precision.

I operated the HiTester in hardware autorange mode, with an internal trigger, 16 times averaging of every measurement, and normal 21 ms testing speed. HiTester has a low basic accuracy of 0.08 %, but real accuracy is bigger because it depends on the sample impedance and measurement range. Accuracy for my measurements was below 1 % according to [310]. Test signal amplitudes can be chosen in the range from 50 mV up to 1 V with an accuracy of $\pm 10\% \pm 10$ mV. The frequency range is from 42 Hz up to 3 MHz with steps in the range from 0.1 Hz up to 1 kHz depending on the range, the frequency accuracy is below 0.005 %.

7.2.2 Setup for measurements of SiPM response to LED and noise

Based on the hardware available in our laboratory and borrowed from the Moscow PSD team, I assembled a simple setup for measurements of SiPM signal response and noise as a function of overvoltage, i.e. S(V) mode in the Dharma software, see the next section. Figure 7.4 presents the scheme of electric connections in this setup. The setup is placed inside the light-tight black box shown in figure 5.7 (bottom). A special holder is used for the optical alignment: SiPM is inserted on one side, LED is inserted on the other side. Two holders are used: one for Zecotek SiPMs which have rounded metallic shell, another one for all the other SiPMs which do not have such shell and all have the same square area, see figure 6.5.

Keithley 6517A Electrometer [312] is used for the bias supply to SiPM. Custom pulse generator drives the LED diode at a constant 1 kHz rate. It was initially developed by V. Červenka from HiLaSe company in Dolní Břežany for tests of the HADES ECAL. Hebei 330MUV9C LED

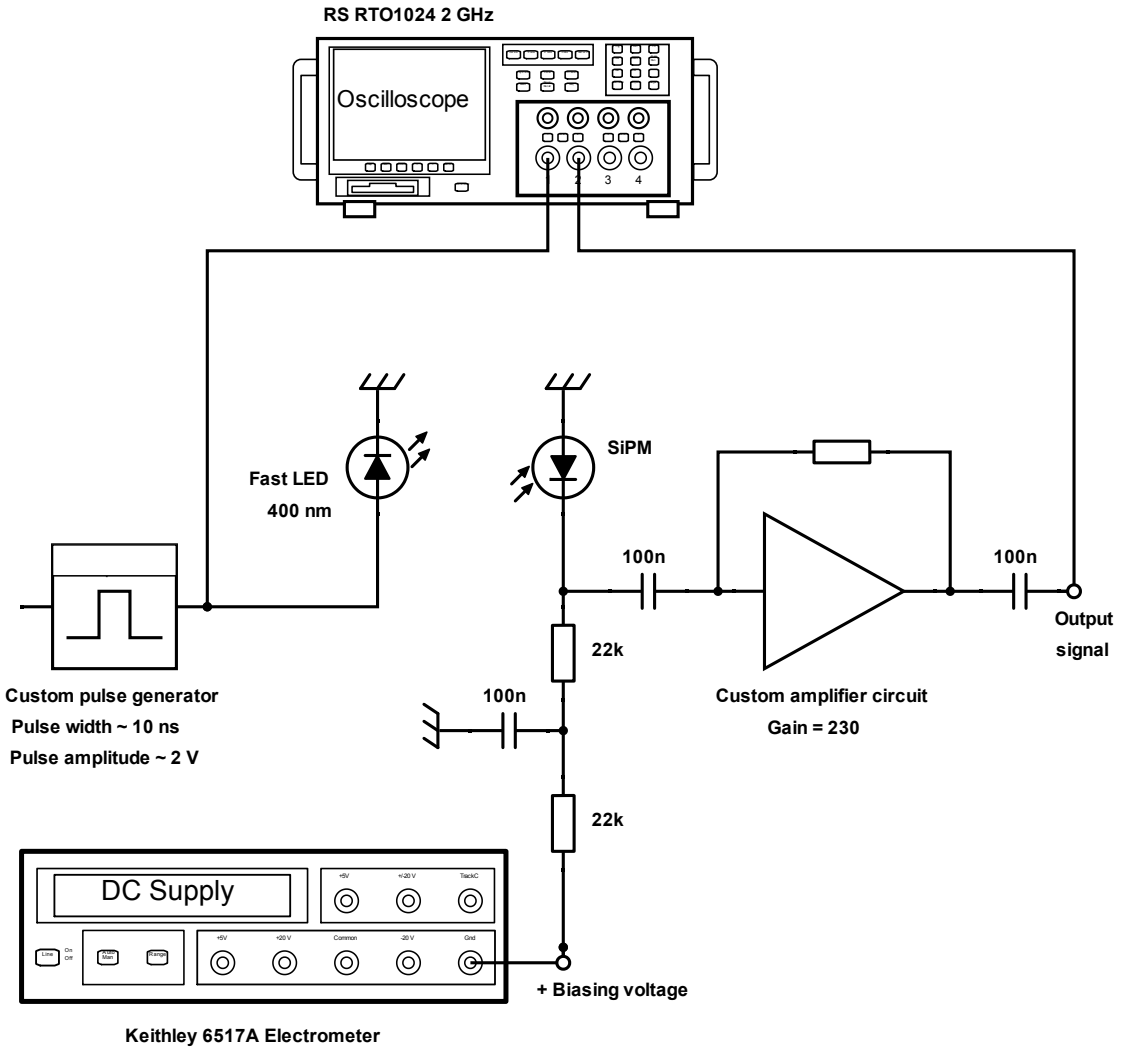

Figure 7.4: Connection scheme for the setup used for the measurement of SiPM noise and response to LED.

is used, it emits 400 nm light with low luminous power of 4 mW. The resulting pulse width is about 10 ns (Full Width at Half Maximum, FWHM), pulse amplitude is held constant, see figure 7.29. I aimed to perform the measurements of SiPMs of the same type during a single day to minimize the uncertainties due to the pulse generator and LED re-powering. When it was not possible or when different SiPMs were tested, I used one non-irradiated SiPM as a reference to adjust the signal amplitude.

SiPM signal is read out by custom transimpedance amplifier with a gain of 230 developed by our colleagues from the PSD team of Moscow Institute for Nuclear Research. It is designed for timing measurements of single photon response, so it has high gain, bandwidth of 300 MHz, input impedance of 10 Ω and output impedance of 50 Ω, but also relatively high noise compared to charge sensitive amplifiers. It's schematics can be found in appendix C. Data acquisition is performed with the digital oscilloscope RTO1024 produced by Rohde&Schwarz [285] at 2

GHz bandwidth, which is capable to record 1 million waveforms per second. It has vertical DC measurement accuracy of about 1.5 – 3 %, and horizontal accuracy of 0.0005 %. The signal from the pulse generator is used as a trigger. Both SiPM output and trigger channels are connected in 50 Ω low impedance mode.

I performed all the measurements at room temperature. Precise K thermocouple connected to Keithley 6517A is used for online room temperature monitoring. Unfortunately, after the measurements I realized that its calibration is incorrect, namely, it shows the temperature which is above the real by 4.5 – 5.5 °C. However, I also used a simple table thermometer with internal and external sensors and a sensitivity of 0.3 °C was to monitor the temperature in the room and inside the black box.

All the measurement devices from both setups are connected via a common GPIB bus to the data acquisition system produced by National Instruments (NI) which we call NI DAQ. It is based on the 2.5 GHz Dual-Core Processor PXI Controller PXI-8115 [313] and runs Windows 7. The devices are operated with help of the software (SW) that I describe in the next subsection.

7.3 Dharma - Software for (not-only) SiPM measurements

To automate the measurements I developed the dedicated software which I called "Dharma – Software for (not-only) SiPM measurements"[2]. Older software prototypes which were called R.D.S.D. and LabTest are now deprecated. I used the NI LabWindows/CVI ANSI C programming environment which is aimed at test and measurement. In my point of view, it allows better customizability of the software functionality than better known NI LabVIEW, because one can unambiguously code everything needed. Both mentioned products use the same libraries and data-acquisition modules.

7.3.1 Software operation and features

Software source consists of: project file Dharma.prj, 2646 lines long main C source code long Dharma.c, user interface (UI) file Dharma.uir, and a bunch of auto-generated files, notably header file Dharma.h and executable file Dharma.exe. Full source code can be downloaded at GitLab `https://gitlab.com/vasily_mikhaylov/dharma-sipm-software`. I will be glad if anyone will find it useful, so please use, redistribute and/or modify it for free, but please add an attribution to me. If you do not have the NI LabWindows/CVI, you can use the distribution installer, which I provide along with the source files, it will install all necessary libraries, drivers, registry keys, executables, etc.

User interface (UI) is divided into five tabs, four of them are dedicated to different measurement modes, and the fifth tab is used for development and debugging. Figure 7.5 shows the screenshot of the software performing the SiPM signal response measurement. On the left side of every tab, a user defines the measurement settings, acquired data are plotted in real time in the middle, operation buttons, general information, and SW setting are situated outside the tabs.

Measurements are designed to acquire the dependence of chosen SiPM parameter (current, capacitacne, signal, etc.) on the bias voltage (or frequency in C-R(F) mode). Before the measurement, a user sets values of the measurement parameters, i.e. Start Voltage, Stop Voltage, Step Voltage, Max Voltage, Wait time, File name, etc. The measurement in the chosen mode is

[2]Dharma in Hinduism, Buddhism, Jainism, Sikhism and other religions, one of its possible definitions is "to do things the right way" or "to follow the path of righteousness". I decided to name my software after Dharma, because I aimed to make the final SW version as well-written and clear in terms of the code, and as productive and compatible in terms of the operation, as I could, in other words, I aimed to do it right.

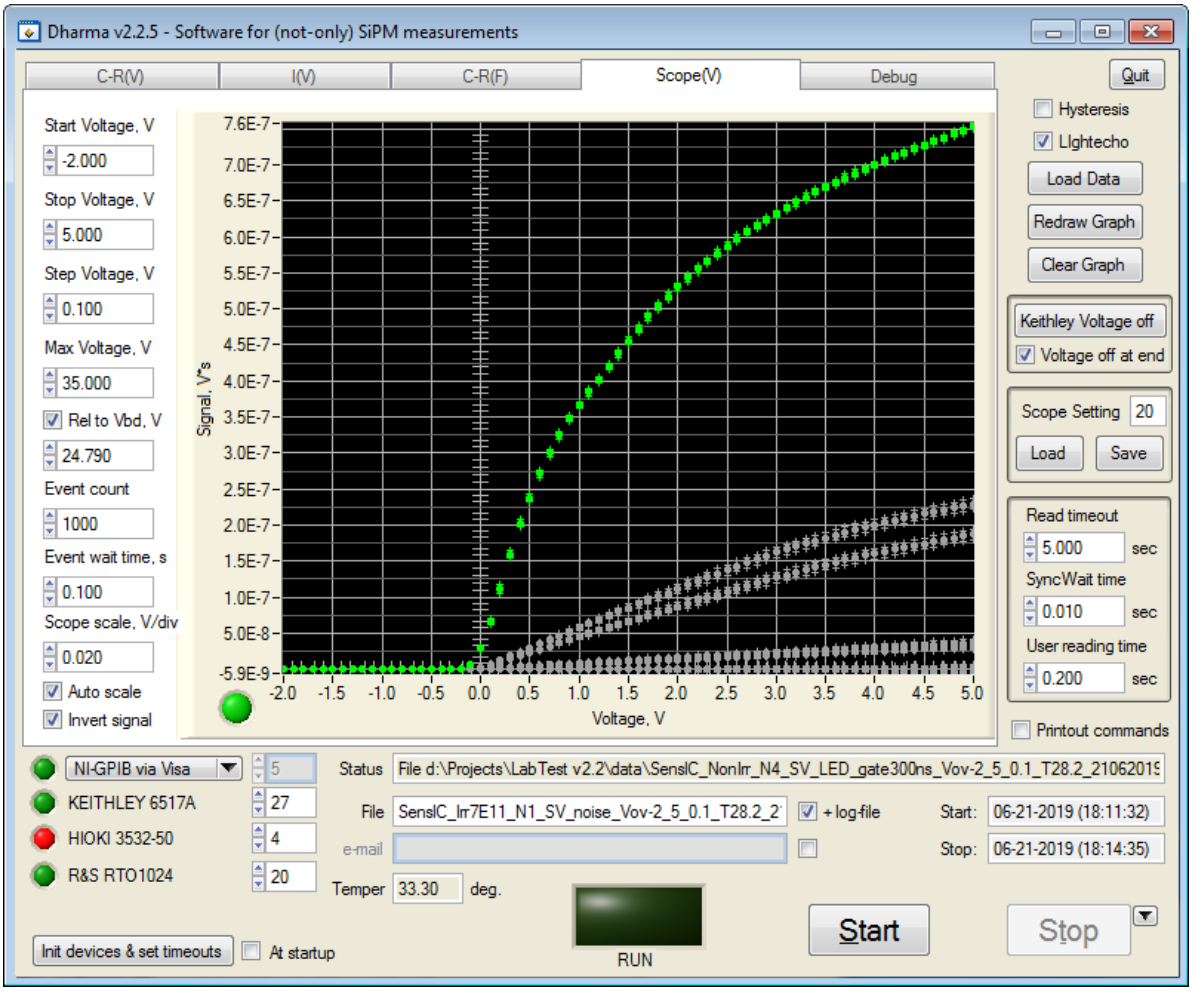

Figure 7.5: Screenshot of Dharma v2.2.5 - Software for (not-only) SiPM measurements during the measurement of SiPM response to LED as a function of overvoltage.

started by pressing the Start button. Measurement goes in a cycle, at every step bias voltage (or frequency in C-R(F) mode) is increased until Stop Voltage (or Stop Frequency in C-R(F) mode) is reached. Alternatively, measurement can be stopped any time by the Stop button.

The very first thing that is performed by the SW after the measurement start, is the initialization of communication protocols and check if all the devices required for chosen measurement are connected and ready. There is a checkbox that allows the SW to perform this initialization right after the SW startup. Measurement will not start if some devices are not ready, Stop Voltage is larger than Max Voltage, or if the files with chosen name can not be created or already exist. Though measurement can start from the negative voltage and there is currently no control if its value is too high, so the user has to be careful about it. During the measurement, the big RUN indicator is green, all the tabs except the current one, and all the buttons except Stop are inactive (otherwise the user could accidentally disturb the measurement cycle).

At measurement start number of steps is calculated and shown in the status bar, so the user can estimate the measurement time. At every step measured data are displayed numerically in the status bar and drawn on the graph as green dots (also yellow dots if the second parameter is chosen for C-R(V) or C-R(F) modes). Also, data and time of the measurement start and stop,

and temperature reading from Keithley 6517A are indicated in dedicated UI.

In earlier versions, there was an option to send an email to the user address which will notify the user the measurement is finished. It was introduced by V. Kushpil with help of a small software executable smail.exe, but when I tested it recently, it did not work, so I disabled it now. It was quite handy for previous software versions when slow device connection via custom USB-GPIB was used and a single measurement could take up to a few hours. Now with faster connection via the VISA-GPIB module, I did not need to use email notifications because measurements typically take 5 – 30 minutes.

SW configuration, i.e. all the values and settings in UI, is automatically saved in file cfg.ini after exit and it is loaded at SW startup. Acquired data are saved in the directory "data" inside the main directory. If cfg.ini and/or data folder do not exist, they are created automatically. Two files are created for each measurement: acquired data are stored in ".dat" file and time log in ".log" file, log-files can be turned off with the corresponding checkbox. Every line in both files represent single measurement point. In log-file it is printed in following format: "V = X.XXXXXX at hh:mm:ss" (or "f = X.XXXXXX at hh:mm:ss" for C-R(F)). For compatibility with older SW versions, values in dat-files are printed in different manner for different measurement modes, see next subsection for description. Files are saved after the measurement is stopped, i.e. finished by itself or stopped by the user. Therefore, I advise to wait and not to "kill" the software even in case of accidental errors, because it will cause data loss for the current measurement.

Already acquired data can be loaded onto the graph via the "Load data button", which allows users to manually choose the data path in a standard Windows popup. If checkbox Printout commands are on, data values are also printed out in a separate cmd terminal. If checkbox Lightecho is on, dots from previous measurements on the graph become grey when a new measurement is started or data are loaded. This helps to distinguishable currently acquired data from the new data, see figure 7.5. Clear Graph button allows to manually clear all the data on current graph tab, button Redraw Graph redraws the last data set on the current tab, either acquired online or loaded.

7.3.2 Specifics of different measurement modes and debug mode

In C-R(V) and C-R(F) modes, Frequency and Voltage (amplitude) of the testing signal can be chosen, see figures 7.6 and 7.7. Two out of four parameters (C_{series}, $C_{parallel}$, R_{series}, $R_{parallel}$) can be simultaneously displayed on the graph. In C-V(F) mode, measurement goes from Start Voltage till Stop Voltage with Voltage. There is also an option to measure the Hysteresis (checkbox is in the right top corner), i.e. measurement will go from Start Voltage till Stop Voltage, and then back to Start Voltage (with negative steps). In C-R(F) mode, measurement goes from Start Frequency till Stop Frequency with Step Frequency. Frequency can be displayed on the graph on a linear or logarithmic scale. Order of values in dat-files of C-R(V) measurement is: measured bias voltage, temperature, requested bias voltage, C_{series}, $C_{parallel}$, R_{series}, $R_{parallel}$. Order of values in dat-files of C-R(V) measurement is: frequency, C_{series}, $C_{parallel}$, R_{series}, $R_{parallel}$, bias voltage, temperature. In both modes, measured values are printed with an accuracy of 6 decimal places and are separated by commas.

Figure 7.8 presents a screenshot of example I(V) measurement. In I(V) mode Maximal Current can be chosen, and measurement will stop automatically if it will be exceeded. Note that Keithley 6517A which is used for the measurement can not detect current above 11 mA, so if a higher value will be chosen current protection will not work. Because the current is not measured in other modes, I recommend always start the sample investigation from the I(V) measurement to determine the safe operating range in terms of bias voltage. The current range is also set here, so the user can tune the measurement accuracy according to the expected

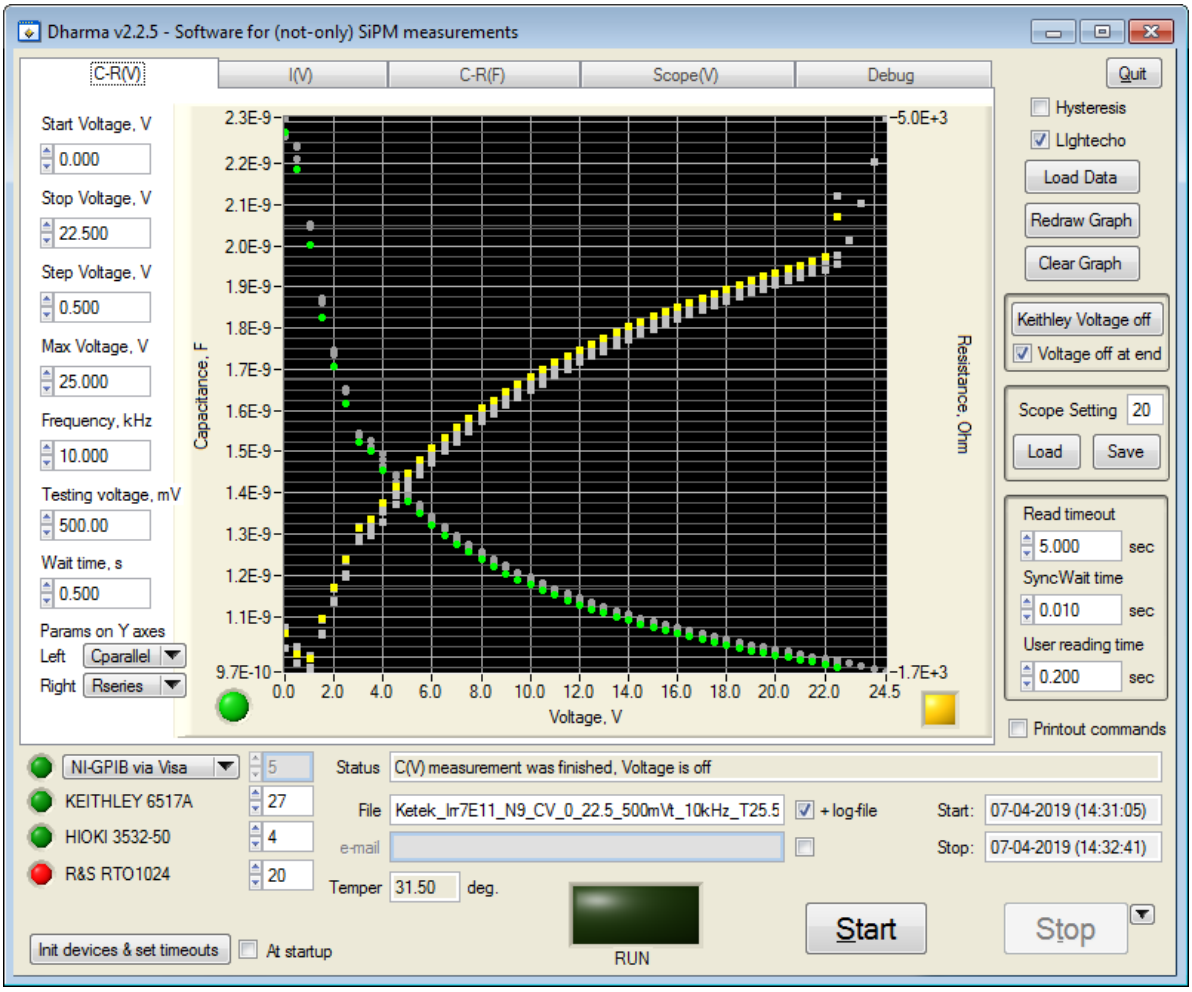

Figure 7.6: Screenshot of Dharma Software during the the measurement of SiPM parallel capacitance and series resistance as a function of reverse bias voltage.

current values. If the user has no anticipation on the range, there are two options for auto-range: hardware autorange which is performed by Keithley 6517A itself, or software autorange which is performed by my software. I implemented the latter option because I encountered unreliable operation of the hardware autorange which sometimes got stuck and could not change the range. To improve the measurement accuracy, after every measurement cycle Zerocheck is performed, i.e. input amplifier is reconfigured to shunt the input signal to low. Format of values in dat-files of I(V) measurement is: bias voltage, current, temperature. Values are printed with an accuracy of 6 decimal places and are separated by tabulators.

In S(V) mode, results from the measurement №1 are acquired from the RTO1024 oscilloscope. The user manually sets the measurement №1 in the oscilloscope. I used measurement of the signal area in a time gate of 100 – 300 ns (depending on the signal shape for different SiPMs). Since the user can define different measurements in the oscilloscope (i.e. different gate lengths in my case), I implemented the button to load and save predefined measurements. Up to 99 measurements can be saved, buttons are situated on the right in UI. A vertical scale for the oscilloscope is also chosen in UI, with an option to use the software autoscale. Autoscale is based on the data from the oscilloscope measurement №2 which is the peak-to-peak value of the

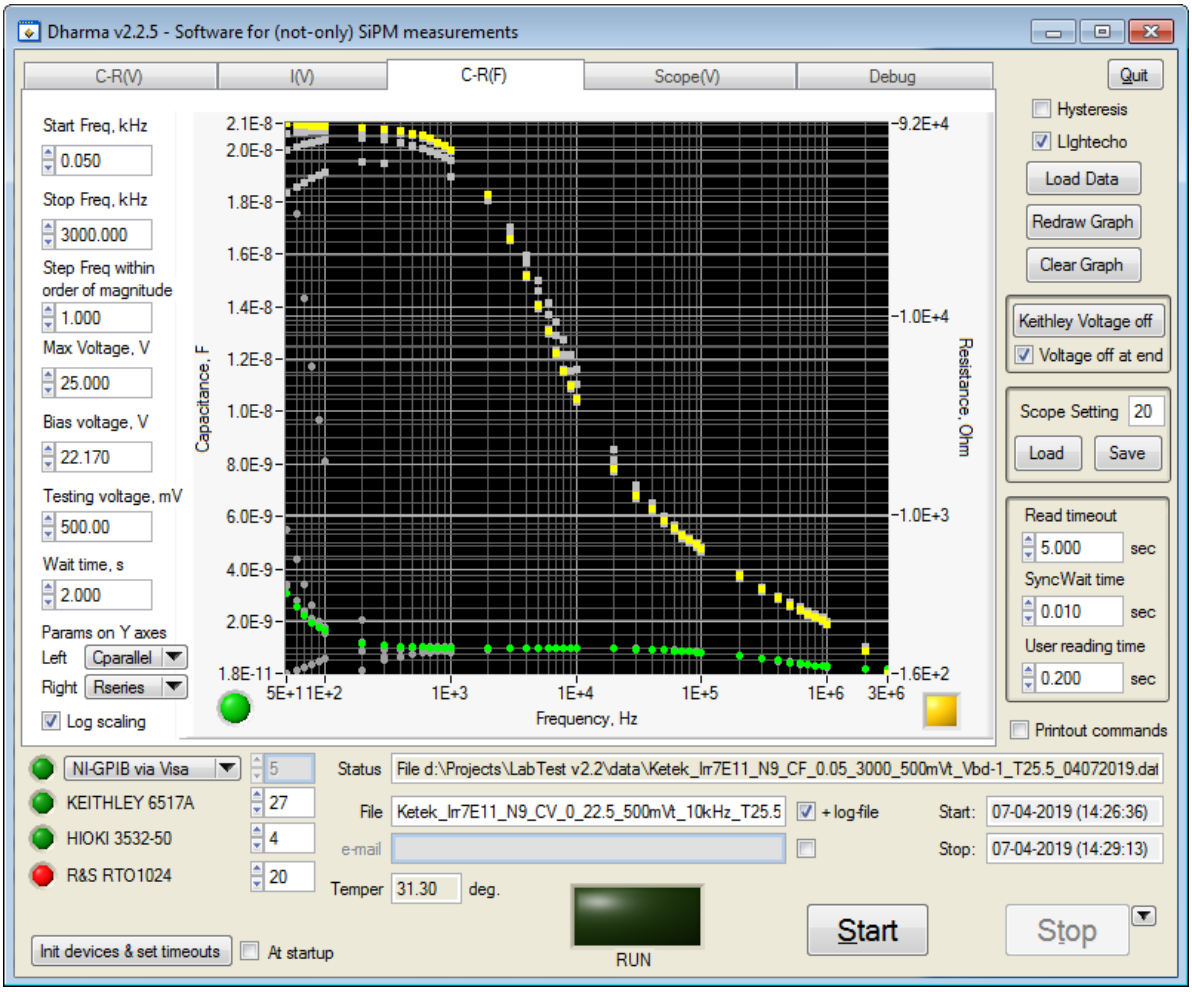

Figure 7.7: Screenshot of Dharma Software during the the measurement of SiPM parallel capacitance and series resistance as a function of the testing signal frequency.

measured waveform. When this value becomes comparable to the vertical range, the range is increased. I also implemented the signal inversion checkbox, though signal inversion can also be chosen in the oscilloscope itself.

The software S(V) measurement (not to be confused with the oscilloscope measurement described earlier) can be performed both as a function of bias voltage, or as a function of overvoltage. In the latter case, user shall manually set the breakdown voltage for each sample (i.e. based on previously analyzed I(V) data). Because the black box is situated further from Keithley 6517A, I used a long cable to connect the bias voltage source, which had non-negligible resistance and resulted in a slight voltage drop at the amplifier input. I measured the magnitude of this effect and introduced the software correction for it, i.e. real bias voltage is set in Keithley 6517A to the value of requested bias voltage multiplied by a factor of 1.006. This correction is only 0.12 V for 20 V, but it is 0.48 V for 80 V which is important for SiPMs with high operating voltage.

In S(V) mode user also defines the number of events to be acquired by the oscilloscope for every measurement point. I empirically found that 1000 events provide reasonable speed and precision for a signal area or amplitude measurements. Format of values in dat-files of S(V)

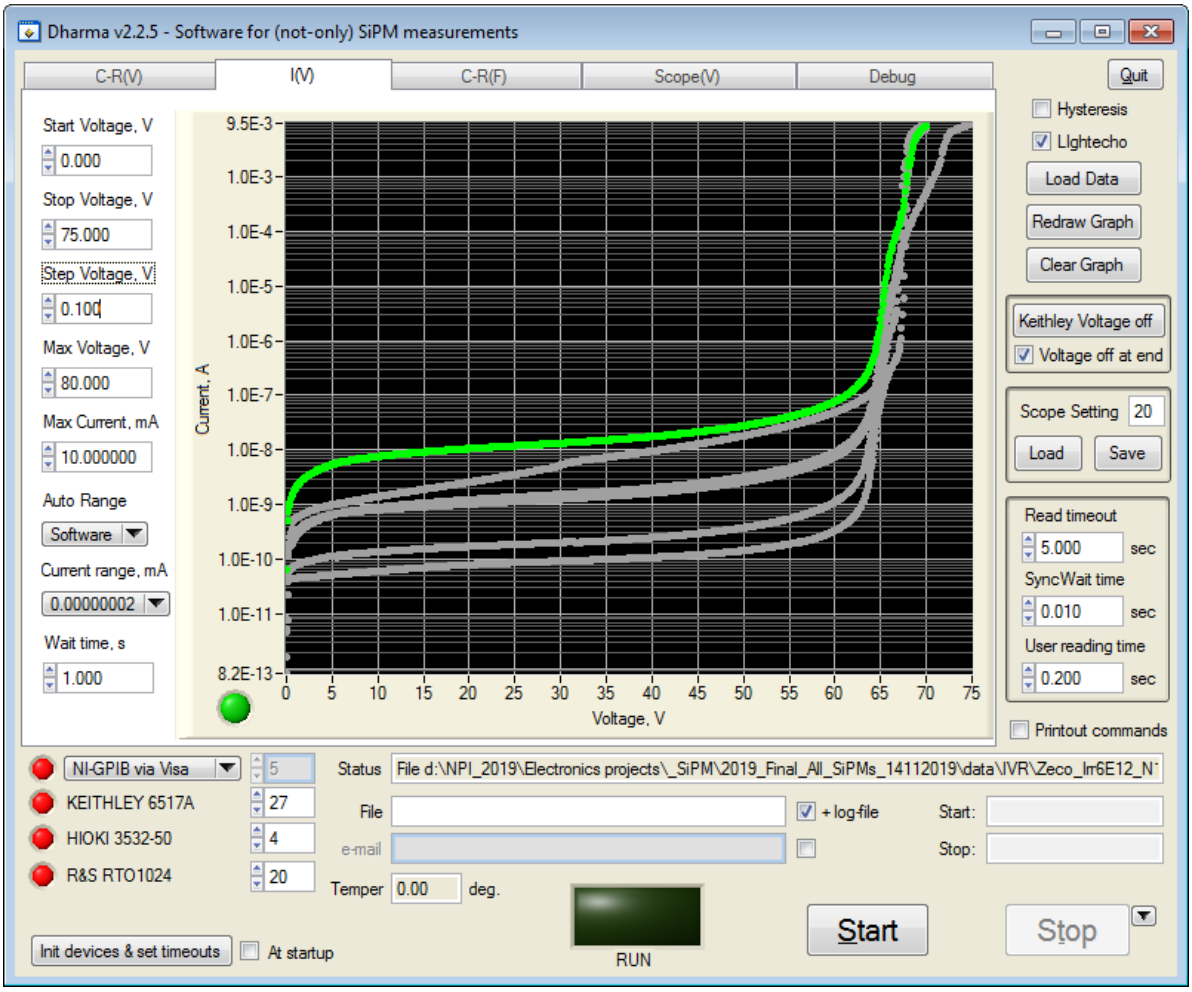

Figure 7.8: Screenshot of Dharma Software during the the measurement of SiPM dark current as a function of reverse bias voltage.

measurement is: bias voltage, temperature, current measured value, maximal peak measured value, minimal peak measured value minus, average measured value, RMS, standard deviation, event count, waveform count. Values are printed with an accuracy of 6 decimal places for bias voltage and temperature, 0 decimal places for event count and waveform count, and 12 decimal places for the other measured and calculated values. All the values are separated by tabulators. The total bias voltage is always printed out, even if the measurement is done relative to the overvoltage. Software plots the average measured value on the graph, with uncertainty bars which are calculated as "average measured value - standard deviation" and "average measured value + standard deviation". In this way, user can use the same SW measurement routine and settings for both signal and noise measurements.

Figure 7.9 presents the last tab which is dedicated to the debugging mode. Here user can directly send any desired commands to any device connected to NI DAQ via GPIB or serial COM-port, including devices that are not supported in the measurement modes. User can set the device address and baud rate for serial connection. See the next subsection for details on the hardware connectivity. Protocol and device initialization is performed before the command is sent if it was not performed before. Note, that not to disrupt the operation of the main

measurement modes, the established connection is not terminated afterward. So to disconnect all the devices which were initialized this way, the user needs to exit the software.

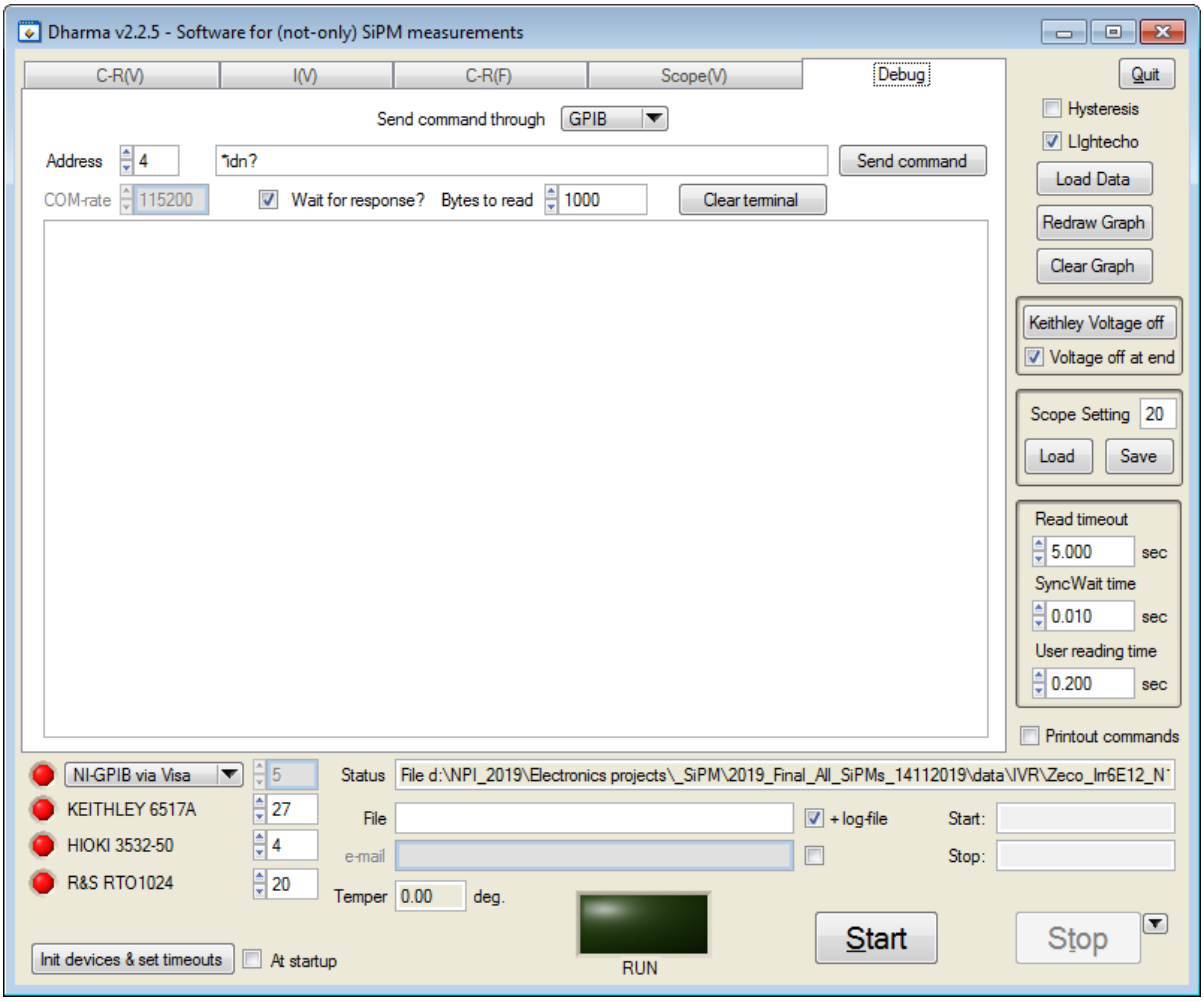

Figure 7.9: Screenshot of Dharma Software tab used for software development and debugging.

7.3.3 Hardware communication, software behavior, and code description

Normally, devices are connected via the NI-GPIB module of NI DAQ, and communication is performed via NI Virtual Instrument Software Architecture (VISA) I/O instrument driver. VISA is an application programming interface (API) standard for communication-based on GPIB, VXI, PXI, serial, Ethernet, and USB interfaces. VISA is used by several major companies in the test and measurement industry, including National Instruments, Rohde & Schwarz, Keithley, and others. In the older version, devices were connected via a custom USB-GPIB converter developed by V. Kushpil, and though it functions much slower, I did my best to preserve compatibility with this connection option. Caution: when switching the GPIB connection mode, one should re-initialize the devices, or even better to restart the SW to prevent errors during the operation. Yet another connection option is the regular COM-port which is often used for simple devices connected via USB. I implemented it to control the XY moving table, but tests involving it were canceled, so it is not yet supported in the SW. However, one can connect it or any other COM

device to NI DAQ and communicate with it in the Debug tab.

The main command for device communication is called SendCommand

```
SendCommand(int port, int devnum, char *command, int responsewait, int
  maxNOREDO, int bytestoread, char *response)
```

where the port is the COM-port number for USB-GPIB converter or any other device connected via COM (not used for NI-GPIB), devnum is the GPIB device address (if it is < 0, regular COM-port is used), *command and *response are the text buffers for the command and response, responsewait = 1 means that SW shall wait for the device response to the command, maxNOREDO was intended to allow the re-tries of the command sending if the response is shorter than expected but it is not currently used, bytestoread is the expected response length (if unknown, a large number like 1000 is used).

Full listings of the SendCommand and other functions that I mention here can be found in appendix C. SendCommand has a unified structure that allows communication to any devices connected via NI-GPIB, USB-GPIB, or COM-port (usually USB port operated via RS232 interface). Error handling is implemented either via VISA status request or RS232 error request, the error message is shown to the user in the status bar of the user interface. Also, a request for the full system error list is sent to the GPIB-connected device, and the answer is printed out in a separate cmd terminal, because there can be many errors at once that might not fit into the status bar.

Since most of the devices need some time to process the command, perform the requested action and return the response, I implemented several waiting variables/functions. Variable readtimeout defines the timeout to wait for the command response, its value is set only during the initialization of VISA or COM interface, so to change it the user should re-initialize it.

Function SyncWaitLoop(double waittime) puts the SW in an idle state in specific moments of operation, e.g. after interface and device initialization, before the response request or just to give the user some time to read an important status message. Variable waittime is defined in seconds. waittime = -1 corresponds to standard SyncWait time, i.e. after SW waits this time at the end of every SendCommand call. If waittime = -2, standard User reading time is used. Read timeout, SyncWait time and User reading time can be changed on the right side of UI. Standard SyncWait time can be changed during the measurement, other ones shall be set in advance.

In earlier SW versions, waiting was realized in a single time interval, but it caused the SW to freeze for the entire waiting time. Now waiting time is divided into smaller time intervals, in between of which the system events are checked, so the user can interact with the SW, i.e. stop the measurement.

Yet another one is the Wait time setting situated on the left in every measurement tab in UI (not to be confused with the waittime variable mentioned before). Wait time setting is used to give the device enough time to perform the data acquisition and its value is unique for every measurement mode. After the new bias voltage value is set at the new measurement step (or frequency value at the new step for C-R(F)), SW waits for this amount of time to wait until relaxation processes in the sample after the step increase are finished, and that the device can perform all the required measurements and calculations to acquire the stable current or impedance value at the new step. In S(V) mode, the Event wait time is slightly different - it determines the time between the data requests, so the expected amount of events can be collected.

During the software and hardware tests and debugging, I empirically determined safe optimal values for the aforementioned wait times, i.e. when the measurement value stabilizes and the HW connection does not crash. Now, default values in the UI are for the case of GPIB connection

via VISA. Namely, Read timeout of 5 s, SyncWait time of 0.01 s, and User reading time of 0.2 s, obviously the latter one depends only on the reaction speed of the user. Wait time setting is 0.5 s for C-R(V), 1 s for I(V) and 2 s for C-F(V). When very small currents (below 100 pA) are measured in I(V) mode, I advise increasing the Wait time setting to achieve the optimal measurement accuracy, because full relaxation and stabilization of the current takes a longer time. Event wait time is 0.1 s, though this one is based purely on my liking. In the case of GPIB connection via USB-COM interface, I suggest significantly increase all the wait times, i.e. start from 5 – 10 s and then try to minimize them. I tested that the software operated well with such long wait times, but their optimization was not that important for me.

I implemented two options to stop the measurement which can be chosen in a small ring button near the Stop button: if "stop" is chosen, the current measurement step will be finished before the stop, but if "terminate" is chosen, it will be instantly terminated. The latter is important in case if some crucial mistake happened, i.e. if the voltage was accidentally set wrongly and damage to the tested sample may happen, but it may cause some data loss or unpredictable SW behavior, so it is generally not recommended. For the same reason, I added checkbox Voltage off at the end, which is used to turn off the bias voltage supplied by Keithley 6517A after measurement end, stop, or termination. Also, there is an extra button Keithley Voltage off, which turns off the voltage, but it can be used only if the measurement is not running (otherwise it could cause the SW to crash).

7.4 Measurement conditions, parameter variations and data analysis

I conducted all the SiPM measurements presented in this section in 2019, i.e. after more than two years after irradiation, see table 6.3, so I consider the self-annealing to be completely finished. The only exception are new samples of Hamamatsu S14160-1310PS and Ketek PM3315-WB-A0 SiPMs which were measured after two months after irradiation. They exhibit slightly worse characteristics than samples irradiated in 2016 which can be seen in the data presented in this section. Note that for Hamamatsu SiPMs irradiated on 02.03.2018 I measured only dark current dependencies because they were transferred to CERN for the beamtest soon after the irradiation and remain there for further tests. I performed few measurements for some samples right after the irradiation, and observed substantial self-annealing effects during the first several days, however, I did not study these effects systematically. General information on the SiPM annealing can be found in subsection 3.6.8.

During the measurements, samples were situated inside the special boxes described in section 7.2, so they were completely covered from light. I conducted all the SiPM measurements at room temperature which ranged from 23 up to 28 °C during the year. However, measurements of the same characteristics (dark current, response to LED, etc.) were done within a single month, which resulted in a temperature variation only up to ±1 °C. Temperature variation during a single measurement was on the order of temperature sensor sensitivity of 0.3 °C. Because the breakdown voltage exhibits a temperature correlation on the order of 0.1 %/°C, for measurements that were done at significantly different temperatures I adjusted the measured value of V_{bd} according to manufacturers data on dV_{bd}/dT.

Uncertainties of measured parameters for samples irradiated by different neutron fluences are dominated by sample-to-sample variability. Due to technical and time reasons, I tested the most SiPMs within the same time span, i.e. already after irradiation, so data before irradiation are mostly based on the measurements done for other samples. The only general exception is I(V) data that was measured for almost all the SiPMs both before and after irradiation.

Depending on the SiPM model and measured characteristics, the standard deviation of the measured parameters for SiPMs of the same type irradiated with the same fluence is in the range of 7 – 30 %, which also confirms the uniformity of the sample irradiation. The only exception is the capacitance, which exhibited variability of the only 1 %. In further sections, I discuss in detail the measurement uncertainties, individually for each measurement type.

I measured the dependencies of various SiPM parameters on the bias voltage and fluence for all the investigated SiPMs (54 irradiated and many non-irradiated) with help of the measurement setup and the Dharma software which I described in previous sections. For voltage dependencies, I chose a 0.1 V voltage step to achieve optimal measurement accuracy, except for I(V) measurement at forwarding bias, where I chose 0.01 V due to the very narrow measurement range. I performed all the data analysis presented in this chapter with help of CERN Root software. It is a C++ based cross-platform open-source data analysis framework used by high-energy physics and others [280]. I made an individual analysis macro for every measurement type, the length of code ranges from 331 up to 1374 lines for my macros (though usually the first half of the code just lists the input data sets). I would like to thank internship student S. Belyavsky from Tomsk Polytechnic University, who under my guidance made the macro for analysis of dark currents versus forwarding bias voltage and determination of the quenching resistance, see subsection 7.6.

7.5 SiPM dark current at reverse bias. Breakdown voltage

Measurement of the dark current is very important for the SiPM characterization because it defines the level of noise and power consumption, and be used for the breakdown voltage determination. In this section I present the main results for the analysis of SiPM dark currents in reverse bias, detailed plots for all the investigated SiPM samples are available in appendix D.

7.5.1 Dark current analysis and breakdown voltage determination

Figure 7.10 presents several measurements of dark current for different SiPMs before and after neutron irradiation. Before irradiation, I_{dark} below the breakdown voltage is almost flat which means that it is dominated by carriers generated at depleted Si-SiO2 interface of SiPM surface. This surface current misses the strong electric field region of a p-n junction, so avalanche amplification does not occur. On contrary, above the breakdown magnitude of the electric field increases rapidly with voltage which produces a huge number of avalanches. One can see that Hamamatsu SiPMs exhibit a sudden step in the dark current just below 30 V which is probably related to full depletion voltage, see figure 7.24 (left) for comparison. A similar effect can be seen for Ketek PM3315-WB-A0 around 5 – 6 V, see figure D.4. After irradiation dark current increases drastically both below and above the breakdown, which indicates that both surface and bulk current increased due to electrically active defects produced in the silicon lattice.

I estimated values of the breakdown voltage by the first derivative method, proposed in [184]. Namely, I found a maximum of the first derivative of the dark current and divided it by the current value, see equation (7.2). Sometimes it is also referred to as logarithmic derivative method since $d\ln(I_{dark})dV_{reverse} = (1/I_{dark}) \times dI_{dark}/dV_{reverse}$. Value of V_{bd} vary by $\pm$ 100 mV depending on the method used to extract it from the curve [161]. In my macro, the maximum is determined with help of the Gaussian fit function. All the calculation is done automatically, and sequence of five fits is performed to find an optimal fit range. The same procedure is described in details in subsection 8.2.7.

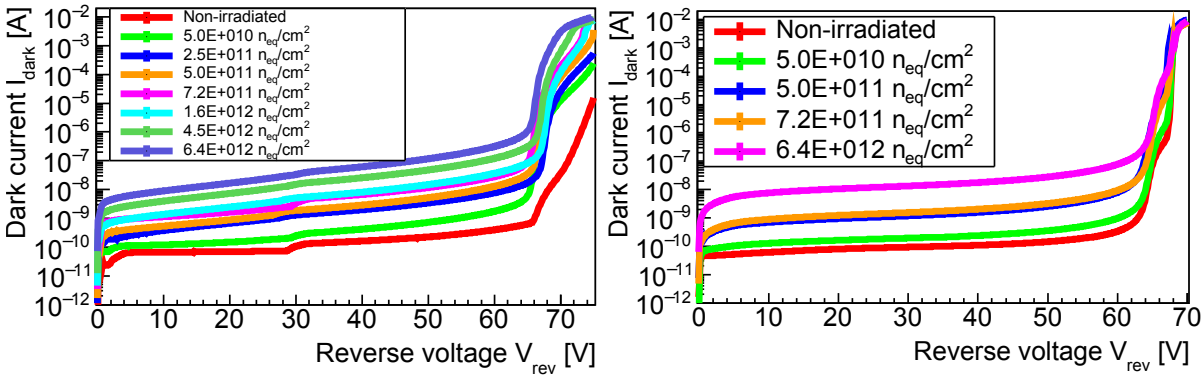

Figure 7.10: Dark current measured as a function of reverse bias voltage for Hamamatsu S12572-010P (left) and Zecotek MAPD-3A (right) SiPMs before and after irradiation with different 1 MeV equivalent neutron fluence.

$$V_{bd} = \max\left(\frac{1}{I_{dark}} \times \frac{dI_{dark}}{dV_{reverse}}\right) \tag{7.2}$$

Before irradiation SiPMs with low dark current have a significant contribution from the non-amplified surface current which results in a very slow dark current increase with voltage, small derivative value and a poor fit, see red curves in figure 7.11. In this case, it is advised to perform an extra current measurement with a slight pulsed or continuous illumination to increase the current and derivative value [161]. I used the continuous light, i.e. I opened the cover of the measurement mini-box a bit. However, it observed slightly different values of V_{bd} depending on the amount of incoming light (opening angle of the box cover). For instance, for non-irradiated Hamamatsu S12572-010P sample N15 I obtained values of V_{bd}: 66.65 ± 0.05 without light, 66.43 ± 0.02 for low light, 66.26 ± 0.02 for medium light, and 66.16 ± 0.01 for high light. To unify my measurements, I used the same medium illumination for all the measurements where the dark current increased slowly, namely for all the non-irradiated SiPMs except for Zecotek MAPD-3A.

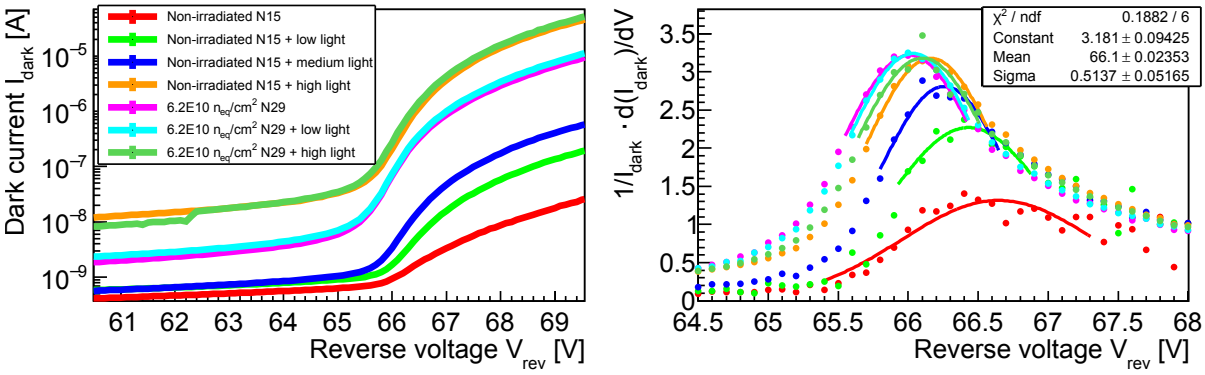

Figure 7.11: Determination of the breakdown voltage for one non-irradiated and one irradiated Hamamatsu S12572-010P SiPMs under different levels of illumination.

I did not encounter such measurement problems for Zecotek MAPD-3A, which were already slightly irradiated during the operation at NA61, as well as for all the SiPMs after irradiation,

see data in appendix D. For them, I determined the breakdown voltage from the dark current measured without illumination. However, I note that V_{bd} slightly varies for irradiated Hamamatsu SiPMs depending on the light level, see figure 7.11. I obtained values of V_{bd}: 66.01 ± 0.01 without light, 66.04 ± 0.01 for low light, and 66.10 ± 0.02 for high light. Also, note that dark current is practically the same for non-irradiated and irradiated SiPMs if measured with high illumination. This means that light-induced carrier generation overcomes the generation due to produced defects. Typical values of the breakdown voltage which I estimated for the investigated SiPMs are summarized in table 7.1.

Figure 7.12 shows the dark current for Hamamatsu S12572-010P SiPMs as a function of overvoltage $V_{ov} = V_{reverse} - V_{bd}$. One can see the dramatic increase of I_{dark} from tens nanoamperes up to milliamperes in the operation region. According to equation (3.15), dependence of I_{dark} on V_{ov} is rather complex, i.e. it can not be described by simple linear or quadratic fit, which can be seen in the figure 7.12 (left).

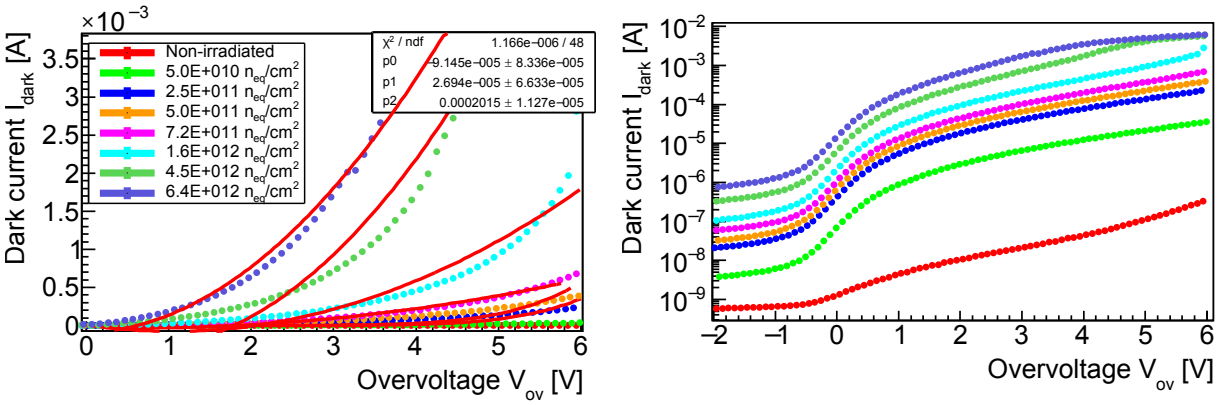

Figure 7.12: Dependence of dark current in linear (left) and logarithmic (right) scale on overvoltage for Hamamatsu S12572-010P SiPMs before and after irradiation. Failed attempts to perform a quadratic fit are visible in (left).

7.5.2 Dependence of dark current on fluence. Effective depletion width

Figure 7.13 shows that the SiPM dark current at fixed overvoltage increases linearly with fluence. This is in agreement with observations presented for regular silicon sensors and SiPMs in subsections 3.4.3 and 3.6.1, respectively.

One can see that the point corresponding to $\Phi_{eq} = 6.4 \times 10^{12}$ n_{eq}/cm^2 is significantly higher compared to the common trend, so I excluded this point from the fit. This is explained by the fact that this SiPM sample was the very first one under investigation, and it was irradiated in several experiments before the final irradiation. Consequently, it achieved higher fluence but at that time fluence was not properly estimated, so its value is unknown. Based on the extracted linear fits and value of its dark current, the actual fluence for this sample is in the range of $(9 - 11) \times 10^{12}$ n_{eq}/cm^2, depending on the overvoltage. Nevertheless, for the simplicity of data comparison with other SiPMs, I will further use the original value of 6.4×10^{12} n_{eq}/cm^2 in this chapter.

Figure 7.14 (left) shows that slope of $I_{dark}(\Phi_{eq})$ function exhibits quadratic dependence on overvoltage. Similar dependencies measured for other SiPMs are shown in figure D.8. Therefore, it is not possible to measure the characteristic slope parameter α based on this data, see description of α for standard silicon sensors in subsection 3.4.3. Another complication arises

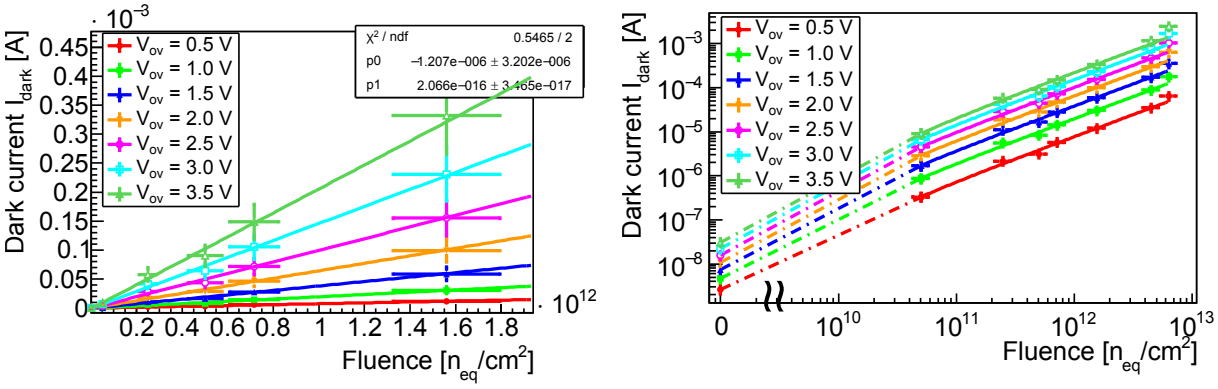

Figure 7.13: Dependence of dark current in linear (left) and logarithmic (right) scale on 1 MeV equivalent neutron fluence at different overvoltages for Hamamatsu S12572-010P SiPMs.

from the fact that α depends on the active sensor volume, i.e. sensor area and active thickness. Furthermore, bulk dark current in SiPMs is amplified by its gain, while standard silicon sensors or PIN diodes do not have any built-in gain.

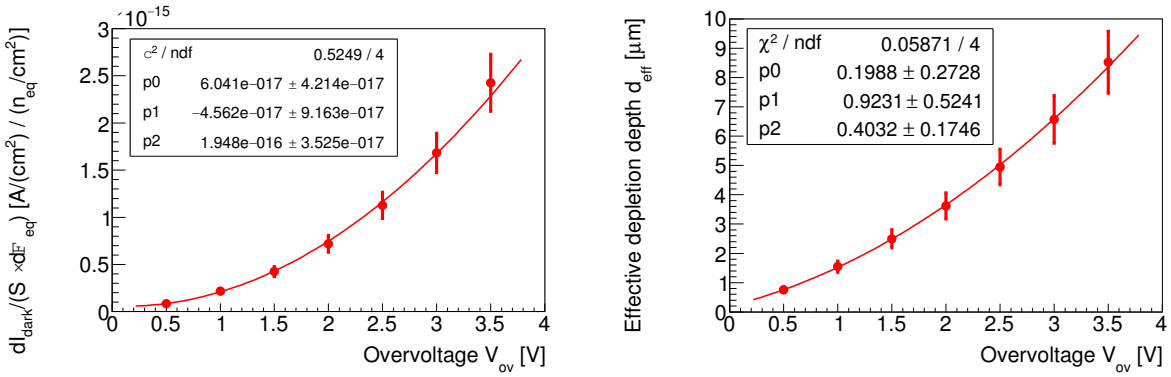

Figure 7.14: Dependence of the $dI/d\Phi_{eq}$ divided by SiPM area (left) and its effective depletion width (right) on overvoltage for Hamamatsu S12572-010P SiPMs after irradiation. Uncertainties are inherited from the linear fitting procedure shown in figure 7.13.

The active thickness of SiPM corresponds to the width of a depletion region where avalanche multiplication of carriers happens. S. Baccaro et al. [314] and Yu. Musienko et al. [315] proposed the term effective depletion width for regular APDs. This is the thickness of a conventional PIN diode required to produce the same charge Q as APD when traversed by a charged particle: $d_{eff} = d_{PIN} \cdot Q_{APD}/(Q_{PIN} \cdot G_{APD})$. Note that the APD signal is divided by its gain. With this approach authors determined $d_{eff}^{APD} \simeq 5-10$ µm at gain = 50, which was about ten times smaller than value of actual depletion width provided by manufacturers. They consequently determined $alpha_{eff}^{APD} = (10-13) \times 10^{-17}$ A/cm after 2 – 3 days of room temperature annealing, which is slightly higher but still within the range of measurements for silicon sensors presented in subsection 3.4.3.

A possible explanation of the quadratic dependence of $I_{dark}(\Phi_{eq})$ slope is the dependence of effective depletion width on overvoltage. Based on the measured gain and assuming *alpha* parameter to be similar to the aforedescribed observations, one may estimate the dependence

of depletion width of SiPM on overvoltage as

$$d_{eff}^{SiPM} = \frac{I_{dark}}{\Phi_{eq} \cdot S \cdot \alpha \cdot G} \tag{7.3}$$

where S is the SiPM area, and G is the SiPM gained defined for non-irradiated SiPMs from the measurement of the single-photon peak described in subsection 7.8.1.

Figure 7.14 (right) shows the results of calculation for effective depletion width for Hamamatsu SiPMs. I calculated gain by equation (3.19), however, it is not entirely clear yet, whether this describes the gain after irradiation correctly, see subsection 3.19 for discussion. I used a value of $\alpha = 3 \times 10^{-17}$ A/cm corresponding to the dark current measured for standard silicon sensors after a year of room temperature annealing which is similar to my situation. M. Danilov et al. [168] used similar method to calculate $d_{eff} = 25$ µm for SiPMs with 32 µm pixel pitch and 1.1×1.1 mm^2 area produced by MEPhI/Pulsar. A. Yu. Musienko and A. Heering et al. [173,182] reported similar data, namely 4 – 50 µm effective depletion width. This is significantly higher than the shallow depletion width of 1 – 2 *um* expected for blue-sensitive p-on-n SiPMs, which have a p-n junction located close to the entrance window [130, 161].

However, in SiPM depletion region does not have an exact border as it slowly grows further into the epitaxial and substrate regions with the increase of bias voltage, see figure 3.20 and discussion in section 7.7.2. Another possible explanation proposed in [173] is that SiPM dark current is significantly enhanced by high electric field effects like phonon-assisted tunneling and field enhanced generation. Further analysis of SiPM internal behavior after irradiation is complicated due to the fact that actual doping profiles are usually kept as a commercial secret by a manufacturer, while DLTS and TSC techniques of defect characterization are not applicable to SiPMs due to large capacitance and high dopant concentration [130]. Therefore, I must note that it is not yet clear whether calculated effective depletion width underlines a physical process in SiPM, or it is just a useful tool for comparison with conventional PIN photodiodes.

7.5.3 Dark current comparison for all SiPMs

Figure 7.15 presents the change of dark current for the investigated SiPM after irradiation by different fluences. Since different SiPMs have significantly different bias voltages, I present I_{dark} in terms of overvoltage. Before irradiation both Hamamatsu SiPMs exhibit the lowest dark current on the order of tens nanoamperes, while Ketek SiPMs with 50 µm pixel pitch exhibit the highest current on the order of microamperes. One can note that Zecotek SiPMs have a second breakdown above $V_{ov} = 3$ V, which increases the current up to tens of microamperes and therefore limits their operation region.

After irradiation with 2.5×10^{11} n_{eq}/cm^2 both Hamamatsu SiPMs with 10 µm pixels show comparable current on the order of 10 – 100 µA, while Ketek PM3315-WB-A0 with 15 µm pixels has an order of magnitude higher current. The fact that the new Hamamatsu S14160-1310PS version has up to 2 times higher I_{dark} than the old Hamamatsu S12572-010P is because the new version was measured after only 2 months after irradiation, while the old one was stored for more than 2 years and undergone more annealing. See subsection 3.6.8 for details on SiPM annealing. SiPM dark current reaches milliampere region for all SiPMs after irradiation with $7.2 \times 10^{11} - 6.4 \times 10^{12}$ n_{eq}/cm^2 which makes them barely applicable for experiments. SiPMs with pixel pitch ≥ 29 µm reach 1 mA already after 7.2×10^{11} n_{eq}/cm^2 and below $V_{ov} = 1$ V, while for SiPMs with pixel pitch ≤ 10 µm this happens only after irradiation with 6.4×10^{12} n_{eq}/cm^2 and above $V_{ov} = 2$ V.

Figure 7.15 shows the dependence $I_{dark}(\Phi_{eq})$ for all the investigated SiPMs. At higher fluences, several SiPMs reached a 10 mA level already above $V_{ov} = 1$ V, which resulted in the

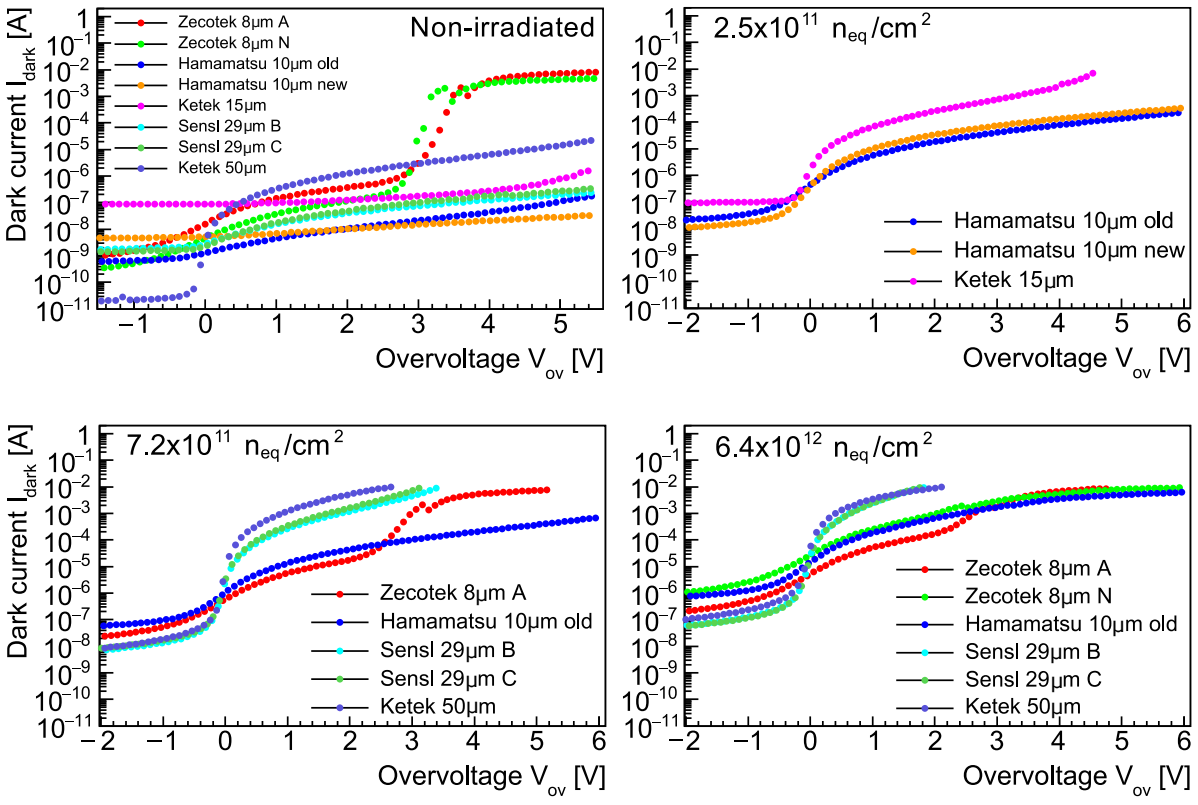

Figure 7.15: Dependences of the dark current on overvoltage for different SiPMs before (top left) and after irradiation with 2.5×10^{11} n_{eq}/cm^2 (top right), 7.2×10^{11} n_{eq}/cm^2 and 6.4×10^{12} n_{eq}/cm^2 (bottom right).

saturation of measured current due to the limit of Keithley 6517A Electrometer. Therefore, I present the current-fluence dependence only at an overvoltage of 1 V. More detailed current data for all the investigated SiPMs are available in appendix D. There one can also find calculated dependences of the $dI/d\Phi_{eq}$ divided by SiPM area and its effective depletion width on overvoltage. However, I must once again note that the change in effective depletion width does not necessarily represent a real physical process but is probably rather a helpful estimation tool.

One can see that dark current scales with the pixel pitch, i.e. the larger the pixels – the larger is the I_{dark}. Furthermore, slope of $I_{dark}(\Phi_{eq})$ is steeper for SiPMs with larger pixels. Data in table 7.2 shows that dark current increases approximately 10 times faster for SiPMs with $\geq$ 15 µm pixels compared to SiPMs with $\leq$ 10 µm pixels irradiated with the same fluence. This is comparable with values of $dI_{dark}/(S\cdot d\Phi_{eq})$ in range of $10^{-9}-10^{-6}$ $\mu A/cm^2/[n_{eq}/cm^2]$ reported for SiPMs with 35 – 50 µm pixels at nominal overvoltage (typically 3 – 4 V) in literature [169, 171, 175, 178, 201].

Table 7.2 also summarizes the maximal changes in SiPM breakdown voltage after irradiation with maximal fluence. On can see quite significant increase in V_{bd} of 0.45 – 0.89 V for SiPMs with high breakdown voltage after the highest irradiation up to 6.4×10^{12} n_{eq}/cm^2. Although this is a shift by only 0.7 – 1 %, it can be crucial for the sensor operation. SiPMs with low breakdown voltage exhibited only very small shifts of 0.05 – 0.18 V (0.2 – 0.5 %) which can be at least partially attributed to measurement uncertainties. Observed results are in agreement with data presented in the literature, see subsection 3.6.3. Based on this data I estimated that Zecotek

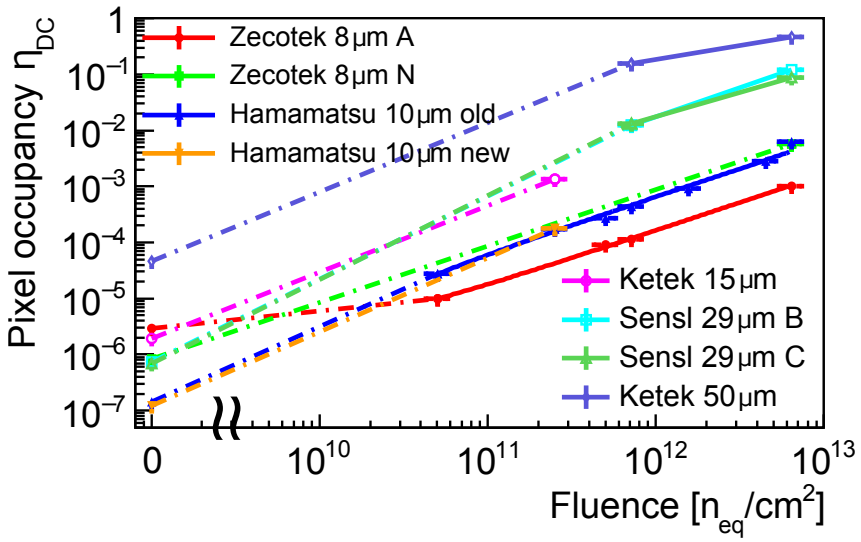

Figure 7.16: Dependences of the dark current on 1 MeV equivalent neutron fluence SiPMs with different pixel pitch measured at fixed overvoltage = 1 V. Note the linear fits for Hamamatsu S12572-010P and Zecotek MAPD-3A.

	Zecotek MAPD		Hamamatsu MPPC		Ketek SiPM PM33		Sensl SiPM	
	3A	3N	S12572 -010P old	S14160 -1310PS new	15 -WB-A0	50	B-series 30020	C-series 30020
Pitch, µm	8	8	10	10	15	50	29	29
Φ_{eq}^{max}, n_{eq}/cm^2	6.4×10^{12}	6.4×10^{12}	6.4×10^{12}	2.5×10^{11}	2.5×10^{11}	6.4×10^{12}	6.4×10^{12}	6.4×10^{12}
ΔV_{bd}^{max}, V	+0.57	+0.89	+0.45	-0.18	-0.07	+0.05	-0.08	+0.06
$dI_{dark}/(S \cdot d\Phi_{eq})$								
at 1 V	8.5×10^{-11}	4.6×10^{-10}	2.2×10^{-10}	4.0×10^{-10}	3.2×10^{-9}	4.6×10^{-9}	4.5×10^{-9}	3.6×10^{-9}
at 2 V	2.8×10^{-10}	1.7×10^{-9}	7.2×10^{-10}	1.4×10^{-9}	1.2×10^{-8}	1.5×10^{-8}	1.9×10^{-8}	2.47×10^{-8}
at 3 V	–	–	1.7×10^{-9}	3.1×10^{-9}	3.4×10^{-8}	–	–	–
$(\mu A/cm^2)/(n_{eq}/cm^2)$								

Table 7.2: Changes in SiPM parameters extracted from dark current measurements after irradiation, including maximal observed shifts of the breakdown voltage after irradiation and relative increase of the dark current divided by SiPM area per fluence at two different overvoltages. Data is available at an overvoltage of 3 V only for SiPMs with low dark currents due to the Electrometer current limit. Note that linear slopes of $dI_{dark}/d\Phi_{eq}$ were unambiguously determined only for Hamamatsu S12572-010P and Zecotek MAPD-3A based on 4 and 6 fluence points, respectively. For Sensl B30020, Sensl C30020, and Ketek PM33-50 they are based only on 2 fluence points which are not enough for an accurate linear fit. For other SiPMs where only single irradiation took place, I just divided the value of I_{dark} by the value of Φ_{eq}.

MAPD-3A samples which were operated at NA61 PSD for several years probably achieved a fluence in the range of $1.4 - 1.8 \times 10^{10}$ n_{eq}/cm^2.

7.5.4 Uncertainty estimation

I assessed the measurement uncertainties based on the sample-to-sample variability for SiPMs of the same type irradiated with the same fluence. Figure 7.17 shows that in general SiPMs exhibit relatively low variability both before and after irradiation. Similar data for other SiPMs are presented in appendix D. For instance, at overvoltage of 1 V standard deviation of I_{dark} for different samples is on the order of 5 – 15 %. However, there are several exceptions. Samples of Zecotek MAPD-3A before irradiation $\sigma = 26$ % because they were operated at NA61 experiment in CERN before my studies, and achieved some low damage there, which is different for each sample depending on its position in the detector. However, after uniform irradiation σ was reduced to 10 – 15 % for them, see figure D.10. Sensl SiPMs are another exception with extremely high dark current variations before irradiation on the order of 40 – 70 %, probably due to process instabilities during the manufacturing, see figure D.12. To mitigate this and to improve the data consistency, I used samples Sensl B30020 №5 and Sensl C30020 №4 which exhibited very similar I_{dark} with $\sigma = 7$ % before irradiation. As expected, dark currents of other samples became very similar after irradiation, see data for Sensl B30020 and C30020 in figure 7.15.

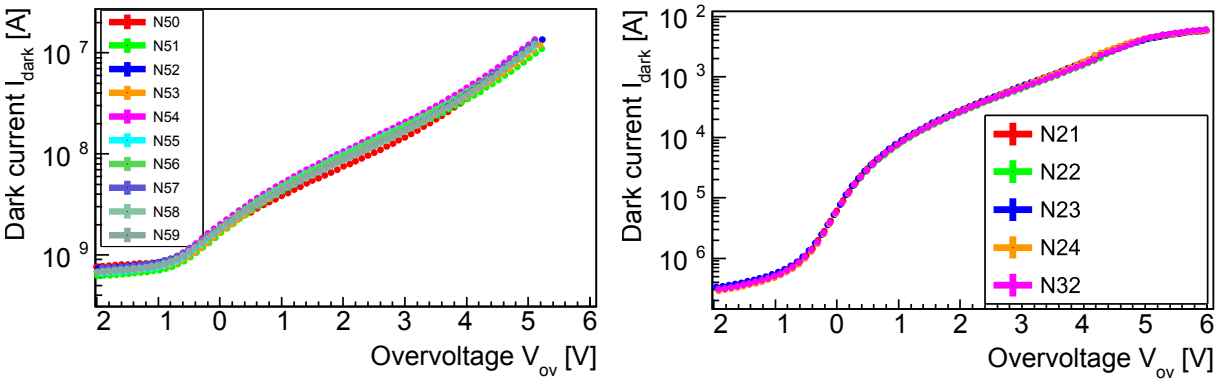

Figure 7.17: Dark current variability for Hamamatsu S12572-010P SiPMs before (left) and after irradiation by 4.5×10^{12} n_{eq}/cm^2 (right).

Dark current measurements were performed at room temperature of 24 ± 1 °C. Dark current strongly increases with temperature for any silicon sensor, including SiPMs, see sections 3.4.3 and 3.6.1. For SiPMs it was observed that dI_{dark}/dT decreases from 9 – 11 %/°C before down to 4 – 6 %/°C after irradiation. However, comprehensive data on the change of dI_{dark}/dT with fluence does not yet exist, so there is no straightforward way to compensate for this effect. Therefore, it can be considered as a part of the overall measurement variability presented above.

Breakdown voltage also increases with temperature, typically by 0.1 % per °C. Data provided by SiPM manufacturers are: 80 mV/°C for Zecotek MAPD-3N [316], 60 mV/°C for Hamamatsu S12572-010P [155], 34 mV/°C for Hamamatsu S14160-1310PS [155], 22 mV/°C for Ketek PM3315-WB-A0 [153], 18 mV/°C for PM3350 [153] and 21.5 mV/°C for both Sensl SiPMs [152]. Since no data are available for Zecotek MAPD-3A, I assume it to be 0.09 %/°C or 58 mV/°C, similar to other SiPMs with high breakdown voltage. Note that no change in dV_{bd}/dT after irradiation was observed in currently the only study performed on this matter by S. Cerioli et al. [193].

Breakdown voltage stability is particularly important for dark current and signal response measurements. In case of I_{dark} measurements shown in figure 7.16 at overvoltage of 1 V, tem-

perature increase by ±1 °C results in V_{bd} shift by 20 – 80 mV/°C leading to up to 10 % increase in I_{dark}. Since I used a voltage step of 100 mV in my measurements, I can not easily compensate for this effect, so I consider it as a part of the overall measurement variability. In the case of signal and noise data presented in section 7.8, I introduced the V_{bd} corrections to compensate for higher V_{bd} shifts.

In summary, the measurement uncertainty of dark current is dominated by the sample variability which is on the order of 5 – 15 %, and temperature-induced variations of current and breakdown voltage below 11 % and 10 %, respectively. Therefore, total uncertainty is generally below 21 %. The uncertainty introduced by the accuracy of current measurement, which is 0.1 – 1 %, is negligible. In view of the dark current increase by many orders of magnitude after irradiation, this does not pose a problem for data interpretation.

The precision of breakdown voltage estimation for every sample is determined by the voltage setting precision which is on the order of 10 – 30 mV, consistency of light illumination for non-irradiated samples which is on the order of 10 – 30 mV, and accuracy of Gaussian fit which is on the order of 10 – 20 mV, see figure 7.11. Therefore, the total uncertainty of V_bd estimation is below 50 mV, which is two times lower than the voltage step which I used for the measurements.

7.6 SiPM dark current at forward bias. Quenching resistance

Measurement of the dark current when SiPM is forward-biased provides a possibility to determine its quenching resistance. In this section, I present the main results for the analysis of SiPM dark currents in forwarding bias, detailed plots for all the investigated samples are available in appendix E.

7.6.1 Dark current analysis and quenching resistance determination

Figure 7.18 presents several measurements of dark current for forward-biased SiPMs for different SiPMs before and after neutron irradiation. Since the p-n junction is opened in this regime, the current increases very quickly with an increase in voltage and reaches the 10 mA limit of the electrometer already around voltage of 1 V. One can see that after irradiation the rapid current increase starts earlier and the limit is reached by 0.1 – 0.2 V earlier as well. This is again due to the electrically active defects produced in the silicon lattice by irradiation, which increases the thermal carrier generation.

When built-in voltage is exceeded, the dependence of forwarding current on voltage becomes a straight line whose slope represents the bulk resistance. I extracted values of quenching resistance from these measurements with help of the first derivative of the dark current with respect to forward voltage as

$$R_q = N_{pix}/(dI_{dark}/dV_{forw}) \tag{7.4}$$

In figure 7.18 one can see that the slope depends on the fit range, so the derivative approaches, but does not reach a constant value. Therefore, the closest fit is achieved in the very last region below the current limit. I estimated (dI_{dark}/dV_{forw}) for each curve by linear fit in the region of the last 0.15 V below the current limit. To achieve the best precision, I used the voltage step of 0.01 V for the measurements, which resulted in 15 measurement points in the fit area.

Figure 7.19 shows the change in the quenching resistance after irradiation for different SiPMs. One can see that no change is visible for Zecotek MAPD-3A, but increase up to 25 % for some samples of Hamamatsu MPPC S12572-010P above 2.5×10^{11} n_{eq}/cm^2 can be seen. I investigated multiple non-irradiated and irradiated samples of Hamamatsu MPPC S12572-010P, and conclude

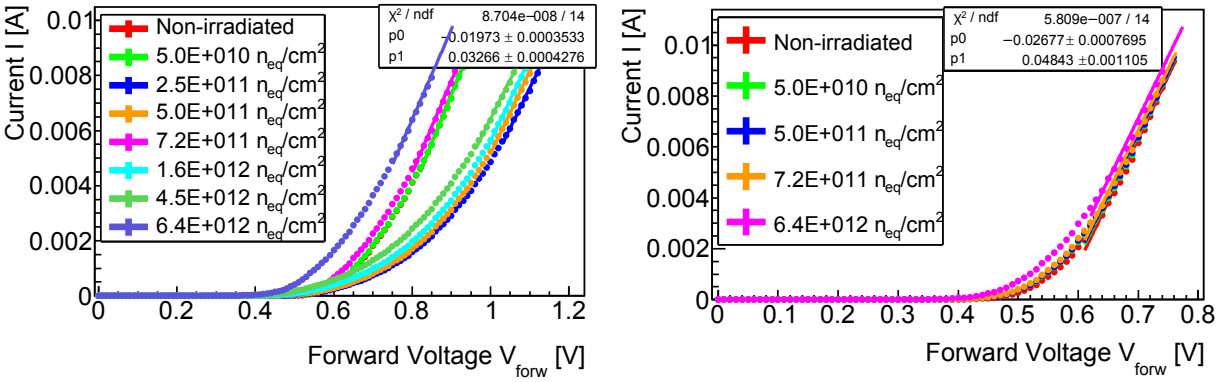

Figure 7.18: Dark current measured as a function of forwarding bias voltage for Hamamatsu S12572-010P (left) and Zecotek MAPD-3A (right) SiPMs before and after irradiation with different 1 MeV equivalent neutron fluence.

that it is most likely caused by the fact that I used SiPMs produced in different batches, so they had initially different R_q. Namely, samples which received fluences of 0, 5×10^{10} n_{eq}/cm^2, 7.2×10^{11} n_{eq}/cm^2 and 6.4×10^{12} n_{eq}/cm^2, were purchased and studied a few years before the samples which received fluences of 2.5×10^{11} n_{eq}/cm^2, 5×10^{11} n_{eq}/cm^2, 1.6×10^{12} n_{eq}/cm^2 and 4.5×10^{12} n_{eq}/cm^2. This is also confirmed by the fact that SiPMs which were purchased later had the breakdown higher by about 1.5 V.

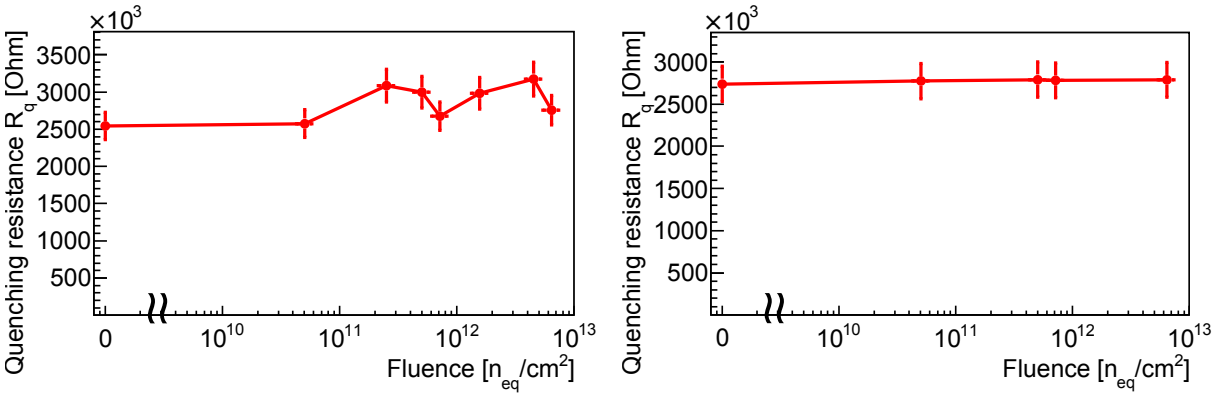

Figure 7.19: Values of quenching resistance extracted from the dark current curves as a function of 1 MeV equivalent neutron fluence for Hamamatsu S12572-010P (left) and Zecotek MAPD-3A (right) SiPMs.

7.6.2 Quenching resistance comparison for all SiPMs

Figure 7.20 shows the relative change in the quenching resistance after irradiation for all the investigated SiPMs. No change is observed below 2.5×10^{11} n_{eq}/cm^2, which is consistent with findings of other studies reviewed in subsection 3.6.4. Typical absolute values of R_q before irradiation can be found in table 7.1.

Increase by up to 40 % is visible for several SiPMs above 2.5×10^{11} n_{eq}/cm^2. However, only a non-irradiated sample of Sensl B30200 №5 was measured before the irradiation and it exhibited

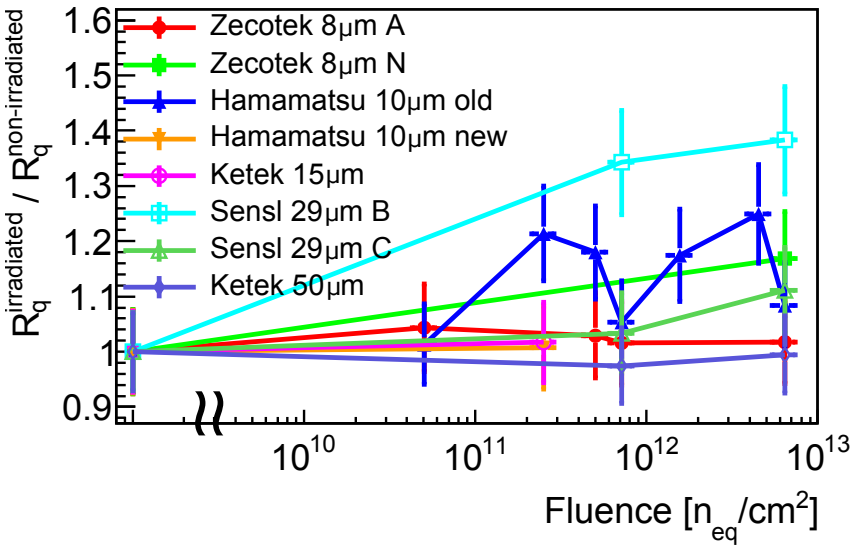

Figure 7.20: Relative change in quenching resistance for different irradiated SiPMs with respect to the values obtained for non-irradiated SiPMs, presented as a function of 1 MeV equivalent neutron fluence.

a much lower dark current at the reverse bias than samples №2 and №4 which were irradiated, which I mentioned in subsection 7.5.3. Due to technical reasons, I measured irradiated samples only after irradiation, so they might just have higher R_q already before irradiation. The situation is similar for Zecotek MAPD-3N, i.e. only single non-irradiated and single irradiated sample were measured. And the last, I elaborated on the Hamamatsu SiPMs in the previous subsection. Similar increase of R_q up to 20 – 50 % above 10^{11} n_{eq}/cm^2 was reported by group of S. Ceriloli and M. C. Vignali [193, 194], see figure 3.33. However, authors also indicate that it can be explained by initially different R_q values in different SiPM samples, e.g. by sample-to-sample variability. Therefore, I conclude that no change in the quenching resistance was observed.

7.6.3 Uncertainty estimation

I assessed the measurement uncertainties based on the sample-to-sample variability for SiPMs of the same type irradiated with the same fluence. Figure 7.21 shows an example of dark current variation at forwarding bias before and after irradiation. In most cases before and after irradiation the curves are really close to each other except for the several samples of Hamamatsu S12572-010P and Ketek PM3315-WB-A0 which exhibit really different trends of $I_{dark}(V_{forw})$, probably due to process variations during the manufacturing, see figures 7.21 (left) and E.5. Nevertheless, even for these samples, it results in $\sigma(R_q)$ of only 4.5 – 8.5 %, while in the case of close curves variability of R_q is in the range of 0.5 – 2.5 %. To improve the consistency of the results, I excluded the most deviated samples from the comparison.

Dark current measurements were performed at room temperature of 24±1 °C. Although dark current strongly increases with temperature which resulted in significant variations of I_{dark} with temperature as was mentioned in subsection 7.5.4, it does not affect the quenching resistance as much. For instance, N. Otte determined dR_q/dT coefficients in the temperature range of -40 °C – +40 °C for SiPMs produced by Hamamatsu, Sensl and FBK as 0.2 %/°C, 0.25 %/°C and 0.5 %/°C, respectively. Therefore, I consider the temperature dependence of R_q to be negligible for the room temperature operation.

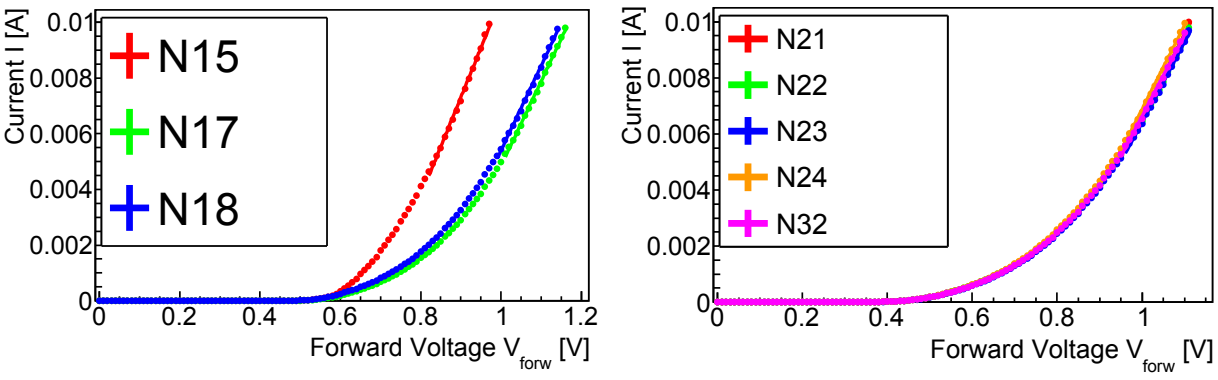

Figure 7.21: Variability of dark current in forward bias for Hamamatsu S12572-010P SiPMs before (left) and after irradiation by 4.5×10^{12} n_{eq}/cm^2 (right).

In summary, the uncertainty of R_q measurement is composed of the sample variability which is on the order of 0.5 – 5 % for most samples, and accuracy of the linear fit which is on the order of 1 – 5 %, see figure 7.18. The uncertainty introduced by the accuracy of current measurement, which is 0.1 % for currents above 2 μA, is negligible. Therefore, total uncertainty is estimated to be below 7 %. Although, I must note that values of quenching resistance obtained from dI_{dark}/dV_{forw} are usually by 5 – 30 % higher than values obtained from impedance measurements, see figure 3.33 (right), and there is yet no understanding which value is correct.

7.7 Capacitance measurements

Measurement of the capacitance can be used to obtain the value of pixel capacitance for SiPM, and estimate its gain even after irradiation when single photons are not resolvable due to noise. In this section, I present the main results for the analysis of SiPM dark currents in forwarding bias, detailed plots for all the investigated samples are available in appendix F.

7.7.1 SiPM capacitance versus frequency. Pixel capacitance, gain

I measured the SiPM capacitance with the LCR-meter in parallel mode with the test signal amplitude of 500 mV. The acquired value of complex admittance is expressed in terms of can be presented in terms of parallel resistance R_{par} and capacitance C_{par} as

$$Y(f) = \frac{1}{R_{par}(f)} + j\omega C_{par}(f) \tag{7.5}$$

According to equations 3.14 and neglecting the parasitic components, total SiPM admittance can be expressed as

$$Y(tot) = N_{tot} Y_{pix} = N_{tot} \cdot \left[\frac{1}{j\omega C_{pix}} + \frac{1}{R_q^{-1} + j\omega C_q} \right]^{-1} \tag{7.6}$$

For intermediate frequencies it's capacitive component is dominated by the diode capacitance C_{pix}, i.e. $C_{par} \approx N_{tot} \cdot C_{pix}$. At high frequencies quenching capacitance starts to dominate because $\omega C_q \gg 1/R_q$, so $C_{par} \approx N_{tot}(1/C_{pix} + 1/C_q)^{-1}$ [161].

Since we are interested in the capacitance during the operation, it is generally advised to conduct the measurement as close as possible to the breakdown, e.g. 0.5 or 1 V below V_{bd}. Though

depletion region thickness may grow also above the breakdown, direct impedance measurement in this region is generally difficult [157].

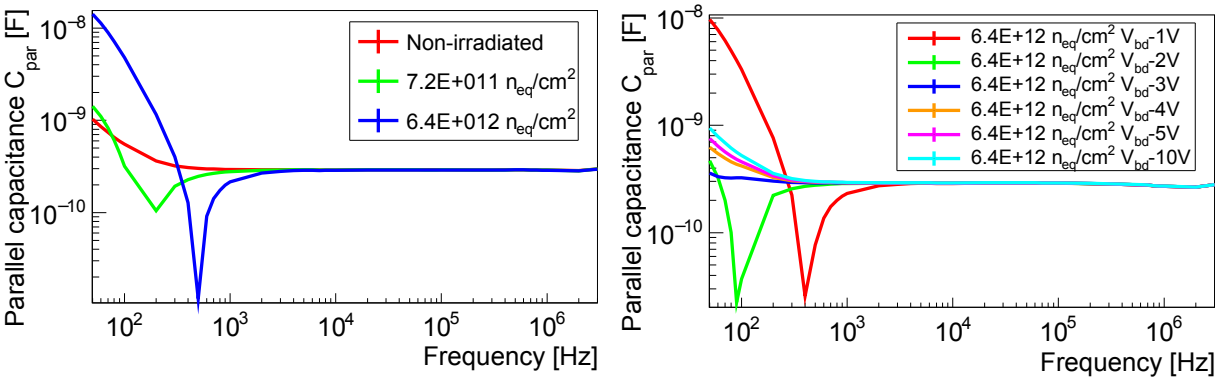

Figure 7.22: (left) Parallel capacitance measured as a function of frequency for Hamamatsu S12572-010P SiPMs at $V_{bd} - 1$ V before and after irradiation with different 1 MeV equivalent neutron fluence. (right) Same measurements for SiPM irradiated by 4.5×10^{12} n_{eq}/cm^2 at different voltages below the breakdown. Frequency step is automatically chosen so, that there are 10 steps per decade.

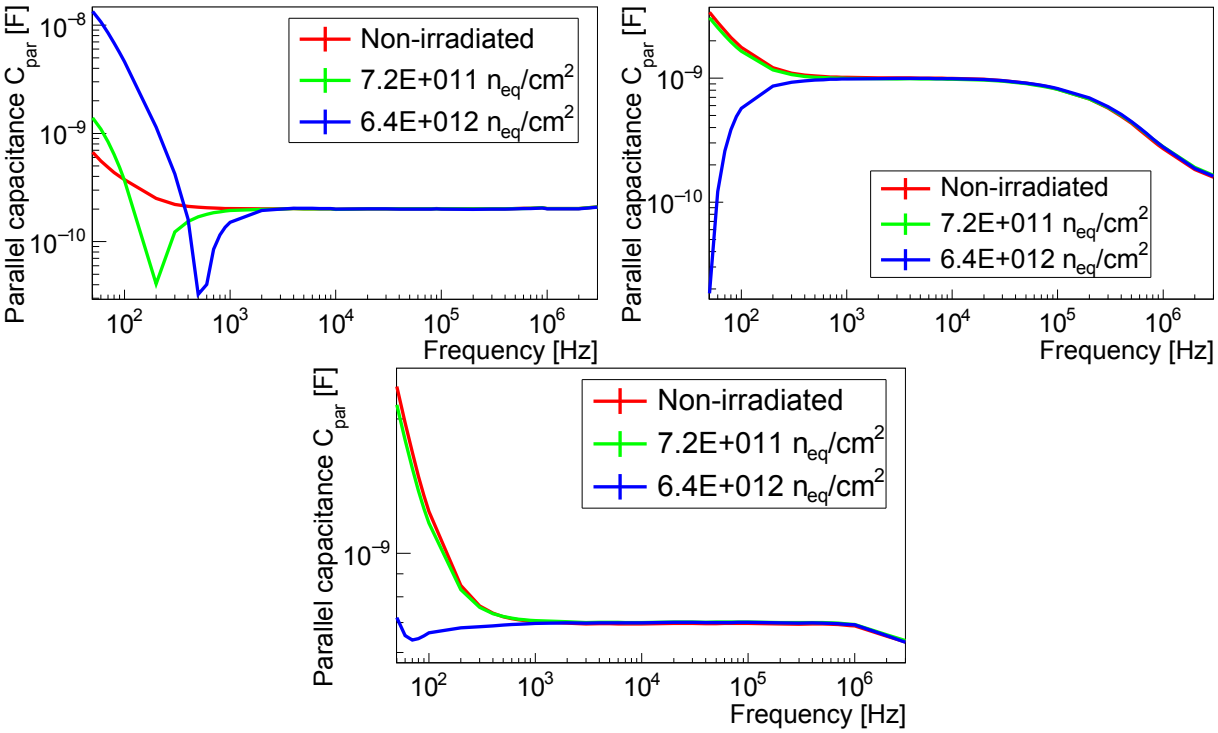

Figure 7.23: Parallel capacitance measured as a function of frequency for different SiPMs at $V_{bd} - 1$ V, before and after irradiation with different 1 MeV equivalent neutron fluence. The frequency step is automatically chosen so, that there are 10 steps per decade.

Figure 7.22 (left) shows an example measurement of parallel capacitance versus frequency for Hamamatsu SiPMs before and after neutron irradiation which was performed with SiPMs biased

at $V_{bd} - 1$ V. One can see significant distortions at frequencies below 2 kHz after irradiation. Figure 7.22 (right) shows that these distortions cease with the decrease of reverse voltage. Therefore, they are probably related to electrically active defects produced near the depletion region, which become activated at higher voltages when the value of the electric field in SiPM reaches certain values. The fact that they are visible only at low frequencies can be explained by the assumption that they have relatively long lifetimes on the order of milliseconds. Two other studies by E. Garutti et al. [317] and M. Nitschke [191] reported changes of capacitance at low frequencies was published after irradiation with X-rays, but again no exact explanation for this effect exists. Therefore, further investigations and possibly model simulations with help of SPICE and/or TCAD are required to achieve a detailed understanding of this effect, which is beyond the scope of this thesis.

Figure 7.23 shows that aforementioned distortions also appear for other SiPMs. Nevertheless, above 1 – 5 kHz they always cease. Interestingly, for SiPMs with low overvoltage and small pixel count, they occur only after $\Phi_{eq} = 6.4 \times 10^{12}$ n_{eq}/cm^2, which might be connected to the differences in radiation hardness of different SiPMs. Also, one can see that for those SiPMs at high frequencies quenching capacitance starts to play a significant role, because they have relatively low quenching resistance. Therefore, one can conclude that capacitance value is very stable at a frequency of 10 kHz where all the aforementioned effects do not play a role. This frequency is generally recommended for measurements of the sensor capacitance, see e.g documents by RD50 collaboration [125], so I performed further measurements at this frequency.

7.7.2 SiPM capacitance versus voltage. Pixel capacitance

Figure 7.24 presents two example measurements of parallel capacitance versus reverse voltage for Hamamatsu and Ketek SiPMs before and after neutron irradiation which was performed at 10 kHz. For Hamamatsu S12572-010P one can see an abrupt step down in capacitance around 26 – 28 V which indicates that the active region became (almost) fully depleted. However, based on the very slow but still noticeable capacitance decrease above this border, one can conclude that the active region widens further. This effect is even more pronounced for SiPMs with small operating voltage like Ketek PM3350 shown in figure 7.24 (right), which means that their p-n junctions are much less abrupt and slowly extend with the voltage increase. Some of them also show subtle border effects, like Ketek PM3315-WB-A0 which has a little capacitance step around 5 – 6 V, see figure F.2 (bottom).

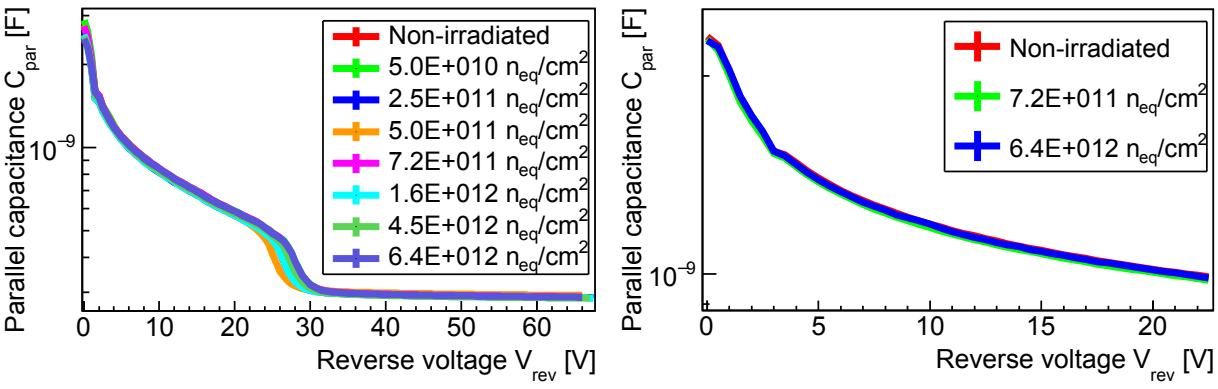

Figure 7.24: Parallel capacitance measured as a function of bias voltage for Hamamatsu S12572-010P (left) and Ketek PM-3350 (right) SiPMs at 10 kHz, before and after irradiation with different 1 MeV equivalent neutron fluence.

One can see that there is virtually no change in the value of the measured capacitance. The only exclusion is the depletion region width of the Hamamatsu S12572-010P SiPMs, however, this is most probably related to the sample-to-sample variability, see figure 7.28.

I also checked the effect of the different amplitude of the test signals. Figure 7.25 shows that no significant difference can be observed between the 50 mV and 500 mV signals used for the measurements.

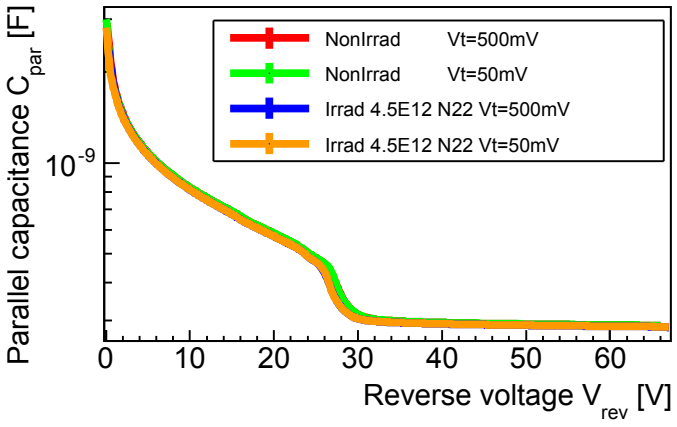

Figure 7.25: Parallel capacitance measured as a function of bias voltage for Hamamatsu S12572-010P before (left) and after irradiation with 4.5×10^{12} n_{eq}/cm^2. Test signals of 50 mV and 500 mV amplitudes were used for the comparison.

Based on acquired data I calculated the value of pixel capacitance from parallel capacitance as $C_{pix} \approx C_{par}/N_{pix}$ measured at $V_{bd} - 1$ V at 10 kHz. Here it is usually assumed that the change of C_{par} above V_{bd} is not too big compared to a value below V_{bd}. Figure 7.26 shows that the change in C_{pix} after irradiation estimated with this method is negligible.

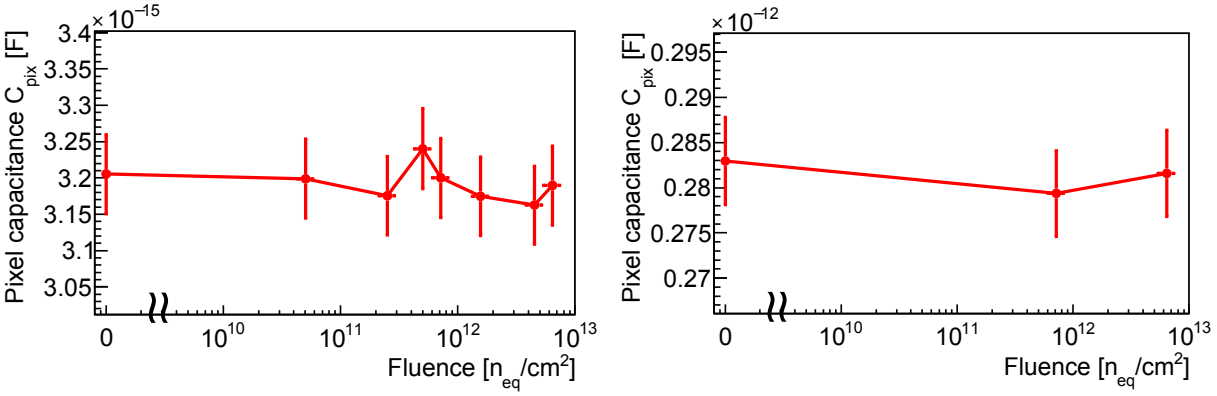

Figure 7.26: Pixel capacitance measured as a function of 1 MeV equivalent neutron fluence for Hamamatsu S12572-010P (left) and Ketek PM-3350 (right) SiPMs.

7.7.3 Pixel capacitance and gain comparison for all SiPMs

Figure 7.27 shows that that pixel capacitances did not change after the irradiation for most SiPMs. Only for Zecotek MAPD-3N C_{pix} increased by 3 % which is comparable to the typical

uncertainty of 1.7 %. Moreover, this uncertainty is based on the variability of other samples, while only single irradiated and single non-irradiated Zecotek MAPD-3N samples were investigated, therefore their variability might be higher.

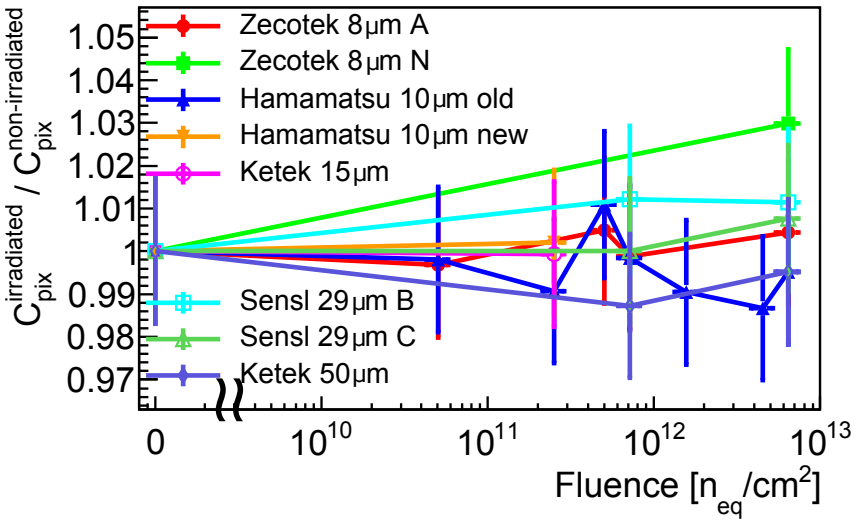

Figure 7.27: Relative change of pixel capacitance after irradiation as a function of 1 MeV equivalent neutron fluence for all the investigated SiPMs. Capacitance was measured at V_{bd}-1 V and 10 kHz.

According to equation (3.19) SiPM gain is defined as $G(V_{rev}) \approx (C_{pix}+C_q)\cdot(V_{rev}-V_{off})/q_0$, where quenching capacitance C_q is typically an order of magnitude lower than C_{pix} [161]. Based on that one might expect that SiPM gain did not change after irradiation as well as C_{pix}. However, this is based on assumptions that capacitance above the breakdown does not change significantly from the capacitance below the breakdown, and that V_{off} only slightly changes after irradiation similarly to V_{bd}. Neither of those is known as a fact. Furthermore, distortions observed at low frequencies are also not understood yet.

7.7.4 Uncertainty estimation

I assessed the measurement uncertainties based on the sample-to-sample variability for SiPMs of the same type irradiated with the same fluence. Figure 7.28 shows that SiPMs exhibit very low variability of the capacitance both before and after irradiation. Similar data for other SiPMs are presented in appendix F. The standard deviation of C_{pix} estimated for different samples is on the order of 0.05 – 1 %.

Capacitance measurements were performed at room temperature. Since capacitance is executed to depend only mildly at all on temperature as elaborated in subsection 3.4.4 for silicon sensors, I did not strive to perform the measurements in the same conditions. In the end, different measurements were performed in the temperature range of 23 – 28 °C. N. Otte determined dC_{pix}/dT coefficients in the temperature range of -40 °C – +40 °C for SiPMs produced by Hamamatsu, Sensl and FBK as 0.014 %/°C, 0.05 %/°C and 0.013 %/°C, respectively. The trend was convincing only for Sensl SiPMs, for FBK and Hamamatsu capacitance rather randomly oscillated around the mean value. Therefore, I consider the temperature dependence of R_q to be negligible for room temperature operation. S. Cerioli et al. also observed virtually no change of capacitance with for measurements at -30 °C and 20 °C before and after irradiation. Therefore, I consider the temperature dependence of C_{pix} to be negligible for the room measurements.

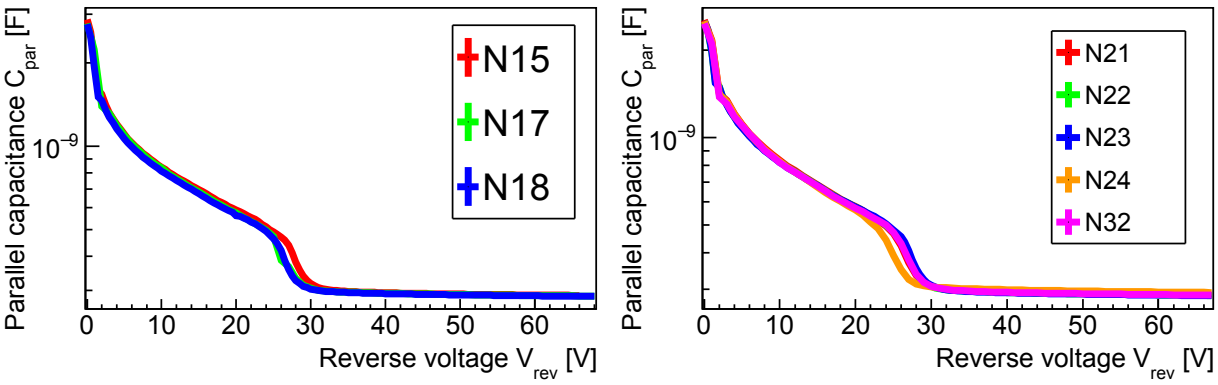

Figure 7.28: Variability of parallel capacitance for Hamamatsu S12572-010P SiPMs before (left) and after irradiation by 4.5×10^{12} n_{eq}/cm^2 (right).

The breakdown voltage shifts significantly with temperature variations, i.e. shift of 100 – 400 mV can be expected for 5 °C variation, see subsection 7.5.4 for temperature coefficients of different SiPMs. However, since capacitance below the breakdown decreases very slowly, this could result in only up to 1 % variation.

In summary, the uncertainty of C_{pix} measurement is composed by the sample variability which is on the order of 0.05 – 1 % for the most samples, accuracy of the LCRmeter which is below 1 %, and possible variations due to temperature changes also below 1 %. Therefore, total uncertainty is estimated to be below 1.7 %.

7.8 SiPM response to LED

The most important during the characterization is to evaluate SiPM's ability to serve as a photodetector after the irradiation. In this section I present the main results for the analysis of SiPM response to LED, detailed plots for all the investigated SiPM samples are available in appendixes G and H.

7.8.1 Single-photon detection with SiPMs. Gain

One of the greatest SiPM qualities is the ability to detect light on a single-photon level. I exposed different SiPMs to very low light levels to demonstrate their ability to distinguish single photons. I measured the response to light as an area integral of SiPM signal pulse with fixed window gate, result is therefore expressed in nV·s. Gate width was chosen individually for every SiPM to contain the pulse only to reduce the amount of integrated noise. For SiPMs with pixels $\leq$ 15 µm produced by Hamamatsu, Ketek and Zecotek are were about 20 – 50 ns, for SiPMs with pixels $\geq$ 29 µm produce by Ketek and Sensl it was 80 – 100 ns since they have higher gains and longer pulse shapes.

Figure 7.29 presents an example of measurement for non-irradiated Hamamatsu SiPM. One can see that peaks corresponding to single photons are clearly visible on the spectrum. Peak near 0 nV·s on the right is produced by the noise, and other peas to the left correspond to 1 photoelectrons, 2 photoelectrons, 3 photoelectrons, etc., respectively.

Measurement of the distance between single-photon peaks allows determining the SiPM gain according to

Figure 7.29: Waveform and collected spectrum of response to very low illumination by UV LED measured for Hamamatsu MPPC S12572-010P before irradiation. Signal from the SiPM is connected to Channel 2 (green) and trigger from the pulser is connected to Channel 3 (orange). Scale of horizontal axis is 20 ns/div, vertical is 40 mV/div for signal and 1 V/div for trigger. Measurement histogram on the bottom has horizontal axis with 0.47 nV·s/div, vertical axis shows arbitrary values due to oscilloscope software bug. Overvoltage is 3 V.

$$G = \frac{Q_{1p.e.}}{e} = \frac{\int I_{1p.e.}(t)dt}{e} = \frac{\int V_{1p.e.}(t)dt}{R_{input} \cdot G_{amplifier} \cdot e} \tag{7.7}$$

where $\int V_{pulse}(t)dt$ is the area integral of the signal at oscilloscope, $G_{amplifier}$ is the amplifier gain = 230, R_{load} is the oscilloscope input impedance = 50 Ω, and e is the electron charge.

I measured the SiPM single-photon spectra for different SiPMs before irradiation at different overvoltages in the range of 0.5 – 2 V or 1 – 4 V to achieve the dependence of SiPM gain on overvoltage. An example of this measurement is presented in figure 7.30 (top left). Every peak is fitted by the Gaussian function, then mean values are plotted versus a number of photoelectrons as shown in figure 7.30 (top right). Resulted in curves for different overvoltages are fitted by linear function to obtain $dQ/dN_{p.e.}$ which is exactly the charge produced by a single photon. It is used to calculate the gain by equation (7.7) at different values of overvoltage. Finally, it is again fitted by linear function to obtain the dependence of gain on overvoltage dG/dV_{ov} as shown in figure 7.30 (bottom). Typical values of dG/dV_{ov} for different SiPMs are presented in table 7.1.

This measurement also allows to estimate the difference between the breakdown voltage (voltage at which avalanche turns on) and offset voltage (voltage at which avalanche turns off), see subsection 3.6.3 for discussion. By a convention proposed by V. Chmill et al. [220], I determined V_{bd} from the bending point of $I(V_{reverse})$ curve, see subsection 7.5.1. V_{off} is defined

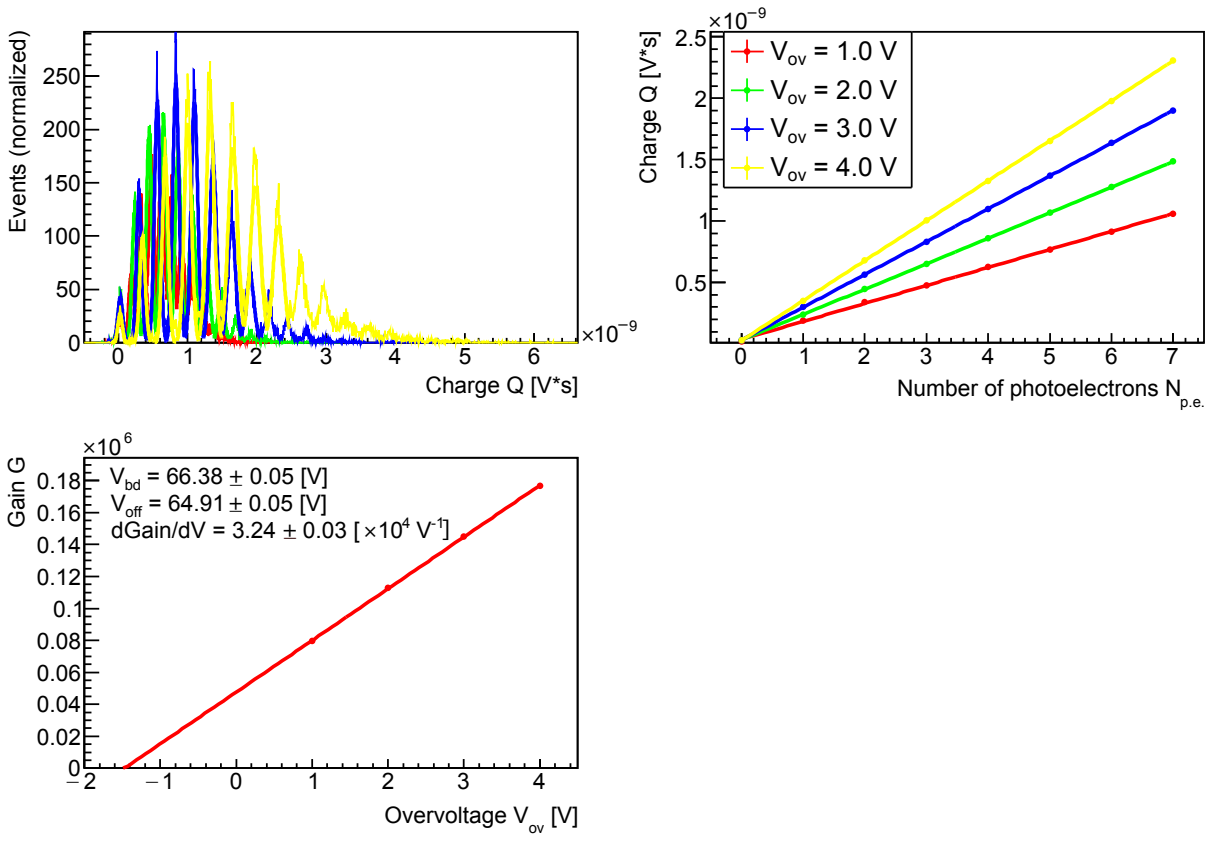

Figure 7.30: (top left) Collected spectra of response to the same amount of light from UV LED measured for Hamamatsu MPPC S12572-010P operated at different overvoltages. The left-most peak around zero is produced by noise, further peaks to the right correspond to individual photons. (top right) Dependence of collected charge on the number of photoelectrons at different overvoltages, extracted from (top left) plot. (bottom) Dependence of gain on overvoltage and main extracted parameters. Uncertainties here are extracted solely from fitting procedures for V_{bd} and dG/dV_{ov}, for complete uncertainty treatment see subsection 7.8.4.

as voltage at which $G(V_{ov})$ dependence crosses zero as shown in figure figure 7.30 (bottom).

I observed that $V_{bd} - V_{off}$ decreases with the pixel size as shown in table 7.1. This is consistent with the data reported by V. Chmill et al. [220], see figure 3.32 (right). The only SiPM falling out from this trend is Zecotek MAPD-3N, which could be explained by its specific triple-junction design, see [306, 308] for details. But since I was able to test only a single sample of Zecotek MAPD-3N which had not so well distinguishable photon peaks, this might as well be caused by production error or sample aging.

Similar data was obtained for other SiPMs before irradiation except for devices produced by Zecotek, all the results can be found in appendix G. I tested many samples of Zecotek MAPD-3A, but all of them were not able to distinguish single photons at any light level and overvoltage setting. This is explained by the fact that before my measurements all of them were utilized at NA61 PSD for several years and were already slightly irradiated, according to an estimation presented in subsection 7.5.3, they achieved about $1.4 - 1.8 \times 10^{10}$ n_{eq}/cm^2. This is consistent with observations reported by other investigations that SiPMs lose the ability to resolve single photons after $10^9 - 10^{10}$ n_{eq}/cm^2, see subsection 3.6.5. During tests, I had only one sample

of non-irradiated Zecotek MAPD-3N, and it could just barely differentiate between the single-photon peaks, because the spectrum was very blurred by noise, see figure G.1. This can be explained by relatively high noise of the high gain amplifier, relatively low overvoltage of 2 V, relatively high intrinsic SiPM noise, and/or SiPM aging during several years that it was stored before the measurement. Due to the second breakdown effect, it was not possible to choose higher overvoltage, see figures 7.10 and 7.15.

Already after irradiation by fluence 5×10^{10} n_{eq}/cm^2 or higher, all the investigated SiPMs lost their ability to resolve single photons due to a drastic increase of the noise, which is presented in figure 7.31. For instance, for Hamamatsu SiPMs the noise increased by almost an order of magnitude, see figure 7.35 in the next subsection. This is again consistent data reported in literature, see subsection 3.6.5. Therefore, it is not possible to utilize this kind of measurement for radiation hardness comparison.

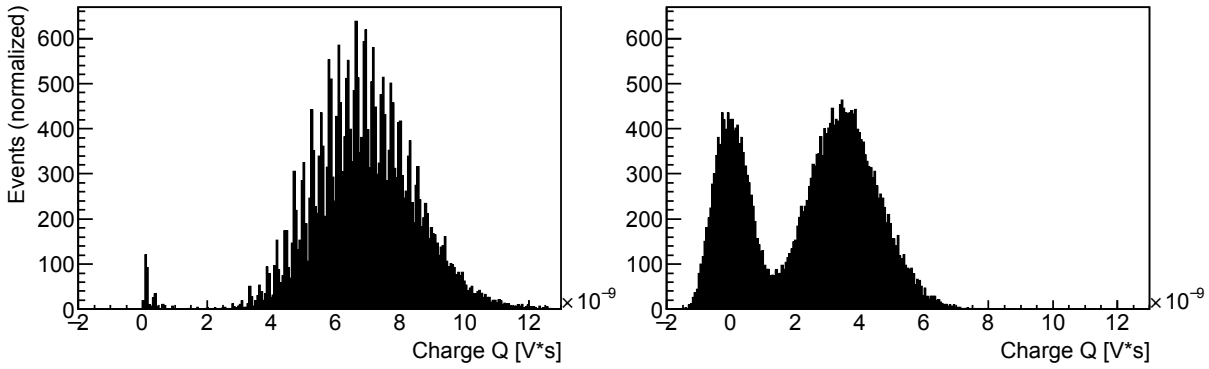

Figure 7.31: Collected spectra of response to the same amount of light from UV LED, measured for Hamamatsu MPPC S12572-010P before (left) and after irradiation by 5×10^{10} n_{eq}/cm^2 (right). Overvoltage is 3 V in both measurements. The left-most peak around zero on both spectra is produced by the noise. Further peaks to the right correspond to individual photons in the case of non-irradiated SiPM, but for irradiated SiPM no single peaks are visible.

7.8.2 SiPM noise and response to LED. signal-to-noise ratio

Figure 7.32 presents several measurements of SiPM response to illumination by UV LED for different SiPMs before and after neutron irradiation. Measured signal charge $\bar{Q}$ is defined as the mean of the signal area measurement with fixed window gate and is expressed in nV·s. Gate width was chosen so, that it will accommodate the maximal light pulse, i.e light pulse of the non-irradiated SiPM at overvoltage of 5 V. It 100 ns for Hamamatsu SiPMs, 200 ns for Zecotek and Sensl SiPMs, 300 ns for Ketek PM3315-WB-A0, and 1000 ns for Ketek PM3350. One can see an abrupt increase of the SiPM signal right above the breakdown voltage. Tremendous signal decrease by several orders of magnitude after irradiation up to 6.4×10^{12} n_{eq}/cm^2 can be observed.

Measuring the signal response when amplitude changes by many orders of magnitude is a tricky task. I chose an amount of light for the measurements in such a way that the signal from the most irradiated SiPM would be still measurable, which is on the order of 10^4 photons. Because of that, signals for non-irradiated SiPMs become very high, which resulted in non-linear dependence of the measured charge on overvoltage due to saturation of amplifier output amplitude around 3.1 V, so it continued to grow only in width, see figure 7.33 (left). But for irradiated SiPMs with smaller signals which did not reach 3.1 V, dependence is generally linear

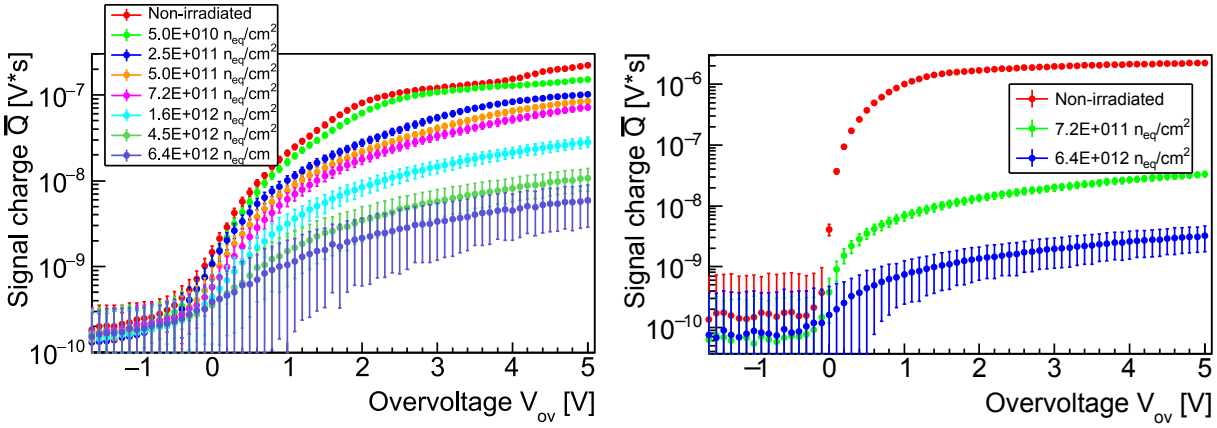

Figure 7.32: SiPM response to illumination by UV LED measured as a function of overvoltage for Hamamatsu S12572-010P (left) and Ketek PM3350, before and after irradiation with different 1 MeV equivalent neutron fluence. Note that error bars correspond to standard deviation of the signal, which is much higher than the measurement uncertainty for the mean, see subsection 7.8.4 for details.

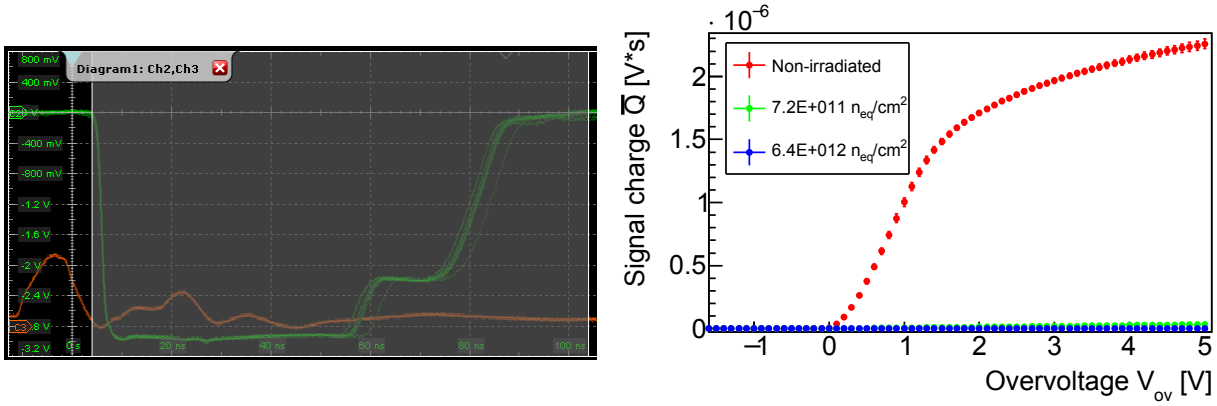

Figure 7.33: (left) Waveform of saturated signal for Hamamatsu MPPC S12572-010P measured at overvoltage of 5 V. Signal from the SiPM is connected to Channel 2 (green) and trigger from the pulser is connected to Channel 3 (orange). Scale of horizontal axis is 20 ns/div, vertical is 400 mV/div for signal and 1 V/div for trigger. (right) Response to illumination by UV LED measured as a function of overvoltage for Ketek PM3350 in linear scale before and after irradiation with different 1 MeV equivalent neutron fluence. Note that error bars correspond to standard deviation of the signal which is much higher than the measurement uncertainty for the mean, see subsection 7.8.4 for details.

above 1 V, see figure 7.34. This reflects the linear increase of the gain with overvoltage that was presented in figure 7.30. SiPMs with a smaller amount of pixels, e.g. Ketek PM3350 with just 3600 pixels, even started to saturate above 1 V, see figure 7.33 (right). Due to this, I present the signals in comparative figures at an overvoltage of 1 V. For lower overvoltages SiPM response is extremely dependent on the variation of V_{bd}, also it can be too small for highly irradiated samples.

Figure 7.35 shows the SiPM noise after irradiation. Noise estimation is based on standard

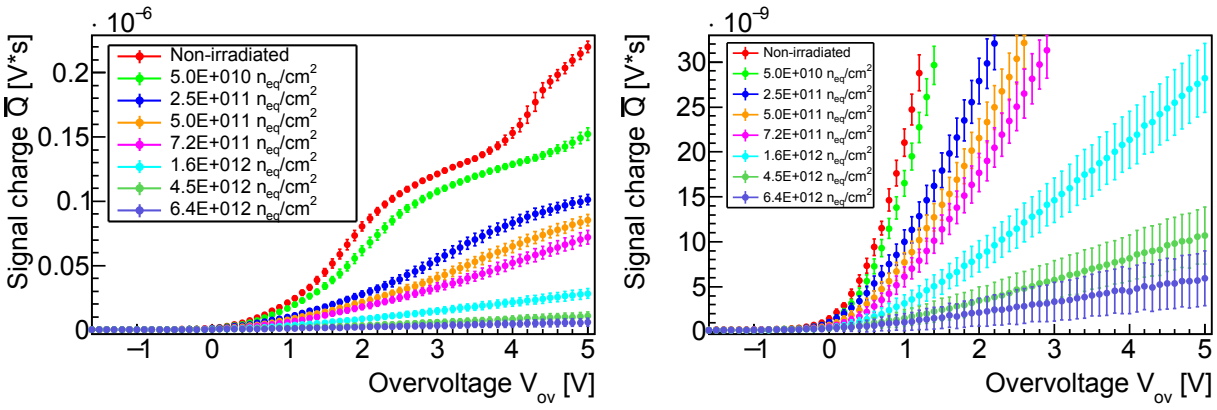

Figure 7.34: SiPM response to illumination by UV LED measured as a function of overvoltage for Hamamatsu MPPC S12572-010P in linear scale before and after irradiation with different 1 MeV equivalent neutron fluence. (left) presents a full scale, (right) is magnified for highly irradiated SiPMs. Note that error bars correspond to the standard deviation of the signal which is much higher than the measurement uncertainty for the mean, see subsection 7.8.4 for details.

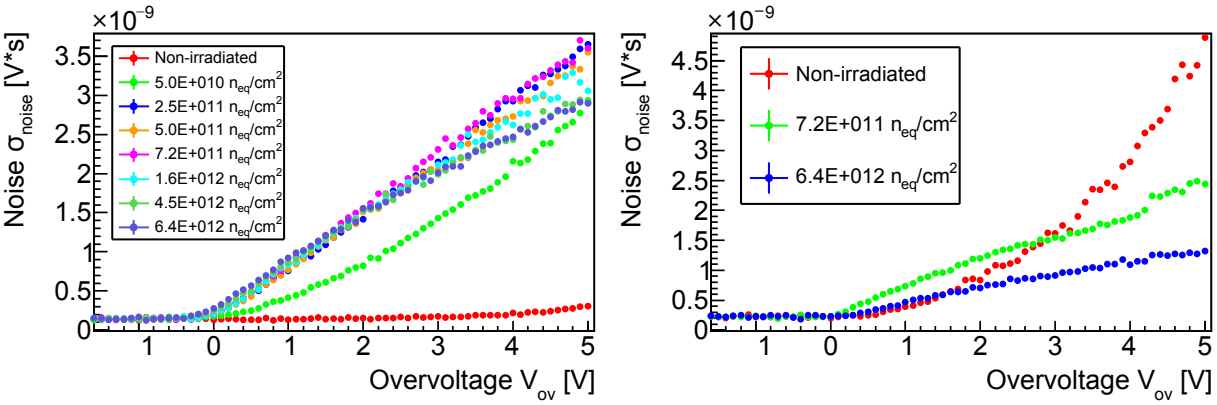

Figure 7.35: Standard deviation of SiPM noise measured as a function of overvoltage for Hamamatsu MPPC S12572-010P (left) and Ketek PM3350 (right) before and after irradiation with different 1 MeV equivalent neutron fluence.

deviation σ_{Noise} of the measured signal area without the light exposure, and is expressed in nV·s. Already after irradiation by 5×10^{10} n_{eq}/cm^2 noise increased by several times due to the increase in dark current. However, for fluences above 2.5×10^{11} n_{eq}/cm^2 it surprisingly saturated, and for SiPMs with big pixels like Ketek PM3350 it even decreased, see figure 7.35 (right). One can see that before irradiation noise was almost flat, which means that it was dominated by the internal noise of the amplifier. Therefore, measured results shall be considered as a lower limit of the noise.

Figure 7.36 presents the results on signal-to-noise ratio and signal resolution for Hamamatsu MPPC S12572-010P after irradiation. They were calculated as $SNR = \bar{Q}/\sigma_{Noise}$, and $Res_Q = \sigma_Q/\bar{Q}$, respectively. SNR tends to decrease rapidly with fluence, starting from the value about one thousand before irradiation and dropping to ~ 1 after the highest fluence of 6.4×10^{12} n_{eq}/cm^2, in case if SiPM is operated at $V_{ov} = 3$ V. One can see that they improve with an increase in overvoltage, but maximum can be found around 2 – 3 V because signal starts

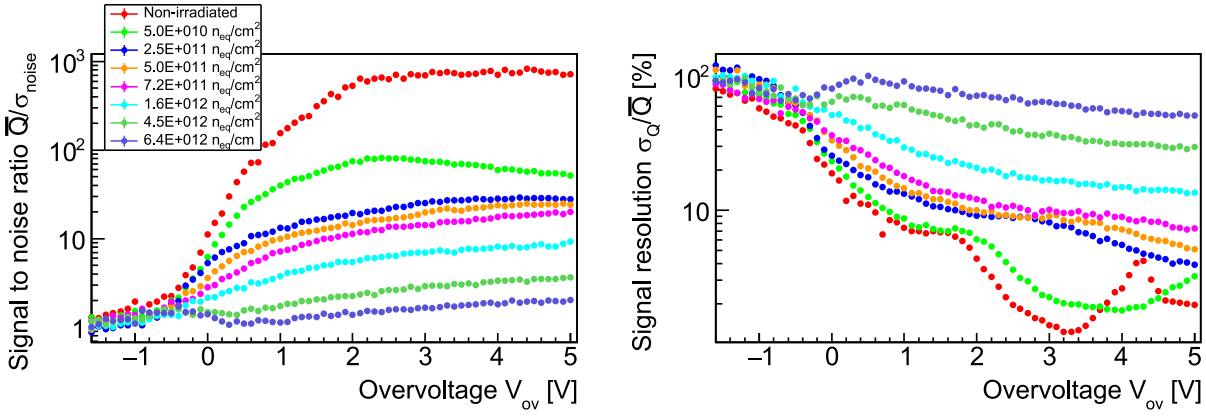

Figure 7.36: signal-to-noise ratio (left) and signal resolution (right) measured as a function of overvoltage for Hamamatsu MPPC S12572-010P before and after irradiation with different 1 MeV equivalent neutron fluence.

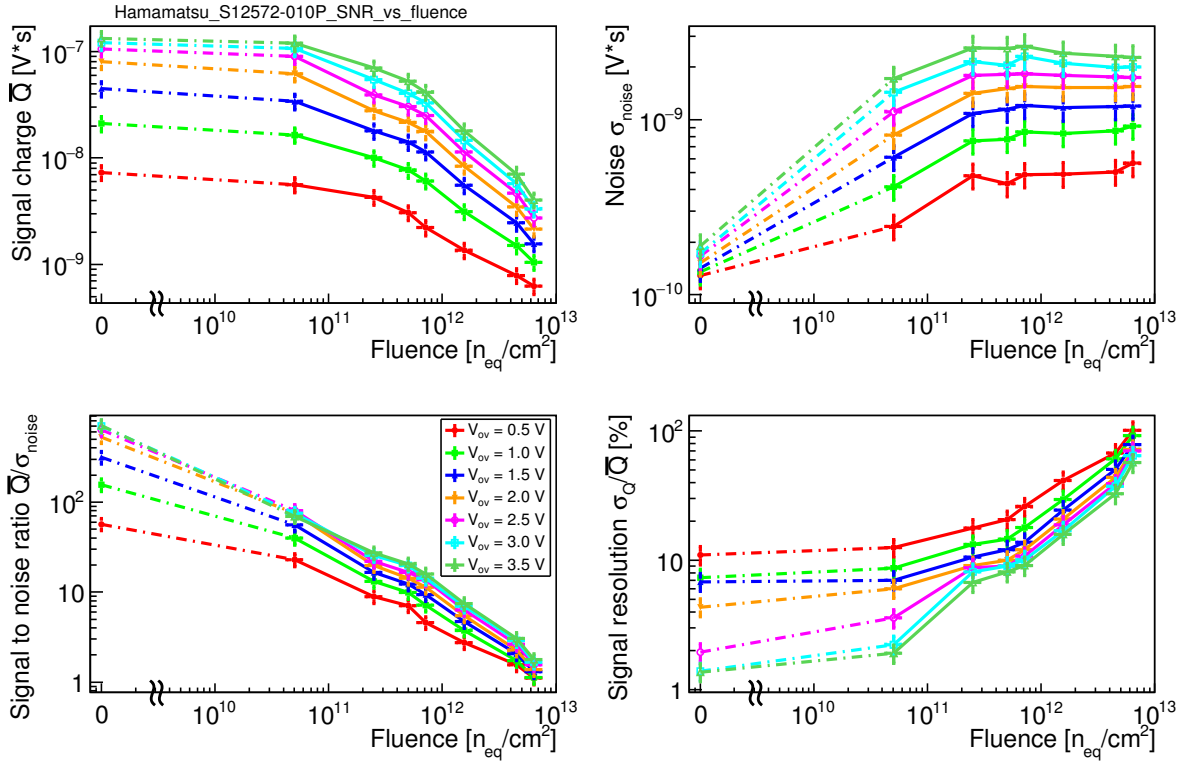

Figure 7.37: Signal response (top left), standard deviation of noise (top right), signal-to-noise ratio (bottom left) and signal resolution (bottom right) for Hamamatsu MPPC S12572-010P as a function of 1 MeV equivalent neutron fluence at different values of overvoltage.

to grow slower than noise. The strange behavior of resolution above 3.5 V is due to amplifier amplitude saturation. Obtained results on SNR are similar to data reported by Yu. Musienko et al. [184,196,196,197,213], for example, see figure 3.39. Unfortunately, no other measurements of SiPM signal-to-noise ratio after irradiation is reported in the literature up to my knowledge.

Figure 7.37 presents all the aforementioned signal parameters as a function of fluence at fixed overvoltages. Monotonic degradation of signal parameters with an increase in fluence is observed, except for noise which saturates above 2.5×10^{11} n_{eq}/cm^2. Degradation by more than 10 times can be seen after the highest fluence of 6.4×10^{12} n_{eq}/cm^2. Parameters improve with overvoltage, but this improvement considerably slows down above 2 V. Similar graphs for every tested SiPMs can be found in appendix H.

7.8.3 SiPM response and signal-to-noise ratio comparison for all SiPMs

Since investigated SiPMs have very different gain ($6 \times 10^4 - 6 \times 10^6$) and photon detection efficiency (10 – 40 %), resulting signal amplitudes vary in up to two orders of magnitude for them. Therefore, one can compare their radiation hardness only in relative terms. Figure 7.38 presents the change of SiPM signal parameters after irradiation relative to values before irradiation. Drastic degradation of signal response to LED (top left) and signal-to-noise ratio (bottom left) by up to three orders of magnitude is observed after irradiation. No response degradation is observed after 5×10^{10} n_{eq}/cm^2, however, only SiPMs with small pitch were irradiated by such low fluences. Around 10^{12} n_{eq}/cm^2 signal decrease is much lower for SiPMs with pixel pitch $\leq$ 15 µm than for SiPMs with pixel pitch $\geq$ 29 µm. Obtained results on SNR are comparable to data reported by A. Heering et al. [183], which is shown in figure 3.35. Discrepancies with other published measurements of SiPM degradation are discussed in detail in subsection 7.9.

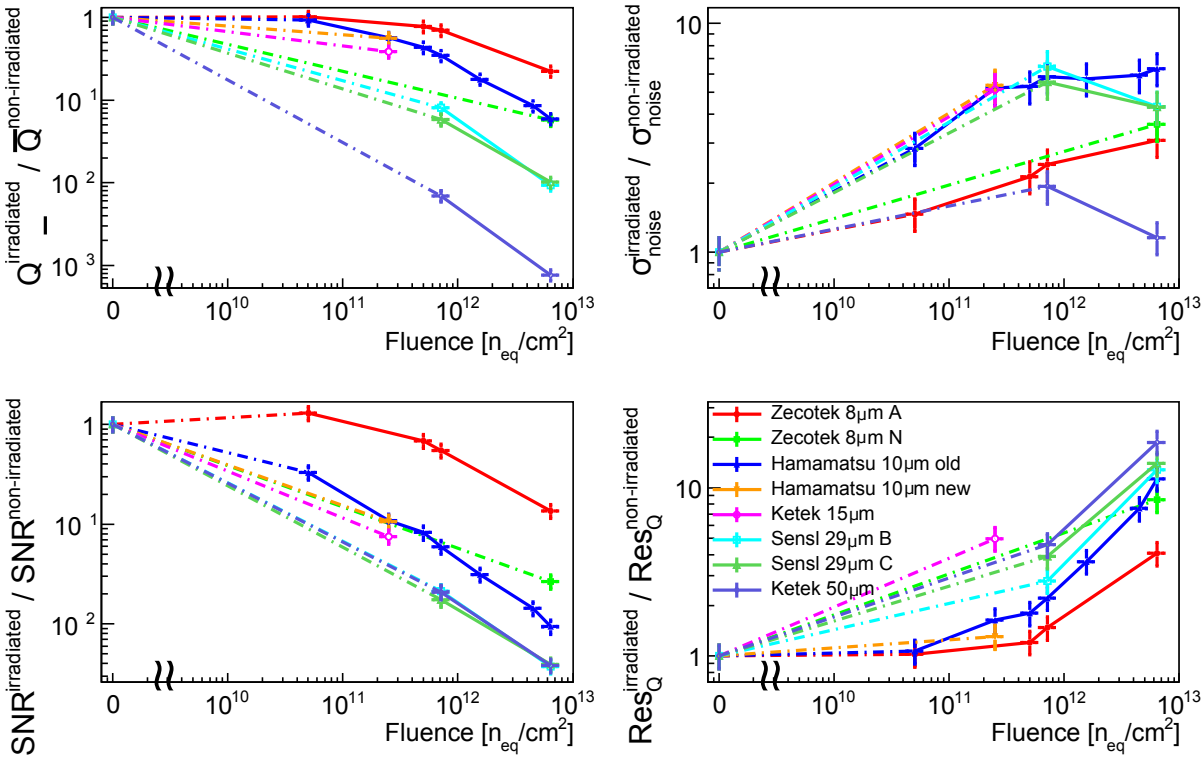

Figure 7.38: Signal response (top left), the standard deviation of noise (top right), signal-to-noise ratio (bottom left) and signal resolution (bottom right) for all the investigated SiPMs as a function of 1 MeV equivalent neutron fluence at overvoltage of 1 V. All the values are relative to values before irradiation.

Note that all the samples of Zecotek MAPD-3A, including ones that I call "non-irradiated"

were already slightly irradiated by about $1.4 - 1.8 \times 10^{10}$ n_{eq}/cm^2 before I studied them because they were used during several years of NA61 PSD operation, see subsection 7.5.3 for details on the fluence estimation. This explains the fact that no signal degradation is visible for them after fluence of 5×10^{10} n_{eq}/cm^2. Therefore, the presented relative decrease of their signal shall be regarded as the lower limit, while the degree of real degradation can be visually assessed by comparison with Zecotek MAPD-3N provided in figure 7.39. Note that before irradiation for MAPD-3A gain is 6×10^4 and PDE is 20 %, but for MAPD-3N gain is 10^5 and PDE is 30 %, which results in approximately three times higher signals for the latter. After irradiation difference is only 1.7 times, which suggests that after irradiation defects produced in silicon lattice play a very significant role in the signal formation.

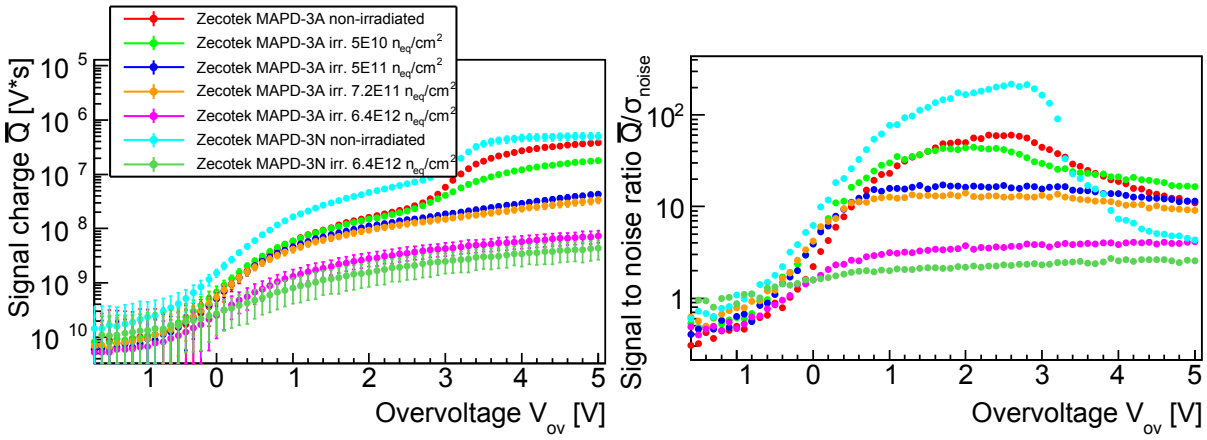

Figure 7.39: Signal response to LED (left) and signal-to-noise ratio (right) for Zecotek MAPD-3A and MAPD-3N as a function of overvoltage before and after irradiation with different 1 MeV equivalent neutron fluence.

Figure 7.38 (bottom left) shows SiPM noise increased in only 2 – 10 times for $\Phi \leq 7.2 \times 10^{12}$ n_{eq}/cm^2 and then saturated, or even decreased for SiPMs with small pixels. Note that the presented relative decrease of SiPM noise shall be regarded as the lower limit because the noise of non-irradiated SiPMs at $V_{ov} = 1$ V is mostly produced by amplification and readout circuitry.

SiPM resolution degraded by more than factor 10 as can be seen in figure 7.38 (bottom right). Relative degradation is smaller for resolution than for SNR because the standard deviation of LED response σ_Q before irradiation is more than 10 times higher than the standard deviation of noise σ_{Noise} but after irradiation they become comparable. σ_Q depends on Poisson statistics of light counting, so it scales with the measured charge $\bar{Q}$ which is very big before irradiation. Noise on the contrary does not depend on $\bar{Q}$ and can be very small before irradiation. After irradiation, $\bar{Q}$ become very small and σ_Q become dominated by σ_{Noise}, so both become comparable. For example, at $V_{ov} = 1$ V MPPC S12572-010P before irradiation had $SNR \approx 2.4 \times 10^{-8}/1.4 \times 10^{-10} \approx 170$ and $Res_Q \approx 1.7 \times 10^{-9}/2.4 \times 10^{-8} \times 100\% \approx 7\%$. After the highest irradiation it became $SNR \approx 1.1 \times 10^{-9}/9.9 \times 10^{-10} \approx 1.1$ and $Res_Q \approx 9.7 \times 10^{-10}/1.1 \times 10^{-9} \times 100\% \sim 88\%$.

The most important conclusion is that SiPM radiation hardness in terms of response to LED and signal-to-noise ratio scales with the pixel size, i.e. the bigger the pixels – the more the SiPM response degrades with accumulated fluence. Namely, they decrease by several times faster for SiPMs with ≥ 29 μm pixels compared to SiPMs with ≤ 15 μm pixels irradiated with the same fluence. This is similar to results for dark currents presented in figure 7.16.

7.8.4 Uncertainty estimation

I assessed the measurement uncertainties based on the sample-to-sample variability for SiPMs of the same type irradiated with the same fluence. Figure 7.40 shows that in general SiPMs exhibit relatively low variability of signal charge and noise, both before and after irradiation. Similar data for other SiPMs are presented in appendix H. This variability also contains the contribution from the SiPM positioning in the holder. For instance, at overvoltage of 1 V standard deviation for all the measured and estimated quantities for different samples is on the order of 3 – 10 %. Few samples, which showed higher parameter variation and increased variability up to 15 %, were excluded from the comparison.

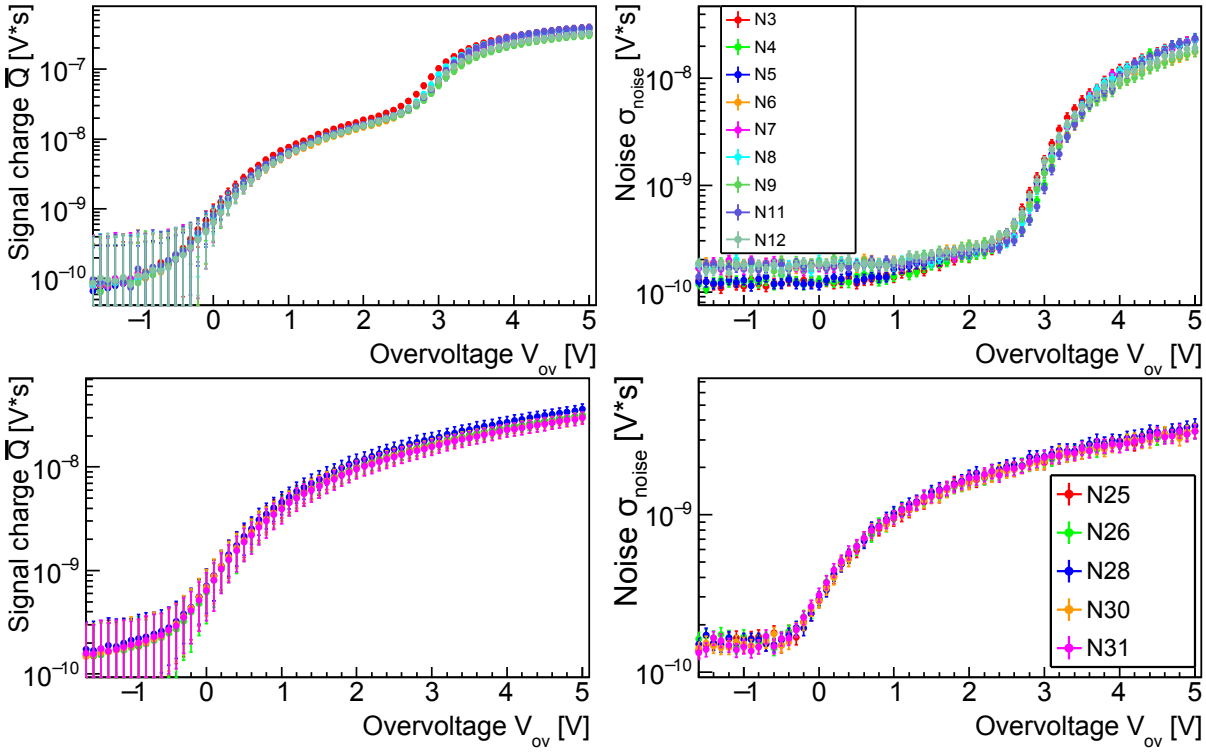

Figure 7.40: Variability of signal charge (left) and noise (right) for: Zecotek MAPD-3A before irradiation (top) and Hamamatsu S12572-010P SiPMs after irradiation by 1.6×10^{12} n_{eq}/cm^2 (bottom).

Measurements were performed at room temperature of 27.5 ± 1 °C. It is by 3 – 4 °C higher than the temperature during the dark current measurements. To account for this, I corrected the values of breakdown voltage determined from current measurements with help of dV_{bd}/dT coefficients provided in subsection 7.5.4. Accuracy of breakdown voltage setting is very important for signal response measurements. Accuracy of V_{bd} estimation is below 50 mV, but the measurement step is 100 mV and finer correction is not easy to introduce resulting in correction accuracy of ± 50 mV. Therefore, the total accuracy of the breakdown voltage setting is below 70 mV. This may result in up to 9 % variation in the measured charge and noise, which can be considered as a part of the overall measurement variability presented above. Since noise increases with temperature as $sqrt(I_{dark})$ as shown in equation (3.16), noise variation up to 4 %/°C can be expected, which is again considered as part of the overall measurement variability.

The uncertainty introduced by the oscilloscope measurement accuracy, which is 1.5 – 3 %, is

much smaller. The uncertainty caused by the measurement statistics of each spectrum can be calculated as the standard error of the mean by equation (5.1). For charge measurements, values of standard deviation are 5 – 30 % of the mean depending on the measurement, and a number of collected events are 1000, so $\sigma_{\overline{Q}}$ is on the order of 0.2 – 1 % of the mean. Therefore, collected statistics are considered to be high enough to make uncertainty due to statistics negligible.

In summary, measurement uncertainty of signal response, noise, signal-to-noise ratio, and signal resolution is comprised by the sample-to-sample variability and precision of the sample positioning which is on the order of 3 – 10 %, and temperature variations which can cause changes up to 9 %. Therefore, conservative total uncertainty is generally below 14 %. In view of the parameter change by several orders of magnitude after irradiation, this does not pose a problem for data interpretation.

Uncertainty of V_{off} and gain estimation is dominated by breakdown voltage setting accuracy, including possible temperature variations, i.e. up to 70 mV total shifts might be expected. Fit accuracy is generally an order of magnitude lower, i.e. up to 5 mV. In the case of absolute gain determination from the single-photon peaks, voltage shift may cause a variation on the order of 2 – 7 % depending on the SiPM sensitivity. For relative gain dG/dV_{ov}, the main uncertainty source is the fit accuracy, which is usually below 1.5 %, except for Zecotek MAPD-3N for which it is about 7 % due to poor peak resolution.

7.9 Summary and discussion of the measurement results

The achieved data revealed the drastic degradation of the SiPM operational characteristics after neutron irradiation with 1 MeV equivalent neutron fluence in the range from 5×10^{10} up to 6.4×10^{12} n_{eq}/cm^2.

7.9.1 Dark current and electrical parameters

Dark current increased from the nano- or microamperes up to milliamperes, so the electrometer used for the measurements even saturated for some SiPMs at overvoltages above 1 – 2 V, where dark current reached 10 mA. Linear dependence of the current on fluence was observed, which is consistent with data from other studies reviewed in subsection 3.6.1 in the review chapter. Relative increment of dark current with fluence is on the order of $10^{-3} - 10$ A/cm^2 per 10^9 n_{eq}/cm^2 depending on the SiPM, which is also similar to published data. I also found that it strongly increases with overvoltage, namely, it increases by approximately an order of magnitude after an increase of V_{ov} by 2 V. Based on this data I estimated the dependence of effective depletion width on overvoltage to be on the order of 1 μm/V for Hamamatsu S12572-010P SiPMs. Up to my knowledge, both observations of the overvoltage dependencies are unique.

Electrical parameters, including the quenching resistance and the pixel capacitance, changed only in a minor way if at all after irradiation, which agrees well with investigations from other studies discussed in subsection 3.6.4. Based on that one may assume that the recovery time $\approx C_d R_q$ did not change as well. Relatively high breakdown voltage shifts up to 0.8 V were detected for SiPMs with high operation voltage which is consistent with published data, see subsection 3.6.3. All SiPMs lost the ability to detect single photons already after irradiation with 5×10^{10} n_{eq}/cm^2, which is also consistent with published data, see subsection 3.6.5.

7.9.2 SiPM response to LED and signal-to-noise ratio. Pixel occupancy and gain

SiPM response to LED and signal-to-noise ratio gradually decreased with increase in fluence. For instance, signal response almost halved after irradiation with 2.5×10^{11} n_{eq}/cm^2, and further decreased by a factor of 10 – 1000 (depending on the SiPM) after 6.4×10^{12} n_{eq}/cm^2, which is presented in figure 7.41. This is mostly in agreement with published data reviewed in subsection 3.6.6. However, several studies [182, 193, 213] made observations of the stability of SiPM response up to $10^{13} - 10^{14}$ n_{eq}/cm^2.

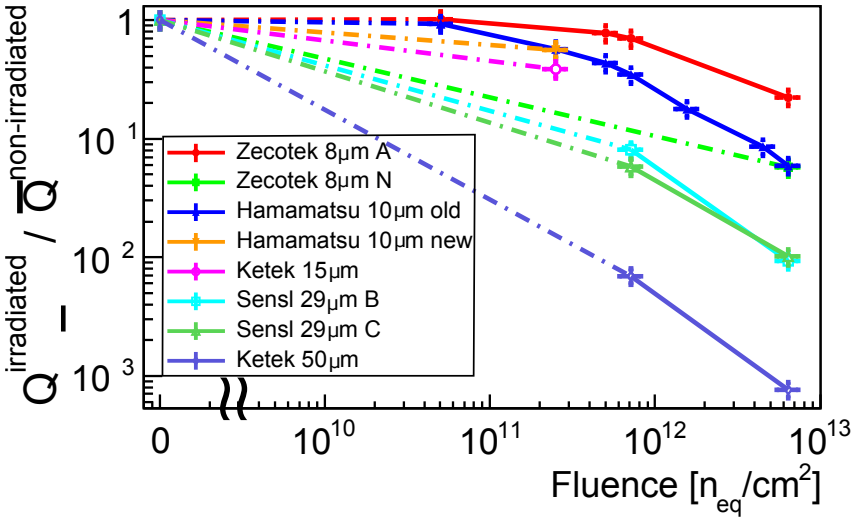

Figure 7.41: Degradation of the signal response to UV LED as a function of 1 MeV equivalent neutron fluence for different SiPMs at overvoltage of 1 V.

The observed decrease of the performance after the irradiation can be described by several concurrent effects. The first effect is an introduction of new states in the silicon band structure, which act as generation-recombination centers for the charge carriers. Therefore, more carriers are generated unrelated to the useful signal increasing the dark current and noise. These dark counts occupy the pixels and make them unavailable for photon detection. Figure 7.42 presents an estimation of the pixel occupancy for the investigated SiPMs. It is based on the method proposed by E. Garutti and M. C. Vignali [192, 194, 195]. Pixel occupancy due to dark counts is calculated as a ratio of measured dark current to the maximal current, which corresponds to the occupation of all the pixels, as

$$\eta_{DC} = \frac{I_{dark}}{I_{max}} = I_{dark} \cdot \frac{R_q}{V_{ov} \cdot N_{pix}} \tag{7.8}$$

One can see that pixel occupancy indeed increased dramatically after irradiation, for instance, pixels of Ketek PM-3350 SiPM became almost fully occupied after 6.4×10^{12} n_{eq}/cm^2, which is consistent with information for 50 µm SiPMs discussed by A. Heering et al. in [182]. However, for other SiPMs η_{DC} is on the order of $10^{-3} - 10^{-1}$, i.e. only 0.1 – 10 % of the pixels are occupied after 6.4×10^{12} n_{eq}/cm^2, which can not explain the observed signal degradation by several orders of magnitude. This could be because an effect of the pixel being in a recovery state after the dark count is not included in this simplistic approach, i.e. it provides only a qualitative evaluation of the occupancy. Detailed dependencies of the pixel occupancy on overvoltage before and after irradiation for different SiPMs can be found in appendix D.9.

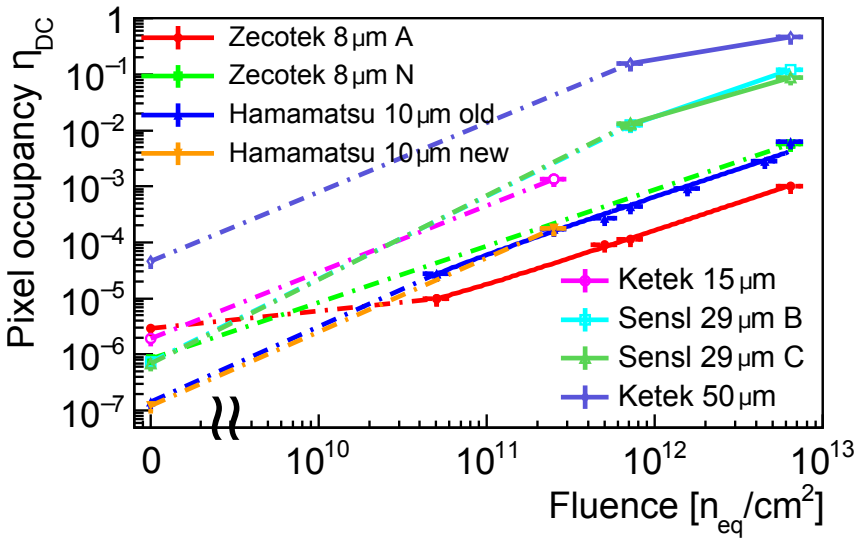

Figure 7.42: Increase of the pixel occupancy estimated by the dark current measurement as a function of 1 MeV equivalent neutron fluence for different SiPMs at overvoltage of 1 V.

Furthermore, E. Garutti [192] showed that the dark current and pixel occupancy scales with temperature, see figure 3.36. Up to an order of magnitude decrease in occupancy was observed for SiPMs cooled down to -30 °C compared to SiPMs operated at room temperature. This at least partially explains why studies which measured SiPMs under similar cooling [193, 213] reported no signal degradation below $5 \times 10^{13} - 5 \times 10^{14}$ n_{eq}/cm^2. However, only a small degradation was also measured by A. Heering et al. [182] at room temperature after irradiation by 2×10^{14} n_{eq}/cm^2. This could be explained by the utilization of specific novel radiation-hardened SiPMs, while I used standard commercially available ones. However, the exact source of the discrepancy remains a question.

The second effect is that radiation produced defects also assist trapping and recombination of carriers, which are generated by a useful signal and should be collected. Therefore, equivalent carrier lifetime is reduced, which leads to a decrease in the charge collection efficiency and total photon detection efficiency, and finally to a decrease in the signal response.

The third possible effect is the self-heating of SiPMs due to very high dark currents after irradiation. M. Cordelli er al. [208] explored the possibilities of the SiPM self-annealing after irradiation when operated at very high overvoltages of 8 – 14 V, which is beyond the range recommended by the manufacturers. This resulted in very high currents of 200 – 400 mA flowing through the SiPM which significantly helped to reduce the radiation produced defects, but sometimes it also resulted in uncontrolled overheating with temperatures reaching 150 – 200 °C. Although, SiPMs which I tested exhibited currents only up to 10 mA, it may possibly be enough to create localized overheated regions in the bulk. This in turn can lead to the effective temporal increase in the breakdown voltage resulting in the decrease of overvoltage and consequently gain. However, such effects were not carefully studied yet.

The fourth effect is a change in the initial doping concentration profile, i.e. electric field distribution around the p-n junction, which is specifically designed to provide the high gain of SiPM. This might lead to the gain decrease due to reduced avalanche triggering probability, and consequently an even more rapid signal decrease. This would also explain the stabilization/decrease of noise, which I observed after fluence about 10^{12} n_{eq}/cm^2. Similar effect was reported by S. Cerioli et al. [161] above 5×10^{13} n_{eq}/cm^2, see figure 3.27 in the review chapter. Gain

determines how many carriers are created in an avalanche, which applies to both carriers of useful signal and "noisy" carriers. One can assume that after a certain fluence threshold, the contribution of gain degradation to decrease of noise starts to dominate over the increase of noise caused by a linear growth of the leakage current. However, capacitance measurements showed no change in pixel capacitance, which suggests that the gain also remained unchanged. But it was measured only below the breakdown voltage, and no trustworthy information is available on the capacitance value above it. Furthermore, during measurements at low frequencies, strange distortions in the capacitance were encountered in my data and data from another group [191,317], which are not yet understood. Therefore, further methods and studies are required to address the gain degradation which is left as an open question now.

7.9.3 Miniaturization of SiPM pixels

One of the most important observations is the improvement of the SiPM radiation hardness with the decrease of the pixel size. Namely, SiPMs with small pixels on the order of 10 – 15 μm exhibit significantly lower dark current, and much slower degradation of the signal response and signal-to-noise ratio after irradiation.

Scaling of the dark current with pixel size was already reported by several studies, see subsection 3.6.1 in the review chapter. I found that SiPMs with small pixels not only have initially smaller dark currents but also show a slower current increase per fluence. The latter is in contradiction to the results of M. Andreotti et al. [175] who reported no visible change in the trends of $dI_{dark}/d\Phi_{eq}$. Since I observed the slower trends only for SiPMs with 8 – 10 μm pixels compared to SiPMs with ≥ 15 μm pixels for fluences above 5×10^{10} n_{eq}/cm^2, while M. Andreotti et al. studied SiPMs with ≥ 25 μm pixels for fluences below 6.2×10^{9} n_{eq}/cm^2, further studies are required to understand this subject.

Only a single study by A. Heering et al. [183] reported scaling of the response to light with pixel size for SiPMs with 8 and 50 μm pixels. Up to my knowledge, the signal-to-noise ratio was studied only by Yu. Musienko et al. [184,196,196,197,213] for SiPMs with small pixels, and no comparison of SiPMs with different pixel sizes exists. The general lack of information on this topic makes my results unique and signifies the high importance of such studies.

SiPM pixel miniaturization is beneficial because it lowers pixel capacitance resulting in a shorter charge collection time and higher collection efficiency contributing to the PDE improvement. It also reduces the sensor deadtime and therefore increases the total dynamic range for the high frequency signals. Decreased active volume and surface of a single-pixel results in the decrease of generated dark current, and lowered probability of both the after-pulsing and the cross-talk. This suggests the use of SiPMs with the smallest available pixels for the harsh radiation environment.

7.10 Choice of the SiPM for PSD

To summarize the aforementioned information, Zecotek MAPD-3A and MAPD-3N SiPMs were found to be inapplicable at the CBM PSD due to the very slow pixel recovery time which resulted in the reduced dynamic range and inability to operate at high particle rates. Ketek PM-3350, Sensl B30020 and Sensl C30020 SiPMs were found to be inapplicable due to the drastic increase of the dark current and noise, and decrease of signal response after irradiation.

Hamamatsu S12572-010P SiPM was found to fit the CBM PSD general requirements at least up to an accumulated fluence of 2.5×10^{11} n_{eq}/cm^2, which corresponds to 1 year of CBM operation at 1 MHz collision rate. Dark current increased significantly up to 50 μA in the operation range from 0.5 up to 3 V, which is near the limit that current power supply boards can deliver.

Signal response to LED illumination halved, which can be fixed during the detector operation by the online adjustment of the overvoltage and/or readout chain recalibration. Observed change of V_{br} up to 0.5 V can be resolved in the same manner. Large signals are still visible even for SiPMs irradiated by 6.4×10^{12} n_{eq}/cm^2. It means that highly irradiated sensors could be still of use for the very central PSD modules, where signal amplitude will be maximal due to the close proximity to the beam axis.

The most important thing to consider is that the signal-to-noise ratio for SiPMs irradiated by 2.5×10^{11} n_{eq}/cm^2 decreased by more than an order of magnitude, which resulted in the shortening of the dynamic range. Before irradiation, the standard deviation of noise was below 0.3 p.e., which allow resolving single photons. After irradiation it increased up to 3 p.e [3], so single photons were not resolvable anymore. However, this is not required at PSD. The practical minimal signals which are important for PSD are minimum ionizing particles (MIPs), namely muons which are used during the calibration. PSD team from INR Moscow [318] reported that they produce a signal on the level of 50 ph.e. per section, i.e. per SiPM. However, noise levels at the calorimeter are significantly higher than in the laboratory.

The upper limit of the dynamic range is defined by the maximal signal, and since the SiPM response to light is halved, the upper limit possibly halved as well. PSD team from INR Moscow [261] measured that the light yield in each section, i.e. for each SiPM, measured with beam muons is about 8–10 ph.e./MeV. Therefore, about 10^5 photons are expected to arrive for the energy deposition of 10 GeV in the central module. The intrinsic dynamic range of Hamamatsu SiPMs before irradiation is defined by the number of pixels, and saturation may theoretically start above 2×10^5 photons, or even less after irradiation. However, a small recovery time effectively increases the dynamic range. Furthermore, tuning of the SiPM overvoltage is a powerful and versatile tool to adjust the dynamic range for an application. For example, at modules of NA61 PSD which are situated in the center of the calorimeter where signals are the highest, SiPMs are usually operated at 1 – 2 V lower V_{ov} to avoid the ADC overflow. Because the complex interplay of all the aforementioned effects at the calorimeter is hard to study in the laboratory conditions, I decided to investigate the SiPM performance at PSD test module at CERN, which is described in the next chapter.

Since the SiPM technology is rapidly evolving, it is advised to regularly check for updates from the manufacturers and use the latest version of SiPMs. For instance, in 2019 I received several Hamamatsu MPPC S14160-1310PS SiPMs. They are successors of the old model Hamamatsu MPPC S12572-010P which I extensively used for irradiation tests. They have very similar general characteristics, i.e. pixel pitch of 10 μm, a gain of 10^5 and recovery time of about 10 ns, but also they possess significantly improved photon detection efficiency of 18 % versus 10 % for the old model and lowered breakdown voltage of 38 V versus 67 V for the old model. Improved PDE provides higher signal amplitudes while the noise remains similar, which notably increases the signal-to-noise ratio, see figure 7.43. Reduced V_{bd} offers better voltage stability against temperature changes, namely 34 mV/°C versus 60 mV/°C for the old model.

Several new Ketek PM3315-WB-A0 SiPMs with a pixel pitch of 15 μm (they do not produce SiPMs with smaller pixels) were also recently acquired, see figure 7.43 for comparison. As expected, bigger pixels provide a higher gain of 3×10^5 and PDE of 22 %, but also an order of magnitude higher dark current and noise (see figure 7.16) and a slightly longer recovery time of 13 ns. This results in higher signals and signal-to-noise ratio, but also in higher noise both before and after irradiation. On the one hand, PM3315-WB-A0 provides higher signals and a better signal-to-noise ratio both before and after irradiation. On the other hand, due to bigger pixels, it

[3] The estimation is based on the measurement of single-photon peaks before irradiation assuming that gain did not change after irradiation.

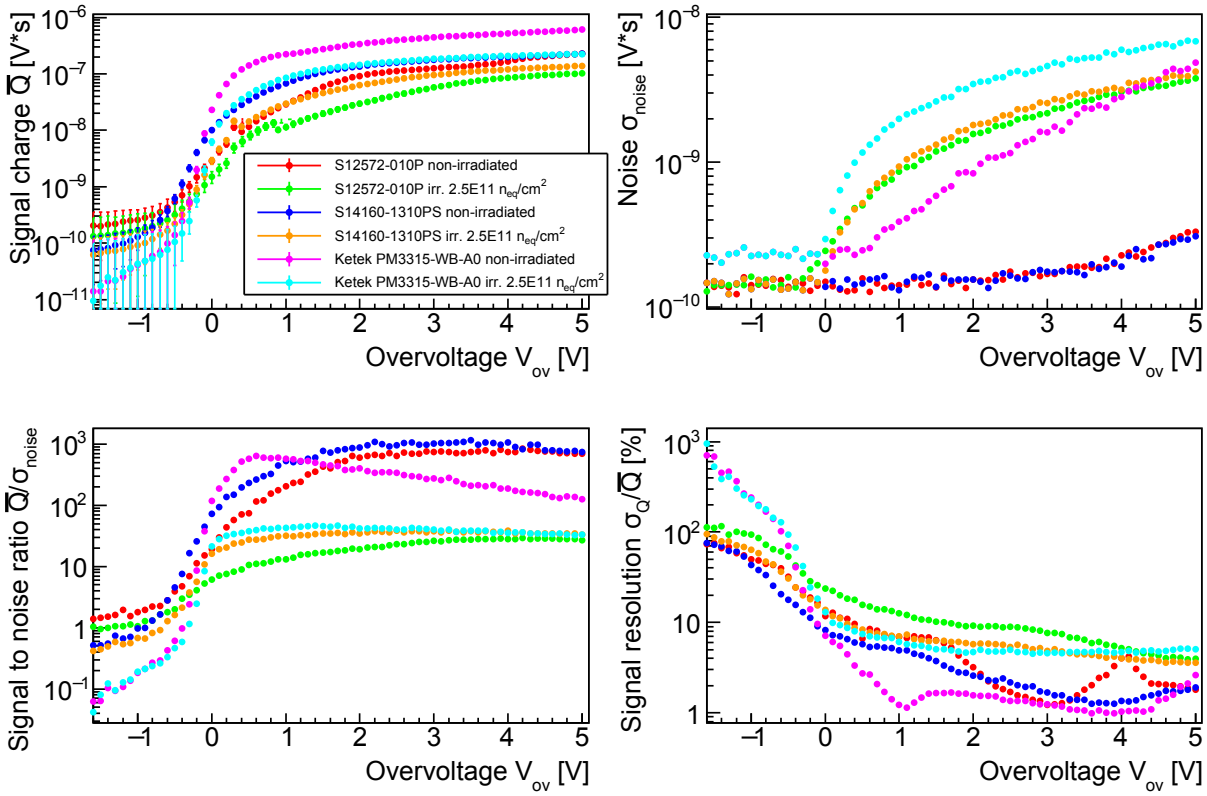

Figure 7.43: Comparison of signal response to LED (top left), noise (top right), signal-to-noise ratio (bottom left) and resolution (bottom left) for Hamamatsu MPPC S12572-010P, Hamamatsu MPPC S14160-1310PS and Ketek PM3315-WB-A0 as a function of overvoltage before and after irradiation with 2.5×10^{11} n_{eq}/cm^2.

has an intrinsically lower dynamic range and higher relative degradation after irradiation, so its applicability for CBM shall be carefully assessed. In principle, Hamamatsu also produces 15 µm SiPMs, so they can also be studied in the future. However, we are generally more interested in devices with the smallest pixels which would benefit the dynamic range. And since SiPM pixel miniaturization is a trend now, one can expect more manufacturers to evolve in this direction.

Chapter 8

Performance of PSD module with irradiated SiPMs at CERN

The truly perfect way to assess the calorimeter radiation hardness is to test its performance after the irradiation. However, its merely impossible to irradiate the whole detector, and researchers normally do not go beyond laboratory tests of most irradiation susceptible detector parts. I decided to go further and test the performance of a PSD module equipped with irradiated SiPMs at CERN. This chapter describes the conducted tests and explores how much the radiation-induced SiPM degradation affects the energy resolution of the real calorimeter.

8.1 CERN beamlines and test conditions

I estimated the dependence of the calorimeter resolution on the neutron fluence achieved by SiPMs with help of the module equipped with SiPMs irradiated by the same neutron fluence. PSD single module response to proton beams was studied in the momentum range of 2 – 80 GeV/c, including tests at CERN PS T9/T10 beamlines for 2 – 10 GeV/c, and tests at CERN SPS NA61/SHINE beamline for 10 – 80 GeV/c. This study was done during the beamtimes allocated by the PSD team from INR, Moscow. I am especially thankful to F. Guber for the beamtime organization and to S. Morozov who believed in my idea and taught me all he could about the PSD calorimeter, beam control and operation, and data analysis. I thank the CBM and NA61 collaborations for their support in the tests and thank CERN staff M. Jeckel and L. Gatignon for their help in test preparation at the beamlines.

8.1.1 T9, T10 and NA61 (H2) beamlines at CERN

During the tests at NA61, the proton beam was provided by the CERN Super Proton Synchrotron (SPS) accelerator complex and further reduced by the Beryllium target system T2 of the via H2 beamline down to 20 – 80 GeV/c [319]. During the tests at T9 and T10 beamlines, the beam was extracted from the CERN Proton Synchrotron (PS) and also reduced by the Beryllium target system down to 2 – 10 GeV/c and 2 – 6 GeV/c, respectively [320]. Therefore, all the beamlines provided mixed hadron and electron beam, which composition depends on the primary beam momentum and target properties, see figure 8.1 for example.

At T9 beamline protons were identified by time-of-flight (TOF) method using two quartz Cherenkov detectors installed in front of the PSD supermodule with a time resolution of about 60 ps [321]. The effective identification range was 3.5 – 10 GeV/c. At T9 beamline protons TOF method was realized with help of scintillator counters installed in front and behind the

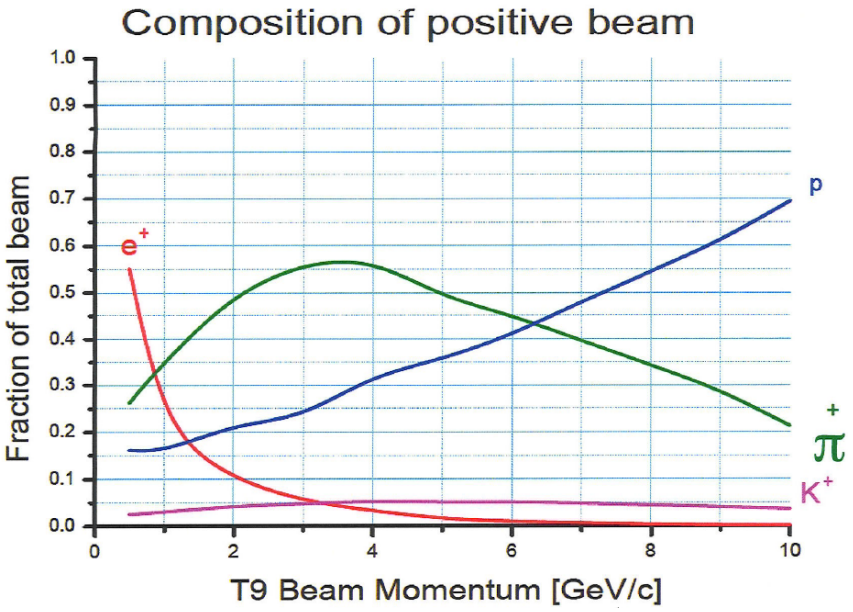

Figure 8.1: Beam composition at T9 beamline [320].

supermodule which covered a range of 2 – 4.5 GeV/c. No PID system was available during the tests at NA61.

8.1.2 Detector setup and data acquisition

I investigated the response of a single PSD module equipped with irradiated SiPMs to proton beams. At NA61 beamline desired PSD module was centered around the beam with the dedicated system capable of the movement of 22 tons heavy calorimeter in the transverse plane, see figure 4.10 (left). At T9 and T10 beamlines PSD supermodule consisting of 9 regular modules was installed in a fixed position, see figure 4.8. The beam was aligned to the central module, which was utilized for the tests. All the other modules of NA61 PSD or PSD supermodule were in an idle state during my measurements.

Together with A. Izvestnyy and S. Morozov we soldered irradiated SiPMs to the PSD readout boards, the result is presented in figure 8.2. Old boards used at NA61 provided a signal amplification of 50, while new boards designed for CBM provided an amplification factor of 10. At the old boards, SiPMs were covered with the optical medium, which was supposed to enhance the light transmission from the WLS-fibers to SiPMs. However, it did not bring enough benefit because it also produced unwanted light reflections, so it was decided not to use it for the new boards.

The SiPM boards were mounted to the back of the module as shown in figure 8.3. At NA61 PSD data was read out with the standard readout system. Data acquisition at PSD supermodule was performed with the help of the CAEN DT5742 16 channel 12 bit 5 GS/s digitizer [322], which can be seen on top of the power supply module depicted in figure 8.4 (right). Note that data measured for SiPMs irradiated by 2.5×10^{11} n_{eq}/cm^2 at high energies were actually measured at the PSD supermodule which was transported to the NA61 cave and tested there standalone.

System power supply module SM32 used at NA61 PSD was developed by V. Astakhov from the HVSys company in Dubna, Russia [323], which is presented in figure 8.4 (left). I utilized it

Figure 8.2: Photographies of irradiated SiPMs soldered to PSD readout boards. (left) presents the old board used at NA61 PSD, (right) presents the new board developed for CBM PSD. Note that on the NA61 board old Zecotek MAPD-3A SiPMs are soldered at the 5 slots corresponding to the last 5 sections of the module, but they were ot used during the tests due to ambiguity of data interpretation for SiPMs with very different parameters.

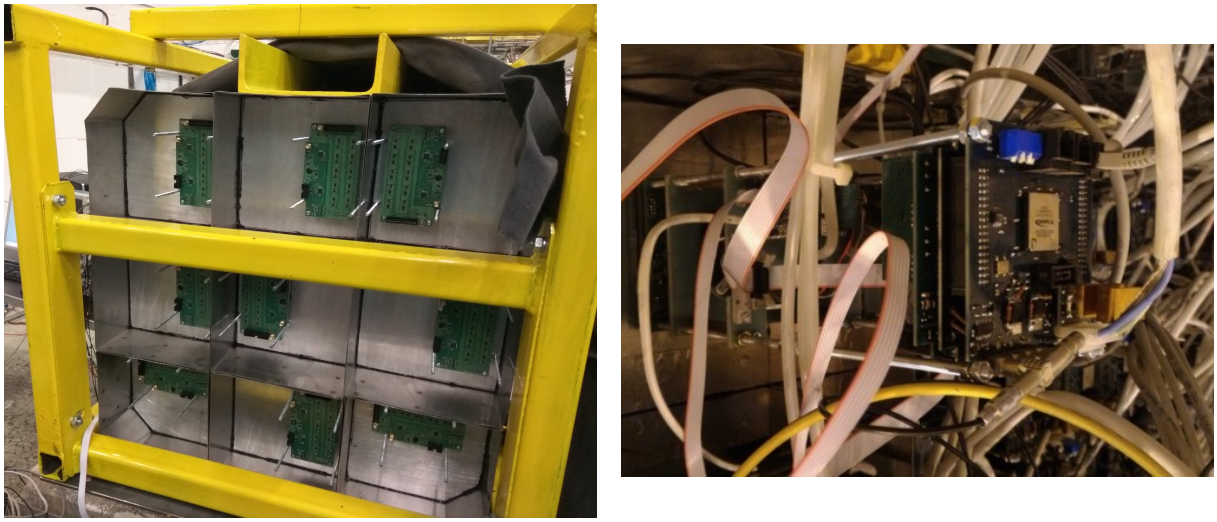

Figure 8.3: Readout boards with SiPMs mounted to the back sides of the PSD supermodule (left) and NA61 PSD module (right)

for SiPMs irradiated by $5 \times 10^{10} - 5 \times 10^{11}$ n_{eq}/cm^2 which had dark currents below 50 μA. But it could not be used for SiPMs irradiated by $1.6 \times 10^{12} - 4.5 \times 10^{12}$ n_{eq}/cm^2 which had much higher dark currents. At the first tests at NA61, high power WIENER Mpod 8 channel low voltage module [324], which can provide up to up to 120 V and 50 W per channel, was used, however it was quite noisy. Figure 8.4 (right) shows the power supply assembled by A. Izvestnyy based on the standard laboratory modules, which exhibited much lower noise and was used for

the further tests of highly irradiated SiPMs at T9 and T10.

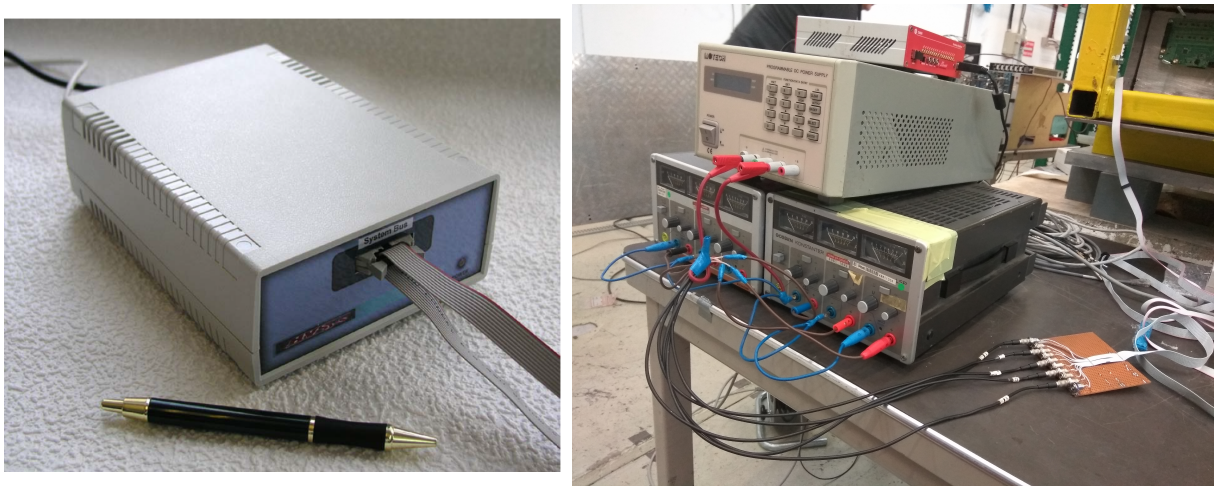

Figure 8.4: (left) SiPM power supply module SM32 used at NA61 PSD developed by V. Astakhov [323]. (right) External power supply assembled from the laboratory modules.

8.1.3 Proton selection

Protons were selected as reference particles for the energy resolution assessment because they are abundant in the beam mixture and showers produced by them have large hadron component. At the T9 beamline, the identification of beam particles was carried out by the Cherenkov detectors installed upstream of the PSD supermodule, which provided good proton identification for the 3.5 – 10 GeV/c momentum range. At the T10 beamline, it was done by the TOF scintillator counters, which provided good proton identification for the 2 – 5 GeV/c momentum range. See subsection 8.1.1 for details. Some deviations from the expected data were observed due to the incomplete PID covering of the energy range. Namely, underestimated energy resolution at 2 – 3 GeV/c for T9 beamline. For non-irradiated SiPMs the most appropriate data intervals were merged to mitigate this effect. For the data collected with highly irradiated SiPMs, I had to exclude the 2 – 3 GeV/c points since they were only measured at the T9 beamline.

No particle identification system was available at the NA61 beamline. In subsection 8.2.5 I described how I excluded the electrons from the data during the offline analysis. Unfortunately, no such simple method is available for pion/proton distinction, which led to slightly better resolution measured at high energies, see figure 8.22. This is explained by the fact that pions tend to deposit more energy in electromagnetic showers than protons, see subsection 2.4.4. Hadron showers spend part of the energy to overcome the nuclear binding, therefore this part is lost for detection and is called "invisible", while this effect is not present for electromagnetic showers. Calorimeter's compensation condition is specifically tuned so, that hadron and EM showers would produce an equal signal, but it is never ideal. The PSD design is slightly under-compensating, i.e. electromagnetic showers produce slightly more energy, which results in slightly better resolution.

8.1.4 Temperature monitoring and stabilization

During the very first tests at NA61 in July 2016 and June 2017, a temperature stabilization system based on the Peltier elements was used. One side was cooled down with pressurized air

from the nearby tank. Another side was connected to the metal plates within the SiPM boards, which allowed to keep it at a constant temperature of 20 or 22 °C depending on the ambient temperature. Unfortunately, this system also produced very high noise, see subsection 8.2.3, and therefore it was decided to use the temperature monitoring for CBM PSD instead.

The main problem, which arises from the ambient temperature variations, is the change of the SiPM breakdown voltage. This leads to the change of overvoltage and consequently gain. In subsection 3.6.3 I showed that the temperature coefficient dV_{bd}/dT is constant for the chosen SiPM type and does not change after irradiation. Therefore, one can adjust the supply voltage for every SiPM board based on the known temperature to keep the breakdown voltage stable, which is demonstrated in figure 8.5. Such a system is implemented in the new SiPM boards and was used for the gain adjustment of SiPMs irradiated by 2.5×10^{11} n_{eq}/cm^2 during the tests in April and May 2018.

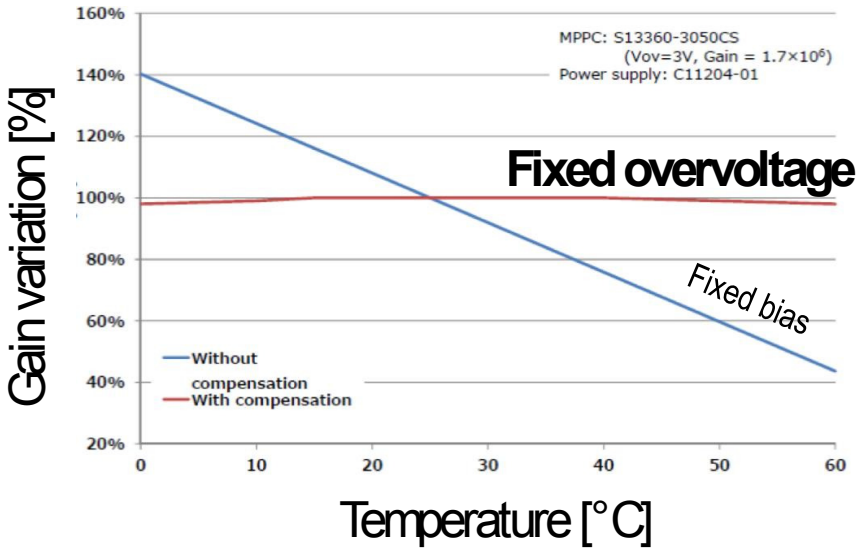

Figure 8.5: SiPM gain stabilization with help of temperature monitoring [325].

It was decided to keep the SiPMs irradiated by 1.6×10^{12} and 4.5×10^{12} n_{eq}/cm^2 on the old electronics boards due to the lack of extra ew boards and very tricky process of SiPM re-soldering, which sometimes results in SiPM failure. This would be unacceptable, since only exactly 5 SiPM pieces were irradiated by the same fluence which are required for the tests.

8.1.5 Investigated SiPMs

Results presented in this thesis were achieved with several batches of Hamamatsu MPPCs S12572-010P irradiated by 1 MeV equivalent neutron fluence of $5 \times 10^{10} - 4.5 \times 10^{12}$ n_{eq}/cm^2. These SiPMs were chosen for the superior radiation hardness, dynamic range and time characteristics with respect to other SiPMs produced by Ketek, Sensl, and Zecotek manufacturers as I described in the previous chapter. However, recently I studied new Hamamatsu MPPC S14160-1310PS and Ketek PM3315-WB-A0 SiPMs and concluded that it might be worthy to continue the investigation with them.

PSD module was consequently equipped with each batch to test its performance with SiPMs irradiated by different fluences. Electronic board equipped with irradiated SiPM batches were mounted to the single calorimeter module and tested in course. Each batch consisted of either 5

or 10 SiPM samples, each SiPM was used for the readout of a single section within the module. All the samples in one batch were irradiated by the same neutron fluence.

To save the budget it was decided to irradiate only 5 SiPMs by 1.6×10^{12} and another 5 SiPMs by 4.5×10^{12} n_{eq}/cm^2. This, unfortunately, resulted in some bias during the measurements caused by the lateral shower leakage, since only the first 5 sections of the module were equipped with SiPMs and available for detection, see figures 8.12 and 8.13. These SiPMs were tested at NA61 in June 2017 and at T9 in November 2017. The fluence was chosen according to the estimation of a yearly radiation load based on the old PSD design, which is presented in PSD TDR [252].

To solve the issue of the shower leakage, it was finally decided to irradiate 10 SiPMs with 2.5×10^{11} n_{eq}/cm^2 to equip the whole 10 sections of the module with them. The fluence was chosen according to the new estimation of a yearly radiation load reduced by the neutron shielding and increased beam hole, which is described in section 5.1.

Two other batches, each consisting of 5 SiPMs of the same type and irradiated by 5×10^{10} and 5×10^{11} n_{eq}/cm^2, respectively, were studied at the very first tests at NA61 in July 2016 and June 2017. However, due to the technical problem at the beamline, it was possible to use only 80 GeV/c protons at that time. After that it was decided to re-irradiate these SiPM samples at fluences of 1.6×10^{12} and 4.5×10^{12} n_{eq}/cm^2 to save the budget. I saved just one sample of each for laboratory tests, which I discussed in chapter 7. Although, I present the data ached during the beam tests with these SiPMs in figure 8.21, one can clearly see that it is obsolete compared to the new data acquired with the whole module equipped with SiPMs irradiated by 2.5×10^{11} n_{eq}/cm^2. More data was collected during two more beamtimes in May 2016 (NA61) and in September 2017 (T10). But due to technical and organizational reasons, its quality was very poor, so I do not present it in my thesis as it does not bring any new information compared to reported data.

Operating voltage was chosen for every SiPM individually based on the measured breakdown voltages and calibration by LED. Non-irradiated SiPMs and SiPMs irradiated by 2.5×10^{11} n_{eq}/cm^2 were operated at the overvoltage of 4.5 V which is recommended by Hamamatsu. Due to the very high dark currents and noise of SiPMs irradiated by 1.6×10^{12} and 4.5×10^{12} n_{eq}/cm^2, they were operated at overvoltage of 3 V.

Table 8.1 summarizes the information on the beamtime conditions and SiPMs used during the different tests.

Beamtime	Beamline	Used momentum range, GeV/c	PID range	Number of SiPMs (sections)	Fluence, n_{eq}/cm^2
July 2016	NA61 (H2)	80	N.a.	5 5	5×10^{10} 5×10^{11}
June 2017	NA61 (H2)	20 – 80	N.a.	5 5	1.6×10^{12} 4.5×10^{12}
November 2017	T9	2 – 10	3.5 – 10	5 5	1.6×10^{12} 4.5×10^{12}
April 2018	T10	2 – 5	2 – 5	10	2.5×10^{11}
May 2018	NA61 (H2)	20 – 80	N.a.	10	2.5×10^{11}

Table 8.1: Summary on the schedule and conditions for tests conducted with irradiated SiPMs.

8.2 Data analysis method

8.2.1 Signal waveforms and raw data conversion

I performed all the data analysis presented in this chapter with help of CERN Root software [280]. I made several individual analysis macros for different analysis tasks type, the length of code ranges from 200 up to 500 lines for my macros.

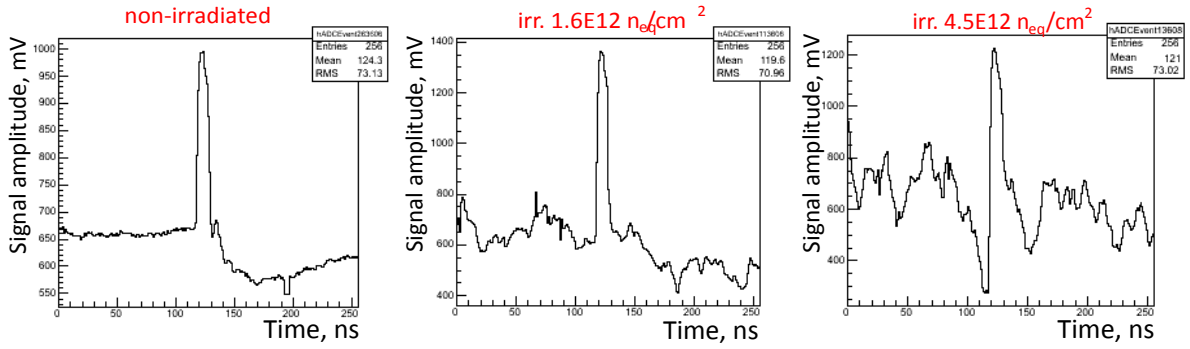

Figure 8.6: Signal and noise waveforms collected with NA61 PSD readout electronics for non-irradiated SiPMs (left), and SiPMs irradiated by 1.6×10^{12} n_{eq}/cm^2 (middle) and 4.5×10^{12} n_{eq}/cm^2 (right).

I converted the raw data collected with the NA61 DAQ system to root format with help of the NA61 SHINE data analysis toolkit installed at CERN servers. Figure 8.6 present typical waveforms for proton signals acquired with non-irradiated and irradiated SiPMs. To reduce the noise standard processing integrates only a narrow time region of 6 ns (6 data point) at the highest point of the signal peak out of the whole 250 ns time acquisition window.

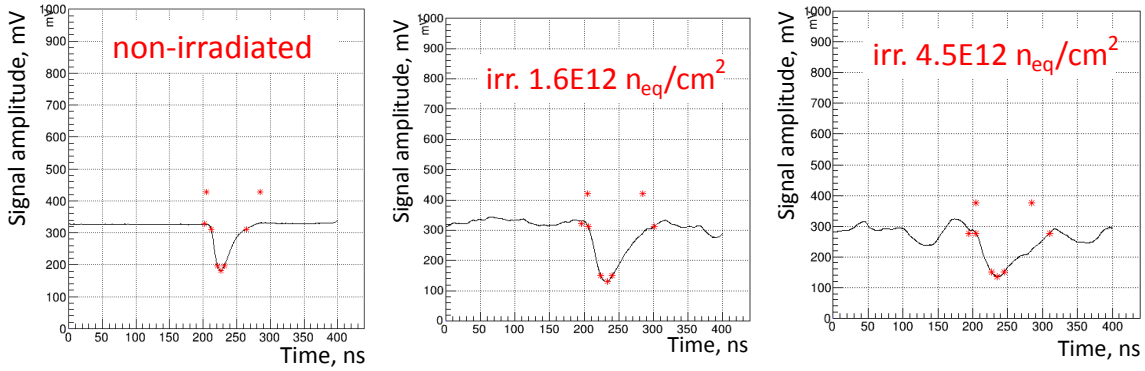

Figure 8.7: Signal and noise waveforms collected with CAEN DT5742 digitizer for non-irradiated SiPMs (left), and SiPMs irradiated by 1.6×10^{12} n_{eq}/cm^2 (middle) and 4.5×10^{12} n_{eq}/cm^2 (right).

For conversion of the raw data collected with help of the CAEN DT5742 digitizer, I used the software toolkit bigdataprocessing. It is an offline analysis toolkit based on CERN Root software. It was created by D. Finogeev who is a member of the PSD team from INR Moscow. Examples of the signal waveforms are shown in figure 8.7. For the signal processing, I chose the very narrow time region of 80 ns out of the whole 450 ns time acquisition window, which

allowed me to significantly reduce the noise. Signal was calculated as an area integral over the narrow time region of 80 ns.

I made a slight modification to the source codes of both processing routines to adapt them for data acquired from irradiated SiPMs. Originally reference zero level of the signal was chosen based on the most stable region within the acquisition time window. But high noise after irradiation resulted in significant variations of the zero level making it impossible to find any stable region. Therefore, I calculated the zero level as an average signal outside the narrow time region that contained the detected signal shape.

8.2.2 Energy distribution in the module and resolution

Figure 8.8 presents a typical energy distribution at every section and sum over the whole module which was acquired with the NA61 DAQ system.

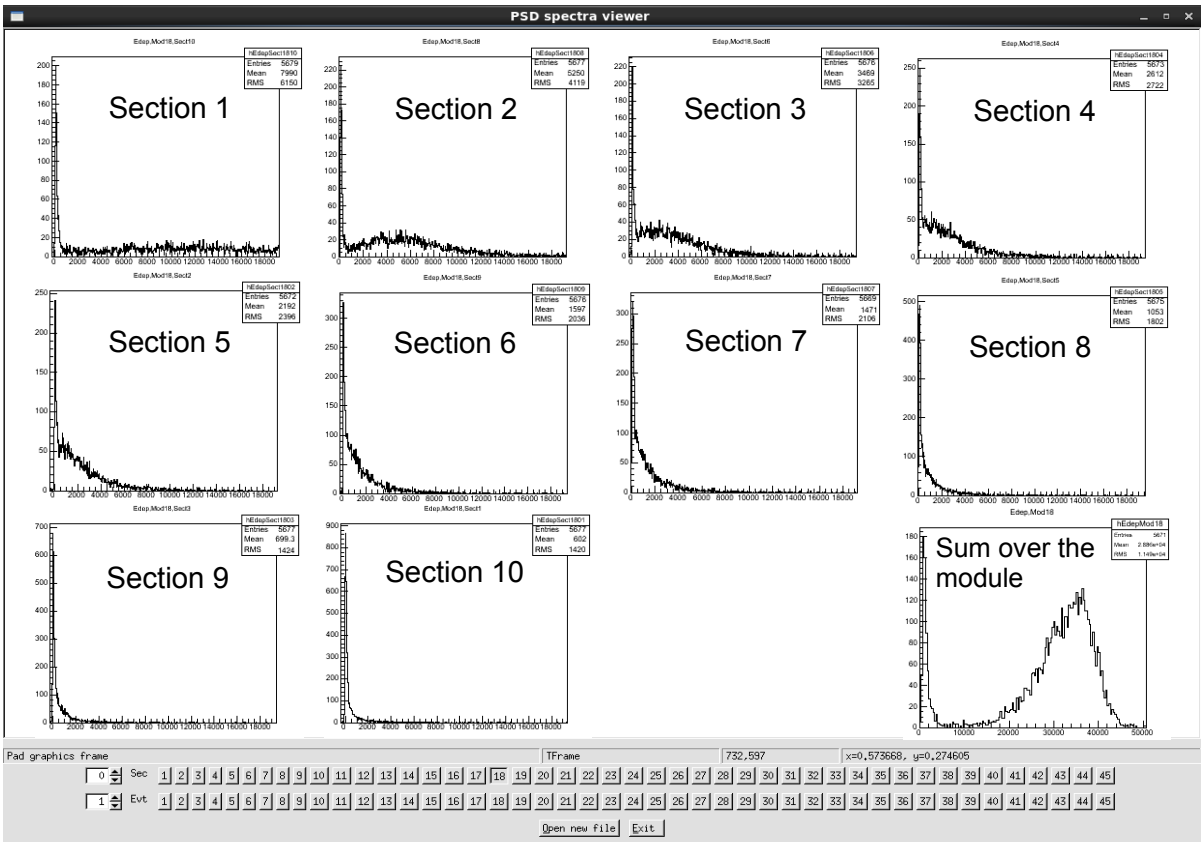

Figure 8.8: Energy distributions in 10 sections of the PSD module for 80 GeV/c proton beam. The bottom left plot presents the sum over all the sections. The skew on the left of the sum distribution is due to the longitudinal shower leakage.

Figure 8.9 presents example distributions of the sum of energy deposited by protons of different momentum in the calorimeter module. Every distribution is fitted automatically with a Gaussian function, and the resulting values of mean and standard deviation are extracted along with corresponding fit uncertainties. For more details on the fitting procedure see subsection 8.2.7. I calculated the module energy resolution R_E as

$$R_E = \sigma_E / E = \frac{\sigma_E^{Gaussian}}{\overline{E}^{Gaussian}} \tag{8.1}$$

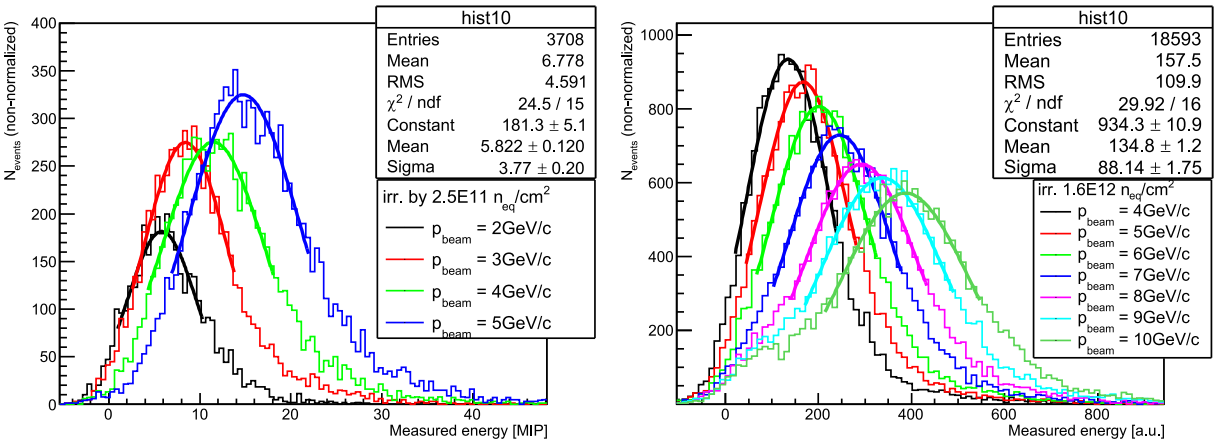

Figure 8.9: Energy distributions for the energy deposition in the PSD module measured with proton beams of different momentum. (left) presents the measurement for module equipped with 10 SiPMs irradiated by 2.5×10^{11} n_{eq}/cm^2. Note that the energy is presented in units of response to MIP particles after calibration. (right) presents the measurement for first 5 sections of the module equipped with SiPMs irradiated by 1.6×10^{12} n_{eq}/cm^2.

To plot the dependences of energy resolution on beam energy I calculated the latter based on the known beam momentum as

$$E_{kin_beam} = \sqrt{m_p^2 c^4 + p_{beam}^2 c^2} - m_p c \tag{8.2}$$

8.2.3 Noise mitigation on the hardware level

The extremely high noise level was encountered during the very first tests at NA61 in July 2016 and June 2017. It was generated by the generally high noise at the NA61 PSD caused by a complicated readout and control electronics system installed directly at the detector. For instance, the high-power Peltier-based thermoelectric coolers [326] were generating the sinusoidal baseline distortion in the signal which is shown in figure 8.6. This could be easily compensated for non-irradiated SiPMs with the correction based on the anticipated baseline from, but for irradiated SiPMs, it became impossible to distinguish any form. In particular, this led to the decision to shift from temperature stabilization to online temperature monitoring and gain adjustment within the new readout electronics developed for CBM PSD.

Another very significant noise source was the power supply used for SiPMs. The dark currents of SiPMs irradiated by $1.6 - 4.5 \times 10^{12}$ n_{eq}/cm^2 were on the order of 0.2 – 1 mA. This was too high for the standard power supply, which could deliver only up to 50 µA per SiPM, see subsection 8.1.2. Therefore, it was necessary to use an external power supply. At the first tests at NA61 in the summer of 2016 and summer of 2017, the available but noisy high power WIENER Mpod 8 channel low voltage module [324] was used. To solve this problem, A .Izvestnyy from the PSD team from INR Moscow assembled the new power supply chain based on several low-noise laboratory supply modules, which were used for the next tests at T9 and T10 in November 2017 – May 2018, see figure 8.4 (right). Figures 8.7 and 8.10 show the

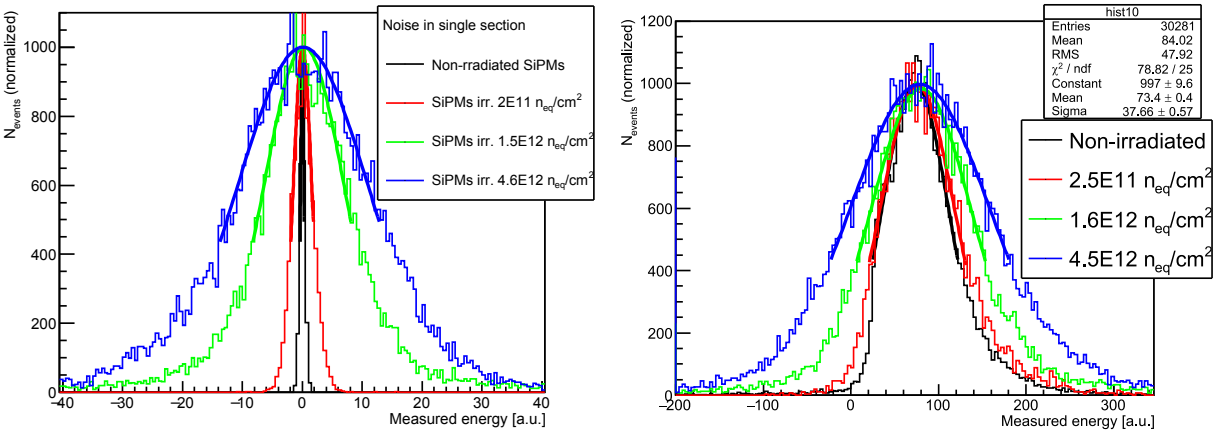

Figure 8.10: (left) Energy distributions of noise measured for single section equipped with non-irradiated and irradiated SiPMs. (right) Energy distributions of response to protons measured with the first five sections of the module equipped with non-irradiated and irradiated SiPMs.

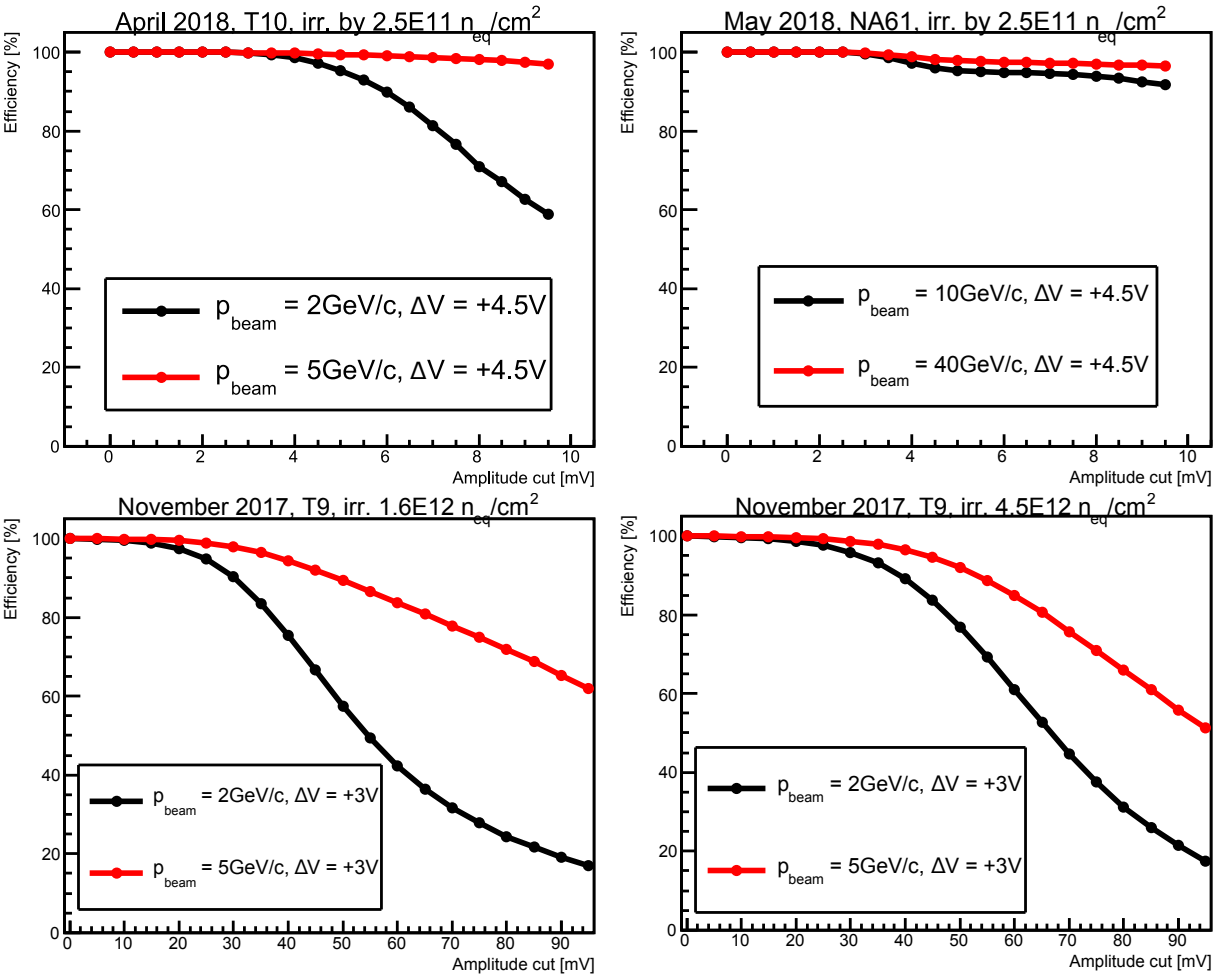

Figure 8.11: Detection efficiencies for detection of beam protons of different energies for SiPMs irradiated with different fluences. It is shown as a function of the amplitude cut in every section which can be used for the noise suppression.

significantly improved situation during the T9 and T10 tests, albeit noise level was still quite high even after the improvement.

8.2.4 Noise reduction with amplitude cutoff

In chapter 7 I described the SiPM noise increase by 2 – 10 times after the irradiation. Figure 8.10 (left) shows the similar effect measured with help of the PSD data acquisition electronics at CERN. Here the relative increase of σ_{noise} in 5 – 50 times was observed for SiPMs irradiated by 2.5×10^{11} – 4.5×10^{12} n_{eq}/cm^2, respectively. This can be explained by the high amount of SiPM readout channels and various hardware components involved in the tests which produced a lot of interferences. Also during the laboratory measurements, the noise was dominated by the amplifier, so only the upper limit was evaluated.

Figure 8.10 (right) shows the deterioration of the energy resolution with the increase of the noise. σ_E/E decreased only by about 5 % (total value) after 2.5×10^{11} n_{eq}/cm^2. But after 1.5×10^{12} n_{eq}/cm^2 the decrease was about 20 %, and after 4.5×10^{12} n_{eq}/cm^2 it became 50 %, namely σ_E/E decreased from 51 % before irradiation down to 100 % after irradiation.

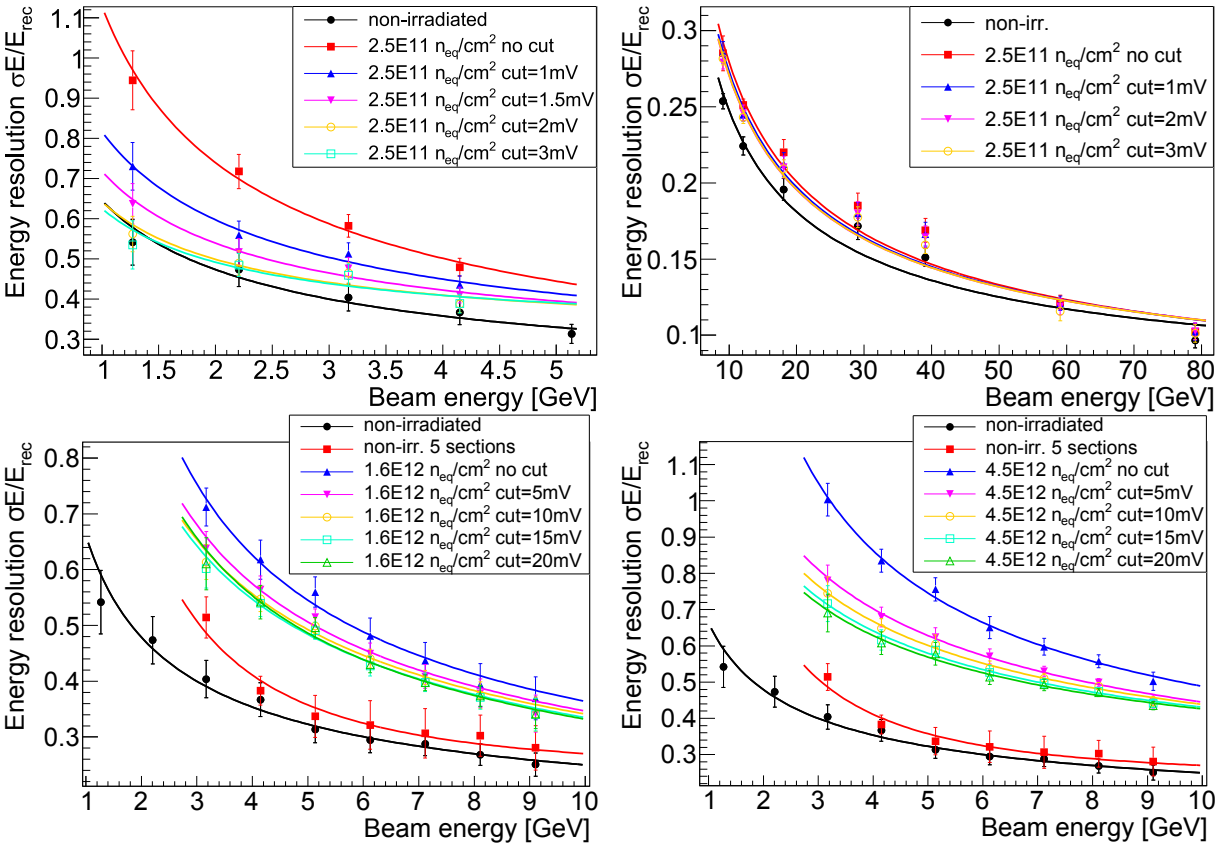

Figure 8.12: Energy resolutions for proton beams of different energies estimated with different amplitude cuts used for noise suppression. All the investigated SiPM batches irradiated with different fluences are presented.

I implemented the cuts on the signal amplitude at every section to discard the noisy sections without useful signal event-by-event. But the cut magnitude shall be chosen carefully to avoid the loss of the actual signal. Figure 8.11 shows the efficiency of the proton detection calculated

for different levels of the amplitude cut. Due to differences in the signal amplitudes for old and new amplification boards, I had to choose different cut values for them.

Figure 8.12 shows that a very significant improvement of the energy resolution can be achieved with help of this simple offline method. Namely, it allowed recovering the energy resolution by up to 40 % for low energies. As expected, for energies above 10 GeV it produced only a negligible effect, since the total signals were much higher. Based on this data I chose the value of amplitude cut of 2 mV for SiPMs soldered to new electronics, and 15 mV for SiPMs soldered to old electronics. This allowed to keep the detection efficiency above 99 % and still be able to see the muons, i.e. retain the full dynamic range.

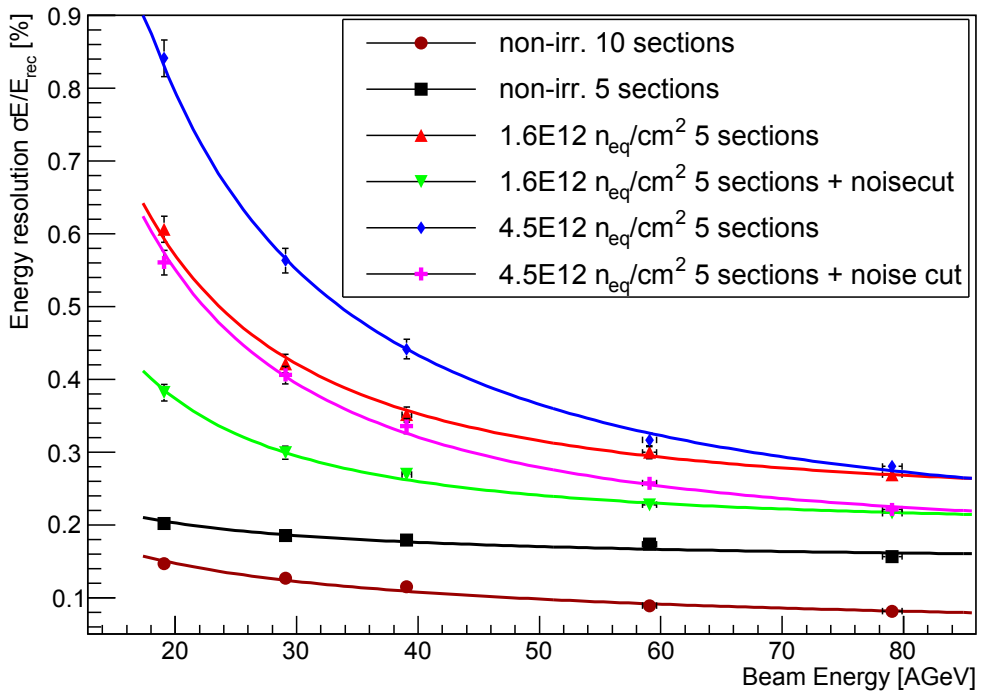

Figure 8.13: Energy resolutions for proton beams measured at high energy range at NA61 for highly irradiated SiPMs with and without the noise cuts. Effects of the utilization of 5 sections instead of 10 are visible for non-irradiated SiPMs.

I also applied similar amplitude cuts during the very first tests which were performed at NA61 PSD in July 2016 and June 2017, which is shown in figure 8.12. Although, it allowed to improve the energy resolution by up to 30 % (total value), the noise level was still too high. Therefore, this data can only be referred to as the upper limit on the σ_E/E.

8.2.5 Electrons exclusion

Another analysis step that improves the energy resolution is the exclusion of electrons. Figure 8.14 (left) shows the energy distributions for incident beam particles measured at the NA61 beamtime. One can see that the distributions are slightly skewed on the right side of the peak. This is explained by the presence of electrons which produce much shorter showers with less energy spread than hadrons. They also do not spend energy to overcome nuclear binding energies. The latter is called the "invisible" energy of the hadron shower, since it is not directly measured by the calorimeter, see subsection 2.4.4 for details. Since PSD can be described as

"almost compensating" calorimeter with e/h ratio about 1.1, election shower have slightly higher energy deposition in the modules.

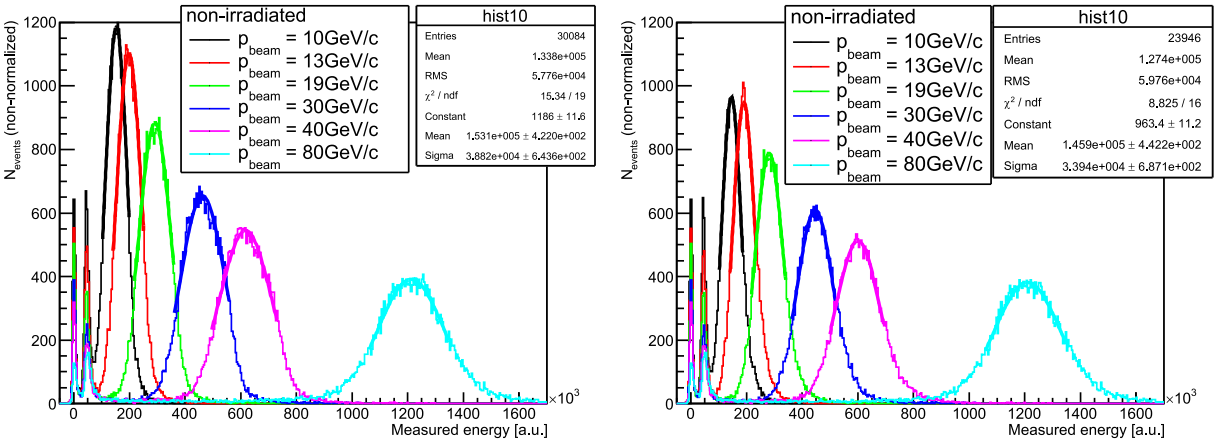

Figure 8.14: Energy distributions for proton beams of different momenta measured with non-irradiated SiPMs before (left) and after the electron exclusion (right). The left-most narrow peak corresponds to noise, the next one – to muons. Following peaks to the right correspond to protons.

The most energy is deposited by electrons in the first section of a module. This effect is compensated by the condition that every event shall do have more than 80 % of energy deposited in the first section. Figure 8.14 (right) shows that after application of the condition the skew on the energy distributions is gone. Figure 8.14 presents the magnitude of this effect on the energy resolution. It consistently improves the resolution by 1 – 3 % for high energies. As expected it produces virtually no change in the energy resolution for low energies where protons were selected by the TOF scintillators.

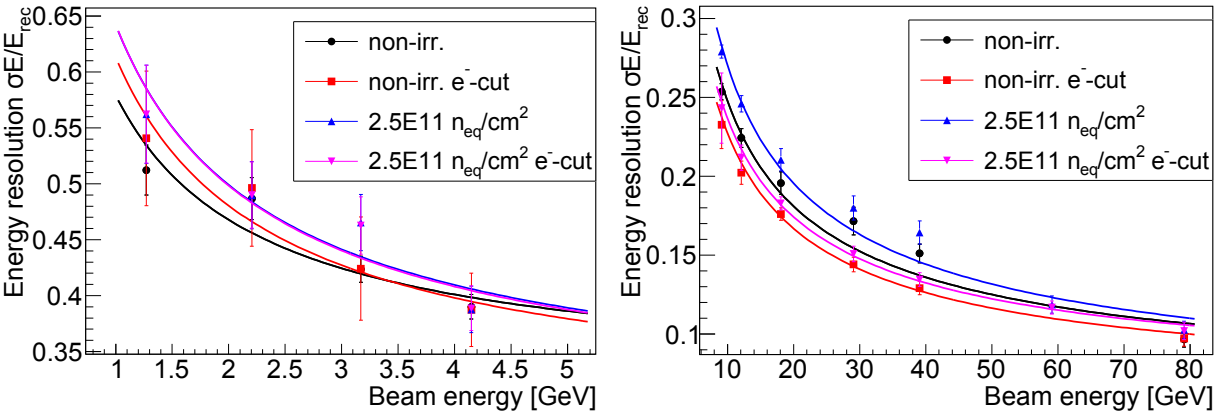

Figure 8.15: Effect induced by the electron exclusion cut on energy resolution measured with non-irradiated and irradiated SiPMs in the low (left) and high (right) energy ranges.

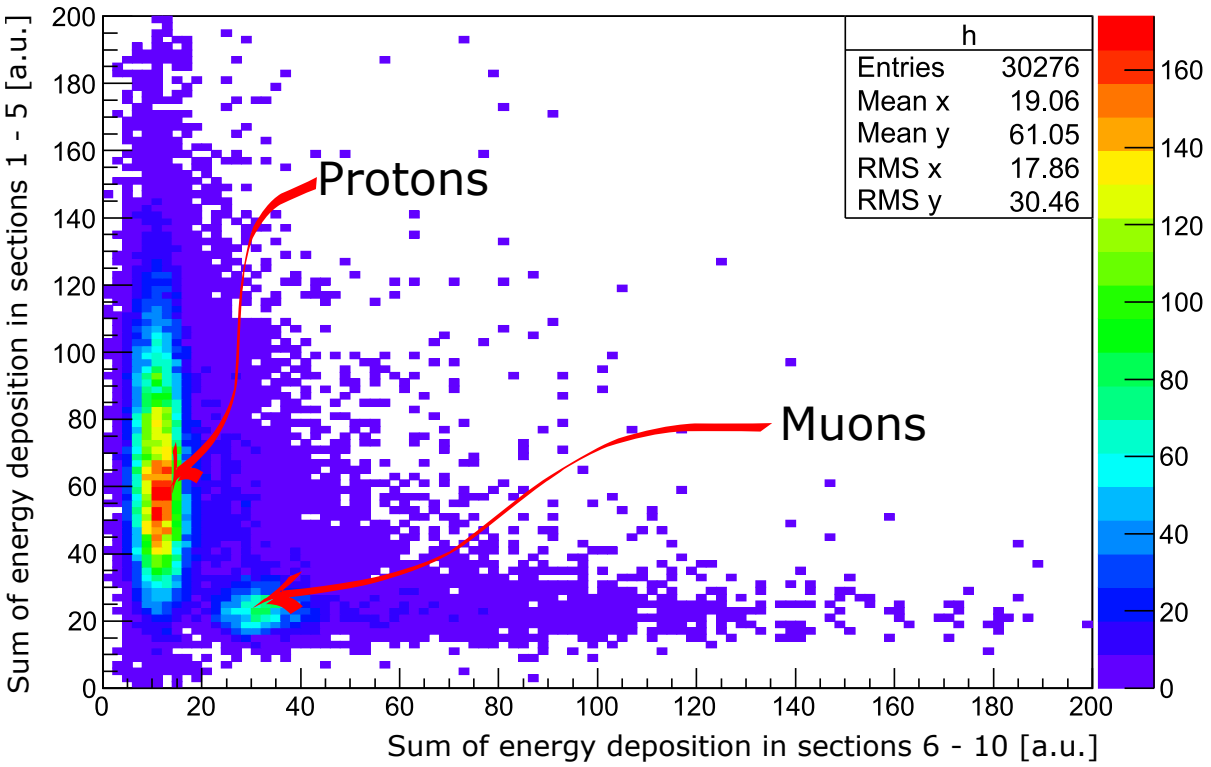

Figure 8.16: Two-dimensional correlation of the sum of signals in first 5 sections versus sum of signals in last five sections measured with SiPMs irradiated by 2.5×10^{11} n_{eq}/cm^2.

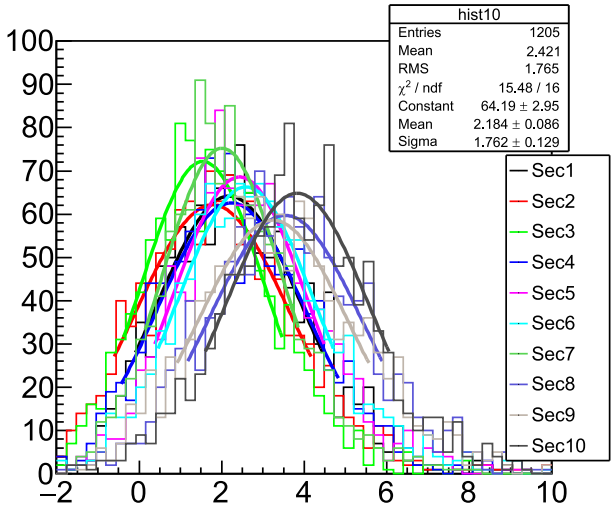

Figure 8.17: Energy distributions for muons selected for the cross calibration of all the 10 sections measured with SiPMs irradiated by 2.5×10^{11} n_{eq}/cm^2.

8.2.6 Calibration of section-to-section response by muons

Longitudinal segmentation of our calorimeters allows unifying the signals in all the sections with help of minimum ionizing particles, e.g. muons. For the performed tests the accelerator created muons that are part of the beam mixture were used, while at CBM it is planned to utilize cosmic

muons. Muons produce the light yield of about 8 – 10 photoelectrons/MeV in each section, i.e. collected by single SiPM [261].

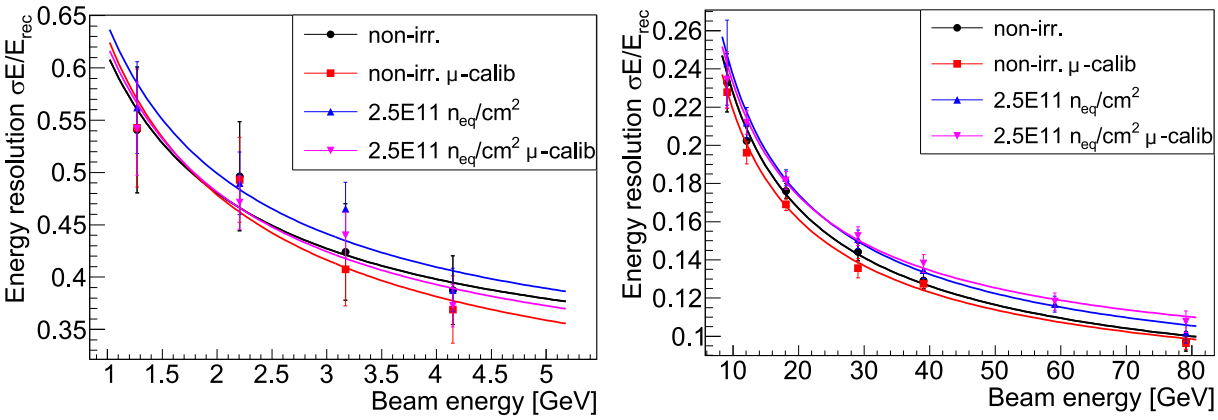

Figure 8.18: Effect of muon-calibration on the energy resolution measured with non-irradiated and irradiated SiPMs at low (left) and high (right) energy regimes.

Figure 8.16 shows the 2D energy distribution in the first 5 sections versus the last 5 sections, where the proton and muon spots are clearly visible. Figure 8.17 shows the energy distribution in every section for the muons selected by the cut on energy window corresponding to the muon spot in figure 8.16. Every distribution is fitted by the Gaussian function and the mean values are extracted. This data is used for the scaling of the response to protons in every section, see energy distributions shown in figures 8.9 and 8.14. Measured energy for protons is divided by the mean values extracted from muons section-by-section.

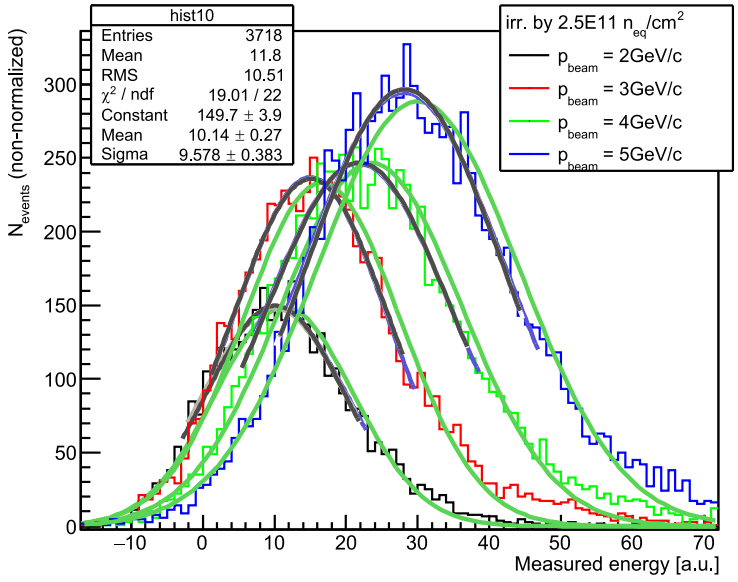

Figure 8.19: Procedure used for the automatic fitting of energy distributions and also for uncertainty estimation based on the fit ranges.

Figure 8.18 shows the benefit which is introduced by the muon calibration in terms of the energy resolution. One can see that the effect is on the order of 2 – 5 % for low energies and below

1 % for higher energies above 10 GeV. This is due to the stochastic nature of the hadron showers which is not easy to account for, compared to muons which produce only ionizing energy loss. I applied this calibration for the data measured with SiPMs irradiated by 2.5×10^{11} n_{eq}/cm^2. For other SiPMs, it was not possible, because the noise levels were too high, and only the first 5 sections of the module were equipped with them.

8.2.7 Uncertainty estimation

I estimated the uncertainty caused by the measurement statistics of each spectrum as the accuracy of the Gaussian fit utilized to extract values of the energy and energy resolution. It was on the order of 1 – 5 % depending on the number of collected events, which was in the range of 4000 – 40000 due to the limitations present in each individual run.

In addition to this, I accounted for the uncertainty caused by the choice of the fitting interval during the automatic fitting procedure. To find an ideal fitting interval, series of five fits is performed. During the first iteration, the fit range corresponds to the full energy range of the measured data. At every next step, the range is chosen as a mean of the Gaussian fit $\pm$ 1.3σ. The results of every iteration are visualized in figure 8.19. The total uncertainty due to statistics and fitting was on the order of 3 – 10 %.

8.3 Discussion of results

8.3.1 Low energy range of 1 – 9 GeV

The low energy region is the most important for the assessment of the calorimeter energy resolution. First of all, CBM will study heavy ions collisions in this range, e.g. SIS100 complex will accelerate gold ions in the range of 4 – 10 AGeV. Furthermore, according to equation (2.15) calorimeter energy resolution improves with the energy increase, therefore it is the most challenging to achieve good σ_E/E at low energies. This is especially the case for the irradiated photon sensors which have an increased noise level because the contribution of the noise to the energy resolution scales with 1/E.

Figure 8.20 shows the change in the energy resolution of the PSD module equipped with irradiated SiPMs. One can see that there is only very minor decrease in σ_E/E after irradiation by 2.5×10^{11} n_{eq}/cm^2, and fitted value is about 70 $\%/\sqrt{\text{E (GeV)}}$ in case of for both irradiated and non-irradiated SiPMs. SiPMs exhibited a very high dark current up to 50 μA, see figure 7.13, but it was still compatible with the standard low noise power supply. The overall noise increased by about 5 times, see figure 7.37, and the signal response of SiPMs to light halved, see figure 7.37. Despite that, with help of the simple offline noise cut, I was able to almost fully restore the energy resolution compared to a module equipped with non-irradiated SiPMs.

Situation is very different for SiPMs irradiated with 1 MeV equivalent neutron fluences of 1.6×10^{12} and 4.5×10^{12} n_{eq}/cm^2, for which σ_E/E became 108 $\%/\sqrt{\text{E (GeV)}}$ and 132 $\%/\sqrt{\text{E (GeV)}}$, respectively. This striking degradation of energy resolution in up to two times is clearly visible in figure 8.20. The main reason is the dramatic increase of the dark current by four orders of magnitude (from 20 nA up to 200 – 500 μA at overvoltage of 3 V, see figure 7.13), which resulted in the increased noise by up to 50 times shown in figure 8.10. It was accompanied by the decrease in the signal amplitude 10 – 20 times shown in figure 7.37. Together these effects resulted in the reduction of the signal-to-noise ratio by up to two orders of magnitude. With help of the noise cuts I significantly improved the resolution, but it was not enough to fully restore it considering the magnitude of the observed effects.

As I discussed in subsections 8.2.3 and 8.2.4, the decrease of σ_E/E at high neutron fluences is also partially explained by the utilization of the external power supply. Although a much better power supply was assembled for the low energy tests at T9/T10, it still could not compare to the specially designed low noise power supply used for SiPMs which had low dark currents. The next contribution arises from the fact that only the first sections of the module were equipped with highly irradiated SiPMs which resulted in the longitudinal shower leakage. And the third reason for the poor resolution is the unavailability of temperature stabilization or gain stabilization during the measurements. Therefore, this data shall be only considered as the upper limit of the radiation-induced degradation.

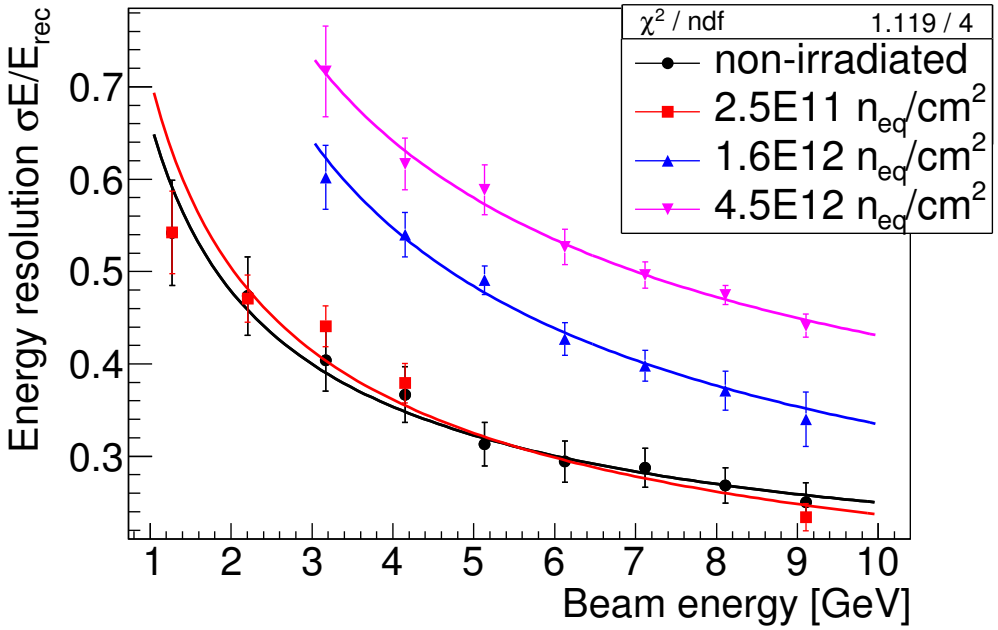

Figure 8.20: Change of the PSD module energy resolution at low energy regime, corresponding to CBM SIS100, after SiPM irradiation with different fluences.

8.3.2 Full energy range of 1 – 79 GeV

High energy region is rather important for the performance of the NA61 calorimeter. However, SIS100 can accelerate protons up to 30 GeV, and SIS300 will extend it up to 90 GeV, which makes it interesting to check the high-energy data as well. Since energy resolution scales with $1/\sqrt{\mathrm{E}}$, and noise contribution from irradiated SiPMs scales with 1/E, the situation is expected to be much better than for low energies.

As one can see in figure 8.21, it is not straightforward to combine all the acquired results. The main problem is the very high noise during the very first tests at NA61 in July 2016 and June 2017, which I described in subsections 8.2.3 and 8.2.4. It resulted in a very poor energy resolution which is visible in the plot. Another complication arises from the fact that the only tests of the full 10 sections of the calorimeter module equipped with irradiated SiPMs were performed in April – May 2018 for SiPMs irradiated by 2.5×10^{11} $\mathrm{n_{eq}/cm^2}$. For other tests, only the first 5 sections were equipped with irradiated SiPMs, which resulted in an artificial

worsening of the resolution due to longitudinal shower leakages, see figures 8.12 and 8.13.

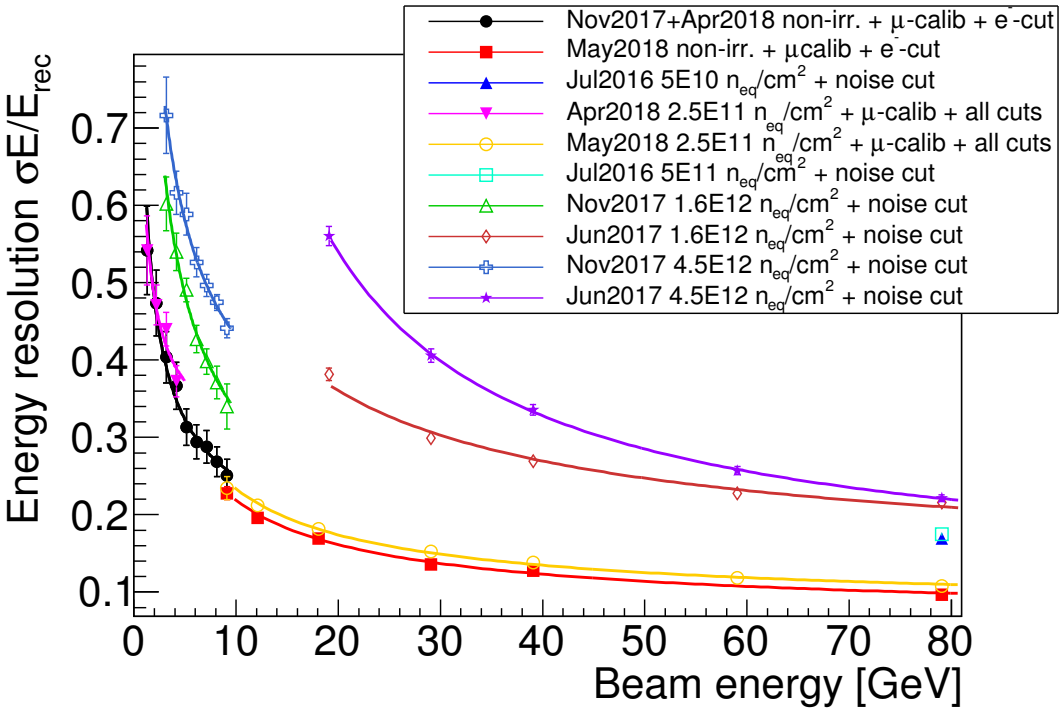

Figure 8.21: Change of the PSD module energy resolution at both low and high energy regimes after SiPM irradiation with different fluences.

The first observation that strikes the eye is the huge discrepancy between the energy resolutions measured at low and high energies for SiPMs irradiated by 1.6×10^{12} and 4.5×10^{12} n_{eq}/cm^2. One can clearly see the mismatch of σ_E/E on the order of 10 – 30 % around the energy 10 – 20 GeV.

Secondly, longitudinal shower leakages play the very important role, especially at the high energy range. For example, at 80 GeV/c σ_E/E is about 10 % for both non-irradiated SiPMs and SiPMs irradiated by 2.5×10^{11} n_{eq}/cm^2 tested in April – May 2018. But for SiPMs irradiated by 5×10^{10} and 5×10^{11} n_{eq}/cm^2 which were tested in July 2016, σ_E/E is about 17 %, because only half of the module was equipped with SiPMs.

The main conclusion that can be drawn from the data is, that it is essential to carefully adjust the power supply and the readout electronics chain to minimize the noise.

However, I combined the data for non-irradiated SiPMs and SiPMs irradiated with 2.5×10^{11} n_{eq}/cm^2 for the whole examined energy range of 1 – 79 GeV. Figure 8.22 shows the resulting data on the energy resolution. One can notice a slight step down in the resolution at 9.11 GeV which is caused by the absence of particle identification for high energies measured at NA61 beamline, see subsection 8.1.3. Simple fit with a single parameter which I used for low energy regime is not enough in this case, so I utilized formula 2.15 to fit the data, the fit parameters are shown in the figure.

Stochastic term $a = 68\ \%/\sqrt{\mathrm{E\ (GeV)}}$ here is slightly worse than $58 - 66\ \%/\sqrt{\mathrm{E\ (GeV)}}$ reported by PSD team from INR Moscow in [318]. This can be explained by the minor differences in the data analysis technique that I used, e.g. zero level determination, and the fact that my fit does not include the noise term. I tried to fix the values of the noise term at 0.5 and 0.6

for non-irradiated and irradiated SiPMs, respectively, which is consistent with data reported in [318]. This indeed improved a which became 65 $\%/\sqrt{\mathrm{E\ (GeV)}}$, but the fit quality in terms of χ^2/ν went from 10.5/11 and 9.9/8 down to 15.9/12 and 29.6/9, for non-irradiated and irradiated SiPMs, respectively. This can be explained by the fact that SiPM does not only contribute to the noise term c of the energy resolution via the increase of the dark current and noise. It also contributes to the stochastic term a via the change in the signal response and the excess noise factor, and to the constant term b via gain sensitivity to voltage and temperature variations [renker]. Therefore, given the available data, it is not simple to unambiguously estimate the change of the individual resolution parameters defined in 2.15.

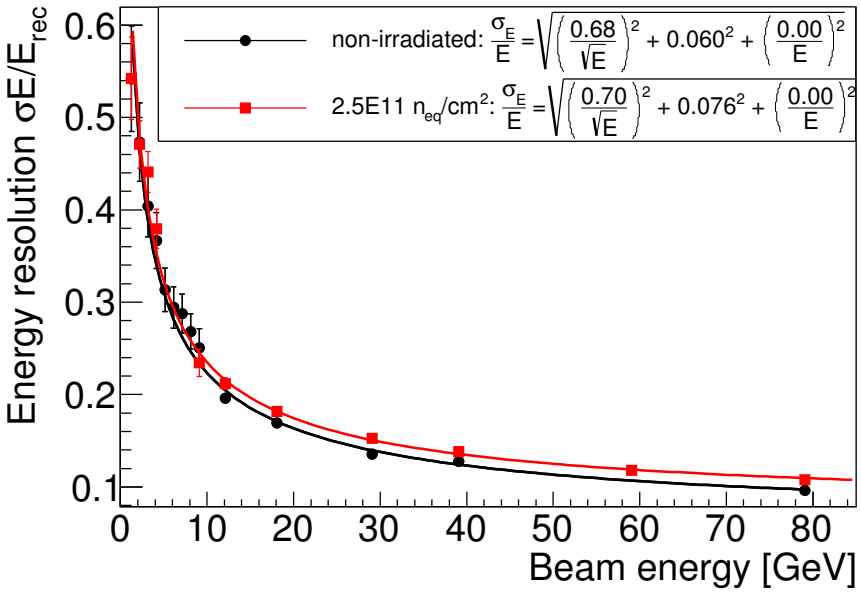

Figure 8.22: Change of the PSD module energy resolution at both low and high energy regimes after SiPM irradiation by 2.5×10^{11} $\mathrm{n_{eq}/cm^2}$.

8.4 Summary

I measured the calorimeter module response to proton beams in the momentum range of 2 – 80 GeV/c, which corresponds to the anticipated range of SIS100 for Au ions and protons. Figure 8.23 shows that PSD module energy resolution changed only slightly in case of light readout with SiPMs irradiated by 2.5×10^{11} $\mathrm{n_{eq}/cm^2}$. This corresponds to SiPMs located closest to the beam hole after a year of CBM operation at 1 MHz collision rate (assumed to be 2 months of an uninterrupted run, see section 5.1 for details).

For SiPMs irradiated by 1.6×10^{12} and 4.5×10^{12} 2.5×10^{11} $\mathrm{n_{eq}/cm^2}$ energy resolution halved. However, this represents only the upper limit of the degradation, because energy resolution for highly irradiated SiPMs was measured only for the first half of the calorimeter module which resulted in shower leakages and an external power supply was used which also introduced additional noise.

Despite the increased noise level, the possibility of the calibration with minimum ionizing particles was proven for SiPMs irradiated by 2.5×10^{11} $\mathrm{n_{eq}/cm^2}$. For SiPMs irradiated with

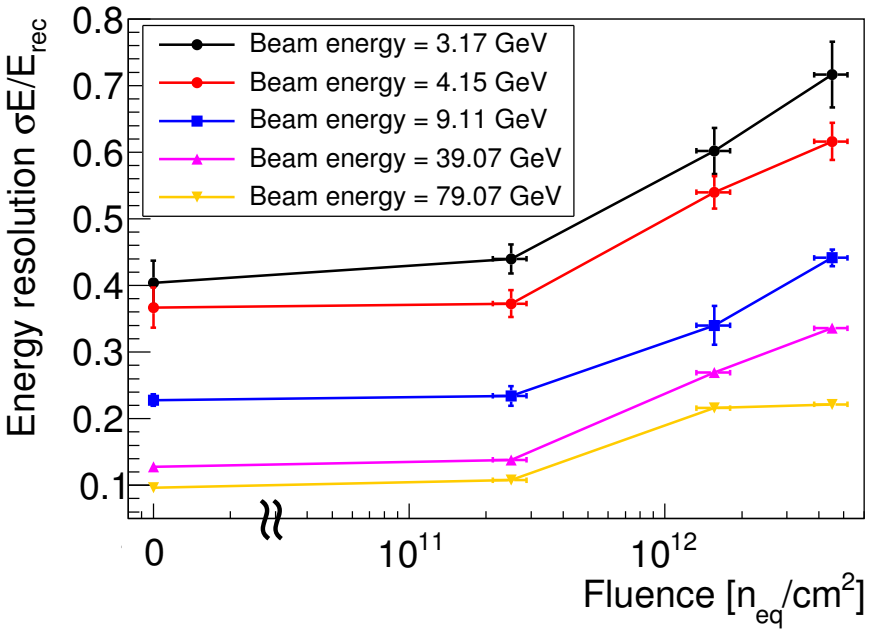

Figure 8.23: Change of the PSD module energy resolution after SiPM irradiation as a function of 1 MeV equivalent neutron fluence achieved by SiPMs, measured with proton beams of different energies.

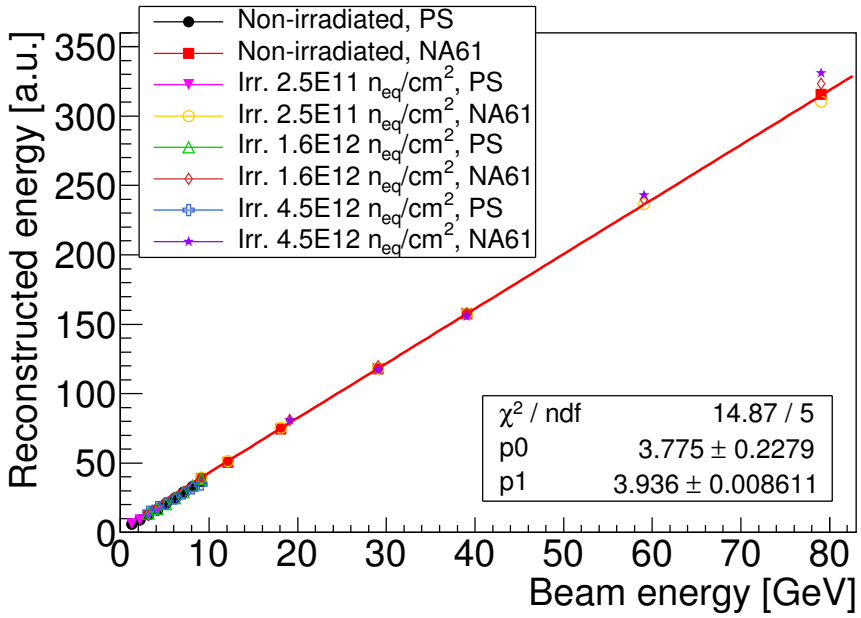

Figure 8.24: Linearity of the PSD module response to proton beams in momentum range of 2 – 80 GeV/c before and after SiPM irradiation with different fluences.

high neutron fluences it was not possible due to utilization of only 5 sections and increased

external noise, so is not possible to draw a certain conclusion whether muon calibration would be possible for the full module and low noise power supply. Figure 8.24 shows that the energy linearity remained consistent with data measured with non-irradiated SiPMs. I noticed only minor deviation from linearity up to 1 % in case of SiPMs irradiated with low fluence, and up to 3 % for SiPMs irradiated with high fluences. Therefore, I conclude that utilization of the irradiated SiPMs does not reduce the dynamic range in terms of the CBM PSD requirements.

I significantly improved the energy resolution with offline noise amplitude cut performed event-by-event and individually for every section. Since an extreme noise increase 5 – 50 times was observed, I advise implementing a similar routine into the data acquisition software at CBM PSD. Hardware noise reduction in form of a low-pass filter would be also beneficial. Reduction of SiPM response to light up to two times can be expected during a year of operation, and it will depend on the SiPM position, i.e. SiPMs located closest to the beam hole will receive the maximal neutron fluence and show the highest degradation. This is not an issue for the detector operation, in case if regular recalibration routine will be implemented. It can be based on the existing LED-calibration system, which can be activated during the technical breaks to equalize the SiPM responses with respect to the level before irradiation.

Since signals in the calorimeter modules closest to the beam hole are the largest, even highly irradiated SiPMs could be used there if the degradation in the energy resolution will be acceptable. SiPMs located further from the beam will achieve significantly lower fluence which will extend their lifetime. Furthermore, the modular detector structure of the CBM experiment will allow exchanging the most damaged SiPMs every year if necessary.

Achieved results on the SiPM radiation hardness are as well of interest for BM@N and NA61 (after upgrade in 2020) experiments where very similar calorimeter design including the SiPM light readout is utilized.

Chapter 9

Simulation of CBM PSD performance with different collision models

The analysis of the heavy-ion collision starts with the detailed description of its basic properties such as collision centrality and reaction plane. These properties are estimated by the dedicated detector setup in the experiment which therefore has to meet certain requirements as described in section 4.3 for the CBM PSD. Simulation of a big number of collisions is a great way to assess the expected performance of the designed experiment. It can be conducted with help of different tools depending on the experiment's needs, for instance, various collision generators and analysis methods can be utilized. This chapter describes a comparative analysis of the various collision generators that I performed to choose the most suitable one for the CBM PSD simulations. Subsequently, I conducted the simulation of the CBM PSD performance based on the input from these generators to estimate the possible impact of the choice of a particular generator.

Experimental determination of global event characteristics in nucleus-nucleus collisions such as the centrality of the collision, which is related to the number of participating nucleons, and the reaction plane orientation is a challenging task in any high-energy heavy-ion experiment. These observables are directly connected to the size and evolution of the excited and compressed medium created in the overlapped region of heavy-ion collision carrying out the general information on the initial collision geometry and dynamics.

9.1 Theoretical background

9.1.1 Heavy-ion collision description

To recreate a "little Big Bang" in the laboratory, accelerator technology is applied to accelerate heavy-element nuclei at nearly the speed of light and lead it to the target composed of the same (or not) nuclei to make them collide. The energy that individual nucleon loses during the collisions with others is available for the production of particles. The process of the nucleon slowing down as it passes through the nucleus is called nuclear stopping. The evolution of a heavy-ion collision is depicted in figure 9.1. At a time $\sim$ 0.2 fm/c partonic constituents of the colliding nuclei (quarks and gluons) are liberated by the collision and form the parton cascade [327]. The partons liberated by the collision interact with each other quite strongly and produced partonic matter rapidly approaches towards thermal equilibrium. Shortly after the

reaction ($\sim$ 1 fm/c), an enormous amount of energy is released into a tiny volume ($\sim$ 10 fm in diameter) wherein a quark-gluon plasma (QGP) medium may be formed. The QGP will expand and cool down rapidly in about 10 – 20 fm/c.

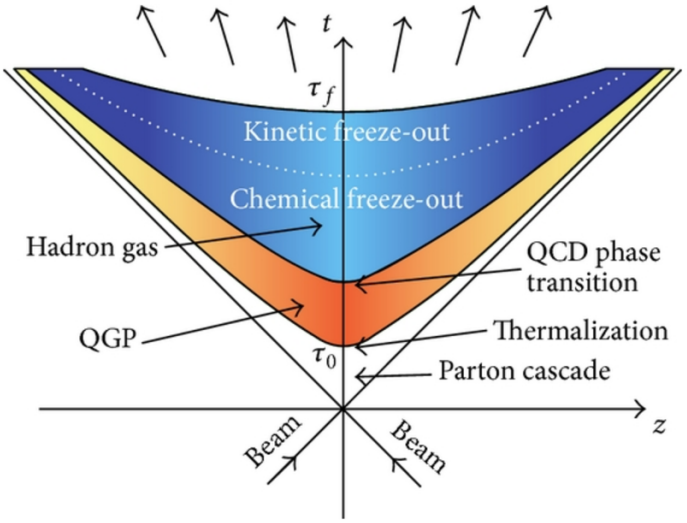

Figure 9.1: The space-time evolution of heavy-ion collision [328].

When the system gets below the critical temperature it enters a mixed-phase until all quarks are again bound inside hadrons by a process called hadronization. This time region is also referred to as quantum chromodynamics (QCD) phase transition, as a quark-gluon phase of matter undergoes the transition to the hadron phase. Depending on the system parameters such as temperature and net baryon density this transition can go directly (high T and low μ_B) or through some extra phase (lower T and high μ_B) where, for example, quarks can be confined, but chiral symmetry – (partially) restored [329]. Study of this transition and corresponding critical point is one of the goals of the RICH BES program, CERN NA61 experiment, and future CBM experiment which is described in detail in section 4.1.

As the energy in the system decreases, inelastic scattering between particles stops and particle species are fixed, this process is called chemical freeze-out. Shortly after that also elastic scattering ceases at kinetic freeze-out. Finally, experimental detectors placed around the reaction point will capture the hadronized particles and reconstruct their trajectories to trace back relevant information during the course of collision. These measurements can then be compared to models like hydrodynamic ones in order to understand the evolution of the collision and determine the temperature and equation of state – the relationship between pressure and volume for the nuclear matter – of the system formed in the collision. For instance, the chemical freeze-out temperature can be determined from fits to measured particle production ratios, because the number of particles produced of a given species depends only on the chemical freeze-out temperature and the net baryon density [330].

Particle flow measurements at SIS18 and AGS provided the first insight into the equation of state in the energy range from 0.1 up to 11 AGeV, but left a number of features to be addressed by second-generation experiments. At AGS, experiment E895 measured the proton elliptic flow and reported a transition from out-of-plane to in-plane emission around 6 AGeV [331]. These data also indicate an evolution from a stiff equation-of-state below 2 AGeV to a softer one at higher beam energies. Such softening of the EOS is suggestive of a phase transition to a

deconfined state. Flow measurements by the FOPI [332] and KaoS [333] collaborations at SIS18, however, seem to exclude a stiff equation of state. Therefore, modern experiments capable of flow measurements with high precision are designed nowadays in order to clarify the situation.

9.1.2 Collision centrality determination

Due to the fact that heavy-ions are extended objects, the system created in a central head-on collision is different from that created in a peripheral collision, where the nuclei just graze each other. Therefore, collisions can be characterized on the basis of their ***centrality***. This is widely used for event selection during the comparison of various experimental results with theoretical calculations. In heavy-ion interactions the event-by-event determination of the collision centrality is used to study observables like the collective flow, particle multiplicities, and fluctuations which vary strongly with centrality.

Geometrically, centrality is defined by the impact parameter b – the distance between the centers of two colliding nuclei in a plane transverse to the beam axis, see figure 9.2. Centrality is thus related to the fraction of the geometrical cross-section that overlaps, which is proportional to $\pi b^2/\pi(2R_A)^2$, where R_A is the nuclear radius [334]. Consequently, b can scale from 0 up to $2R_A$, where collisions with a small b are referred to as central and collisions with a large b as peripheral. It is customary in heavy-ion physics to characterize the centrality of a collision in terms of the number of ***participants*** (N_{part}), i.e. the number of nucleons that undergo at least one collision, or in terms of the number of binary collisions among nucleons from the two nuclei (N_{coll}) [335]. The nucleons and fragments that do not participate in any collision – the ***spectators*** – essentially keep traveling unaffected, close to the beam direction.

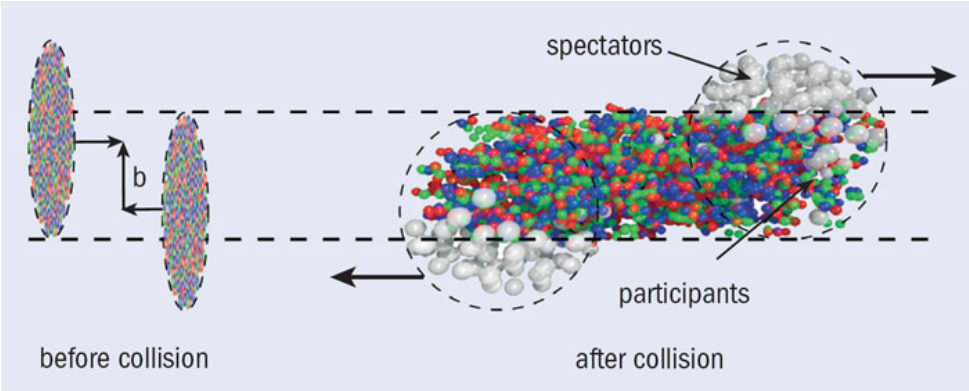

Figure 9.2: Left: Two heavy-ions before collision with impact parameter b. Right: The spectator nucleons remain unaffected while particle production takes place in the participants zone [334].

The magnitude of the impact parameter b or the number of participating nucleons for a given heavy-ion collision is not known experimentally. Instead, the multiplicity of the produced particles in the overlap zone of the nuclei is used as an experimental proxy of the b value. Since the b value and particle multiplicity are correlated only on average, the measured multiplicity can be only used to estimate the average impact parameter value $\langle b \rangle$ and its spread σ_b for a given multiplicity (centrality) class of events. In practice, all events are sorted in centrality classes, with the most central ($b \approx 0$ or $centrality \approx 0\%$) being the collisions with the highest multiplicity of the produced particles and peripheral ($b \approx 2R_A$ or $centrality \approx 100\%$) with low multiplicity [336].

The multiplicity of the spectators (collision fragments) can be also used for collision centrality determination. Spectators provide an independent way to determine centrality which is important for physics studies such as event-by-event fluctuations at midrapidity of various physics observables. In the case of spectator measurements, the most central events correspond to a low spectator multiplicity (or a small energy deposition in the very forward hadron calorimeter), while peripheral events result in a large number of spectators (and typically in a large energy deposition in the forward calorimeter).

9.1.3 Reaction plane reconstruction

In addition to the centrality, reaction plane XZ defined by the impact parameter b and axis of the beam z is used to describe the initial collision geometry [337], see figure 9.5. The ***reaction plane angle*** Ψ_{RP} is a very important characteristic of the collision allowing to measure such effects as a collective flow which is defined with respect to the reaction plane [338].

Similar to the magnitude of the impact parameter, Ψ_{RP} is not known experimentally. To estimate the reaction plane orientation it is common to use the azimuthal asymmetry of participant particle production in the transverse plane to the beam direction [339]. This method works the best for the central collisions. Alternatively, as spectators are deflected in the direction of the impact parameter, the most direct method to determine the reaction plane is to measure the position and energy of the spectators at a certain distance downstream of the target. This approach can be realized by the measurement of transverse energy deposition in a very forward hadron calorimeter and it is very profitable for the non-central collisions.

The finite number of fragments and the fluctuation of the particle multiplicity from one collision to another at fixed impact parameter orientation result in a difference between the orientation of the true reaction plane of the collision and its ***event plane*** which is measured experimentally. Hereby, experimentally determined reaction plane angle Ψ_{EP} is used to denote the event plane angle. The described angular difference is usually called the ***event plane resolution*** or ***reaction plane resolution*** and defined as a Gaussian width of the $\Psi_{\mathrm{EP}} - \Psi_{\mathrm{RP}}$ distribution.

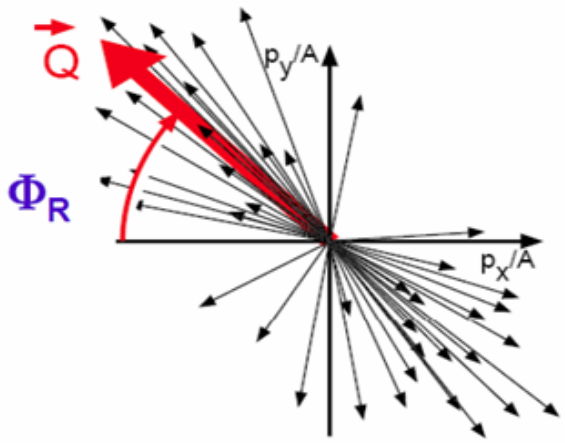

Figure 9.3: Schematic representation of the Q-vector reconstruction for the reaction plane determination.

The event plane angle is calculated from the spectator energy deposition in a given module of the forward hadron calorimeter or with reconstructed participant particles in the tracking system

by constructing a so-called flow ***Q-vector*** which is shown in figure 9.3. It is a two-dimensional vector in the plane transverse to the beam defined as [340]

$$\mathbf{Q} \equiv (Q_x,\ Q_y) = \sum_i \omega_i \left(\cos n\phi_i,\ \ \sin n\phi_i\right) \tag{9.1}$$

where ϕ_i is the azimuthal angle of the i-th particle reconstructed by the tracking or azimuthal angle of the center in the transverse plane of the i-th calorimeter module. w_i is a weight that is used to improve the sensitivity of the event plane to the reaction plane. In the case of the tracking, the weight w_i is usually set to the rapidity of the particle i. In the case of the calorimeter, the weight w_i is typically set to the energy in a given module i. Therefore, the event plane angle Ψ_{EP} can be calculated from the $Q-vector$ components

$$\Psi_{\mathrm{EP}} = \mathrm{atan}\left(\frac{Q_y}{Q_x}\right). \tag{9.2}$$

9.1.4 Particle flow decomposition

The collective motion of the final-state hadrons created in the non-central heavy-ion collision contains important information on the collision dynamics. The isotropic, radial flow allows characterizing the collision system at kinetic freeze-out, i.e. when elastic collisions of the produced particles cease. Anisotropic flow results from the conversion of anisotropies in the initial density distribution into pressure gradients, and thus gives access to the equation of state [341].

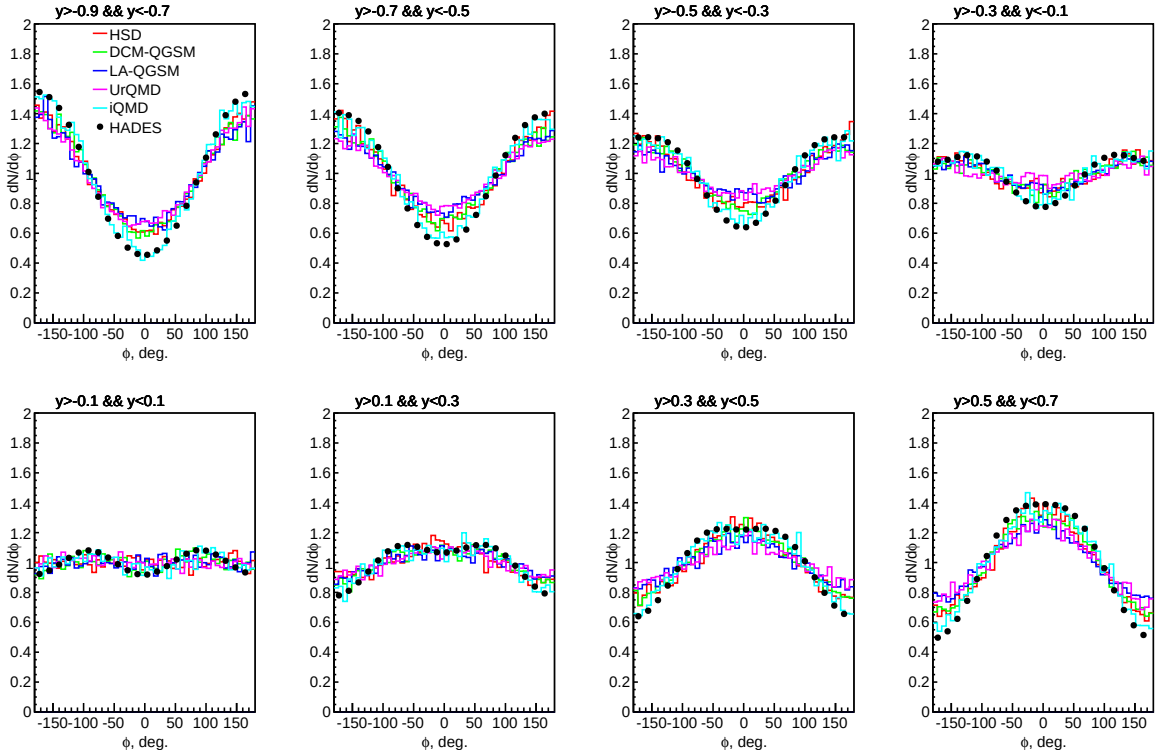

Figure 9.4: Particle distribution with respect to the azimuthal angle for different rapidity bins. Data was extracted from collision simulations which I performed with different models, see following sections. Data measured by HADES collaboration were provided by A .Sadovsky [342].

Given the known reaction plane orientation, one can study physics observables relatively to the reaction plane orientation. An example of the particle azimuthal distribution relative to the reaction plane is shown in figure 9.4. It can be decomposed via Fourier series as [340]

$$\frac{dN}{d\phi} \sim 1 + 2\sum_{n} v_n \cos n(\phi - \Psi_{\mathrm{RP}}) \tag{9.3}$$

where ϕ is the particle azimuthal angle and v_n are called the anisotropic transverse flow coefficients.

The first few coefficients have special names, in particular the first, v_1, and second, v_2, are called the directed and elliptic flow, respectively. The flow coefficients v_n can be derived from the equation (9.3) as

$$v_n = \langle \cos n(\phi - \Psi_{\mathrm{RP}}) \rangle \tag{9.4}$$

where the brackets $\langle ... \rangle$ denote the average overall particles in a given event and over a large ensemble of events.

The value of v_n is typically represented either with respect to the transverse momentum p_T or to the rapidity y. The y is usually employed for the relativistic particles and defined by [343]

$$y = \frac{1}{2} \ln \left(\frac{E + p_z c}{E - p_z c} \right) \tag{9.5}$$

where E is the total particle energy and p_z is its longitudinal momentum. Therefore $v_n(y)$ reflects all the three projections of the particle momentum vector in space. To simplify the rapidity value for different collision energies, one can normalize the rapidity y to the rapidity of the center of mass y_{cm}, which in case of the beam + target interaction is described by

$$y_{cm} = \frac{y_{target} + y_{beam}}{2} = \frac{1}{4} \ln \left(\frac{E_{beam} + p_{beam} c}{E_{beam} - p_{beam} c} \right) \tag{9.6}$$

where E_{beam} and p_{beam} are the beam energy and momentum, correspondingly. Subsequently, normalized rapidity can be defined as

$$y_{norm} = \frac{y - y_{cm}}{y_{cm}} \tag{9.7}$$

After this normalization, beam rapidity will correspond to 1 and target rapidity will correspond to -1.

Figure 9.5 represents the typical geometry of the heavy-ion collision. The collision is generally divided into two regions – the spectators and participants region by its physical origin [345]. The directed flow v_1 represents an overall shift of the total azimuthal particle distribution in the transverse plane that can be measured by the spectators or participants. It is also called in-plane flow, as it propagates in the reaction plane. In a symmetric colliding system $\langle cos(\phi - \Psi_{\mathrm{RP}}) \rangle$ is an odd function of rapidity, therefore it is zero at midrapidity [330]. Directed flow is a result of the pressure in the system and therefore it is sensitive to the compressibility of the created matter. It depends on collision centrality: it is maximum for semi-central collisions and vanishes for central collisions, due to symmetry, and for very peripheral collisions due to the lack of a sizable pressure gradient.

Elliptic flow v_2 is measured with help of participants and can be both in- and out-of-plane depending on the system energy as it is shown in section 9.2. Elliptic flow is the most dominant modulation of the azimuthal particle production at midrapidity and can only build up if an

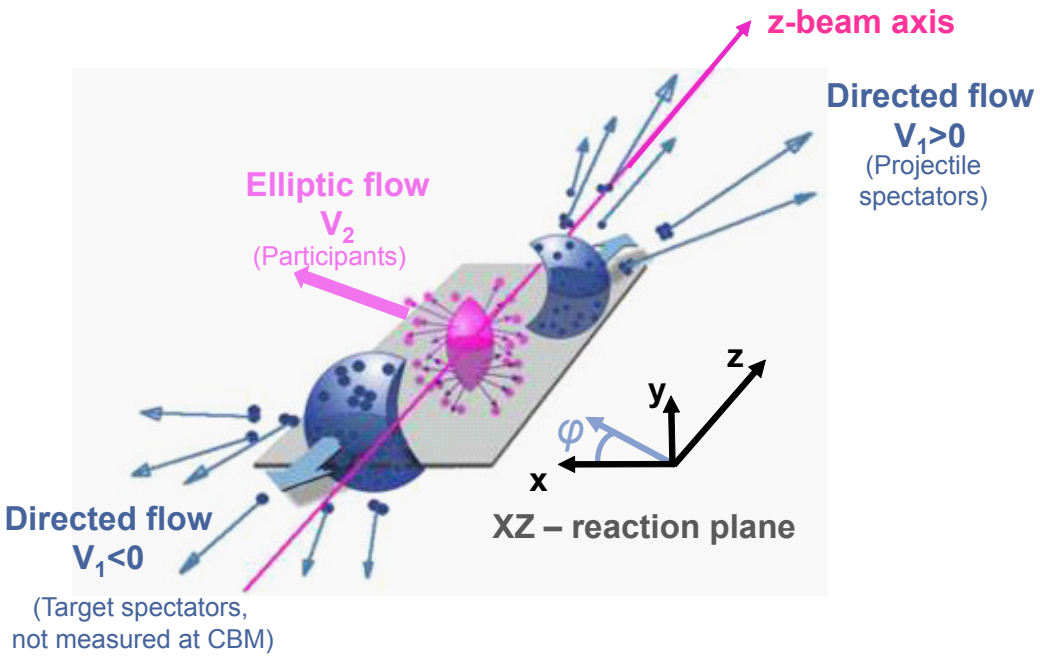

Figure 9.5: Schematic illustration of the collision zone between two incoming nuclei explaining the reaction plane, spectators and participants regions and corresponding directed and elliptic collective flow. Modified artwork from [344].

anisotropic reaction volume is present as well as multiple interactions between the particles. Due to multiple interactions, the initial spatial anisotropy of the reaction volume is transferred into an anisotropic transverse momentum distribution. Most of it comes from the early stage of the evolution of the system making elliptic flow-sensitive to the partonic phase, if present, of the system [346]. The further flow harmonics can be related to the modulation of the participants region shape such as triangular v_3 and squared v_4 flow.

In the experiment, estimate of v_n can be obtained with the event plane method using the event plane angle Ψ_{EP} [340]

$$v_n\{\Psi_{\mathrm{EP}}\} = \frac{\langle \cos n(\phi - \Psi_{\mathrm{EP}}) \rangle}{R_{\mathrm{n}}} \tag{9.8}$$

The reaction or event plane resolution correction factor R_{n} corrects for the finite event plane angle resolution relatively to the reaction plane and it is defined for n-th flow harmonics as

$$R_{\mathrm{n}} = \langle \cos n(\Psi_{\mathrm{EP}} - \Psi_{\mathrm{RP}}) \rangle \tag{9.9}$$

R_{n} value ranges between zero (very poor resolution) and unity (very good resolution) [338]. I estimated only reaction plane resolution correction factor R_1 corresponding to the first flow harmonic because it is used in practice for the true reaction plane estimation.

In order to estimate the event plane resolution experimentally, i.e. when the actual value of the reaction plane angle is unknown, one can divide the full event into two independent sub-events of equal multiplicity [347]. Since the sub-events are positively correlated because each is correlated with the reaction plane, the event plane resolution for the sub-events is just the square-root of this correlation

$$R_{\mathrm{n,sub}} = \sqrt{\langle \cos n(\Psi^A_{\mathrm{EP}} - \Psi^B_{\mathrm{EP}}) \rangle} \tag{9.10}$$

where A and B denote the two subgroups of particles.

9.1.5 Heavy-ion collision event generators

Input data in form of the list of particles and their momenta which were created in the collision is requested to perform further physical analysis. They can be obtained by running heavy-ion collision event generator codes with given input parameters, such as a colliding system and energy. Nowadays, there are a variety of generators available based on different collision description approaches [2]. A collision can be treated macroscopically as an ideal or viscous fluid or several fluids by the so-called fluid dynamics models. They were found to be very useful for the description of bulk matter properties of the system such as the equation of state. Unfortunately, the dedicated freeze-out procedure is required to convert the fluid into individual particles, which is not straightforward.

Another approach is to describe the colliding system microscopically in terms of individual particles and their interactions. Cascade models are the simplest ones treating collisions and decays on the basis of vacuum cross-sections and decay rates but neglecting the interplay of the particles inside the collision zone. They are justifiable for energies higher than 6 AGeV, where the nuclear mean field becomes less important as direct elastic and inelastic collisions start to dominate the reaction dynamics. To properly describe the inter-particle interactions a variety of true quantum many-body approaches were developed, which are however technically extremely demanding and quite complicated to apply for a wide range of observables. Alternatively, the dynamics of the system can be described in terms of certain well-chosen relevant observables that are supposed to contain the most relevant information. For instance, Boltzmann Uhling-Uhlenbeck dynamics (BUU) reduces the many-body problem to one-body by adding an effective mean-field averaging the influence from all the particles to a given one. Quantum molecular dynamics (QMD) codes exploit density- and momentum-dependent effective two-body forces instead of a single mean-field. Furthermore, the string concept can be utilized, where very heavy hadrons are treated as "strings" in order to extend the range of applicability to higher energies. The formation of composite particles or fragments such as deuterons or α-s can be also included through the specific techniques within the code itself. However, more often additional post transport codes are employed to form clusters by a specific set of rules, e.g. combining particles that have very close momenta after a freeze-out.

Different combinations of the aforementioned and other approaches were used to develop a variety of collision generation and transport codes. Typical examples of a cascade model are ARC and LUZIFER [348], at the same time some other models can be run in a cascade mode as well to increase the computation speed. At the lower collision energies up to 10 AGeV models that rely on purely hadron degrees of freedom and a mean-field are typically utilized such as iQMD, VUU/BUU, ART, and BEM [348]. Widely known models extended to higher energies with help of strings are RQMD, UrQMD, and HSD [2]. At RHIC and CERN energies strings and hadrons may be substituted by quarks and gluons interacting through hard scattering for the appropriate description of the deconfinement as in VNI/BMS and AMPT [348]. For the detailed description, and comparison of the various models and approaches, some of which were mentioned here, please refer to the Part III of the CBM Physics Book [2].

In this study four well known heavy-ion collision event generators that can be applied in the full CBM energy range, i.e. from 2 up to 35 AGeV, were chosen for the comparison:

- Ultrarelativistic Quantum Molecular Dynamics (UrQMD) [349] model is described as the most stringent extension of the QMD concept towards relativistic and ultra-relativistic energies. It has an impressive particle list, namely 55 different baryon species (including

nucleon, Δ and hyperon resonances with masses up to 2.25 GeV/c^2) and 32 different meson species (including strange meson resonances), which are supplemented by their corresponding antiparticles and all isospin-projected states. It is one of the most widely utilized models in the corresponding energy range due to its versatility, for instance, most of the general CBM simulations are currently done with it. Data generated with UrQMD version 3.3 were provided by V. Friese [350].

- The Hadron-String Dynamics (HSD) [351] transport approach is another multi-purpose model aiming to gain an understanding of the nuclear dynamics, the creation of dense and hot hadron matter and the modification of hadron properties in a medium in the energy range from SIS to RHIC. It is based on quark, diquark, string, and hadron degrees of freedom and is notable due to the implementation of the string concept, however many other models like UrQMD have it implemented as well. There is also another version called Parton-Hadron-String Dynamics (PHSD) which is the extension of HSD for higher energies including the partonic phase. However, several simulations performed with it up to the energy of 30 AGeV were found to give the same results as HSD, and therefore it is not discussed in this thesis. I generated the data with HSD version 3.3, access to the code was granted by E. Bratkovskaya [352].

- Dubna intranuclear Cascade Model coupled with Quark-Gluon String Model (DCM-QGSM) [353] used within the SHIELD [354] transport code is an alternative string model realization. It is dedicated to simulating the interaction of hadrons and arbitrary atomic nuclei with complex extended targets in an energy range up to 1 TeV/A. It incorporates the string fragmentation, formation of resonances, and rescattering of hadrons, but simplifies the nuclear effects neglecting mean fields or multi-particle interactions. This code is beneficial in the way that it inherently includes nuclear fragmentation and therefore is of big interest for the PSD simulations as many fragments are expected to be detected there [252]. Data generated with the last version of DCM-QGSM were provided by M. Golubeva [355].

- Los Alamos Quark-Gluon String Model (LA-QGSM) [353] is another somewhat refined version of the previously described code. Data generated with the last version of LA-QGSM were provided by K. Gudima [356].

Additionally, one more model was utilized for the comparison with recent flow data acquired by the HADES experiment at 1.23 AGeV [357]:

- The Isospin Quantum Molecular Dynamics model (iQMD) [2] is an extension of the original QMD code with respect to the isospin dependence of the nuclear forces determining the mean-field and the cross-sections for the binary scatterings. In addition to neutrons and protons, the four charge states of Δ resonances and the three ones of the pion are included. Fragmentation is included in the code as well. Unfortunately, the model is by design suitable for an application only below 2 AGeV and therefore cannot be applied for the CBM simulations. But I used it for comparison with data acquired by HADES collaboration. Data generated with iQMD were provided by Y. Leifels [358].

9.2 Proton collective flow at CBM energies: models vs data

To assess their applicability for the CBM PSD simulations, the aforeindicated models were used to generate data for semi-central Au+Au collisions in the projectile beam energy range $E_b = 1 - 30$ AGeV, which covers the range from SIS18 at GSI up to SIS100/SIS300 at FAIR.

Statistics of 10^5 minimum bias events were used for every model at each energy to archive the best accuracy. With help of the collision data, I calculated the directed v_1 and elliptic v_2 flow produced by the models by formula 9.4. The collective flow was compared for the models and available experimental data achieved by FOPI [332], HADES [357], E895 [359], E877 [360], and STAR [361] collaborations. HADES data presented here were kindly provided by A. Sadovsky [342]. I applied the cuts on transverse momentum p_{T} and impact parameter b in the simulations to match the cuts used by corresponding experimental groups as presented in table 9.1.

Experiment	E_b, AGeV	b, fm	*Centrality*, %	p_{T}, GeV/c
FOPI	1.2	3.3 – 6.0	6 – 21	> 0.3
HADES	1.23	3.3 – 6.0	6 – 21	> 0.3
E895	2	5 – 7	12 – 25	> 0.1
	4	5 – 7	12 – 25	> 0.1
	6	5 – 7	12 – 25	> 0.2
	8	5 – 7	12 – 25	> 0.4
STAR	30	4.5 – 9.2	10 – 42	> 0.2

Table 9.1: Summary of cuts on transverse momentum p_{T} and impact parameter b used for the collective flow simulations for consistency with the experimental data.

Centrality classes roughly corresponding to the impact parameter b cuts are also presented for convenience. However, they were estimated very approximately according to data acquired by V. Klochkov [259], who estimated the inherent uncertainty of the centrality determination as 5 – 10 %. In other words, I analyzed the semi-central collisions, which fits the purpose of the comparison quite well – v_1 flow is largest in this centrality region while v_2 is also very well visible. Protons were primarily chosen for this general flow comparison as the most abundant particles in the corresponding energy region and therefore carrying most of the flow (about 90 %).

An example of the collective flow of protons as function of the normalized rapidity y_{norm} at SIS100 energies is shown in figure 9.6 (top) for $E_b = 4$ AGeV and figure 9.6 (bottom) for $E_b = 8$ AGeV. Proton flow calculated for other energies, i.e. 1.23, 2, 6 and 30 AGeV can be found in appendix I. One can see that all the event generators produced the v_1 that exhibited the correct trend expected by the data, i.e. $v_1(y_{norm})$ is an odd function symmetric to midrapidity and crossing zero at $y_{norm} = 0$. However, the slope of $v_1(y_{norm})$ varied significantly for the different event generators, which is very well seen by an eye for $E_b = 8$ AGeV. In the case of v_2 the situation was observed to be even worse. The only iQMD at $E_b = 1.23$ AGeV actually followed the $v_2(y_{norm})$ data trend, see figure I.1, while other models did not show much agreement with data. Unfortunately, for the energy range of $E_b = 2 - 30$ AGeV only the magnitude of the elliptic flow at midrapidity $v_2|y_{norm} = 0$ is available from the experimental data sets, and therefore it is not straightforward to judge which model follows the closer trend of $v_2(y_{norm})$. Based only on a comparison of $v_2|y_{norm} = 0$ significant discrepancies with data were observed for all the generators at these energies.

Finally, I compared the slope of proton directed flow (dv_1/dy_{norm} fitted for $y_{norm} \in$ [-0.5; 0.5]) and elliptic flow at midrapidity ($v_2|y_{norm} = 0$) as a function of beam energy E_b simulated by different generators with the experimental data. Results of comparison are presented in figure 9.7. I observed a strong variation in the flow magnitude for different collision event generators. At the lowest energy $E_b = 1.23$ AGeV which corresponds to the data measured by FOPI, and by HADES at SIS18, the iQMD agrees very well with the data.

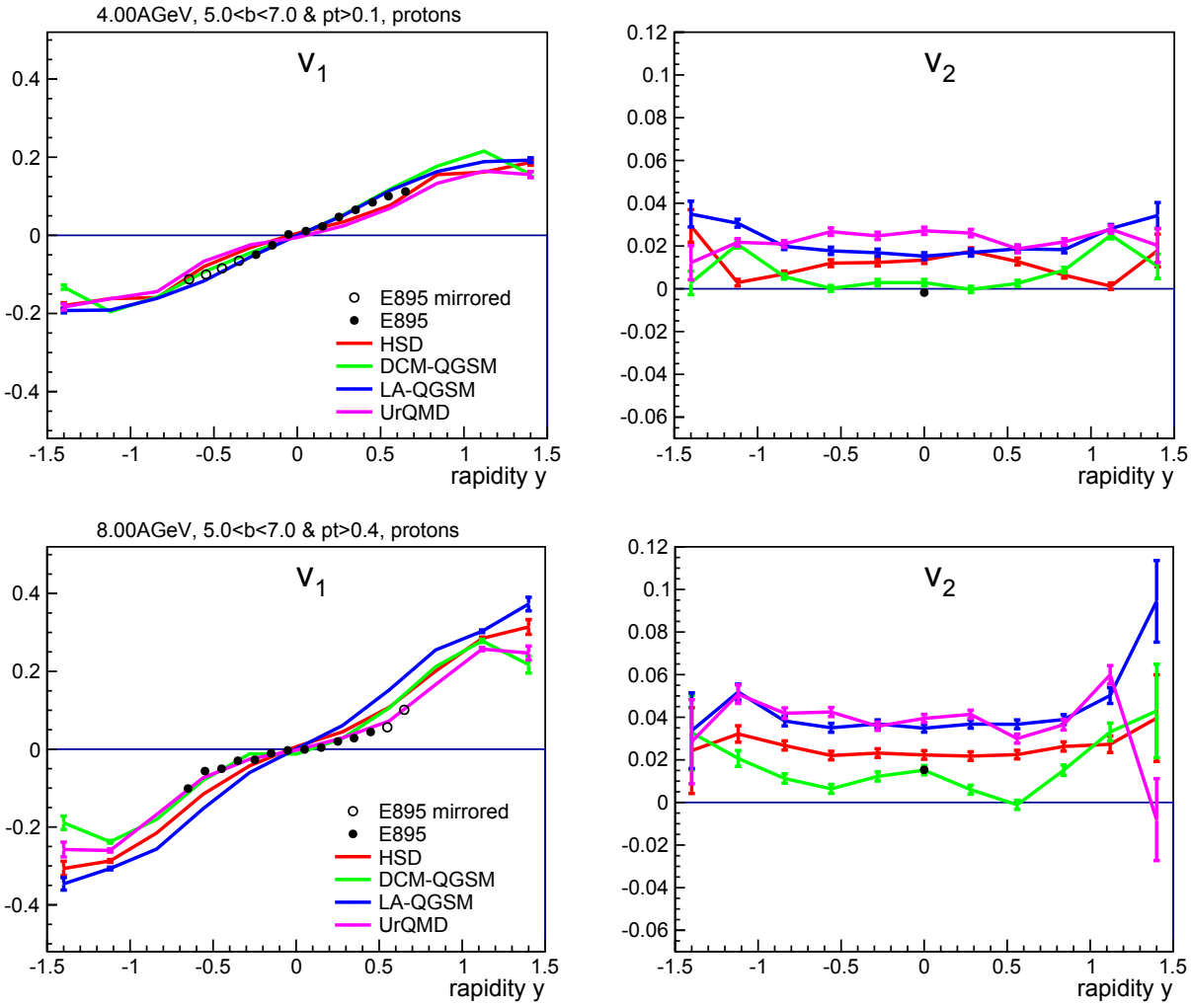

Figure 9.6: Dependence of directed v_1 (left) and elliptic v_2 (right) proton flow on normalized rapidity at $E_b = 4$ (top) and 8 (bottom) AGeV.

At the full SIS100/SIS300 energy range $E_b = 2-30$ AGeV which corresponds to the designed CBM experiment, the DCM-QGSM model seemed to be the most consistent with data achieved by E877, E895 and STAR. This event generator closely followed the experimental data for directed flow v_1 in contrast to other models and even seemed to exhibit the out-of-plane to in-plane change for the elliptic flow magnitude of $v_2|y_{norm} = 0$ around $E_b \sim 4-6$ AGeV similar to what was observed by E895 [331]. Another important fact is that DCM-QGSM also exhibited the overall strongest v_1 or in other words the strongest azimuthal anisotropy. Consequently, one can expect it to give better resolution for the determination of $Q-vector$ (see equation (9.1)) or event plane Ψ_{EP}.

Utilized models exhibit variation in the directed particle flow v_1 which describes the asymmetry in the azimuthal distributions of produced particles with respect to the initial reaction plane. The substantial difference in v_1 strength is observed for the midrapidity region of -0.5<y_{norm}<0.5 as presented in figure 9.7 (left). However, figure 9.8 shows much smaller difference in v_1 around the beam rapidity $y_{norm} \sim 1$.

In summary, the availability of fragments in the spectator region and the closest qualitative

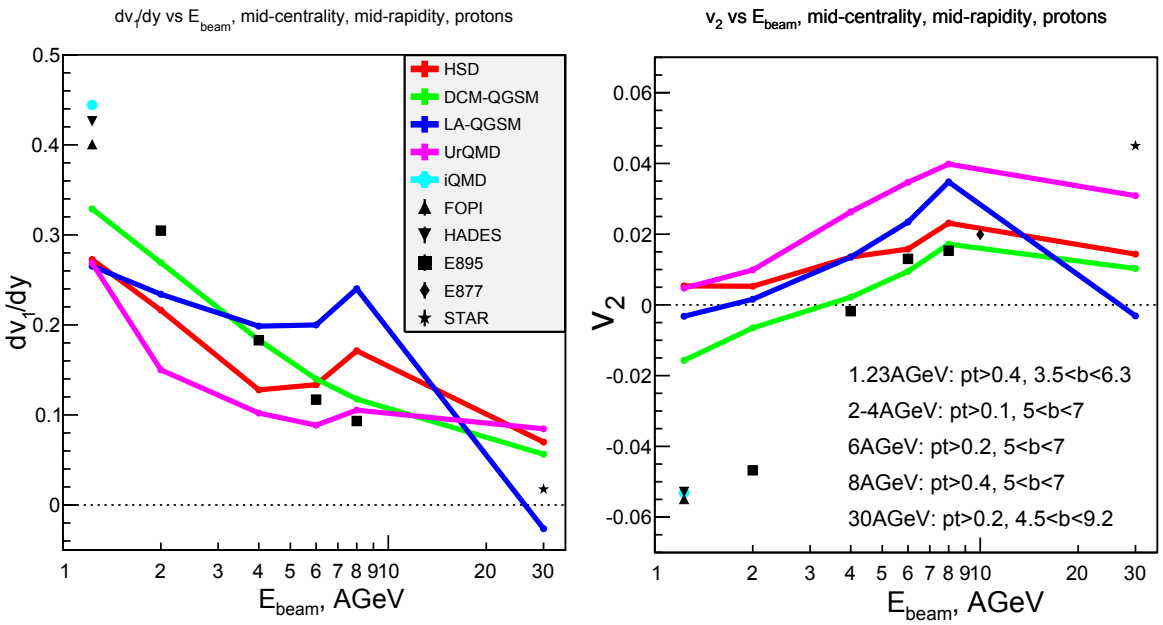

Figure 9.7: Dependence of the slope of proton directed flow (dv_1/dy, left) and elliptic flow at midrapidity ($v_2|y = 0$, right) on beam energy.

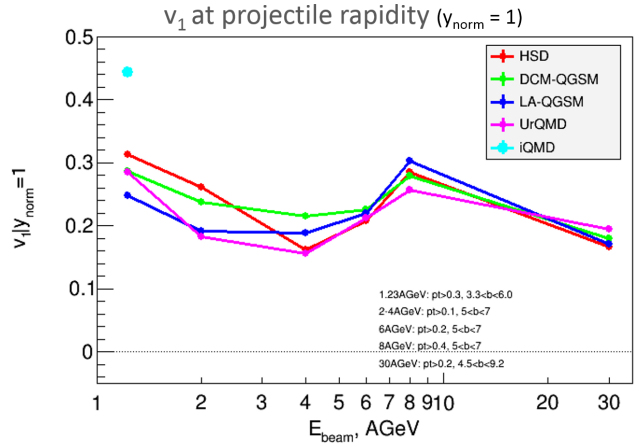

Figure 9.8: Directed particle flow vs beam energy around projectile rapidity. Simulations are done with help of different collision models for proton directed flow at Au+Au collisions at semi-centrality with b and p_T cuts corresponding to indicated experimental data.

agreement with the experimental data for the directed flow suggested the use of DCM-QGSM for the CBM PSD performance study.

9.3 PSD performance with various configurations and collision models

I studied the PSD performance within the CbmRoot environment in conjunction with the GEANT4 Monte-Carlo simulation framework. It was created and maintained by S. Seddiki, who was in charge of PSD simulations at that time. I utilized four aforedescribed collision gen-

erators (models), and three different detector setups for the comparison. I opted for statistics of 10^4 minimum bias events to decrease the computational time.

9.3.1 Simulated CBM detector geometry setup

Figure 9.9 (top left) shows the full realistic simulated geometry of the CBM detector subsystems used for the PSD simulation studies. The realistic geometry includes a 250 μm thick Au target, eight silicon tracking stations (STS) [362] located 30 – 100 cm far from the target inside the dipole magnet, the vacuum-filled aluminum beam pipe with a variable cross-section and thickness of a few millimeters, and PSD. The optimal PSD distance z_{dist} was chosen to be 8 (15) meters from the target for collision energies at SIS100 $E_b = 2 - 8$ AGeV (SIS300 $E_b = 30$ AGeV), see figure 13 in PSD TDR [252]. The transverse segmentation of PSD is illustrated in figure 9.9 (top right). It includes 44 modules with a 20×20 cm^2 the cross-section in the transverse plane and a beam hole formed by the inner corners of the four central modules which are marked by a red color in the figure. The new geometry with enlarged beam hole which I described in subsection 5.1.2 was not yet proposed at the time when I conducted simulations.

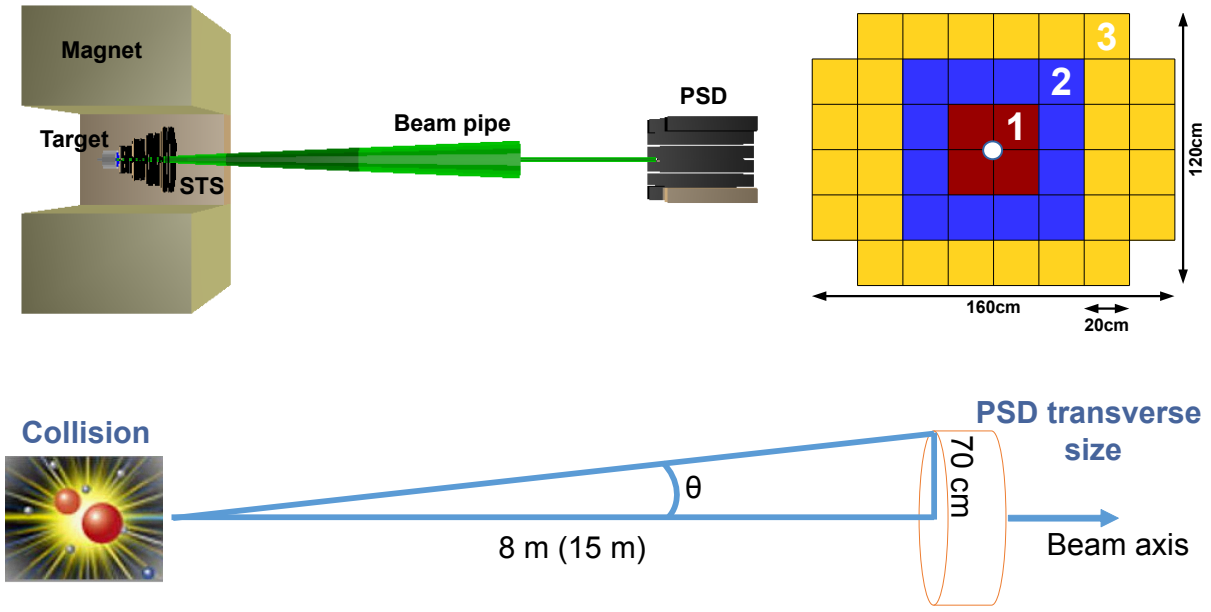

Figure 9.9: (top, left) The realistic simulated CBM setup including STS and PSD detector geometries. (top, right) The detailed view of PSD transverse geometry and modules used to construct subevents for the simulation [252]. (bottom) The concept of a simple simulation setup without realistic detector geometry.

Figure 9.9 (bottom) shows the concept of the simulation setup without the detector geometry and corresponding GEANT transport procedure. It was utilized to assess the performance of the ideal forward calorimeter which registers all the particles hitting it. Here the MC-tracks of particles coming within the PSD acceptance were chosen from the generated input data by corresponding θ-angle cut. Considering the PSD transverse dimensions and optimal PSD location, θ was calculated to be within [0.215ř; 5.0ř] for $E_b = 2 - 8$ AGeV and within [0.115ř; 2.7ř] for $E_b = 30$ AGeV. This setup is further referred to as "PSD-accept.".

In order to study how much distortion arises from the deflection of charged particles by the magnetic field, two configurations of the realistic setup were tested, namely setup with a

turned-on and turned-off dipole magnet, which has a nominal field integral of about 1 Tm. They are further referred to as "PSD-geom.,B=0" and "PSD-geom.,B>0", respectively.

FAIR accelerator ring	E_b, AGeV	PSD x_{shift}, cm	Magnetic field, $B \times \rho$, Tm
SIS100 (PSD z_{dist} = 8 m)	2	21.4	0.5
	4	15.5	0.63
	6	10.9	0.63
	8	10.9	0.82
SIS300 (PSD z_{dist} = 15 m)	30	7.5	1

Table 9.2: Summary of values of magnetic field and PSD x_{shift} corresponding to different E_{beam}, FAIR accelerator rings and PSD z_{dist} used during the reaction plane performance simulations for "PSD-geom.,B>0" configuration. Optimization simulations were carried out by S. Seddiki, and are presented in PSD TDR [252].

In the case of the "PSD-geom.,B>0" configuration, the ion beam is horizontally deflected by the magnetic field along the x direction in the laboratory frame. Consequently, PSD was shifted by x_{shift} for each collision energy, magnetic field strength, and detector distance to the target z_{dist}, such that the beam always pass PSD via its beam hole. This is also the reason why the PSD geometry was chosen to be elongated along the x direction. The magnetic field values and PSD x_{shift} used in simulations for different beam energies corresponding to expected FAIR accelerator rings and PSD z_{dist} are shown in table 9.2.

Values of all the parameters were chosen for the optimal PSD performance during the comprehensive preceding studies described in PSD TDR [252]. For example, simulations performed with a smaller (and more expensive) module size of 10×10 cm^2 showed only marginal improvement of the reaction plane resolution.

9.3.2 Reaction plane reconstruction method

I studied the performance of the reaction plane reconstruction with PSD with help of the simulations in the CbmRoot environment. I estimated the reconstructed event plane angle Ψ_{EP} from the anisotropy of energy deposition in PSD modules by the construction of a $Q - vector$ described by equations 9.1 and 9.2. I directly extracted the true reaction plane angle Ψ_{RP} of the collision from the data generated by models.

In the case of the "PSD-geom.,B>0" configuration, the azimuthal distribution of particles in PSD was distorted by the magnetic field, which resulted in off-centered values (mainly in the x direction) of the **Q**-vector. In order to correct for this effect a **Q**-vector recentering procedure was applied

$$Q'_{x,y} = \frac{Q_{x,y} - \langle Q_{x,y} \rangle}{\sigma_{Q_{x,y}}} \tag{9.11}$$

where $\langle Q_{x,y} \rangle$ and $\sigma_{Q_{x,y}}$ are event averaged mean and Gaussian width of the $Q_{x,y}$ distribution. CBM performance simulations conducted by S. Seddiki proven that the recentering procedure removes the strong energy dependence of $\langle Q_x \rangle$ and flattens the event plane distribution, which results in a significant improvement of PSD event plane resolution, see section 5.5.1 in PSD TDR [252].

9.3.3 PSD performance with various configurations and event generators

I studied PSD performance for the reaction plane reconstruction utilizing the input from different event generators and various detector setups described in sections 9.1.5 and 9.3.1. I used the common setup for the PSD simulations shown in figure 9.9 (top left), but I did not analyze signals from the STS detector because this study was dedicated to PSD standalone performance. Gold target was also added purely for compatibility reasons, since I used event data generated already after the collision. Input data was generated for semi-central Au+Au collisions in the projectile beam energy range $E_b = 2-30$ AGeV, which covers the expected energy range of SIS100/SIS300 at FAIR. I chose the broad range of collision centrality corresponding to midcentral events. I used the range of impact parameter indicated in the generated data of 5 fm $< b <$ 10 fm, which roughly corresponds to the centrality of 12 – 48 %, according to estimation by V. Klochkov [259].

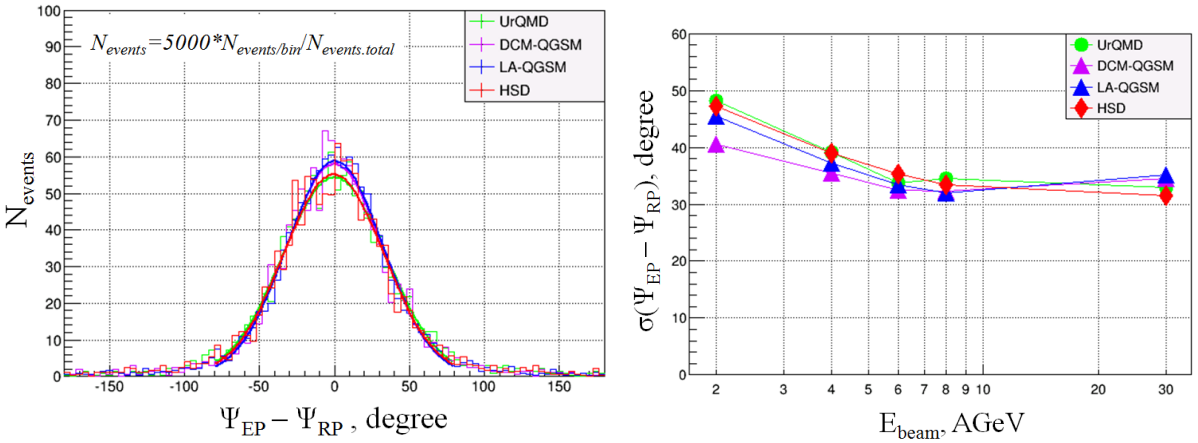

Figure 9.10: Comparison of the reaction plane resolution of PSD for the four generators. (left) Distribution of registered events for $E_{beam} = 8$ AGeV by difference in $\Psi_{\mathrm{EP}} - \Psi_{\mathrm{RP}}$, fitted by Gaussian distribution. (right) Reaction plane resolution $\sigma(\Psi_{\mathrm{EP}} - \Psi_{\mathrm{RP}})$ as function of beam energy. Simulations were performed for the full PSD geometry "PSD-geom.,B>0".

Comparison of the reaction plane resolution simulated for the full PSD geometry "PSD-geom.,B>0" with help of data generated with UrQMD, DCM-QGSM, LA-QGSM and HSD is shown in figure 9.10. Figure 9.10 (left) represents the distribution of events registered in PSD at $E_{beam} = 8$ AGeV with respect to the difference in $\Psi_{\mathrm{EP}} - \Psi_{\mathrm{RP}}$. I fitted it by Gaussian function. Standard deviation of the fit $\sigma(\Psi_{\mathrm{EP}} - \Psi_{\mathrm{RP}})$ as a function of the beam energy is presented in figure 9.10 (right).

For all the utilized generators reaction plane resolution $\sigma(\Psi_{\mathrm{EP}} - \Psi_{\mathrm{RP}})$ was found to be below 40 degrees which fulfills the PSD requirements. Despite the observed strong variation of the proton collective flow v_1 in models, $\sigma(\Psi_{\mathrm{EP}} - \Psi_{\mathrm{RP}})$ did not differ much between event generators. It is explained by the fact that the substantial difference in v_1 was observed only for the midrapidity region. However, PSD detects the spectators around the beam rapidity, approximately $0.7 < y_{norm} < 1.3$, where much lower difference in v_1 was observed, especially for $E_b > 4$ AGeV. However, slight variation in $\sigma(\Psi_{\mathrm{EP}} - \Psi_{\mathrm{RP}})$ was observed, primarily around $E_b =$ 2 AGeV, where usage of DCM-QGSM data showed the best resolution. It could be related to the inherit presence of fragments in this generator which is considered to be significantly important for the PSD physics performance and justified the use of DCM-QGSM for PSD simulations.

I also assessed the PSD performance with different models in terms of the reaction plane resolution correction factor R_1 calculated by 9.9 as shown in figure 9.11 (left). Similarly to

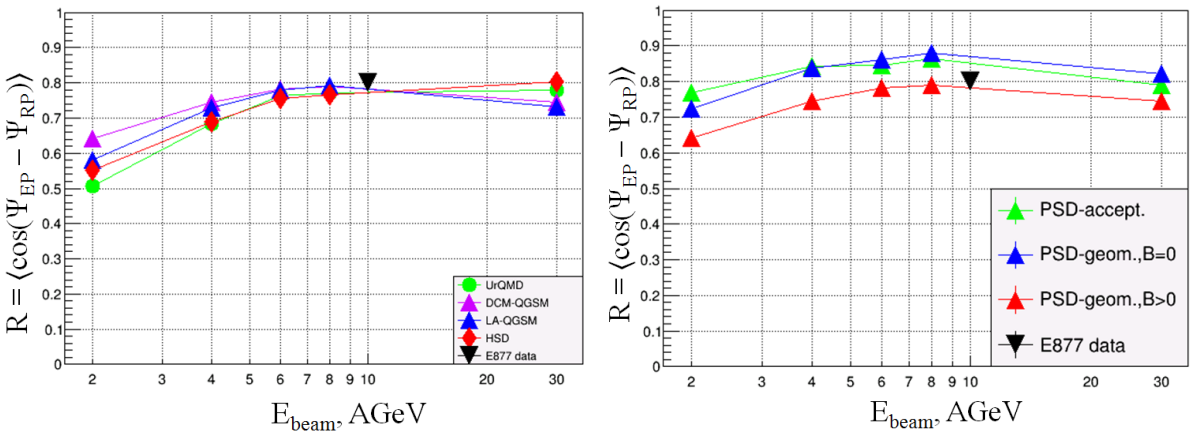

Figure 9.11: Comparison of the reaction plane resolution correction factor R of PSD as function of beam energy for the four generators (left) and three PSD configurations (right).

$\sigma(\Psi_{\mathrm{EP}} - \Psi_{\mathrm{RP}})$, value of R_1 did not differ much for various event generators being reasonably close to 1 (ideal resolution). The correction factor around $E_b = 8$ AGeV (and thus the PSD reaction plane resolution) was found to be similar to that of the target (TCal) and participant (PCal) calorimeters used for the collective flow measurements in Au+Au collisions by the E877 experiment at AGS, which had a maximum of $R_1 \approx 0.8$ at 10 AGeV in semi-central collisions, see figure 5 in [360].

Moreover, I studied the effects introduced by the detector design with help of the data from the DCM-QGSM generator. Figure 9.11 (right) represents the reaction plane resolution correction factor of PSD as a function of the beam energy for three different detector configurations. The comparison of the reaction plane resolution correction factor achieved with "PSD-accept." and "PSD-geom.,B=0" setups, for details see section 9.3.1, showed that the azimuthal segmentation of PSD did not introduce any significant bias into the measurement. The splitting of the beam into neutral and charged particles and fragments due to magnetic field decreased R_1 over the whole beam energy range ("PSD-geom.,B=0" vs "PSD-geom.,B>0" setups). However, the introduced bias was found to be relatively small on the order of 10 %.

Chapter 10

Conclusion and outlook

As a member of the international CBM@FAIR experiment, I performed a detailed investigation of the radiation hardness for the Projectile Spectator Detector. It is a compensating lead/scintillator hadron calorimeter with a light readout based on wavelength shifting fibers coupled to Silicon Photomultipliers. PSD is designed to measure the energy distribution of non-interacting nucleons and fragments emitted at very low polar angles in the forward direction in nucleus-nucleus collisions which provides the determination of collision centrality and reaction plane orientation.

Summarizing the development of my thesis, I can certainly say that the extensive amount of information and investigations required to fully understand the detector radiation hardness was totally underestimated. During my research, I made an extensive review of radiation hardness for active detector components, namely plastic scintillators, WLS-fibers and SiPMs. I performed 8 experiments at NPI cyclotron during 2016 – 2018 where I irradiated 54 different SiPMs, I evaluated the achieved fluence with help of the activation foils. For detailed SiPM characterization after irradiation, I assembled a laboratory setup and developed dedicated software to automate the measurements. I performed series of experiments at CERN, where I measured the change in performance of the test calorimeter module which was read out by irradiated SiPMs.

Furthermore, I participated in two experiments at NPI cyclotron to irradiate the scintillators. I supervised two internship students from TPU, Tomsk, Russia who conducted final measurements and data analysis. Also, during the first years of my study, I organized internships in NPI for other 5 students from TPU. At the beginning of my PhD work, I performed simulations of nucleus-nucleus collisions to assess the most appropriate collision model for PSD performance studies. I also did a similar study for the HADES experiment.

I presented the data discussed in this work on 9 international conferences, and 15 internal meetings organized by CBM and HADES collaborations, and by FAIR-CZ project. I am the main author of 8 articles and proceedings in peer-reviewed journals, including two articles in journals with impact factor > 1. I am co-author of 11 other articles and proceedings in peer-reviewed journals published by members of PSD team, CBM and HADES collaborations.

Review of radiation hardness studies

Even though plastic scintillators and Silicon Photomultipliers are already successfully used in nuclear physics, the comprehensive references that would unambiguously cover the data are still lacking. This is in striking contrast to silicon sensors and electronics, for which many books covering the radiation effects are available nowadays. This led me to a decision to review and compare all the available data on radiation hardness for polymer scintillators, WLS-fibers and SiPMs. This review is presented in chapter 3. Below I will briefly summarize the state of the art.

SiPMs mostly suffer from damage caused by non-ionizing energy loss because it produces electrically active defects in the silicon lattice which enhance the thermal carrier generation and disrupt the designed operation. This manifests in the drastic increase of the dark current and noise, and in rapid degradation of their response to light. Dark current increases from the nanoampere up to milliampere level after 1 MeV neutron equivalent fluence of $10^{11} - 10^{12}$ n_{eq}/cm^2. The ability to resolve single photons usually vanishes around 10^9 to 10^{10} n_{eq}/cm^2 due to high noise levels. Electrical characteristics, including quenching resistance and quenching capacitance, change only in a minor way or do not change at all. However, due to the device novelty and high design variation, there is no general agreement on the radiation tolerance level in terms of the light response. The latter ranges between 10^9 to 10^{14} n_{eq}/cm^2 depending on the study.

Operation temperature is of great importance for SiPMs similar to standard silicon sensors as it significantly reduces the dark current and noise. Several studies showed that even single photons can be still resolvable after 10^{10} n_{eq}/cm^2 or even 10^{14} n_{eq}/cm^2 if SiPMs are cooled down to -30 °C or even cryogenic temperatures, respectively. Annealing at a high temperature can reduce the dark current by up to an order of magnitude, however, it has to be applied carefully to avoid damage or destruction. Studies with ionizing energy sources indicate only little degradation at least up 10 kGy, but possibly even up to much higher doses.

Polymer scintillators and fibers are on the contrary more susceptible to damage caused by ionizing energy loss which produces highly active radicals, disrupts polymer chains, and results in the formation of color centers. In consequence, the scintillator's ability to emit light decreases along with the transparency degradation which causes the overall light yield deterioration. After careful data comparison, I concluded that for fast irradiation in normal conditions radiation tolerance level of scintillators and fibers, used individually or together, is on the order of 10 kGy. Operation up to 100 kGy is often still feasible but with significantly reduced light yield.

The dose rate effect observed by many researchers is of great importance. When irradiation rate is below 100 Gy/h and/or oxygen pressure is high, oxygen penetrates the scintillator easier enhancing the radical formation which was observed to decrease the radiation tolerance level by up to an order of magnitude depending on the conditions. In the case of neutron irradiation, only minor effects in scintillators are observed up to $10^{13} - 10^{14}$ n/cm^2.

Radiation level at PSD

My main goal was to provide a comprehensive evaluation of the PSD radiation hardness. Since my study is the first PhD thesis focused on PSD, in chapters 4 and 5 I did my best to cover the most important design aspects and changes that were implemented since the Technical Design Report approval in 2015. The calorimeter is designed to operate at a very high collisions rate up to 1 MHz (beam rates up to 10^8 ions/s) which will produce significant radiation load, therefore the radiation tolerance of its components is of utmost importance.

Total ionizing dose up to 10 kGy and 1 MeV neutron equivalent fluence up to 10^{13} n_{eq}/cm^2 is expected in its innermost parts close to the beam hole after 10 years of CBM operation (assumed as 2 months of non-interrupted run time per year at collision rate of 1 MHz). Therefore, scintillators are not likely to suffer significant damage, but they were still briefly studied to verify the assumption above.

To ensure the stability of the readout electronics, it will be placed 10 – 40 meters from the detector. Silicon Photomultipliers are placed right behind PSD to ensure the best light collection from the wavelength shifting fibers that transport the light through the modules. Extension of WLS fibers outside the module could solve this problem, but it would very likely cause excessive fiber bending and damage during the PSD movement. CBM experiment has a modular structure which means that individual detectors can be easily accessible and moved between the beamtimes to accommodate the physics plans, however, it imposes higher requirements on the detector's

mechanical rigidity. SiPMs are soldered onto the simple amplifier boards based on standard commercial components which are expected to withstand the fluence up to 10^{15} n_{eq}/cm^2 based on the existing data from other experiments.

PSD is a lead/scintillator sandwich calorimeter, so it will act as a spallation target and produce high neutron flux behind it. For the original PSD design presented in TDR, a dose of 300 Gy and a fluence of 3×10^{12} n_{eq}/cm^2 for SiPMs placed closest to the beam hole were expected after a year of CBM operation. From the initial results of my radiation hardness investigation for SiPMs, it was clear that degradation even during a single year will be too high. Fortunately, O. Svoboda came up with an idea of neutron shielding based on the borated polyethylene, which was successfully implemented in between of PSD module end and SiPMs during the assembly of modules. This allowed reducing the neutron flux by multiple times. Furthermore, the radius of the beam hole was enlarged from 3 up to 11 cm (20×20 cm^2). Now the expected radiation load behind the PSD where SiPMs are placed corresponds to a dose of 100 Gy and a fluence of 2×10^{11} n_{eq}/cm^2 for the same run scenario. Therefore, little to no SiPM degradation due to ionizing energy loss is expected, but degradation due to the neutron fluxes remained an issue.

SiPM irradiation tests and measurement process

The main practical part of my work was to perform irradiation tests for the most susceptible PSD components, namely Silicon Photomultipliers. I investigated the suitability of 8 commercially available models: Hamamatsu MPPC S12572-010P and S14160-1310PS, Ketek PM-3350 and 15-WB-A0, Sensl B-series 30020 and C-series 30020, Zecotek MAPD-3A and MAPD-3N for the CBM PSD light readout in terms of their performance before and after neutron irradiation.

I conducted multiple neutron irradiation tests at NPI cyclotron for this purpose exploring the wide fluence range from 5×10^{10} up to 6.4×10^{12} n_{eq}/cm^2. I achieved the funding for these experiments via CANAM program. I evaluated neutron fluences with help of thin gold activation foils which were placed together with SiPMs during the irradiation. With help of HPGe gamma spectrometer, I measured the decay data for $^{197}Au(n,2n)Au^{196}$ reaction. It has a well-known microscopic activation cross-section with a maximum below 30 MeV which corresponds to the maximum of the neutron spectra at cyclotron. I applied all the standard spectroscopic corrections to achieve the best measurement accuracy. Based on the known neutron spectra and NIEL damage function for silicon I converted the fluence results to equivalent fluence for 1 MeV neutrons. Achieved fluence results are consistent with an estimation based on the data from the cyclotron team within the measurement uncertainty of 15 %.

I assembled a new setup for tests of SiPM response to light based on available hardware, while I used a setup developed by my supervisor V. Kushpil to measure SiPM dark currents and electrical parameters. To acquire data I connected all the devices to NI DAQ system. To control the measurements automatically, I developed a dedicated software which I called "Dharma - Software for (not-only) SiPM measurements". I used NI LabWindows development environment. My software allows to measure current, capacitance, resistance, and signal response for SiPMs or any other electrical components and sensors, e.g. MOS-capacitors, pin-diodes, or avalanche photodiodes. During the development and optimization, I put an extra effort to ensure operational stability, good measurement accuracy, and high measurement speed. In the end, measurement time was within 3 – 30 minutes depending on the sample and measurement type (in earlier versions it was up to several hours).

Results on the SiPM degradation due to irradiation

I conducted in-depth laboratory tests for all the irradiated and non-irradiated samples (54 irradiated and many non-irradiated). This allowed me to estimate the measurement uncertainties which are in most cases dominated by sample-to-sample variability, and range from 0.5 up to 30 % depending on the SiPM and measurement type. I observed a linear increase in dark current

with fluence, which is similar to what is reported for standard silicon sensors. Dark current up to ten milliamperes is reached after the irradiation with the highest fluence. Breakdown voltage increased by 0.45 – 0.89 V for SiPMs with high operating voltage of 60 – 80 V after 6.4×10^{12} n_{eq}/cm^2, while little to no change was observed below 2.5×10^{11} n_{eq}/cm^2. For SiPMs with an operating voltage of 20 – 30 V change was insignificant as well, i.e. approximately 0.1 – 0.2 V which is close to the measurement uncertainty. When irradiated above 5×10^{10} n_{eq}/cm^2 all the SiPMs lost the ability to distinguish single photons. No change in quenching resistance and pixel capacitance that would be incompatible with the measurement uncertainty was observed. All the aforementioned results are consistent with the findings from other studies which I reviewed. Beyond the above, the complex dependence of dI_{dark}/dV_{ov} on the overvoltage was reported for the first time in my experiments. I was able to describe it in terms of the effective depletion width, which has a quadratic dependence on overvoltage.

The situation is even more interesting in the case of the SiPM performance measurements. Response to LED decreased extremely by a factor of 10 – 1000 after the highest fluence depending on the SiPM model. Noise also increased significantly by up to 10 times after fluence above 7.2×10^{11} n_{eq}/cm^2. However, with the further fluence increase, the saturation and even decrease of noise level was observed, which was only briefly reported in a single existing publication. The exact reason for the observed degradation is not established yet and can become a subject of further research. The signal degradation is at least partially explained by the increased pixel occupancy due to the dark counts which temporarily reduce the detection efficiency. Another complementary explanation may be the change of the electric field distribution in the active volume which led to the permanent decrease of SiPM gain and/or detection efficiency. This would also explain the noise saturation/decrease as well as capacitance decrease at low frequency, both of which are observed at high fluences. Similar data on the noise saturation/decrease was reported by another group, but as far as I know, I am the first one to discover the capacitance decrease at low frequency after irradiation. Regardless of the underlying mechanism, a combination of the aforementioned effects manifested in the decrease of signal to noise ratio which can be seen as a decrease of the dynamic range by 10 – 1000 times depending on the SiPM model and fluence.

I observed both dark current and signal to noise ratio improve significantly with the reduction of the pixel area. This is explained by the consequent decrease of active volume which leads to the reduction of afterpulsing, crosstalk, pixel capacitance, recovery time, as well as an increase of dynamic range and charge collection efficiency. Therefore, I conclude that the pixel miniaturization is essential for SiPM's radiation hardness, similarly to thickness miniaturization which is exploited in the radiation hardening of standard silicon sensors. Furthermore, pixel miniaturization increases the dynamic range.

Comparatively, Zecotek SiPMs with 8×8 μm^2 pixels exhibit the best radiation tolerance. But it can not withstand event rates above 10 kHz due to very long pixel recovery time which makes it inapplicable at CBM. Ketek and Sensl SiPMs with large pixels have too short dynamic range and a much weaker radiation hardness in comparison with both Hamamatsu and Zecotek SiPMs.

The best fit to PSD requirements is the Hamamatsu SiPMs with 10×10 μm^2 pixels which have the second-best radiation hardness. The new model seems even better because it exhibits similar performance in terms of dark current and signal response, but it has initially higher detection efficiency and lower operation voltage which improves the light collection, reduces the power consumption, and mitigates larger shifts in breakdown voltage. New Ketek SiPMs with 15×15 μm^2, which recently became available for testing, have relatively good radiation hardness and can be in principle considered as an alternative for PSD.

Nevertheless, characteristics of Hamamatsu SiPMs degraded significantly after irradiation with 2.5×10^{11} n_{eq}/cm^2 or one year of CBM operation at the highest rate. The dark current of Hamamatsu SiPMs increased from 10 nA up to 50 μA which is close to the maximum that the current version of the amplifier board can deliver. Signal decreased by a factor of 2 and signal to noise ratio decreased by a factor of 25 which significantly reduced the dynamic range. The dynamic range is directly related to amplifier noise and the amount of impinging light. Those factors are very different for laboratory setup and PSD, therefore the best way to study it is during the detector operation.

Tests of irradiated SiPMs at PSD module at CERN

I devised and carried out the radiation hardness investigation of irradiated SiPMs at CERN. For this, I participated in tests allocated by PSD team from INR, Moscow at T9, T10 and NA61 beamlines where I measured the performance of PSD module equipped with irradiated SiPMs. I performed the complete data analysis and implemented a simple technique of noise reduction which significantly improved the observed energy resolution.

SiPMs were found to be capable of operation with a relatively small deterioration of energy resolution after neutron irradiation with fluence of 2.5×10^{11} n_{eq}/cm^2. It roughly corresponds to one year of CBM experiment operation for SiPMs located close to the beam and several years of operation for SiPMs located farther. The practical dynamic range of PSD is defined from the minimal up to the maximal signal. A minimal signal is produced by minimum ionizing particles, for example, muons which were still distinguishable from other species by the detector. This also confirmed the possibility to use muons for section calibration after this fluence. Linear module response was observed for proton beams from 2 up to 80 GeV. These results ensured that the dynamic range will not become a limiting factor for a calorimeter operation.

After higher fluences the energy resolution deteriorated up to two times, however, it is not necessarily a problem because signals in inner calorimeter modules are very large. Linearity to proton beam remained unchanged. However, muons were completely indistinguishable from the noise which makes section calibration by muons impossible. In principle, this can be solved by initial module calibration, followed by LED recalibration after high irradiation. But in this case, SiPMs shall never be disconnected from the module to avoid calibration problems due to SiPM repositioning. Alternatively, the modular detector structure of the CBM experiment allows exchanging the most damaged SiPMs every year if necessary.

The results of my investigation are completely unique, i.e. no study of calorimeter performance with irradiated SiPMs was reported so far by other groups. Achieved results on the radiation hardness and provided recommendations are also applicable for both BM@N and NA61 experiments, which plan to operate at quite high interaction rates of $10^6 - 10^7$ ions/second, which raises the question of radiation hardness. Due to the fact that the new version of Hamamatsu SiPM was proven to perform similarly to an old one during the laboratory tests, I suggest using it at all the mentioned calorimeters.

Investigation of scintillator radiation hardness

Additionally, I participated in proton irradiations at NPI cyclotron to confirm that polystyrene scintillator tile samples that are used at PSD have the required radiation hardness. I supervised two internship students who tested the scintillator light yield deterioration after the irradiation in a laboratory. No light yield deterioration was observed for samples that achieved 1 kGy of ionizing dose, which corresponds to maximal radiation load after one year of CBM operation. Light yield decreased by up to 20 % after 10 kGy which corresponds to 10 years of operation near the PSD beam hole. This confirms that the quality of scintillators produced by Uniplast, Vladimir, Russia satisfies the requirements for radiation hardness of PSD.

In order to achieve realistic results for the CBM run scenario, I corrected the observed data

for the dose rate effect. Light yield deterioration of 20 % after 10 kGy at 1.3 kGy/h translated into 40 % 0.69 Gy/h assumed for CBM. Nevertheless, an average expected absorbed dose is an order of magnitude lower, and therefore only a slight if any overall scintillator degradation is expected at CBM PSD. This is further backed up by the results reported by ZEUS collaboration, who observed no degradation of energy resolution for ECAL module assembled with scintillators irradiated by 10 kGy. Moreover, due to the PSD modular structure, four innermost modules can be replaced by outer modules. For such an occasion, four outer modules are produced with edges cut to accommodate the beam pipe.

Simulation of gold-gold collisions

I performed a simulation of collective particle flow exploiting four generators of heavy-ion collisions based on models – UrQMD, HSD, DCM-QGSM and LA-QGSM – at the CBM energy range, i.e. from 2 up to 35 AGeV. The DCM-QGSM showed the overall closest agreement with the data acquired by E895, E877 and STAR collaborations and exhibited overall the strongest v_1 in the midrapidity region ($y_{norm} \in$ [-0.5; 0.5]). However, discrepancies with data were observed for all the generators: typically underestimated v_1 and overestimated v_2 which indicates possibilities of further improvements in the generator codes.

Additionally, I performed the same simulation for the HADES collaboration at a beam energy of 1.23 AGeV. In addition to the initial set of generators, iQMD was added to the study. It showed the best agreement with experimental data from FOPI and HADES. Unfortunately, it is not applicable to higher energies, and therefore it was not used for CBM simulations.

I simulated the PSD reaction plane determination with input data from the aforementioned generators in the same energy range. On the contrary to large differences in v_1 in different generators, the difference in the reaction plane resolution was rather small. It can be explained by the fact that the largest difference in v_1 was observed for the midrapidity region, while PSD detects the spectators around the beam rapidity where a much lower difference in v_1 produced by different generators was observed. However, DCM-QGSM showed slightly better resolution compared to other generators for the lower energies, probably due to the presence of fragments and the strongest v_1. As a consequence, the detailed studies of the PSD physics performance demonstrated in the PSD TDR [252] were performed with either DCM-QGSM which exhibits the closest agreement with the experimental data, or UrQMD which is a common reference used for all the CBM simulations.

Recommendations and suggestions

While this study helped to resolved multiple important issues for the design of the new experiment, it became evident that the topic of the SiPM radiation hardness provides many further opportunities and challenges for future research. Next, some of the most promising future research directions are briefly summarized.

- Implement a continuous recalibration system to compensate for the changes in SiPM response and operation voltage during irradiation. Such system is essential since without additional calibration (as of now) SiPM response can decrease up to two times during a year of operation. In between beamtimes, regular calibration with cosmic muons and beam protons can be done. During the operation, e.g. at technical breaks, LED calibration system can be used to renormalize the section-to-section and module-to-module response.
- Incorporate noise reduction for readout electronics. It can be implemented on the hardware level by the bandwidth limitation to cut out the HF part of radiation-induced noise. Such possibility should be carefully investigated to avoid performance deterioration at high

collision rates of CBM. Another complementary approach is to carefully adjust the acquisition time window and set the cut-out threshold for noise, it can be applied individually to each SiPM depending on its noise.

- Study the detector performance with irradiated SiPMs at next miniCBM, NA61, BM@N and CBM beamtimes. Tests of irradiated SiPMs' performance with various readout electronics employed at calorimeters of these experiments are also of high interest.
- Implement the high-temperature annealing after the beamtimes to reduce the radiation damage. This can be done by unmounting the most damaged SiPMs from the detector and baking them in the oven. Alternatively, very high overvoltage or forward bias voltage can be applied which will heat them from inside. Such an approach does not require unmounting. However, dedicated studies must be carried out beforehand to determine the safe limits of heating or bias supply.
- Expand the software for calorimeter performance simulation to include anticipated SiPM degradation validated against available experimental data.
- Investigate of the new SiPM candidates as these devices are rapidly evolving. Following directions are the most promising in terms of radiation hardness

  - SiPM pixel miniaturization is beneficial both in terms of radiation hardness and dynamic range. For instance, devices with pixel sizes of 7.5×7.55 μm^2 and 5×5 μm^2 are expected to arrive in the near future. However, pixel miniaturization also significantly reduces gain and detection efficiency, so the benefits shall be carefully evaluated. For instance, Hamamatsu or Ketek SiPMs with 15×15 μm^2 might still be acceptable in terms of dynamic range and radiation hardness, and may even provide a significant boost in terms of initial performance.
  - SiPMs with low operation voltages on the order of 20 – 30 V are advisable because they exhibit lower changes in breakdown voltage after irradiation. Furthermore, they have a lower temperature coefficient which will benefit the temperature stability.
  - "Better red than dead" strategy. In SiPMs tuned for green-red spectrum, electrons are collected at n+ electrodes and have a much lower chance to be trapped by irradiation-induced defects because they have to travel only a few micrometers to reach the electrode, opposed to traveling the whole sensor depth (300 – 500 μm) in case of p+ in n-type substrate. A single available study showed that they exhibit a much lower dark current after irradiation, see subsection 3.6.16 for details. Such SiPMs are currently produced by Hamamatsu, Sensl and Advansid. Unfortunately, the detection spectrum of Hamamatsu SiPMs does not match well with the emission spectrum of Kuraray Y-11 WLS-shifting fibers, Sensl SiPMs are produced only in 1×1 mm^2 size while PSD requires 3×3 mm^2, and Advansid SiPMs have only 40×40 μm^2 pixels which will not provide enough dynamic range for PSD. Therefore, new green-red optimized SiPMs are highly anticipated by the HEP community.

- Continue the deep investigation of the SiPM internal parameters and technology improvement via TCAD and SPICE simulations. Cooperation with manufacturers is strongly desired for this.

Furthermore, since event collision generators also evolve, it would be of high interest to repeat and extend my performance studies with new versions, or even new models.

References

[1] C. A. Salgado, *Lectures on high-energy heavy-ion collisions at the LHC*, in *2008 European School of High-Energy Physics, Herbeumont-sur-Semois, Belgium, 8-21 June 2008*, pp. 239–280, 2009, arXiv:0907.1219.

[2] B. Friman *et al.*, *The CBM physics book: Compressed baryonic matter in laboratory experiments*, Lect.Notes Phys. **814**, 1 (2011), doi:10.1007/978-3-642-13293-3.

[3] STAR Collaboration, A. Schmah, *Highlights of the Beam Energy Scan from STAR*, Central Eur.J.Phys. **10**, 1238 (2012), arXiv:1202.2389, doi:10.2478/s11534-012-0149-1.

[4] NA61 Collaboration, A. Aduszkiewicz, *NA61/SHINE at the CERN SPS: Plans, status and first results*, Acta Phys.Polon. **B43**, 635 (2012), arXiv:1201.5879, doi:10.5506/APhysPolB.43.635.

[5] NA61/SHINE, L. Turko, *Looking for the Phase Transition—Recent NA61/SHINE Results*, Universe **4**, 52 (2018), arXiv:1801.06919, doi:10.3390/universe4030052.

[6] BM@N Collaboration, T. O. Ablyazimov, *Conceptual Design Report of BM@N*, http://nica.jinr.ru/files/BM@N/BMN_CDR.pdf .

[7] NICA Collaboration, V. D. Kekelidze, *Design and Construction of Nuclotron-based Ion Collider fAcility. Conceptual Design Report*, http://nica.jinr.ru/files/NICA_CDR.pdf .

[8] *Primary Radiation Damage in Materials*, https://www.oecd-nea.org/jcms/pl_19620, NEA/NSC/DOC(2015)9.

[9] *Lockheed Martin Corporation*, https://www.lockheedmartin.com/.

[10] V. Wagner, *Introduction to Nuclear Spectroscopy*, http://ojs.ujf.cas.cz/~wagner/prednasky/spektroskopie/osnovaen.html, Lectures at FNPI CTU at Prague.

[11] P. D. Group *et al.*, *Review of particle physics*, Progress of Theoretical and Experimental Physics **2020**, 083C01 (2020).

[12] *Stopping-Power & Range Tables for Electrons, Protons, and Helium Ions, NIST Standard Reference Database 124* .

[13] M. Chadwick *et al.*, *ENDF/B-VII.1 Nuclear Data for Science and Technology: Cross Sections, Covariances, Fission Product Yields and Decay Data*, Nuclear Data Sheets **112**, 2887 (2011), Special Issue on ENDF/B-VII.1 Library, doi:https://doi.org/10.1016/j.nds.2011.11.002.

[14] *JANIS Java-based Nuclear Data Information System*, OECD / NEA Data Bank (2013).

[15] *X-Ray Mass Attenuation Coefficients*, NIST Standard Reference Database 126 (2004).

[16] A. Lechner, *Particle interactions with matter*, CERN Yellow Rep. School Proc. **5**, 47. 22 p (2018), doi:10.23730/CYRSP-2018-005.47.

[17] S. Pomp, *Tutorial on neutron physics in dosimetry*, Radiation Measurements **45**, 1090–1095 (2010), doi:10.1016/j.radmeas.2010.06.021.

[18] *International Commission on Radiation Units and Measurements (ICRU)*, https://www.icru.org/.

[19] V. A. J. V. Lint, T. M. Flanagan, R. E. Leadon, J. A. Naber and V. C. Rogers, *Mechanisms of Radiation Effects in Electronic Materials (Volume 1)*, 1 ed. (Wiley, 1980), [link].

[20] M. Moll, *Radiation damage in silicon particle detectors: Microscopic defects and macroscopic properties*, PhD thesis, Hamburg U., 1999.

[21] S. R. Messenger, E. A. Burke, G. P. Summers, M. A. Xapsos, R. J. Walters, E. M. Jackson and B. D. Weaver, *Nonionizing energy loss (NIEL) for heavy ions*, IEEE Transactions on Nuclear Science **46**, 1595 (1999), doi:10.1109/23.819126.

[22] A. Vasilescu, *The NIEL scaling hypothesis applied to neutron spectra of irradiation facilities in the ATLAS and CMS SCT*, RD48 Technical report, ROSE/TN/97-2, CERN (1997).

[23] *Displacement Damage in Silicon*, https://rd50.web.cern.ch/NIEL/.

[24] H. Feick, *Radiation tolerance of silicon particle detectors for high-energy physics experiments*, Dr., Universität Hamburg, 1997, Universität Hamburg, Diss., 1997.

[25] M. Moll, *Displacement damage in silicon detectors for high energy physics*, IEEE Trans. Nucl. Sci. **65**, 1561 (2018), doi:10.1109/TNS.2018.2819506.

[26] F. Honniger, *Radiation damage in silicon: Defect analysis and detector properties*, PhD thesis, Hamburg U., 2008, doi:10.3204/DESY-THESIS-2008-002.

[27] *The Stopping and Range of Ions in Matter (SRIM) 2013 software package* .

[28] P. Novotnỳ and V. Linhart, *Radiation damage study of thin YAG: Ce scintillator using low-energy protons*, Journal of Instrumentation **12**, P07021 (2017).

[29] C. W. Fabjan and F. Gianotti, *Calorimetry for particle physics*, Reviews of Modern Physics **75**, 1243 (2003).

[30] P. Loch, *Calorimetry in High Energy and High Intensity Particle Phyiscs Applications*, https://indico.cern.ch/event/697598/contributions/2871229/attachments/1594649/2525097/CalorimetersUniGoettingen.12.01.2017.pdf, 2017.

[31] A. Krása, *Spallation reaction physics*, Manuscript for the Lecture "Neutron Sources for ADS" for Students of the Faculty of Nuclear Sciences and Physical Engineering at Czech Technical University, Prague , 1 (2010).

[32] K. Pauwels, M. Lucchini, A. Benaglia and E. Auffray, *Calorimeter designs based on fibre-shaped scintillators*, in *International Conference on Engineering of Scintillation Materials and Radiation Technologies*, pp. 231–241, Springer, 2016.

[33] R. Wigmans, *New developments in calorimetric particle detection*, Prog. Part. Nucl. Phys. **103**, 109 (2018), arXiv:1807.03853, doi:10.1016/j.ppnp.2018.07.003.

[34] L. D. Hansen and R. M. Hart, *The art of calorimetry*, Thermochimica Acta **417**, 257 (2004), Honour Issue on the Retirement of Prof A. E. Beezer, doi:https://doi.org/10.1016/j.tca.2003.07.023.

[35] ZEUS Calorimeter Group, ZEUS, A. Andresen *et al.*, *Construction and beam test of the ZEUS forward and rear calorimeter*, Nucl. Instrum. Meth. A **309**, 101 (1991), doi:10.1016/0168-9002(91)90095-8.

[36] DREAM, R. Wigmans, *The DREAM project: Towards the ultimate in calorimetry*, Nucl. Instrum. Meth. A **617**, 129 (2010), doi:10.1016/j.nima.2009.09.118.

[37] R. Wigmans, *Calorimetry*International Series of Monographs on Physics (Oxford University Press, 2017).

[38] J. Zmeskal, *Detector and detector systems for particle and nuclear physics*, OEAW University Lecture (2015).

[39] S. V. Golovkin, A. A. Konstantinchenko, V. A. Kozlov, A. E. Kushnirenko, A. I. Pyshchev, V. M. Shershukov, V. G. Vasil'chenko and K. V. Zimyn, *Radiation damage studies on new liquid scintillators and liquid core scintillating fibers*, Nucl. Instrum. Meth. A **362**, 283 (1995), doi:10.1016/0168-9002(95)00225-1.

[40] B. D. Leverington, *An overview of scintillators and their applications in High Energy Physics*, https://indico.cern.ch/event/602044/contributions/2429699/attachments/1426301/2188333/scintillatorseminar.pdf, 2017.

[41] C. D'Ambrosio *et al.*, *A short Overview on Scintillators.*

[42] Y. N. Kharzheev, *Radiation Hardness of Scintillation Detectors Based on Organic Plastic Scintillators and Optical Fibers*, Phys. Part. Nucl. **50**, 42 (2019), doi:10.1134/S1063779619010027.

[43] S. Berns *et al.*, *A novel polystyrene-based scintillator production process involving additive manufacturing*, Journal of Instrumentation **15**, P10019–P10019 (2020), doi:10.1088/1748-0221/15/10/p10019.

[44] E. Biagtan, E. Goldberg, R. Stephens, E. Valeroso and J. Harmon, *Gamma radiation dose rate effects on a polymer scintillator containing a large Stokes shift dye, 3-hydroxyflavone*, Nuclear Instruments and Methods in Physics Research Section B: Beam Interactions with Materials and Atoms **114**, 88 (1996).

[45] K. C. Ltd., *Scintillator Fiber Products*, (1994).

[46] V. Salimgareeva and S. Kolesov, *Plastic scintillators based on polymethyl methacrylate: A review*, Instruments and Experimental Techniques **48**, 273 (2005).

[47] *Saint-Gobain Scintillating Fibers*, https://www.crystals.saint-gobain.com/products/scintillating-fiber.

[48] V. Hagopian, *Optical fibers light yield and radiation damage*, Nucl. Phys. B Proc. Suppl. **61**, 355 (1998), doi:10.1016/S0920-5632(97)00586-0.

[49] L. Peralta, *Temperature dependence of plastic scintillators*, Nucl. Instrum. Meth. A **883**, 20 (2018), arXiv:1709.06458, doi:10.1016/j.nima.2017.11.041.

[50] C. Zorn, *A pedestrian's guide to radiation damage in plastic scintillators*, Nucl. Phys. B Proc. Suppl. **32**, 377 (1993), doi:10.1016/0920-5632(93)90049-C.

[51] *Frontmatter* (John Wiley & Sons, Ltd, 2012), pp. i–xxviii, https://onlinelibrary.wiley.com/doi/pdf/10.1002/9781118162798.fmatter, arXiv: https://onlinelibrary.wiley.com/doi/pdf/10.1002/9781118162798.fmatter, doi:https://doi.org/10.1002/9781118162798.fmatter, [link].

[52] S. Banerjee, M. Deka, A. Kumar and U. De, *Ion Irradiation Effects in some Electro-Active and Engineering Polymers Studies by Conventional and Novel Techniques*, in *Defect and Diffusion Forum* Vol. 341, pp. 1–49, Trans Tech Publ, 2013.

[53] H. Virk, *Radiation Damage Effects in Solids: Special Topic Volume with Invited Peer Reviewed Papers Only*Defect and Diffusion Forum (Trans Tech Publications, 2013), [link].

[54] H. Padleckas, *Scheamtic of polystyrene formation*, https://commons.wikimedia.org/wiki/File:Polystyrene_formation.PNG, 2005.

[55] G. Small, *The impact of exposure to chemicals on thermoplastic polymers*, https://www.victrex.com/en/blog/2017/the-impact-of-exposure-to-chemicals-on-thermoplastic-polymers, 2017.

[56] K. Arshak, *Advanced materials and techniques for radiation dosimetry* (Artech, 2006).

[57] A. Belloni, *Radiation Effects on Plastic Scintillators for Current and Future HEP Experiments*, https://indico.fnal.gov/event/18739/contributions/48811/attachments/30467/37475/181120_fnalrts.pdf, 2018.

[58] S. V. Afanasiev *et al.*, *An improvement of a radiation hardness of the CMS hadron endcap calorimeters under increased LHC luminosity*, in *CMS Workshop: Perspectives on Physics and on CMS at Very High Luminosity, HL-LHC*, 2013.

[59] CMS, A. M. Sirunyan *et al.*, *Measurements with silicon photomultipliers of dose-rate effects in the radiation damage of plastic scintillator tiles in the CMS hadron endcap calorimeter*, JINST **15**, P06009 (2020), arXiv:2001.06553, doi:10.1088/1748-0221/15/06/P06009.

[60] A. D. Bross and A. Pla-Dalmau, *Radiation damage of plastic scintillators*, IEEE Trans. Nucl. Sci. **39**, 1199 (1992), doi:10.1109/23.173178.

[61] Y. M. Protopopov and V. G. Vasilchenko, *Radiation damage on plastic scintillators and optical fibers*, Instrum. Exp. Tech. **37**, 53 (1994).

[62] V. G. Vasilchenko, V. G. Lapshin, A. I. Peresypkin, A. A. Konstantinchenko, A. I. Pyshchev, V. M. Shershukov, B. V. Semenov and A. S. Solovev, *New results on radiation damage studies of plastic scintillators*, Nucl. Instrum. Meth. A **369**, 55 (1996), doi:10.1016/0168-9002(95)00774-1.

[63] G. I. Britvich *et al.*, *Radiation damage studies on polystyrene based scintillators*, Nucl. Instrum. Meth. A **326**, 483 (1993), doi:10.1016/0168-9002(93)90849-D.

[64] A. Nemashkalo *et al.*, *Study of tile/fiber systems manufactured from Kharkov injection molded and Kuraray SCSN-81 scintillators*, Nucl. Instrum. Meth. A **419**, 609 (1998), doi:10.1016/S0168-9002(98)00838-9.

[65] E. Biagtan, E. Goldberg, J. Harmon and R. Stephens, *Effect of gamma radiation dose rate on the light output of commercial polymer scintillators*, Nuclear Instruments and Methods in Physics Research Section B: Beam Interactions with Materials and Atoms **93**, 296 (1994).

[66] S. Afanasiev *et al.*, *Light yield measurements of "finger" structured and unstructured scintillators after gamma and neutron irradiation*, Nuclear Instruments and Methods in Physics Research Section A: Accelerators, Spectrometers, Detectors and Associated Equipment **818**, 26 (2016).

[67] ATLAS, R. Pedro, *Optics robustness of the ATLAS Tile Calorimeter*, J. Phys. Conf. Ser. **1162**, 012004 (2019), arXiv:1905.01160, doi:10.1088/1742-6596/1162/1/012004.

[68] ATLAS, B. Pereira, *Radiation hardness of the ATLAS Tile Calorimeter optical components*, J. Phys. Conf. Ser. **1690**, 012053 (2020), doi:10.1088/1742-6596/1690/1/012053.

[69] CMS HCAL, V. Khachatryan *et al.*, *Dose rate effects in the radiation damage of the plastic scintillators of the CMS Hadron Endcap Calorimeter*, JINST **11**, T10004 (2016), [Erratum: JINST 14, E08001 (2019)], arXiv:1608.07267, doi:10.1088/1748-0221/11/10/T10004.

[70] L. Zhao *et al.*, *Properties of plastic scintillators after irradiation*, Nucl. Instrum. Meth. A **552**, 449 (2005), doi:10.1016/j.nima.2005.06.075.

[71] H. Jivan, E. Sideras-Haddad, R. Erasmus, S. Liao, M. Madhuku, G. Peters, K. Sekonya and O. Solvyanov, *Radiation hardness of plastic scintillators for the Tile Calorimeter of the ATLAS detector*, J. Phys. Conf. Ser. **645**, 012019 (2015), doi:10.1088/1742-6596/645/1/012019.

[72] H. Jivan, J. Mdhluli, E. Sideras-Haddad, B. Mellado, R. Erasmus and M. Madhuku, *Radiation damage effects on the optical properties of plastic scintillators*, Nuclear Instruments and Methods in Physics Research Section B: Beam Interactions with Materials and Atoms **409**, 224 (2017).

[73] I. Bohnet, D. Kummerow and K. Wick, *Influence of radiation damage on the performance of a lead / scintillator calorimeter investigated with 1-GeV to 6-GeV electrons*, Nucl. Instrum. Meth. A **490**, 90 (2002), doi:10.1016/S0168-9002(02)01057-4.

[74] G. I. Britvich, A. E. Dorokhov, R. I. Dzhelyadin, A. K. Konoplyannikov and V. Matveev, *The HCAL optics radiation damage study*, (2000).

[75] S. Han *et al.*, *Radiation hardness tests of tile / fiber calorimeter structures for SDC*, (1992).

[76] A. Gomes, M. David, A. Henriques and A. Maio, *Comparative study of WLS fibres for the ATLAS tile calorimeter*, Nucl. Phys. B Proc. Suppl. **61**, 106 (1998), doi:10.1016/S0920-5632(97)00547-1.

[77] M. J. Varanda, M. David, A. Gomes and A. Maio, *Recent results on radiation hardness tests of WLS fibers for the ATLAS Tilecal hadronic calorimeter*, Nucl. Instrum. Meth. A **453**, 255 (2000), doi:10.1016/S0168-9002(00)00642-2.

[78] A. N. Karyukhin, V. V. Lapin, Y. M. Protopopov and V. G. Vasilchenko, *Radiation hardness study on molded scintillation tiles and wavelength shifting fibers*, Nucl. Instrum. Meth. **117**, 415 (1996), doi:10.1016/0168-583X(96)00301-1.

[79] A. Maio, M. David and A. Gomes, *Dose rate effects in WLS fibers*, Nuclear Physics B - Proceedings Supplements **54**, 222 (1997), doi:https://doi.org/10.1016/S0920-5632(97)00116-3.

[80] A. Fazely *et al.*, *Radiation damage studies for the SDC electromagnetic calorimeter*, Radiation Physics and Chemistry **41**, 243 (1993).

[81] S. Barsuk, A. Golutvin, V. Kirichenko, I. Korolko, S. Malyshev, V. Y. Rusinov and E. Tarkovski, *Radiation damage of LHCb electromagnetic calorimeter*, (2000).

[82] R. Alfaro, E. Cruz, M. I. Martinez, L. M. Montano, G. Paic and A. Sandoval, *Radiation hardness tests of a scintillation detector with wavelength shifting fiber readout*, AIP Conf. Proc. **857**, 218 (2006), doi:10.1063/1.2359259.

[83] J. Ernwein, *Radiation damage in tile - fiber calorimeter modules*, in *2nd International Conference on Calorimetry in High-energy Physics*, 1991.

[84] M. David, A. Gomes and A. Maio, *Radiation hardness of WLS fibres for the ATLAS tile calorimeter*, (2009).

[85] A. D. Bross and A. Pla-Dalmau, *Radiation induced hidden absorption effects in polystyrene based plastic scintillator*, ACS Symp. Ser. **475**, 578 (1991).

[86] V. G. Senchishin *et al.*, *A New radiation stable plastic scintillator*, Nucl. Instrum. Meth. A **364**, 253 (1995), doi:10.1016/0168-9002(95)00470-X.

[87] M. M. Hamada, P. R. Rela, F. E. da Costa and C. H. de Mesquita, *Radiation damage studies on the optical and mechanical properties of plastic scintillators*, Nuclear Instruments and Methods in Physics Research Section A: Accelerators, Spectrometers, Detectors and Associated Equipment **422**, 148 (1999).

[88] N. Buechel, S. Garrett, M. Lomnitz, A. Schmah, X. Sun, J. Van Dyke, J. Xu and J. Zhang, *Radiation Hardness Test of Eljen EJ-500 Optical Cement*, 1703.10606, arXiv:1703.10606.

[89] A. Artikov *et al.*, *Light yield and radiation hardness studies of scintillator strips with a filler*, Nucl. Instrum. Meth. A **930**, 87 (2019), arXiv:1711.11393, doi:10.1016/j.nima.2019.03.087.

[90] T. Kirn, M. Haering, D. Schmitz and W. Schulz, *Absorption length, radiation hardness and ageing of different optical glues*, (1999).

[91] A. Dbeyssi *et al.*, *Tests of optical glues for the PANDA electromagnetic calorimeter*, Nucl. Instrum. Meth. A **722**, 82 (2013), doi:10.1016/j.nima.2013.04.057.

[92] M. Montecchi and C. H. Q. Ingram, *Study of some optical glues for the Compact Muon Solenoid at the Large Hadron Collider of CERN*, Nucl. Instrum. Meth. A **465**, 329 (2001), doi:10.1016/S0168-9002(01)00678-7.

[93] A. Cemmi *et al.*, *Radiation hardness and stability of optical coupling materials for BelleII electromagnetic calorimeter*, PoS **TIPP2014**, 255 (2015), doi:10.22323/1.213.0255.

[94] A. D. Bross and A. Pla-Dalmau, *Radiation effects in intrinsic 3HF scintillator*, Nucl. Instrum. Meth. A **327**, 337 (1993), doi:10.1016/0168-9002(93)90699-I.

[95] P. Bertolucci, J. Harmon, E. Biagtan, G. Schueneman, E. Goldberg, P. Schuman and W. Schuman, *Radiation effects of low refractive index, fluorinated methacrylate polymers for fiber cladding*, Polymer Engineering & Science **38**, 699 (1998).

[96] N. Bol'bit, V. Taraban, I. Shelukhov, E. Klinshpont and V. Milinchuk, *A new type of plastic scintillators with excellent radiation resistance*, Instruments and Experimental Techniques **43**, 460 (2000).

[97] N. Akchurin, E. Kendir, c. Yaltkaya, J. Damgov, F. D. Guio and S. Kunori, *Radiation-hardness studies with cerium-doped fused-silica fibers*, JINST **14**, P03020 (2019), doi:10.1088/1748-0221/14/03/P03020.

[98] CMS, E. Tiras, *Radiation Hard \& High Light Yield Scintillator Search for CMS Phase II Upgrade*, in *Meeting of the APS Division of Particles and Fields*, 2015, arXiv:1510.08572.

[99] M. Dettmann *et al.*, *Radiation Hard Plastic Scintillators for a New Generation of Particle Detectors*, JINST **12**, P03017 (2017), doi:10.1088/1748-0221/12/03/P03017.

[100] S. W. Han *et al.*, *Radiation hardness tests of scintillating tile / WLS fiber calorimeter modules*, Nucl. Instrum. Meth. A **365**, 337 (1995), doi:10.1016/0168-9002(95)00429-7.

[101] G. Anzivino *et al.*, *Radiation induced effects on lead and scintillating fiber calorimeters at the LHC*, Nucl. Instrum. Meth. A **346**, 153 (1994), doi:10.1016/0168-9002(94)90699-8.

[102] A. B. R. Cavalcante, B. Dey, L. Gavardi, L. Gruber, C. Joram, R. Kristic, O. Shinji and V. Zhukov, *Refining and testing 12,000 km of scintillating plastic fibre for the LHCb SciFi tracker*, JINST **13**, P10025 (2018), doi:10.1088/1748-0221/13/10/P10025.

[103] B. Bodmann, S. Göb and U. Holm, *LET effects of neutron irradiated plastic scintillators*, Nuclear Instruments and Methods in Physics Research Section B: Beam Interactions with Materials and Atoms **208**, 495 (2003).

[104] L. Torrisi, *Radiation damage in polyvinyltoluene (PVT)*, Radiation Physics and Chemistry **63**, 89 (2002).

[105] B. Bodmann and U. Holm, *Neutron-irradiated plastic scintillators*, Nuclear Instruments and Methods in Physics Research Section B: Beam Interactions with Materials and Atoms **185**, 299 (2001).

[106] V. Baranov *et al.*, *Effects of neutron radiation on the optical and structural properties of blue and green emitting plastic scintillators*, Nucl. Instrum. Meth. B **436**, 236 (2018), arXiv:1810.05000, doi:10.1016/j.nimb.2018.10.002.

[107] G. Buss, A. Dannemann, U. Holm and K. Wick, *Radiation damage by neutrons to plastic scintillators*, IEEE Trans. Nucl. Sci. **42**, 315 (1995), doi:10.1109/23.467829.

[108] J. E. Mdhluli *et al.*, *Neutron induced radiation damage of plastic scintillators for the upgrade of the Tile Calorimeter of the ATLAS detector.*, J. Phys. Conf. Ser. **878**, 012008 (2017), doi:10.1088/1742-6596/878/1/012008.

[109] B. Bicken, U. Holm, T. Marckmann, K. Wick and M. Rohde, *Recovery and permanent radiation damage of plastic scintillators at different dose rates*, IEEE Trans. Nucl. Sci. **38**, 188 (1991), doi:10.1109/23.289295.

[110] U. Holm and K. Wick, *Radiation Stability of Plastic Scintillators and Wave Length Shifters*, IEEE Trans. Nucl. Sci. **36**, 579 (1989), doi:10.1109/23.34504.

[111] U. Holm, D. Horstmann and S. Schacht, *Oxygen diffusion and recovery of damage in irradiated polystyrene*, Nuclear Instruments and Methods in Physics Research Section B: Beam Interactions with Materials and Atoms **151**, 453 (1999).

[112] H. Klose, M. Krause, W. Pfeiffer, J. Rauchfuss, G. Sinn, D. Fink and M. Wilhelm, *On radiation damage of scintillating organic fibres in dependence on energetic electron bombardment*, in *Proceedings of the Third European Conference on Radiation and its Effects on Components and Systems*, pp. 525–530, IEEE, 1995.

[113] B. Bicken, A. Dannemann, U. Holm, T. Neumann and K. Wick, *Influence of temperature treatment on radiation stability of plastic scintillator and wavelength shifter*, IEEE Trans. Nucl. Sci. **39**, 1212 (1992), doi:10.1109/23.173180.

[114] T. Zhou, H. He and X. Sheng, *The long-term stability of plastic scintillator for electromagnetic particle detectors*, Proceedings of the 32nd International Cosmic Ray Conference, ICRC 2011 **4**, 346 (2011), doi:10.7529/ICRC2011/V04/0267.

[115] K. Wick, R. Hornung and T. Gosau, *Reduction of the permanent radiation induced absorption by illumination of plastic scintillators during γ-irradiation*, Nuclear Instruments and Methods in Physics Research Section A: Accelerators, Spectrometers, Detectors and Associated Equipment **538**, 668 (2005).

[116] A. Artikov *et al.*, *Properties of the Ukraine polystyrene-based plastic scintillator UPS 923A*, Nuclear Instruments and Methods in Physics Research Section A: Accelerators, Spectrometers, Detectors and Associated Equipment **555**, 125 (2005).

[117] I. Bohnet, R. P. Feller, N. Krumnack, E. Moller, H. Prause, H. Salehi and K. Wick, *Long-term studies of the optical components in the ZEUS calorimeter using a moving Co-60 source*, Nucl. Instrum. Meth. A **599**, 53 (2009), doi:10.1016/j.nima.2008.10.035.

[118] J. Silva, A. Maio, J. Pina, J. Santos and J. G. Saraiva, *Ageing studies of wavelength shifter fibers for the TILECAL/ATLAS experiment*, Nucl. Instrum. Meth. A **580**, 318 (2007), doi:10.1016/j.nima.2007.05.165.

[119] S. Mthembu, Y. Davydov, V. Baranov, B. Mellado Garcia, J. Mdhluli and E. Sideras-Haddad, *The influence of neutron radiation damage on the optical properties of plastic scintillator UPS 923A*, J. Phys. Conf. Ser. **889**, 012019 (2017), doi:10.1088/1742-6596/889/1/012019.

[120] C. Pelwan, H. Jivan, D. Joubert, J. Keartland, S. Liao, G. Peters and E. Sideras-Haddad, *Characterization of plastic scintillators using magnetic resonance techniques for the upgrade of the Tile Calorimeter in the ATLAS detector*, J. Phys. Conf. Ser. **645**, 012023 (2015), doi:10.1088/1742-6596/645/1/012023.

[121] L. Maphanga, R. Erasmus, H. Jivan, B. Mellado, G. Peters and E. Sideras-Haddad, *Characterization of damage in in-situ radiated plastic scintillators at the Tile calorimeter of the ATLAS*, in *59th Annual Conference of the South African Institute of Physics*, 2015.

[122] V. Manzari, *Silicon Detectors*, https://indico.cern.ch/event/453690/sessions/99350/attachments/1184199/1726996/2015-11_SiliconDetectors_manzari_Lecture1.pdf, 2015, Lectures at The 5th Egyptian School on High Energy Physics.

[123] M. Krammer, *Silicon Detectors*, https://fisica.cab.cnea.gov.ar/particulas/html/icfa/pdf/Krammer01.pdf, 2015, Lectures at XI ICFA School on Instrumentation.

[124] K. Iniewski, editor, *Radiation Effects in Semiconductors (Devices, Circuits, and Systems)*, 1 ed. (CRC Press, 2010), [link].

[125] *RD50 - Recommendations for performing sensor measurements*, https://rd50.web.cern.ch/doc/recommendations.html.

[126] H. Spieler, *Semiconductor Detector Systems (Series on Semiconductor Science and Technology)*, 1 ed. (Oxford University Press, 2005), [link].

[127] J. Gebelein, *FPGA fault tolerance in radiation environments*, PhD thesis, Goethe University Frankfurt, 2016.

[128] K. E. Holbert, *Single Event Effects*, http://holbert.faculty.asu.edu/eee560/see.html (2006).

[129] H. E. Boesch and T. L. Taylor, *Charge and Interface State Generation in Field Oxides*, IEEE Transactions on Nuclear Science **31**, 1273 (1984), doi:10.1109/TNS.1984.4333495.

[130] E. Garutti and Y. Musienko, *Radiation damage of SiPMs*, Nucl. Instrum. Meth. A **926**, 69 (2019), arXiv:1809.06361, doi:10.1016/j.nima.2018.10.191.

[131] D. Zontar, *Study of radiation damage in silicon detectors for high luminosity experiments at LHC*, PhD thesis.

[132] B. Linnik, T. Bus, M. Deveaux, D. Doering, P. Kudejova, F. M. Wagner, A. Yazgili and J. Stroth, *Radiation damage caused by cold neutrons in boron doped CMOS active pixel sensors*, Journal of Instrumentation **12**, C05011 (2017).

[133] Y. Shi, D. X. Shen, F. M. Wu and K. J. Cheng, *A numerical study of cluster center formation in neutron irradiated silicon*, Journal of Applied Physics **67**, 1116 (1990), arXiv:http://dx.doi.org/10.1063/1.345799, doi:10.1063/1.345799.

[134] C. Poivey, *TNID Total Non Ionizing Dose or DD Displacement Damage*, ESA–CERN–SCC Workshop, 2017.

[135] P. Larionov, *Systematic Irradiation Studies and Quality Assurance of Silicon Strip Sensors for the CBM Silicon Tracking System*, PhD thesis, Goethe-Universität Frankfurt am Main, 2016.

[136] C. Claeys and E. Simoen, *Radiation Effects in Advanced Semiconductor Materials and Devices* (Springer Berlin Heidelberg, 2002), doi:10.1007/978-3-662-04974-7.

[137] *PN Junction Diode tutorial*, https://www.electronics-tutorials.ws/diode/diode_3.html.

[138] Y. Unno *et al.*, *Proton irradiation on AC-coupled silicon microstrip detectors*, IEEE Trans. Nucl. Sci. **42**, 675 (1995), doi:10.1109/23.467878.

[139] M. Moll, *An introduction to Silicon Detectors with focus on High Energy Physics applications*, presentation at SIMDET2016 thematic school.

[140] A. Chilingarov, *Temperature dependence of the current generated in Si bulk*, Journal of Instrumentation **8**, P10003 (2013), doi:10.1088/1748-0221/8/10/P10003.

[141] P. Hofmann, *Solid State Physics: An Introduction*Physics textbook (Wiley, 2015), [link].

[142] D. Campbell, A. Chilingarov and T. Sloan, *Frequency and temperature dependence of the depletion voltage from CV measurements for irradiated Si detectors*, Nucl. Instrum. Meth. A **492**, 402 (2002), doi:10.1016/S0168-9002(02)01353-0.

[143] G. Kramberger, M. Batic, V. Cindro, I. Mandic, M. Mikuz and M. Zavrtanik, *Annealing studies of effective trapping times in silicon detectors*, Nucl. Instrum. Meth. **A571**, 608 (2007), doi:10.1016/j.nima.2006.10.399.

[144] G. Kramberger, V. Cindro, I. Mandic, M. Mikuz and M. Zavrtanik, *Effective trapping time of electrons and holes in different silicon materials irradiated with neutrons, protons and pions*, Nucl. Instrum. Meth. A **481**, 297 (2002), doi:10.1016/S0168-9002(01)01263-3.

[145] D. Contardo, M. Klute, J. Mans, L. Silvestris and J. Butler, Report No. CERN-LHCC-2015-010. LHCC-P-008. CMS-TDR-15-02, 2015 (unpublished), Upgrade Project Leader Deputies: Lucia Silvestris (INFN-Bari), Jeremy Mans (University of Minnesota) Additional contacts: Lucia.Silvestris@cern.ch, Jeremy.Mans@cern.ch, [link].

[146] C. Da Via *et al.*, *Radiation hardness properties of full-3D active edge silicon sensors*, Nucl. Instrum. Meth. **A587**, 243 (2008), doi:10.1016/j.nima.2007.12.027.

[147] T. Rohe *et al.*, *Fluence dependence of charge collection of irradiated pixel sensors*, Nucl. Instrum. Meth. A **552**, 232 (2005), arXiv:physics/0411214, doi:10.1016/j.nima.2005.06.037.

[148] P. P. Allport, G. Casse, M. Lozano, P. Sutcliffe, J. J. Velthuis and J. Vossebeld, *Performance of P-type micro-strip detectors after irradiation to 7.5 x 10**15 p cm**(-2)*, IEEE Trans. Nucl. Sci. **52**, 1903 (2005), doi:10.1109/TNS.2005.856747.

[149] RD42, W. Adam *et al.*, *Radiation hard diamond sensors for future tracking applications*, Nucl. Instrum. Meth. A **565**, 278 (2006), doi:10.1016/j.nima.2006.05.127.

[150] M. Moll, *An introduction to Silicon Detectors with focus on applications at Hadron Colliders*, https://indico.in2p3.fr/event/17763/contributions/66813/attachments/50770/64925/2018-10-29-Paris-SIMDET-Silicon_Sensors.pdf, 2018.

[151] F. Yu *et al.*, *Overview of Radiation Hardening Techniques for IC Design*, Information Technology Journal **9**, 1068 (2010), doi:10.3923/itj.2010.1068.1080.

[152] *Sensl (now ON Semiconductor) Silicon Photomultipliers*, https://www.onsemi.com/products/sensors/silicon-photomultipliers-sipm.

[153] *Silicon Photomultipliers (SiPMs) from KETEK*, https://www.ketek.net/sipm/.

[154] Zecotek, *Zecotek MAPD*, (2015), Multi-pixel Avalanche Photo Diode White Paper.

[155] *Hamamatsu Multi-Pixel Photon Counters*, https://www.hamamatsu.com/eu/en/product/optical-sensors/mppc/index.html.

[156] G. Collazuol, *The Silicon Photo-Multiplier Status and Perspectives*, presentation at Vienna Conference of Instrumentation.

[157] F. Acerbi and S. Gundacker, *Understanding and simulating SiPMs*, Nucl. Instrum. Meth. A **926**, 16 (2019), doi:10.1016/j.nima.2018.11.118.

[158] F. Simon, *Silicon Photomultipliers in Particle and Nuclear Physics*, Nucl. Instrum. Meth. A **926**, 85 (2019), arXiv:1811.03877, doi:10.1016/j.nima.2018.11.042.

[159] D. Renker and E. Lorenz, *Advances in solid state photon detectors*, Journal of Instrumentation **4**, P04004 (2009).

[160] S. Gundacker and A. Heering, *The silicon-photomultiplier: fundamentals and applications of a modern solid-state photon detector*, Phys. Med. Biol. **65**, 17TR01 (2020), doi:10.1088/1361-6560/ab7b2d.

[161] R. Klanner, *Characterisation of SiPMs*, Nucl. Instrum. Meth. A **926**, 36 (2019), arXiv:1809.04346, doi:10.1016/j.nima.2018.11.083.

[162] F. S. Robert Klanner, *Silicon Photomultipliers: Technology, Characterisation and Applications*, Special volume 926 of NIMA.

[163] *Physics and operation of the MPPC silicon photomultiplier*, https://hub.hamamatsu.com/jp/en/technical-note/sipm-physics-operation/index.html.

[164] M. Grodzicka-Kobylka, M. Moszyński and T. Szczęśniak, *Silicon photomultipliers in gamma spectroscopy with scintillators*, Nuclear Instruments and Methods in Physics Research Section A: Accelerators, Spectrometers, Detectors and Associated Equipment **926**, 129 (2019).

[165] C. Xu, *Study of the Silicon Photomultipliers and Their Application in Positron Emission Tomography*, PhD thesis, 2014.

[166] N. Dinu, *Instrumentation on silicon detectors: from properties characterization to applications*, Habilitation à diriger des recherches, Université Paris Sud - Paris XI, 2013.

[167] K. Ueno, S. Sahu, K. Peng, W. Hou and C. Wang, *Detection of minimum-ionizing particles and nuclear counter effect with pure BGO and BSO crystals with photodiode readout*, NIM A **396**, 103 (1997), doi:http://dx.doi.org/10.1016/S0168-9002(97)00791-2.

[168] M. Danilov, *Novel Photo-Detectors and Photo-Detector Systems*, Nucl. Instrum. Meth. A **604**, 183 (2009), arXiv:0812.1098, doi:10.1016/j.nima.2009.01.208.

[169] Z. Li *et al.*, *Characterization of radiation damage caused by 23 MeV protons in Multi-Pixel Photon Counter (MPPC)*, Nuclear Instruments and Methods in Physics Research Section A: Accelerators, Spectrometers, Detectors and Associated Equipment **822**, 63 (2016), doi:https://doi.org/10.1016/j.nima.2016.03.092.

[170] T. Matsumura *et al.*, *Effects of radiation damage caused by proton irradiation on Multi-Pixel Photon Counters (MPPCs)*, Nucl. Instrum. Meth. A **603**, 301 (2009), arXiv:0901.2430, doi:10.1016/j.nima.2009.02.022.

[171] A. Ulyanov *et al.*, *Radiation Damage Study of SensL J-Series Silicon Photomultipliers Using 101.4 MeV Protons*, 2007.10919, arXiv:2007.10919, doi:10.1016/j.nima.2020.164203.

[172] E. Tarkovsky, *Performance of a scintillating strip detector with G-APD readout*, Nuclear Instruments and Methods in Physics Research Section A: Accelerators, Spectrometers, Detectors and Associated Equipment **628**, 372 (2011), {VCI} 2010Proceedings of the 12th International Vienna Conference on Instrumentation, doi:https://doi.org/10.1016/j.nima.2010.07.004.

[173] A. Heering, Y. Musienko, J. Gonzales, A. Karneyeu, M. Wayne, R. Ruchti and M. Moll, *Low temperature characteristics of SiPMs after very high neutron irradiation*, Nucl. Instrum. Meth. A **936**, 671 (2019), doi:10.1016/j.nima.2018.09.111.

[174] M. Andreotti *et al.*, *Silicon photo-multiplier radiation hardness tests with a white neutron beam*, in *3rd International Conference on Advancements in Nuclear Instrumentation Measurement Methods and their Applications*, 2013, doi:10.1109/ANIMMA.2013.6728033.

[175] M. Andreotti *et al.*, *Study of the radiation damage of Silicon Photo-Multipliers at the GELINA facility*, Journal of Instrumentation **9**, P04004 (2014).

[176] P. W. Cattaneo, T. Cervi, A. Menegolli, M. Oddone, M. Prata, M. C. Prata and M. Rossella, *Radiation Hardness tests with neutron flux on different Silicon photomultiplier devices*, JINST **12**, C07012 (2017), arXiv:1705.08786, doi:10.1088/1748-0221/12/07/C07012.

[177] I. Nakamura, *Radiation damage of pixelated photon detector by neutron irradiation*, Nuclear Instruments and Methods in Physics Research Section A: Accelerators, Spectrometers, Detectors and Associated Equipment **610**, 110 (2009), New Developments In Photodetection {NDIP08Proceedings} of the Fifth International Conference on New Developments in Photodetection, doi:https://doi.org/10.1016/j.nima.2009.05.086.

[178] Y. Qiang, C. Zorn, F. Barbosa and E. Smith, *Radiation hardness tests of SiPMs for the {JLab} Hall D Barrel calorimeter*, Nuclear Instruments and Methods in Physics Research Section A: Accelerators, Spectrometers, Detectors and Associated Equipment **698**, 234 (2013), doi:https://doi.org/10.1016/j.nima.2012.10.015.

[179] T. Tsang, T. Rao, S. Stoll and C. Woody, *Neutron radiation damage and recovery studies of SiPMs*, Journal of Instrumentation **11**, P12002 (2016).

[180] L. J. Mitchell, B. Phlips, W. N. Johnson, M. Johnson-Rambert, A. N. Kansky and R. Woolf, *Radiation damage assessment of SensL SiPMs*, Nucl. Instrum. Meth. A **988**, 164798 (2021), arXiv:2003.08213, doi:10.1016/j.nima.2020.164798.

[181] T. Tolba, D. Grzonka, T. Sefzick and J. Ritman, *Study of Silicon Photomultiplier Radiation Hardness with Proton Beam from the JULIC Cyclotron*, 2003.04933, arXiv:2003.04933.

[182] A. Heering, Y. Musienko, R. Ruchti, M. Wayne, A. Karneyeu and V. Postoev, *Effects of very high radiation on SiPMs*, Nuclear Instruments and Methods in Physics Research Section A: Accelerators, Spectrometers, Detectors and Associated Equipment **824**, 111 (2016), Frontier Detectors for Frontier Physics: Proceedings of the 13th Pisa Meeting on Advanced Detectors, doi:https://doi.org/10.1016/j.nima.2015.11.037.

[183] A. H. Heering *et al.*, *Radiation damage studies on SiPMs for calorimetry at the Super LHC*, in *2008 IEEE Nuclear Science Symposium Conference Record*, pp. 1523–1526, 2008, doi:10.1109/NSSMIC.2008.4774702.

[184] Y. Musienko, *Radiation Damage Studies of Silicon Photomultipliers for for the CMS HCAL Phase I Upgrade*, presentation at International Conference NDIP-2014.

[185] Y. Musienko, A. Heering, M. Wayne, R. Ruchti, A. Karneyeu and V. Postoev, *Studies of SiPMs for the CMS HCAL Upgrade*, PoS **PhotoDet2015**, 038 (2016), doi:10.22323/1.252.0038.

[186] F. Barbosa, J. McKisson, J. McKisson, Y. Qiang, W. Steinberger, W. Xi and C. Zorn, *Radiation tolerance survey of selected silicon photomultipliers to high energy neutron irradiation*, in *2012 IEEE Nuclear Science Symposium and Medical Imaging Conference Record (NSS/MIC)*, pp. 385–390, IEEE, 2012.

[187] B. Biró *et al.*, *A Comparison of the Effects of Neutron and Gamma Radiation in Silicon Photomultipliers*, IEEE Trans. Nucl. Sci. **66**, 1833 (2019), arXiv:1809.04594, doi:10.1109/TNS.2019.2921102.

[188] M. Calvi, P. Carniti, C. Gotti, C. Matteuzzi and G. Pessina, *Single photon detection with SiPMs irradiated up to 10^{14} cm^{-2} 1-MeV-equivalent neutron fluence*, Nucl. Instrum. Meth. A **922**, 243 (2019), arXiv:1805.07154, doi:10.1016/j.nima.2019.01.013.

[189] Y. Sudo, *Study of the multi pixel photon counter for the ILC scintillator-strip calorimeter*, PoS **PD09**, 005 (2010), doi:10.22323/1.090.0005.

[190] T. Tsang, *Silicon photomultipliers radiation damage and recovery via high temperature annealing*, JINST **13**, P10019 (2018), doi:10.1088/1748-0221/13/10/P10019.

[191] M. S. Nitschke, *Characterization of Silicon Photomultipliers Before and After Neutron Irradiation*, PhD thesis, MSC Thesis, 1989.

[192] E. Garutti, R. Klanner, D. Lomidze, J. Schwandt and M. Zvolsky, *Characterisation of highly radiation-damaged SiPMs using current measurements*, 1709.05226, arXiv:1709.05226.

[193] S. Cerioli, E. Garutti, R. Klanner, S. Martens, J. Schwandt and M. Zvolsky, *Analysis methods for highly radiation-damaged SiPMs*, Nucl. Instrum. Meth. A **958**, 162729 (2020), arXiv:1904.07023, doi:10.1016/j.nima.2019.162729.

[194] M. C. Vignali, V. Chmill, E. Garutti, R. Klanner, M. Nitschke, J. Schwandt and S. Sonder, *Neutron induced radiation damage of KETEK SiPMs*, in *2016 IEEE Nuclear Science Symposium, Medical Imaging Conference and Room-Temperature Semiconductor Detector Workshop (NSS/MIC/RTSD)*, pp. 1–5, IEEE, 2016.

[195] M. Centis Vignali, E. Garutti, R. Klanner, D. Lomidze and J. Schwandt, *Neutron irradiation effect on SiPMs up to $\Phi_{neq} = 5 \times 10^{14}$ cm^{-2}*, Nucl. Instrum. Meth. A **912**, 137 (2018), arXiv:1709.04648, doi:10.1016/j.nima.2017.11.003.

[196] Y. Musienko, A. Heering, R. Ruchti, M. Wayne, Y. Andreev, A. Karneyeu and V. Postoev, *Radiation damage in silicon photomultipliers exposed to neutron radiation*, JINST **12**, C07030 (2017), doi:10.1088/1748-0221/12/07/C07030.

[197] Y. Musienko, A. Heering, R. Ruchti, M. Wayne, Y. Andreev, A. Karneyeu and V. Postoev, *Radiation damage of prototype SiPMs for the CMS HCAL Barrel phase I upgrade*, Nucl. Instrum. Meth. A **912**, 359 (2018), doi:10.1016/j.nima.2017.12.059.

[198] E. Garutti, M. Gensch, R. Klanner, M. Ramilli and C. Xu, *Afterpulse effect in SiPM and neutron irradiation studies*, in *2014 IEEE Nuclear Science Symposium and Medical Imaging Conference (NSS/MIC)*, pp. 1–7, 2014, doi:10.1109/NSSMIC.2014.7430746.

[199] K. D. Bartlett, D. D. S. Coupland, D. Beckman and K. E. Mesick, *Proton Irradiation Damage and Annealing Effects in ON Semiconductor J-Series Silicon Photomultipliers*, Nucl. Instrum. Meth. A **969**, 163957 (2020), arXiv:1911.08270, doi:10.1016/j.nima.2020.163957.

[200] K. Lacombe, I. Belkacem, B. Houret, J. Knödlseder, P. Ramon, A. Bardoux and T. Gimenez, *Impact of Proton Irradiation on SiPM Dark Current for High-Energy Space Instruments*, JPS Conf. Proc. **27**, 012006 (2019), doi:10.7566/JPSCP.27.012006.

[201] T. Matsumura *et al.*, *Effects of radiation damage caused by proton irradiation on Multi-Pixel Photon Counters (MPPCs)*, Nuclear Instruments and Methods in Physics Research Section A: Accelerators, Spectrometers, Detectors and Associated Equipment **603**, 301 (2009), doi:https://doi.org/10.1016/j.nima.2009.02.022.

[202] T. Matsumura *et al.*, *Radiation damage to MPPCs by irradiation with protons*, PoS **PD07**, 033 (2007).

[203] CMS, P. Bohn *et al.*, *Radiation Damage Studies of Silicon Photomultipliers*, Nucl. Instrum. Meth. A **598**, 722 (2009), arXiv:0809.4786, doi:10.1016/j.nima.2008.10.027.

[204] Y. Musienko, D. Renker, Z. Charifoulline, K. Deiters, S. Reucroft and J. Swain, *Study of radiation damage induced by 82 MeV protons on multi-pixel Geiger-mode avalanche photodiodes*, Nuclear Instruments and Methods in Physics Research Section A: Accelerators, Spectrometers, Detectors and Associated Equipment **610**, 87 (2009), New Developments In Photodetection {NDIP08Proceedings} of the Fifth International Conference on New Developments in Photodetection, doi:https://doi.org/10.1016/j.nima.2009.05.052.

[205] M. Angelone *et al.*, *Silicon photo-multiplier radiation hardness tests with a beam controlled neutron source*, Nuclear Instruments and Methods in Physics Research Section A: Accelerators, Spectrometers, Detectors and Associated Equipment **623**, 921 (2010), doi:https://doi.org/10.1016/j.nima.2010.07.057.

[206] R. Faccini *et al.*, *Results from silicon photo-multiplier neutron irradiation test*, in *11th ICATPP Conference on Astroparticle, Particle, Space Physics, Detectors and Medical Physics Applications*, 2009, doi:10.1142/9789814307529_0092.

[207] T. Cervi *et al.*, *Radiation hardness tests with neutrons of timing counter MEGII SiPMs*, in *2016 IEEE Nuclear Science Symposium, Medical Imaging Conference and Room-Temperature Semiconductor Detector Workshop (NSS/MIC/RTSD)*, pp. 1–4, IEEE.

[208] M. Cordelli, E. Diociaiuti, R. Donghia, A. Ferrari, S. Miscetti, S. Muller, G. Pezzullo and I. Sarra, *Electrical Induced Annealing technique for neutron radiation damage on SiPMs*, 1804.09792, arXiv:1804.09792.

[209] M. Cordelli, E. Diociaiuti, R. Donghia, A. Ferrari, S. Miscetti, S. Müller and I. Sarra, *Neutron irradiation test of Hamamatsu, SensL and AdvanSiD UV-extended SiPMs*, JINST **13**, T03005 (2018), arXiv:1710.06239, doi:10.1088/1748-0221/13/03/T03005.

[210] M. Y. Barnyakov, T. Frach, S. A. Kononov, I. A. Kuyanov and V. G. Prisekin, *Radiation hardness test of the Philips Digital Photon Counter with proton beam*, Nucl. Instrum. Meth. A **824**, 83 (2016), doi:10.1016/j.nima.2015.10.098.

[211] F. Diblen, T. Buitenhuis, T. Solf, P. Rodrigues, E. van der Graaf, M.-J. van Goethem, S. Brandenburg and P. Dendooven, *Radiation hardness of dsipm sensors in a proton therapy radiation environment*, IEEE Transactions on Nuclear Science **64**, 1891 (2017).

[212] S. Mianowski, J. Baszak, Y. Gledenov, Y. Kopatch, Z. Mianowska, M. Moszynski, P. Sibczynski and T. Szczesniak, *Study of MPPC damage induced by neutrons*, Nuclear Instruments and Methods in Physics Research Section A: Accelerators, Spectrometers, Detectors and Associated Equipment **906**, 30 (2018), doi:https://doi.org/10.1016/j.nima.2018.07.080.

[213] Y. Musienko, A. Heering, A. Karneyeu and M. Wayne, *Change of SiPM parameters after very high neutron irradiation*, JINST **15**, C09036 (2020), doi:10.1088/1748-0221/15/09/C09036.

[214] Y. Musienko, A. Heering, R. Ruchti, M. Wayne, A. Karneyeu and V. Postoev, *Radiation damage studies of silicon photomultipliers for the {CMS} {HCAL} phase I upgrade*, NIM A **787**, 319 (2015), New Developments in Photodetection {NDIP14}, doi:https://doi.org/10.1016/j.nima.2015.01.012.

[215] S. Mianowski *et al.*, *SiPM proton irradiation for application in cosmic space*, JINST **15**, P03002 (2020), arXiv:2003.09731, doi:10.1088/1748-0221/15/03/P03002.

[216] E. Engelmann, *Dark Count Rate of Silicon Photomultipliers*, PhD thesis, Universität Hamburg, 2018.

[217] T. Matsubara, H. Tanaka, K. Nitta and M. Kuze, *Radiation damage of MPPC by gamma-ray irradiation with Co-60*, PoS **PD07**, 032 (2007).

[218] H. Photonics, *Opto-semiconductor handbook / Chapter 03 Si APD, MPPC* (, 2011), [link].

[219] A. Vacheret *et al.*, *Characterization and Simulation of the Response of Multi Pixel Photon Counters to Low Light Levels*, Nucl. Instrum. Meth. A **656**, 69 (2011), arXiv:1101.1996, doi:10.1016/j.nima.2011.07.022.

[220] V. Chmill, E. Garutti, R. Klanner, M. Nitschke and J. Schwandt, *Study of the breakdown voltage of SiPMs*, Nucl. Instrum. Meth. A **845**, 56 (2017), arXiv:1605.01692, doi:10.1016/j.nima.2016.04.047.

[221] S. Mianowski, J. Baszak, Y. Gledenov, K. Nikolaevich, Z. Mianowska, M. Moszynski, P. Sibczynski and T. Szczesniak, *Evolution of MPPC properties as a function of neutron fluence*, pp. 1–3, 2017, doi:10.1109/NSSMIC.2017.8532616.

[222] C. Leroy and P. G. Rancoita, *Silicon Solid State Devices and Radiation Detection* (, 2012), doi:10.1142/8383.

[223] Y. Musienko, D. Renker, S. Reucroft, R. Scheuermann, A. Stoykov and J. Swain, *Radiation damage studies of multipixel Geiger-mode avalanche photodiodes*, Nuclear Instruments and Methods in Physics Research Section A: Accelerators, Spectrometers, Detectors and Associated Equipment **581**, 433 (2007), {VCI} 2007Proceedings of the 11th International Vienna Conference on Instrumentation, doi:https://doi.org/10.1016/j.nima.2007.08.021.

[224] S. Baccaro *et al.*, *Irradiation study of UV Silicon Photomultipliers for the Mu2e calorimeter*, Journal of Instrumentation **12**, C02022 (2017).

[225] Sensl, *An Introduction to the Silicon Photomultiplier*, (2017), Technical note.

[226] *Linearity of the Silicon Photomultiplier*, https://www.onsemi.com/pub/Collateral/AND9776-D.PDF.

[227] *Silicon Photomultiplier (SiPM) Signal to Noise Ratio*, https://www.onsemi.com/pub/Collateral/AND9794-D.PDF.

[228] D. Durini, C. Degenhardt, H. Rongen, A. Feoktystov, M. Schlösser, A. Palomino-Razo, H. Frielinghaus and S. van Waasen, *Evaluation of the dark signal performance of different SiPM-technologies under irradiation with cold neutrons*, Nuclear Instruments and Methods in Physics Research Section A: Accelerators, Spectrometers, Detectors and Associated Equipment **835**, 99 (2016), doi:https://doi.org/10.1016/j.nima.2016.08.016.

[229] S. Kumar, D. Durini, C. Degenhardt and S. van Waasen, *Photodetection characterization of SiPM technologies for their application in scintillator based neutron detectors*, Journal of Instrumentation **13**, C01042 (2018).

[230] S. Kumar, L. Niraula, D. Arutinov, A. Dalla Mora and S. Van Waasen, *Timing resolution of SiPM technologies before and after neutron irradiation*, Journal of Instrumentation **15**, C01023 (2020).

[231] M. Usami *et al.*, *Radiation damage effect on time resolution of 6 series-connected SiPMs for MEG II positron timing counter*, Nucl. Instrum. Meth. A **936**, 572 (2019), doi:10.1016/j.nima.2018.10.053.

[232] G. Boca *et al.*, *Timing resolution of a plastic scintillator counter read out by radiation damaged SiPMs connected in series*, Nucl. Instrum. Meth. A **999**, 165173 (2021), arXiv:2005.05027, doi:10.1016/j.nima.2021.165173.

[233] S. Sanchez Majos *et al.*, *Noise and radiation damage in silicon photomultipliers exposed to electromagnetic and hadronic radiation*, Nucl. Instrum. Meth. **A602**, 506 (2009), doi:10.1016/j.nima.2009.01.176.

[234] S. Sanchez Majos, P. Achenbach and J. Pochodzalla, *Characterisation of radiation damage in silicon photomultipliers with a Monte Carlo model*, Nucl. Instrum. Meth. A **594**, 351 (2008), arXiv:0805.4158, doi:10.1016/j.nima.2008.06.021.

[235] R. Pagano, S. Lombardo, F. Palumbo, D. Sanfilippo, G. Valvo, G. Fallica and S. Libertino, *Radiation hardness of silicon photomultipliers under 60Co gamma-ray irradiation*, Nuclear Instruments and Methods in Physics Research Section A: Accelerators, Spectrometers, Detectors and Associated Equipment **767**, 347 (2014), doi:https://doi.org/10.1016/j.nima.2014.08.028.

[236] C. Xu, R. Klanner, E. Garutti and W.-L. Hellweg, *Influence of X-ray irradiation on the properties of the Hamamatsu silicon photomultiplier S10362-11-050C*, Nuclear Instruments and Methods in Physics Research Section A: Accelerators, Spectrometers, Detectors and Associated Equipment **762**, 149 (2014), doi:https://doi.org/10.1016/j.nima.2014.05.112.

[237] F. Nishikido, Y. Hirano, A. Mohammadi and T. Yamaya, *Radiation damage of the multi-pixel photon counter to be used for in-beam PET in carbon therapy*, in *2014 IEEE Nuclear Science Symposium and Medical Imaging Conference (NSS/MIC)*, pp. 1–2, 2014, doi:10.1109/NSSMIC.2014.7430978.

[238] T. Tanaka, Y. Itow, T. Mase, K. Masuda, H. Menjo, T. Sako and H. Watanabe, *Radiation damage test of MPPC by a 290-MeV/u C beam at HIMAC*, PoS **PD07**, 045 (2007).

[239] J. Link *et al.*, *SIPM use in Future Space Instruments*, PoS **ICRC2017**, 235 (2018), doi:10.22323/1.301.0235.

[240] F. Acerbi *et al.*, *Irradiation and performance of RGB-HD Silicon Photomultipliers for calorimetric applications*, JINST **14**, P02029 (2019), arXiv:1901.08430, doi:10.1088/1748-0221/14/02/P02029.

[241] FAIR, *FAIR Baseline Technical Report 2006*, www.fair-center.eu/fileadmin/fair/publications_FAIR/FAIR_BTR_6.pdf (2006).

[242] W. Ehehalt and W. Cassing, *Relativistic transport approach for nucleus nucleus collisions from SIS to SPS energies*, Nucl.Phys. **A602**, 449 (1996), doi:10.1016/0375-9474(96)00097-8.

[243] CBM, S. Chattopadhyay *et al.*, *Challenges in QCD matter physics - The Compressed Baryonic Matter experiment at FAIR*, 1607.01487, arXiv:1607.01487.

[244] CBM, J. M. Heuser, *Status of the CBM experiment*, EPJ Web Conf. **95**, 01006 (2015), doi:10.1051/epjconf/20149501006,10.1051/epjconf/20159501006.

[245] HADES, G. Agakishiev *et al.*, *The High-Acceptance Dielectron Spectrometer HADES*, Eur. Phys. J. **A41**, 243 (2009), arXiv:0902.3478, doi:10.1140/epja/i2009-10807-5.

[246] CBM Collaboration, *Pre-Construction Memorandum of Understanding for the Execution of the Initial Phase of the Compressed BaryonicMatter (CBM) Experiment at FAIR – Annex 9*, (Mar. 2012).

[247] CBM collaboration, *CBM public documents*, http://www.fair-center.eu/en/for-users/experiments/cbm/documents.html .

[248] R. Turchetta *et al.*, *A monolithic active pixel sensor for charged particle tracking and imaging using standard VLSI CMOS technology*, Nucl. Instrum. Meth. **A458**, 677 (2001), doi:10.1016/S0168-9002(00)00893-7.

[249] V. Akishina, *4D Event Reconstruction in the CBM Experiment*, PhD thesis, Goethe University Frankfurt, 2017.

[250] M. Zyzak, *Online selection of short-lived particles on many-core computer architectures in the CBM experiment at FAIR*, PhD thesis, Goethe University Frankfurt, 2016.

[251] I. Kisel, *Event reconstruction in the CBM experiment*, Nucl. Instrum. Meth. **A566**, 85 (2006), doi:10.1016/j.nima.2006.05.040.

[252] F. Guber and I. Selyuzhenkov, editors, *Technical Design Report for the CBM Projectile Spectator Detector (PSD)* (GSI, Darmstadt, 2015), [link].

[253] A. Senger, *FLUKA calculations for PSD*, 21th CBM Collaboration Meeting (Apr. 2013).

[254] Janda, M. and others, *Status of PSD support platform development*, presentations at CBM Collaboration Meetings, martin.janda@(at)fs.cvut.cz.

[255] P. F. F. Silva Filho, *A multichannel digitizer for the PANDA experiment*, Master's thesis, DUniversitat Politècnica de València, 2014.

[256] N. Karpushkin, F. Guber and A. Ivashkin, *Application of the Prony least squares method for fitting signal waveforms measured by sampling ADC*, AIP Conf. Proc. **2163**, 030006 (2019), doi:10.1063/1.5130092.

[257] *CBM Data Acquisition (DAQ) webpage*, https://fair-center.eu/for-users/experiments/nuclear-matter-physics/cbm/projects/daq.html.

[258] CBM, D. Finogeev, F. Guber, N. Karpushkin, A. Makhnev, S. Morozov and D. Serebryakov, *The readout system of the CBM Projectile Spectator Detector at FAIR*, JINST **15**, C09015 (2020), doi:10.1088/1748-0221/15/09/C09015.

[259] Klochkov, I. Selyuzhenkov and C. collaboration, *Centrality determination in heavy-ion collisions with the CBM experiment*, Journal of Physics: Conference Series **798**, 012059 (2017).

[260] V. Klochkov, *Anisotropic flow measurements at FAIR and SPS energies*, PhD thesis, Goethe University Frankfurt, 2019.

[261] CBM, N. Karpushkin *et al.*, *The Projectile Spectator Detector for measuring the geometry of heavy ion collisions at the CBM experiment on FAIR*, Nucl. Instrum. Meth. A **936**, 156 (2019), doi:10.1016/j.nima.2018.10.054.

[262] R. Wigmans, *On the Energy Resolution of Uranium and Other Hadron Calorimeters*, Nucl.Instrum.Meth. **A259**, 389 (1987), doi:10.1016/0168-9002(87)90823-0.

[263] S. Uozumi *et al.*, *Performance of a compensating lead / plastic-scintillator tile / fiber calorimeter*, Nucl.Instrum.Meth. **A487**, 291 (2002), doi:10.1016/S0168-9002(01)00891-9.

[264] G. A. Alekseev *et al.*, *Study of the compensated lead hadron calorimeter on hadron, electron and lead-ion beams*, Nucl.Instrum.Meth. **A461**, 381 (2001), doi:10.1016/S0168-9002(00)01250-X.

[265] JLC Calorimeter Group, Y. Fujii, *Performance of compensated tile-fiber hadron calorimeter*, Nucl.Instrum.Meth. **A453**, 237 (2000), doi:10.1016/S0168-9002(00)00638-0.

[266] F. Guber, *Synergy in the development of Forward Hadron Calorimeters for NA61/SHINE, BM@N, MPD and CBM experiments*, https://indico.cern.ch/event/802303/sessions/318516/attachments/1931612/3199384/Guber_NICA_days_Oct_2019.pdf, 2019, presentation at NICA days.

[267] NA61 Collaboration, *NA61 Experiment web page*, https://na61.web.cern.ch/na61 .

[268] M. Golubeva *et al.*, *Forward hadron calorimeter for measurements of projectile spectators in heavy-ion experiment*, Phys.Atom.Nucl. **75**, 673 (2012), doi:10.1134/S1063778812060142.

[269] CBM Collaboration, *Memorandum of Understanding between the CBM Experiment at FAIR and NA61 Experiment at CERN*, (Dec. 2015).

[270] O. Svoboda *et al.*, *Neutron shielding for PSD readout with SiPM* (GSI, Darmstadt, 2017), Contribution to the CBM Progress Report 2016, [link].

[271] e. D. B. Pelowitz, *MCNPX (Monte Carlo N-Particle eXtended) User's Manual, Version 2.7.0*, Los Alamos National Laboratory report LA-CP-11-00438 (Apr. 2011).

[272] M. Golubevaber *et al.*, *Status of PSD construction and tests* (GSI, Darmstadt, 2017), Contribution to the CBM Progress Report 2016, [link].

[273] T. T. Böhlen *et al.*, *The FLUKA Code: Developments and Challenges for High Energy and Medical Applications*, Nuclear Data Sheets **120**, 211 (2014), doi:10.1016/j.nds.2014.07.049.

[274] A. Ivashkin, CBM PSD group of INR RAS, Moscow, Russia, private communication .

[275] A. Senger, *CBM Radiation simulations wikipage*, https://cbm-wiki.gsi.de/foswiki/bin/view/Radiationstudies .

[276] *mCBM at SIS18 - A CBM full system test-setup for high-rate nucleus-nucleus collisions at GSI/FAIR*, https://fair-center.eu/for-users/experiments/nuclear-matter-physics/cbm/projects/mcbm.html.

[277] *Uniplast*, Vladimir, Russia .

[278] A. Mefodiev and Y. Kudenko, *The design of the totally active scintillator detector*, Journal of Physics: Conference Series **653**, 012016 (2015), doi:10.1088/1742-6596/653/1/012016.

[279] *Description of optical cement EJ-500 produced by Eljen Technology*, https://eljentechnology.com/products/accessories/ej-500.

[280] R. Brun and F. Rademakers, *ROOT—an object oriented data analysis framework*, Nuclear Instruments and Methods in Physics Research Section A: Accelerators, Spectrometers, Detectors and Associated Equipment **389**, 81 (1997).

[281] J. Dixon *et al.*, *Evaluation of a Silicon Sr-90 Betavoltaic Power Source*, SCIENTIFIC REPORTS **6** (2016), doi:{10.1038/srep38182}.

[282] *The ESTAR program for calculattion of stopping power, range, and radiation yield tables for electrons in various materials.*, https://physics.nist.gov/PhysRefData/Star/Text/ESTAR.html.

[283] *The 9903KB photomultiplier with an enhanced green sensitive bialkali photocathode produced by ETEnterprises.*, https://et-enterprises.com/products/photomultipliers/product/p9903kb-series.

[284] *CAEN DT1470ET 4 Channel Reversible 8 kV/3 mA (8 W) Desktop HV Power Supply Module*, https://www.caen.it/products/dt1470et/.

[285] *Technical information on RS RTO1000 Digital Oscilloscope*, `https://www.rohde-schwarz.com/tr/product/rto1000-productstartpage_63493-191808.html`.

[286] *Laboratory of Cyclotron and Fast Neutron Generators at Center of Accelerators and Nuclear Analytical Methods*, `http://www.ujf.cas.cz/cs/vyzkum-a-vyvoj/velke-vyzkumne-infrastruktury-a-centra/canam/laboratories/Laboratory1/` (2019).

[287] M. Majerle, P. Bém, J. Novák, E. Šimečková and M. Štefánik, *Au, Bi, Co and Nb cross-section measured by quasimonoenergetic neutrons from p + 7Li reaction in the energy range of 18–36 MeV*, Nuclear Physics A **953**, 139 (2016), `doi:https://doi.org/10.1016/j.nuclphysa.2016.04.036`.

[288] M. Stefanik, P. Bem, M. Gotz, K. Katovsky, M. Majerle, J. Novak and E. Simeckova, *High-flux white neutron source based on p(35)-Be reactions for activation experiments at {NPI}*, Radiation Physics and Chemistry **104**, 306 (2014), 1st International Conference on Dosimetry and its Applications, `doi:https://doi.org/10.1016/j.radphyschem.2014.06.009`.

[289] *Neutron Beams at Center of Accelerators and Nuclear Analytical Methods*, `http://www.ujf.cas.cz/cs/vyzkum-a-vyvoj/velke-vyzkumne-infrastruktury-a-centra/canam/laboratories/Laboratory1/neutron-beams.html` (2019).

[290] *SAND-II-SNL: Neutron flux spectra determination by multiple foil activation-iterative method*, RSICC Shielding Routine Collection PSR-345, Oak Ridge (1996).

[291] *Radioactive Waste Repository Authority of the Czech Republic (SÚRAO)*, `http://www.surao.cz/` (2016).

[292] A. J. K. et al., *TALYS-1.0.*, Proceedings of the International Conference on Nuclear Data for Science and Technology - ND2007 , 211 (2007).

[293] O. Svoboda, J. Vrzalová, A. Krása, A. Kugler, M. Majerle and V. Wagner, *Cross-Section Measurements of (n, xn) Threshold Reactions in Au, Bi, I, In and Ta*, Journal of the Korean Physical Society **59** (2011), `doi:10.3938/jkps.59.1709`.

[294] P. Chudoba, *Study of reaction cross-sections important for advanced nuclear systems*, PhD thesis, Charles University in Prague, 2018.

[295] O. Svoboda, *Experimental Study of Neutron Production and Transport for ADTT*, PhD thesis, Czech Technical University in Prague, 2011.

[296] P. Chudoba and M. Fikrle, *Kalibrace detektoru Canberra GC3018 - CAN35*, Nuclear spectroscopy department of Nuclear physics institute of CAS (2015).

[297] S. Sudar, *'TrueCoinc' software utility for calculation of the true coincidence correction (IAEA-TECDOC–1275)*, International Atomic Energy Agency (IAEA) .

[298] *Genie 2000 Spectroscopy software manual*, Canberra (2000).

[299] F. J., *Program DEIMOS32 for Gamma-Ray Spectra Evaluation*, Journal of Radioanalytical and Nuclear Chemistry **3**, 583 (2003), doi:10.3938/jkps.59.1709.

[300] L. E. S.Y.F. Chu and R. Firestone, *WWW Table of Radioactive Isotopes*, The Lund/LBNL Nuclear Data Search (1999).

[301] *Experimental Nuclear Reaction Data (EXFOR)*, (2019).

[302] F. Křížek *et al.*, *Irradiation setup at the U-120M cyclotron facility*, Nuclear Instruments and Methods in Physics Research Section A: Accelerators, Spectrometers, Detectors and Associated Equipment **894**, 87 (2018), doi:https://doi.org/10.1016/j.nima.2018.03.066.

[303] *PTW Freiburg*, Germany .

[304] *Precision positioning system MCL*, LANG GmbH & CO KG, Hütteberg .

[305] X. Llopart, R. Ballabriga, M. Campbell, L. Tlustos and W. Wong, *Timepix, a 65k programmable pixel readout chip for arrival time, energy and/or photon counting measurements*, Nuclear Instruments and Methods in Physics Research Section A: Accelerators, Spectrometers, Detectors and Associated Equipment **581**, 485 (2007), VCI 2007, doi:https://doi.org/10.1016/j.nima.2007.08.079.

[306] *Zecotek MAPD White Paper*, http://zecotek.com/wp-content/uploads/2015/10/MAPD_White_Paper_v_19__26_Jan_12_.pdf.

[307] M. Golubeva *et al.*, *Hadron calorimeter (PSD) with new photo-detectors (MPPC) in NA61 experiment at CERN*, J. Phys. Conf. Ser. **798**, 012073 (2017), doi:10.1088/1742-6596/798/1/012073.

[308] Z. Sadygov *et al.*, *Performance of new Micro-pixel Avalanche Photodiodes from Zecotek Photonics*, Nuclear Instruments and Methods in Physics Research Section A: Accelerators, Spectrometers, Detectors and Associated Equipment **610**, 381 (2009), New Developments In Photodetection NDIP08, doi:https://doi.org/10.1016/j.nima.2009.05.123.

[309] Y. Musienko, *SiPM - status and prospects*, presentation at 2nd CHIPP Workshop on Detector RnD 2013.

[310] *Technical information on Hioki LCR Meters, Impedance Analyzers and Capacitance Meters*, https://www.hioki.com/en/products/list/?category=10.

[311] *Hioki manual. LCR Meters, Impedance Analyzers, Capacitance Meters How to Use*, https://www.hioki.com/.

[312] *Tektronix (Keithley) Model 6517A Electrometer User's Manual Rev. C*, https://www.tek.com/manual/model-6517a-electrometer-users-manual-rev-d-manual.

[313] *Technical information on NI PXI Controller PXI-8115*, https://www.ni.com/cs-cz/support/model.pxi-8115.html.

[314] S. Baccaro *et al.*, *Radiation damage effect on avalanche photodiodes*, Nucl. Instrum. Meth. A **426**, 206 (1999), doi:10.1016/S0168-9002(98)01493-4.

[315] Y. Musienko, S. Reucroft, D. Ruuska and J. Swain, *Studies of neutron irradiation of avalanche photodiodes using Cf-252*, Nucl. Instrum. Meth. A **447**, 437 (2000), doi:10.1016/S0168-9002(99)01019-0.

[316] A. F. U. Rychter and l'Universite de Strasbourg], *Measurement Based Characterisation and Modelling of Micropixel Avalanche Photodiodes*, PhD thesis, Warsaw University of Technology, 2016, https://cds.cern.ch/record/2265844.

[317] E. Garutti, R. Klanner, S. Laurien, P. Parygin, E. Popova, M. Ramilli and C. Xu, *Silicon Photomultiplier characterization and radiation damage investigation for high energy particle physics applications*, Journal of Instrumentation **9**, C03021 (2014).

[318] F. Guber *et al.*, *Transverse and longitudinal segmented forward hadron calorimeters with SiPMs light readout for future fixed target heavy ion experiments*, Nuclear Instruments and Methods in Physics Research Section A: Accelerators, Spectrometers, Detectors and Associated Equipment **958**, 162728 (2020), Proceedings of the Vienna Conference on Instrumentation 2019, doi:https://doi.org/10.1016/j.nima.2019.162728.

[319] NA61, N. Abgrall *et al.*, *NA61/SHINE facility at the CERN SPS: beams and detector system*, JINST **9**, P06005 (2014), arXiv:1401.4699, doi:10.1088/1748-0221/9/06/P06005.

[320] *Webpage of the East experimental area with T9 and T10 beamlines*, http://sba.web.cern.ch/sba/BeamsAndAreas/East/East.html.

[321] *Information about the T9 beam line and experimental facilities*, https://home.cern/sites/home.web.cern.ch/files/file/spotlight_students/information_about_the_t9_beam_line_and_experimental_facilities.pdf.

[322] *Technical information on CAEN DT5742 16 channel 12 bit 5 GS/s digitizer*, https://www.caen.it/products/dt5742/.

[323] *Website of HVSys company located in Dubna, Russia*, http://hvsys.ru/en/.

[324] *Technical information on WIENER Mpod 8 channel low voltage module*, http://www.wiener-d.com/sc/power-supplies/mpod--lvhv/mpod-lv-module.html.

[325] S. Piatek, *Webinar Silicon Photomultiplier Operation, Performance & Possible Applications organized by Hamamatsu company*, https://www.hamamatsu.com/sp/hc/osh/sipm_webinar_1.10.pdf.

[326] A. Ivashkin, *Temperature stabilization of PSD photodetectors*, https://indico.gsi.de/event/2184/, 2011, presentation at 23rd CBM collaboration meeting.

[327] E. Iancu, *QCD in heavy ion collisions*, in *Proceedings, 2011 European School of High-Energy Physics (ESHEP 2011): Cheile Gradistei, Romania, September 7-20, 2011*, pp. 197–266, 2014, arXiv:1205.0579, doi:10.5170/CERN-2014-003.197.

[328] H. Wang, *Study of particle ratio fluctuations and charge balance functions at RHIC*, PhD thesis, Michigan State U., 2012, 1304.2073, arXiv:1304.2073.

[329] A. Andronic *et al.*, *Hadron production in ultra-relativistic nuclear collisions: Quarkyonic matter and a triple point in the phase diagram of QCD*, Nuclear Physics A **837**, 65 (2010), doi:http://dx.doi.org/10.1016/j.nuclphysa.2010.02.005.

[330] N. van der Kolk, *To flow or not to flow: A study of elliptic flow and nonflow in proton-proton collisions in ALICE*, PhD thesis, Utrecht U., 2012.

[331] E895, C. Pinkenburg *et al.*, *Elliptic flow: Transition from out-of-plane to in-plane emission in Au + Au collisions*, Phys. Rev. Lett. **83**, 1295 (1999), arXiv:nucl-ex/9903010, doi:10.1103/PhysRevLett.83.1295.

[332] FOPI, W. Reisdorf *et al.*, *Systematics of azimuthal asymmetries in heavy ion collisions in the 1 A GeV regime*, Nucl. Phys. **A876**, 1 (2012), arXiv:1112.3180, doi:10.1016/j.nuclphysa.2011.12.006.

[333] KAOS, C. T. Sturm *et al.*, *Evidence for a soft nuclear equation of state from kaon production in heavy ion collisions*, Phys. Rev. Lett. **86**, 39 (2001), arXiv:nucl-ex/0011001, doi:10.1103/PhysRevLett.86.39.

[334] A. Toia, *Participants and spectators at the heavy-ion fireball*, http://cerncourier.com/cws/article/cern/53089 (2013).

[335] M. L. Miller, K. Reygers, S. J. Sanders and P. Steinberg, *Glauber Modeling in High-Energy Nuclear Collisions*, Annual Review of Nuclear and Particle Science **57**, 205 (2007), arXiv:http://dx.doi.org/10.1146/annurev.nucl.57.090506.123020, doi:10.1146/annurev.nucl.57.090506.123020.

[336] M. B. Golubeva *et al.*, *Nuclear-nuclear collision centrality determination by the spectators calorimeter for the MPD setup at the NICA facility*, Physics of Atomic Nuclei **76**, 1 (2013), doi:10.1134/S1063778812120046.

[337] H. Schlagheck, *Reaction Plane Event by Event*, http://www.uni-muenster.de/Physik.KP/santo/thesis/phd/schlagheck/node39.html (1998).

[338] J.-Y. Ollitrault, *Determination of the reaction plane in ultrarelativistic nuclear collisions*, Phys. Rev. **D48**, 1132 (1993), arXiv:hep-ph/9303247, doi:10.1103/PhysRevD.48.1132.

[339] W. Reisdorf and H. G. Ritter, *Collective flow in heavy-ion collisions*, Ann. Rev. Nucl. Part. Sci. **47**, 663 (1997), doi:10.1146/annurev.nucl.47.1.663.

[340] A. M. Poskanzer and S. Voloshin, *Methods for analyzing anisotropic flow in relativistic nuclear collisions*, Phys.Rev. **C58**, 1671 (1998), arXiv:nucl-ex/9805001, doi:10.1103/PhysRevC.58.1671.

[341] W. G. Lynch, *Collective Flow: nuclear equation of state*, https://people.nscl.msu.edu/ lynch/flow1.html (1997).

[342] A. Sadovsky, HADES analysis working group, sadovsky@inr.ru, private communication .

[343] E. Daw, *Lecture 7 - Rapidity and Pseudorapidity*, http://www.hep.shef.ac.uk/edaw/PHY206/Site/2012_course_files/phy206rlec7.pdf .

[344] STAR, B. I. Abelev *et al.*, *Azimuthal Charged-Particle Correlations and Possible Local Strong Parity Violation*, Phys. Rev. Lett. **103**, 251601 (2009), arXiv:0909.1739, doi:10.1103/PhysRevLett.103.251601.

[345] H. Schlagheck, *Collective Flow*, http://www.uni-muenster.de/Physik.KP/santo/thesis/phd/schlagheck/node10.html (1998).

[346] A. Tang, *ELLIPTIC FLOW IN AU + AU COLLISIONS AT $\sqrt{s_{\rm NN}}$ = 130 GEV*, PhD thesis, Kent State University, 2002.

[347] S. A. Voloshin, A. M. Poskanzer and R. Snellings, *Collective phenomena in non-central nuclear collisions*, 0809.2949, arXiv:0809.2949.

[348] S. A. Bass, *Strangeness production in microscopic transport models*, J. Phys. **G28**, 1543 (2002), arXiv:nucl-th/0112046, doi:10.1088/0954-3899/28/7/304.

[349] UrQMD Group, *The UrQMD Model webpage*, http://urqmd.org/ .

[350] V. Friese, CBM Computing working group, V.Friese@gsi.de, private communication .

[351] HSD Group, *The HSD Model webpage*, http://fias.uni-frankfurt.de/~brat/HSD/index1.html .

[352] E. Bratkovskaya, P/HSD code development group, Elena.Bratkovskaya@th.physik.uni-frankfurt.de, private communication .

[353] K. Gudima, Stepan G. Mashnik, and Arnold J. Sierk, *User Manual for the Code LAQGSM* , http://permalink.lanl.gov/object/tr?what=info:lanl-repo/lareport/LA-UR-01-6804 (2001).

[354] Nikolai Sobolevsky, *Shield: Multipurpose hadron transport code webpage*, http://www.inr.ru/shield/ .

[355] M. Golubeva, CBM Computing working group, marina@inr.ru, private communication .

[356] K. Gudima, LAQGSM code development group, gudima@theor.jinr.ru, private communication .

[357] B. Kardan, *Flow harmonics of Au+Au collisions at 1.23 AGeV with HADES*, Journal of Physics: Conference Series **742**, 012008 (2016).

[358] Y. Leifels, iQMD code development group, Y.Leifels@gsi.de, private communication .

[359] E895 Collaboration, H. Liu *et al.*, *Sideward flow in Au + Au collisions between 2-A-GeV and 8-A-GeV*, Phys.Rev.Lett. **84**, 5488 (2000), arXiv:nucl-ex/0005005, doi:10.1103/PhysRevLett.84.5488.

[360] E877, J. Barrette *et al.*, *Energy and charged particle flow in a 10.8-A/GeV/c Au + Au collisions*, Phys. Rev. **C55**, 1420 (1997), [Erratum: Phys. Rev.C56,2336(1997)], arXiv:nucl-ex/9610006, doi:10.1103/PhysRevC.55.1420,10.1103/PhysRevC.56.2336.

[361] STAR Collaboration, L. Adamczyk *et al.*, *Beam-Energy Dependence of Directed Flow of Protons, Antiprotons and Pions in Au+Au Collisions*, Phys.Rev.Lett. **112**, 162301 (2014), arXiv:1401.3043, doi:10.1103/PhysRevLett.112.162301(2014),10.1103/PhysRevLett.112.162301.

[362] CBM Collaboration, J. e. a. Heuser, *Technical Design Report for the CBM Silicon Tracking System (STS)*, http://repository.gsi.de/record/54798 **GSI-2013-05499** (2013).

[363] V. Mikhaylov, F. Guber, A. Ivashkin, A. Kugler, V. Kushpil, S. Morozov, O. Svoboda and P. Tlustý, *Characterisation of SiPM radiation hardness for application in hadron calorimeters at FAIR, CERN and NICA*, JINST **15**, C02005 (2020), arXiv:2001.10322, doi:10.1088/1748-0221/15/02/C02005.

[364] CBM, V. Mikhaylov *et al.*, *The very forward hadron calorimeter PSD for the future CBM@FAIR experiment*, EPJ Web Conf. **204**, 11004 (2019), doi:10.1051/epjconf/201920411004.

[365] V. Mikhaylov, F. Guber, A. Ivashkin, A. Kugler, V. Kushpil, S. Morozov, O. Svoboda and P. Tlustý, *Radiation hardness of Silicon Photomultipliers for CBM@FAIR, NA61@CERN and BM@N experiments*, Nucl. Instrum. Meth. A **912**, 241 (2018), doi:10.1016/j.nima.2017.11.066.

[366] V. Mikhaylov, A. Kugler, V. Kushpil, I. Selyuzhenkov and P. Tlusty, *Performance study of the anisotropic flow and reaction plane reconstruction in the CBM experiment*, J. Phys. Conf. Ser. **742**, 012023 (2016), doi:10.1088/1742-6596/742/1/012023.

[367] V. Mikhaylov *et al.*, *Performance of the forward calorimeters for heavy-ion experiments at FAIR, NICA, and CERN SPS*, PoS **EPS-HEP2015**, 281 (2015).

[368] V. Mikhaylov, A. Kugler, V. Kushpil, S. Kushpil, O. Svoboda, P. Tlusty and V. P. Ladygin, *Radiation hardness tests of Avalanche Photodiodes for FAIR, NICA, and CERN SPS experiments*, PoS **EPS-HEP2015**, 282 (2015).

[369] V. Mikhaylov, A. Kugler, V. Kushpil, P. Tlusty, S. Seddiki and I. Selyuzhenkov, *Particle flow and reaction plane reconstruction in the CBM experiment*, PoS **EPS-HEP2015**, 208 (2015).

[370] V. Mikhaylov, A. Kugler, V. Kushpil, S. Seddiki, I. Selyuzhenkov and P. Tlusty, *Anisotropic flow and the reaction plane reconstruction with the CBM experiment*, in *Proceedings, 18th Conference of Czech and Slovak Physicists, with participation of Hungarian and Polish Physical Societies: Olomouc, Czech Republic, September 16-19, 2014*, pp. 75–76, 2015.

[371] N. Karpushkin *et al.*, *The Projectile Spectator Detector for measuring the geometry of heavy ion collisions at the CBM experiment on FAIR*, Nuclear Instruments and Methods in Physics Research Section A: Accelerators, Spectrometers, Detectors and Associated Equipment **936**, 156 (2019), Frontier Detectors for Frontier Physics: 14th Pisa Meeting on Advanced Detectors, doi:https://doi.org/10.1016/j.nima.2018.10.054.

[372] V. Kushpil, V. Mikhaylov, V. P. Ladygin, A. Kugler, S. Reznikov, S. Kushpil, O. Svoboda and P. Tlusty, *Neutron irradiation study of silicon photomultipliers from different vendors*, Nucl. Instrum. Meth. **A845**, 114 (2017), doi:10.1016/j.nima.2016.06.101.

[373] V. Kushpil, V. Mikhaylov, A. Kugler, S. Kushpil, V. P. Ladygin, O. Svoboda and P. Tlusty, *Radiation hardness of semiconductor avalanche detectors for calorimeters in future HEP experiments*, J. Phys. Conf. Ser. **675**, 012039 (2016), doi:10.1088/1742-6596/675/1/012039.

[374] V. Kushpil, V. Mikhaylov, V. P. Ladygin, A. Kugler, S. Kushpil, O. Svoboda and P. Tlusty, *Investigation of avalanche photodiodes radiation hardness for baryonic matter studies*, Phys. Part. Nucl. Lett. **13**, 120 (2016), arXiv:1505.01297, doi:10.1134/S1547477116010143.

[375] V. Kushpil, V. Mikhaylov, S. Kushpil, P. Tlusty, O. Svoboda and A. Kugler, *Radiation hardness investigation of avalanche photodiodes for the Projectile Spectator Detector readout at the Compressed Baryonic Matter experiment*, Nucl. Instrum. Meth. **A787**, 117 (2015), doi:10.1016/j.nima.2014.11.071.

[376] S. Kushpil, V. Kushpil and V. Mikhaylov, *Setup for laboratory studies of the environmental conditions influence on the fixed charge state in silicon dioxide*, JINST **10**, C02045 (2015), doi:10.1088/1748-0221/10/02/C02045.

[377] CBM, P. Senger, *Astrophysics with heavy-ion beams*, Phys. Scripta **96**, 054002 (2021), arXiv:2102.08908, doi:10.1088/1402-4896/abebfe.

[378] CBM, V. Klochkov, *The Compressed Baryonic Matter Experiment at FAIR*, Nucl. Phys. A **1005**, 121945 (2021), doi:10.1016/j.nuclphysa.2020.121945.

[379] CBM, P. Senger, *Probing dense QCD matter in the laboratory—The CBM experiment at FAIR*, Phys. Scripta **95**, 074003 (2020), arXiv:2005.03321, doi:10.1088/1402-4896/ab8c14.

[380] HADES, J. Adamczewski-Musch *et al.*, *Two-pion production in the second resonance region in $\pi^- p$ collisions with the High-Acceptance Di-Electron Spectrometer (HADES)*, Phys. Rev. C **102**, 024001 (2020), arXiv:2004.08265, doi:10.1103/PhysRevC.102.024001.

[381] HADES, B. Ramstein *et al.*, *Time-Like Baryon Transitions studies with HADES*, EPJ Web Conf. **199**, 01008 (2019), doi:10.1051/epjconf/201919901008.

[382] HADES, J. Adamczewski-Musch *et al.*, *Strong absorption of hadrons with hidden and open strangeness in nuclear matter*, Phys. Rev. Lett. **123**, 022002 (2019), arXiv:1812.03728, doi:10.1103/PhysRevLett.123.022002.

[383] CBM, T. Ablyazimov *et al.*, *Challenges in QCD matter physics –The scientific programme of the Compressed Baryonic Matter experiment at FAIR*, Eur. Phys. J. **A53**, 60 (2017), arXiv:1607.01487, doi:10.1140/epja/i2017-12248-y.

List of publications

Publications as the main author

1. V. Mikhaylov, F. Guber, A. Ivashkin, A. Kugler, V. Kushpil, S. Morozov, O. Svoboda and P. Tlustý, *Characterisation of SiPM radiation hardness for application in hadron calorimeters at FAIR, CERN and NICA*, JINST **15**, C02005 (2020), arXiv:2001.10322, doi:10.1088/1748-0221/15/02/C02005

2. CBM, V. Mikhaylov *et al.*, *The very forward hadron calorimeter PSD for the future CBM@FAIR experiment*, EPJ Web Conf. **204**, 11004 (2019), doi:10.1051/epjconf/201920411004

3. V. Mikhaylov, F. Guber, A. Ivashkin, A. Kugler, V. Kushpil, S. Morozov, O. Svoboda and P. Tlustý, *Radiation hardness of Silicon Photomultipliers for CBM@FAIR, NA61@CERN and BM@N experiments*, Nucl. Instrum. Meth. A **912**, 241 (2018), doi:10.1016/j.nima.2017.11.066

4. V. Mikhaylov, A. Kugler, V. Kushpil, I. Selyuzhenkov and P. Tlusty, *Performance study of the anisotropic flow and reaction plane reconstruction in the CBM experiment*, J. Phys. Conf. Ser. **742**, 012023 (2016), doi:10.1088/1742-6596/742/1/012023

5. V. Mikhaylov *et al.*, *Performance of the forward calorimeters for heavy-ion experiments at FAIR, NICA, and CERN SPS*, PoS **EPS-HEP2015**, 281 (2015)

6. V. Mikhaylov, A. Kugler, V. Kushpil, S. Kushpil, O. Svoboda, P. Tlusty and V. P. Ladygin, *Radiation hardness tests of Avalanche Photodiodes for FAIR, NICA, and CERN SPS experiments*, PoS **EPS-HEP2015**, 282 (2015)

7. V. Mikhaylov, A. Kugler, V. Kushpil, P. Tlusty, S. Seddiki and I. Selyuzhenkov, *Particle flow and reaction plane reconstruction in the CBM experiment*, PoS **EPS-HEP2015**, 208 (2015)

8. V. Mikhaylov, A. Kugler, V. Kushpil, S. Seddiki, I. Selyuzhenkov and P. Tlusty, *Anisotropic flow and the reaction plane reconstruction with the CBM experiment*, in *Proceedings, 18th Conference of Czech and Slovak Physicists, with participation of Hungarian and Polish Physical Societies: Olomouc, Czech Republic, September 16-19, 2014*, pp. 75–76, 2015

Publications in co-authorship

1. F. Guber *et al.*, *Transverse and longitudinal segmented forward hadron calorimeters with SiPMs light readout for future fixed target heavy ion experiments*, Nuclear Instruments and Methods in Physics Research Section A: Accelerators, Spectrometers, Detectors and Associated Equipment **958**, 162728 (2020), Proceedings of the Vienna Conference on Instrumentation 2019, doi:https://doi.org/10.1016/j.nima.2019.162728

2. N. Karpushkin *et al.*, *The Projectile Spectator Detector for measuring the geometry of heavy ion collisions at the CBM experiment on FAIR*, Nuclear Instruments and Methods in Physics Research Section A: Accelerators, Spectrometers, Detectors and Associated Equipment **936**, 156 (2019), Frontier Detectors for Frontier Physics: 14th Pisa Meeting on Advanced Detectors, doi:https://doi.org/10.1016/j.nima.2018.10.054

3. V. Kushpil, V. Mikhaylov, V. P. Ladygin, A. Kugler, S. Reznikov, S. Kushpil, O. Svoboda and P. Tlusty, *Neutron irradiation study of silicon photomultipliers from different vendors*, Nucl. Instrum. Meth. **A845**, 114 (2017), doi:10.1016/j.nima.2016.06.101

4. V. Kushpil, V. Mikhaylov, A. Kugler, S. Kushpil, V. P. Ladygin, O. Svoboda and P. Tlusty, *Radiation hardness of semiconductor avalanche detectors for calorimeters in future HEP experiments*, J. Phys. Conf. Ser. **675**, 012039 (2016), doi:10.1088/1742-6596/675/1/012039

5. V. Kushpil, V. Mikhaylov, V. P. Ladygin, A. Kugler, S. Kushpil, O. Svoboda and P. Tlusty, *Investigation of avalanche photodiodes radiation hardness for baryonic matter studies*, Phys. Part. Nucl. Lett. **13**, 120 (2016), arXiv:1505.01297, doi:10.1134/S1547477116010143

6. V. Kushpil, V. Mikhaylov, S. Kushpil, P. Tlusty, O. Svoboda and A. Kugler, *Radiation hardness investigation of avalanche photodiodes for the Projectile Spectator Detector readout at the Compressed Baryonic Matter experiment*, Nucl. Instrum. Meth. **A787**, 117 (2015), doi:10.1016/j.nima.2014.11.071

7. S. Kushpil, V. Kushpil and V. Mikhaylov, *Setup for laboratory studies of the environmental conditions influence on the fixed charge state in silicon dioxide*, JINST **10**, C02045 (2015), doi:10.1088/1748-0221/10/02/C02045

Example publications as a member of CBM and HADES collaborations (about 60 total)

1. CBM, P. Senger, *Astrophysics with heavy-ion beams*, Phys. Scripta **96**, 054002 (2021), arXiv:2102.08908, doi:10.1088/1402-4896/abebfe

2. CBM, V. Klochkov, *The Compressed Baryonic Matter Experiment at FAIR*, Nucl. Phys. A **1005**, 121945 (2021), doi:10.1016/j.nuclphysa.2020.121945

3. CBM, P. Senger, *Probing dense QCD matter in the laboratory—The CBM experiment at FAIR*, Phys. Scripta **95**, 074003 (2020), arXiv:2005.03321, doi:10.1088/1402-4896/ab8c14

4. HADES, J. Adamczewski-Musch *et al.*, *Two-pion production in the second resonance region in $\pi^- p$ collisions with the High-Acceptance Di-Electron Spectrometer (HADES)*, Phys. Rev. C **102**, 024001 (2020), arXiv:2004.08265, doi:10.1103/PhysRevC.102.024001

5. HADES, B. Ramstein *et al.*, *Time-Like Baryon Transitions studies with HADES*, EPJ Web Conf. **199**, 01008 (2019), doi:10.1051/epjconf/201919901008

6. HADES, J. Adamczewski-Musch *et al.*, *Strong absorption of hadrons with hidden and open strangeness in nuclear matter*, Phys. Rev. Lett. **123**, 022002 (2019), arXiv:1812.03728, doi:10.1103/PhysRevLett.123.022002

7. CBM, T. Ablyazimov *et al.*, *Challenges in QCD matter physics –The scientific programme of the Compressed Baryonic Matter experiment at FAIR*, Eur. Phys. J. **A53**, 60 (2017), arXiv:1607.01487, doi:10.1140/epja/i2017-12248-y

Appendix A

Detailed distributions of dose and neutron fluence in PSD

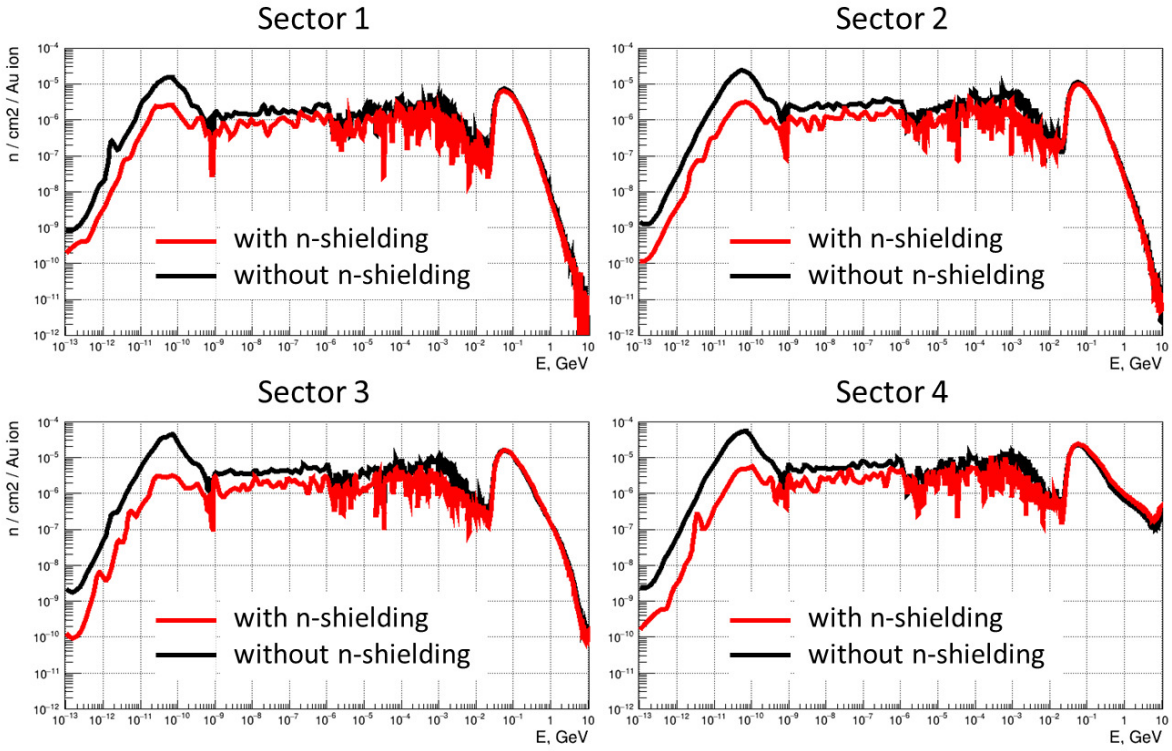

Figure A.1: Neutron spectrum in a plane where SiPMs are located in PSD for different radial sectors with and without shielding of 8 cm 3.5 borated polyethylene. Division into sectors is visualized in figure 6.3 (right). Neutron fluence is in range from 10−12 to 10^{-4} n/cm^2 per Au ion, neutron energy is in the range from 10^{-13} to 10 GeV. Simulations were done by A. Senger [275] for a typical calendar year of operation with the maximal beam settings, i.e. total 2 months of non-stop operation with 10 AGeV collision at 1 MHz collision rate.

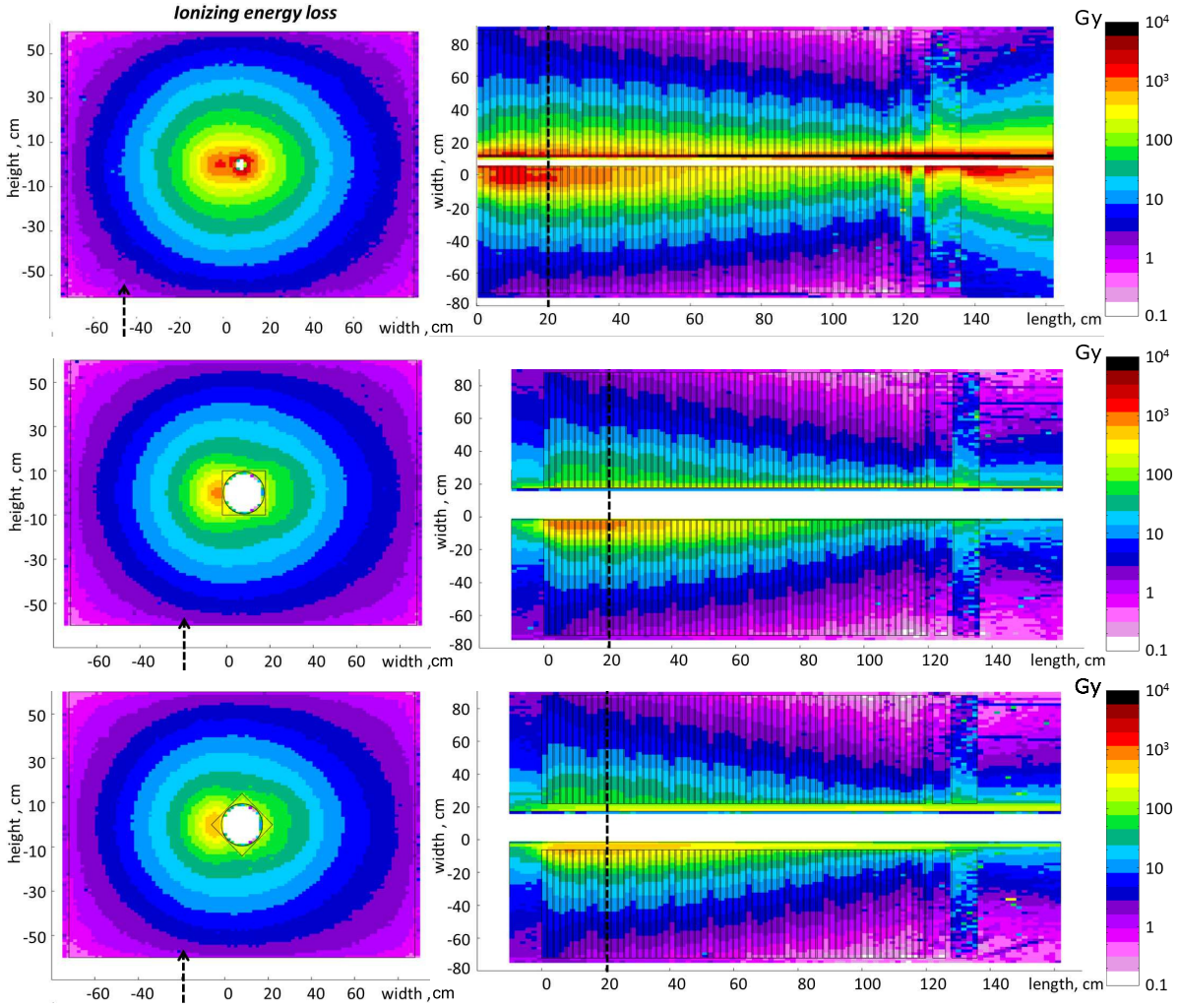

Figure A.2: Radial Y-X (left) and longitudinal-radial Z-X (right) distributions of the dose in the PSD module with different beam hole designs. Namely, beam hole of 3 cm radius (top), square-shaped (middle) and diamond-shaped geometry (bottom) of the 20 × 20 cm^2 beam hole. Radial distributions are showed for the layer 10 which is located 20 cm deep from the head of PSD as shown in figures. Dose ranges from 0.1 up to 10000 Gy. Simulations were done by A. Senger [275] for a typical calendar year of operation with the maximal beam settings, i.e. total 2 months of non-stop operation with 10 AGeV collision at 1 MHz collision rate. Note that data here correspond to older simulations with outdated CBM geometry, so results are somewhat different from data presented in figure 5.5.

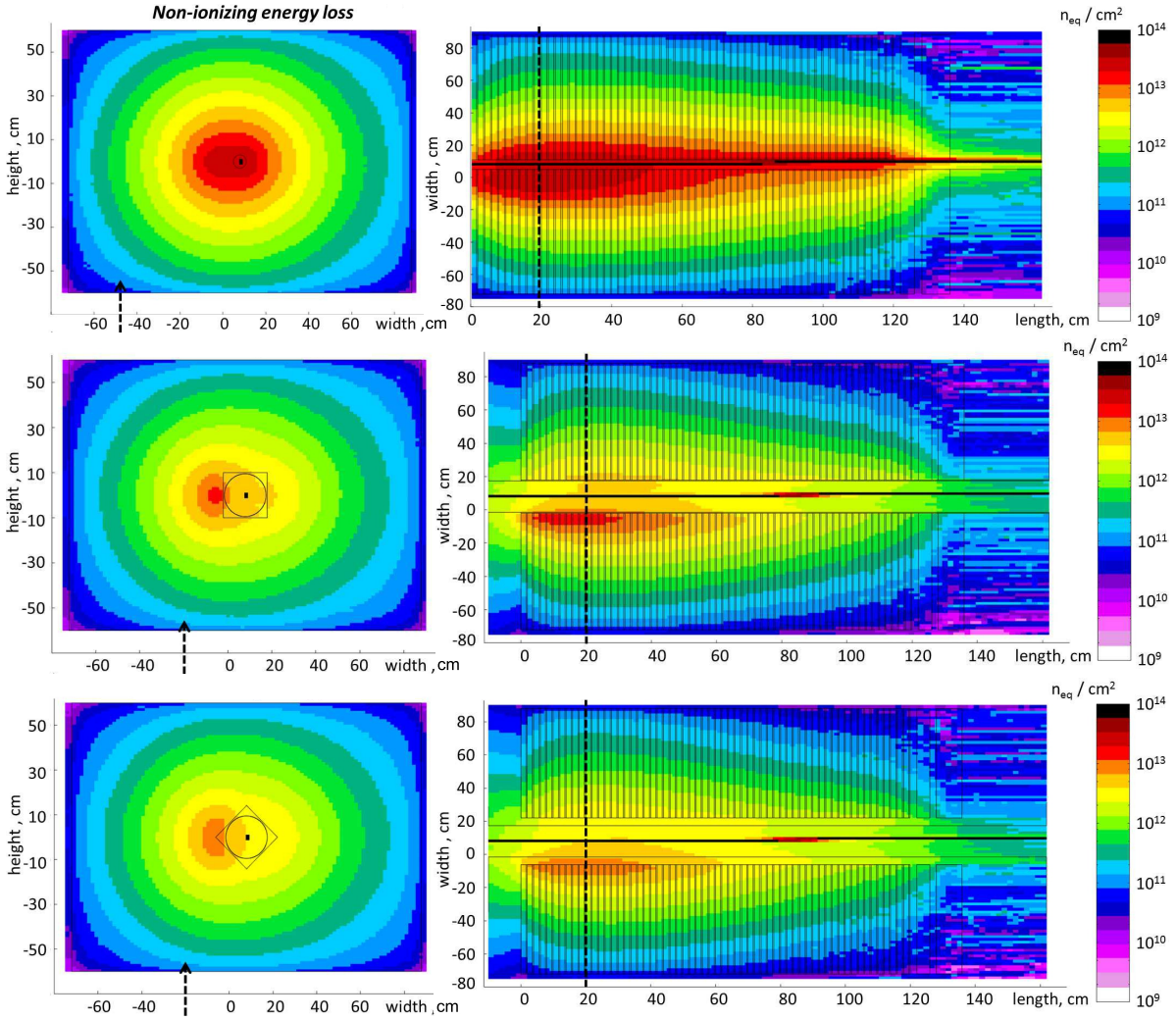

Figure A.3: Radial Y-X (left) and longitudinal-radial Z-X (right) distributions of the 1 MeV equivalent neutron fluence in the PSD module with different beam hole designs. Namely, beam hole of 3 cm radius (top), square-shaped (middle) and diamond-shaped geometry (bottom) of the 20 $\times$ 20 cm^2 beam hole. Radial distributions are showed for the layer 10 which is located 20 cm deep from the head of PSD as shown in figures. Dose ranges from 0.1 up to 10000 Gy. Simulations were done by A. Senger [275] for a typical calendar year of operation with the maximal beam settings, i.e. total 2 months of non-stop operation with 10 AGeV collision at 1 MHz collision rate. Note that data here correspond to older simulations with outdated CBM geometry, so results are somewhat different from data presented in figure 5.4.

Appendix B

Beam stability during irradiations

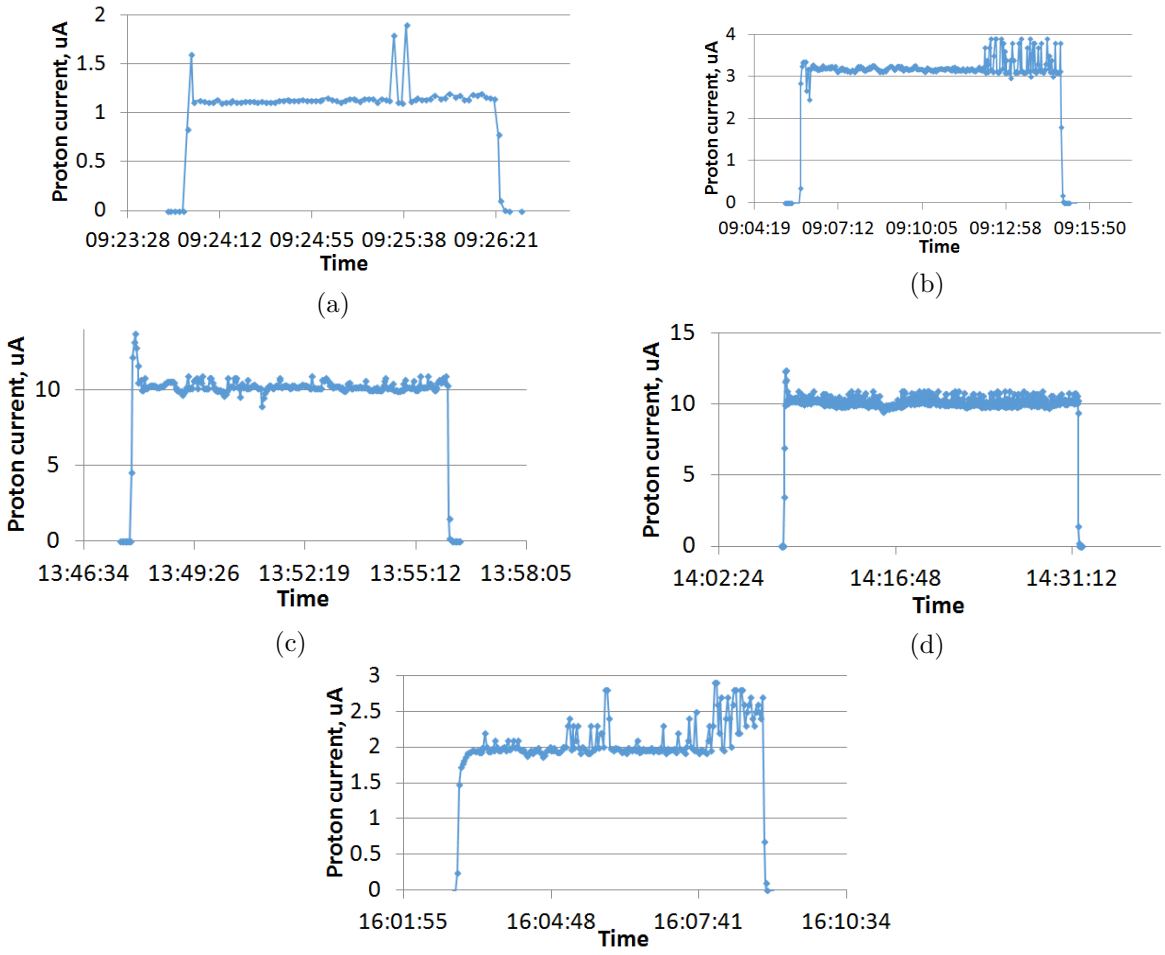

Figure B.1: Time series of beam currents for irradiation experiments with a white spectrum at 10.06.2016 for low (a) and high fluence (b), at 23.11.2016 for low (c) and high fluence (d), at 02.03.2018 (e).

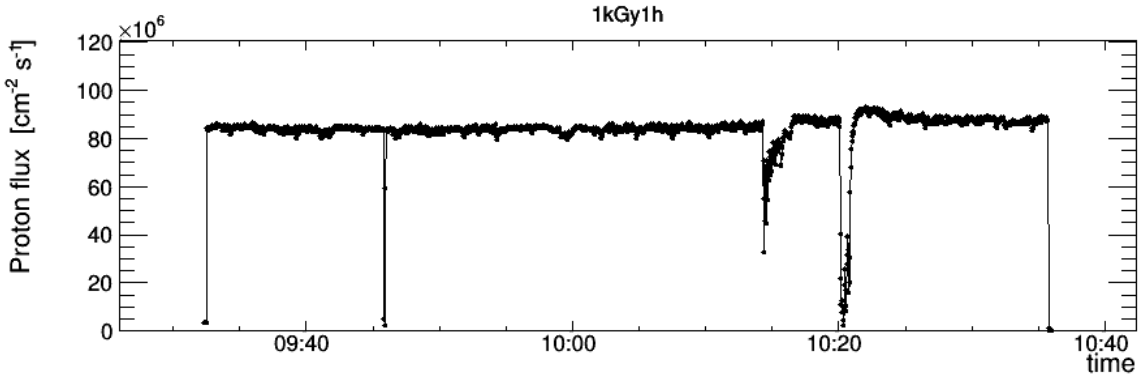

(a)

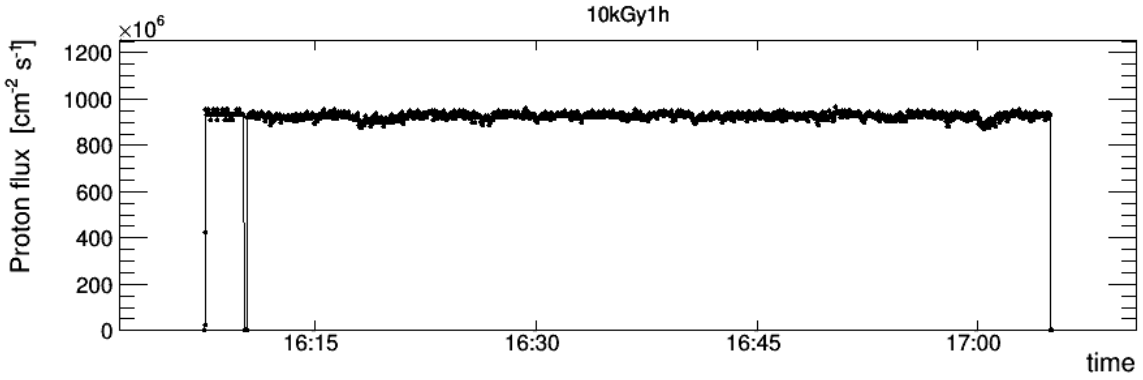

(b)

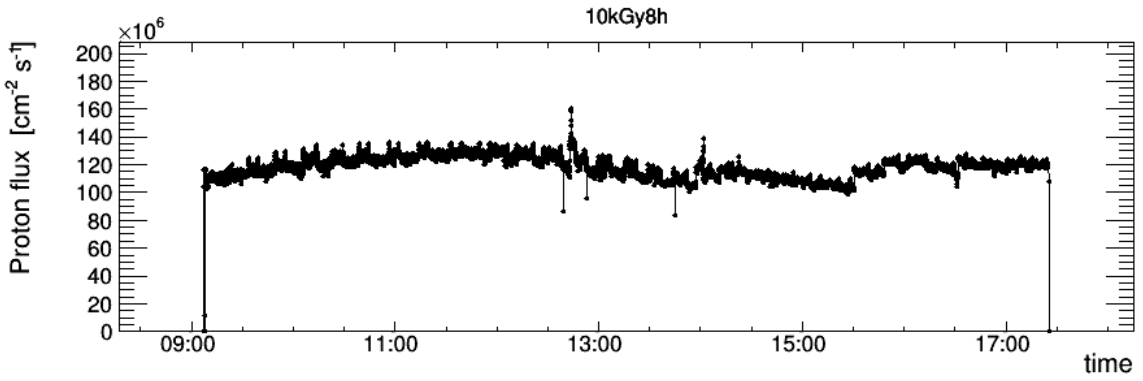

(c)

Figure B.2: Time series of proton fluxes for irradiation experiments at 27.03.2019 and 29.03.2019 for different total ionizing doses and irradiation times: 1 kGy in 1 hour (a), 10 kGy in 1 hour (b) and 10 kGy in 8 hours (c).

Appendix C

Details on chosen hardware and software components

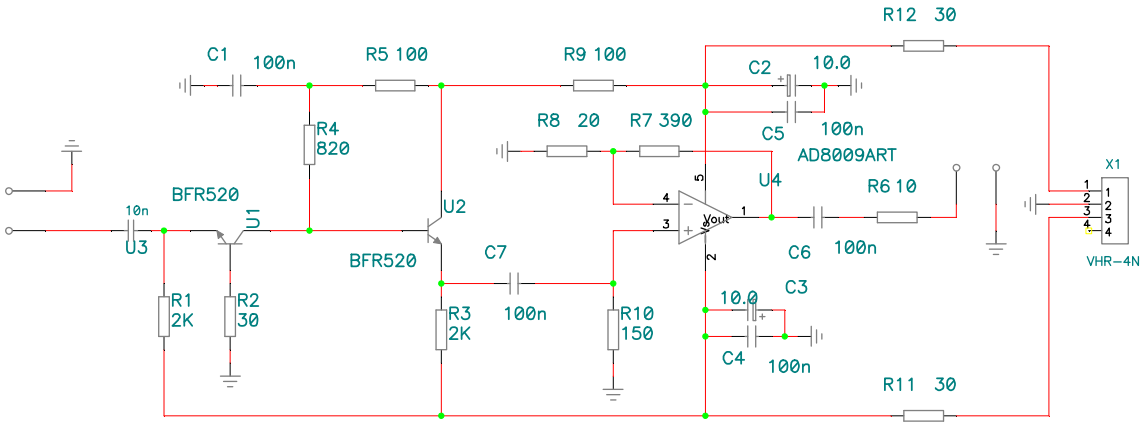

Figure C.1: Schematics of the transimpedance amplifier, which I used for SiPM signal response measurements. It was developed by the PSD team of Moscow Institute for Nuclear Research.

Listings of SendCommand and SyncWaitLoop functions utilized in Dharma – Software for (not-only) SiPM measurements, which I developed for the SiPM measurements, see section 7.3.

```
/*************************************************************/
// Send command to any device by USB-GPIB, NI-GPIB or COM-port
// For COM-ports (non-GPIB) use devnum < 0
/*************************************************************/

int SendCommand(int port, int devnum, char *command, int responsewait, int
    maxNOREDO, int bytestoread, char *response)
{
int nbytes, redo = 1, error = 1, errW=0, errR=0, devHandle = 0;
ViUInt32 returnCount = 0;
char errDescription[1024], conName[100]="", commandLF[1024]="";
char *errDescriptionN=NULL;
char status[300], buf[4096]="", *buf2;

```

```
14 sprintf(currentCommand,"%s",command);
15 currentDevnum=devnum;
16
17 if (GPIBMODE == 1)
18 {
19 if (devnum == K6517A)  devHandle = K6517AHandle;
20 else if (devnum == HIOKICV) devHandle = HIOKICVHandle;
21 else if (devnum == RS1024)  devHandle = RS1024Handle;
22 }
23 else devHandle = 1;
24
25 if ((popen == 0 && devHandle > 0 && devnum > 0) || (popenX == 0 && devnum < 0)
       || (port==comport2D && popen2D == 0 && devnum < 0))
26 {
27 while (redo > 0)
28 {
29 // send command
30 //if (SyncWaitLoop(-1) == -1) {error = -1; break;}
31 if (GPIBMODE == 0 && devnum > 0)
32 {
33 if (devnum != RS1024) USBGPIBClear(port, USBGPIB);   // clear USBGPIB interface
34 if (devnum == RS1024 && RS1024attention == 0) USBGPIBgetAttention (port, devnum)
       ;  // needed for RS1024 instead of clear USBGPIB interface
35 errW = USBGPIBsend (port, devnum, command);
36 if (errW < 0)
37 {
38 errDescriptionN = GetRS232ErrorString (errW);
39 printf("\nCommand [%s] was not sent to device [%d] with error:\n%s\n",command,
       devnum, errDescriptionN);
40 }
41 }
42 else if (GPIBMODE == 1 && devnum > 0)
43 {
44 sprintf(commandLF, "%s\n", command);
45 errW = viWrite(devHandle, (ViBuf)commandLF, (ViUInt32)strlen(commandLF), VI_NULL
       );
46 if (errW < 0)
47 {
48 viStatusDesc(devHandle, errW, errDescription);
49 printf("\nCommand [%s] was not sent to device [%d] with error:\n%s\n",command,
       devnum, errDescription);
50 }
51 }
52 else if (devnum < 0)
53 {
54 sprintf(commandLF, "%s\r\n", command);
55 errW = ComWrt (port, commandLF, strlen(commandLF));
56 if (errW < 0)
57 {
58 errDescriptionN = GetRS232ErrorString (errW);
59 printf("\nCommand [%s] was not sent to device [%d] with error:\n%s\n",command,
       devnum, errDescriptionN);
60 }
61 }
62
63 // get responce if reqested
64 if (responsewait == 1)
65 {
66 //if (SyncWaitLoop(-1) == -1) {error = -1; break;}
67 SyncWaitLoop(-1);
```

```
68 ClearBuff(buf,4096);
69 ClearBuff(response,bytestoread);
70
71 if (GPIBMODE == 0 && devnum > 0)
72 {
73 // 5 service bytes of USB-GPIB: (02) before message and (0A,10,03,06) after // (
       HEX format)
74 errR = USBGPIBenter (port, devnum, buf, bytestoread+5);
75 buf2 = &buf[1];
76 Scan (buf2,"%s>%s[t10]",response); // changed to t10
77 nbytes = NumFmtdBytes ();
78 if (errR < 0)
79 {
80 errDescriptionN = GetRS232ErrorString (errR);
81 printf("\nResponse to command [%s] was not received from device [%d] with error
       :\n%s\n",command, devnum, errDescriptionN);
82 }
83 }
84 else if (GPIBMODE == 1 && devnum > 0)
85 {
86 errR = viRead(devHandle, (ViBuf)buf, bytestoread+1, &returnCount);
87 Scan (buf,"%s>%s[t10]",response);
88 nbytes = NumFmtdBytes ();
89 //nbytes = returnCount;
90 if (errR < 0)
91 {
92 viStatusDesc(devHandle, errR, errDescription);
93 printf("\nResponse to command [%s] was not received from device [%d] with error
       :\n%s\n",command, devnum, errDescription);
94 }
95 }
96 else if (devnum < 0)
97 {
98 nbytes = ComRd (port, buf, bytestoread+2);
99 if (nbytes < 0) errR = nbytes;
100 Scan (buf,"%s>%s[t13]",response);
101 nbytes = NumFmtdBytes ();
102 if (errR < 0)
103 {
104 errDescriptionN = GetRS232ErrorString (errR);
105 printf("\nResponse to command [%s] was not received from device [%d] with error
       :\n%s\n",command, devnum, errDescriptionN);
106 }
107 }
108 response[nbytes] = 0; //terminate the string properly
109 if (debugging) printf(buf);
110
111 if (nbytes == bytestoread) redo = 0;
112 else
113 maxNOREDO--;
114 if (maxNOREDO < 0) redo = 0;
115 }
116 else redo = 0;
117
118 if (SyncWaitLoop(-1) == -1) {error = -1; return error;}
119 }
120 }
121 else
122 {
123 if (GPIBMODE == 0 || devnum < 0) sprintf (conName, "COM%i-port", port);
```

```
124 else sprintf (conName, "VisaRM or remote device");
125 sprintf (status, "Cannot send the command: %s is not opened", conName);
126 SetCtrlVal (pnlvar, PNL_STATUS, status);
127 error = 0;
128 }
129
130 if (errW < -1) error = errW;
131 if (errR < -1) error = errR;
132
133 return error;
134 }
```

```
1 /******* Synchronisation with SyncWait insead of delay  ****************/
2 // if time is 0, it just checks for events
3 int SyncWaitLoop(double waittime)
4 {
5 int ret = 0;
6 double interval = 0.01;
7
8 if (waittime == -1) // default sync wait time
9 {
10 GetCtrlVal (pnlvar, PNL_SYNCWAITTIME, &syncwaittime);
11 waittime = syncwaittime;
12 }
13 else if (waittime == -2) // time for user reading
14 {
15 GetCtrlVal (pnlvar, PNL_USERTIME, &usertime);
16 waittime = usertime;
17 }
18
19 if (waittime>=0 && waittime<0.1) interval = 0.01;
20 else if (waittime>=0.1 && waittime<1.0) interval = 0.1;
21 else if (waittime>=1.0) interval = waittime/10.;
22
23 while (waittime > 0)
24 {
25 ProcessSystemEvents();
26 SyncWait (Timer(), interval);
27 waittime -= interval;
28 }
29 if (waittime == 0.0) ProcessSystemEvents();
30
31 if (runflag == 0 && stophow == -1) ret = -1;
32
33 return ret;
34 }
```

Appendix D

SiPM dark current at reverse bias

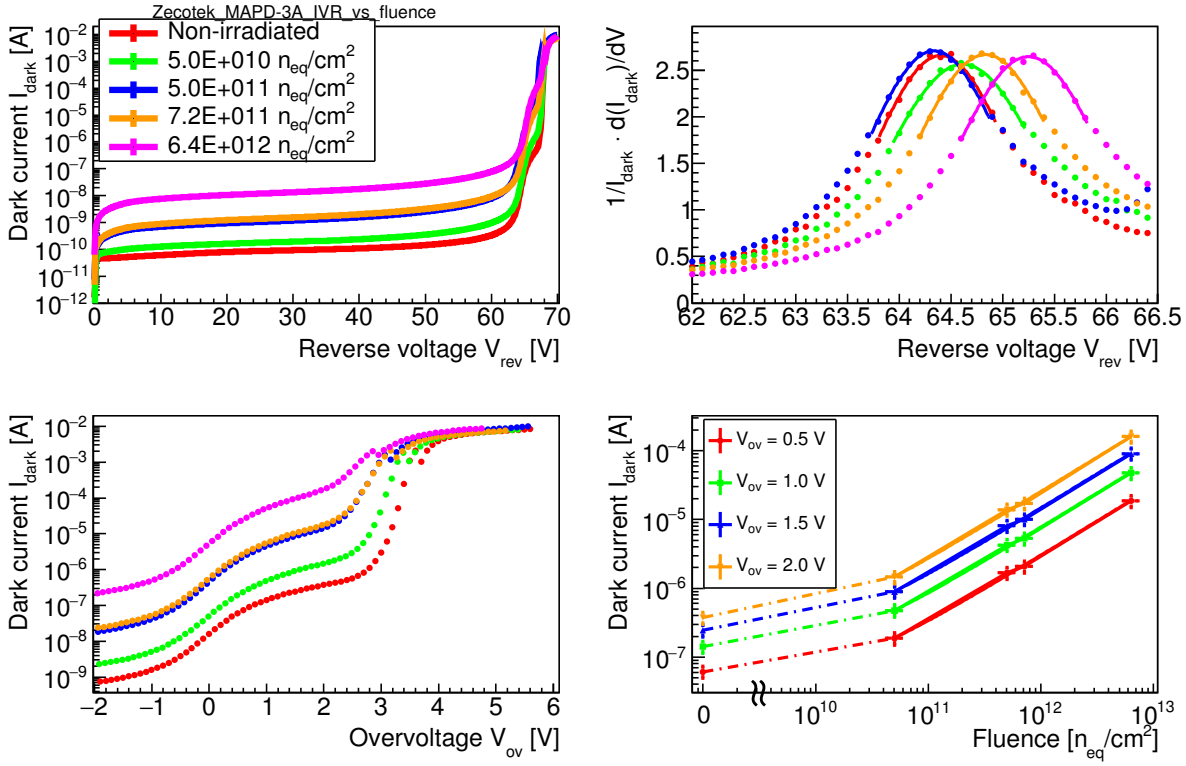

Figure D.1: Dark current and breakdown voltage determination for Zecotek MAPD-3A before and after irradiation. Detailed description can be found in section 7.5.

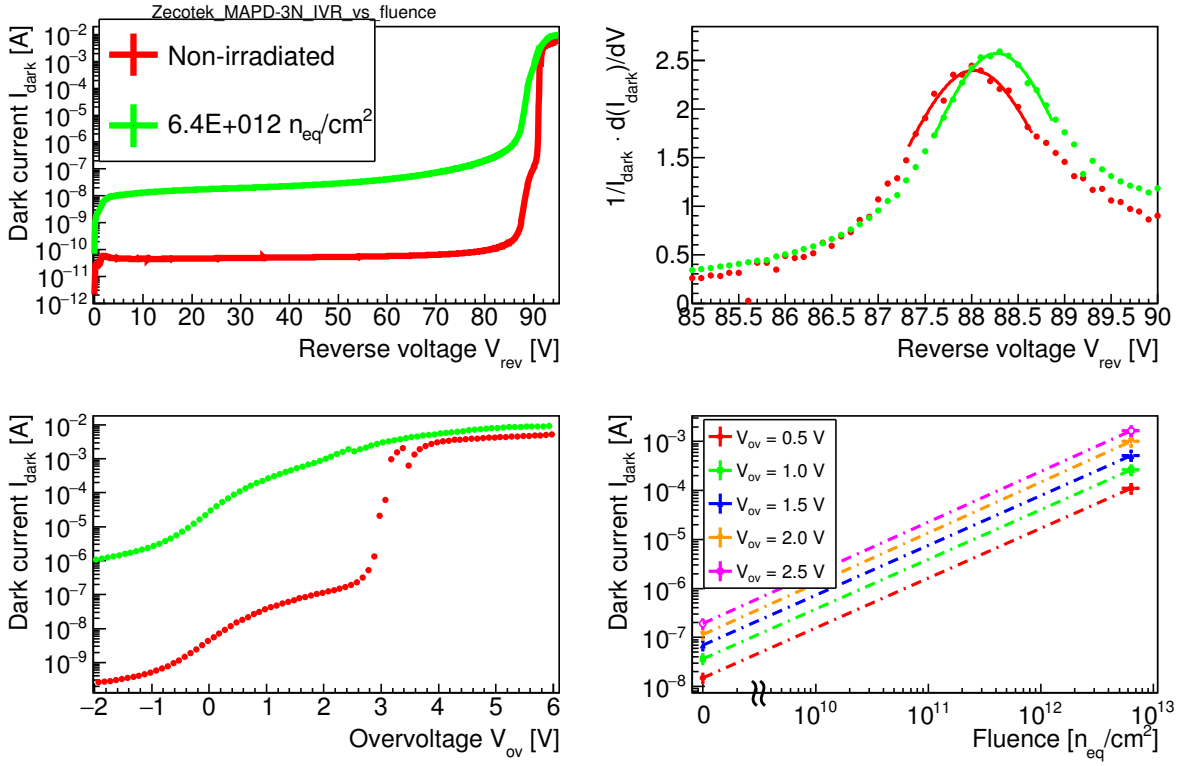

Figure D.2: Dark current and breakdown voltage determination for Zecotek MAPD-3N before and after irradiation. Detailed description can be found in section 7.5.

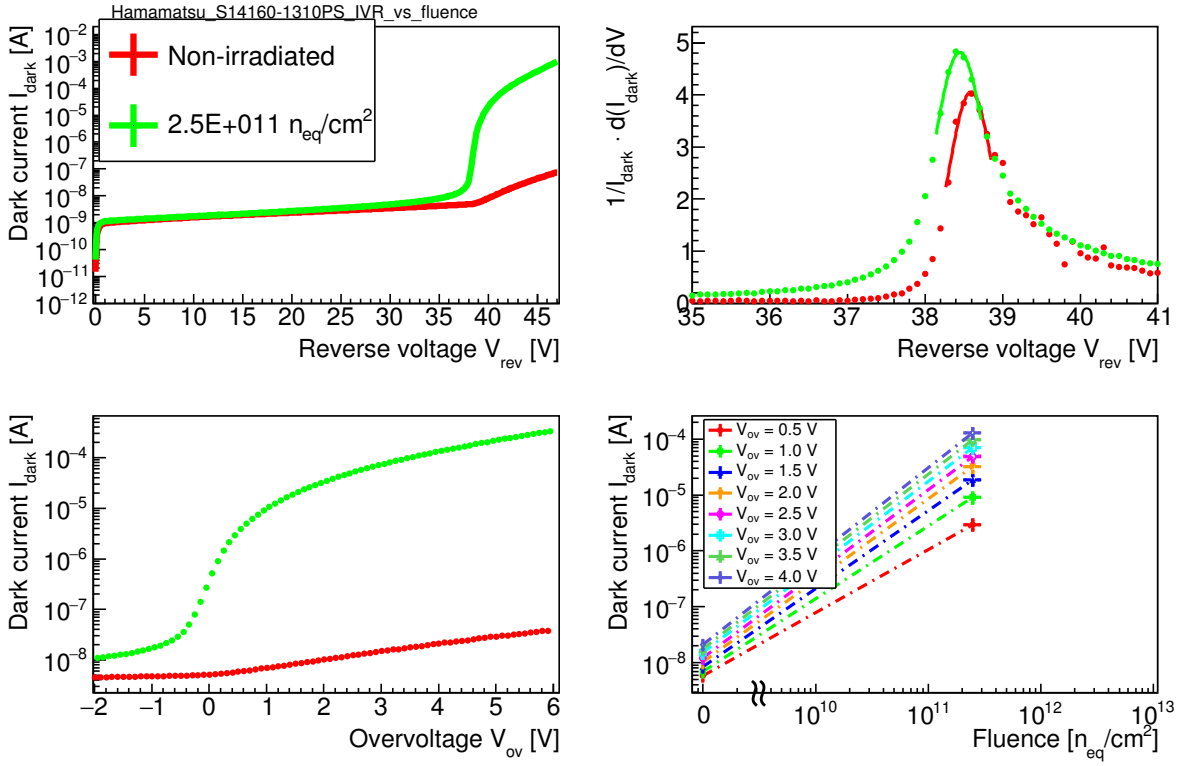

Figure D.3: Dark current and breakdown voltage determination for Hamamatsu MPPC S14160-1310PS before and after irradiation. Detailed description can be found in section 7.5.

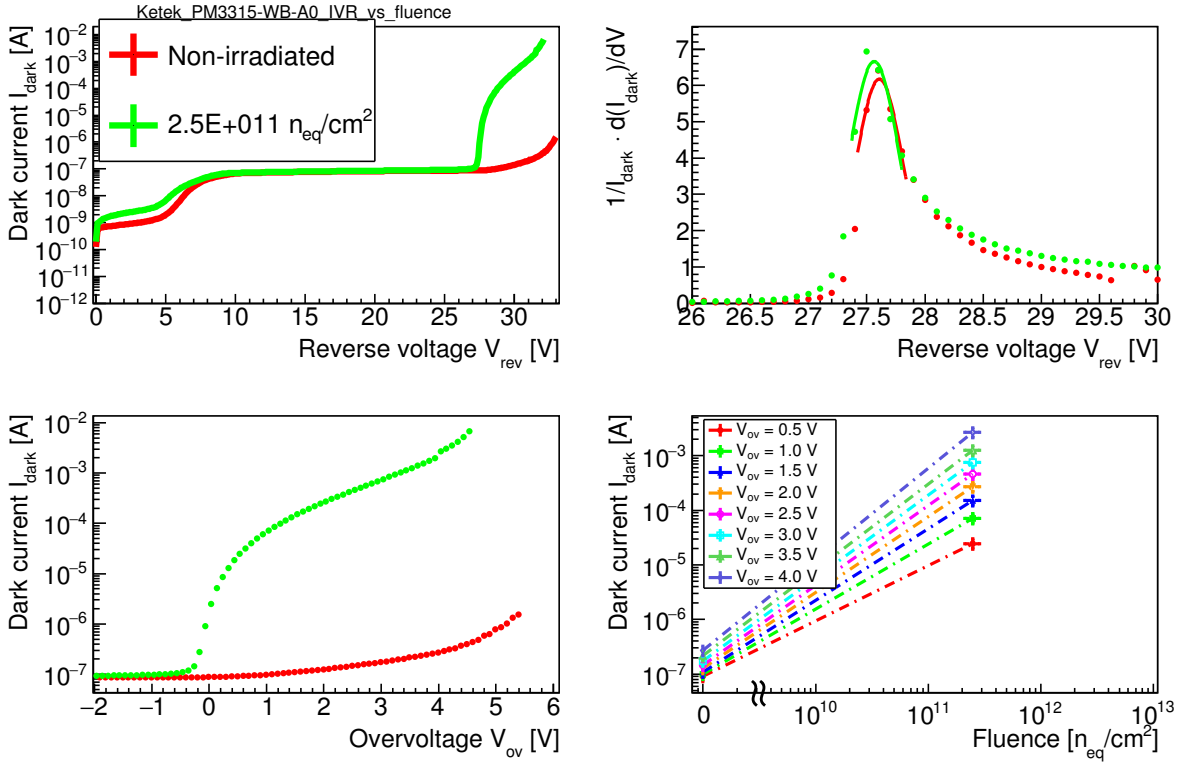

Figure D.4: Dark current and breakdown voltage determination for Ketek SiPM PM3315-WB-A0 before and after irradiation. Detailed description can be found in section 7.5.

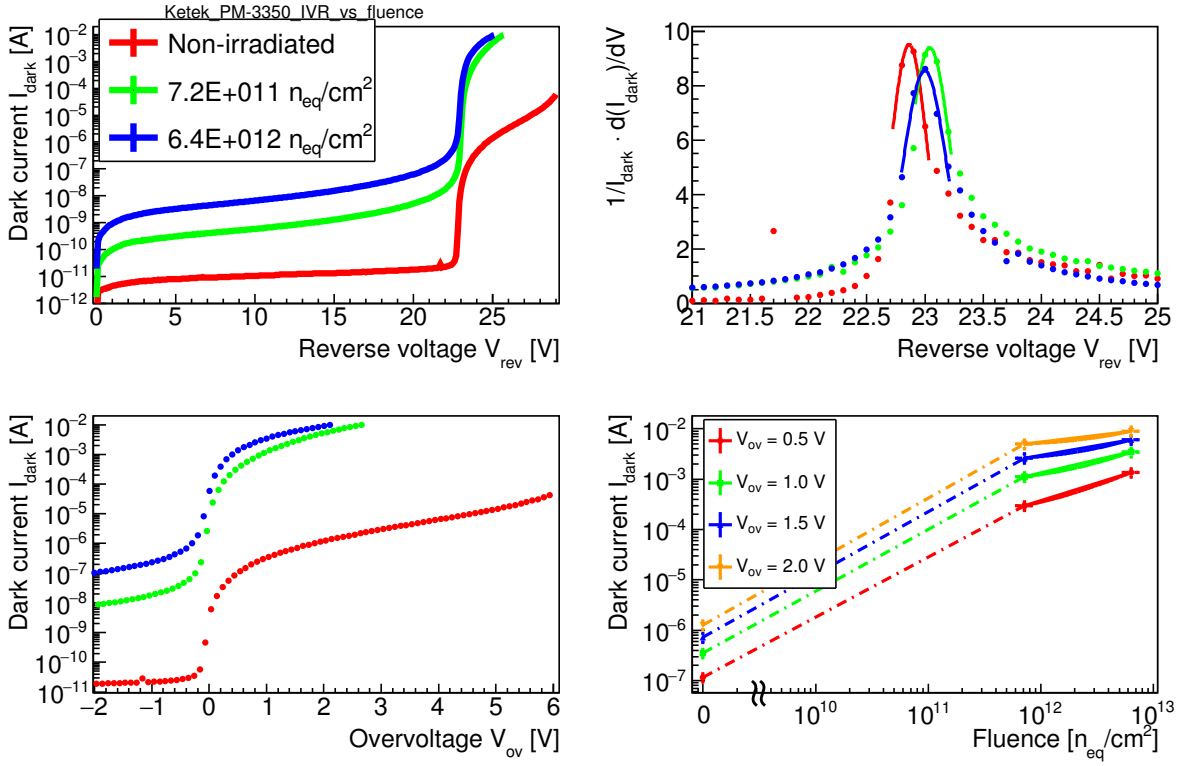

Figure D.5: Dark current and breakdown voltage determination for Ketek SiPM PM3350 before and after irradiation. Detailed description can be found in section 7.5.

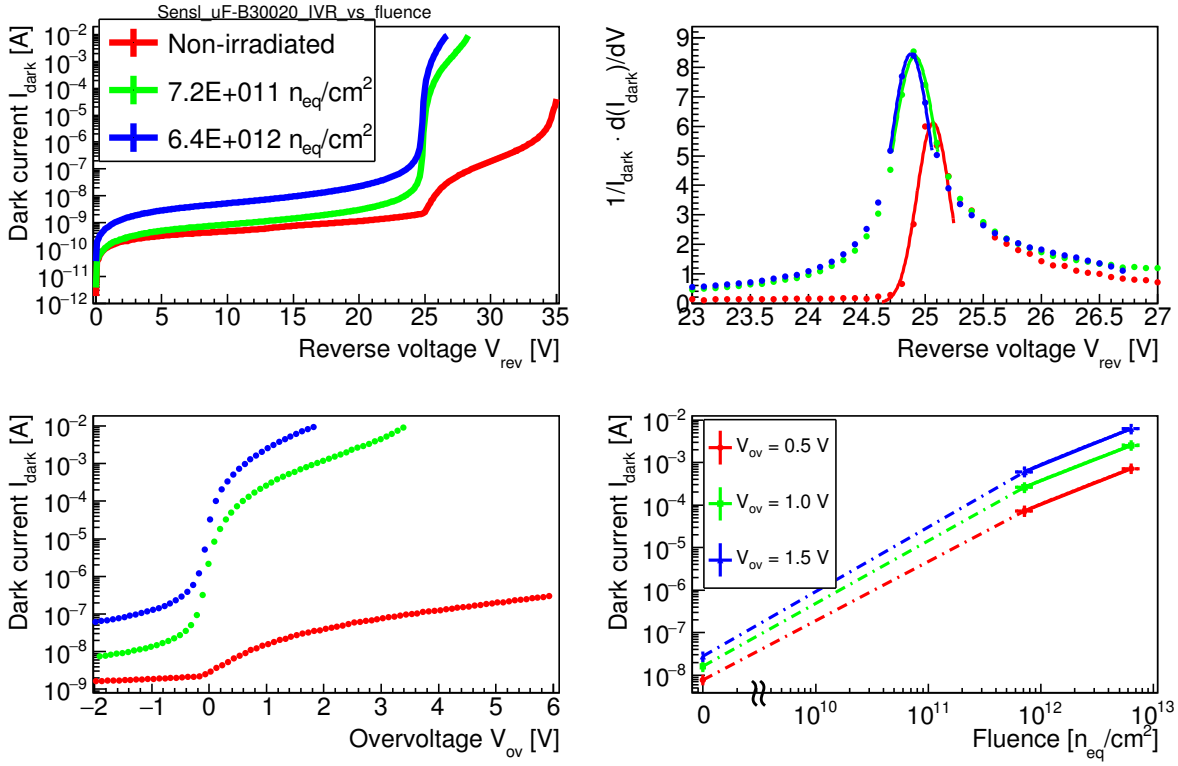

Figure D.6: Dark current and breakdown voltage determination for Sensl SiPM B-series 30020 before and after irradiation. Detailed description can be found in section 7.5.

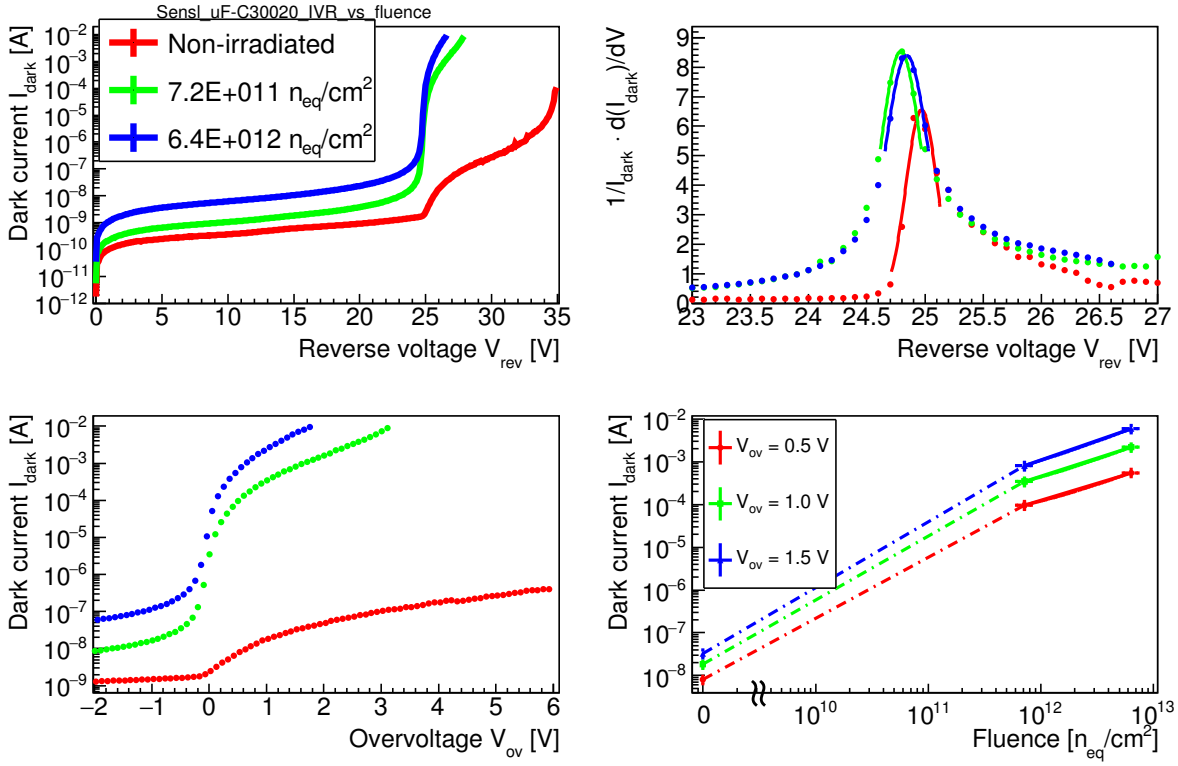

Figure D.7: Dark current and breakdown voltage determination for Sensl SiPM C-series 30020 before and after irradiation. Detailed description can be found in section 7.5.

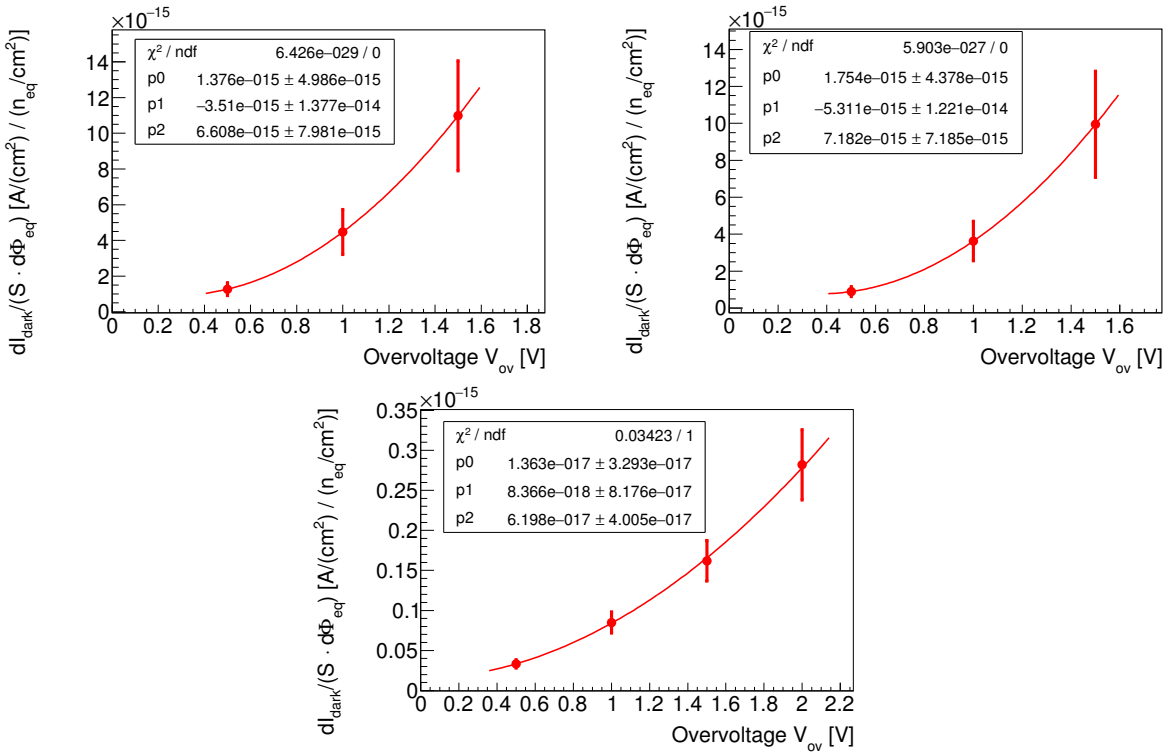

Figure D.8: $I_{dark}/S(\Phi_{eq})$ slope as function of overvoltage for Sensl B-series (top left), Sensl C-series (top right), and Zecotek MAPD-3A SiPMs. Detailed description can be found in section 7.5.2.

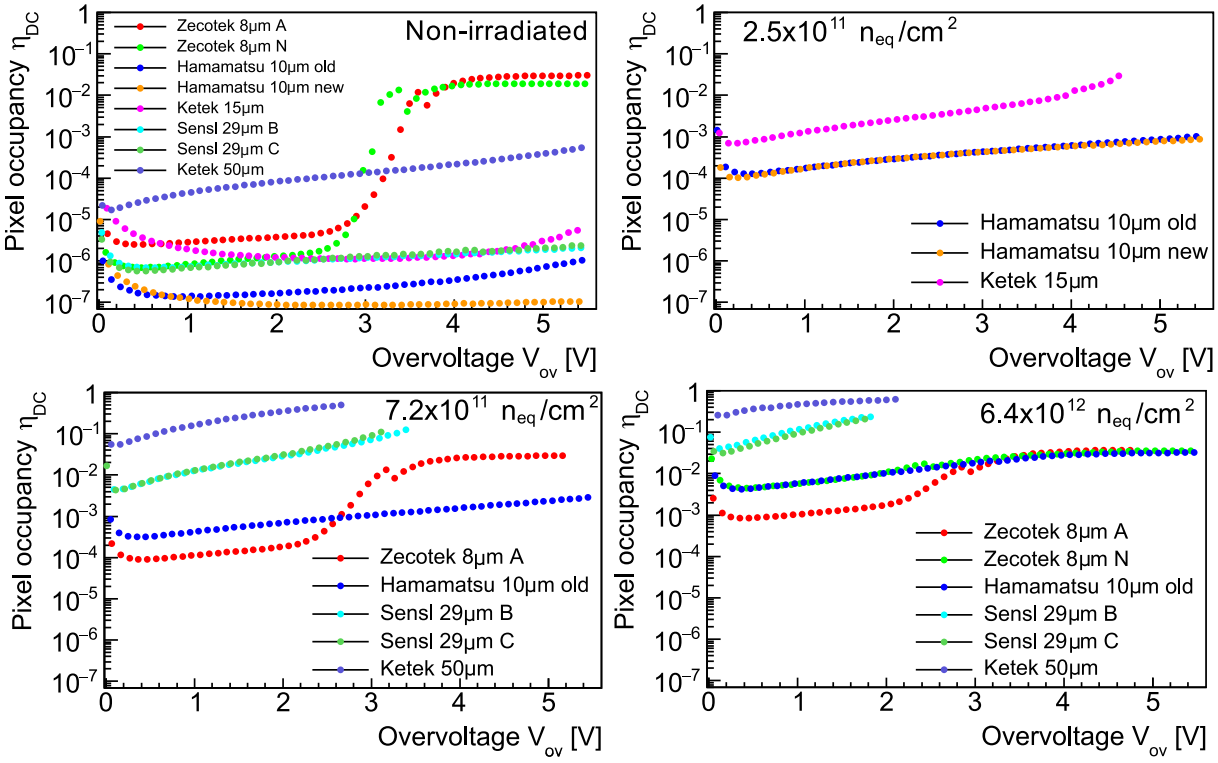

Figure D.9: Pixel occupancy as function of overvoltage for all the investigated SiPMs before (top left) and after irradiation with 2.5×10^{11} n_{eq}/cm^2 (top right), 7.2×10^{11} n_{eq}/cm^2 and 6.4×10^{12} n_{eq}/cm^2 (bottom right). Detailed description of the occupancy estimation from the dark current can be found in section 7.9.2.

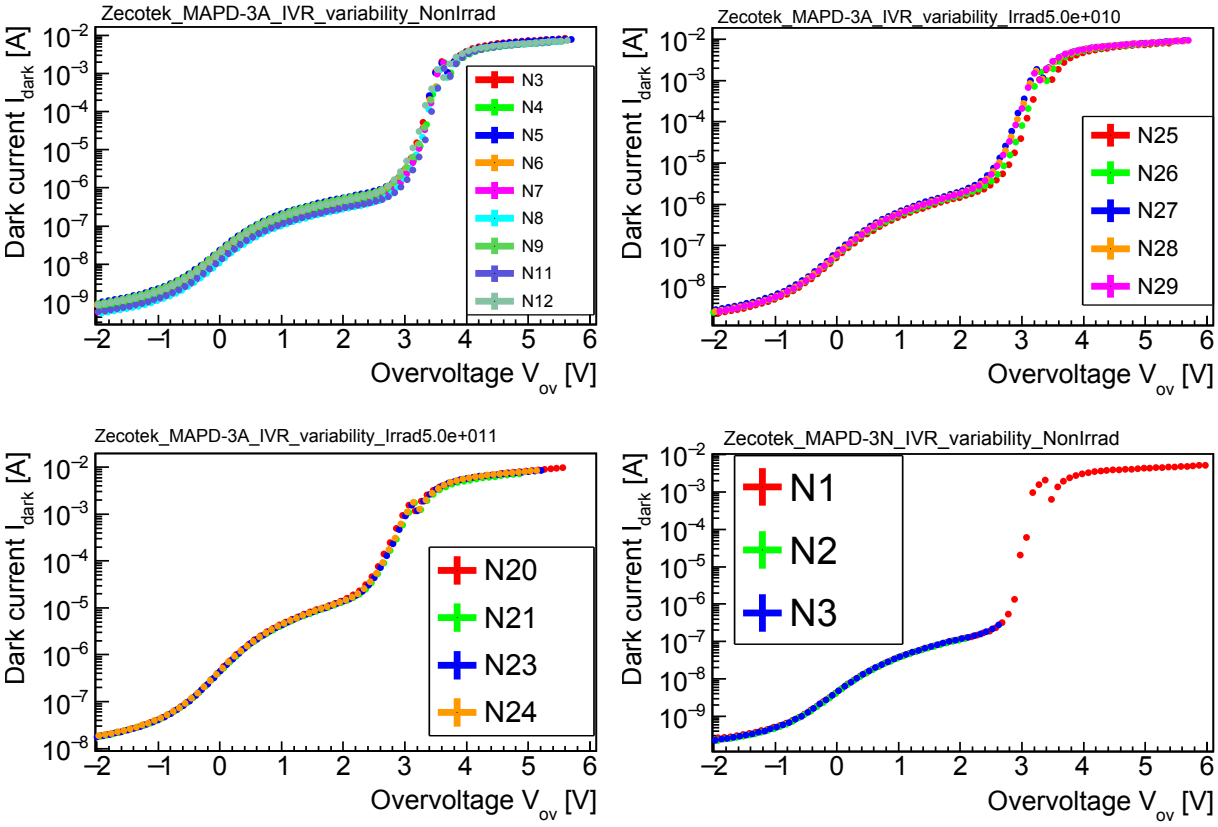

Figure D.10: Dark current sample-to-sample variability for Zecotek MAPDs before and after irradiation, see captions above the plots. Detailed description can be found in section 7.5.

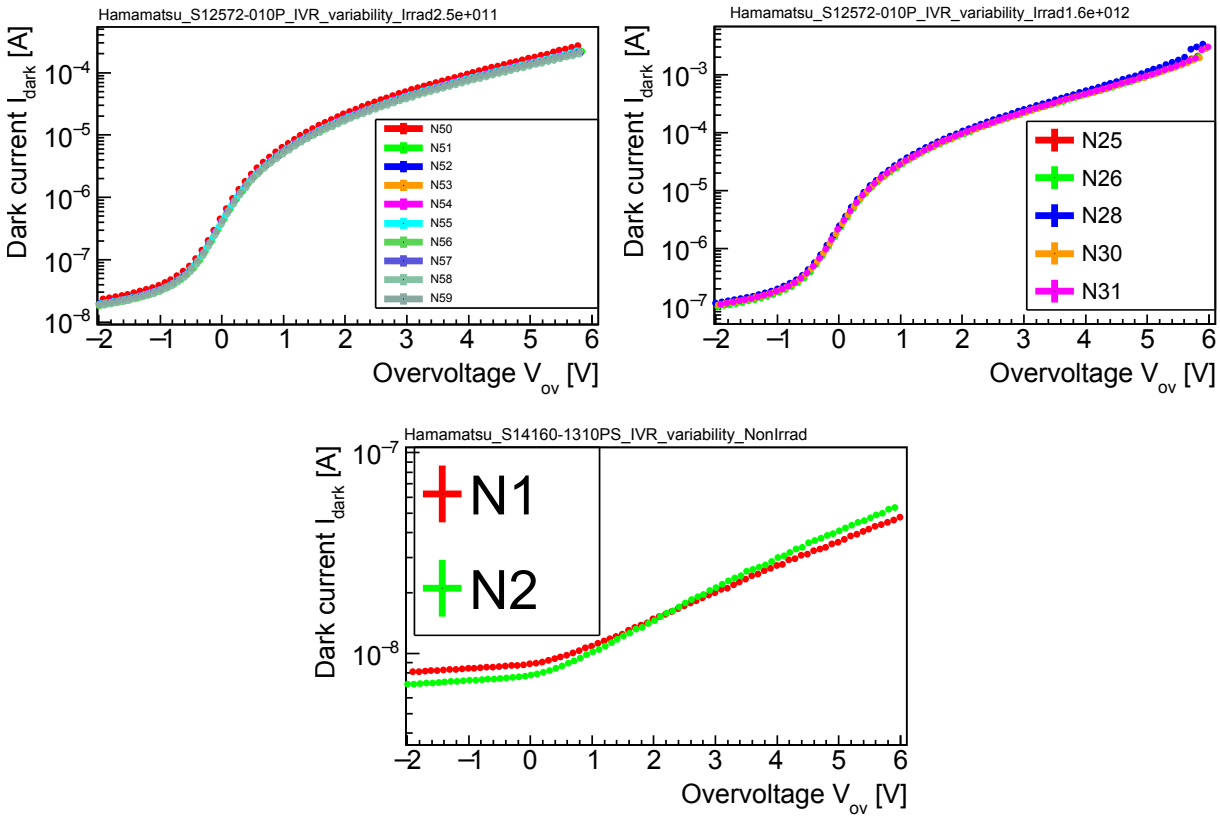

Figure D.11: Dark current sample-to-sample variability for Hamamatsu MPPCs before and after irradiation, see captions above the plots. Detailed description can be found in section 7.5.

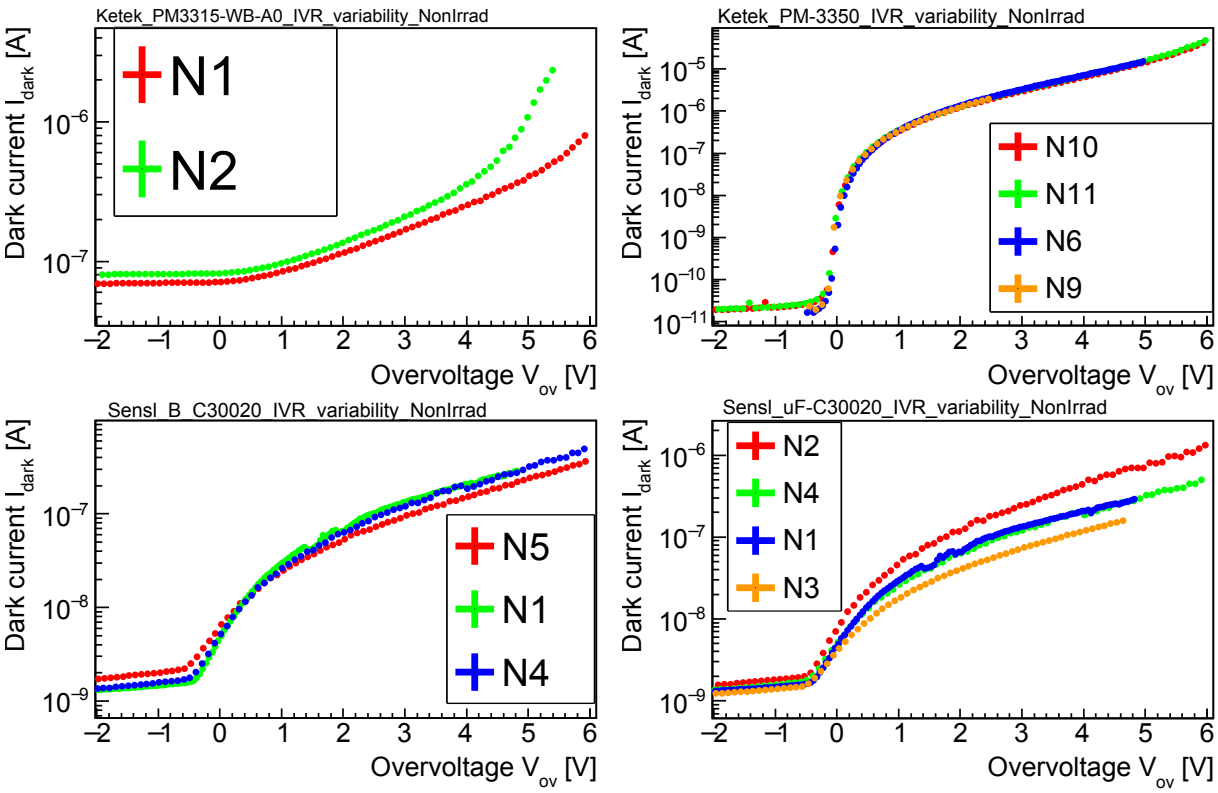

Figure D.12: Dark current sample-to-sample variability for Ketek and Sensl SiPMs before irradiation, see captions above the plots. Detailed description can be found in section 7.5.

Appendix E

SiPM dark current at forward bias

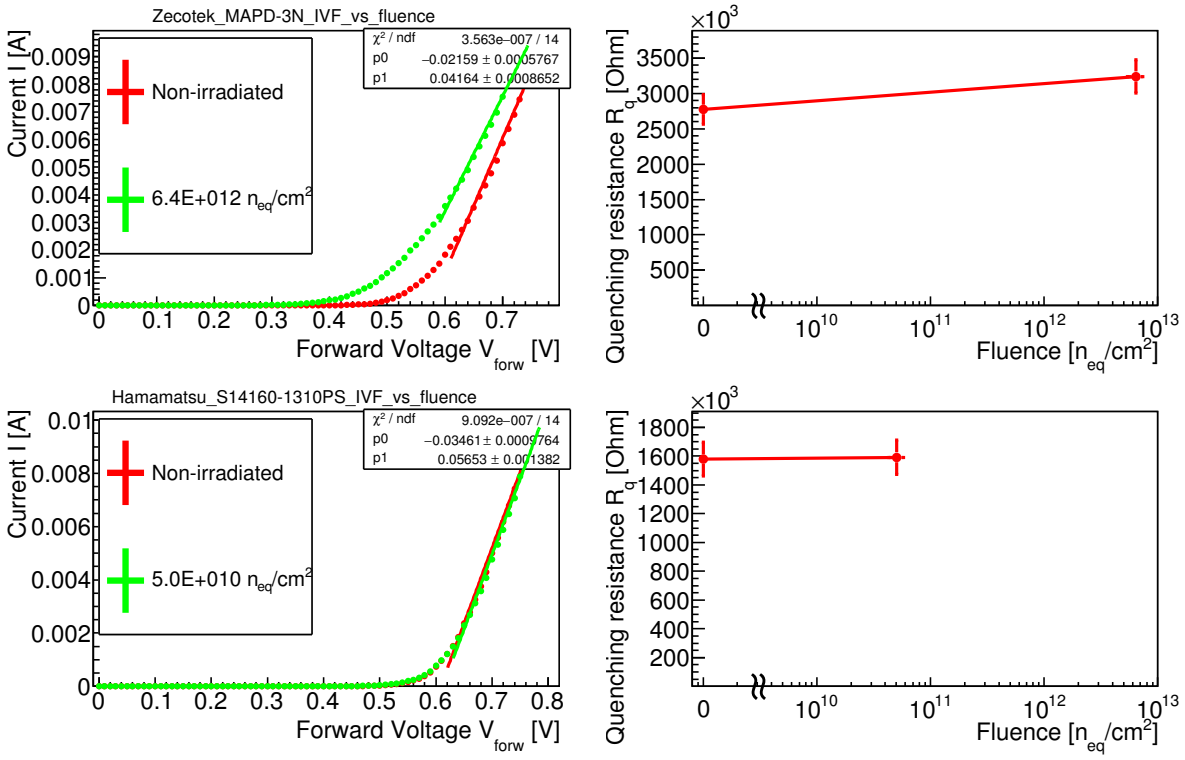

Figure E.1: Dark current at forward bias and quenching resistance determination for Zecotek MAPD-3N (top) and Hamamatsu MPPC S14160-1310PS (bottom) before and after irradiation. Detailed description can be found in section 7.6.

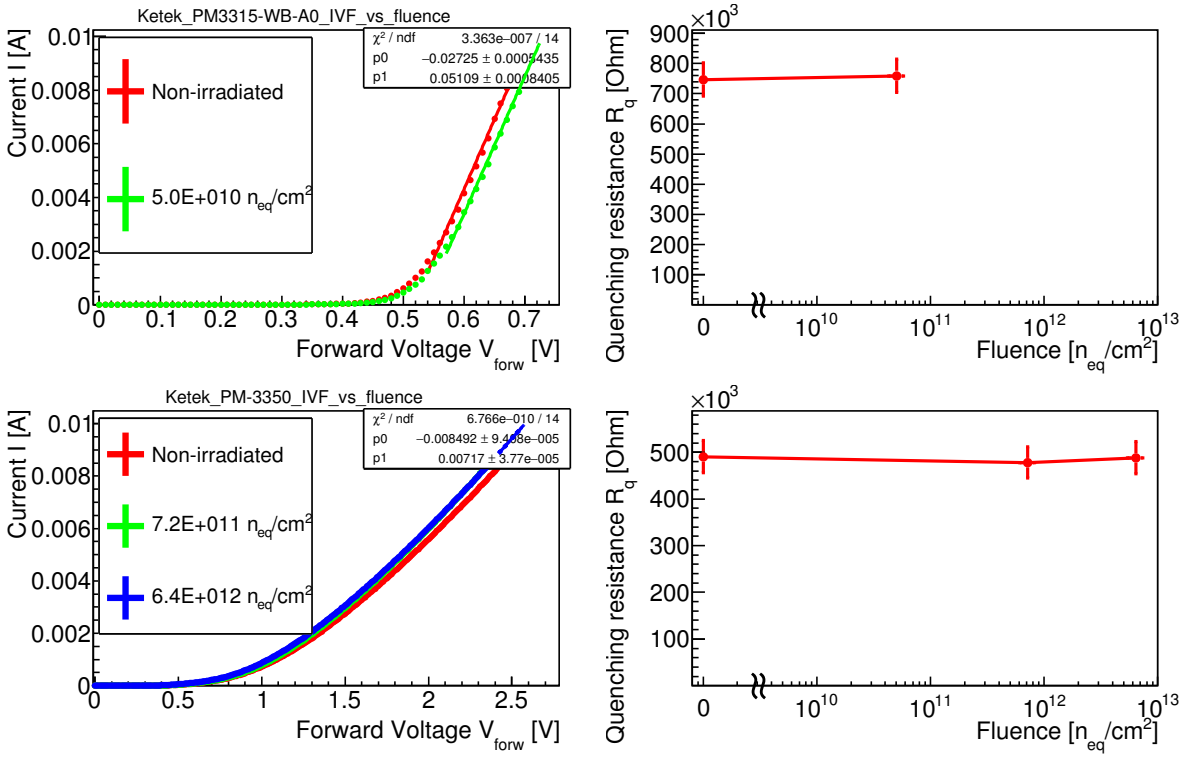

Figure E.2: Dark current at forward bias and quenching resistance determination for Ketek PM3315-WB-A0 (top) and Ketek PM-3350 (bottom) SiPMs before and after irradiation. Detailed description can be found in section 7.6.

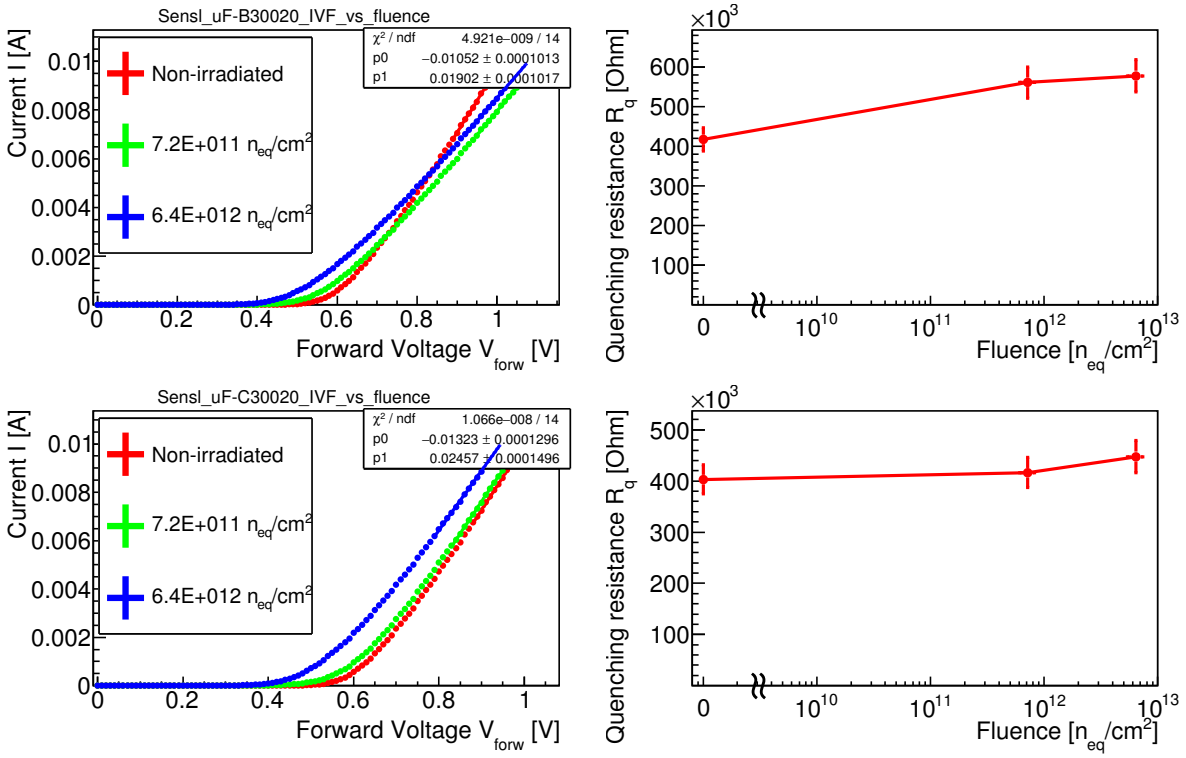

Figure E.3: Dark current at forward bias and quenching resistance determination for Sensl B-series 30020 (top) and Sensl C-series 30020 (bottom) SiPMs before and after irradiation. Detailed description can be found in section 7.6.

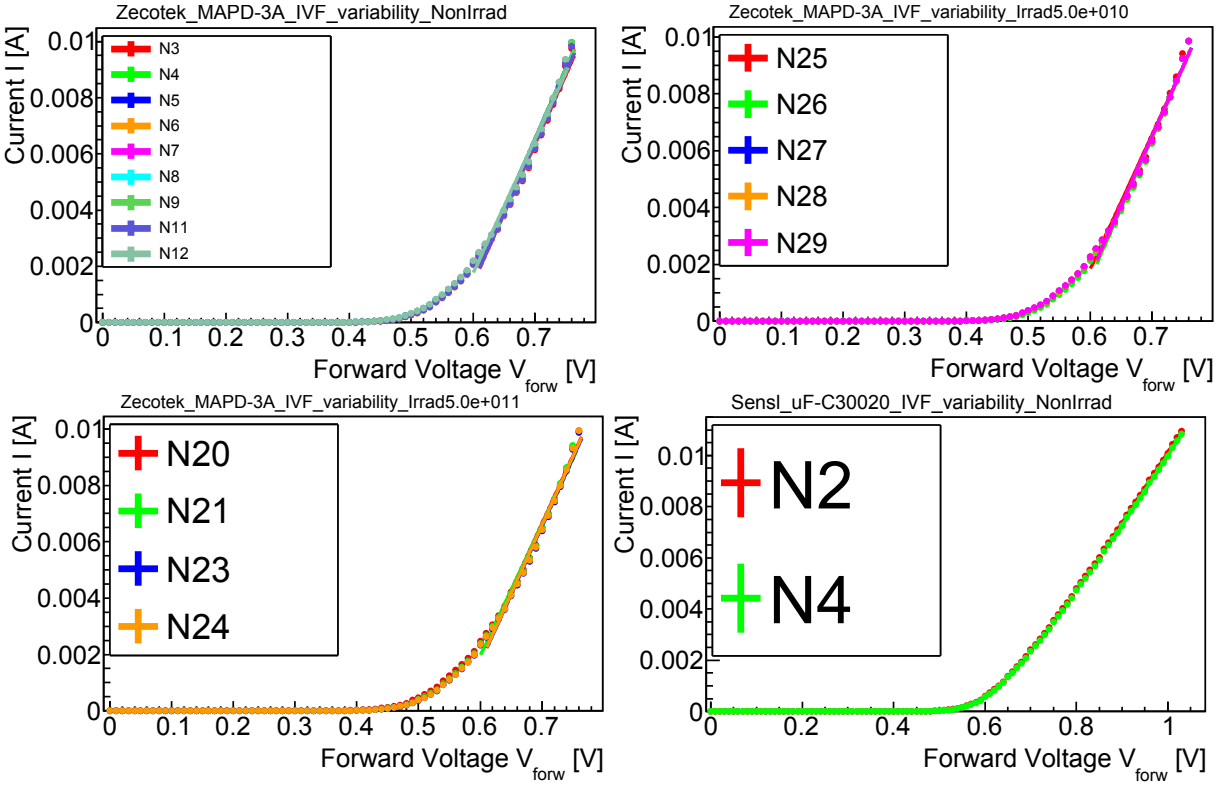

Figure E.4: Sample-to-sample variability of dark current at forward bias for Zecotek MAPD-3A and Sensl C-series 30020 SiPMs before and/or after irradiation, see captions above the plots. Detailed description can be found in section 7.6.

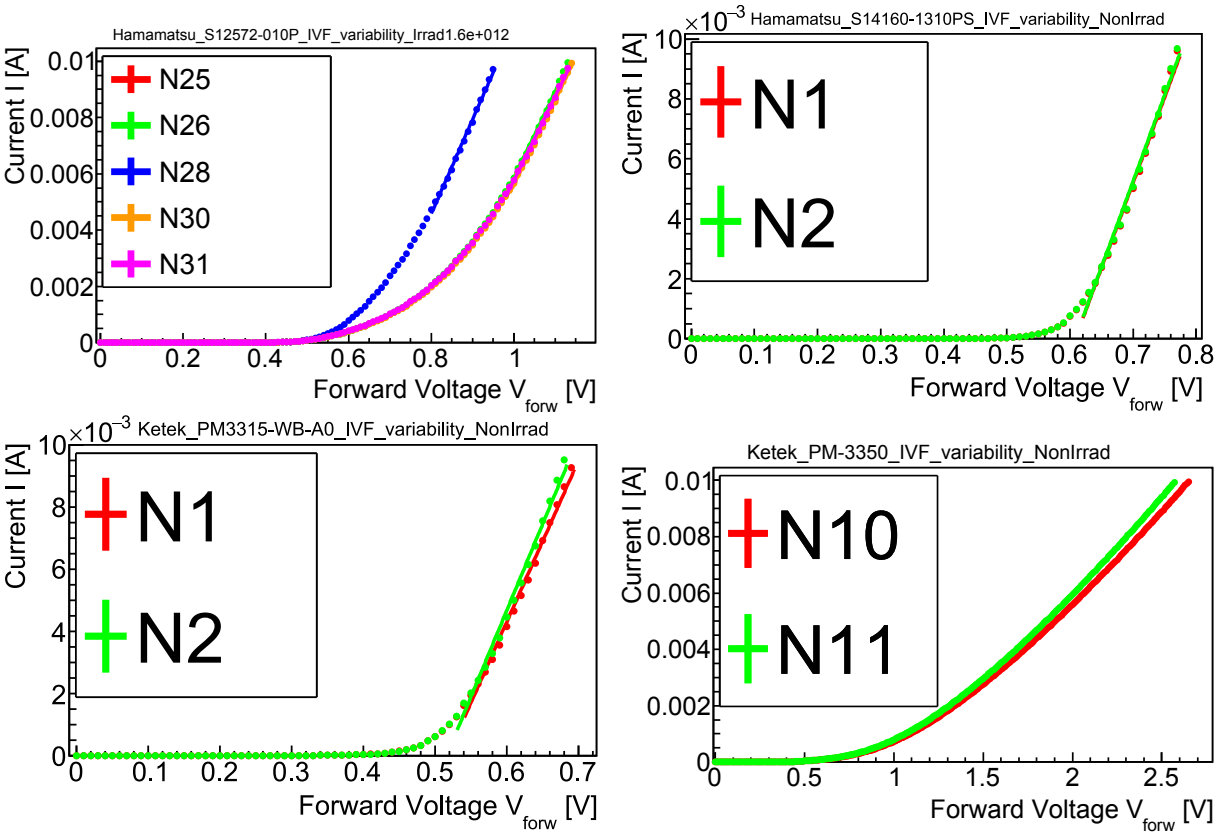

Figure E.5: Sample-to-sample variability of dark current at forward bias for Hamamatsu and Ketek SiPMs before and/or after irradiation, see captions above the plots. Detailed description can be found in section 7.6.

Appendix F

SiPM capacitance

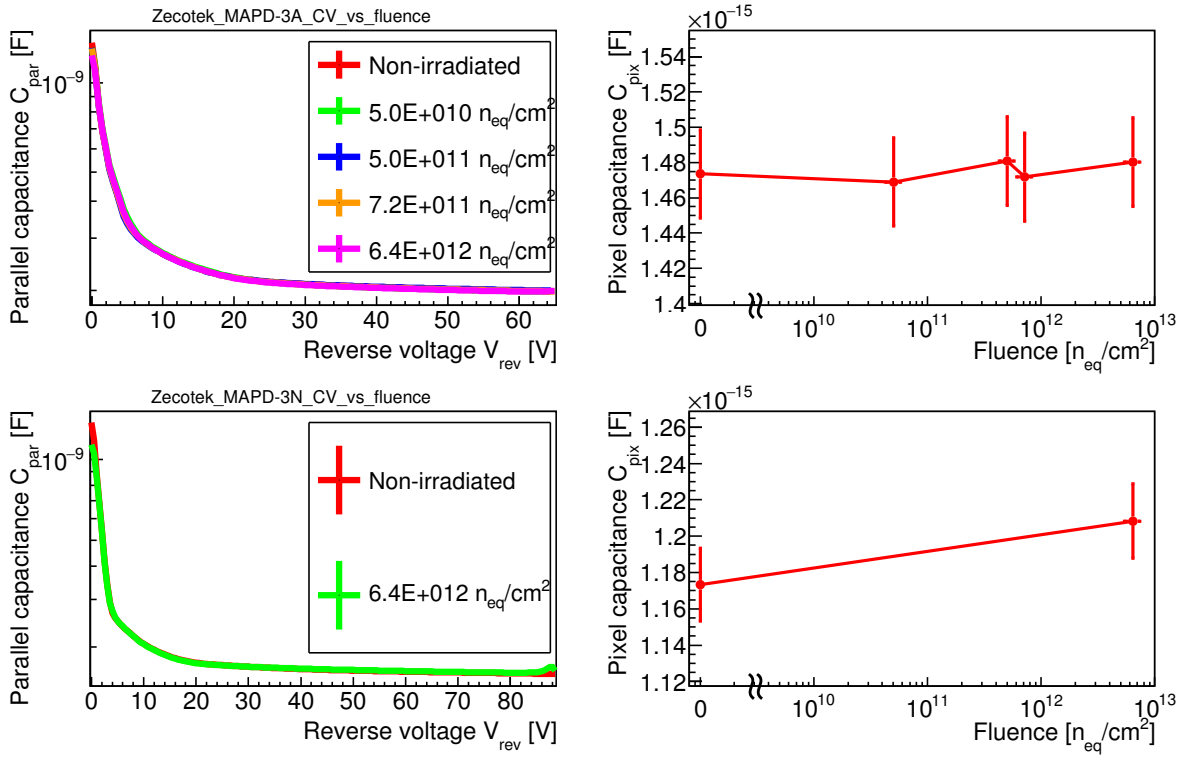

Figure F.1: Parallel capacitance as function of reverse voltage and pixel capacitance determination for Zecotek MAPD-3A (top) and MAPD-3N (bottom) before and after irradiation. Detailed description can be found in section 7.7.

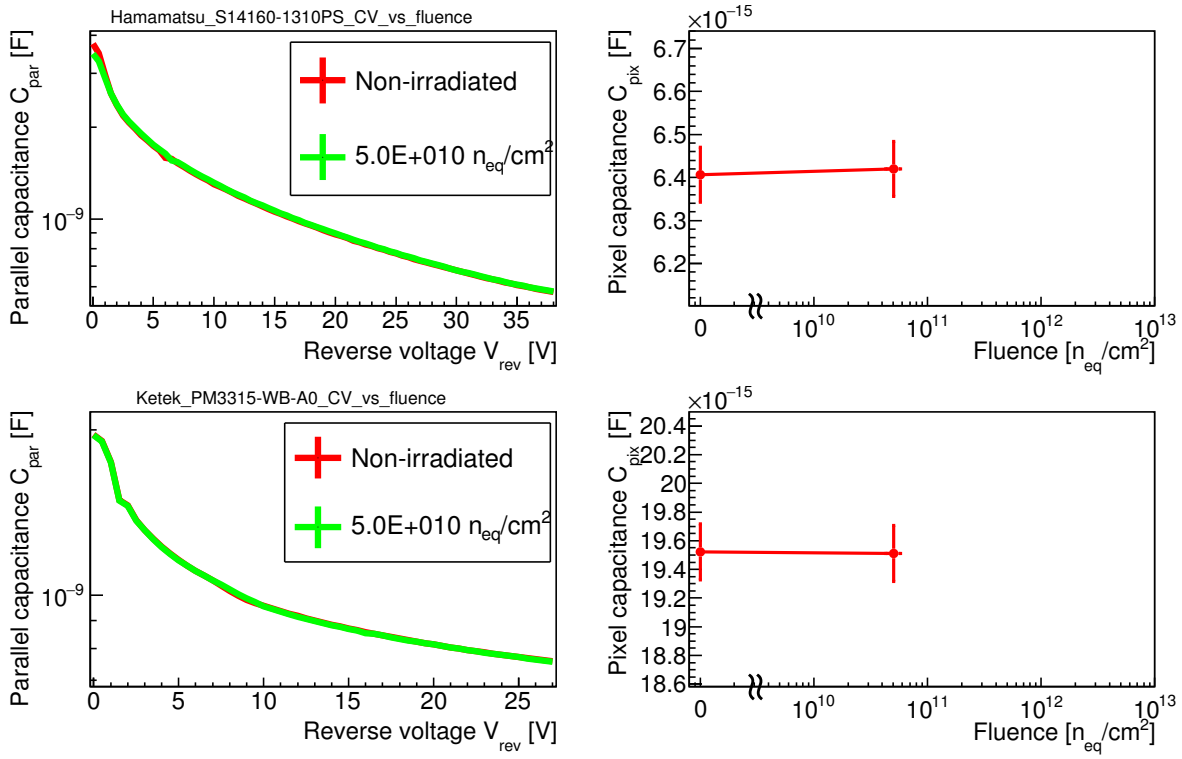

Figure F.2: Parallel capacitance as function of reverse voltage and pixel capacitance determination for Hamamatsu MPPC S14160-1310PS (top) and Ketek PM3315-WB-A0 SiPM (bottom) before and after irradiation. Detailed description can be found in section 7.7.

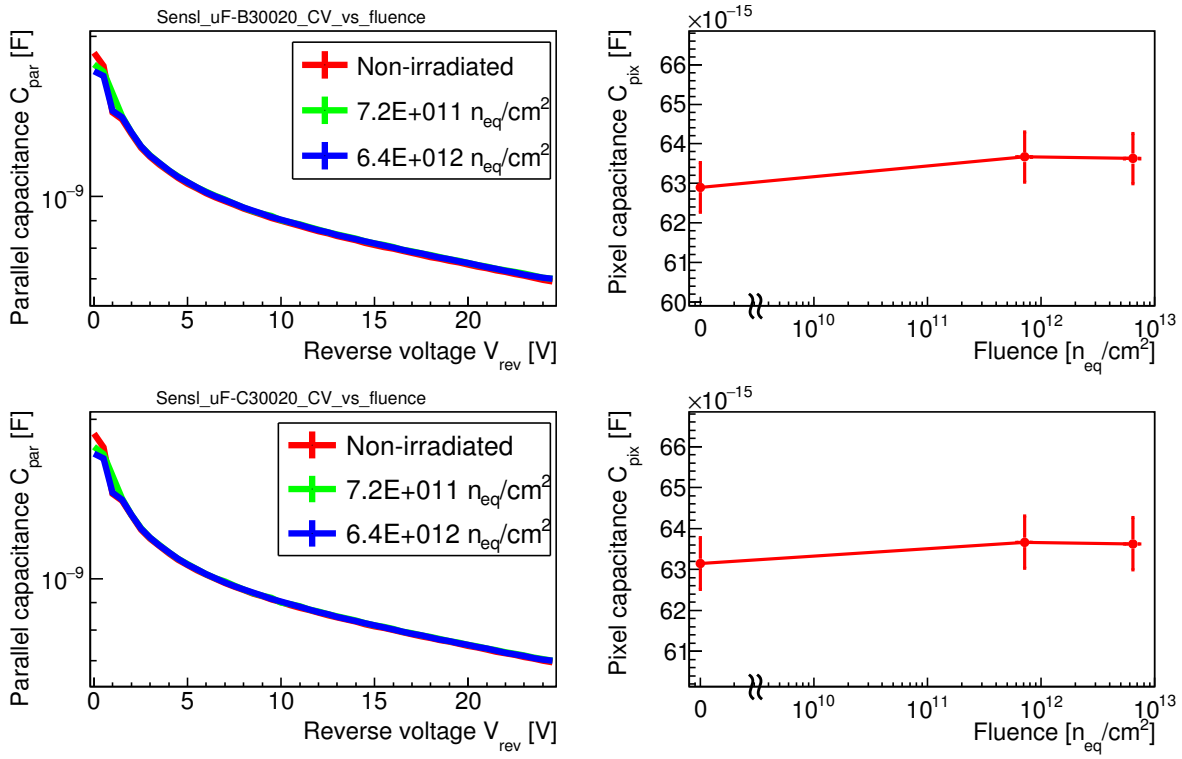

Figure F.3: Parallel capacitance as function of reverse voltage and pixel capacitance determination for Sensl B-series 30020 (top) and C-series 30020 (bottom) SiPMs before and after irradiation. Detailed description can be found in section 7.7.

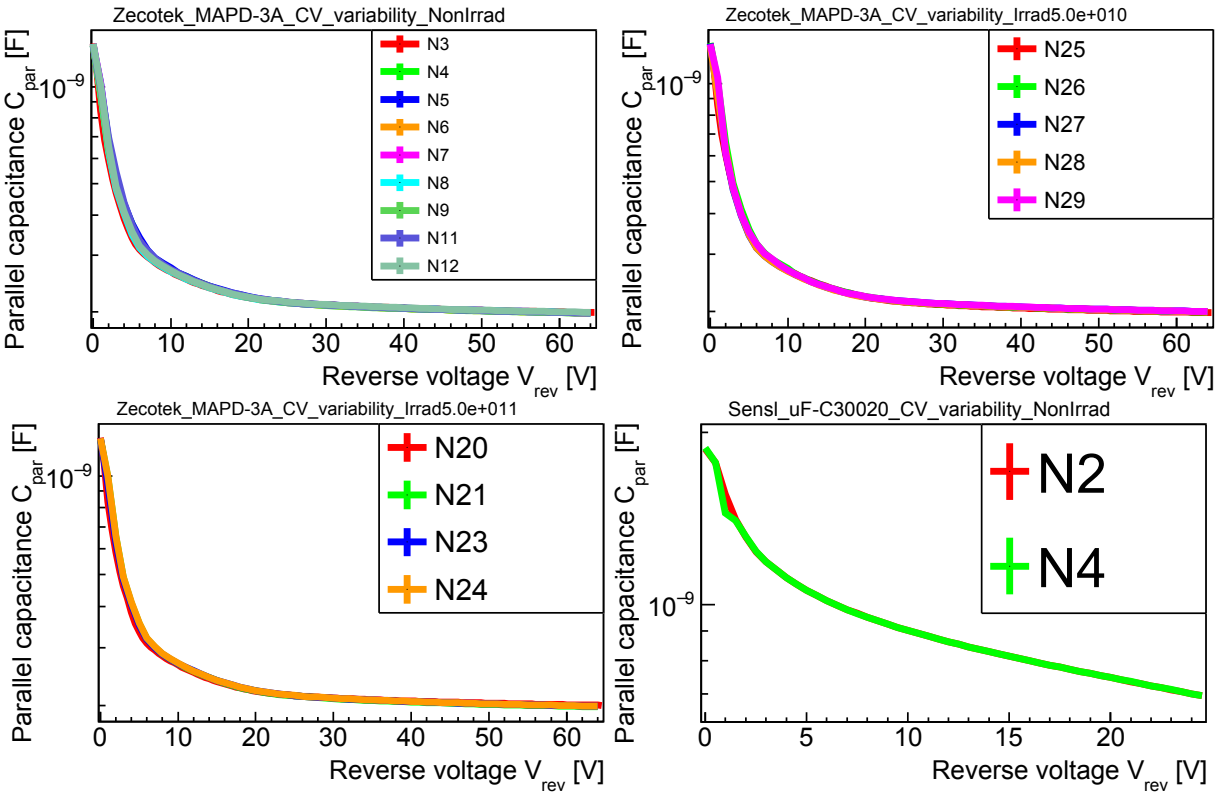

Figure F.4: Sample-to-sample variability of parallel capacitance at reverse voltage for Zecotek MAPD-3A and Sensl C-series 30020 SiPMs before and/or after irradiation, see captions above the plots. Detailed description can be found in section 7.6.

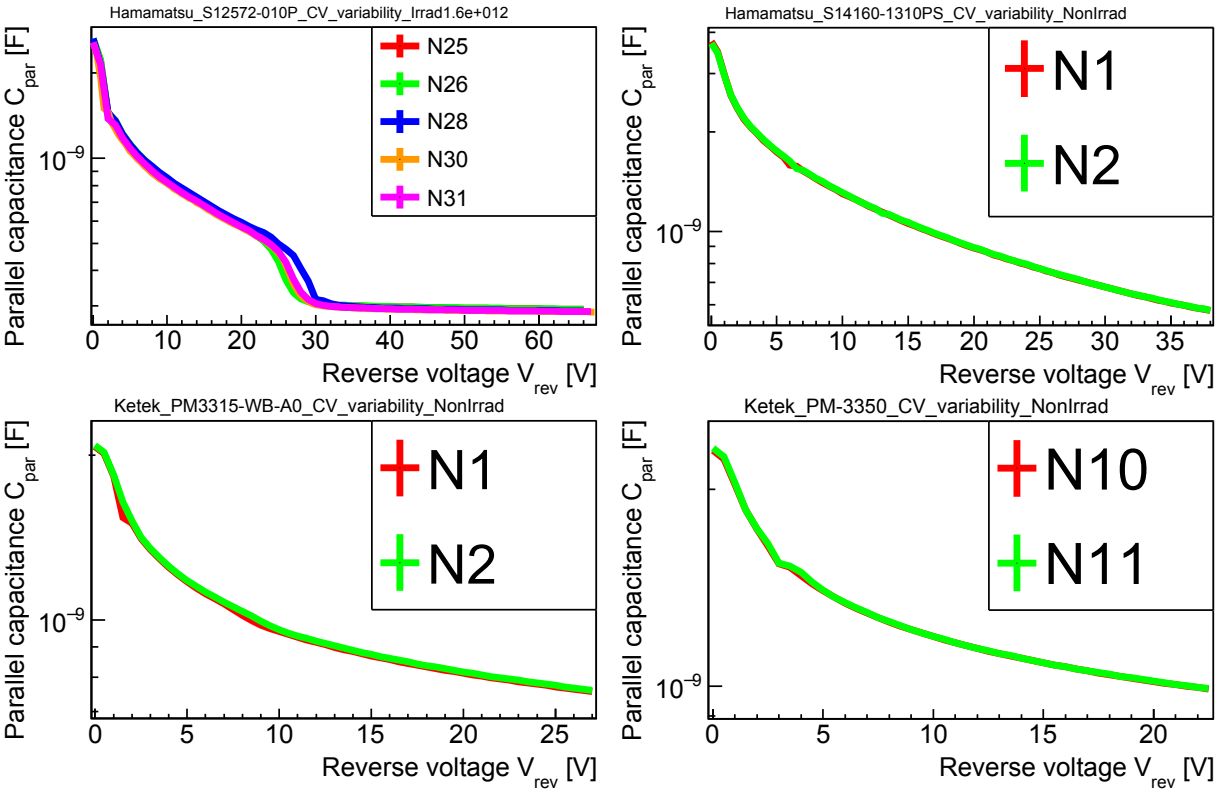

Figure F.5: Sample-to-sample variability of parallel capacitance at reverse voltage for Hamamatsu and Ketek SiPMs before and/or after irradiation, see captions above the plots. Detailed description can be found in section 7.6.

Appendix G

Spectra of SiPM response to LED

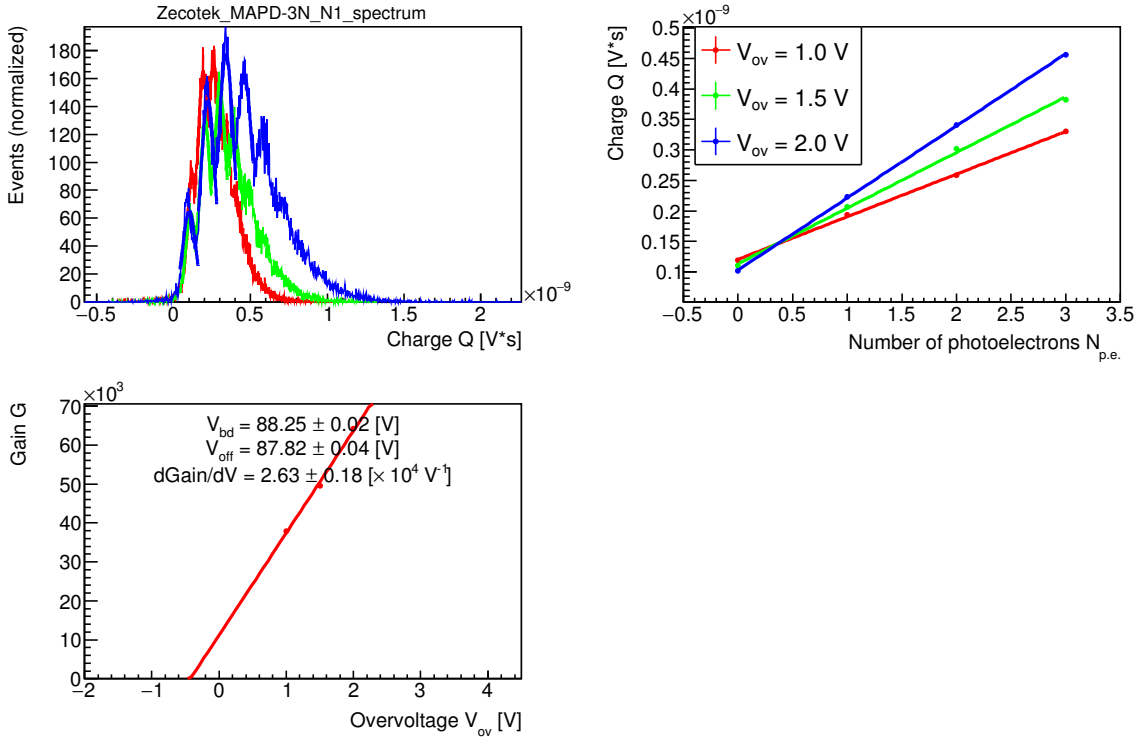

Figure G.1: Single photon spectrum, and determination of gain and offset voltage for Zecotek MAPD-3N before irradiation. Detailed description can be found in section 7.8.1.

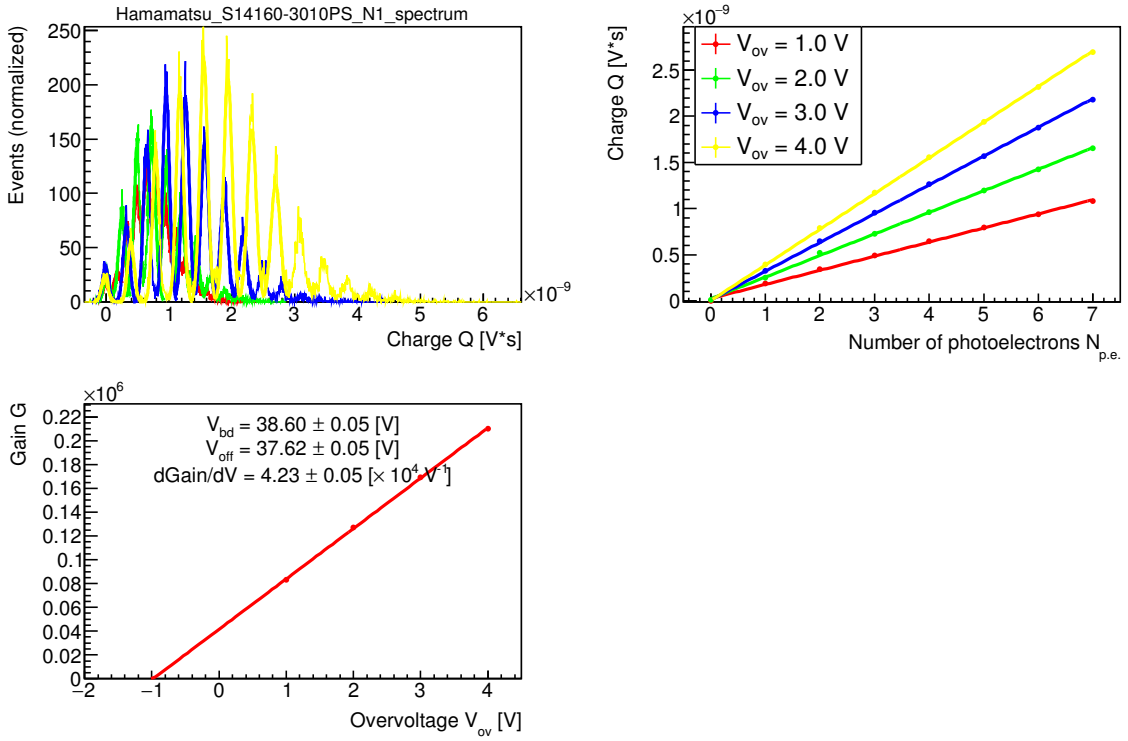

Figure G.2: Single photon spectrum, and determination of gain and offset voltage for Hamamatsu MPPC S14160-3010PS before irradiation. Detailed description can be found in section 7.8.1.

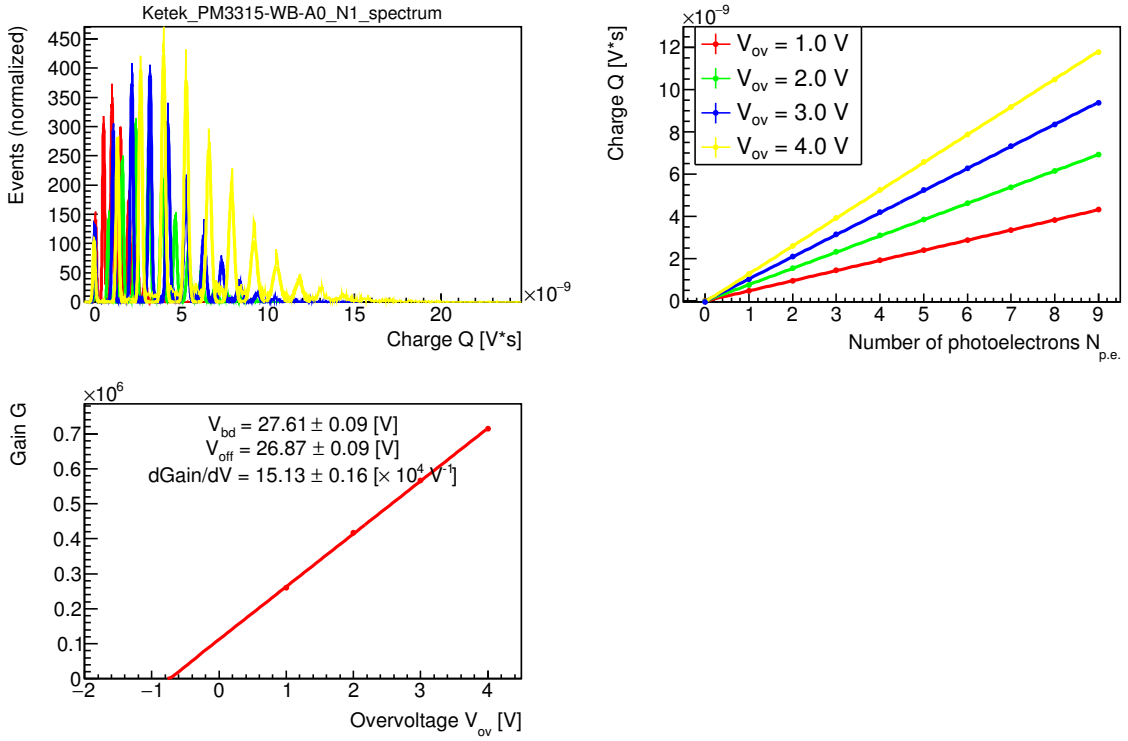

Figure G.3: Single photon spectrum, and determination of gain and offset voltage for Ketek PM3315-WB-A0 SiPM before irradiation. Detailed description can be found in section 7.8.1.

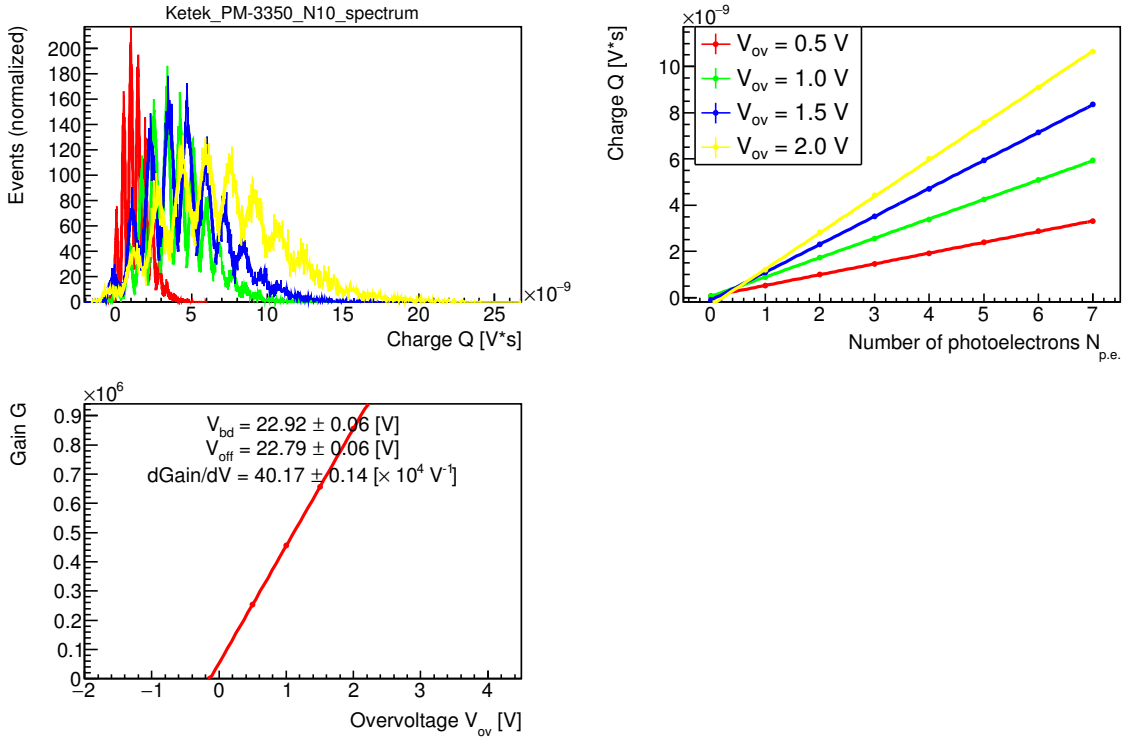

Figure G.4: Single photon spectrum, and determination of gain and offset voltage for Ketek PM3350 SiPM before irradiation. Detailed description can be found in section 7.8.1.

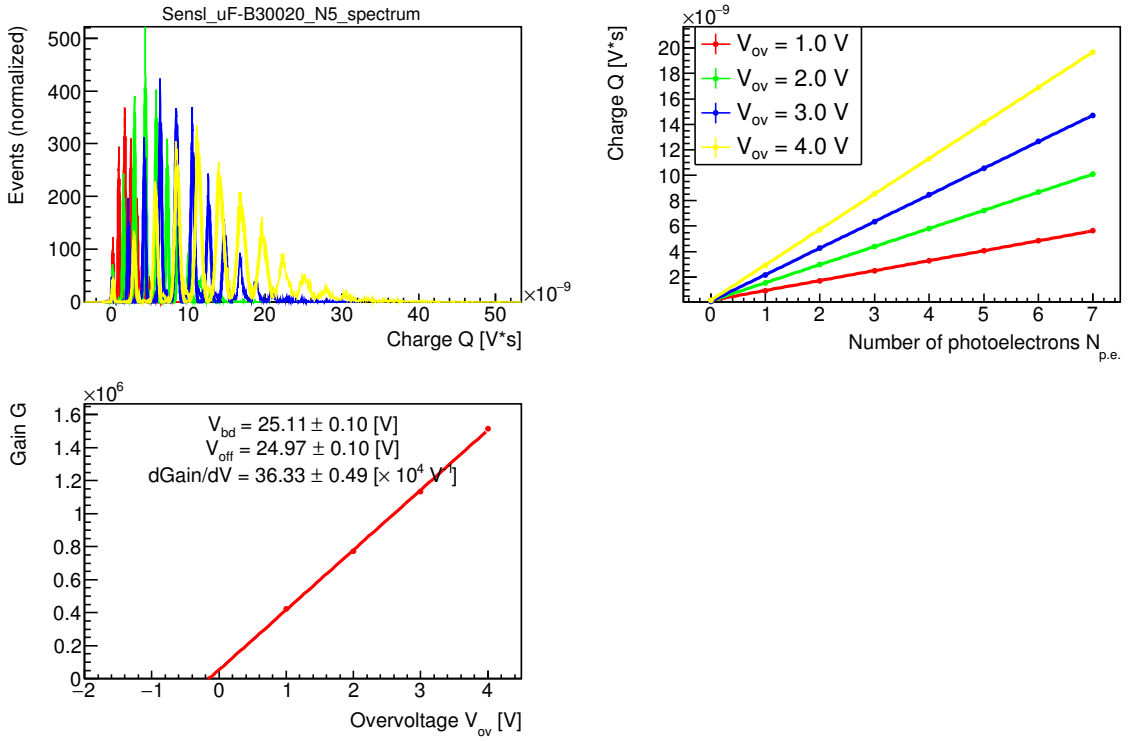

Figure G.5: Single photon spectrum, and determination of gain and offset voltage for Sensl B-series 30020 SiPM before irradiation. Detailed description can be found in section 7.8.1.

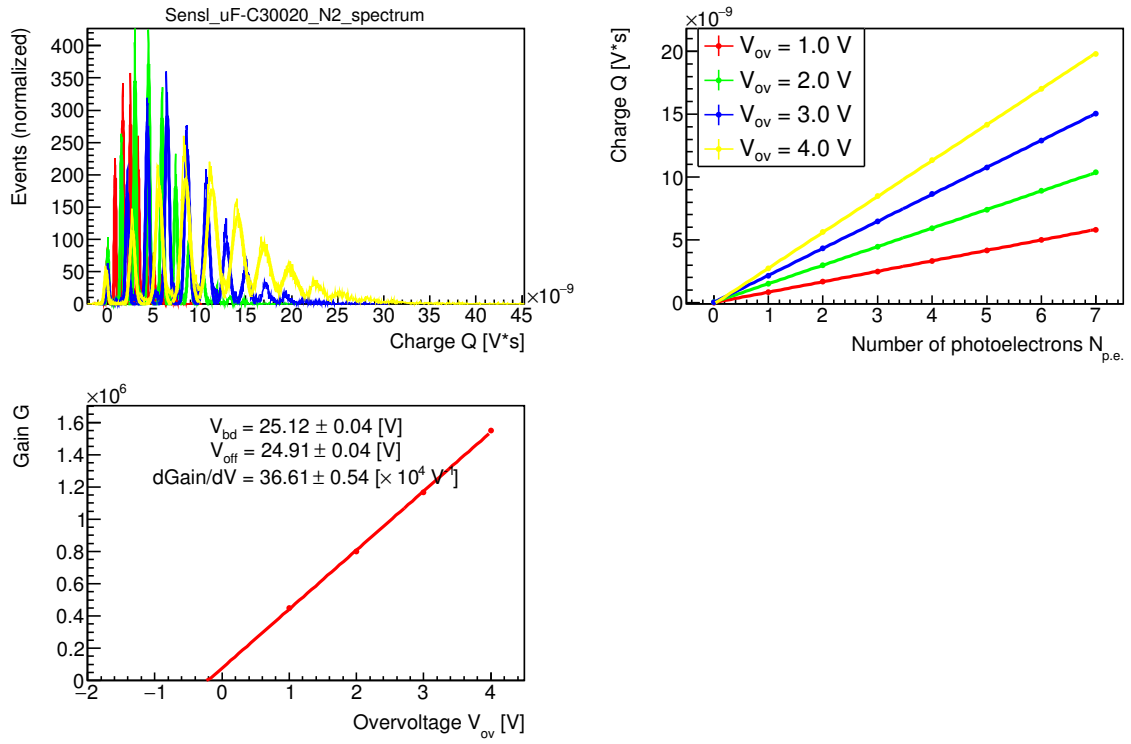

Figure G.6: Single photon spectrum, and determination of gain and offset voltage for Sensl C-series 30020 SiPM before irradiation. Detailed description can be found in section 7.8.1.

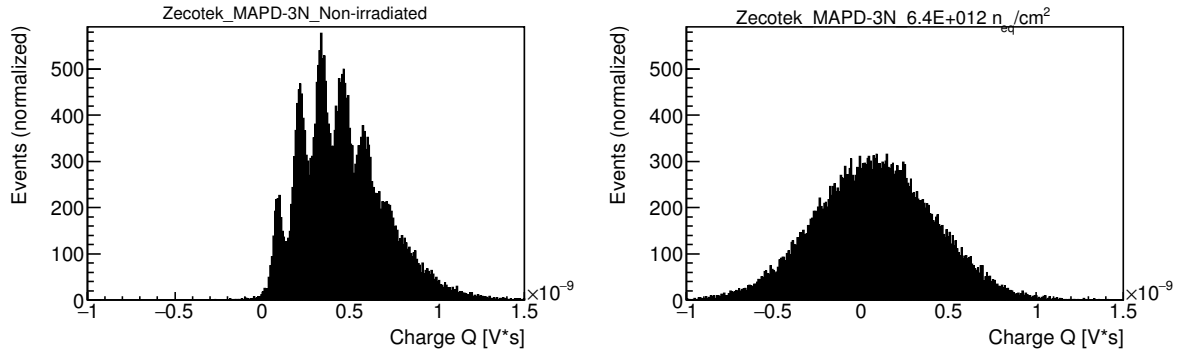

Figure G.7: Spectrum of response to the same LED pulse for Zecotek MAPD-3N before (left) and after irradiation (right). Detailed description can be found in section 7.8.1.

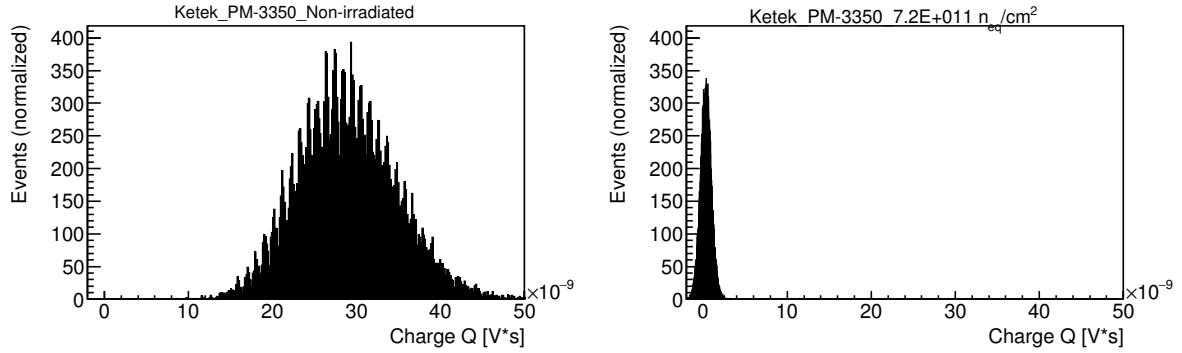

Figure G.8: Spectrum of response to the same LED pulse for Ketek PM-3350 SiPM before (left) and after irradiation (right). Overvoltage = 2 V. One can see that SiPM can not detect low light levels after irradiation.Detailed description can be found in section 7.8.1.

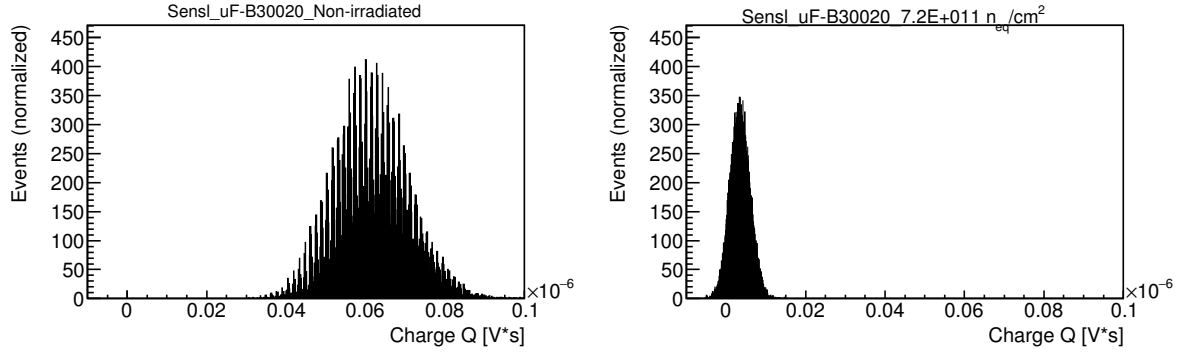

Figure G.9: Spectrum of response to the same LED pulse for Sensl B-series 30020 SiPM before (left) and after irradiation (right). Overvoltage = 2 V. One can see that SiPM can not detect low light levels after irradiation. Detailed description can be found in section 7.8.1.

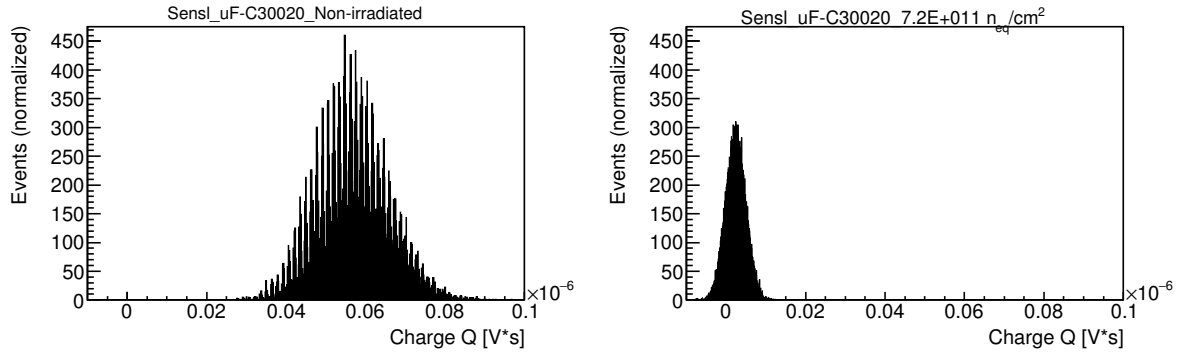

Figure G.10: Spectrum of response to the same LED pulse for Sensl C-series 30020 SiPM before (left) and after irradiation (right). Overvoltage = 2 V. One can see that SiPM can not detect low light levels after irradiation. Detailed description can be found in section 7.8.1.

Appendix H

SiPM noise and response to LED

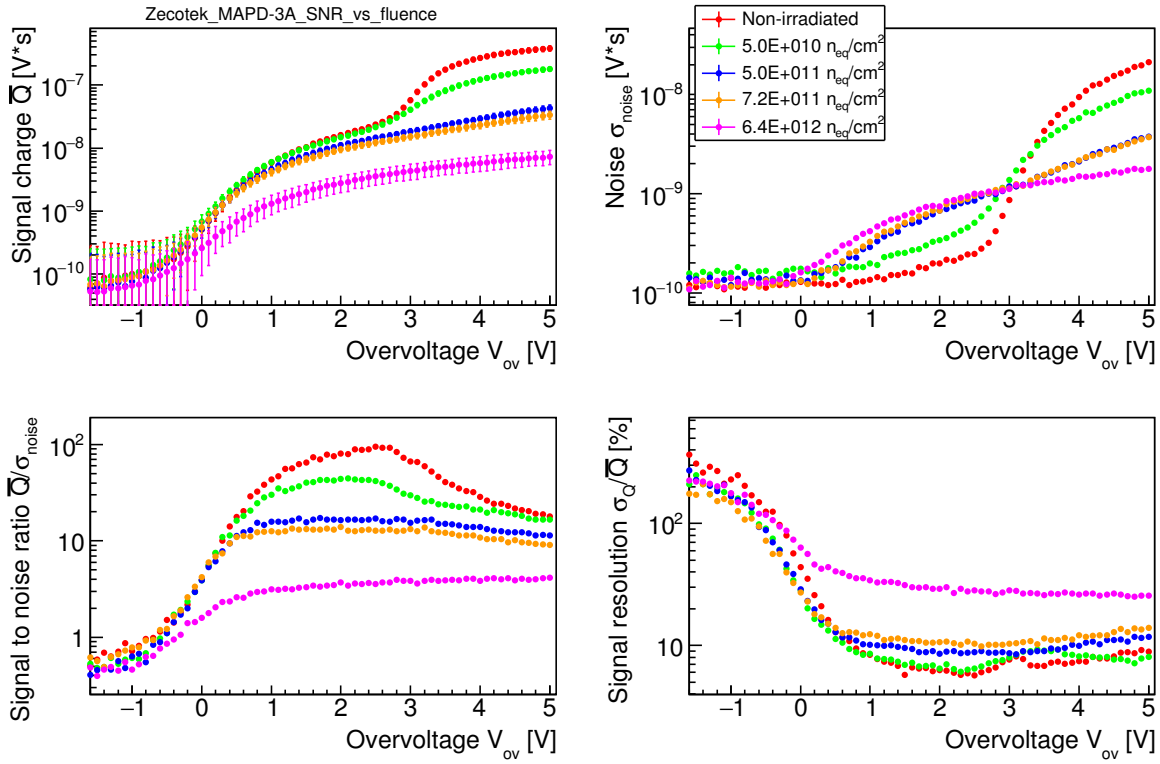

Figure H.1: Signal response to LED (top left), noise (top right), signal-to-noise ratio (bottom left), and resolution (bottom right) for Zecotek MAPD-3A before and after irradiation. Detailed description can be found in section 7.8.2.

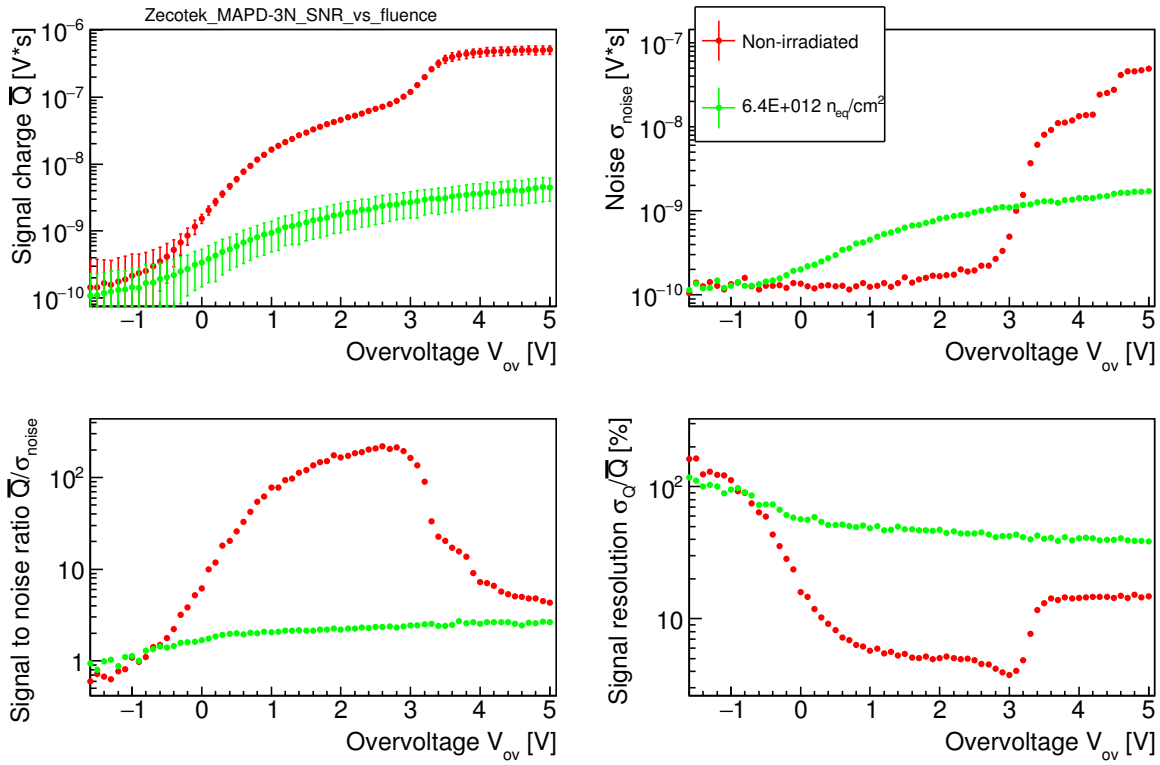

Figure H.2: Signal response to LED (top left), noise (top right), signal-to-noise ratio (bottom left), and resolution (bottom right) for Zecotek MAPD-3N before and after irradiation. Detailed description can be found in section 7.8.2.

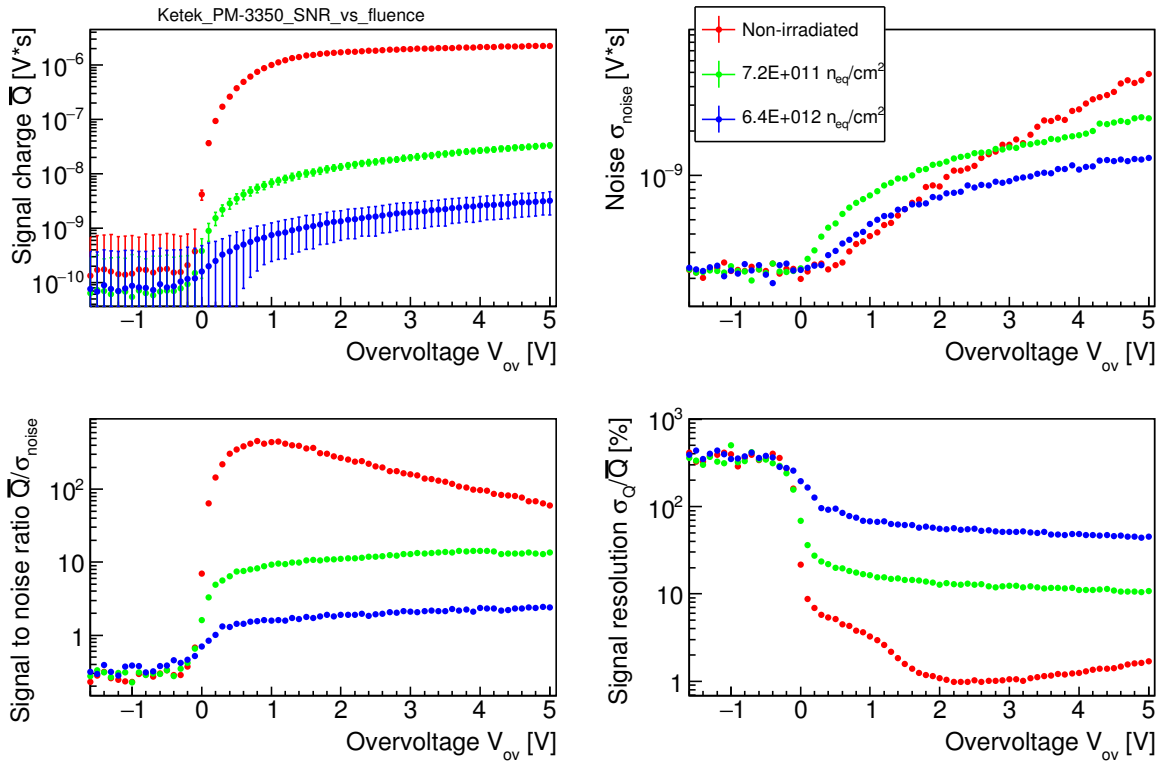

Figure H.3: Signal response to LED (top left), noise (top right), signal-to-noise ratio (bottom left), and resolution (bottom right) for Ketek PM-3350 SiPM before and after irradiation. Detailed description can be found in section 7.8.2.

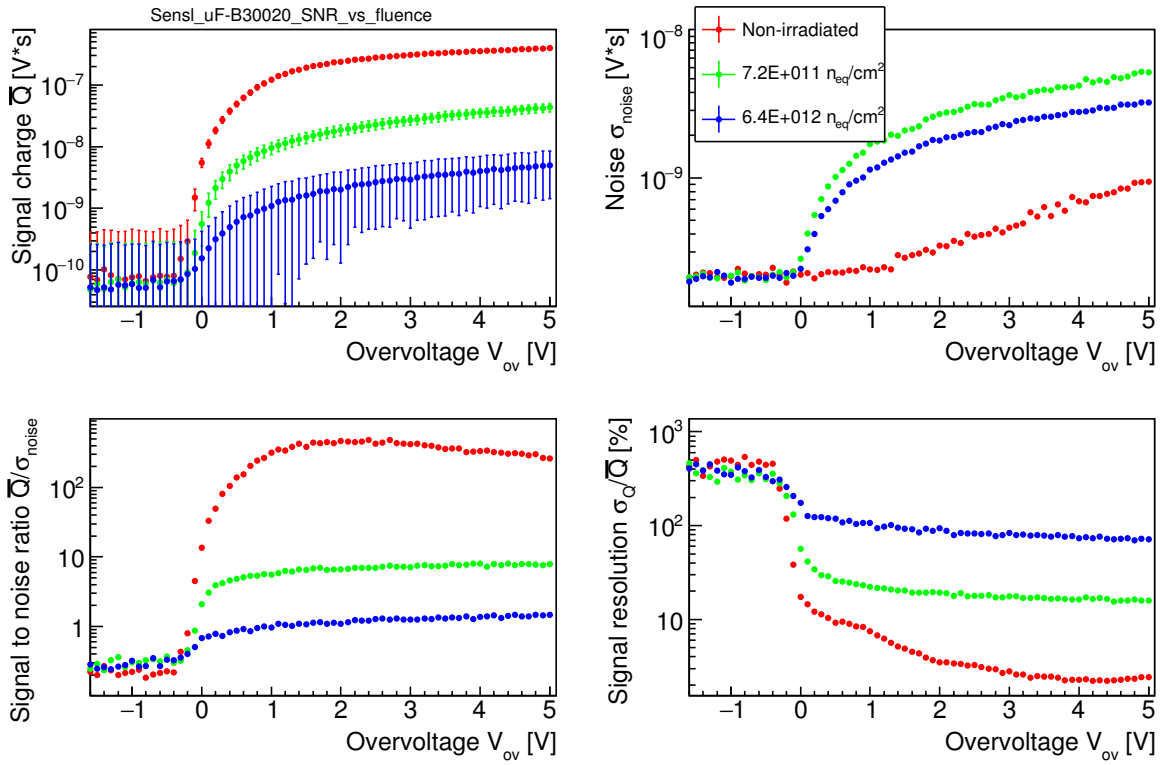

Figure H.4: Signal response to LED (top left), noise (top right), signal-to-noise ratio (bottom left), and resolution (bottom right) for Sensl B-series 30020 SiPM before and after irradiation. Detailed description can be found in section 7.8.2.

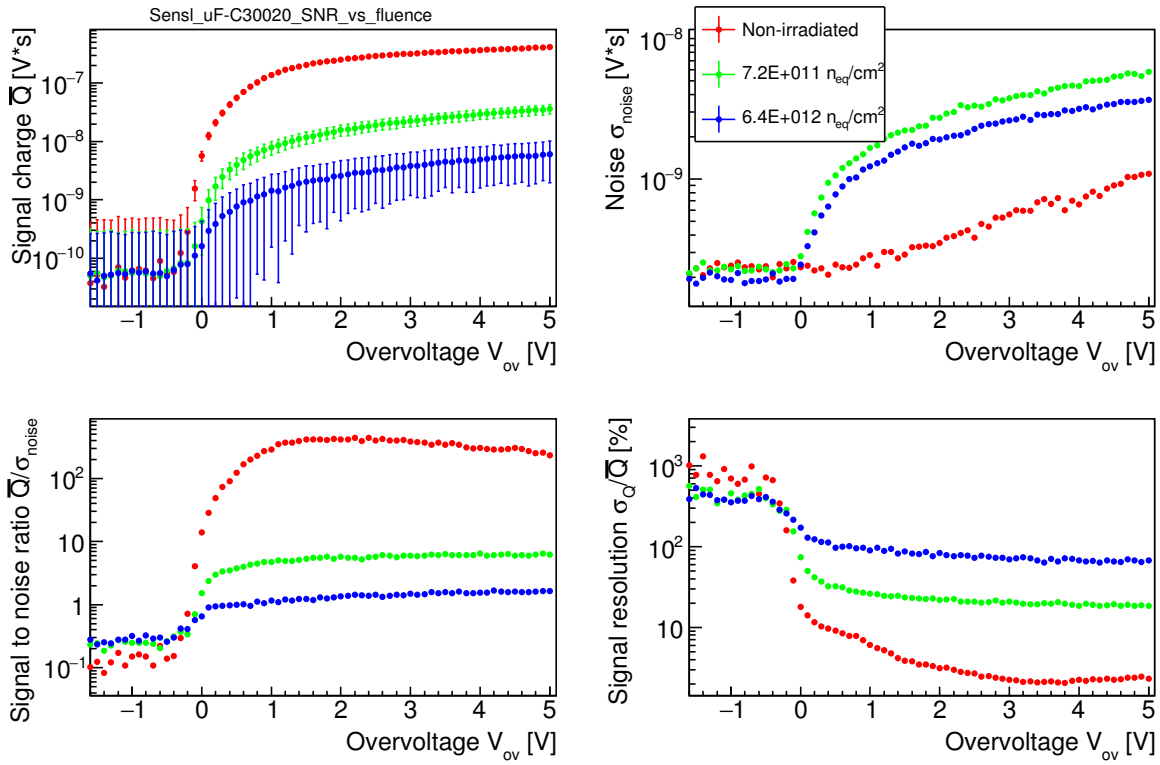

Figure H.5: Signal response to LED (top left), noise (top right), signal-to-noise ratio (bottom left), and resolution (bottom right) for Sensl C-series 30020 SiPM before and after irradiation. Detailed description can be found in section 7.8.2.

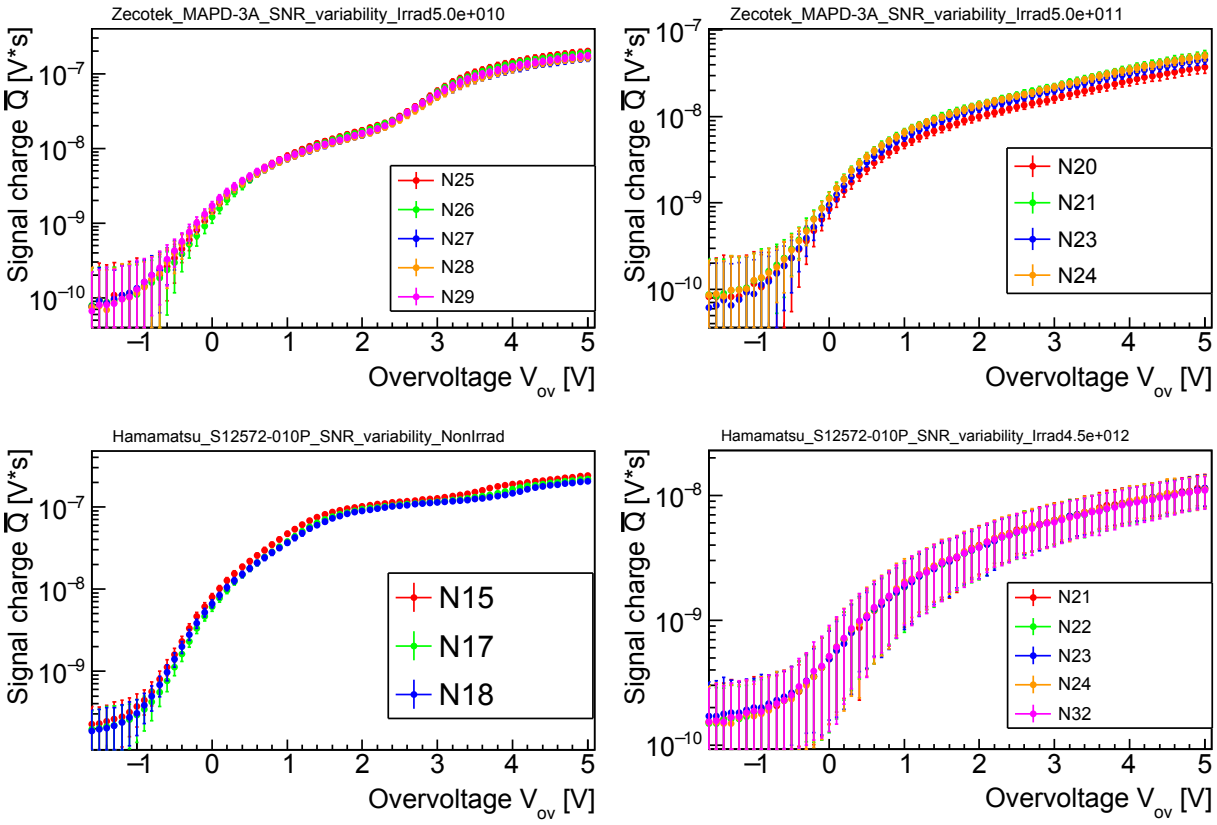

Figure H.6: Sample-to-sample variability of response to LED for Zecotek MAPDs and Hamamatsu MPPCs before and/or after irradiation, see captions above the plots. Detailed description can be found in section 7.8.2.

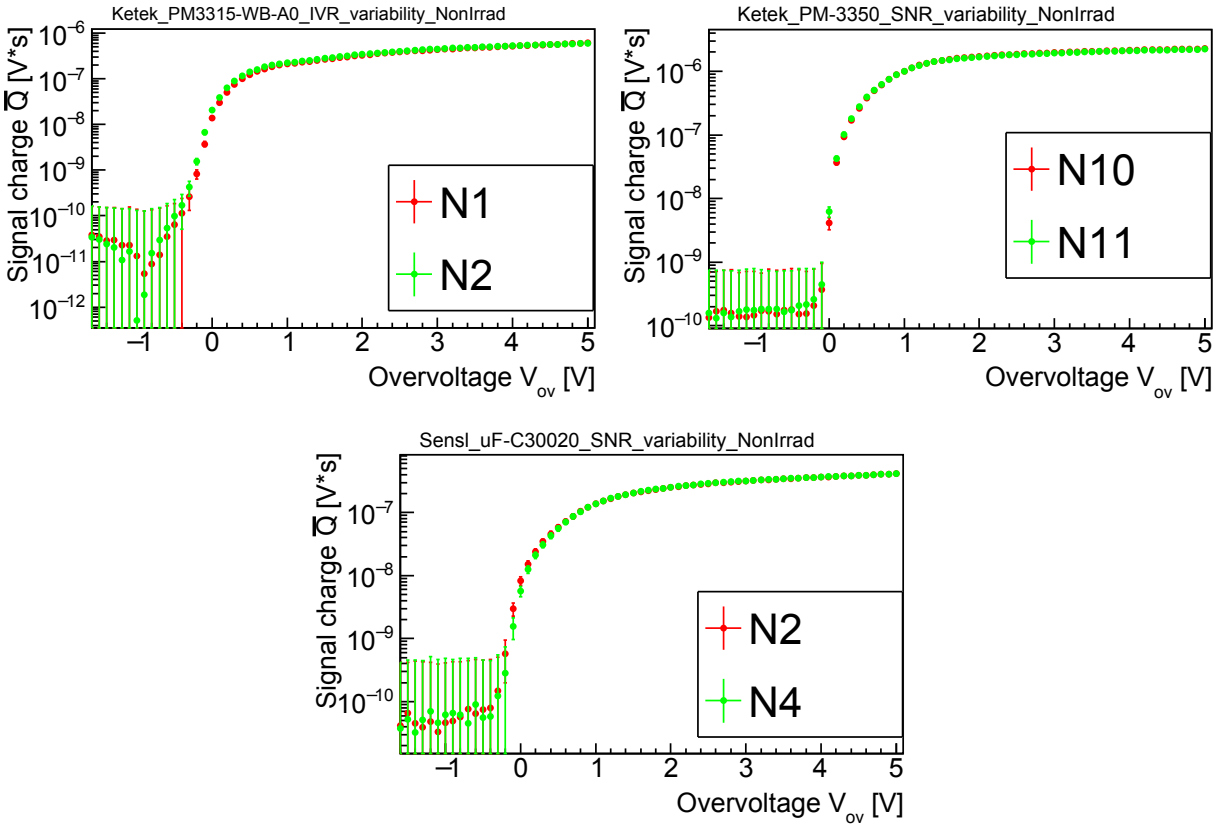

Figure H.7: Sample-to-sample variability of response to LED for Ketek and Sensl SiPMs before irradiation, see captions above the plots. Detailed description can be found in section 7.8.2.

Appendix I

Proton collective flow calculated at 1.23, 2, 6 and 30 AGeV

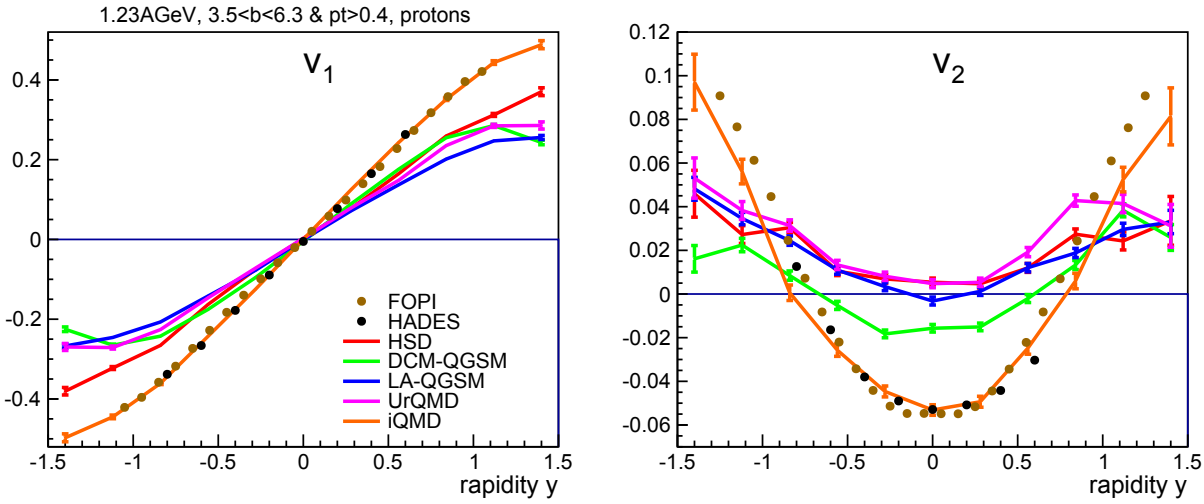

Figure I.1: Dependence of directed v_1 (left) and elliptic v_2 (right) proton flow on normalized rapidity at $E_b = 1.23$ AGeV. Detailed description can be found in section 9.2.

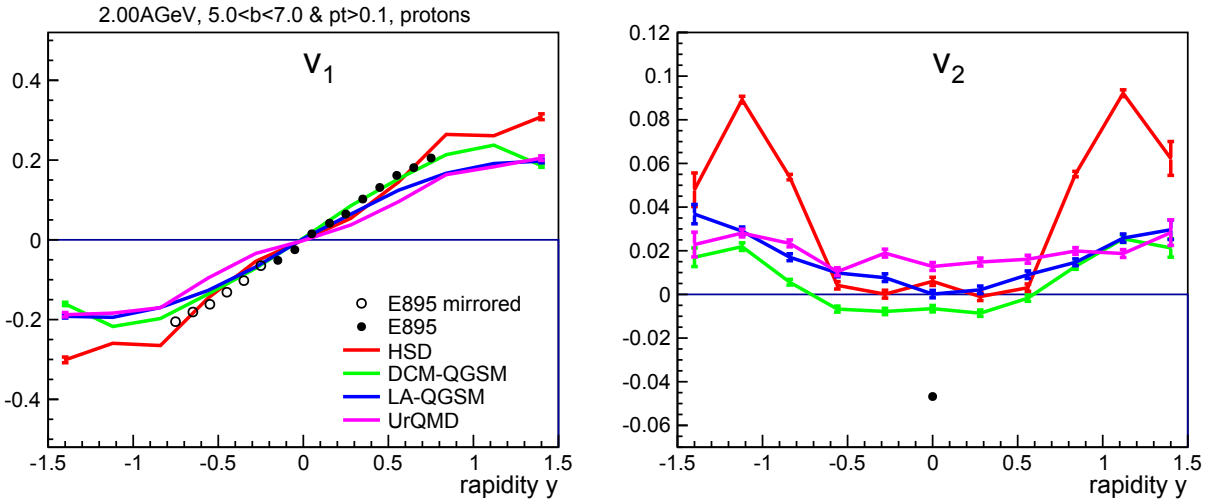

Figure I.2: Dependence of directed v_1 (left) and elliptic v_2 (right) proton flow on normalized rapidity at $E_b = 2$ AGeV. Detailed description can be found in section 9.2.

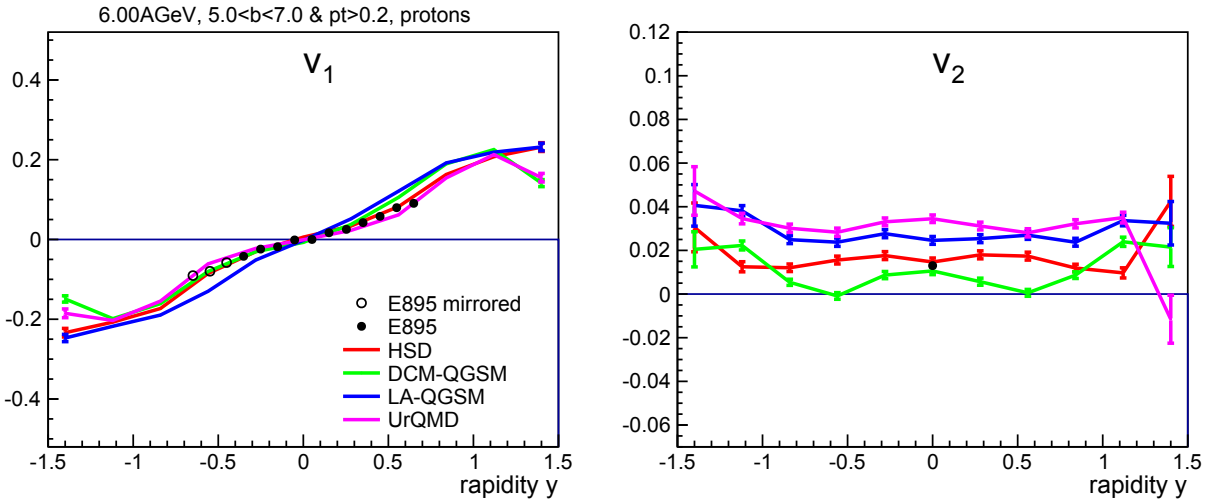

Figure I.3: Dependence of directed v_1 (left) and elliptic v_2 (right) proton flow on normalized rapidity at $E_b = 6$ AGeV. Detailed description can be found in section 9.2.

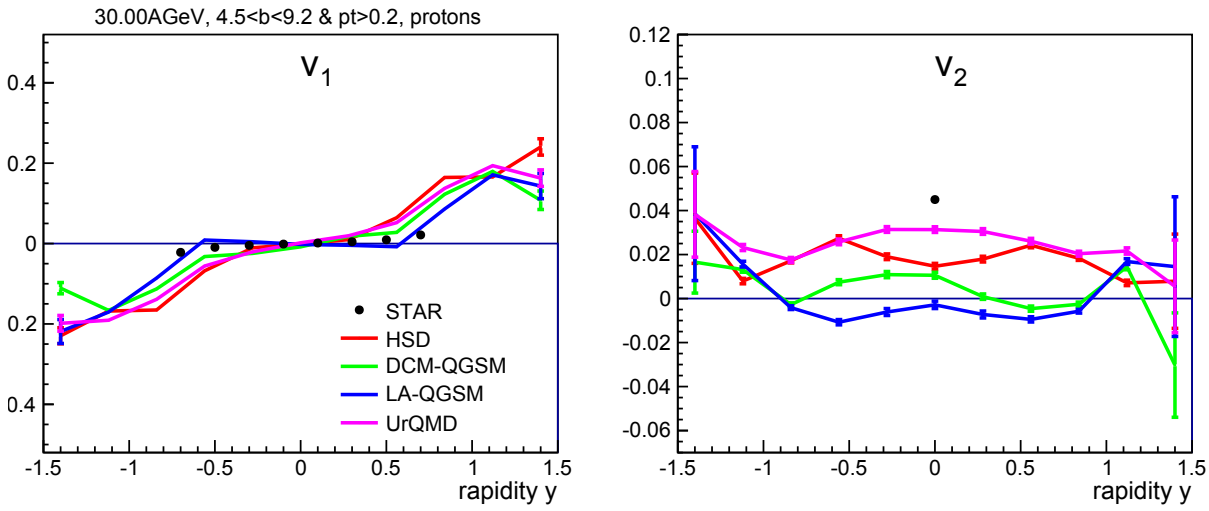

Figure I.4: Dependence of directed v_1 (left) and elliptic v_2 (right) proton flow on normalized rapidity at $E_b = 30$ AGeV. Detailed description can be found in section 9.2.